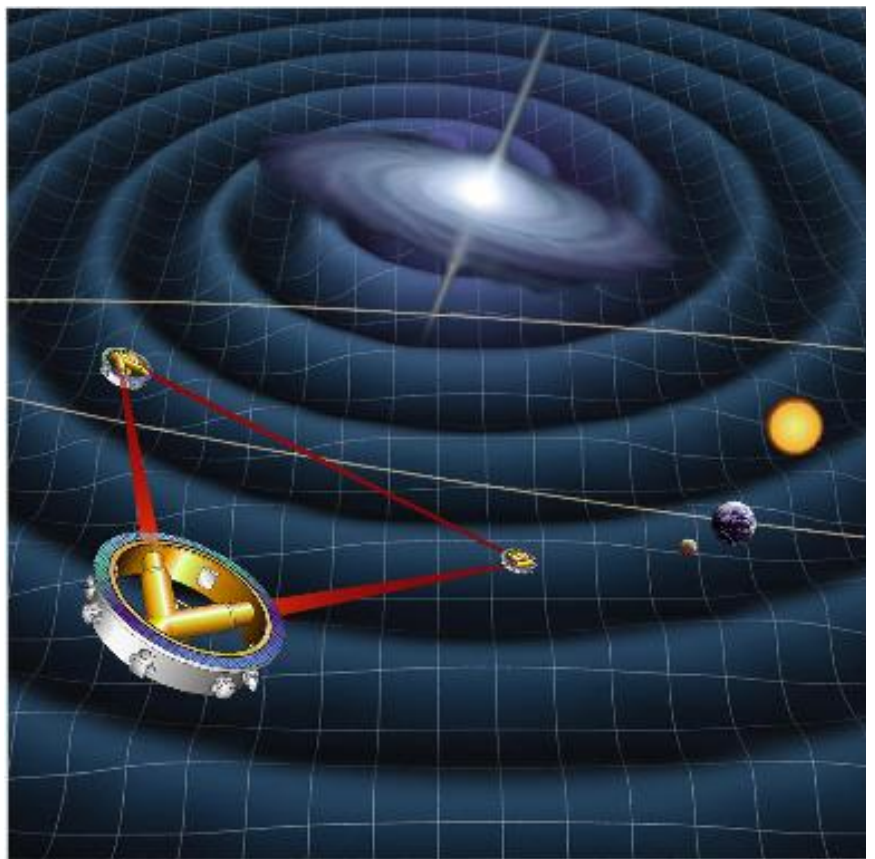


# LISA

## Laser Interferometer Space Antenna: A Cornerstone Mission for the Observation of Gravitational Waves



**System and Technology Study Report**



# LISA

Laser Interferometer Space Antenna

A Cornerstone Mission for the observation of  
gravitational waves

System and Technology Study Report

**Front cover figure :**

*Artist's concept of the LISA configuration, bathing in the gravitational waves emitted from a distant cosmic event.*

*Three spacecraft, each with a Y-shaped payload, form an equilateral triangle with sides of 5 million km in length. The two branches of the Y at one corner, together with one branch each from the spacecraft at the other two corners, form one of up to three Michelson-type interferometers, operated with infrared laser beams. The interferometers are designed to measure relative path changes  $\delta\ell/\ell$  due to gravitational waves, so-called strains in space, down to  $10^{-23}$ , for observation times of the order of 1 year.*

*The diameters of the spacecraft are about 2.5 m, the distances between them  $5 \times 10^9$  m.*

**Rear cover figure :**

*Schematic diagram of LISA configuration, with three spacecraft in an equilateral triangle. The plane of this triangle is tilted by  $60^\circ$  out of the ecliptic. The center of this triangle moves around the Sun in an Earth-like orbit, about  $20^\circ$  behind the Earth, with the plane of the [LISA](#) formation revolving once per year on a cone of  $30^\circ$  half-angle.*

*The drawing is not to scale, the triangular formation of the LISA interferometer, with sides of 5 million km, is blown up by a factor of 5.*



LISA Mission Summary	
Objectives:	<p>Detection of low-frequency (<math>10^{-4}</math> to <math>10^{-1}</math> Hz) gravitational radiation with a strain sensitivity of <math>4 \times 10^{-21}/\sqrt{\text{Hz}}</math> at 1 mHz.</p> <p>Abundant sources are galactic binaries (neutron stars, white dwarfs, etc.); extra-galactic targets are supermassive black hole binaries (SMBH-SMBH and BH-SMBH), SMBH formation, and cosmic background gravitational waves.</p>
Payload:	<p>Laser interferometry with six electrostatically controlled drag-free reference mirrors housed in three spacecraft; arm lengths <math>5 \times 10^6</math> km.</p> <p>Each spacecraft has two lasers (plus two spares) which operate in a phase-locked transponder scheme.</p> <p>Diode-pumped Nd:YAG lasers: wavelength <math>1.064 \mu\text{m}</math>, output power 1 W, Fabry-Perot reference cavity for frequency-stability of <math>30 \text{ Hz}/\sqrt{\text{Hz}}</math>.</p> <p>Quadrant photodiode detectors with interferometer fringe resolution, corresponding to <math>4 \times 10^{-5} \lambda/\sqrt{\text{Hz}}</math>.</p> <p>30 cm diameter f/1 Cassegrain telescope (transmit/receive), <math>\lambda/10</math> outgoing wavefront quality.</p> <p>Drag-free proof mass (mirror): 40 mm cube, Au-Pt alloy of extremely low magnetic susceptibility (<math>&lt; 10^{-6}</math>); Ti-housing at vacuum <math>&lt; 10^{-6}</math> Pa; six-degree-of-freedom capacitive sensing.</p>
Orbit:	<p>Each spacecraft orbits the Sun at 1 AU. The inclinations are such that their <i>relative</i> orbits define a circle with radius <math>3 \times 10^6</math> km and a period of 1 year. The plane of the circle is inclined <math>60^\circ</math> with respect to the ecliptic. On this circle, the spacecraft are distributed at three vertices, defining an equilateral triangle with a side length of <math>5 \times 10^6</math> km (interferometer baseline).</p>
Launcher:	<p>This constellation is located at 1 AU from the Sun, <math>20^\circ</math> behind the Earth.</p> <p>Delta II 7925 H, 10 ft fairing, housing a stack of three composites consisting of one science and one propulsion module each.</p> <p>Each spacecraft has its own jettisonable propulsion module to provide a <math>\Delta V</math> of 1300 m/s using solar-electric propulsion.</p>
Spacecraft: mass: propulsion module: propellant: total launch mass: power: power: Drag-free performance: Pointing performance: Payload, mass: power: Science data rate: Telemetry:	<p>3-axis stabilized drag-free spacecraft (three)</p> <p>274 kg, <i>each spacecraft in orbit</i></p> <p>142 kg, <i>one module per spacecraft</i></p> <p>22 kg, <i>for each propulsion module</i></p> <p>1380 kg</p> <p>940 W, <i>each composite during cruise</i></p> <p>315 W, <i>each spacecraft in orbit</i></p> <p><math>3 \times 10^{-15} \text{ m/s}^2</math> (rms) in the band <math>10^{-4}</math> to <math>3 \times 10^{-3}</math> Hz, achieved with <math>6 \times 4</math> Cs or In FEEP thrusters</p> <p>few nrad/<math>\sqrt{\text{Hz}}</math> in the band <math>10^{-4}</math> Hz to 1 Hz</p> <p>70 kg, <i>each spacecraft</i></p> <p>72 W, <i>each spacecraft</i></p> <p>672 bps, <i>all 3 spacecraft</i></p> <p>7 kbps, for about 9 hours inside two days</p> <p>Ground stations: Deep Space Network</p>
Mission Lifetime:	2 years (nominal); 10 years (extended)



## Foreword

The first mission concept studies for a space-borne gravitational wave observatory began 1981 at the Joint Institute for Laboratory Astrophysics (JILA) in Boulder, Colorado. In the following years this concept was worked out in more detail by P.L. Bender and J. Faller and in 1985 the first full description of a mission comprising three drag-free spacecraft in a heliocentric orbit was proposed, then named Laser Antenna for Gravitational-radiation Observation in Space (LAGOS). LAGOS already had many elements of the present-day Laser Interferometer Space Antenna (LISA) mission.

In May 1993, the center of activity shifted from the US to Europe when LISA was proposed to ESA in response to the *Call for Mission Proposals* for the third Medium-Size Project (M3) within the framework of ESA's long-term space science programme "Horizon 2000". The proposal was submitted by a team of US and European scientists coordinated by K. Danzmann, Max-Planck-Institut für Quantenoptik and Universität Hannover. It envisaged LISA as an ESA/NASA collaborative project and described a mission comprising four spacecraft in a heliocentric orbit forming an interferometer with a baseline of  $5 \times 10^6$  km.

The SAGITTARIUS proposal, with very similar scientific objectives and techniques, was proposed to ESA at the same time by another international team of scientists coordinated by R.W. Hellings, JPL. The SAGITTARIUS proposal suggested placing six spacecraft in a geocentric orbit forming an interferometer with a baseline of  $10^6$  km.

Because of the large degree of commonality between the two proposals ESA decided to merge them when accepting them for a study at assessment level in the M3 cycle. It was one of the main objectives of the Assessment Study to make an objective trade-off between the heliocentric and the geocentric option. The Study Team decided to adopt the heliocentric option as the baseline because it has the advantage that it provides for reasonably constant arm lengths and a stable environment that gives low noise forces on the proof masses, and because neither option offered a clear cost advantage.

Because the cost for an ESA-alone LISA (there was no expression of interest by NASA in a collaboration at that time) exceeded the M3 cost limit, it became clear quite early in the Assessment Study that LISA would not be selected for a study at Phase A level in the M3 cycle. In December 1993, LISA was therefore proposed as a cornerstone project for "Horizon 2000 Plus", involving six spacecraft in a heliocentric orbit. Both the Fundamental Physics Topical Team and the Survey Committee realised the enormous discovery potential and timeliness of the LISA Project and recommended it as a cornerstone of "Horizon 2000 Plus".

Being a cornerstone in ESA's space science programme implies that, in principle, the mission is approved and that funding for industrial studies and technology development is provided right away. The launch year, however, is dictated by the availability of funding.

In 1996 and early 1997, the LISA team made several proposals how to drastically reduce the cost for LISA without compromising the science in any way, most importantly to reduce the number of spacecraft from six to three, where each of the new spacecraft would replace a pair of spacecraft at the vertices of the triangular configuration, with essentially two instruments in each spacecraft. With these and a few other measures the total launch mass could be reduced from 6.8 t to 1.4 t.

Perhaps most importantly, it was proposed by the LISA team and by ESA's Fundamental Physics Advisory Group (FPAG) in February 1997 to carry out LISA in collaboration with NASA. A launch in the time frame 2010 would be ideal from the point of view of technological readiness of the payload and the availability of second-generation detectors in ground-based interferometers

making the detection of gravitational waves in the high-frequency band very likely.

In January 1997, a candidate configuration of the three-spacecraft mission was developed by the [LISA](#) science team, with the goal of being able to launch the three spacecraft on a Delta-II. The three-spacecraft [LISA](#) mission was studied by [JPL](#)'s Team-X in January, 1997. The purpose of the study was to assist the science team, represented by P.L. Bender and R.T. Stebbins ([JILA](#)/University of Colorado), and W.M. Folkner ([JPL](#)), in defining the necessary spacecraft subsystems and in designing a propulsion module capable of delivering the [LISA](#) spacecraft into the desired orbit. The result of the Team-X study was that it appeared feasible to fly the three-spacecraft [LISA](#) mission on a single Delta-II 7925 H launch vehicle by utilizing a propulsion module based on a solar-electric propulsion, and with spacecraft subsystems expected to be available by a 2001 technology cut-off date.

In June 1997, a [LISA](#) Pre-Project Office was established at [JPL](#) with W.M. Folkner as the Pre-Project Manager and in December 1997, an ad-hoc [LISA](#) Mission Definition Advisory Team was formed by [NASA](#). Representatives from [ESA](#)'s [LISA](#) Study Team are invited to participate in the activities of the [LISA](#) Mission Definition Team.

The revised version of [LISA](#) (three spacecraft in a heliocentric orbit, ion drive, Delta-II launch vehicle; [NASA](#)/[ESA](#) collaborative) has been endorsed by the [LISA](#) Science Team and served as the basis for a detailed payload definition study by the [LISA](#) team. After a payload review in April 1998, [ESA](#)'s Fundamental Physics Advisory Group ([FPAG](#)) concluded that the payload had reached a sufficient level of maturity and recommended to enter into the industrial study phase.

This industrial System and Technology Study was performed by a consortium consisting of Dornier Satellitensysteme (Germany) as the prime and Alenia (Italy) and Matra (France) as subcontractors with intensive involvement of the [LISA](#) Science Team throughout the study. The System and Technology Study was begun in June 1999 and the final report delivered to [ESA](#) in June 2000. It is based on a collaborative [ESA](#)/[NASA](#) mission with equal shares and a launch in 2010. This is the baseline scenario that is now also part of [NASA](#)'s Strategic Plan.

The industrial study was performed by the following team members:

Industrial Team Manager:

A. Hammesfahr, Dornier Satellitensysteme

Industrial Team:

H. Faulks, K. Gebauer, K. Honnen, U. Johann, G. Kahl, M. Kersten, L. Morgenroth, M. Riede, and H.-R. Schulte from Dornier Satellitensysteme,

M. Bisi and S. Cesare from Alenia Aerospazio,

O. Pierre, X. Sembely, and L. Vaillon from Matra Marconi Space,

D. Hayoun, S. Heys, and B.J. Kent from Rutherford Appleton Laboratory,

F. Rüdenauer from Austrian Research Center Seibersdorf,

S. Marcuccio and D. Nicolini from Centrosazio,

L. Maltecca from Laben S.p.A. and

I. Butler from University of Birmingham.

ESOC Support:

Jose Rodriguez-Canabal

The ESA personnel from the Directorate of the Scientific Programme associated with the study were :

R. Reinhard (acting Study Scientist and ESA-HQ Fundamental Physics Missions Coordinator)

T. Edwards (Study Manager under contract to ESA, Rutherford Appleton Laboratory)

LISA Study Team :

P. Bender, Joint Institute for Laboratory Astrophysics, Boulder, Colorado, USA

A. Brillet, Observatoire de la Côte d'Azur, Nice, France

A.M. Cruise, University of Birmingham, UK

C. Cutler, Albert-Einstein Institut, Potsdam, Germany

K. Danzmann, Max-Planck-Institut für Quantenoptik and Universität Hannover, Germany

F. Fidecaro, INFN, Pisa, Italy

W.M. Folkner, Jet Propulsion Laboratory, Pasadena, California, USA

J. Hough, University of Glasgow, UK

P. McNamara, University of Glasgow, UK

M. Peterseim, Max-Planck-Institut für Quantenoptik, Hannover, and [LZH](#), Germany

D. Robertson, University of Glasgow, UK

M. Rodrigues, ONERA, France

A. Rüdiger, Max-Planck-Institut für Quantenoptik, Garching, Germany

M. Sandford, Rutherford Appleton Laboratory, Chilton, UK

G. Schäfer, Universität Jena, Germany

R. Schilling, Max-Planck-Institut für Quantenoptik, Garching, Germany

B. Schutz, Albert-Einstein Institut, Potsdam, Germany

C. Speake, University of Birmingham, UK

R.T. Stebbins, Joint Institute for Laboratory Astrophysics, Boulder, Colorado, USA

T. Sumner, Imperial College, London, UK

P. Touboul, ONERA, France

J.-Y. Vinet, Observatoire de la Côte d'Azur, Nice, France

S. Vitale, Università di Trento, Italy

H. Ward, University of Glasgow, UK

W. Winkler, Max-Planck-Institut für Quantenoptik, Garching, Germany

For further information please contact Karsten Danzmann <kvd@mpq.mpg.de>



# Contents

<b>Mission Summary Table</b>	<b>iii</b>
<b>Foreword</b>	<b>v</b>
<b>Executive Summary</b>	<b>1</b>
The nature of gravitational waves . . . . .	1
Sources of gravitational waves . . . . .	2
Complementarity with ground-based observations . . . . .	3
The <a href="#">LISA</a> mission . . . . .	4
<b>1 Scientific Objectives</b>	<b>7</b>
1.1 Theory of gravitational radiation . . . . .	7
1.1.1 General relativity . . . . .	7
1.1.2 The nature of gravitational waves in general relativity . . . . .	12
1.1.3 Generation of gravitational waves . . . . .	14
1.1.4 Other theories of gravity . . . . .	16
1.2 Low-frequency sources of gravitational radiation . . . . .	18
1.2.1 Galactic binary systems . . . . .	21
1.2.2 Massive black holes in distant galaxies . . . . .	25
1.2.3 Primordial gravitational waves . . . . .	31
<b>2 Different Ways of Detecting Gravitational Waves</b>	<b>35</b>
2.1 Detection on the ground and in space . . . . .	35
2.2 Ground-based detectors . . . . .	36
2.2.1 Resonant-mass detectors . . . . .	36
2.2.2 Laser Interferometers . . . . .	37
2.3 Pulsar timing . . . . .	39
2.4 Spacecraft tracking . . . . .	40
2.5 Space interferometer . . . . .	40
2.6 Early concepts for a laser interferometer in space . . . . .	41
2.7 Heliocentric versus geocentric options . . . . .	43
<b>3 The LISA Concept – An Overview</b>	<b>45</b>
3.1 The LISA flight configuration . . . . .	45
3.2 The LISA orbits . . . . .	45
3.3 The three LISA spacecraft . . . . .	46
3.4 The payload . . . . .	48

3.4.1	The proof mass . . . . .	49
3.4.2	The inertial sensor . . . . .	49
3.4.3	The optical bench . . . . .	49
3.4.4	The telescope . . . . .	50
3.4.5	The support structure . . . . .	50
3.4.6	The thermal shield . . . . .	50
3.4.7	The star trackers . . . . .	50
3.5	Lasers . . . . .	51
3.6	Data extraction . . . . .	51
3.7	Drag-free and attitude control . . . . .	52
3.8	Ultrastable structures . . . . .	52
3.9	System options and trade-off . . . . .	53
3.10	Summary tables . . . . .	53
<b>4</b>	<b>Measurement Sensitivity</b>	<b>57</b>
4.1	Interferometer response . . . . .	57
4.2	Noises and error sources . . . . .	59
4.2.1	The noise effects . . . . .	59
4.2.2	The noise types . . . . .	59
4.2.3	Shot noise . . . . .	60
4.2.4	Optical-path noise budget . . . . .	60
4.2.5	Acceleration noise budget . . . . .	62
<b>5</b>	<b>The Interferometer</b>	<b>65</b>
5.1	Introduction . . . . .	65
5.2	Phase locking and heterodyne detection . . . . .	65
5.3	Interferometric layout . . . . .	66
5.3.1	The optical bench of <a href="#">PPA 2</a> . . . . .	67
5.3.2	Optical bench, revisited . . . . .	68
5.3.3	Telescope assembly . . . . .	72
5.4	System requirements . . . . .	72
5.4.1	Laser power and shot noise . . . . .	72
5.4.2	Beam divergence . . . . .	72
5.4.3	Efficiency of the optical chain . . . . .	72
5.4.4	Shot noise limit . . . . .	73
5.5	Laser system . . . . .	73
5.5.1	Introduction . . . . .	73
5.5.2	Laser system components . . . . .	75
5.6	Laser performance . . . . .	76
5.6.1	Laser frequency noise . . . . .	76
5.6.2	Laser power noise . . . . .	77



5.6.3	On-board frequency reference . . . . .	77
5.7	Beam pointing . . . . .	78
5.7.1	Pointing stability . . . . .	78
5.7.2	Pointing acquisition . . . . .	79
5.7.3	Final focusing and pointing calibration . . . . .	79
5.7.4	Point-ahead angle . . . . .	79
5.8	Thermal stability . . . . .	82
<b>6</b>	<b>Inertial Sensor and Drag-Free Control</b>	<b>85</b>
6.1	The inertial sensor . . . . .	85
6.1.1	Overview . . . . .	85
6.1.2	<b>CAESAR</b> sensor head . . . . .	86
6.1.3	Electronics configuration . . . . .	87
6.1.4	Evaluation of performances . . . . .	90
6.1.5	Sensor operation modes . . . . .	91
6.1.6	Proof-mass charge control . . . . .	91
6.2	Drag-free/attitude control system . . . . .	92
6.2.1	Description . . . . .	92
6.2.2	<b>DFACS</b> controller modes . . . . .	93
6.2.3	Autonomous star trackers . . . . .	94
6.3	Accelerations directly affecting the proof-mass . . . . .	95
<b>7</b>	<b>Signal Extraction and Data Analysis</b>	<b>97</b>
7.1	Signal extraction . . . . .	97
7.1.1	Phase measurement . . . . .	97
7.2	Frequency-domain cancellation of laser noise . . . . .	97
7.2.1	Laser noise . . . . .	97
7.2.2	Clock noise . . . . .	99
7.2.3	Other approaches . . . . .	100
7.3	Time-domain cancellation of laser phase noise . . . . .	100
7.4	Alternative laser-phase and optical-bench noise-canceling methods . . . . .	101
7.4.1	Notation and geometry . . . . .	102
7.4.2	Gravitational wave signal transfer function to single laser link . . . . .	104
7.4.3	Noise transfer function to single laser link . . . . .	104
7.4.4	Combinations that eliminate laser noises and optical bench motions . . . . .	104
7.4.5	Gravitational wave sensitivities . . . . .	109
7.5	Data analysis . . . . .	112
7.5.1	Data reduction and filtering . . . . .	113
7.5.2	Angular resolution . . . . .	115
7.5.3	Polarization resolution and amplitude extraction . . . . .	121
7.5.4	Results for <b>MBH</b> coalescence . . . . .	123

7.5.5	Estimation of background signals . . . . .	124
<b>8</b>	<b>Payload Design</b>	<b>127</b>
8.1	Payload structure design concept . . . . .	127
8.2	Payload structural components . . . . .	128
8.2.1	Optical assembly . . . . .	128
8.2.2	Optical bench . . . . .	128
8.2.3	Payload thermal shield . . . . .	130
8.3	Mass estimates . . . . .	130
8.4	Payload thermal requirements . . . . .	131
8.5	Payload thermal design . . . . .	132
8.6	Thermal analysis . . . . .	133
8.7	Telescope assembly . . . . .	135
8.7.1	General remarks . . . . .	135
8.7.2	Telescope concept . . . . .	135
8.7.3	Telescope development . . . . .	136
8.8	Payload processor and data interfaces . . . . .	136
8.8.1	Payload processor . . . . .	136
8.8.2	Payload data interfaces . . . . .	137
<b>9</b>	<b>Spacecraft Design</b>	<b>139</b>
9.1	The Pre-Phase A spacecraft design . . . . .	139
9.1.1	The spacecraft . . . . .	139
9.1.2	Propulsion module . . . . .	140
9.1.3	Launch configuration . . . . .	141
9.2	Spacecraft subsystem design . . . . .	141
9.2.1	Structure . . . . .	141
9.2.2	Thermal control . . . . .	142
9.2.3	Coarse attitude control . . . . .	142
9.2.4	On-board data handling . . . . .	143
9.2.5	Tracking, telemetry and command . . . . .	143
9.2.6	Power subsystem and solar array . . . . .	143
9.3	The revised spacecraft design . . . . .	144
9.3.1	The constraints . . . . .	144
9.4	Structure and Mechanisms . . . . .	150
9.4.1	Requirements . . . . .	150
9.4.2	Structure Design . . . . .	151
9.4.3	Structure Performance . . . . .	154
9.4.4	Mechanism Design . . . . .	154
9.5	Thermal control . . . . .	155
9.5.1	Requirements . . . . .	155

9.5.2	Thermal design . . . . .	155
9.5.3	Thermal performance . . . . .	157
9.5.4	<a href="#">LISA</a> spacecraft system options and trade-off . . . . .	159
9.6	Spacecraft electrical subsystems . . . . .	163
9.6.1	System electrical architecture . . . . .	164
9.6.2	Electrical power subsystem . . . . .	166
9.6.3	Command and data handling/avionics . . . . .	169
9.6.4	<a href="#">RF</a> communications . . . . .	173
9.6.5	Electromagnetic compatibility . . . . .	175
9.7	Micronewton ion thrusters . . . . .	176
9.7.1	History of <a href="#">FEEP</a> development . . . . .	177
9.7.2	The Field Emission Electric Propulsion System . . . . .	177
9.7.3	Advantages and critical points of <a href="#">FEEP</a> systems . . . . .	178
9.7.4	Alternative solutions for <a href="#">FEEP</a> systems . . . . .	179
9.7.5	Current status . . . . .	180
9.8	Mass and power budgets . . . . .	182
<b>10</b>	<b>Mission Analysis</b>	<b>185</b>
10.1	Orbital configuration . . . . .	185
10.2	Launch and orbit transfer . . . . .	185
10.3	Injection into final orbits . . . . .	186
10.4	Orbit configuration stability . . . . .	187
10.5	Orbit determination and tracking requirements . . . . .	189
10.6	Launch phase . . . . .	191
10.6.1	Launcher and launcher payload . . . . .	191
10.6.2	Analysis of launch phase . . . . .	192
10.7	Operational orbit injection and composite separation . . . . .	193
10.7.1	Composite spacecraft . . . . .	193
10.7.2	Analysis of injection into operational orbit . . . . .	193
10.7.3	Analysis of composite separation . . . . .	195
10.8	Evolution of the operational orbit . . . . .	195
<b>11</b>	<b>Technology Demonstration in Space</b>	<b>199</b>
11.1	<a href="#">SMART 2</a> technology demonstration flight . . . . .	199
11.1.1	Introduction . . . . .	199
11.1.2	Mission goals . . . . .	199
11.1.3	Background requirements . . . . .	200
11.2	<a href="#">SMART 2</a> mission profile . . . . .	202
11.2.1	Orbit – baseline option . . . . .	202
11.2.2	De-scoped option . . . . .	202
11.2.3	Coarse attitude control . . . . .	202

11.3	SMART 2 technologies . . . . .	203
11.3.1	Capacitive sensor . . . . .	203
11.3.2	Laser interferometer . . . . .	203
11.3.3	Ion thrusters . . . . .	203
11.3.4	Drag-free control . . . . .	204
11.4	SMART 2 satellite design . . . . .	204
11.4.1	Power subsystem . . . . .	205
11.4.2	Command and Data Handling . . . . .	205
11.4.3	Telemetry and mission operations . . . . .	205
<b>12</b>	<b>Science and Mission Operations</b>	<b>207</b>
12.1	Science operations . . . . .	207
12.1.1	Relationship to spacecraft operations . . . . .	207
12.1.2	Scientific commissioning . . . . .	207
12.1.3	Scientific data acquisition . . . . .	208
12.2	Mission operations . . . . .	208
12.3	Operating modes . . . . .	209
12.3.1	Ground-test mode . . . . .	209
12.3.2	Launch mode . . . . .	209
12.3.3	Orbit acquisition . . . . .	209
12.3.4	Attitude acquisition . . . . .	209
12.3.5	Science mode . . . . .	210
12.3.6	Safe mode . . . . .	210
12.4	Operational strategy . . . . .	210
12.4.1	Nominal operations concept . . . . .	210
12.4.2	Advanced operations concept . . . . .	210
12.4.3	Autonomy . . . . .	211
12.4.4	Failure detection, isolation and recovery . . . . .	212
12.4.5	Ground control . . . . .	213
12.5	Mission phases . . . . .	213
12.6	Operating modes and mode transitions . . . . .	215
12.7	Ground segment . . . . .	218
<b>13</b>	<b>International Collaboration, Management, Schedules, Archiving</b>	<b>221</b>
13.1	International collaboration . . . . .	221
13.2	Science and project management . . . . .	222
13.3	Schedule . . . . .	222
13.4	Archiving . . . . .	223
	<b>Appendix</b>	<b>225</b>
A.1	Detailed Noise Analysis . . . . .	225

A.1.1	Overview . . . . .	225
A.1.2	Pathlength Difference Measurement . . . . .	228
A.1.3	Residual Proof Mass Acceleration . . . . .	249
A.1.4	Optical Path-Noise Budget . . . . .	250
A.1.5	Conclusion . . . . .	255
A.2	Proof-mass charging by energetic particles . . . . .	257
A.2.1	Disturbances arising from electrical charging . . . . .	257
A.2.2	Modelling the charge deposition . . . . .	258
A.2.3	Lorentz forces . . . . .	261
A.2.4	Coulomb forces . . . . .	263
A.2.5	Summary of charge limits . . . . .	264
A.2.6	Charge measurement using force modulation . . . . .	265
A.2.7	Momentum transfer . . . . .	266
A.3	Disturbances due to minor bodies and dust . . . . .	267
A.4	Alternative Proof-Mass Concepts . . . . .	271
A.4.1	Single (spherical) proof mass . . . . .	271
A.4.2	IRS optical read out . . . . .	272
A.4.3	IRS internal all optical control . . . . .	273
A.4.4	Laser metrology harness . . . . .	274
A.4.5	Single proof mass as accelerometer . . . . .	274
A.5	Laser Assembly Concepts . . . . .	275
A.5.1	Laser requirements . . . . .	275
A.5.2	Single-frequency solid state laser alternatives . . . . .	275
A.5.3	Laser components identification and trades . . . . .	280
A.5.4	Photodiodes . . . . .	283
A.6	Telescope . . . . .	285
A.6.1	Telescope design drivers . . . . .	285
A.6.2	Review of possible optical and mechanical telescope designs . . . . .	285
A.6.3	Selection of the telescope optical design . . . . .	292
A.6.4	Design and performance summary . . . . .	293
A.7	Line-of-Sight Orientation Mechanism . . . . .	295
A.7.1	Configuration . . . . .	295
A.7.2	Pointing mechanism requirements . . . . .	296
A.7.3	Mechanism design drivers . . . . .	297
A.7.4	Location of the centre of rotation. . . . .	298
A.7.5	Candidate technologies . . . . .	300
A.7.6	Mechanism concept . . . . .	300
A.7.7	Dynamic simulations . . . . .	303
A.7.8	Conclusion . . . . .	304

<b>References</b>	<b>307</b>
<b>Acronyms</b>	<b>316</b>

## Executive Summary

The primary objective of the Laser Interferometer Space Antenna ([LISA](#)) mission is to detect and observe gravitational waves from massive black holes and galactic binaries in the frequency range  $10^{-4}$  to  $10^{-1}$  Hz. This low-frequency range is inaccessible to ground-based interferometers because of the unshieldable background of local gravitational noise and because ground-based interferometers are limited in length to a few kilometres.

### The nature of gravitational waves

In Newton's theory of gravity the gravitational interaction between two bodies is instantaneous, but according to Special Relativity this should be impossible, because the speed of light represents the limiting speed for all interactions. If a body changes its shape the resulting change in the force field will make its way outward at the speed of light. It is interesting to note that already in 1805, Laplace, in his famous *Traité de Mécanique Céleste* stated that, if Gravitation propagates with finite speed, the force in a binary star system should not point along the line connecting the stars, and the angular momentum of the system must slowly decrease with time. Today we would say that this happens because the binary star is losing energy and angular momentum by emitting gravitational waves. It was no less than 188 years later in 1993 that Hulse and Taylor were awarded the Nobel prize in physics for the indirect proof of the existence of Gravitational Waves using exactly this kind of observation on the binary pulsar PSR 1913+16. A direct detection of gravitational waves has not been achieved up to this day.

Einstein's paper on gravitational waves was published in 1916, and that was about all that was heard on the subject for over forty years. It was not until the late 1950s that some relativity theorists, H. Bondi in particular, proved rigorously that gravitational radiation was in fact a physically observable phenomenon, that gravitational waves carry energy and that, as a result, a system that emits gravitational waves should lose energy.

General Relativity replaces the Newtonian picture of Gravitation by a geometric one that is very intuitive if we are willing to accept the fact that space and time do not have an independent existence but rather are in intense interaction with the physical world. Massive bodies produce "indentations" in the fabric of spacetime, and other bodies move in this curved spacetime taking the shortest path, much like a system of billiard balls on a springy surface. In fact, the Einstein field equations relate mass (energy) and curvature in just the same way that Hooke's law relates force and spring deformation, or phrased somewhat poignantly: spacetime is an elastic medium.

If a mass distribution moves in an asymmetric way, then the spacetime indentations travel outwards as ripples in spacetime called gravitational waves. Gravitational waves are fundamentally different from the familiar electromagnetic waves. While electromagnetic waves, created by the acceleration of electric charges, propagate IN the framework of space and time, gravitational waves, created by the acceleration of masses, are waves of the spacetime fabric ITSELF.

Unlike charge, which exists in two polarities, masses always come with the same sign. This is why the lowest order asymmetry producing *electro-magnetic* radiation is the dipole moment of the charge distribution, whereas for *gravitational* waves it is a change in the quadrupole moment of the mass distribution. Hence those gravitational effects which are spherically symmetric will not give rise to gravitational radiation. A perfectly symmetric collapse of a supernova will produce no waves, a non-spherical one will emit gravitational radiation. A binary system will always radiate.

Gravitational waves distort spacetime, in other words they change the distances between free macroscopic bodies. A gravitational wave passing through the Solar System creates a time-

varying strain in space that periodically changes the distances between all bodies in the Solar System in a direction that is perpendicular to the direction of wave propagation. These could be the distances between spacecraft and the Earth, as in the case of [ULYSSES](#) or [CASSINI](#) (attempts were and will be made to measure these distance fluctuations) or the distances between shielded proof masses inside spacecraft that are separated by a large distance, as in the case of [LISA](#). The main problem is that the relative length change due to the passage of a gravitational wave is exceedingly small. For example, the periodic change in distance between two proof masses, separated by a sufficiently large distance, due to a typical white dwarf binary at a distance of 50 pc is only  $10^{-10}$  m. This is not to mean that gravitational waves are weak in the sense that they carry little energy. On the contrary, a supernova in a not too distant galaxy will drench every square meter here on earth with kilowatts of gravitational radiation intensity. The resulting length changes, though, are very small because spacetime is an extremely stiff elastic medium so that it takes extremely large energies to produce even minute distortions.

## Sources of gravitational waves

The two main categories of gravitational waves sources for [LISA](#) are the galactic binaries and the massive black holes ([MBHs](#)) expected to exist in the centres of most galaxies.

Because the masses involved in typical binary star systems are small (a few solar masses), the observation of binaries is limited to our Galaxy. Galactic sources that can be detected by [LISA](#) include a wide variety of binaries, such as pairs of close white dwarfs, pairs of neutron stars, neutron star and black hole ( $5-20 M_{\odot}$ ) binaries, pairs of contacting normal stars, normal star and white dwarf (cataclysmic) binaries, and possibly also pairs of black holes. It is likely that there are so many white dwarf binaries in our Galaxy that they cannot be resolved at frequencies below  $10^{-3}$  Hz, leading to a confusion-limited background. Some galactic binaries are so well studied, especially the X-ray binary 4U1820-30, that it is one of the most reliable sources. If [LISA](#) would not detect the gravitational waves from known binaries with the intensity and polarisation predicted by General Relativity, it will shake the very foundations of gravitational physics.

The main objective of the [LISA](#) mission, however, is to learn about the formation, growth, space density and surroundings of massive black holes ([MBHs](#)). There is now compelling indirect evidence for the existence of [MBHs](#) with masses of  $10^6$  to  $10^8 M_{\odot}$  in the centres of most galaxies, including our own. The most powerful sources are the mergers of [MBHs](#) in distant galaxies, with amplitude signal-to-noise ratios of several thousand for  $10^6 M_{\odot}$  black holes. Observations of signals from these sources would test General Relativity and particularly black-hole theory to unprecedented accuracy. Not much is currently known about black holes with masses ranging from about  $100 M_{\odot}$  to  $10^6 M_{\odot}$ . [LISA](#) can provide unique new information throughout this mass range.



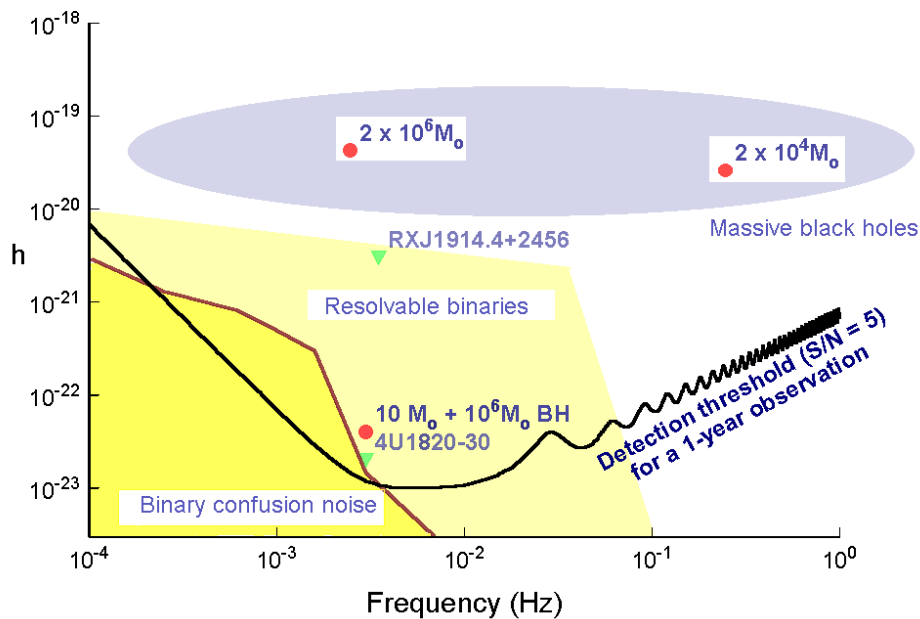


**Figure 1** *LISA* Sensitivity to binary star systems in our Galaxy and black holes in distant galaxies. The heavy black curve shows the *LISA* detection threshold, giving the noise amplitude of  $5\sigma$  after a 1-year observation. At frequencies below 3 mHz, binaries in the Galaxy are so numerous that *LISA* will not resolve them, and they form a noise background; this is also indicated at its expected  $5\sigma$  level, coloured dark yellow. In lighter yellow is the region where *LISA* should resolve thousands of binaries that are closer to the Sun than most or that radiate at higher frequencies. The signals expected from two known binaries are indicated by the green triangles. Many other systems are known to be observable, but are not indicated here. The blue shaded area is where signals are expected from coalescences of massive black holes in galaxies at redshifts of order  $z = 1$ . These signals are complex and may last less than 1 year, so the region is drawn to indicate the expected signal-to-noise ratio above the *LISA* instrumental noise. Two signals are indicated, for coalescences of binaries consisting of two  $10^6 M_\odot$  and two  $10^4 M_\odot$  black holes. These show how sensitive *LISA* will be, reaching amplitude signal-to-noise ratios exceeding several thousand. While such events may occur only once per year, signals from small black holes falling into larger ones should be very common. Their strength is indicated by giving one example, where a  $10 M_\odot$  black hole falls into a  $10^6 M_\odot$  black hole at  $z = 1$ .

## Complementarity with ground-based observations

The ground-based interferometers *LIGO*, *VIRGO*, *TAMA 300* and *GEO 600* and the *LISA* interferometer in space complement each other in an essential way. Just as it is important to complement the optical and radio observations from the ground with observations from space at submillimetre, infrared, ultraviolet, X-ray and gamma-ray wavelengths, so too is it important to complement the gravitational wave observations done by the ground-based interferometers in the high-frequency regime (10 to  $10^3$  Hz) with observations in space in the low-frequency regime ( $10^{-4}$  Hz to 1 Hz).

Ground-based interferometers can observe the bursts of gravitational radiation emitted by galactic binaries during the final stages (minutes and seconds) of coalescence when the frequencies are high and both the amplitudes and frequencies increase quickly with time. At low frequencies,

which are only observable in space, the orbital radii of the binary systems are larger and the frequencies are stable over millions of years. Coalescences of MBHs are only observable from space. Both ground- and space-based detectors will also search for a cosmological background of gravitational waves. Since both kinds of detectors have similar energy sensitivities their different observing frequencies are ideally complementary: observations can provide crucial spectral information.

## The LISA mission

The LISA mission comprises three identical spacecraft located  $5 \times 10^6$  km apart forming an equilateral triangle. LISA is basically a giant Michelson interferometer placed in space, with a third arm added to give independent information on the two gravitational wave polarizations, and for redundancy. The distance between the spacecraft – the interferometer arm length – determines the frequency range in which LISA can make observations; it was carefully chosen to allow for the observation of most of the interesting sources of gravitational radiation. The centre of the triangular formation is in the ecliptic plane, 1 AU from the Sun and  $20^\circ$  behind the Earth. The plane of the triangle is inclined at  $60^\circ$  with respect to the ecliptic. These particular heliocentric orbits for the three spacecraft were chosen such that the triangular formation is maintained throughout the year with the triangle appearing to rotate about the centre of the formation once per year.

While LISA can be described as a big Michelson interferometer, the actual implementation in space is very different from a laser interferometer on the ground and is much more reminiscent of the technique called spacecraft tracking, but here realized with infrared laser light instead of radio waves. The laser light going out from the center spacecraft to the other corners is not directly reflected back because very little light intensity would be left over that way. Instead, in complete analogy with an RF transponder scheme, the laser on the distant spacecraft is phase-locked to the incoming light providing a return beam with full intensity again. After being transponded back from the far spacecraft to the center spacecraft, the light is superposed with the on-board laser light serving as a local oscillator in a heterodyne detection. This gives information on the length of one arm modulo the laser frequency. The other arm is treated the same way, giving information on the length of the other arm modulo the same laser frequency. The difference between these two signals will thus give the difference between the two arm lengths (i.e. the gravitational wave signal). The sum will give information on laser frequency fluctuations.

Each spacecraft contains two optical assemblies. The two assemblies on one spacecraft are each pointing towards an identical assembly on each of the other two spacecraft to form a Michelson interferometer. A 1 W infrared laser beam is transmitted to the corresponding remote spacecraft via a 30-cm aperture  $f/1$  Cassegrain telescope. The same telescope is used to focus the very weak beam (a few pW) coming from the distant spacecraft and to direct the light to a sensitive photodetector where it is superimposed with a fraction of the original local light. At the heart of each assembly is a vacuum enclosure containing a free-flying polished platinum-gold cube, 4 cm in size, referred to as the proof mass, which serves as an optical reference (“mirror”) for the light beams. A passing gravitational wave will change the length of the optical path between the proof masses of one arm of the interferometer relative to the other arm. The distance fluctuations are measured to sub-Ångström precision which, when combined with the large separation between the spacecraft, allows LISA to detect gravitational-wave strains down to a level of order  $\Delta\ell/\ell = 10^{-23}$  in one year of observation, with a signal-to-noise ratio of 5.

The spacecraft mainly serve to shield the proof masses from the adverse effects due to the solar

radiation pressure, and the spacecraft position does not directly enter into the measurement. It is nevertheless necessary to keep all spacecraft moderately accurately ( $10^{-8}$  m/ $\sqrt{\text{Hz}}$  in the measurement band) centered on their respective proof masses to reduce spurious local noise forces. This is achieved by a “drag-free” control system, consisting of an accelerometer (or inertial sensor) and a system of electrical thrusters.

Capacitive sensing in three dimensions is used to measure the displacements of the proof masses relative to the spacecraft. These position signals are used in a feedback loop to command micro-Newton ion-emitting proportional thrusters to enable the spacecraft to follow its proof masses precisely. The thrusters are also used to control the attitude of the spacecraft relative to the incoming optical wavefronts, using signals derived from quadrant photodiodes. As the three-spacecraft constellation orbits the Sun in the course of one year, the observed gravitational waves are Doppler-shifted by the orbital motion. For periodic waves with sufficient signal-to-noise ratio, this allows the direction of the source to be determined (to arc minute or degree precision, depending on source strength).

Each of the three [LISA](#) spacecraft has a launch mass of about 400 kg (plus margin) including the payload, ion drive, all propellants and the spacecraft adapter. The ion drives are used for the transfer from the Earth orbit to the final position in interplanetary orbit. All three spacecraft can be launched by a single Delta II 7925H. Each spacecraft carries a 30 cm steerable antenna used for transmitting the science and engineering data, stored on board for two days, at a rate of 7 kb/s in the X-band to the 34-m network of the DSN. Nominal mission lifetime is two years.

[LISA](#) is envisaged as a [NASA/ESA](#) collaborative project, with [NASA](#) providing the launch vehicle, the X-band telecommunications system on board the spacecraft, mission and science operations and about 50 % of the payload, [ESA](#) providing the three spacecraft including the ion drives, and European institutes, funded nationally, providing the other 50 % of the payload. The collaborative [NASA/ESA LISA](#) mission is aimed at a launch in the 2010 time frame.

Based on the [LISA Pre-Phase A Report \[1\]](#), a Technical Study had been performed, under the auspices of Dornier Satellitensysteme ([DSS](#)). Also involved in this study were Matra Marconi Space ([MMS](#)) and Alenia Aerospazio and various subcontractors.

Their Final Technical Report ([FTR](#), [ESTEC](#) Contract no. 13631/99/NL/MS, Report No. LI-RP-DS-009) has been made available to [ESA](#) Headquarters in June 2000. In the following System and Technology Study Report, this [FTR](#) will be cited as Reference [2].

The [FTR](#) has deepened, verified, corroborated, and optimised findings given in [1], and has shown up various options for improvements and alternatives. The trade-offs given in [FTR](#) will allow the [LISA](#) Study Team and associated institutions to make informed choices between the alternatives offered.

In the report at hand, some of the alternatives will still be shown side by side. As will become apparent, the differences are not large, and minor advantages may sway the final decision one way or the other. The very encouraging result of the [FTR](#) was that at no place in the Pre-Phase A Study had claims been made that could not be confirmed in the subsequent [FTR](#) study.



# 1 Scientific Objectives

By applying Einstein’s theory of general relativity to the most up-to-date information from modern astronomy, physicists have come to two fundamental conclusions about gravitational waves:

- Both the *most predictable* and the *most powerful* sources of gravitational waves emit their radiation predominantly at very low frequencies, below about 10 mHz.
- The terrestrial Newtonian gravitational field is so noisy at these frequencies that gravitational radiation from astronomical objects can only be detected by space-based instruments.

The *most predictable* sources are binary star systems in our galaxy; there should be thousands of resolvable systems, including some already identified from optical and X-ray observations. The *most powerful* sources are the mergers of supermassive black holes in distant galaxies; if they occur their signal power can be more than  $10^7$  times the expected noise power in a space-based detector. Observations of signals involving massive black holes (MBHs) would test general relativity and particularly black-hole theory to unprecedented accuracy, and they would provide new information about astronomy that can be obtained in no other way.

This is the motivation for the LISA Cornerstone Mission project. The experimental and mission plans for LISA are described in Chapters 3–13 below. The technology is an outgrowth of that developed for ground-based gravitational wave detectors, which will observe at higher frequencies; these and other existing gravitational wave detection methods are reviewed in Chapter 2. In the present Chapter, we begin with a non-mathematical introduction to general relativity and the theory of gravitational waves. We highlight places where LISA’s observations can test the fundamentals of gravitation theory. Then we survey the different expected sources of low-frequency gravitational radiation and detail what astronomical information and other fundamental physics can be expected from observing them.

## 1.1 Theory of gravitational radiation

### 1.1.1 General relativity

There are a number of good textbooks that introduce general relativity and gravitational waves, with their astrophysical implications [3, 4, 5, 6]. We present here a very brief introduction to the most important ideas, with a minimum of mathematical detail. A discussion in the same spirit that deals with other experimental aspects of general relativity is in Reference [7].

#### Foundations of general relativity.

General relativity rests on two foundation stones: the equivalence principle and special relativity. By considering each in turn, we can learn a great deal about what to expect from general relativity and gravitational radiation.

- **Equivalence principle.** This originates in Galileo’s observation that all bodies fall in a gravitational field with the same acceleration, regardless of their mass. From the modern

point of view, that means that if an experimenter were to fall with the acceleration of gravity (becoming a *freely falling local inertial observer*), then every local experiment on free bodies would give the same results as if gravity were completely absent: with the common acceleration removed, particles would move at constant speed and conserve energy and momentum.

The equivalence principle is embodied in Newtonian gravity, and its importance has been understood for centuries. By assuming that it applied to light — that light behaved just like any particle — eighteenth century physicists predicted black holes (Michell and Laplace) and the gravitational deflection of light (Cavendish and von Söldner), using only Newton’s theory of gravity.

The equivalence principle leads naturally to the point of view that gravity is geometry. If all bodies follow the same trajectory, just depending on their initial velocity and position but not on their internal composition, then it is natural to associate the trajectory with the spacetime itself rather than with any force that depends on properties of the particle. General relativity is formulated mathematically as a geometrical theory, but our approach to it here will be framed in the more accessible language of forces.

The equivalence principle can only hold locally, that is in a small region of space and for a short time. The inhomogeneity of the Earth’s gravitational field introduces differential accelerations that must eventually produce measurable effects in any freely-falling experiment. These are called *tidal effects*, because tides on the Earth are caused by the inhomogeneity of the Moon’s field. So tidal forces are the part of the gravitational field that cannot be removed by going to a freely falling frame. General relativity describes how tidal fields are generated by sources. Gravitational waves are time-dependent tidal forces, and gravitational wave detectors must sense the small tidal effects.

Ironically, the equivalence principle never holds exactly in real situations in general relativity, because real particles (*e.g.* neutron stars) carry their gravitational fields along with them, and these fields always extend far from the particle. Because of this, no real particle experiences only the local part of the external gravitational field. When a neutron star falls in the gravitational field of some other body (another neutron star or a massive black hole), its own gravitational field is accelerated with it, and far from the system this time-dependent field assumes the form of a gravitational wave. The loss of energy and momentum to gravitational radiation is accompanied by a gravitational radiation reaction force that changes the motion of the star. These reaction effects have been observed in the Hulse-Taylor binary pulsar [8], and they will be observable in the radiation from merging black holes and from neutron stars falling into massive black holes. They will allow [LISA](#) to perform more stringent quantitative tests of general relativity than are possible with the Hulse-Taylor pulsar. The reaction effects are relatively larger for more massive “particles”, so the real trajectory of a star will depend on its mass, despite the equivalence principle. The equivalence principle only holds strictly in the limit of a particle of small mass.

This “failure” of the equivalence principle does not, of course, affect the self-consistency of general relativity. The field equations of general relativity are partial differential equations, and they incorporate the equivalence principle as applied to matter in infinitesimally small volumes of space and lengths of time. Since the mass in such regions is infinitesimally small, the equivalence principle does hold for the differential equations. Only when the effects of gravity are added up over the whole mass of a macroscopic body does the motion begin to deviate from that predicted by the equivalence principle.

- **Special relativity.** The second foundation stone of general relativity is special relativity.

Indeed, this is what led to the downfall of Newtonian gravity: as an instantaneous theory, Newtonian gravity was recognized as obsolete as soon as special relativity was accepted. Many of general relativity's most distinctive predictions originate in its conformance to special relativity.

General relativity incorporates special relativity through the equivalence principle: local freely falling observers see special relativity physics. That means, in particular, that nothing moves faster than light, that light moves at the same speed  $c$  with respect to all local inertial observers at the same event, and that phenomena like time dilation and the equivalence of mass and energy are part of general relativity.

Black holes in general relativity are regions in which gravity is so strong that the escape speed is larger than  $c$ : this is the Michell-Laplace definition as well. But because nothing moves faster than  $c$ , all matter is trapped inside the black hole, something that Michell and Laplace would not have expected. Moreover, because light can't stand still, light trying to escape from a black hole does not move outwards and then turn around and fall back in, as would an ordinary particle; it never makes any outward progress at all. Instead, it falls inwards towards a complicated, poorly-understood, possibly singular, possibly quantum-dominated region in the center of the hole.

The source of the Newtonian gravitational field is the mass density. Because of  $E = mc^2$ , we would naturally expect that all energy densities would create gravity in a relativistic theory. They do, but there is more. Different freely falling observers measure different energies and different densities (volume is Lorentz-contracted), so the actual source has to include not only energy but also momentum, and not only densities but also fluxes. Since pressure is a momentum flux (it transfers momentum across surfaces), relativistic gravity can be created by mass, momentum, pressure, and other stresses.

*Among the consequences of this that are observable by [LISA](#) are gravitational effects due to spin.*

These include the Lense-Thirring effect, which is the gravitational analogue of spin-orbit coupling, and gravitational spin-spin coupling. The first effect causes the orbital plane of a neutron star around a spinning black hole to rotate in the direction of the spin; the second causes the orbit of a spinning neutron star to differ from the orbit of a simple test particle. (This is another example of the failure of the equivalence principle for a macroscopic "particle".) Both of these orbital effects create distinctive features in the waveform of the gravitational waves from the system.

Gravitational waves themselves are, of course, a consequence of special relativity applied to gravity. Any change to a source of gravity (*e.g.* the position of a star) must change the gravitational field, and this change cannot move outwards faster than light. Far enough from the source, this change is just a ripple in the gravitational field. In general relativity, this ripple moves at the speed of light. In principle, all relativistic gravitation theories must include gravitational waves, although they could propagate slower than light. Theories will differ in their polarization properties, described for general relativity below.

Special relativity and the equivalence principle place a strong constraint on the source of gravitational waves. At least for sources that are not highly relativistic, one can decompose the source into multipoles, in close analogy to the standard way of treating electromagnetic radiation. The electromagnetic analogy lets us anticipate an important result. The monopole moment of the mass distribution is just the total mass. By the equivalence principle, this is conserved, apart from the energy radiated in gravitational waves (the



part that violates the equivalence principle for the motion of the source). As for all fields, this energy is quadratic in the amplitude of the gravitational wave, so it is a second-order effect. To first order, the monopole moment is constant, so there is no monopole emission of gravitational radiation. (Conservation of charge leads to the same conclusion in electromagnetism.)

The dipole moment of the mass distribution also creates no radiation: its time derivative is the total momentum of the source, and this is also conserved in the same way. (In electromagnetism, the dipole moment obeys no such conservation law, except for systems where the ratio of charge to mass is the same for all particles.) It follows that the dominant gravitational radiation from a source comes from the time-dependent *quadrupole moment* of the system. Most estimates of expected wave amplitudes rely on the quadrupole approximation, neglecting higher multipole moments. This is a good approximation for weakly relativistic systems, but only an order-of-magnitude estimate for relativistic events, such as the waveform produced by the final merger of two black holes.

The replacement of Newtonian gravity by general relativity must, of course, still reproduce the successes of Newtonian theory in appropriate circumstances, such as when describing the solar system. General relativity has a well-defined Newtonian limit: when gravitational fields are weak (gravitational potential energy small compared to rest-mass energy) and motions are slow, then general relativity limits to Newtonian gravity. This can only happen in a limited region of space, inside and near to the source of gravity, the *near zone*. Far enough away, the gravitational waves emitted by the source must be described by general relativity.

### **The field equations and gravitational waves.**

The Einstein field equations are inevitably complicated. With 10 quantities that can create gravity (energy density, 3 components of momentum density, and 6 components of stress), there must be 10 unknowns, and these are represented by the components of the metric tensor in the geometrical language of general relativity. Moreover, the equations are necessarily nonlinear, since the energy carried away from a system by gravitational waves must produce a decrease in the mass and hence of the gravitational attraction of the system.

With such a system, exact solutions for interesting physical situations are rare. It is remarkable, therefore, that there is a unique solution that describes a black hole (with 2 parameters, for its mass and angular momentum), and that it is exactly known. This is called the Kerr metric. Establishing its uniqueness was one of the most important results in general relativity in the last 30 years. The theorem is that any isolated, uncharged black hole must be described by the Kerr metric, and therefore that any given black hole is completely specified by giving its mass and spin. This is known as the “no-hair theorem”: black holes have no “hair”, no extra fuzz to their shape and field that is not determined by their mass and spin.

*If [LISA](#) observes neutron stars orbiting massive black holes, the detailed waveform will measure the multipole moments of the black hole. If they do not conform to those of Kerr, as determined by the lowest 2 measured moments, then the no-hair theorem and general relativity itself may be wrong.*

There are no exact solutions in general relativity for the 2-body problem, the orbital motion of two bodies around one another. Considerable effort has therefore been spent over the last 30 years to develop suitable approximation methods to describe the orbits. By expanding about the Newtonian limit one obtains the *post-Newtonian* hierarchy of approximations. The first post-Newtonian equations account for such things as the perihelion shift in binary orbits. Higher



orders include gravitational spin-orbit (Lense-Thirring) and spin-spin effects, gravitational radiation reaction, and so on. These approximations give detailed predictions for the waveforms expected from relativistic systems, such as black holes spiralling together but still well separated, and neutron stars orbiting near massive black holes.

When a neutron star gets close to a massive black hole, the post-Newtonian approximation fails, but one can still get good predictions using linear perturbation theory, in which the gravitational field of the neutron star is treated as a small perturbation of the field of the black hole. This technique is well-developed for orbits around non-rotating black holes (Schwarzschild black holes), and it should be completely understood for orbits around general black holes within the next 5 years.

The most difficult part of the 2-body problem is the case of two objects of comparable mass in a highly relativistic interaction, such as when two black holes merge. This can only be studied using large-scale numerical simulations. One of the NSF's Grand Challenge projects for supercomputing is a collaboration among 7 university groups in the USA to solve the problem of inspiralling and merging black holes. Within 10 years good solutions could be available.

Mathematically, the field equations can be formulated in terms of a set of 10 fields that are components of a symmetric  $4 \times 4$  matrix  $\{h_{\alpha\beta}, \alpha = 0 \dots 3, \beta = 0 \dots 3\}$ . These represent geometrically the *deviation* of the metric tensor from that of special relativity, the Minkowski metric. In suitable coordinates the Einstein field equations can be written

$$\left[ \nabla^2 - \frac{1}{c^2} \frac{\partial^2}{\partial t^2} \right] h_{\alpha\beta} = \frac{G}{c^4} (\text{source}), \quad (1.1)$$

where “(source)” represents the various energy densities and stresses that can create the field, as well as the non-linear terms in  $h_{\alpha\beta}$  that represent an effective energy density and stress for the gravitational field. This should be compared with Newton's field equation,

$$\nabla^2 \Phi = 4\pi G \varrho, \quad (1.2)$$

where  $\varrho$  is the mass density, or the energy density divided by  $c^2$ . Since  $\varrho$  is dimensionally (source)/ $c^2$ , we see that the potentials  $h_{\alpha\beta}$  are generalisations of  $\Phi/c^2$ , which is dimensionless. This correspondence between the relativistic  $h$  and Newton's  $\Phi$  will help us to understand the physics of gravitational waves in the next section.

Comparing Equation 1.1 with Equation 1.2 also shows how the Newtonian limit fits into relativity. If velocities inside the source are small compared with  $c$ , then we can neglect the time-derivatives in Equation 1.1; moreover, pressures and momentum densities will be small compared to energy densities. Similarly, if  $h$  is small compared to 1 (recall that it is dimensionless), then the nonlinear terms in “(source)” will be negligible. If these two conditions hold, then the Einstein equations reduce simply to Newton's equation in and near the source.

However, Equation 1.1 is a wave equation, and time-dependent solutions will always have a wavelike character far enough away, even for a nearly Newtonian source. The transition point is where the spatial gradients in the equation no longer dominate the time-derivatives. For a field falling off basically as  $1/r$  and that has an oscillation frequency of  $\omega$ , the transition occurs near  $r \sim c/\omega = \lambda/2\pi$ , where  $\lambda$  is the wavelength of the gravitational wave. Inside this transition is the “near zone”, and the field is basically Newtonian. Outside is the “wave zone”, where the time-dependent part of the gravitational acceleration ( $\nabla\Phi$ ) is given by  $\Phi/\lambda$  rather than  $\Phi/r$ . Time-dependent gravitational effects therefore fall off only as  $1/r$ , not the Newtonian  $1/r^2$ .

### 1.1.2 The nature of gravitational waves in general relativity

#### Tidal accelerations.

We remarked above that the observable effects of gravity lie in the tidal forces. A gravitational wave detector would not respond to the acceleration produced by the wave (as given by  $\nabla\Phi$ ), since the whole detector would fall freely in this field, by the equivalence principle. Detectors work only because they sense the changes in this acceleration across them. If two parts of a detector are separated by a vector  $\vec{L}$ , then it responds to a *differential* acceleration of order

$$\vec{L} \cdot \nabla(\nabla\Phi) \sim L\Phi/\lambda^2. \quad (1.3)$$

Since we have seen that  $\Phi \sim hc^2$  (dropping the indices of  $h_{\alpha\beta}$  in order to simplify this order-of-magnitude argument), the differential acceleration is of order  $L\omega^2 h$ .

If the detector is a solid body, such as the bar detectors described in Section 2.2.1, the differential acceleration will be resisted by internal elastic stresses, and the resulting mechanical motion can be complex. Bars are made so that they will “ring” for a long time after a gravitational wave passes, making detection easier. If the detector consists of separated masses that respond to the gravitational wave like free particles, then the situation is easier to analyse. This is the case for interferometers, including LISA.

For two free masses separated by the vector  $\vec{L}$ , the differential acceleration given by Equation 1.3 leads to an equation for the change in their separation  $\delta\vec{L}$ , of order

$$\frac{d^2\delta L}{dt^2} \sim L\omega^2 h.$$

Since the time-derivatives on the left-hand-side just bring down factors of  $\omega$ , we arrive at the very simple equation  $\delta L/L \sim h$ . A careful derivation shows that this is exact with a further factor of 2:

$$\frac{\delta L}{L} = \frac{1}{2} h. \quad (1.4)$$

Here we make contact with the geometrical interpretation of general relativity. The distances  $L$  and  $\delta L$  should be interpreted as *proper* distances, the actual distances that a meter-stick would measure at a given time. Then we see that  $h$  is indeed a metric, a distance measure: as a gravitational wave passes, it stretches and shrinks the proper distance between two free bodies. This equation also explains why interferometric detectors should be made large: the technical problem is always to measure the small distance change  $\delta L$ , and for a given wave amplitude  $h$  this distance change increases in proportion to  $L$ .

#### Polarization of gravitational waves.

We have managed to discover much about gravitational waves by ignoring all the indices and the full complexity of the field equations, but this approach eventually reaches its limit. What we cannot discover without indices is how the differential accelerations depend on the direction to the source of the wave. Here there are two important results that we simply quote without proof:

- Gravitational waves are **transverse**. Like electromagnetic waves, they act only in a plane perpendicular to their direction of propagation. This means that the two separated masses will experience the maximum relative distance change if they are perpendicular to the direction to the source; if they lie along that direction there will be no change  $\delta L$ .

- In the transverse plane, gravitational waves are **area preserving**. This means that if a wave increases the proper distance between two free masses that lie along a given direction, it will simultaneously decrease the distance between two free masses lying along the perpendicular direction in the transverse plane. The consequence of this is illustrated in the standard polarization diagram, Figure 1.1.

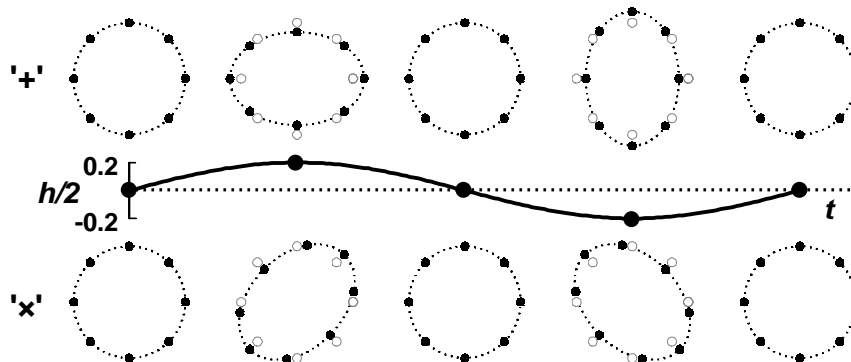


**Figure 1.1 Illustration of the polarisation of a gravitational wave.** Two linearly independent polarisations of a gravitational wave are illustrated by displaying their effect on a ring of free particles arrayed in a plane perpendicular to the direction of the wave. The wave-form is shown between the two sequences, for a wave with the (large) dimensionless amplitude  $h = 0.2$ . Shown to scale are the distortions in the original circle that the wave produces if it carries the  $+$ -polarisation (above) and the  $\times$ -polarisation (below). The motion of each particle can be discovered by comparing it to its original position, shown as the “shadow” circles. In general relativity, there are only two independent polarisations. The ones shown here are orthogonal to one another — notice that individual particles move in orthogonal directions in the two illustrations. These polarisations are transverse to the direction of the wave.

It follows that there are only two independent linear polarizations. It is conventional to take them as the two area-preserving distortions illustrated in Figure 1.1, which are called “+” and “ $\times$ ”. The rotation by  $45^\circ$  from one polarisation to the other makes them orthogonal: notice that for each particle the motion in one diagram is perpendicular to its motion in the other. In the language of quantum field theory, one expects only two independent polarisations for a pure spin-2 massless graviton, because such a particle has only two independent helicity states. But note that, despite this language, observable gravitational waves are not quantum fields: they contain such enormous numbers of “gravitons” ( $10^{80}$  or more for some sources) that they are completely classical.

### Radiation and antenna patterns.

We shall turn in the next section to the way waves are generated by source motions. But again we will not get directional information from our approach. We fill this gap by noting here that, happily, the directions of polarization follow closely the mass motions in the source. Suppose for simplicity that the source consists of two masses moving back and forth along a given line, as if on a spring; then the polarization ellipse of the waves will align its major axis with this line. Thus, two detector masses separated along a direction parallel to the separation of the source masses move back and forth in synchronisation with the source masses, at the same retarded time (*i.e.* allowing for the travel time of the wave from source to detector). It follows that the two oscillating source masses emit no radiation along the direction of the line joining them,

because when seen from this direction they have no transverse motion at all.

It is possible from this information to build up the radiation patterns and antenna patterns of more complicated sources and detectors. For example, a binary star system will emit circularly polarised radiation along its orbital angular momentum axis, since from this direction its mass motions are circular. By contrast, it will emit linearly polarised radiation along directions in the orbital plane, since from these directions the transverse mass motions are simple linear oscillations.

*By measuring the degree of circular polarization in a wave and its orientation, [LISA](#) can determine the angle of inclination of a binary orbit, and even the direction of this inclination projected on the sky (to within a 90° ambiguity).*

This information cannot usually be obtained by conventional observations of binary systems, and is crucial to determining stellar masses. Note also that we see that the frequency of the gravitational radiation from a binary is twice the frequency of the orbital motion, since after half an orbital period the two stars have replaced one another and the mass distribution is the same as at the beginning. (This is true even if the stars have dissimilar masses, at least for the quadrupole radiation described below.)

Similarly, [LISA](#) will be most sensitive to sources located along a line perpendicular to the plane containing its spacecraft, but it will have some sensitivity to sources in its plane.

*As [LISA](#) orbits the Sun, its orientation in space changes (see [Chapter 3](#) and especially [Section 7.5](#)). This produces an amplitude modulation in a signal received from a long-lived source, which gives some information about its direction. Further directional information comes from [LISA](#)'s changing orbital velocity. This results in a Doppler-induced phase modulation that can, for sufficiently high frequencies, give very accurate positions.*

This is similar to the way radio astronomers determine precise pulsar positions using only single radio antennas with very broad antenna patterns. These issues are discussed in detail in [Section 7.5](#).

For frequencies above about 3 mHz, [LISA](#)'s arm length is long enough that it can measure the differences between the arrival times of the gravitational wave at the different corners. This can in principle be used to triangulate positions on the sky, provided the telemetry returns enough information to extract these timing signals. Further study is required to determine whether the added information justifies providing the extra telemetry bandwidth.

### 1.1.3 Generation of gravitational waves

We mentioned above the different approximation methods that are used to decide how much radiation to expect from a given source. The simplest approximation, and the one that is used for most estimates, is the lowest-order post-Newtonian formula, called the “quadrupole formula”. Recall that the quadrupole radiation is the dominant radiation, because conservation of energy and momentum kill off monopole and dipole gravitational radiation. The interested reader can find a derivation of the quadrupole formula, using only the assumptions and mathematical level we have adopted here, in [Reference \[9\]](#).

If we define the second moment integral of the mass distribution of the source to be the integral

$$I_{jk} = \int \varrho x_j x_k d^3x, \quad (1.5)$$

where the integral is over the entire volume of the source, then the standard trace-free quadrupole tensor is

$$Q_{jk} = I_{jk} - \frac{1}{3}I\delta_{jk}, \quad (1.6)$$

where  $I$  is the trace of the moment tensor. (The tensor  $Q$  is sometimes called  $I$  in textbooks. Note that  $I_{jk}$  is not the moment of inertia tensor, despite the notation.) The radiation amplitude is, for a nonrelativistic source at a distance  $r$ ,

$$h = \frac{2G}{c^4} \frac{\ddot{Q}}{r}, \quad (1.7)$$

where we have left off indices because we have not been quantitative about the antenna and radiation patterns. The total luminosity in gravitational waves is given by

$$L_{\text{GW}} = \frac{G}{c^5} \left\langle \sum_{jk} \left( \frac{d^3 Q_{jk}}{dt^3} \right)^2 \right\rangle, \quad (1.8)$$

where the angle brackets  $\langle \dots \rangle$  denote an average over one cycle of the motion of the source. In this formula we have put in all the correct factors and indices.

There are simple order-of-magnitude approximations for these formulas, which are both easy to use and instructive to look at. For example, one can write

$$\ddot{I}_{jk} = \frac{d^2}{dt^2} \int \varrho x_j x_k d^3x \sim \int \varrho v_j v_k d^3x.$$

Now, the quantity  $v_j v_k$  will, by the virial theorem, be less than or of the order of the internal gravitational potential  $\Phi_{\text{int}}$ . Combining this with Equation 1.7 gives

$$h \leq \frac{G}{c^4} \frac{\Phi_{\text{int}}}{r} \int \varrho d^3x = \frac{\Phi_{\text{ext}}}{c^2} \frac{\Phi_{\text{int}}}{c^2}, \quad (1.9)$$

where  $\Phi_{\text{ext}}$  is the external gravitational potential of the source at the observer's position,  $GM/r$ .

This simple expression provides an upper bound. It is attained for binary systems where all the mass is participating in asymmetrical motions. The exact formula was first derived by Peters and Mathews [10]. For a circular orbit the radiation is a sinusoid whose maximum amplitude can be expressed in terms of the frequency of the emitted waves and the masses of the stars by

$$h_0 = 1.5 \times 10^{-21} \left( \frac{f}{10^{-3} \text{Hz}} \right)^{2/3} \left( \frac{r}{1 \text{ kpc}} \right)^{-1} \left( \frac{\mathcal{M}}{M_\odot} \right)^{5/3}, \quad (1.10)$$

where  $f$  is the gravitational wave frequency (twice the binary orbital frequency),  $r$  is the distance from source to detector, and  $\mathcal{M}$  is the so-called “chirp mass”, defined in terms of the two stellar masses  $M_1$  and  $M_2$  by

$$\mathcal{M} = \frac{(M_1 M_2)^{3/5}}{(M_1 + M_2)^{1/5}}. \quad (1.11)$$

Equation 1.10 can be derived, to within factors of order unity, by eliminating the orbital radius from Equation 1.9 in favour of the orbital frequency and the masses using Kepler's orbit equation. For equal-mass binaries, for example, one uses

$$\omega_{\text{orbit}} = \left( \frac{GM_T}{d^3} \right)^{1/2}, \quad (1.12)$$

where  $M_T$  is the total mass and  $d$  the orbital diameter. Eccentric binaries emit higher-amplitude radiation with, of course, a more complicated time-dependence.

The most important use of the luminosity formula is to discover the effect of the loss of energy on the radiating system. A binary system consisting of two equal masses  $M$  in a circular orbit of radius  $R$  emits radiation with angular frequency  $\omega = (GM/R^3)^{1/2}$ , amplitude  $h \sim (GM/rc^2)(GM/Rc^2)$  and luminosity  $L_{\text{GW}} \sim GM^2 R^4 \omega^6 / 5c^5$ . The time-scale for the orbit to change due to the loss of energy is the orbital energy  $|E| \sim \frac{1}{2}MR^2\omega^2$  divided by the luminosity  $L_{\text{GW}}$ :

$$\begin{aligned} \tau_{\text{GW}} = \frac{|E|}{L_{\text{GW}}} &\sim \frac{5c^5}{2GMR^2\omega^4} \\ &\sim \frac{5c^5}{2G^3} \frac{R^4}{M^3}, \end{aligned} \quad (1.13)$$

$$\sim \frac{5}{2\omega} \left( \frac{c^3}{GM\omega} \right)^{5/3}, \quad (1.14)$$

where in the last two equations we have alternately eliminated  $\omega$  or  $R$ , respectively, using the orbit equation.

Now we can draw a very important conclusion:

*LISA can measure distances to binaries whose orbits “chirp”, i.e. which change frequency through gravitational radiation emission during the observation time.*

If we combine Equation 1.10 with Equation 1.14, we find

$$h \sim \frac{c}{\omega r} \frac{(GM\omega)^{5/3}}{c^5} \sim \frac{c}{\omega^2 \tau_{\text{GW}} r}. \quad (1.15)$$

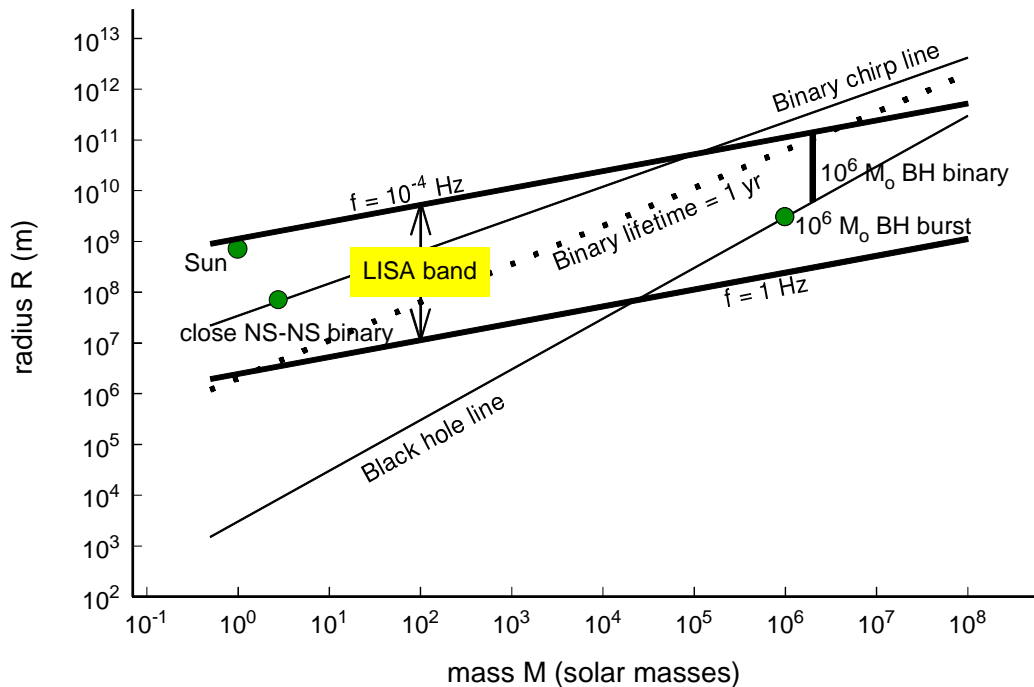
Now, since  $\omega$  and  $\tau_{\text{GW}}$  are observable, a determination of the amplitude  $h$  is enough to determine the distance  $r$  to the binary system. This is a powerful way to determine distances to supermassive black-hole binaries.

Figure 1.2 summarises the content of the equations of this section in the *LISA* context.

### 1.1.4 Other theories of gravity

When using gravitational wave observations to test general relativity, it is important to have an idea of what alternative predictions are possible. While general relativity has successfully passed every experimental and observational test so far [7, 11], it is clear that it must fail on some level, since it is not compatible with quantum mechanics. Direct quantum effects will not be observable in such powerful gravitational waves, but side-effects of quantizing general relativity may be. For example, if by unifying gravity with the other interactions one needs to introduce massless gravitational scalar fields, these can themselves produce observable effects. One should, therefore, be alert to the possibility that some of the sources will show evidence that gravity is governed by a scalar-tensor theory.

Black holes are the same in scalar-tensor theories as in general relativity: the “no-hair” theorem demonstrates that the scalar field is radiated away when the holes are formed. So binary black holes are unlikely to show such effects, but neutron-star orbits around black holes might, as could gravitational waves emitted during the formation of a massive black hole. Not only would the dynamics in such a theory be different, but so would the radiation: scalar waves are



**Figure 1.2 Gravitational dynamics.** This diagram shows the wide range of masses and radii of sources whose natural dynamical frequency is in the *LISA* band. The two heavy lines delineate the outer limits of sources accessible from space, at gravitational wave frequencies of  $10^{-4}$  Hz and 1 Hz. They follow the formula  $f_{\text{GW}} = (GM/R^3)^{1/2}/\pi$ .

The “black hole line” follows  $R = 2GM/c^2$ ; if general relativity is correct, there are no systems below it. The “chirp line” shows the upper limit on binary systems whose orbital frequencies change (due to gravitational-wave energy emission) by a measurable amount ( $3 \times 10^{-8}$  Hz) in one year: any circular binary of total mass  $M$  and orbital separation  $R$  that lies below this line will “chirp” in *LISA*’s observations, allowing *LISA* to determine its distance. (See text.) The curve labelled “binary lifetime = 1 yr” is the upper limit on binaries that chirp so strongly that they coalesce during a *LISA* observation. Any binaries formed of black holes above  $10^6 M_\odot$  that are in the *LISA* band will coalesce as *LISA* observes them.

At the lower-mass end of *LISA*’s range we show the Sun and the shortest-period close neutron-star binary we expect *LISA* to see, which is on the chirp line but not the 1-year lifetime line. Near the upper mass limit we illustrate a  $10^6 M_\odot$  black hole formation burst and a  $10^6 M_\odot$  black hole binary chirp (vertical line).

Ground-based detectors operate only in the mass range between the  $f = 1$  Hz line and the black-hole line.

longitudinally polarised, not transverse, and they would show a distinctive antenna pattern as *LISA* rotates during an observation. Perhaps the best chance to detect scalar radiation is by determining the polarization pattern of white-dwarf binaries, which ought to be abundant; some of them may have signal-to-noise ratios in excess of 1000.



## 1.2 Low-frequency sources of gravitational radiation

In this section we survey some of the low-frequency sources that current astrophysical theory predicts and discuss the information that is likely to come from observations of them. The expected amplitudes will be compared with the predicted noise characteristics of *LISA*. The details of how these noise characteristics are estimated will be given in Chapter 4, which also discusses how the information can be extracted from the signals.

The specific types of sources that *LISA* will see or may see signals from are discussed in Sections 1.2.1 and 1.2.2. However, before discussing the sources, we need to provide some information on the threshold sensitivity expected for the *LISA* antenna. This will be done using the example of the numerous expected signals from compact binaries in our galaxy, as shown in Figure 1.3.

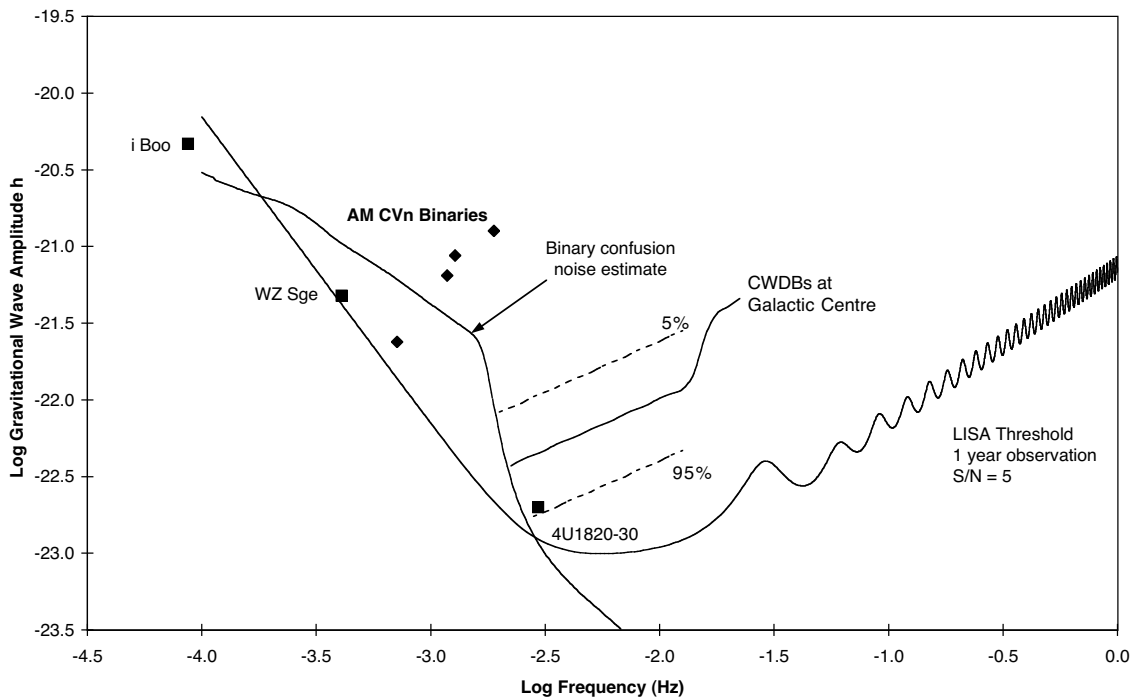


**Figure 1.3** The signal levels and frequencies are given for a few known galactic sources, along with the expected *LISA* threshold sensitivity and an estimate of the binary confusion noise level. In addition, the range of levels for 90 % of the expected thousands of resolvable close white dwarf binary signals from our galaxy is shown.

Later figures in this section will show the possible strength of signals from extragalactic sources. The search for and detailed study of such sources, along with unprecedented tests of gravitational theory under extreme condition, are the main objectives of the *LISA* mission. Most of them involve massive black holes. If massive black holes are indeed present in most galactic nuclei, it seems likely that signals giving information about them will be observable by *LISA* out to cosmological distances.

The solid and roughly U-shaped curve shown in Figure 1.3 is the expected threshold sensitivity over the main observing range for *LISA*, which extends from  $10^{-4}$  Hz to 1 Hz. A 1-year-long observing period is assumed. This is a reasonable length of time, but not the maximum: the nominal mission lifetime is 2 yr, but in principle it might last as long as a decade. The duration of an observation affects, of course, the effective noise in the observation, provided that the level



of spurious signals is sufficiently low. For an observation of length  $T$ , the frequency resolution is just  $1/T$ , and so a longer observation needs to fight against the noise in a smaller bandwidth. Since noise power is proportional to bandwidth, the *rms* noise amplitude is proportional to the square root of the bandwidth, and the result is that the noise at any frequency falls as  $1/\sqrt{T}$ . In a 1-year observation, the frequency resolution is  $3 \times 10^{-8}$  Hz, and there are  $(1 \text{ Hz})/(3 \times 10^{-8} \text{ Hz}) = 3 \times 10^7$  resolvable frequencies in the [LISA](#) band.

For expected signals due to binaries in our galaxy, the *intrinsic* wave amplitude  $h$  is essentially constant during a 1-year observation. Such sources are placed in the diagram to show this  $h$  on the vertical scale. But because of [LISA](#)'s motion, [LISA](#) almost never responds to this maximum amplitude; rather, the full signal-to-noise ratio [SNR](#) over a year is lower by a factor which depends on the exact position of the source relative to [LISA](#)'s orbit. Since the *rms* antenna sensitivity for [LISA](#) averaged over a year is nearly isotropic [12], we can approximate this effect by using the reduction factor averaged over the entire sky, which is  $1/\sqrt{5}$  [6]. This means that, if a source lies above the  $1\text{-}\sigma$  noise level by a certain factor  $s$ , the expected [SNR](#) will be typically  $s/\sqrt{5}$ . To be specific, the threshold sensitivity curve in Figure 1.3 is drawn to correspond to a [SNR](#) of 5 in a 1-year observation. (Accordingly, it is drawn at a factor of  $5\sqrt{5} \approx 11$  above the 1-year,  $1\text{-}\sigma$  noise level.) This [SNR](#) of 5 is a *confidence level*: for a 1-year observation, the probability that Gaussian noise will fluctuate to mimic a source at 5 standard deviations in the [LISA](#) search for sources over the whole sky is less than  $10^{-5}$ , so one can be confident that any source above this threshold curve can be reliably detected. *To estimate the expected [SNR](#) for any long-lived source in the diagram, one multiplies the factor by which it exceeds the threshold curve by the threshold level of 5.* The threshold curve is drawn on the assumption that the dominant noise is the  $1\text{-}\sigma$  instrumental noise level. If any of the random gravitational-wave backgrounds described above are larger, then the threshold must likewise go up, remaining a factor of  $5\sqrt{5}$  above the *rms* gravitational-wave noise.

It is important when looking at Figure 1.3 to realise that even sources near the threshold curve will be strongly detected: the X-ray binary 4U1820-30 is only a factor of 2 above the curve, but that implies an expected [SNR](#) in amplitude of 10, or in power of 100. Any observation by [LISA](#) above the threshold curve will not only be a detection: there will be enough signal to extract other information as well, and that will be important in our discussion below.

Note also that sources can be detected below the threshold curve if we have other information about them. For example, if a binary system is already known well enough to determine its orbital period and position, then the confidence level can be lowered to something like  $3\sigma$ , where the probability would still be less than  $10^{-4}$  that (on Gaussian statistics) the noise was responsible for the observation.

The phase-modulation of a signal produced by [LISA](#)'s orbital motion will require that, in the data analysis, a compensating correction be applied to the data in order to give a signal its expected [SNR](#) as indicated in the diagram. This correction will depend on the assumed location of the source on the sky. At 0.1 Hz, there may be as many as  $10^5$  distinguishable locations, and so there are  $10^5$  different chances for noise to mimic a source at any level. This factor has been taken into account in adopting the threshold level of 5 standard deviations in the diagram: the chances that Gaussian noise will produce a false alarm anywhere in these different locations at this level is still less than  $10^{-4}$ . The data analysis will of course test whether the noise is Gaussian, and may then set the threshold differently if necessary.

In Chapter 4 we describe in some detail how [LISA](#)'s sensitivity is calculated, but here it is appropriate to note where its main features come from. The best sensitivity is between 3 and 10 mHz. In this range the sensitivity is limited by photon shot noise plus a combination of other noise sources that are assumed for simplicity to be roughly white, including variations in the

beam pointing. Above 10 mHz, *LISA*'s sensitivity begins to get worse because the wavelength of the gravitational wave becomes shorter than  $2\pi$  times *LISA*'s arm-length of  $5 \times 10^6$  km. For such waves, light does not have time to go up and back along a *LISA* arm before the wave amplitude changes sign and begins to reverse its action on the arm. This increasing cancellation, when averaged over source direction, accounts for the rising threshold sensitivity at high frequencies.

At low frequencies, the noise curve rises because of the effect of spurious forces on the proof masses. The acceleration noise error budget is taken to be white from 0.1 to 30 mHz, so that the contribution to the instrumental noise in detecting gravitational wave signals varies as the inverse square of the frequency. At lower frequencies  $f$ , it is intended to keep the acceleration from rising faster than  $\sqrt{[0.1 \text{ mHz}/f]}$ , if possible.

The sensitivities shown in Figure 1.3 are *conservative*, for three reasons:

1. The error budgets (Section 4.2) have been calculated realistically. Allowances are included for all of the substantial error sources that have been thought of since early studies of drag-free systems and since the first one was flown over 25 years ago. In most cases, except for shot noise, the error allowance is considerably larger than the expected size of the error and is more like an approximate upper limit. This means that the performance of *LISA* could in principle turn out to be significantly better than shown.
2. *LISA* is likely to have a significantly longer lifetime than one year. The mission is planned for 2 years, but it could last up to 10 years without exhausting on-board supplies. As described above, its sensitivity to long-lived sources improves as the square root of the mission duration. Not only would this lower the noise and threshold curves, but it would also lower any gravitational-wave noise from white-dwarf binaries, since *LISA* would resolve more of those sources and remove them from this confusion-limited background.
3. *LISA* will actually have three arms, not two. *LISA*'s third arm provides necessary redundancy for the success of the mission, but it also has an important scientific benefit: it allows *LISA* to detect two distinct gravitational wave observables, which can be thought of as formed from the signals of two different interferometers, with one arm common to both. This improves both the sensitivity of *LISA* and its ability to measure parameters, particularly the polarisation of the waves. The sensitivity shown in Figure 1.3 is only for a single interferometer.

The two interferometers are not perfectly orthogonal, since they are not oriented at  $45^\circ$  to each other. But they are oriented differently enough so that two distinct, linearly independent gravitational-wave observables can be formed, with similar signal-to-noise ratios. One is the difference in arm length for the two arms of the “primary” interferometer. The other is the length of the third arm minus the average of the lengths of the other two arms.

The fact that the two interferometers share a common arm means that they will have common noise. Most of the signals in Figure 1.3 have signal-to-noise ratios that are so large that the likelihood that the signal is caused by noise will be negligible; in this case, the information from the two interferometers can be used to obtain extra polarization and direction information. This will be particularly helpful for observations of relatively short-lived sources, such as the coalescences of  $10^6 M_\odot$  black holes, where the signal does not last long enough to take full advantage of the amplitude and frequency modulation produced by *LISA*'s orbital motion.

For signals nearer the noise limit, the second observable will still provide some increase in the confidence of detection. Using three arms could increase the effective signal-to-noise ratio by perhaps 20%. And for stochastic backgrounds, the third arm will help to discriminate such backgrounds as produced by binaries and cosmological effects from anomalous instrumental noise. This will be considered in detail in Section 7.5 below.

The frequency of radiation emitted by a source of mass  $M$  and size  $R$  will normally be of the same order as its natural gravitational dynamical frequency, as in Equation 1.12, recalling that the gravitational wave frequency is twice the orbital frequency<sup>1</sup>:

$$f_{\text{GW}} = \frac{1}{2\pi} \omega_{\text{GW}} = \frac{1}{\pi} \left( \frac{GM}{R^3} \right)^{1/2} = 3.7 \times 10^{-3} \left( \frac{M}{1 M_{\odot}} \right)^{1/2} \left( \frac{R}{1 \times 10^8 \text{ m}} \right)^{-3/2} \text{ Hz.} \quad (1.16)$$

Therefore, as we can see in Figure 1.2, a source will radiate above 0.1 mHz (the main *LISA* band) if either (1) it is a stellar system (solar mass) with a dynamical size of order  $10^9$  m, about 0.01 AU or  $1.4 R_{\odot}$ ; or (2) it is supermassive, such as a pair of  $5 \times 10^7 M_{\odot}$  black holes, with a separation of about  $5 \times 10^{11}$  m. Since this separation is about seven times the gravitational radius of a  $5 \times 10^7 M_{\odot}$  black hole, detection of signals from higher mass binaries will require observation at frequencies substantially below 0.1 mHz. Intermediate mass binaries, such as binaries of 300–1000  $M_{\odot}$  black holes, may well exist or have existed in many galactic nuclei, and their coalescences could be observed from cosmological distances.

Stellar-mass sources are weaker emitters of radiation, so they will usually be seen only in the Galaxy. Signals involving massive black holes are much stronger, and can be seen from very far away. So we discuss discrete sources in our Galaxy first, and then discrete sources in other galaxies. After that we go on to discuss primordial gravitational waves.

Oscillations of the Sun disturb its Newtonian gravitational field, and the tidal effects of this disturbance can affect *LISA* in the same way as gravitational waves. Estimates of the possible effects of solar  $g$ -mode oscillations on *LISA* indicate that they might be observable at frequencies near 0.1 mHz if they are close to the limits set by *SOHO* observations.

### 1.2.1 Galactic binary systems

After Mironowskii's [13] early and pioneering work on gravitational radiation from W UMa stars, there was a delay of nearly two decades before other studies appeared which estimated the gravitational radiation luminosity due to various types of binary stars in the galaxy. Iben [14] first described the expected signal level from close white dwarf binaries, and Hils *et al.* [15] presented a brief summary of the later results of Hils, Bender, and Webbink [16], in which other types of binaries also were included. Lipunov and Postnov [17] modelled the evolution of galactic low- and moderate-mass systems by Monte Carlo methods and gave the expected signal strengths, and Lipunov, Postnov, and Prokhorov [18] extended their results to include white dwarf and neutron star binaries plus the background due to other galaxies. Evans, Iben, and Smarr [19] gave detailed calculations on white dwarf binaries. The general picture which has developed is as follows. After an initial period of observations such as 1 yr, most frequency bins below some critical frequency near 1 mHz will contain signals from more than one galactic binary. At higher frequencies, most of the signals from individual binaries can be resolved and fit to determine the source amplitude, phase, and direction. However, the unresolved sources at lower frequencies form a confusion-limited background, which makes observations of individual sources difficult, unless they are particularly strong.

The different types of galactic binaries will be discussed in the following sections. *LISA*'s observations of these systems would have interest both for fundamental physics and for astrophysics. Because *LISA* is a linearly polarised detector that rotates with a 1-year period, it can measure not only the amplitude but also the polarisation of the gravitational waves. If known systems

<sup>1</sup>An exception is a system which is emitting much less radiation than the upper limit in Equation 1.9, such as a slowly rotating neutron star with a small lump on it. We do not expect any such sources to be prominent at low frequencies.

are not seen, or seen with amplitudes or polarisations not predicted by general relativity, then general relativity must be wrong. If they are seen, the polarisation measurement reveals the angle of inclination of the orbit and the orientation of the plane of the orbit on the sky. The inclination angle is usually the crucial missing datum when one tries to infer stellar masses from optical observations. With it astronomers will have more secure models of these systems and will in addition be able to estimate the distance to the binary from the gravitational-wave amplitude and the estimated masses. The orientation angle of the plane of the orbit will be interesting if other orientation-dependent phenomena are observed, such as jets or optical/radio/X-ray polarisation. The large majority of galactic binaries will not be known in advance, but can be located on the sky from the frequency modulation that the motion of [LISA](#) produces in their signals, and to some extent also from the amplitude modulation. This is discussed in Section [7.5](#).

### Neutron star binaries.

The best-known two-neutron-star ([NS-NS](#)) binary is the famous Hulse-Taylor binary pulsar PSR B1913+16, discovered in 1975 [[20](#), [21](#)]. Its orbital period of 7.68 hrs places it below the [LISA](#) band, but it is important to [LISA](#) as the best-studied member of a class of binaries that should be important sources. The Hulse-Taylor binary is decaying due to the loss of orbital energy to gravitational waves at exactly the rate predicted by general relativity [[8](#)]. PSR B1913+16 will coalesce to a single star in  $3 \times 10^8$  years. Two other very similar systems are known. By considering the selection effects in the detection of such systems, a recent detailed study [[22](#)] arrived at a conservative estimate of  $N \sim 10^3$  such systems in the Galaxy, formed at a rate of about one per  $10^5$  yr.

Theoretical calculations of binary evolution give a wide variety of estimates of the number of such systems. Most of them [[23](#), [24](#), [25](#)] give rather higher rates than the observational estimates. It is possible, therefore, that observations give a lower bound on the number of such systems, but that some fraction of the population does not turn up in pulsar surveys. It may be that not all neutron stars turn on as pulsars, or even that binaries like PSR B1913+16 may be merely the long-period tail of a distribution of binaries that are formed with periods as short as an hour and which decay so rapidly through the emission of gravitational radiation that one would not expect to see any such systems in pulsar surveys. In this case the formation rate could be as high as one per 3000 yr, leading to a total population of  $N \sim 3 \times 10^6$  systems. Moreover, recent observations of the binary pulsar PSR J1012+5307, whose companion is a white dwarf that is much younger than the apparent age of the pulsar as estimated from its spin-down rate, have suggested that millisecond pulsar spindown may overestimate the pulsar's true age [[26](#)]. Since binary pulsars tend to be millisecond pulsars, this could also raise the binary neutron-star birthrate. For a recent overview of this subject, see [[27](#)].

Another indication of this population comes from gamma-ray bursts [[28](#)]. From optical identifications of some recent bursts, it is now known that these events occur at immense distances [[29](#)]. Although the events are not understood in detail, it seems that they could involve coalescences of neutron stars with other neutron stars or with black holes. Such events occur at the end of the gravitational-wave evolution of systems in the population of binaries we are considering here. Estimates of the size of the population from observations of gamma-ray bursts are consistent with the observational limits mentioned above. For example, the estimates above suggest that there could be of order  $10^4$  neutron-star/neutron-star coalescences per year out to a redshift of  $z = 1$ . About 1000 observable bursts are thought to occur each year, but it seems probable that bursts are beamed, so that the two rates would be consistent for a 10% beaming factor. If bursts are spread to greater distances (one has been seen beyond  $z = 3$ ), the rates are not consistent unless the beams are very narrow, or unless the more distant bursts come from neutron-star/black-hole mergers (see the next section), which could indeed emit stronger bursts,

according to popular models.

Progress with ground-based gravitational wave detectors makes it likely that [LIGO](#) and [VIRGO](#) will have observed a number of the rare coalescence events by the time [LISA](#) is launched. In this case we will have a much better idea of the rate to expect. But only gravitational wave observations by [LISA](#) would provide a complete census of this population in our Galaxy. This should provide a springboard for further advances in binary evolution theory.

### **Black hole binaries in the Galaxy.**

The evolutionary scenario that is expected to lead to [NS-NS](#) binaries will also form binaries of a neutron star and a black hole ([NS-BH](#)) in some cases. In fact, the formation of a black hole has much less probability of disrupting a binary system, since less mass is lost. For this reason, Narayan, Piran, and Shemi [30] estimated that there could be almost as many neutron star – black hole binaries as there are neutron star – neutron star binaries. Tutukov and Yungelson [23], considering the process in more detail, estimate that there could be about 10 % as many [NS-BH](#) binaries as [NS-NS](#) binaries. However, these estimates are very sensitive to assumptions about mass loss in giant stars during their pre-supernova evolution. If winds are very high, close binaries containing black holes may not form at all [31].

Binaries consisting of two black holes are also predicted in scenarios that lead to neutron-star/black-hole binaries, and it is possible that there are a handful of them in the Galaxy. A prediction of [BH-BH](#) binaries formed in globular clusters also has been made recently [32]. The Virgo cluster has many more galaxies, so the shortest-period one will be faster and more powerful than expected ones in the Galaxy. If the higher birthrate estimates are correct, then the shortest-period [BH-BH](#) binary expected in Virgo might be just detectable.

Unless the binary system chirps during the [LISA](#) observation (*i.e.* unless it lies below the chirp line in Figure 1.2), then gravitational wave observations alone will not normally distinguish between [NS-NS](#) binaries and [BH-BH](#) binaries of the same orbital period, except statistically. The black-hole binaries radiate more strongly because of their larger mass, and so they will be detectable at greater distances. Again, continued work on gamma-ray bursts and future observations by [LIGO](#) and [VIRGO](#) may give us a clearer idea of the number of systems [LISA](#) might observe. But only [LISA](#) can reveal the Galaxy’s black-hole binary population. Its spatial distribution would be a clue to the origin of the population.

### **X-ray and common-envelope binaries.**

An important stage of the evolution of close binary systems is the X-ray binary phase, where one of the stars has become compact (a neutron star or black hole) and the other feeds gas to it. At the end of this stage, the compact star can enter the envelope of its companion and disappear from view in X-rays, while remaining a strong emitter of gravitational waves. The orbits of such systems are larger than the ultimate orbits if they leave behind compact-object binary systems, so most will be below the main [LISA](#) frequency range. But there should be a number of common-envelope and X-ray systems that are in the [LISA](#) range. Indeed, one low-mass X-ray binary, 4U1820-30, is so well-studied that it is one of the most secure of the known binary sources: its orbital period, companion mass, and distance are believed to be very reliable. Its expected signal is shown in Figure 1.3.

### **Close white dwarf binaries.**

The situation for close white dwarf binaries ([CWDBs](#)) unfortunately is rather more complicated than for neutron-star or black-hole binaries. The normal stellar evolution calculations for close binaries indicate that such systems pass through at least one and sometimes two stages of common envelope evolution before [CWDBs](#) are formed. However, it is not known how to calculate



the loss in angular momentum during the common evolution stages, and thus the calculated space density of CWDBs with periods in the range of interest for LISA is more like an upper estimate than an expected value. These estimates suggest that LISA will suffer an embarrassment of riches from this population, so many systems that they will not be resolvable by LISA below a few millihertz frequency, and they will obscure other, rarer systems.

Until recently, searches for this type of binary with orbital periods less than a day have been unsuccessful, but the total number of known non-interacting CWDBs with periods longer than 1 day jumped not long ago from two to six, and two additional ones with periods of 3.47 hr and about 4 hr have been found [33, 34]. These last two have lifetimes before merger of roughly a quarter of the Hubble time, and so further analysis and observations may lead soon to better understanding of the binary population in the LISA range [35].

In view of the theoretical and observational uncertainties, the detailed estimates of Hils *et al.* [16] of the gravitational wave background that could be expected from this population used a space density for non-interacting CWDBs which was a factor 10 less than the evolutionary rough limit (see also [36, 27, 37]). These binaries give the dominant contribution to the gravitational-wave confusion noise level, which is shown in Figure 1.3 based on the factor 10 assumed reduction in space density. The part of the curve above about 3 mHz, where the level has dropped off sharply, is due to the estimated integrated effect of CWDBs in all other galaxies (see also [38, 39]. It should be stressed that the actual confusion noise level might be significantly higher or lower than the level shown. LISA will be able to distinguish the galactic binary background from a cosmological background or instrumental noise because there will be a large number of “outliers” — binaries at high enough frequencies to be individually resolvable. By studying the resolvable systems, one should be able to predict what the background level is, and infer from it what the space density of CWDBs is in other parts of the Galaxy.

The strengths of the signals from the resolvable CWDBs at the galactic centre are shown by the solid curve with that label in Figure 1.3. The curve rises with respect to a constant slope curve above 15 mHz as the lighter CWDBs consisting of two He white dwarfs coalesce, and only the heavier ones consisting of two carbon-oxygen (CO) white dwarfs are left. The dashed curve labeled 5 % gives the rms strength for CWDBs at a distance from the Earth such that only 5 % of those in the galaxy are closer, and the 95 % curve is defined in a similar way. Thus 90 % of the galactic CWDBs give signal strengths between the two dashed curves. Based on the CWDB space density assumed in calculating the binary confusion noise estimate, roughly 5000 CWDBs would be resolvable at frequencies above about 3 mHz.

### Helium cataclysmic variables.

These are systems where a low-mass helium star fills its Roche lobe and transfers mass onto a more massive white dwarf [40]. Such systems have close orbits that place them in the LISA frequency band. Six HeCVs within about 100 pc of the Earth are known, and all have likely gravitational-wave frequencies near 1 mHz. The He star in these cases has been reduced by mass transfer to a few hundredths of a solar mass, so that the strength of the signals is quite low. These sources frequently are called AM CVn binaries, and also interacting white dwarf binaries, even though the He star may be only semi-degenerate. The estimated signal strengths for the four which are best understood (AM CVn, V803 Cen, CP Eri, and GP Com) are shown in Figure 1.3 as the unlabelled squares at and above 1 mHz. The frequencies are known for AM CVn and GP Com, and are probable for the other two.

The initial conditions and evolutionary paths that produce HeCVs are not well known. One plausible assumption [41] is that they evolved through a stage where a CO white dwarf had formed and the secondary was burning He when it made Roche lobe contact. The orbital period

would have shortened rapidly due to gravitational radiation until it reached a minimum of about 600 s when the secondary mass was reduced to roughly  $0.2 M_{\odot}$ . Later evolution due mainly to mass transfer would be to longer periods, and the rate of period change would become slower as the secondary mass decreased.

Hils [42] has estimated the HeCV signal strength under the above scenario. Because of the rapid evolution of these binaries before they reach the AMCVn stage with low secondary masses, and the weakness of the signals from then on, the resulting contributions to the *rms* binary signal strength as a function of frequency are fairly small. However, the estimated number of such sources in the frequency range of interest is large, so they fill many of the frequency bins that otherwise would be open between roughly 1 and 3 mHz.

Another estimate for the HeCV space density based on a different assumption about the nature of their progenitors has been given by Tutukov and Yungelson [43]. It considers the helium star secondary to already be degenerate or semi-degenerate at the time of Roche lobe contact. The resulting estimated space density of AMCVn binaries is much higher than the estimate of Warner [40]. Hils and Bender [44] have recently made a new estimate based on the Tutukov-and-Yungelson scenario, but with 10 % of their calculated space density. The results are quite similar to those from [42]. Until the likelihood of the different assumptions is better understood, the uncertainty in the contribution of HeCVs to the confusion noise should be remembered. However, they will not contribute much at frequencies above about 3 mHz in any of the assumed scenarios. A curve for the confusion noise including the HeCV contribution [42] as well as those from CWDBs and other binaries is given in Figure 1.3 and in later figures.

### Normal detached binaries, contact binaries, and cataclysmic variable binaries.

These three types of binaries have been discussed in some detail [16]. By normal detached binaries we mean binaries consisting of normal, “unevolved” stars whose Roche lobes are not in contact. “Unevolved”, as used here, means that the stars have not yet reached a giant phase or started helium burning. Contact binaries are the WUMa binaries studied first by Mironowskii [13], which are two unevolved stars with their Roche lobes in contact. A cataclysmic variable binary consist of a white dwarf which accretes mass spilling over from a low mass hydrogen-burning secondary.

Some individual binaries of each of these types will be close enough and at high enough frequency, so their signals will be resolvable. This includes the normal detached binary  $\iota$  Boo and the cataclysmic variable WZ Sge, which are the two lowest-frequency circles shown in Figure 1.3. The expected confusion limits for the WUMa and cataclysmic variables are comparable with the LISA noise budget level over the frequency range from 0.1 to 0.4 mHz. Thus, if the spectral amplitudes for the CWDBs and helium cataclysmics should turn out to be low enough, the abundance of these other types of binaries could be determined.

#### 1.2.2 Massive black holes in distant galaxies

It is clear from the preceding sections that LISA will provide valuable information concerning the populations of various types of binaries in different parts of our galaxy. However, the most exciting scientific objectives for LISA involve the search for and detailed study of signals from sources that contain massive black holes (MBHs).

The most spectacular event involving MBHs will be the coalescence of MBH-MBH binaries. Because the signal has the unique signature of a “chirp” and can be followed over many months, and because it is intrinsically very strong, LISA can recognise MBH coalescence events in its frequency band almost anywhere in the Universe they occur. If LISA sees even one such event,

it would confirm beyond doubt the existence of MBHs. From the fundamental physics point of view, the waveforms of signals from such objects at times near coalescence can provide extremely sensitive tests of general relativity for non-Newtonian conditions [45]. Because the phase of the signals over thousands of cycles or longer can be tracked accurately for even fairly weak signals, very minor errors in the predictions of the theory would be detectable [46].

From the astrophysics point of view, sources involving MBHs can provide unique new information on the formation, numbers, mass distribution, and surroundings of MBHs. They also may well provide information on the formation of structure in the universe.

Astronomers invoke MBHs to explain a number of phenomena, particularly quasars and active galactic nuclei. The most well-known cases involve MBHs of masses roughly  $10^8 - 10^{10} M_\odot$ . LISA is sensitive mainly to lower masses, which may be considerably more abundant.

The key question for LISA is to estimate the likely event rate (see e.g. [47] and [48]).

### Identification and abundance of massive black holes.

The initial arguments for the existence of MBHs in quasars and active galactic nuclei were theoretical: there seemed to be no other way of explaining the extremely high and rapidly varying luminosities that were observed in the optical and radio bands. Now, however, direct observational evidence is compelling. For example, Hubble Space Telescope observations of M87 revealed a central brightness cusp and large asymmetric Doppler shifts, indicating a BH mass of order  $3 \times 10^9 M_\odot$  [49, 50]. X-ray observations can see gas much closer to the MBH, and the ASCA satellite provided remarkable evidence that seems definitive. Observing the active galaxy MCG-6-30-15, it has detected an iron X-ray line that is Doppler-broadened by velocities of order  $0.3c$  and that is strongly redshifted, indicating that the radiation is coming from within 3 to 10 Schwarzschild radii of the MBH at the galactic centre [51]. The measured radial distances and Doppler shifts for H<sub>2</sub>O masers in orbit around the centre of NGC 4258 demonstrate the presence of a mass of  $3.6 \times 10^7 M_\odot$  in a region less than 0.13 pc in radius [52].

Evidence for smaller MBHs in the main LISA mass range is also strong. Recent near-IR measurements clearly indicate a  $2.6 \times 10^6 M_\odot$  black hole at the centre of our own galaxy [53, 54, 55]. Even smaller galaxies have them: HST and ground-based observations of M32 [56] imply that this, a nearby dwarf elliptical, a satellite of the Andromeda galaxy M31, contains a  $2.8 \times 10^6 M_\odot$  black hole at its centre. Indeed, M31 itself contains a black hole of mass  $3 \times 10^7 M_\odot$ .

Observational evidence for black holes of about the expected size is turning up in every galaxy that has been studied with enough sensitivity to see them, which restricts the evidence mainly to nearby galaxies. Confident identifications include, besides the ones mentioned above: NGC 3115 ( $2 \times 10^9 M_\odot$ ); M104 ( $5 \times 10^8 M_\odot$ ); NGC 4261 ( $52 \times 10^8 M_\odot$ ); M106 ( $3.6 \times 10^7 M_\odot$ ); and M51 ( $3 \times 10^6 M_\odot$ ). The size of the black hole is reasonable close to proportional to the mass of the bulge of the galaxy, and even more closely related to the velocities of the stars in the bulge [57, 58]. For example, limits below  $10^5 M_\odot$  now exist for MBHs in the Local Group dwarf galaxies M33 and NGC 205. See the articles by Kormendy & Richstone [57] and by Rees [59, 60] for reviews and summaries.

What is particularly important for LISA is that massive black holes must be remarkably abundant, since all the confident black-hole detections are in local galaxies. When the surveys are continued to larger distances, the evidence remains strong, within the limits of the available resolution of the observations. Two recent HST surveys bear this out. Of about 50 sample galaxies outside the Local Group in two studies [61, 62], *not a single one showed a central region that is constant in surface brightness*. Instead, 70 % of the galaxies in the first study showed light profiles similar to the cusps generated by central MBHs, with inferred MBH masses of roughly 0.1 % to a few % of the galaxy core mass. And the second study similarly concluded that the



cores of many galaxies appear to be similar to that of M32, with its modest-mass MBH.

### Formation of massive black holes.

There is still major uncertainty about how MBHs form, although a great deal has been written on this subject. One approach taken by Quinlan and Shapiro [63] is to start from an assumed dense cluster of stars in a galactic nucleus and follow the build-up of  $100 M_{\odot}$  or larger seed MBHs by collisions. The further growth to a MBH would then be mainly by accretion of gas made available to the hole in a number of ways. If the seed MBHs grow to  $500 M_{\odot}$  before they coalesce with each other, these coalescences would give signals observable by LISA out to a redshift of  $z = 5$ . Provided that roughly 10 or more such coalescences occurred per galaxy now having a MBH at its centre, the annual number of such events observable by LISA might be substantial. However, the largest seed may grow sufficiently faster than the others so that it runs away [64] before the others are large enough to give observable signals.

A very different view concerning the formation of MBHs has been presented in a number of papers (see e.g. [65, 59, 60]). In this view, fragmentation and star formation in a massive and dense gas cloud at a young galactic center will stop when the opacity becomes high, and the angular momentum loss will be rapid. The gas will either form a supermassive star, which evolves rapidly to a MBH, or collapse directly to a MBH.

In the paper by Haehnelt and Rees [65], they state that if a density concentration of the order of  $10^8 M_{\odot}$  occurs in a region 1 pc across, it will have no nonrelativistic equilibrium state that can be supported for long, and will collapse to a MBH. Assuming that this scenario is correct for roughly  $10^8 M_{\odot}$  and larger gas clouds, and that it leads to rapid formation of MBHs in the quasars observed at large redshifts, it still is unclear how massive and how dense the gas cloud has to be for the collapse to a MBH to occur. In particular, whether it occurs throughout the MBH mass range of roughly  $10^5$  to  $10^7 M_{\odot}$  of particular interest for LISA has not been established. Alternative ways of forming MBHs in this mass range also have been proposed [66, 67].

If sudden collapses to MBHs do occur for gas clouds large enough to give roughly  $10^5$  to  $10^7 M_{\odot}$  MBHs, an important question is how much angular momentum will be left. If the cloud hasn't lost its angular momentum rapidly enough, a bar instability may occur and cause considerable gravitational radiation in the main LISA frequency band [68]. Thus looking for pulses lasting only a few cycles will be important for LISA, as it is for supernova pulse searches with ground-based detectors.

### MBH-MBH binary coalescence.

A promising source of events for LISA is MBH-MBH coalescence after mergers of galaxies or pre-galactic structures that already contain MBHs [47]. It is assumed that smaller structures form first, and then merge to form successively larger ones. At some point, after MBHs have formed, later mergers will give opportunities for MBH-MBH coalescences. What is required is for dynamical friction to bring the MBHs close to the center of the merged structures, and then to avoid a hang-up in the process when they are still far enough apart so that gravitational radiation cannot bring them together in less than a Hubble time. The problem is a complex one, but the rate may well be several per year or higher. For masses up to at least  $10^6 M_{\odot}$ , such coalescence would be observable from virtually anywhere in the universe. They would give unique and valuable information on the whole process of structure formation in the universe.

Figure 1.4 shows the expected signal strength of coalescing MBH binary events in LISA against the LISA noise curve. The signal strengths and frequencies are displayed as a function of time for some possible MBH-MBH coalescence events at a redshift of 1. The Hubble constant  $H_0$  is assumed to be  $75 \text{ km s}^{-1} \text{ Mpc}^{-1}$ . The straight lines sloping up to the right show the values of the

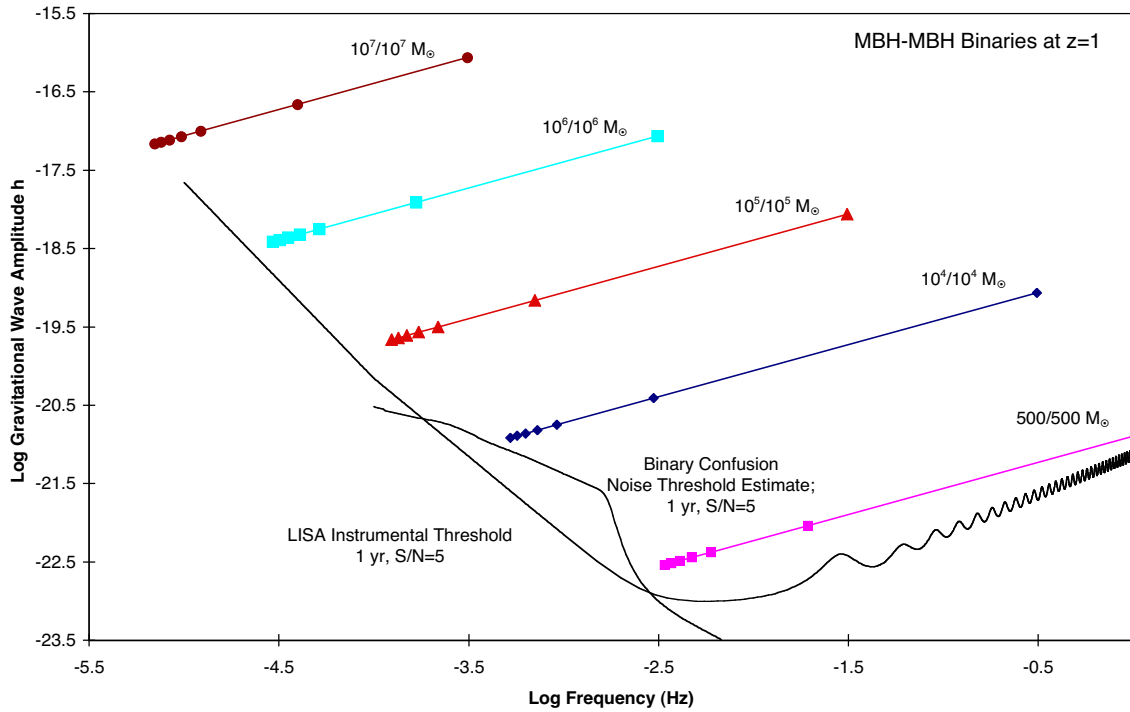


**Figure 1.4** Strain amplitude during the last year before MBH-MBH coalescence.

gravitational wave signal strength  $h$  as a function of time during the last year before coalescence for different pairs of MBH masses. The first 5 symbols from the left correspond to times of 1.0, 0.8, 0.6, 0.4, and 0.2 yr before coalescence, while the 6th symbol is for 0.5 week before coalescence. The final symbol for the four highest mass pairs is at the approximate coalescence frequency. (Note that, at cosmological distances, the apparent chirp mass of a binary is  $1 + z$  times its true chirp mass, its radiation is redshifted by the same factor, and its Euclidian distance is replaced by its luminosity distance. These factors are taken into account in Figure 1.4.) The case of  $500 M_{\odot}$  MBHs is included to correspond to possible coalescences of seed MBHs, rather than to currently plausible events resulting from galaxy mergers.

The LISA instrumental threshold curve for 1 year of observations and  $S/N = 5$  is included in Figure 1.4, along with the corresponding binary confusion noise estimate. The instrumental threshold curve has been extended below 0.1 mHz with a slope of -2.5, corresponding to the goal for LISA.

It is clear that the integrated  $S/N$  ratio for some time interval cannot be obtained by taking the ratio of two curve heights in Figure 1.4. This is because the instrumental and confusion noise curves correspond to 1 year of observation, and the signals of interest sweep through quite a frequency range during this time. Instead, the  $S/N$  ratio has to be integrated over time as the frequency changes, and the results are given in Figure 1.5. Here each symbol starting at the bottom left for each curve gives the integrated  $S/N$  ratio after 1 week, 2 weeks, etc., from the beginning of the last year before coalescence. The last symbol on each curve gives the total integrated  $S/N$  ratio up to roughly the last stable circular orbit, but is plotted at the frequency corresponding to 0.5 weeks before coalescence.

Moreover, by combining the amplitude, polarisation, and chirp-rate information from LISA's observations, we will be able to deduce (as in Section 1.1.3) the distance to the event. In cosmological terms, the distance measured will be the luminosity distance.

The extremely high signal-to-noise ratios that are expected in some cases are remarkable. They

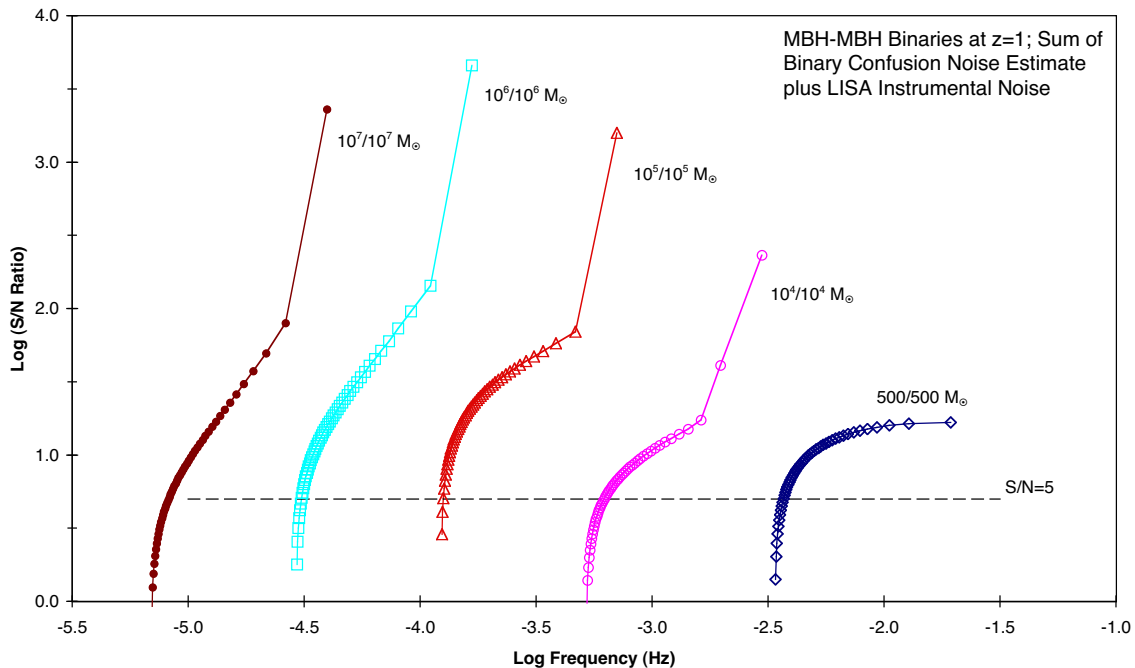


**Figure 1.5** Cumulative weekly  $S/N$  ratios during the last year before MBH-MBH coalescence.

mean that *LISA* will not just detect such events; it will be able to study them in detail. The frequency modulation of the observed signal over a period of 3 months or more will locate the event on the sky, and the amplitude modulation as the plane containing *LISA* rotates will determine the signal's polarisation (see Section 7.5). The scientific payoff of observing such events will be great:

- Detection will confirm the existence of black holes, and details of the orbital evolution will test general relativity.
- Coalescences in the appropriate mass range will be seen essentially anywhere in the Universe they occur.
- Detailed comparison with numerical simulations will reveal the masses, spins and orientations of the two black holes, and this will provide important clues to the history and formation of the binary system.
- An overall test of models for when MBHs of different sizes formed with respect to the times of mergers of pregalactic and galactic structures will be obtained.
- *LISA* offers a slight possibility of an accurate check on both the Hubble constant  $H_0$  and the cosmological deceleration parameter  $q_0$ . If optical signals corresponding to MBH-MBH coalescences at different cosmological distances should be observed, and if the redshifts of the associated galaxies can be obtained, comparison of the redshifts with the luminosity distances from *LISA* would give tight constraints on  $H_0$  and  $q_0$ . However, this method must be used with care: gravitational lensing of distant events by nearby clusters of galaxies could (by magnifying or de-magnifying the amplitude) distort the inferred luminosity distance. The chances of observing optical or other electromagnetic signals may be enhanced by pre-coalescence information from *LISA* on when and roughly where the event will occur, as suggested by Cutler [69].

If the growth of the massive holes is mainly by coalescence (rather than gas accretion), then the physical event rate will be so high that the more distant events will produce a stochastic background of signals rather like the confusion-limited white-dwarf background. An estimate is as follows: if each massive black hole contains  $10^{-5}$  of a galaxy's baryonic mass (probably a conservative number), if the coalescence events that formed it released 10 % of the original mass in gravitational radiation, and if  $10^{-3}$  to  $10^{-2}$  of the infalling mass is stellar-mass black holes, then about  $10^{-9}$  to  $10^{-8}$  of the baryonic mass of the Universe will have been converted into gravitational radiation this way. This corresponds to an energy density greater than  $10^{-11}$  to  $10^{-10}$  of the closure density, a level probably detectable by *LISA* (see Section 1.2.3 below).

### **MBH – compact star binary signals.**

A third possible type of *MBH* signal is from compact stars and stellar-mass black holes orbiting around *MBHs* in galactic nuclei [70, 71]. *MBHs* in active galactic nuclei appear to be fueled partly by accreted gas from ordinary stars that were disrupted by the hole's tidal forces. But white dwarfs, neutron stars and black holes will not be disrupted, and will instead follow complex orbits near the hole. These orbits are very sensitive to relativistic effects that depend on the spin of the *MBH* and of the infalling star. If these events are as frequent as current thinking suggests, then they can be used not only to test general relativity but also to survey the *MBH* population out to redshifts beyond 1.

Estimates of the expected number and strength of signals observable by *LISA* in a one year period have been made by Hils and Bender [71] for the case of roughly solar-mass compact stars. Such events may well be observable if the neutron-star space density in the density cusp around the *MBH* is of the order of 0.1% of the total stellar density, which is not unexpected. Many more coalescence events occur, but the observable event rate is reduced because these stars have highly eccentric orbits, which are easily perturbed by other stars in the cusp. Thus the compact stars usually plunge in rapidly, and the number of orbits one can observe in order to build up the  $S/N$  ratio usually will be small. Also, the confusion noise will obscure many of the more distant events for the higher *MBH* masses.

Recent calculations for  $5\text{--}10 M_{\odot}$  black holes orbiting *MBHs* indicate that these coalescence events will be more easily detected [72, 73, 42]. The signal is stronger, and the more massive black holes are less susceptible to stellar perturbations. If such black holes make up a fraction  $10^{-3}$  of the total stellar numbers near the *MBH*, as they are very likely to do, then the number of signals from *BH-MBH* binaries observable at any time may well be substantial, and a number of such systems may coalesce each year.

Figure 1.6 shows the expected signal strengths and frequencies for  $7 M_{\odot}$  black holes orbiting around *MBHs* with different masses  $M$  and at different redshifts  $z$  [74]. For each factor-2 range in  $M$  and  $z$  about the value given, the signal strength and frequency are plotted for the strongest expected source within those ranges. For a given symbol corresponding to a given *MBH* mass, the plotted points correspond to values of  $z$  from the lowest to the highest value given as a label. Curves corresponding to the *LISA* threshold sensitivity and to the confusion noise estimate for 1 year of observation are included. However, for reasons discussed below, they are given for  $S/N = 10$  instead of  $S/N = 5$ . The frequencies are treated as constant over a year, even though they actually will chirp strongly, and in a number of cases coalescence will occur during the year. The signals are likely to be stronger for rapidly rotating Kerr *MBHs*.

The orbits for such *BH-MBH* binaries will be highly relativistic, and observations would test the predictions of general relativity very accurately in extremely strong fields. The orbital velocity near periapsis is roughly  $0.5c$ , and the period for the relativistic precession of periapsis is similar to the period for radial motion. In addition, if the *MBH* is rapidly rotating, the orbital plane

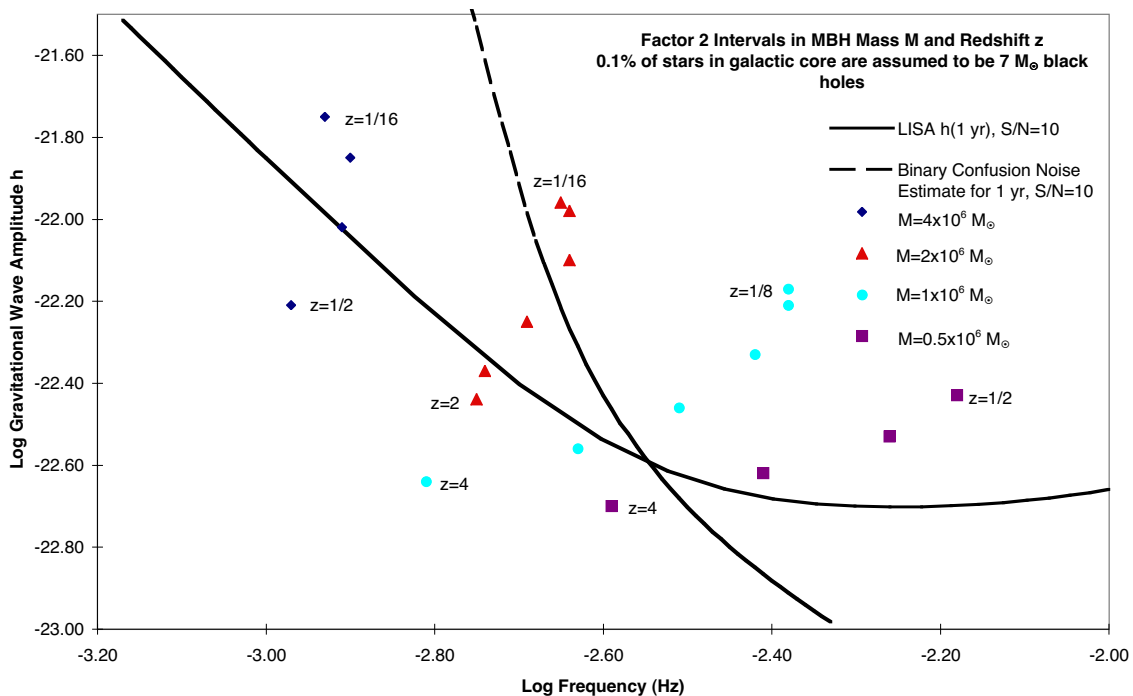


**Figure 1.6** Expected signals from *BH-MBH* binaries.

will rapidly precess. In view of the complexity of the orbits, the number of parameter values to be searched for, and the expected evolution of the orbit parameters, the **SNR** needed to detect the signals reliably probably will be about 10.

If these events are observed, then each one will tell us the mass and spin of the central **MBH**, as well as its distance and direction. The ensemble of events will give us some indication of the numbers of such black holes out to  $z \sim 1$ , and they will give us useful information about the **MBH** population, particularly the distribution of masses and spins.

### 1.2.3 Primordial gravitational waves

Just as the cosmic microwave background is left over from the Big Bang, so too should there be a background of gravitational waves. If, just after the Big Bang, gravitational radiation were in thermal equilibrium with the other fields, then today its temperature would have been redshifted to about 0.9 K. This radiation peaks, as does the microwave radiation, at frequencies above  $10^{10}$  Hz. At frequencies accessible to **LISA**, or indeed even to ground-based detectors, this radiation has negligible amplitude. So if **LISA** sees a primordial background, it will be non-thermal.

Unlike electromagnetic waves, gravitational waves do not interact with matter after a few Planck times ( $10^{-45}$  s) after the Big Bang, so they do not thermalize. Their spectrum today, therefore, is simply a redshifted version of the spectrum they formed with, and non-thermal spectra are probably the rule rather than the exception for processes that produce gravitational waves in the early universe.

The conventional dimensionless measure of the spectrum of primordial gravitational waves is the energy density per unit logarithmic frequency, as a fraction of the critical density to close

the Universe,  $\varrho_c$ :

$$\omega_{\text{GW}}(f) = \frac{f}{\varrho_c} \frac{d\varrho_{\text{GW}}}{df}. \quad (1.17)$$

The background radiation consists of a huge number of incoherent waves arriving from all directions and with all frequencies; it can only be described statistically. The *rms* amplitude of the fluctuating gravitational wave in a bandwidth  $f$  about a frequency  $f$  is

$$h_{\text{rms}}(f, \Delta f = f) = 10^{-15} [\Omega_{\text{GW}}(f)]^{1/2} \left( \frac{1 \text{ mHz}}{f} \right) \left( \frac{H_0}{75 \text{ km s}^{-1} \text{ Mpc}^{-1}} \right), \quad (1.18)$$

where  $H_0$  is the present value of Hubble's constant. That this seems to be large in [LISA](#)'s band is deceptive: we really need to compare this with [LISA](#)'s instrumental noise, and this is best done over the much narrower bandwidth of the frequency resolution of a 1 yr observation,  $3 \times 10^{-8}$  Hz. Since the noise, being stochastic, scales as the square root of the bandwidth, this gives us the relation

$$\begin{aligned} h_{\text{rms}}(f, \Delta f = 3 \times 10^{-8} \text{ Hz}) &= 5.5 \times 10^{-22} \left[ \frac{\Omega_{\text{GW}}(f)}{10^{-8}} \right]^{1/2} \left( \frac{1 \text{ mHz}}{f} \right)^{3/2} \\ &\times \left( \frac{H_0}{75 \text{ km s}^{-1} \text{ Mpc}^{-1}} \right), \end{aligned} \quad (1.19)$$

where we have scaled  $\Omega_{\text{GW}}$  to a plausible value. This is the  $\Omega_{\text{GW}} = 10^{-8}$  curve that is plotted in [Figure 1.7](#), assuming  $H_0 = 75 \text{ km s}^{-1} \text{ Mpc}^{-1}$ . Since  $\Omega_{\text{GW}}$  scales as  $h^2$ , curves for other constant values of  $\Omega_{\text{GW}}$  can be found by simply moving the given curve up or down.

A non-thermal cosmological background of gravitational waves could come from many different sources: density fluctuations produced by cosmic strings or cosmic textures have been much discussed; and there is general agreement that inflation would amplify early quantum fluctuations into a stochastic background. In all of these processes, the typical wavelength for producing gravitational waves is the cosmological horizon size at the time. After that, the waves travel freely and are redshifted by the expansion of the Universe. If we take a typical [LISA](#) frequency of 10 mHz today, and extrapolate it back in time to the point where it would have had a wavelength equal to the horizon size, we find that this occurs at a cosmological time of about  $10^{-14}$  s, when the temperature of the Universe was 100 GeV [[75](#), [76](#)]. This is a domain of physics accessible to modern particle accelerators, and it is associated with the electroweak phase transition.

This has two implications: first, if [LISA](#) measures a background, it could tell us something about electroweak physics; and second, further fundamental physics research, for example using the [LHC](#) at [CERN](#), could make definite predictions about a gravitational wave background in the [LISA](#) frequency band.

Many processes that produce a background do not have an intrinsic scale length; when this is the case, one expects a scale-free spectrum, one whose energy density is independent of frequency. Then the curve plotted in [Figure 1.7](#) has the shape of the expected spectrum. One such process is inflation. Since it would have occurred much earlier than the [LISA](#) “production time” of  $10^{-14}$  s, the spectrum [LISA](#) would see consists of waves that had wavelengths much larger than the horizon size at the end of inflation, and that therefore had no characteristic length scale. Observations of the microwave background by [COBE](#) constrain the time at which inflation occurred, and this in turn constrains the energy density today at [LISA](#) frequencies (and, incidentally, at ground-based frequencies as well) to  $\Omega_{\text{GW}} \leq 8 \times 10^{-14}$  [[75](#), [76](#)].

The most-discussed cosmic gravitational wave background has probably been that produced by cosmic strings. These are defects that could have been left over from a [GUT](#)-scale phase transition

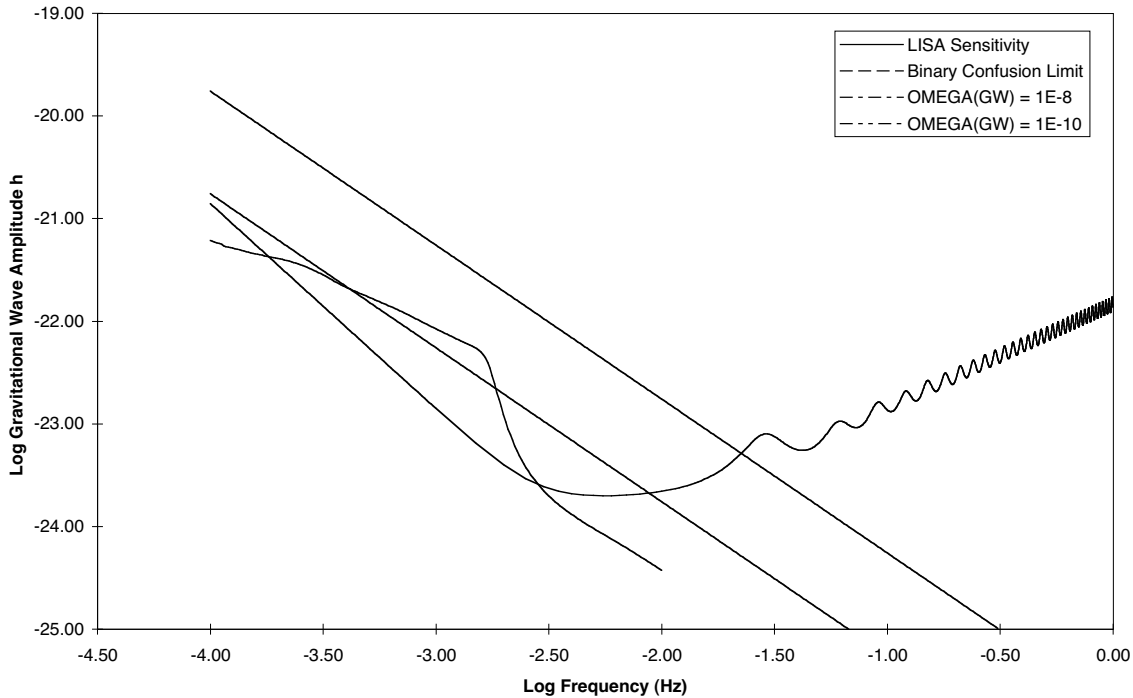


**Figure 1.7** *Sensitivity to a random cosmological gravitational wave background*

at a much earlier epoch than the electroweak transition. Therefore, by the *LISA* production time, the strings would not have had any characteristic length-scale, and the spectrum today would again be essentially scale-free at *LISA* frequencies, rising at lower frequencies [77]. This spectrum is constrained by present observations of frequency fluctuations in millisecond pulsars. This limit suggests that, at *LISA* and ground-based frequencies,  $\Omega_{\text{GW}} \leq 10^{-8}$ . This is still an interesting level for *LISA*, although ground-based detectors are likely to reach this level first.

One example of a process that would produce a spectrum with features in the *LISA* band is the collision of vacuum bubbles in the early Universe. This could occur at the end of a phase transition that occurred randomly throughout space. The expanding bubbles of the “new” vacuum state collide, and the resulting density discontinuities give off gravitational waves. If the electroweak phase transition produced such bubbles, the spectrum might peak at 0.1 mHz with a density  $\Omega_{\text{GW}} \sim 3 \times 10^{-7}$  [78]. This would easily be detected by *LISA*, and it would again be an extremely important and fundamental result. Such radiation from the electroweak transition would not be observable from the ground.

It should be emphasized that the cosmic background of gravitational waves is the least-understood prospective source for *LISA*. The observational constraints are few, and the predictions of possible spectra depend on relatively simple theoretical models of the early Universe and on toy models of high-energy physics. *LISA*’s frequency band is orders of magnitude different from that which is accessible to ground-based detectors or to pulsar timing experiments, and it is very possible that *LISA* will find unexpected surprises here. These would give us unparalleled insight into the mechanics of the early Universe.





## 2 Different Ways of Detecting Gravitational Waves

### 2.1 Complementarity of detection on the ground and in space

Astronomical observations of electromagnetic waves cover a range of 20 orders of magnitude in frequency, from ULF radio waves to high-energy gamma-rays. Almost all of these frequencies (except for visible and radio) cannot be detected from the Earth, and therefore it is necessary to place detectors optimised for a particular frequency range (e.g. radio, infrared, ultraviolet, X-ray, gamma-ray) in space.

The situation is similar for gravitational waves. The range of frequencies spanned by ground- and space-based detectors, as shown schematically in Figure 2.1, is comparable to the range from high frequency radio waves up to X-rays. Ground-based detectors will never be sensitive

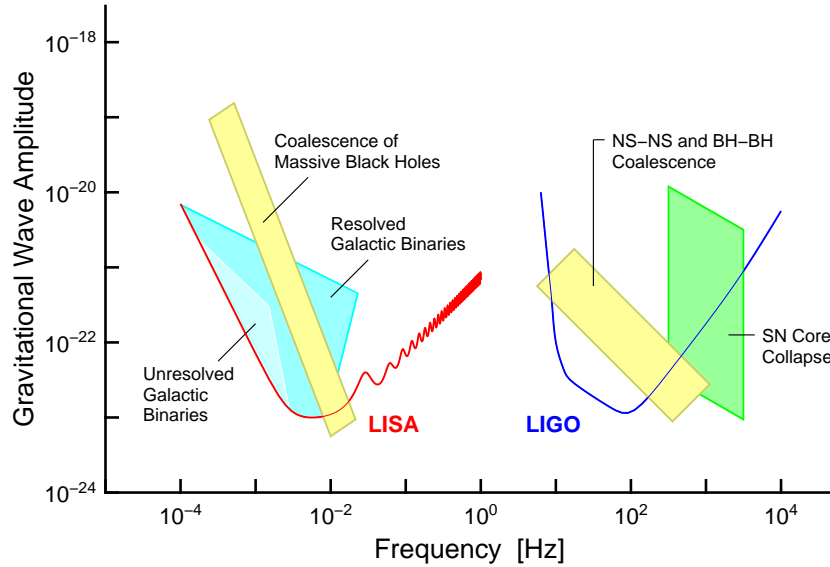


**Figure 2.1** Comparison of frequency range of sources for ground-based and space-based gravitational wave detectors. Only a few typical sources are indicated, ranging in frequency from the kHz region of supernovae and final mergers of binary stars down to mHz events due to formation and coalescence of supermassive black holes, compact binaries and interacting white dwarf binaries. The sources shown are in two clearly separated regimes: events in the range from, say, 10 Hz to several kHz (and only these will be detectable with terrestrial antennas), and a low-frequency regime,  $10^{-4}$  to  $10^{-1}$  Hz, accessible only with a space project. Sensitivities of *LISA* for periodic sources, and of (the “Advanced”) *LIGO* for burst sources, are indicated.

below about 1 Hz, because of terrestrial gravity-gradient noise. A space-based detector is free from such noise and can be made very large, thereby opening the range from  $10^{-4}$  Hz to 1 Hz, where both the most certain and the most exciting gravitational-wave sources radiate most of their power.

The importance of low frequencies is a consequence of Newton's laws. For systems involving solar-mass objects, lower frequencies imply larger orbital radii, and the range down to  $10^{-4}$  Hz includes sources with the typical dimensions of many galactic neutron star binaries, cataclysmic binaries, and some known binaries. These are the most certain sources. For highly relativistic systems, where the orbital velocities approach the speed of light, lower frequencies imply larger masses ( $M \propto 1/f$ ), and the range down to  $10^{-4}$  Hz reaches masses of  $10^7 M_\odot$ , typical of the black holes that are believed to exist in the centres of many, if not most, galaxies. Their formation and coalescences could be seen anywhere in the Universe and are among the most exciting of possible sources. Detecting them would test the strong-field limit of gravitational theory and illuminate galaxy formation and quasar models.

For ground-based detectors, on the other hand, their higher frequency range implies that even stellar-mass systems can last only for short durations, so these detectors will mainly search for sporadic short-lived catastrophic events (supernovae, coalescing neutron-star binaries). Normally, several detectors are required for directional information. If such events are not detected in the expected way, this will upset the astrophysical models assumed for such systems, but not necessarily contradict gravitation theory.

By contrast, if a space-based interferometer does not detect the gravitational waves from known binaries with the intensity and polarisation predicted by General Relativity, it will undermine the very foundations of gravitational physics. Furthermore, even some highly relativistic events, such as massive black hole coalescences with masses below  $10^5 M_\odot$ , last roughly a year or longer. This allows a single space-based detector to provide directional information as it orbits the Sun during the observation.

Both ground- and space-based detectors will also search for a cosmological background of gravitational waves. Since both kinds of detectors have similar energy sensitivities, their different observing frequencies are ideally complementary: observations can supply crucial spectral information.

The space-based interferometer proposal has the full support of the ground-based detector community. Just as it is important to make observations at radio, optical, X-ray, and all other electromagnetic wavelengths, so too is it important to cover different gravitational-wave frequency ranges. Ground-based and space-based observations will therefore complement each other in an essential way.

## 2.2 Ground-based detectors

The highest frequencies expected for the emission of strong gravitational waves are around 10 kHz because a gravitational wave source cannot emit strongly at periods shorter than the light travel time across its gravitational radius. At frequencies below 1 Hz, observations on the ground are impossible because of an unshieldable background due to Newtonian gravity gradients on the earth. These two frequencies define the limits of the high-frequency band of gravitational radiation, mainly populated by signals from neutron star and stellar mass black hole binaries. This band is the domain of ground-based detectors: laser interferometers and resonant-mass detectors.

### 2.2.1 Resonant-mass detectors

The history of attempts to detect gravitational waves began in the 1960s with the famous bar experiments of Joseph Weber [79]. A resonant-mass antenna is, in principle, a simple object. It

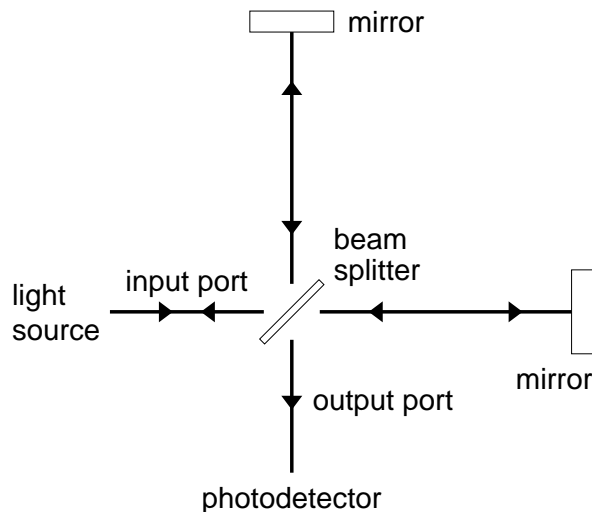


**Figure 2.2** Schematic of a two-arm Michelson interferometer. Interference of the two returning beams on the photodetector gives a measure of their relative phase. Any variation in the mirror distances caused by a passing gravitational wave will modulate this phase signal. By having two arms fed from the same light source, the phase noise inherent to the non-ideal source is the same in each arm. In essence, the interferometry amounts to a differencing of the phases from the light returning along each arm, so the common-mode noise in the light is cancelled. This is the main reason for having two arms in a Michelson interferometer.

consists of a solid body that during the passage of a gravitational wave gets excited similarly to being struck with a hammer, and then rings like a bell.

The solid body traditionally used to be a cylinder, that is why resonant-mass detectors are usually called bar detectors. But in the future we may see very promising designs in the shape of a sphere or sphere-like object like a truncated icosahedron. The resonant mass is usually made from an aluminum alloy and has a mass of several tons. Occasionally, other materials are used, e.g. silicon, sapphire or niobium.

The first bar detectors were operated at room temperature, but the present generation of bars is operating below liquid-helium temperature. A new generation ([NAUTILUS](#) in Frascati and [AURIGA](#) in Legnaro) is now operating at a temperature around 100 mK.

Resonant-mass detectors are equipped with transducers that monitor the complex amplitudes of one or several of the bar's vibrational modes. A passing gravitational wave changes these amplitudes due to its frequency content near the normal mode frequencies. Present-day resonant mass antennas are fairly narrowband devices, with bandwidths of only a few Hz around centre-frequencies in the kHz range. With improved transducer designs in the future, we may see the bandwidth improve to 100 Hz or better.

The sensitivities of bar antennas have steadily improved since the first experiments of Joe Weber. Currently we see a network of antennas at Rome, Legnaro, [CERN](#), Louisiana State and Perth with best detectors operating with a sensitivity to millisecond duration pulses of  $h = 3 \times 10^{-19}$ . In the first decade of the next millennium, planned sphere-like detectors operating near the standard quantum limit may reach burst sensitivities below  $10^{-21}$  in the kHz range [80].

### 2.2.2 Laser Interferometers

Although the seeds of the idea can be found in early papers by Pirani [81] and Gertsenshtein and Pustovoit [82], it was really in the early 1970s that the idea emerged that laser interferometers might have a better chance of detecting gravitational waves, mainly promoted by Weiss [83] and Forward [84].

A Michelson interferometer measures the phase difference between two light fields having propagated up and down two perpendicular directions, i.e. essentially the length difference between the two arms (see Figure 2.2). This is the quantity that would be changed by a properly ori-

<i>Country:</i>	<b>USA</b>	<b>USA</b>	<b>GER</b>	<b>GBR</b>	<b>FRA</b>	<b>ITA</b>	<b>JPN</b>	<b>JPN</b>
<i>Institute:</i>	MIT	Caltech	MPQ	Glasgow	CNRS	INFN	ISAS	NAO

**Prototypes:**

<i>Start:</i>	1972	1980	1975	1977	1983	1986	1986	1991
<i>Laser:</i>	Ar <sup>+</sup>	Ar <sup>+</sup>	Ar <sup>+</sup>	Ar <sup>+</sup>	(Ar <sup>+</sup> )	(Ar <sup>+</sup> )	Ar <sup>+</sup>	YAG
<i>Arm length <math>\ell</math>:</i>	40 m		30 m	10 m	0.5 m		100 m	20 m
<i>Strain sensitivity</i> $\tilde{h}$ [Hz <sup>-1/2</sup> ]:	$1 \cdot 10^{-20}$ 1995		$11 \cdot 10^{-20}$ 1986	$6 \cdot 10^{-20}$ 1992			$8 \cdot 10^{-20}$ 1996	$2 \cdot 10^{-18}$ 1996

**Large Interferometric Detectors:**

<i>Planning (start):</i>	1982	1984	1985	1986	1986	1986	1987	1994
<i>Arm length <math>\ell</math>:</i>	4 km 2 km	4 km	600 m		3 km		300 m	
<i>Site (State)</i>	Hanford (WA)	Livingston (LA)	Hannover GER		Pisa ITA		Mitaka JPN	
<i>Cost (10<sup>6</sup> US\$):</i>	292		7		90		15	
<i>Project name:</i>	<b>LIGO</b>		<b>GEO 600</b>		<b>VIRGO</b>		<b>TAMA 300</b>	

**Table 2.1** Funded ground-based interferometric gravitational wave detectors: List of prototypes (upper part) and long-baseline projects (lower part).

ented gravitational wave. The phase difference measured can be increased by increasing the armlength, or, equivalently, the interaction time of the light with the gravitational wave, up to an optimum for an interaction time equal to half a gravitational wave period. For a gravitational wave frequency of 100 Hz this corresponds to five milliseconds or an armlength of 750 km. On the ground it is clearly impractical to build such large interferometers, but there are ways to increase the interaction time without increasing the physical armlength beyond reasonable limits. Several variants have been developed, all of them relying on storing and enhancing the laser light, or the gravitational-wave induced sidebands, or both.

The technology and techniques for such interferometers have now been under development for nearly 30 years. Table 2.1 gives an impression of the wide international scope of the interferometer efforts. After pioneering work at MIT, other groups at Munich/Garching, at Glasgow, then Caltech, Paris/Orsay, Pisa, and later in Japan, also entered the scene. Their prototypes range from a few meters up to 30, 40, and even 100 m (upper part of Table 2.1).

Today, these prototype interferometers are routinely operating at a displacement noise level of the order  $10^{-19}$  m/ $\sqrt{\text{Hz}}$  over a frequency range from 200 Hz to 1000 Hz, corresponding to an rms gravitational-wave amplitude noise level of better than  $h_{\text{rms}} \approx 10^{-19}$ .

Plans for kilometer-size interferometers had been made since the 1980s. Starting around 1995, the construction of such large detectors was pursued at five different locations, see Table 2.1, lower part.

All of these large-scale projects will use low-noise Nd:YAG lasers (wavelength 1.064  $\mu\text{m}$ ), pumped with laser diodes, just as is intended for LISA, which will greatly benefit from their efforts for achieving extreme stability and high overall efficiency.

The US project LIGO consists of *two* facilities at two widely separated sites [85]. Both house a 4 km interferometer, Hanford an additional 2 km interferometer. At both sites ground-work,

construction, and the vacuum tests (of the “world’s largest vacuum chamber”) have long been finished, installation of optics has well progressed, and first interferometric tests are under way. In the French-Italian project [VIRGO](#), being built near Pisa, an elaborate seismic isolation system will allow this project to measure down to a frequency of 10 Hz or even below [86]. Construction is in full progress. The central housing has been completed, and in it first interferometry tests will be made soon.

A British-German collaboration has de-scoped the project of a 3 km antenna to a length of only 600 m: [GEO 600](#) [87]. It employs advanced optical techniques (tunable signal recycling) to make up for the shorter arms. Ground work, construction and vacuum testing at the site near Hannover have long been completed, installation of optics and first inrterferometric tests are under way.

In Japan, completion of a joint project of [NAO](#), University of Tokyo, and other institutions, is the farthest advanced. In this 300 m project, called [TAMA 300](#) [88], civil engineering, vacuum housing, have long been completed, the ‘locking’ of the two interferometer arms has been demonstrated, and first measurements, albeit not yet at the targeted sensitivity, are being done. Not included in Table 2.1 is the (not yet funded) Australian project of a kilometer-sized detector. A very modern ‘prototype’ of 80 m armlength is being built near Perth. The site would allow later extension to 3 km arms.

[LIGO](#), [GEO 600](#) and [TAMA 300](#) are scheduled to be begin data runs by 2001, [VIRGO](#) perhaps a year later. However, the sensitivity of the first stage detectors may be only marginally sufficient to detect gravitational waves. Therefore, step-by-step improvements will be made, until the network finally reaches the advanced detector sensitivity, sometime between 2005 and 2010. Plans are being made in Japan and Europe for further large detectors, possibly using cryogenic test masses.

With such next-generation detectors, one can be confident that signals will be observed from sources such as supernovae, compact binary coalescences and pulsars, unless something is fundamentally wrong with our current estimates of their strength and distribution.

## 2.3 Pulsar timing

Man-made gravitational wave detectors operate by detecting the effect of gravitational waves on the apparatus. It is also possible to detect gravitational waves by observing their effect on electromagnetic waves as they travel to us from astronomical objects. Such methods of detection are like “one-arm interferometers” – the second arm is not needed if there is another way to provide a reference clock stable enough to sense the changes in propagation time produced by gravitational waves.

Pulsar timing makes use of the fact that the pulsar is a very steady clock. If we have a clock on the Earth that is as stable as the pulsar, then irregularities in the arrival times of pulses that are larger than expected from the two “clocks” can be attributed to external disturbances, and in particular possibly to gravitational waves. Since the physics near a pulsar is poorly known, it might be difficult to prove that observed irregularities are caused by gravitational waves. But where irregularities are absent, this provides an upper limit to the gravitational wave field. This is how such observations have been used so far.

All pulsars slow down, and a few have shown systematic changes in the slowing down rate. Therefore, it is safer to use random irregularities in the pulsar rate as the detection criterion, rather than systematic changes. Such random irregularities set limits on random gravitational

waves: the stochastic background.

The arrival times of individual pulses from most pulsars can be very irregular. Pulsar periods are stable only when averaged over considerable times. The longer the averaging period, the smaller are the effects of this intrinsic irregularity. Therefore, pulsar timing is used to set limits on random gravitational waves whose period is of the same order as the total time the pulsar has been observed, from its discovery to the present epoch. Millisecond pulsars seem to be the most stable over these long periods, and a number of them are being used for these observations.

The best limits come from the first discovered millisecond pulsar, PSR B1937+21. At a frequency of approximately  $1/(10 \text{ yr})$  the pulsar sets an upper limit on the energy density of the gravitational wave background of  $\Omega_{\text{GW}} < 10^{-7}$  [89] (see Section 1.2.3). This is in an ultra-low frequency range that is  $10^5$  times lower than the [LISA](#) band and  $10^{10}$  times lower than the ground-based band. If one believes a theoretical prediction of the spectrum of a cosmic gravitational wave background, then one can extrapolate this limit to the other bands. But this may be naive, and it is probably wiser to regard observations in the higher-frequency bands as independent searches for a background.

More-recently discovered millisecond pulsars are also being monitored and will soon allow these limits to be strengthened. If irregularities are seen in all of them at the same level, and if these are independent of the radio frequency used for the observations, then that will be strong evidence that gravitational waves are indeed responsible.

These observations have the potential of being extended to higher frequencies by directly cross-correlating the data of two pulsars. In this way one might detect a correlated component caused by gravitational waves passing the Earth at the moment of reception of the radio signals from the two pulsars. Higher frequencies are accessible because the higher intrinsic timing noise is reduced by the cross-correlation. Again, seeing the effect in many pairs of pulsars independently of the radio frequency would be strong evidence for gravitational waves.

## 2.4 Spacecraft tracking

Precise, multi-frequency transponding of microwave signals from interplanetary probes, such as the [ULYSSES](#), [GALILEO](#) and [CASSINI](#) spacecraft, can set upper limits on low-frequency gravitational waves. These appear as irregularities in the time-of-communication residuals after the orbit of the spacecraft has been fitted. The irregularities have a particular signature. Searches for gravitational waves have produced only upper limits so far, but this is not surprising: their sensitivity is far short of predicted wave amplitudes. This technique is inexpensive and well worth pursuing, but will be limited for the foreseeable future by some combination of measurement noise, the stability of the frequency standards, and the uncorrected parts of the fluctuations in propagation delays due to the interplanetary plasma and the Earth's atmosphere. Consequently, it is unlikely that this method will realise an *rms* strain sensitivity much better than  $10^{-17}$ , which is six orders of magnitude worse than that of a space-based interferometer.

## 2.5 Space interferometer

The [LISA](#) measurement concept is, in essence, a space-borne implementation of a Michelson interferometer for the purpose of measuring the fluctuations in the distance between widely separated mirrors. There is, however, a fundamental distinction between [LISA](#) and the ground-based interferometers: [LISA](#) will search for the distinctively *low-frequency* (milli-hertz) gravitational



waves (Chapter 1) which will probably *never* be detectable by any terrestrial detectors — existing or planned — because of unshieldable gravitational disturbances. These disturbances are due to the motion of bulk matter in the Earth and the atmosphere which will pull gravitationally on the interferometer mirrors, producing undesirable phase shifts. Since gravity can not be shielded, and there does not seem to be a feasible way of independently measuring the gravitational effects of seismicity, these effects impose a strict lower limit on the gravitational wave frequencies observable on Earth. With its wide separation from Earth, *LISA* is completely free from these terrestrial disturbances.

## 2.6 Early concepts for a laser interferometer in space

The earliest concept for a laser gravitational wave detector in space appears to have been a Shuttle-launched monolithic Gravity Wave Interferometer (*GW*I). R. Weiss was informed in 1974 about *NASA* studies of producing such a device with up to 1 km arm lengths by using an orbiting machine to extrude aluminium beams. A *NASA* publication in March 1978 [90] described an interferometer with a total launch mass of 16.4t, which included four 1000 kg test masses at the ends of a cross-shaped device (see Figure 2.3). The *GW*I's sensitivity was calculated as

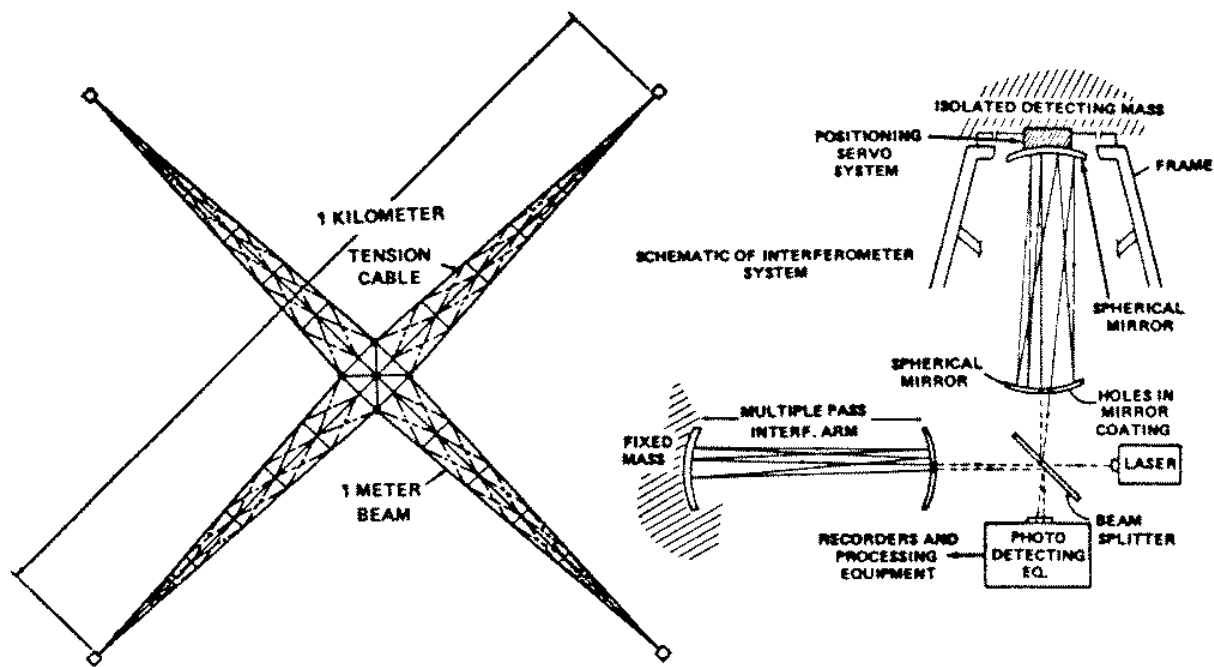


**Figure 2.3** *Conceptual design of the Gravitational Wave Interferometer (GWI). Left: GWI structure after deployment in low-Earth orbit. Right: Schematic of the interferometer system.*

$\delta l/l = 10^{-21}$  in the frequency range from  $10^{-1}$  to  $10^2$  Hz. The total cost of the project was estimated at that time to be \$ 49.5 M.

The idea of a monolithic space gravitational wave interferometer presented to Weiss started discussions in 1974 with P.L. Bender, R.W.P. Drever and J.E. Faller of a much larger space interferometer. The approach considered was to send laser beams between shielded proof masses in three widely separated drag-free spacecraft, using laser transponders rather than mirrors at the ends of the interferometer arms to greatly reduce the shot noise. Both, the separated

spacecraft and monolithic approaches were mentioned in a 1976 committee report by Weiss *et al.* [91] and described by Weiss in a 1979 paper [92]. A more complete discussion of a possible separated spacecraft interferometer with  $1 \times 10^6$  km arm lengths was given by Decher *et al.* [93] in 1980, but it required frequent major adjustments to the orbit of one spacecraft and had other disadvantages.

The first suggestion of a mission using spacecraft orbits similar to those planned for LISA was made in 1981 by Faller and Bender [94, 95]. It included the approach suggested by Faller of using the apparent changes in length of one arm to determine the laser phase noise, and then correcting the arm length difference based on the measured laser phase noise. A full description of this concept, then tentatively named the Laser Antenna for Gravitational-radiation Observation in Space (LAGOS), was given by Faller [96].

LAGOS had already many elements of the present-day LISA mission. It consisted of three drag-free satellites, one master spacecraft in the center and two auxilliary spacecraft at a distance of  $10^6$  km from the central spacecraft, forming a triangle with an angle of  $120^\circ$  at the central spacecraft (see Figure 2.4). This configuration would be placed in a circular heliocentric orbit

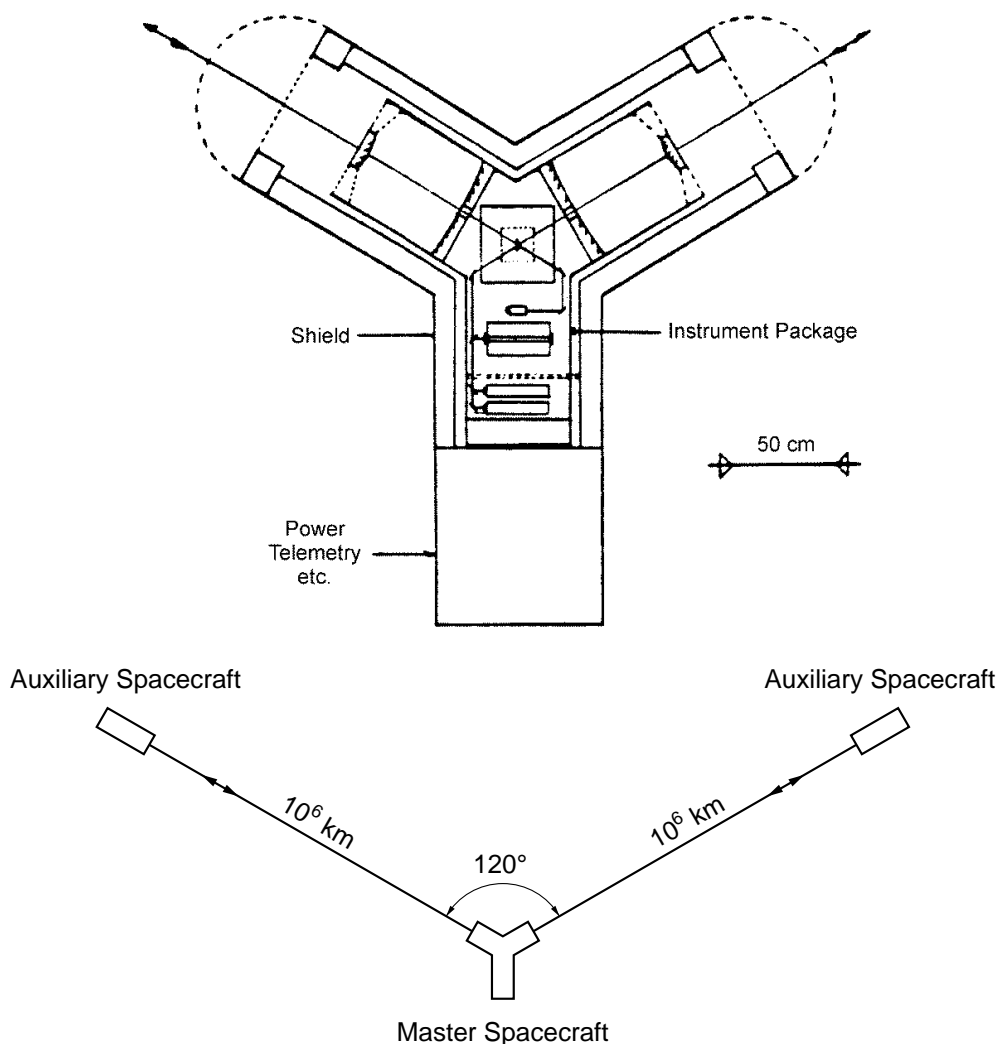


**Figure 2.4** Early version of the LAGOS concept. Top: Central spacecraft. Bottom: The configuration of three drag-free spacecraft in interplanetary space.



at 1 AU from the Sun, about  $4 \times 10^7$  km ( $15^\circ$ ) ahead of the Earth. With 100 mW laser power and 50 cm diameter telescopes for transmitting and receiving the laser beams a strain sensitivity of  $\delta l/l = 10^{-19}$  over the frequency range from  $10^{-4}$  to  $10^{-1}$  Hz appeared feasible. The proof masses in the spacecraft were thought to be cylinders of about 15 cm in length and diameter, freely floating inside a housing of 25 cm. Displacements of the housing by  $10 \mu\text{m}$  with respect to the proof masses would be sensed optically, and the signals could be used to servo-control the position of the spacecraft against perturbations.

## 2.7 Heliocentric versus geocentric options

An alternative gravitational wave mission that uses geocentric rather than heliocentric orbits for the spacecraft has been suggested by R.W. Hellings. An earlier version of this mission called **SAGITTARIUS** was proposed to **ESA** in 1993 as a candidate for the M3 mission. A similar mission called **OMEGA** was proposed to **NASA** in 1996.

The 1996 **OMEGA** proposal involved six spacecraft in retrograde coplanar geocentric orbits with semi-major axes of roughly 600 000 km and periods of about 53 days. Two spacecraft would be close together at each corner of an equilateral triangle, as for the **LISA** Cornerstone proposal, but the triangle would be about 1 million km on a side instead of 5 million km. An inclination of  $11^\circ$  to the ecliptic has been mentioned for the orbits. The proposed telescope diameter was 15 cm, but we will assume a more favourable diameter of 30 cm diameter, as in **LISA**, for a comparison of the heliocentric and geocentric orbit options.

There are three main advantages expected for the geocentric option. One is that the propulsion requirements after the initial launch for placing the spacecraft in the desired orbits are much less. This would cut much of the cost of the interplanetary propulsion modules for **LISA**, and would reduce the launch vehicle cost. The second advantage is a simpler and less expensive telecommunications system for sending down the data. An S-band system with small ground antennas could be used instead of an X-band system with a large ground antenna, and the bandwidth could be much larger. This means that less or no preprocessing and data compression would be needed on the spacecraft. Finally, the time necessary to put the spacecraft in their final orbits would be considerably less than the roughly one year planned for **LISA**.

It unfortunately is difficult to estimate reliably the cost savings for a geocentric mission compared with a heliocentric mission. The **ESA** study of both types of mission during the first half of the M3 study led to an estimated cost difference of only about 15 %, and the **LISA** mission was chosen for consideration in the rest of the study. However, the same launch vehicle was assumed for both types of mission, so the actual savings could be higher. Our present rough estimate is perhaps 20 % for the cost difference.

In terms of expected scientific results, a major question is the error budget allowed for the inertial sensor. For **LISA**, the currently adopted requirement is  $3 \times 10^{-15} \text{ m s}^{-2}/\sqrt{\text{Hz}}$  from 0.1 to 10 mHz for an individual sensor. If a geocentric mission had the same requirement, the overall interferometer sensitivity below about 3 mHz would be five times worse than for **LISA**. In addition, the cross-over point between mainly inertial-sensor noise and mainly distance-measurement noise would move up from 3 to about 7 mHz. If our present estimate of the confusion-noise level due to unresolved galactic and extragalactic binaries is correct, the loss in instrumental sensitivity would be serious for several types of signals that are of high scientific importance. In addition, the potential information on some types of galactic binaries would be degraded. The sensitivity at frequencies above roughly 30 mHz would be improved for the geocentric mission because of the baseline staying shorter than the gravitational wavelength up to higher frequencies. How-

ever, there are no sources expected at present for which the frequency region from 30 mHz to the top of the [LISA](#) band at 1 Hz would be important for detection.

If instead a factor five lower noise level is required for the inertial sensors in a geocentric mission, then the question becomes how difficult it is to meet that requirement. While it is possible that a lower noise level can be achieved if several of the potential noise sources are on the lower end of their potential ranges, it appears difficult at present to design the inertial sensors in such a way as to be sure of this. Thus, we regard a substantially tighter inertial sensor requirement as a major technological hurdle that the mission would have to overcome.

A second important technological issue arising in a geocentric mission is the need to keep sunlight from getting into the telescopes when the optical axes point close to the sun. With six telescopes and  $11^\circ$  inclination of the orbits to the ecliptic, the optical axis of one of the telescopes will pass within  $15^\circ$  of the sun roughly 40 % of the time. Earlier theoretical studies of this problem indicated that a combination of multilayer UV and IR reflecting filters plus a narrowband optical transmitting filter could reduce incident sunlight by a sufficient amount, but such filters have not been designed in detail or constructed. The problem of constructing such filters appears to be made even more difficult if they need to be 30 cm in diameter, rather than the 15 cm diameter assumed in the earlier studies.

A third technological issue concerns the need for generating an extremely stable clock frequency for use in cancelling out the Doppler shifts in the observed signals. For the geocentric mission, the Doppler shifts vary with about 27 day period between plus and minus 300 MHz. This is more than two orders of magnitude larger than the difference in Doppler shifts for the two preferred arms of the [LISA](#) interferometer, for which the initial orbit conditions are chosen to keep the Doppler shifts low, and a factor 20 higher than for the third arm in [LISA](#). Thus, while [LISA](#) can determine the phase noise in its Ultra Stable Oscillators ([USOs](#)) to sufficient accuracy by fairly simple means, as discussed later, this task is considerably more difficult for the geocentric mission.

For [LISA](#), roughly 200 MHz sidebands generated from the [USO](#) are modulated onto the laser beams, with roughly 10 % of the power in the sidebands. Measurements of phase jitter in the beats between the sidetones and the carrier after transmission over an interferometer arm determine the phase noise in the [USO](#). However, for the geocentric mission, two separate lasers with a difference frequency of perhaps 5 GHz probably would need to be used. Thus, the number of lasers that must survive in at least four of the spacecraft is doubled, since the accuracy of the results would be very strongly degraded if accurate corrections for the Doppler shifts were not available. If optical modulators with 5 GHz or higher frequencies and substantial sideband power are used instead of two separate lasers, the efficiency and long term reliability of the modulators are much more significant technological challenges than for the roughly 200 MHz modulators needed for [LISA](#).

In view of the three important technological issues discussed above and the loss in sensitivity for a geocentric mission if tighter requirements are not imposed on the inertial sensors, we believe that the [LISA](#) approach of using heliocentric orbits should be preferred. Cost is clearly a very important issue, but we expect that the main cost drivers for a gravitational-wave mission will continue to be the design and construction of the individual spacecraft and payloads, and in insuring the reliability of all of the systems that have to work simultaneously in at least four of the six optical assemblies.

# 3 The LISA Concept – An Overview

This chapter is to give an overview of the [LISA](#) concept, and in doing so introduce the main components that will be described in a more detailed fashion in the following chapters.

Some details are taken from the original proposal ([PPA 2 \[1\]](#)), while others show the alternatives, options, and improvements resulting from the Industrial Study ([FTR \[2\]](#)) performed in 1999/2000.

## 3.1 The LISA flight configuration

Conceptually, the idea of implementing an interferometer in space is straightforward, but the practical realisation requires an intricate blend of optical technology, spacecraft engineering and control. For a start, the interferometer mirrors can not simply float freely in space — they must be contained inside spacecraft. Nonetheless, they can be arranged to be floating almost freely inside the spacecraft, protected from external disturbances by the spacecraft walls. As long as the spacecraft do not disturb the mirrors, then, ideally, only gravitational waves would perturb their relative motion. “Drag-free control” can be employed to ensure that the spacecraft always remain centred on the mirrors.

A Michelson-type interferometer in space could be realised using three spacecraft: one at the “corner” to house the light source, beam splitter, and detector, plus one at each “end” to house the remote mirrors. But for practical reasons the actual implementation is slightly different. Each spacecraft contains two telescopes, each one pointing at one of the distant spacecraft at the other two corners of the triangle, and two lasers, one per telescope. Each laser is phase-locked either to its companion on the same spacecraft, forming the equivalent of a beam-splitter, or to the incoming light from the distant spacecraft, forming the equivalent of an amplifying mirror, or light transponder. Together the three spacecraft function as a Michelson interferometer with an additional redundant third arm (Figure 3.1). Thus [LISA](#) constitutes a redundant set of redundant Michelson interferometers, designed in such a way as to avoid single-point failures.

Each spacecraft is located at the vertex of a large equilateral triangle whose sides measure  $5 \times 10^6$  km in length. This arm length has been chosen to optimise the sensitivity of [LISA](#) at the frequencies of known and expected sources. A factor of 2 increase may be desirable. However, an arm length increase beyond that would begin to compromise the high-frequency sensitivity when the light in the arms experiences more than half of the gravitational wave period. An interferometer shorter than  $5 \times 10^6$  km would begin to lose the interesting low-frequency massive blackhole sources. It would give less scientific information but would not be any easier to build or operate because the spacecraft and the interferometry would be essentially the same.

## 3.2 The LISA orbits

Each spacecraft is actually in its own orbit around the Sun. The three individual orbits have their inclinations and eccentricities arranged such that, relative to each other, the spacecraft rotate on a circle ‘drawn through’ the vertices of a giant triangle that is tilted by  $60^\circ$  with respect to the ecliptic. The center of this [LISA](#) constellation moves around the Sun in an

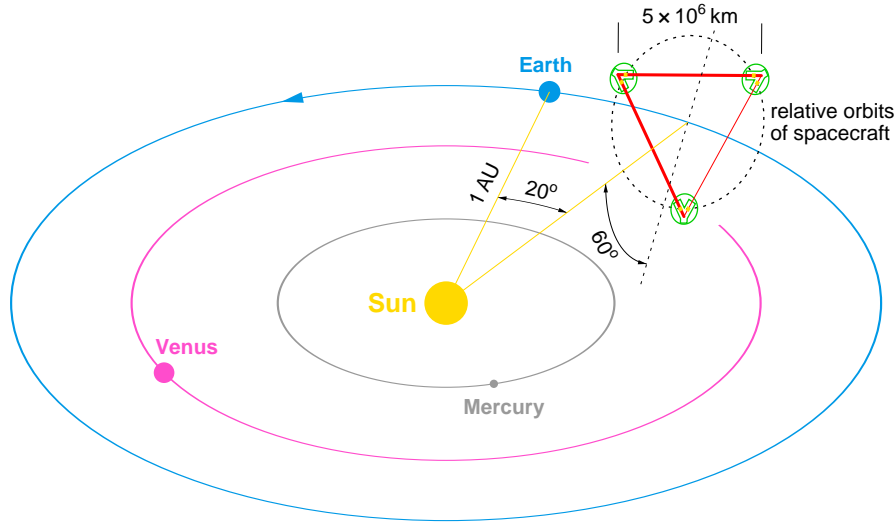


**Figure 3.1** *LISA configuration: three spacecraft in an equilateral triangle. Drawing not to scale: the LISA triangle is drawn one order of magnitude too large.*

earth-like orbit ( $R = 1 \text{ AU}$ ),  $20^\circ$  behind the Earth. As indicated in Figure 3.2, the triangular constellation revolves once around its centre as it completes one orbit in the course of one year. Each spacecraft moves along an elliptic orbit, with major axis  $D = 2 \text{ AU} \approx 3 \times 10^{11} \text{ km}$ , eccentricity  $e \approx L/(D\sqrt{3}) \approx 1/100$  and inclination with respect to the ecliptic  $i = L/D \approx 1^\circ$ . These three orbits (one is shown in Fig. 3.2) are displaced by  $120^\circ$  along the ecliptic. With this special choice of orbits, the triangular geometry of the interferometer is largely maintained throughout the mission. The centre of the triangle is located on the ecliptic —  $20^\circ$  behind the Earth — and follows the Earth on its orbit around the Sun. Ideally, the constellation should be as far from Earth as possible in order to minimise gravitational disturbances. The choice of  $20^\circ$  is a practical compromise based on launch vehicle and telemetry capabilities.

The once-per-year orbital rotation of the LISA constellation around the Sun provides the instrument with angular resolution, i.e. the ability to determine the particular direction to a source. An interferometer is rather omnidirectional in its response to gravitational waves. In one sense this is advantageous — it means that more sources can be detected at any one time — but it has the disadvantage that the antenna cannot be “aimed” at a particular location in space. For a given source direction, the orbital motion of the interferometer Doppler-shifts the signal, and also affects the observed amplitude. By measuring these effects the angular position of the source can thus be determined (see Section 7.5.2). This is analogous to the technique used by radio astronomers to determine pulsar locations.

It is expected that the strongest LISA sources (from very distant supermassive black holes) should be resolvable to better than an arcminute; and even the weaker sources (galactic binaries) should be positioned to within one degree throughout the entire galaxy.

### 3.3 The three LISA spacecraft

A possible layout of the spacecraft housing the payload is indicated in Figure 3.3 (in the earlier version of PPA 2). The top lid, serving as a thermal shield, is removed to allow a view at the Y-shaped enclosure of the scientific package, the “payload”. In a more recent version, the whole top lid will carry solar cells.

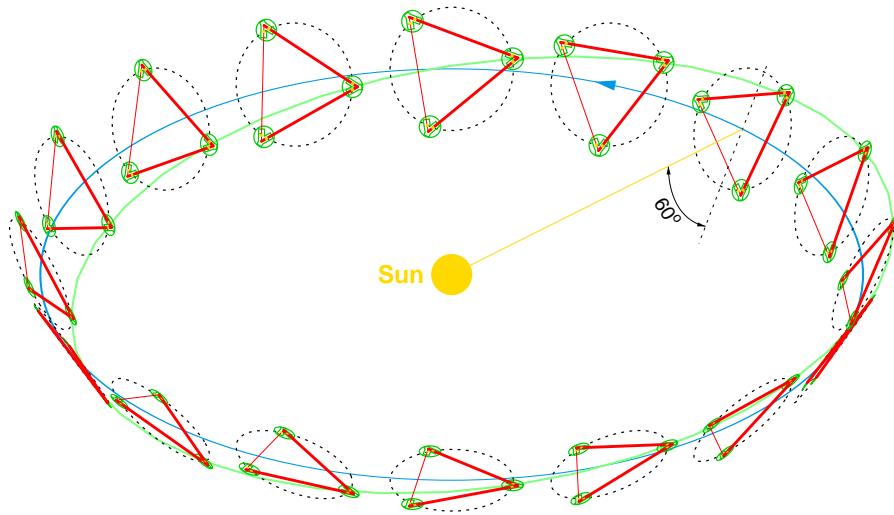


**Figure 3.2** Annual revolution of *LISA* configuration around the Sun, describing a cone with  $60^\circ$  half opening angle. One selected 2-arm interferometer is highlighted by heavier interconnecting laser beams. The green trajectory of one individual spacecraft is shown, inclined with respect to the blue Earth orbit.

These spacecraft, roughly the shape of flat cylindrical boxes, will always have the Sun shining on the same, the “upper”, side, at an angle of incidence of  $30^\circ$ . This provides a thermally very stable environment. Not shown are the down-link antennas, nor the *FEEP* thrusters that control the attitude of the spacecraft.

The two telescope arms of the Y-shaped payload subtend an angle of  $60^\circ$ . Their extensions, the “baffles”, protrude through the spacecraft cylinder, having ends angled at  $30^\circ$  to prevent sunlight from entering the telescope.

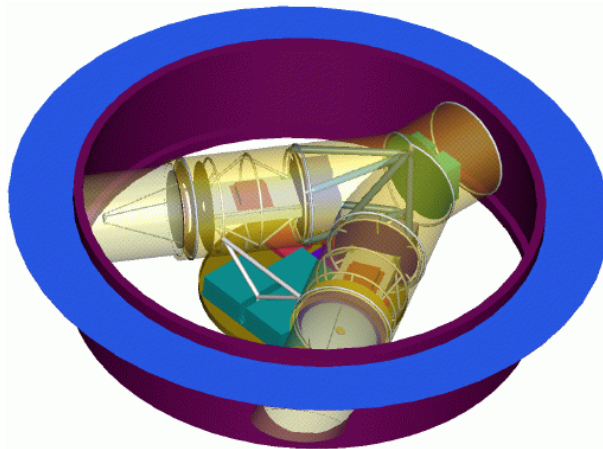


**Figure 3.3** One of the three identical *LISA* spacecraft (the original design of *PPA 2*). Top lid removed to allow view at the Y-shaped thermal shield encasing the two optical assemblies. The Y-shaped enclosure is actually gold-coated carbon-epoxy, but is indicated here as semi-transparent to allow a look at the two optical assemblies.

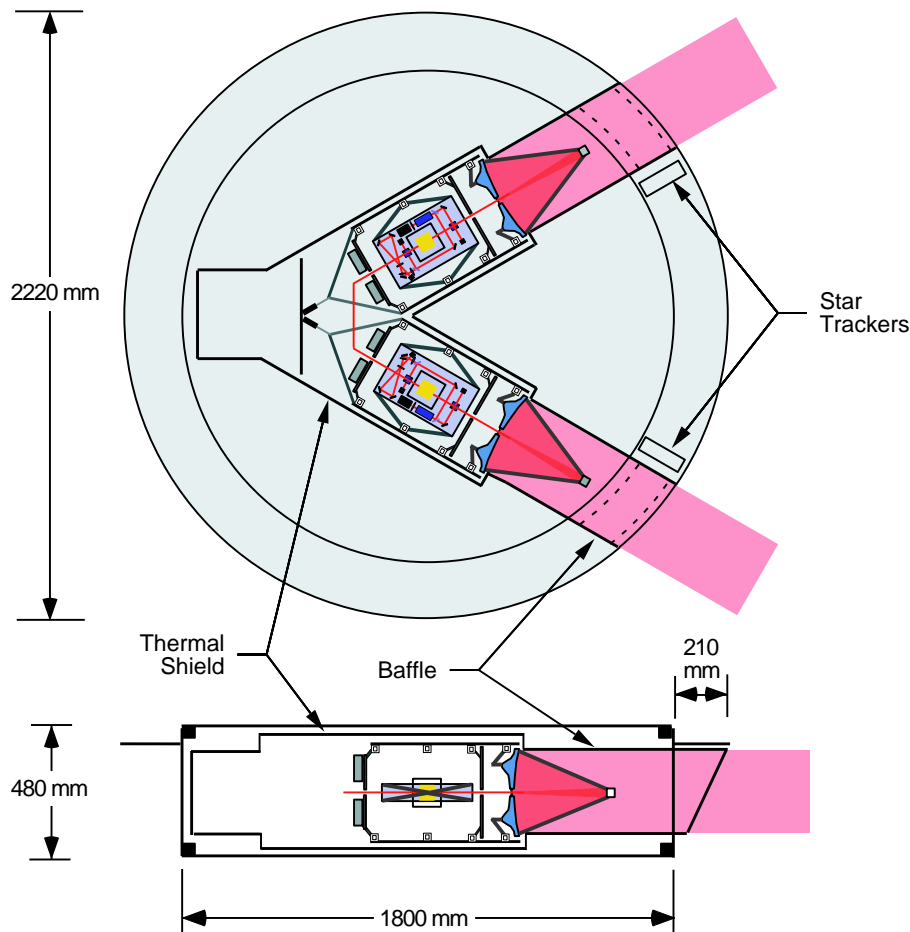


**Figure 3.4** Upper part: top view of the spacecraft showing the payload with its two optical assemblies, as in PPA 2 [1]. Lower part: cut through one payload arm, along its axis.

### 3.4 The payload

In this document, the term “payload” will encompass all items enclosed by and including the Y-shaped thermal shield shown in Figure 3.3, and in addition also the lasers and the electronics required for the science mission.

The two longer branches of the Y-shaped thermal shield subtend an angle of  $60^\circ$ , and they contain two identical optical assemblies. Figure 3.4 indicates in top and side views one configuration of how the two optical assemblies might be positioned in the Y-shaped thermal enclosure. Alternative configurations, with the two optical benches rotated around their telescope axes by either  $90^\circ$  or  $45^\circ$  are also being considered. In all these cases, their symmetry with respect to each other is that of a  $180^\circ$  rotation around the bisector of the two arms.

The configuration of one optical assembly is shown in more detail in Figures 3.5 and 3.6, and will be sketched briefly, starting from the innermost components, in the following subsections.

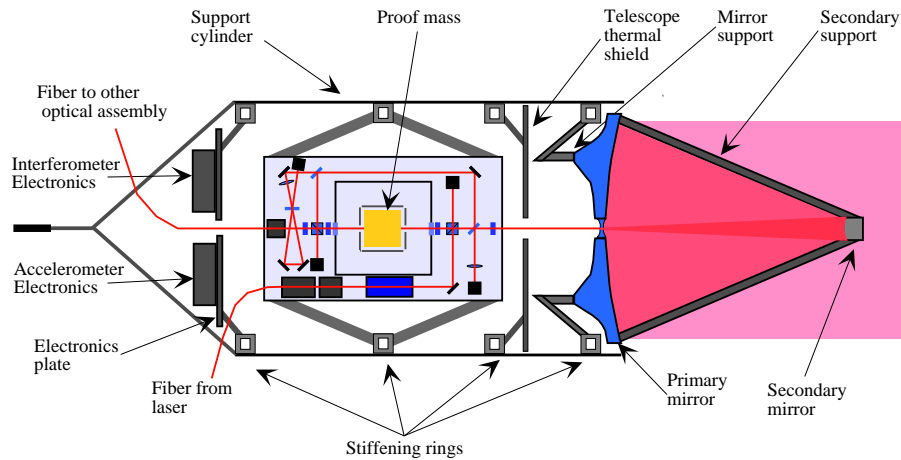


**Figure 3.5** One of the two optical assemblies of the Y-shaped *LISA* payload [1].

### 3.4.1 The proof mass

The interferometry between the spacecraft will be done with respect to proof masses that are (almost) freely floating inside the payload arms. These proof masses are shown as 40 mm cubes in Figs. 3.4–3.6, but other geometries are also considered. They are made from an alloy chosen for its low magnetic susceptibility (90 % Au, 10 % Pt,  $m \sim 1.3$  kg).

### 3.4.2 The inertial sensor

The motions of the proof masses have different constraints in different degrees of freedom. In the direction of the optical axis, the spacecraft is to follow the freely floating proof mass. (Due to the fact that each spacecraft contains two independent proof masses, this cannot be accomplished to the full extent.) With respect to the other degrees of freedom, the alignment of the spacecraft is mainly determined by the lines of sight to the two distant spacecraft, and the proof masses must be made to follow this alignment.

A capacitive scheme, the “inertial sensor”, is used to monitor the relative displacements of proof mass and spacecraft, and elaborate control techniques afford the control required. The drag-free control of the spacecraft uses for actuators a field effect electric propulsion (FEPP) system. These FEPPs are, however, part of the spacecraft, not of the “payload”.

### 3.4.3 The optical bench

The inertial sensor is mounted on the “optical bench” shown in Fig. 3.6, a rigid structure made of ultra-low expansion material (ULE), about 350 mm by 200 mm by 40 mm (length, width, thickness). For rigidity, the optical components are embedded in insets machined into this solid ULE block. All beams propagate in the central plane of this optical bench.

The laser light is conducted onto the optical bench via an optical fibre (mono-mode, polarisation preserving). The light returning from the distant spacecraft is bounced off the proof mass before it is brought to interference with a fraction of the internally generated laser light.



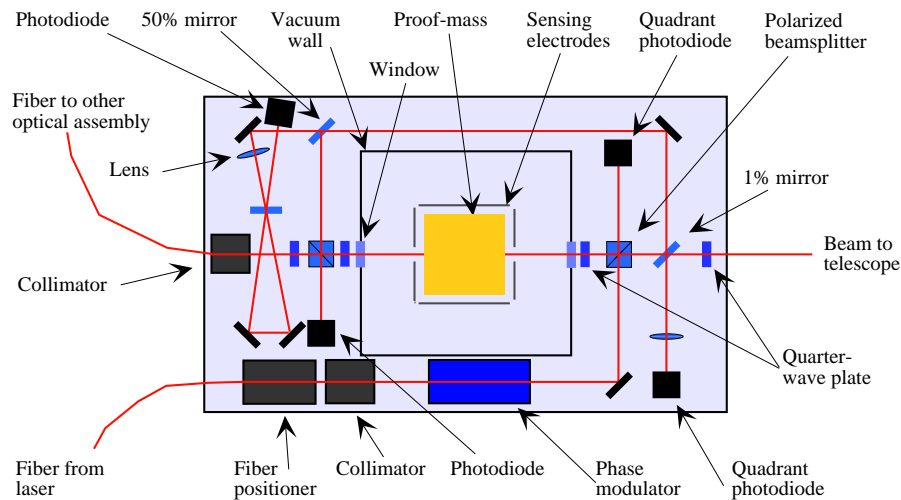


**Figure 3.6** *Top view of the optical bench.*

### 3.4.4 The telescope

The telescope (see right hand part of Fig. 3.5) serves the dual purpose of transmitting the laser beam to the distant spacecraft and of receiving the light from that spacecraft. The telescope was originally conceived as a  $f/1$  Cassegrain design of the Richey-Chrétien type, with a parabolic primary mirror of 300 mm in diameter, and a hyperbolic secondary mirror, 32 mm in diameter, the mirrors to be made of ULE, the secondary mirror being supported by a stiff carbon-epoxy spider. This scheme has been changed somewhat, see Section 8.7 and Appendix A.6.

### 3.4.5 The support structure

Optical bench and telescope, and some further components to be enumerated below, are supported inside a structure made of graphite-epoxy, with 3 mm wall thickness. A disk-shaped telescope thermal shield reduces the heat exchange between the (cold) telescope and the optical bench (roughly at “room temperature”).

### 3.4.6 The thermal shield

In addition to the top lid (not shown in Figure 3.3), constituting a first stage of thermal shielding, the whole science payload is encapsulated in the Y-shaped tubular thermal protection. This consists of gold-coated carbon-epoxy, affording the highly stable environment for the science package. The tubes are 400 mm in diameter, and they are supported by fiberglass tension bands in the spacecraft structure. They provide the anchor for the pointing articulation of the support structure inside.

### 3.4.7 The star trackers

Outside of the payload thermal shield, pointing parallel to the two arms, star trackers are to be mounted either on the “lower side” of the solar panel rim or on standoffs from the payload thermal shield inside the spacecraft cylinder. For redundancy, a total of four star trackers per spacecraft may have to be provided.



### 3.5 Lasers

Lasers have extremely narrow beams that can survive long journeys through space. In addition, they are very stable in frequency (and phase) which is crucial to interferometry since phase “noise” appears just like gravitational waves. Furthermore, the infrared light has a frequency of  $3 \times 10^{14}$  Hz which renders it immune from refraction caused by the charged particles (plasma) which permeate interplanetary space.

The lasers for *LISA* must deliver sufficient power at high efficiency, as well as being compact, stable (in frequency and amplitude), and reliable. The plan is to use solid-state diode-pumped monolithic miniature *Nd:YAG* ring lasers that generate a continuous 1 W infra-red beam with a wavelength of  $1.064 \mu\text{m}$ .

Each spacecraft has two 1 W lasers (actually four, two for redundancy), and two identical payload assemblies, each comprising a two-mirror telescope for sending and receiving light, and an optical bench which is a mechanically-stable structure on which various sensitive optical components are mounted. An optical assembly is shown in Figure 3.5. The mirrors enclosed in each spacecraft are actually 40 mm gold-platinum cubes (also referred to as the ‘proof masses’). Each one is located inside a titanium vacuum can at the centre of the respective optical bench. Quartz windows allow access for the laser light.

Within the corner spacecraft, one laser is the ‘master’, and a fraction of its light (10 mW) is bounced off the back surface of its cube, and used as a reference to ‘slave’ the other local laser. In this way, the main ( $\sim 1$  W) beams going out along each arm can be considered as having originated from a single laser.

### 3.6 Data extraction

The light sent out along an arm is received by the end spacecraft telescope, bounced off its cube, then amplified using its local laser, in such a way as to maintain the phase of the incoming light. The amplified light is then sent to the corner spacecraft. Amplification at the end spacecraft is required due to divergence of the beam over the very large distances. Even though each outgoing beam is extremely narrow — a few micro radians — it is about 20 km wide when it reaches the distant spacecraft. This diffraction effect, together with unavoidable optical losses, means that only a small fraction of the original output power ( $\sim 10^{-10}$ ) finally reaches the end diode. If this was simply reflected and sent all the way back, only about 200 photons per hour would reach the corner diode after the round-trip. The phase-signals they carry would be swamped by shot noise, the quantum-mechanical fluctuations in the arrival times of the photons. The amplification brings the number back up to over  $10^8$  photons per second — which makes the signal detection straightforward using standard photodiodes.

The phase precision requirement for this measurement is seven orders of magnitude less demanding than is routinely achieved (at higher frequencies) in ground-based prototype interferometers ([97, 98, 99]).

The resulting round-trip journey from the corner to the end and back defines one arm of the large interferometer. On its return to the corner spacecraft, the incoming light is bounced off the cube and then mixed with a fraction of the outgoing light on a sensitive photodetector, where interference is detected. The resulting brightness variations contain the phase-shift information for one arm of the interferometer. This signal is then compared (in software on the on-board computer) with the corresponding signals from the other two arms, and some preliminary data processing is done. The results are then transmitted to Earth by radio link.

### 3.7 Drag-free and attitude control

An essential task of the spacecraft is to protect the mirrors from any disturbances which could jostle them around and create phase-signals that appear as gravitational waves. For example, consider the momentum of the light from the Sun which amounts to an average pressure of about  $5 \times 10^{-6} \text{ N/m}^2$ . The internal dynamics of the Sun lead to small variations — less than one percent — in this photon pressure, which occur at the low frequencies within LISA’s range of interest. Although this variable photon pressure may seem rather small, if it were allowed to act on the cubical mirrors, the resulting motion would be  $10^4$  times larger than the tiny motions due to gravitational waves that LISA is looking for.

By simply “wrapping a spacecraft around each one”, the cubes are isolated from the solar pressure — but this is not the complete picture. When the solar pressure blows on the surface of the spacecraft, it will move relative to the freely-floating cube. Left alone, this motion would build up to unacceptable levels — in the extreme case, the cube would eventually “hit the wall”. To stop this from happening, the relative motion can be measured very precisely by monitoring the change in electrical capacitance between the cube and electrodes mounted on the spacecraft. This measurement is then converted into a force-command which instructs thrusters mounted on the outer structure of the spacecraft, to fire against the solar pressure and keep the spacecraft centred on the cube.

This concept is, for historical reasons, known as “drag-free control”, since it was originally invented in the 1960’s to shield Earth-orbiting satellites from the aerodynamic drag due to the residual atmospheric gases. The method was first demonstrated on the TRIAD spacecraft, flown by the US Navy in 1972, where the drag-free controller designed at Stanford University in collaboration with the Johns Hopkins Applied Physics Laboratory, was effective in reducing the effects of atmospheric drag by a factor of  $10^3$ . Since then, the technique has undergone continued development, most notably for use on NASA’s Gravity Probe B mission, which is the proposed space experiment to search for the relativistic precessions of gyroscopes orbiting the Earth.

The thrusters used on conventional spacecraft are far too powerful for LISA. The drag-free system only needs to develop a force of a few micro-newtons. Furthermore, the delivered force must be smoothly controllable so that the varying disturbance forces can be matched without introducing a further disturbance from the thrust system itself. Surprisingly, it is not a trivial task to build a thruster which generates such a small force and yet operates smoothly and does not consume too much power. By good fortune, ESA has been developing them for years, as an alternative to hydrazine rockets for station-keeping of communication satellites.

They are called FEEDs, for Field Emission Electric Propulsion. They operate by accelerating ions in an electric field, and ejecting them to develop the thrust. They are described in Section 9.7.

### 3.8 Ultrastable structures

The small variations in the intensity of sunlight will cause fluctuations in the heat-load applied to the spacecraft. This could lead to thermal gradients across the optical bench, which would upset the stability of the laser cavity. To obtain the required thermal stability, most structural elements are made from carbon-epoxy which has a thermal expansion coefficient of  $4 \times 10^{-7}/\text{K}$  and the optical bench is made from ULE, which has a temperature coefficient at least a factor 4 lower over the possible temperature range of the LISA payload. Furthermore, low emissivity coatings are used on most surfaces inside the spacecraft and a thermal shield surrounds the payload

cylinder, in order to provide isolation from the temperature variations of the spacecraft skin that is exposed to the Sun. These shields are only effective against heat fluctuations faster than a few hours to half a day. The slower variations will get through, thus making the sensitivity of [LISA](#) deteriorate rapidly below roughly  $10^{-4}$  Hz. The use of carbon-epoxy structures also minimises any thermally-induced mechanical distortions which could produce physical changes in the optical path-length, as well as local gravitational disturbances on the mirror-cubes.

### 3.9 System options and trade-off

In studies undertaken on mission and spacecraft level, several system options have been investigated in order to meet operational constraints (launcher, transfer orbit, cost cap). The mission scenario had been baselined as to orbit, constellation, launcher. Major trade-offs therefore were focussing on the propulsion module / science module configuration, the communication link and the internal structural, electrical and thermal concept.

Nevertheless, at the begin of this study a brief qualitative review of alternative concept and design options, which have the potential to:

- Solve technical problems encountered with the baseline approach
- Drastically reduce the technical complexity and hence the risk of failure
- Enhance mission reliability and redundancy
- Allow a better validation of performance in terms of [AIV](#) procedures and costs
- Lead to less stringent tolerances in design parameters and to optimised share of design loads among subsystems
- Lead to significant reduction in cost and development effort

Of course within the scope of the study it was not possible to perform full detailed analyses of alternative payload concept options. Further, the baseline concept as described in the ‘Payload Definition Document’ [100] has been analysed so far in much more detail compared with the potential alternatives. Especially, for the [CAESAR](#) baseline inertial reference sensor, a long heritage of precursor developments exists. In an effort to identify less complex approaches, it may well turn out that a promising alternative (e.g. featuring less control degrees of freedom) may be more complex at the end after detailed investigation. Hence, the alternatives have been identified as a pool of concept options to draw upon only in case principle difficulties would have been encountered with the baseline concept. However, as major result of this study, the baseline concept at the recent level of investigations turns out to be a valid approach indeed, with some modifications necessary on assembly level (e.g. point ahead angle compensation implementation). The further Sections, and the Appendices will give a broader discussion of some of the options.

### 3.10 Summary tables

The new baseline for [LISA](#) is a combination of the revised proposal [1] and improvements, suggestions, favourable options, as given in the Industrial Study [2].

The [LISA](#) project is summarized in the three following tables. The entries are taken mostly from the Industrial Study [2], in most cases they are, however, close to the original [PPA 2](#) data.

These tables provide a short overview of the specifications. These figures will be broken down further in the subsequent chapters.

**Table 3.1** *Main System Requirements*

<i>Item</i>	<i>Value</i>	<i>Comments</i>
<b>Science / Mission</b>		
Measurement error $\Delta L$	$4 \times 10^{-11}$ m	Total measurement error of the variations in path difference, $\Delta(L_2 - L_1)$ , between the two arms.
Strain sensitivity $\Delta L/L$	$10^{-23}$	For one year of observation, with a signal to noise ratio of $S/N = 5$ .
GW frequency range, extended:	$10^{-4} - 10^{-1}$ Hz $10^{-5}$ Hz – 1 Hz	Selected spectral range of measurements. The spectral range determines the required distance between satellites and is a major design driver for the S/C (thermally induced distortions)
Source location accuracy, periodic sources: other sources:	$< 1$ arcmin few degrees	Spatial resolution and wave polarisation are determined by analysing Doppler shift and differential amplitudes in the signals, and from the annual orbit
Data acquisition		Observation data shall be acquired and processed on ground for not less than 90% of the mission time.
Mission duration	2 years at least	(10 years optional)
<b>Orbit Requirements</b>		
Heliocentric orbit		Three satellites form an equilateral triangle. Any two arms form an interferometer.
Distance from Earth, in ecliptic	$20^\circ$ (trailing)	Centre of triangular formation is in ecliptic, in an Earth-like orbit, $20^\circ$ behind the Earth.
Plane of triangular S/C formation	$60^\circ$ (from ecliptic)	$60^\circ$ inclination w.r.t. the ecliptic maintains S/C formation throughout the year. S/C formation rotates about the centre of the triangle once per year.
Distance between the individual S/C	$5 \times 10^9$ m	The arm lengths define both the sensitivity and the spectral response of LISA.
Difference of arm length knowledge of relative position	1 % [101], 30 km [PDD].	TBC during the study. The allowed difference of arm length reflects a requirement for orbit maintenance, i.e. frequency of manoeuvres, thruster performance, propellant, etc. Correction of laser phase noise to achieve the required system sensitivity drives this requirement [101].
Max. relative velocity between the S/C without USO	$< 15$ m/s [101] $0.03$ m/s [PDD]	Needs to be confirmed during the study. The allowed relative velocity of satellites drives the requirement for orbit maintenance, i.e. frequency of manoeuvres, thruster performance, propellant, etc. Measurement of Doppler, heterodyne bandwidth and reduction of USO noise to achieve the required system sensitivity drive this requirement [101].

**Table 3.2** *Optics Requirements*

<i>Item</i>	<i>Value</i>	<i>Comments</i>
<b>Laser</b>		
Number of lasers per S/C	2 + 2 spare	Nd:YAG monolithic non-planar ring laser <b>NPRO</b> . One laser plus one spare laser per optical assembly.
Optical output power	$\geq 1$ W	Drives the laser link budget, together with space loss, receiver area and detection efficiency
Frequency stability at 1 mHz, (spectral density)	$\leq 30 \text{ Hz}/\sqrt{\text{Hz}}$	One laser serves as master (commanded), locked to a Fabry Perot reference cavity. All other lasers are phase (offset) locked to the master. Low frequency noise is reduced from the beat signal by a noise reduction algorithm [101]. The laser phase noise is to be traded against knowledge of arm lengths.
Relative power stability at 1 mHz (spectral density)	$\leq 2 \times 10^{-4}/\sqrt{\text{Hz}}$	The variation of laser power contributes to acceleration noise of the inertial sensors (proof masses)
<b>Optics</b>		
Transmission of optics, Optical isolation, Depolarisation	$\geq 0.3$ <b>TBD</b> <b>TBD</b>	The achievable values in both the transmission and receiving path enter the laser link budget and affect straylight and crosstalk.
<b>Telescope</b>		
Aperture	0.3 m	The current design of [101] assumes a primary mirror of 0.3 m diameter. Low thermal expansion material for the mirrors or athermal design to be used to minimise phase errors due to thermal effects.
Focal length	$f/1$	Cassegrain design of Richey-Chretien type is baseline [101]; Dall-Kirkham as option
Wavefront tolerance	$\lambda/10$	Besides pointing offset sensitivity, heterodyne efficiency and link budget are affected.
Temperature variations at 1 mHz, spectral density	$\leq 10^{-5} \text{ K}/\sqrt{\text{Hz}}$	The required thermal stability of the telescope takes into account low expansion material used for mirrors and the supporting structure. The requirement is driven by the allowed contribution to the distance measurement error.
<b>Optical Bench</b>		
Thermal expansion of bench	$\text{CTE} \approx 10^{-8}/\text{K}$	A trade-off between Ultra Low Expansion ( <b>ULE</b> ) glass and Zerodur is being performed.
Temperature variation (spectral density)	$\leq 10^{-6} \text{ K}/\sqrt{\text{Hz}}$	Temperature variation at 1 mHz due to variation of the solar constant (4 min oscillation). Temperature variation due to power dissipation of any electronics must comply with this requirement.

**Table 3.3** *Other System Requirements*

<i>Item</i>	<i>Value</i>	<i>Comments</i>
<b>Inertial Sensor</b>		
Resolution	$1 \times 10^{-9} \text{ m}/\sqrt{\text{Hz}}$	Resolution required to limit disturbances induced by relative motions between proof mass and S/C.
Acceleration by disturbing forces at 0.1 mHz, per sensor	$3 \times 10^{-15} \text{ ms}^{-2}/\sqrt{\text{Hz}}$	Various disturbances contribute to the acceleration noise. The corresponding distance (phase) error is proportional to $1/f^2$ , i.e. acceleration noise limits the sensitivity of LISA towards low frequencies.
<b>USO</b>		
Allen variance at $10^4 \text{ s}$	$2 \times 10^{-13}$	Requirement as reported in [100]. The proposed algorithm for reducing USO noise shows that after processing no USO noise remains. Thus the Allan variance requirement may possibly be relaxed.
<b>Drag Free Control</b>		
Displacement between S/C and proof mass	$< 2.5 \times 10^{-9} \text{ m}/\sqrt{\text{Hz}}$ in sensitive direction	Requirement in measurement band width.
ditto	$< 2.5 \times 10^{-9} \text{ m}/\sqrt{\text{Hz}}$ orthogonal	The cube positioning in the lateral beam direction must be similar to avoid excessive cross talk.
Relative attitude between S/C and proof mass	$< 1.5 \times 10^{-9} \text{ rad}/\sqrt{\text{Hz}}$	Internal contribution to the beam pointing budget
<b>Pointing</b>		
Offset pointing error (DC)	$< 3 \times 10^{-8} \text{ rad}$	This is a requirement on the allowed angular fluctuation of interfering beams. The distance (phase) error needs to be controlled by a dedicated pointing system that uses the phase information of the quadrupoles that are also used for detection of the beat signal. Since the product of DC pointing error and pointing stability defines the overall phase error a trade-off of both requirements can be performed.
Pointing stability, (spectral density)	$< 8 \times 10^{-9} \text{ rad}/\sqrt{\text{Hz}}$	See above. The values are affected by pointing jitter achieved and by astigmatism primarily
Point-ahead angle	$\approx 3 \times 10^{-6} \text{ rad}$	Nearly time independent angle between incoming and transmitted laser beam due to S/C motion, arm length and speed of light.
<b>Measured Signals</b>		
Number of signals to be acquired per S/C	$4 + 2$	Based on the current design of [101], six signals per S/C have to be acquired for eliminating laser and USO phase noise, as well as for determining the Doppler. After down-conversion and low pass filtering each signal is sampled at 1 to 2 Hz (TBD)

# 4 Measurement Sensitivity

## 4.1 Interferometer response

The sensitivity of the [LISA](#) mission is determined by two competing features: by the response, i.e. the ‘*output signal*’, of the interferometer to a given gravitational wave of strength  $h$  on the one hand, and by the effects of various noise sources that fake such gravitational wave signals on the other. We shall specify that relationship, as well as the terms “sensitivity” and “signal-to-noise ratio” [SNR](#), in this section.

An interferometer of the Michelson type measures the phase difference between the two beams after they have returned from the two arms of length  $L$ , i.e. after each has traversed a total optical path of  $\mathcal{L} = 2L$ . Some noise effects (e.g. shot noise) will also fake such differences in phase (or optical path), and it is therefore a natural choice to express all effects in terms of this total optical path  $\mathcal{L}$ .

The strength of a gravitational wave is described by the “dimensionless amplitude”  $h$ , which, for normal incidence onto the light path, is defined as *twice* the relative change  $\delta L$  of a given distance  $L$ :

$$h := 2 \frac{\delta L}{L}, \quad (4.1)$$

or, in other words, a given length  $L$  will undergo an apparent strain  $\delta L/L$  of  $h/2$ . If we assume a Michelson interferometer with orthogonal arms, a gravitational wave coming from the normal of the interferometer’s plane, and with the appropriate polarization, would cause single-pass changes  $\delta L$  of opposite polarity in the two arms (having nearly equal geometrical lengths  $L_1$  and  $L_2$ ), and the *path length difference*  $\delta \mathcal{L} = 2(\delta L_2 - \delta L_1)$ , divided by the path length becomes

$$\frac{\delta \mathcal{L}}{\mathcal{L}} = h. \quad (4.2)$$

The difference scheme makes the response of a Michelson interferometer by a factor of two larger than that of a single arm.

For gravitational wave frequencies  $f_{\text{GW}}$  at which the interferometer path length  $2L$  becomes an appreciable part of the gravitational wavelength  $\Lambda = c/f_{\text{GW}}$ , the relation Eq. (4.2) has to be modified to

$$\frac{\delta \mathcal{L}}{\mathcal{L}} = h \operatorname{sinc} \left( \frac{2\pi L}{\Lambda} \right), \quad (4.3)$$

again assuming normal incidence and optimum polarization of the gravitational wave.

In the case of [LISA](#), the two arms do not subtend a right angle, but one of only  $60^\circ$ , thus decreasing the response by a factor  $\sin 60^\circ = 0.8660$ . Furthermore, the angle of incidence depends on the position of the source at the sky and on the momentary orientation of [LISA](#) which undergoes a continuous change during its orbit around the Sun, see Figure 3.2. The following Figure 4.1 gives an example of the rather complex dependence of the [LISA](#) response while orbiting the Sun. Shown are, at a gravitational-wave frequency of 45 mHz and a source declination of  $30^\circ$  above the ecliptic, the orbit dependence for four different source azimuths  $\alpha_s$  and six different polarisations each [102].



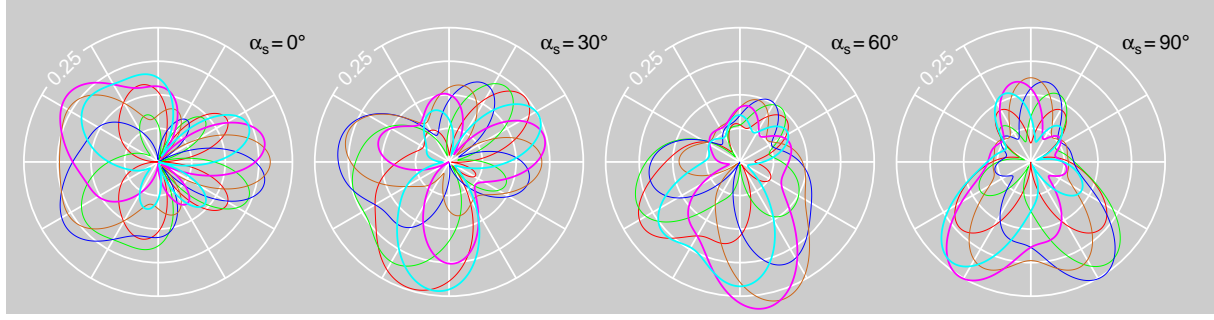


**Figure 4.1** Magnitude of the normalised *LISA* transfer function in dependence upon the orbit azimuth for a source at declination  $30^\circ$  and azimuths of  $0^\circ$ ,  $30^\circ$ ,  $60^\circ$  and  $90^\circ$ , at a frequency of  $45 \text{ mHz}$ . Six curves for different polarisation angles are shown in each diagram:  $0^\circ$  (red),  $15^\circ$  (green),  $30^\circ$  (blue),  $45^\circ$  (yellow),  $60^\circ$  (magenta) and  $75^\circ$  (cyan).

When averaged over the different angles of incidence of the gravitational wave in the course of one year, the antenna response is smoothed out considerably, and the nulls in Eq. (4.3) disappear. Figure 4.2 shows the frequency response of *LISA* for four different source declinations  $\delta$  after averaging over the orbit and all possible source azimuths and polarisations.

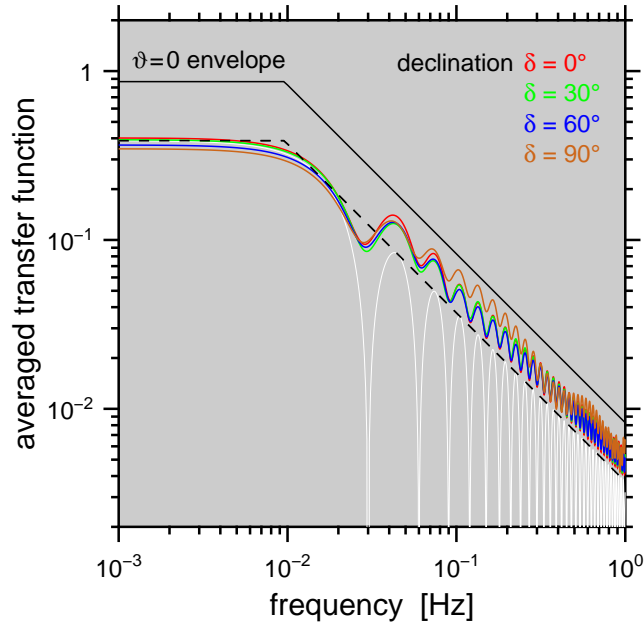


**Figure 4.2** Magnitude of the normalised *LISA* transfer function in dependence upon frequency after averaging over the orbit and all possible source azimuths and polarisations, shown for source declinations of  $0^\circ$  (red),  $30^\circ$  (green),  $60^\circ$  (blue) and  $90^\circ$  (yellow). For comparison, also shown are the envelope for normal incidence (black), the same line reduced by  $\sqrt{5}$  (black, broken line) and the transfer function proper for such a case (white).



## 4.2 Noises and error sources

### 4.2.1 The noise effects

Let us consider noise that will fake path differences of  $\delta\mathcal{L}_{\text{noise}}$ , then the level at which true gravitational wave signals can be reliably detected must be sufficiently above this noise level.

The required *signal-to-noise ratio* (SNR) will be dependent on a multitude of features of the expected signal, the characteristics of the noise, the duration of the measurement, etc. It has become practice to specify a SNR of 5, and a geometric factor of  $\sqrt{5}$  to allow for less optimal directions and polarizations. The measurement time is generally assumed to be 1 year, even though the lifetime of LISA would make longer measurement times possible.

It is with these assumptions that the sensitivity curves in the figures of Section 1.2 have been drawn.

### 4.2.2 The noise types

The sensitivity of LISA is determined by a wide variety of noise sources, and by the degree to which their effects can be kept small. There are two main categories of such sensitivity-limiting noise effects:

- A first one that fakes fluctuations in the lengths of the optical paths, which we will call *optical-path noise*. This category of disturbances includes different types of noise, the most prominent of which are expected to be shot noise and beam pointing instabilities. These contributions will, in general, be uncorrelated, and therefore by adding quadratically the four contributions from the four passes gives the final (apparent) fluctuation in optical path difference.
- The second category is due to forces (or accelerations) acting on the proof masses. The drag-free environment will effectively shield the proof masses from outside influences, but some residual *acceleration noise* will remain. These accelerations will lead to displacement errors  $\delta x$  of the proof masses, and for each pass these errors have to be counted twice to arrive at the (real) fluctuation in optical path difference.

Considering these types of noise and the frequency dependence of the interferometer response as presented in Figure 4.2, one arrives at a typical sensitivity curve shown in Figure 4.3. In the low-frequency range, say below 2 mHz, the noise, and thus the sensitivity, is determined by the acceleration noise, leading to a decrease in sensitivity towards lower frequencies roughly proportional to  $f^{-2}$ . Above about 2 mHz the noise is dominated mainly by the shot noise, where the decline of the antenna transfer function above 10 mHz causes a decrease in sensitivity roughly proportional to the frequency.

The following subsections will discuss the most important noise sources, and means to suppress them. They are given in tabular form, separately for optical-path and acceleration noise.

The entries were conceived as ‘error allocations’, specifications of the maximum allowable effects, if the overall sensitivity goal of LISA is to be met.

The justification was confirmed by an independent assessment made in Industrial Study, starting out from different assumptions. The FTR [2] arrived at a very similar value for the total noise level.

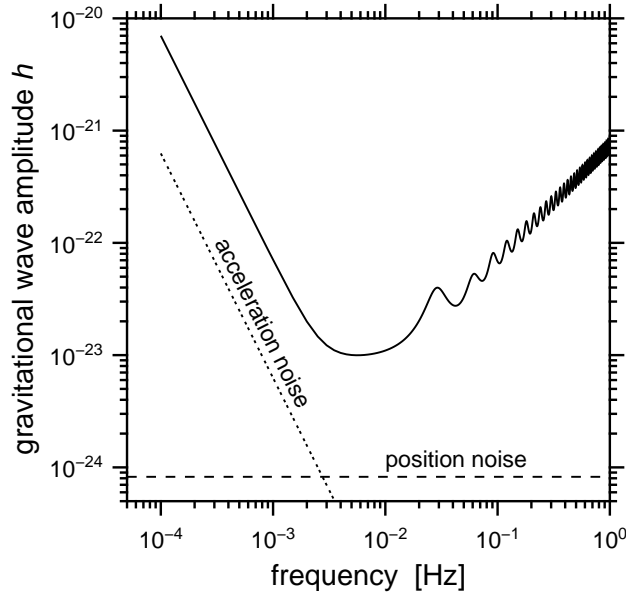


**Figure 4.3** *LISA* sensitivity for one year integration time and a signal-to-noise ratio of 5, averaged over all possible source locations and polarisations. Also indicated are the position noise (dashed line) and the acceleration noise (dotted line).

### 4.2.3 Shot noise

Among the optical-path noise sources, a very fundamental one is *shot noise*, which for each *single* passage through an arm of length  $L$  leads to a *power* spectral density of apparent optical-path fluctuations

$$\mathcal{S}_{\delta L}(f) := \left( \widetilde{\delta L}(f) \right)^2 = \frac{\hbar c}{2\pi} \frac{\lambda}{P_{\text{avail}}} . \quad (4.4)$$

There are four such single paths, their uncorrelated contributions adding up quadratically to the final shot noise value  $\widetilde{\delta \mathcal{L}}$ , the apparent variation of the total path difference  $\mathcal{L}_2 - \mathcal{L}_1$  in one *LISA* interferometer (see also Section 5.4).

The light power available,  $P_{\text{avail}}$ , is extremely low, due to the beam spreading ( $P/P_0 < 2 \times 10^{-10}$ ) and the poor efficiency  $\eta$  of optics and photodiode ( $\eta \approx 0.3$ ). Shot noise would therefore set a limit for the smallest detectable single arm-length variation of  $\widetilde{\delta L} \approx 11 \times 10^{-12} \text{ m}/\sqrt{\text{Hz}}$ , assuming 1 W of laser power, or  $\widetilde{\delta \mathcal{L}} \approx 22 \times 10^{-12} \text{ m}/\sqrt{\text{Hz}}$ , for the total path-length variation.

This fluctuation has to be set in relation to the path length  $\mathcal{L} = 2L = 10^{10} \text{ m}$  over which the light has been subjected to the gravitational wave strain.

### 4.2.4 Optical-path noise budget

It will be our aim to keep all other *optical-path* noise contributions at a level comparable with the shot-noise induced sensitivity limit. A goal of an accumulated path-length noise of  $\widetilde{\delta \mathcal{L}} \approx 40 \times 10^{-12} \text{ m}/\sqrt{\text{Hz}}$  was set as a realistic target.

For the purpose of setting up a detailed error budget, the effects of known noise sources were given error allocations, which are indicated in Table 4.1, [1].

In the Industrial Study [2], an independent noise analysis was undertaken, which has led to a very similar total error value.

**Table 4.1** *Major sources of optical-path noise, and schemes to suppress their effects.*

Error Source	Error*	Number	Error Reduction Approach
Detector shot noise 1 W laser; 30 cm optics	11	4	Optimise efficiency of optical chain
Master clock noise	10	1	Ultra-stable oscillators (USO) and correction procedure
Residual laser phase noise after correction	10	1	Use of phase noise correction algorithm
Laser beam-pointing instability	10	4	Active stabilisation of angular orienta- tion of proof masses and spacecraft
Laser phase measurement and offset lock	5	4	Low noise electro-optic design
Scattered-light effects	5	4	Frequency offset; frequency stabilisa- tion of laser to cavity
Other substantial effects	3	32	Careful mechanical and optical design
<b>Total path difference</b>	<b>40</b>	<b>= measurement error in <math>\mathcal{L}_2 - \mathcal{L}_1</math></b>	

\*) Errors given in units of  $10^{-12} \text{ m}/\sqrt{\text{Hz}}$

In this fashion, detailed noise budgets have been set up, leading to specifications for the structural design, or for the control of various parameters. Many of the design features shown in Chapters 5 and 6 are the result of these noise reduction considerations.

Table 4.1 gives the current error allocation budget, listing the cause of the spurious optical-path fluctuations, the allowed value (in units of  $10^{-12} \text{ m}/\sqrt{\text{Hz}}$ ), the number of such effects entering in one interferometer of four optical assemblies, and in the last column the means to cope with the problem.

Adding all these contributions quadratically, one arrives at the total path length variation of  $40 \times 10^{-12} \text{ m}/\sqrt{\text{Hz}}$  in the bottom line. It is this estimate of  $40 \text{ pm}/\sqrt{\text{Hz}}$  that formed the basis of the sensitivity curves in the figures of Section 1.2.

The shot noise contribution in Table 4.1 was calculated assuming a 1 W laser and a diameter of 0.30 m for the optics (see Section 5).

Some of the major noise effects are discussed in more detail in the remainder of this section or in subsequent sections.

#### 4.2.4.1 Laser phase noise

Another optical noise source creating spurious optical-path signals is the *phase fluctuations* of the master laser. The four lasers on the four spacecraft are phase-locked with each other, but with about 17 s time delays for two of them because of the length of the interferometer arms. The requirements for measuring and correcting for the laser phase noise are discussed in Section 7.2.1.

#### 4.2.4.2 Thermal vibrations

The proof masses and the optical structures have their resonant frequencies orders of magnitude above the frequency range of the gravitational wave signals. Nevertheless, thermal vibrations

(*Brownian noise*) can produce spurious signals. We are searching for signals whose frequencies are well below the lowest resonant frequencies of the optical structure. The ( $kT$ ) thermal vibration noise is composed of the sub-resonant tails of the (various) structural resonances. These vibrations, per proof mass, have *linear* spectral densities  $\widetilde{\delta L}(f)$  of apparent arm-length fluctuations of a general form

$$\widetilde{\delta L}(f) = \left( \frac{4kT}{MQ\omega_0^2\omega} \right)^{1/2} \quad (4.5)$$

if we assume the (noisier) displacement-dependent ‘structural damping’ (imaginary spring constant) [103]. These noise sources will be very small for *LISA*, so they are not included in Table 4.1.

#### 4.2.5 Acceleration noise budget

Table 4.2 gives the error allocation for spurious *accelerations*, mainly of the individual proof masses, the allowed value (in units of  $10^{-15} \text{ m s}^{-2}/\sqrt{\text{Hz}}$  at  $10^{-4} \text{ Hz}$ ), and the number of such effects entering in one inertial sensor.

The allowed total effect of acceleration noise for one inertial sensor is  $3 \times 10^{-15} \text{ m s}^{-2}/\sqrt{\text{Hz}}$ . The effect on the difference in geometrical arm lengths is then  $6 \times 10^{-15} \text{ m s}^{-2}/\sqrt{\text{Hz}}$ . It is with these values, after multiplication with factors 5 (SNR) and  $\sqrt{5}$  (for orientation and polarisation), that the sensitivity curves of Figures 1.3 and 1.4 were drawn.

To ease comparison of these acceleration errors with the allowed errors in optical path, the total was multiplied by two in the final line, to give  $12 \times 10^{-15} \text{ m s}^{-2}/\sqrt{\text{Hz}}$ . A multiplication with  $\omega^{-2}$  will give the optical-path error due to the contributions in Table 4.2.

##### 4.2.5.1 Thermal distortions

Special care must be taken to avoid too strong a deformation of the spacecraft (optical bench) due to partial heating. Such inhomogeneous heating could arise from changing orientation with respect to the sun (which would have been particularly worrisome in an alternative option, the geocentric configuration). Multiple thermal shielding is used to keep the optical bench at a very stable temperature (about  $10^{-6} \text{ K}/\sqrt{\text{Hz}}$  at  $1 \text{ mHz}$ ), with small temperature gradients.

Furthermore, the mass distribution of the main spacecraft structure is designed such that gravitational effects due to homogeneous expansion and even due to inhomogeneous deformation are kept small.

Section 8.1 gives details on how these thermal considerations entered into the design of the *LISA* payload.

##### 4.2.5.2 Brownian acceleration noise due to dielectric losses

Dissipation intervening in the motion of the proof mass relative to the spacecraft is a source of Brownian acceleration noise. While damping due to residual gas is made negligible by the very low pressure, losses in the electrostatic readout remain as a serious candidate for the residual dissipation. It is easy to calculate that any mechanism that results in a loss angle  $\delta_\varepsilon$  in the effective capacitance between the proof mass and the sensing electrodes, also provides a loss angle  $\delta$  to the (negative) stiffness  $m\omega_{\text{int}}^2$  of the effective spring originating from the electrostatic readout. Candidate physical phenomena for such a source of dissipation are surface losses due to adsorbed molecules, to oxide layers and to hopping of electrons among different workfunction

**Table 4.2** Major sources of acceleration noise, and schemes to suppress their effects.

Error Source	Error*	Number	Error Reduction Approach
Thermal distortion of spacecraft	1	1	Carbon epoxy construction and limited power use variations
Thermal distortion of payload	0.5	1	Carbon-epoxy construction with $\alpha = 4 \times 10^{-7}/\text{K}$ , plus two-stage thermal isolation of payload
Noise due to dielectric losses	1	1	Very low electrostatic coupling
Gravity noise due to spacecraft displacement	0.5	1	1 nm/ $\sqrt{\text{Hz}}$ control of spacecraft displacements with <b>FEEP</b> thrusters
Temperature difference variations across cavity	1	1	Three stages of thermal isolation plus symmetrical heat leak paths
Electrical force on charged proof mass	1	1	Small spacecraft displacements, $> 1$ mm position-sensor gaps, and discharging of proof mass
<i>Lorentz</i> force on charged proof mass from fluctuating interplanetary field	1	1	Intermittent discharging of proof mass, e.g. with UV light
Residual gas impacts on proof mass	1	1	Less than $3 \times 10^{-7}$ Pa pressure in proof-mass cavity
Telescope thermal expansion	0.5	1	Low-expansion secondary mounting plus two-stage thermal isolation
Magnetic force on proof mass from fluctuating interplanetary field	0.5	1	$10^{-6}$ proof-mass susceptibility plus moderate spacecraft magnetic-field gradient
Other substantial effects	0.5	4	
Other smaller effects	0.3	16	
Total effect of accelerations:	3	for one inertial sensor	
<b>Effect in optical path:</b>	<b>12</b>	= variation in $\frac{\partial^2}{\partial t^2} (\mathcal{L}_2 - \mathcal{L}_1)$	

\*) Errors given in units of  $10^{-15} \text{ m s}^{-2}/\sqrt{\text{Hz}}$

minima. In addition, leakage of the electric field into lossy dielectric parts of the apparatus may also contribute.

In simple geometries one can expect  $\delta \approx \delta_\varepsilon$ , and the resulting acceleration noise has a spectral density

$$\mathcal{S}_a = \frac{4kT |\omega_{\text{int}}|^2}{m|\omega|} \delta_\varepsilon. \quad (4.6)$$

$|\omega_{\text{int}}|^2$  is proportional to the square of the bias voltage needed to sense the mass displacement. Thus, though  $|\omega_{\text{int}}|^2$  can be reduced by reducing the voltage, this also causes a loss in displacement sensitivity. Fortunately, as repeatedly stated, **LISA** does not need a very high displacement sensitivity. As a consequence,  $|\omega_{\text{int}}|$  can be made as low as  $|\omega_{\text{int}}| \approx 10^{-4} \text{ rad/s}$ . The mission goal is then met for  $\delta_\varepsilon < 10^{-6}$ .



# 5 The Interferometer

## 5.1 Introduction

When a gravitational wave passes through the plane of the [LISA](#) antenna it can be regarded as changing the geometry of the antenna. The precise length of each arm is defined by the distance between the front faces of proof masses positioned inside the three drag free spacecraft. The changes in proof-mass separations are determined by measuring the phase delays for laser beams which have traversed the arms of the interferometer. Due to the wide spread of even a well collimated laser beam over the arm length of  $5 \times 10^6$  km, the beam cannot simply be reflected at the far spacecraft. Rather, the beams are ‘amplified’ with the help of a laser at each craft. So the interferometry is done by comparing the phase of an infra-red laser beam being transmitted out to a far mass with that of the beam transponded back.

In this section, we discuss the layout of the optical system, the performance requirements it must meet and the current plans for measuring the phase of the various heterodyne signals. In [Section 7.1](#) we explain in more detail the planned methods for correcting for the laser phase noise and for removing the effects of clock noise.

To describe the method for measuring the distance changes, it is useful to have a nomenclature for referring to the different spacecraft, optical benches, and arms, as shown in [Figure 5.1](#). The three spacecraft ([S/C](#)) are labelled A, B and C, and each [S/C](#) contains two optical benches, labelled A1, A2, B1, B2 and C1, C2. The arms of the interferometer are defined between the optical benches, *e.g.* arm 1 is between optical benches A1 and C2. Note that all designations progress counterclockwise around the triangle.

In one basic scheme of data acquisition and analysis, the laser associated with optical bench A1 will serve as the master laser for the whole system and will be locked to an on-board reference cavity. All the other lasers in the system will be phase locked to this master laser. The lasers on a spacecraft can thus be considered as essentially identical and the three spacecraft can thus be thought of as forming a Michelson interferometer with an extra arm. Signal information from the other two [S/C](#) will be sent back to [S/C A](#) by modulation put on the laser beams travelling between the spacecraft. This information is then used in [S/C A](#) to correct for laser phase noise and to determine the gravitational wave signal.

## 5.2 Phase locking and heterodyne detection

One spacecraft is designated as the master craft ([S/C A](#)) and one laser (laser A1) in this spacecraft is locked to its reference cavity. The other laser (laser A2) in this craft is offset locked to laser A1. Laser A1 points out to the spacecraft (C) at another vertex of the triangle and the relevant laser in that craft (laser C2) is offset locked to the incoming light from laser A1. Similarly laser A2 points to the remaining spacecraft (B) and laser B1 in that craft is offset locked to laser A2. Laser B2 is offset locked to laser B1 in the same space craft and laser C1 is offset locked to laser C2.

The offset frequencies, all different and around 10 kHz, for the locking are provided by numerically programmed oscillators ([NPOs](#)) on each spacecraft driven from a [USO](#).

We assume that the spacecraft orbits are chosen so that variations in arm length for arms 1

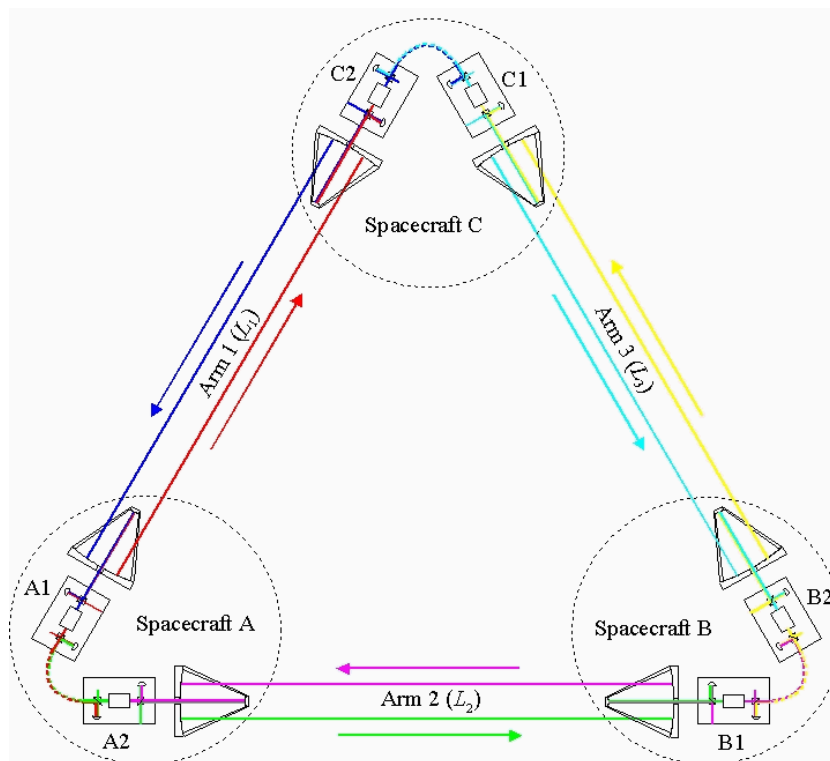


**Figure 5.1** Schematic diagram of the layout of the *LISA* interferometer, showing the labeling scheme adopted.

and 2 remain fairly small without orbit adjustments over periods of several months or longer. The phases of the beat signals over the interferometric arms are determined in all three spacecraft by means of multiple input phase comparison units, (*e.g.* modified Turbostar GPS receivers from Allen Osborne Associates Inc.) at time intervals of perhaps 10 ms as discussed later. The results are then smoothed and sampled at a rate of about 0.5/s and the results from spacecraft B and C are telemetered back to spacecraft A suitable modulation of a carrier ( $\sim 200$  MHz) imposed on the laser light on each craft by the phase modulator on each optical bench. The necessary bit rate is approximately 100 bits/s. The data collected on craft A are processed on-board to essentially remove the effects of laser phase noise and of noise associated with the USOs in the system.

More detailed descriptions of various error-eliminating schemes are discussed in Chapter 7, and in the Appendix.

### 5.3 Interferometric layout

Figure 5.2 shows the payload for one of the three spacecraft. The payload consists of two identical assemblies each containing a proof mass, optical bench and telescope. The two assemblies are joined at the junction of the ‘Y’ by a flexure. The front of each assembly is mounted from the thermal shield by an adjustable strut, allowing the angle between the two telescopes to be adjusted. By varying the length of this strut and the orientation of the spacecraft the pointing of each telescope may independently optimised. At the rear of each optical bench is a steerable mirror to direct light from one optical bench to the other.



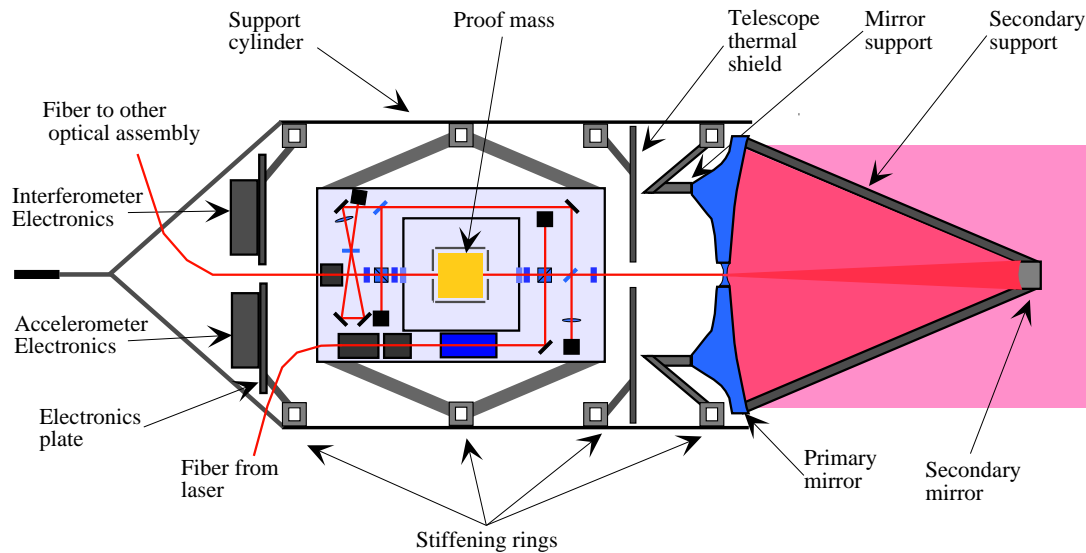


**Figure 5.2** *The payload assembly. Each structure consists of a thermal shield from which are mounted: the 30 cm transmit/receive telescope; a disk shaped thermal shield; the optical bench with laser-injection, cavity for laser stabilisation, beam-shaping optics, photodetectors, and drag-free accelerometer (containing the interferometer “mirror”); a preamplifier disk which carries the accelerometer preamplifiers, the USO and the small steerable mirror for the laser-link between the two optical benches.*

### 5.3.1 The optical bench of PPA 2

The main optical components are located on an ‘optical bench’, containing the laser beam injection, detection and beam shaping optics, and the drag-free sensor (or “accelerometer”). The proof mass of the drag-free sensor acts as the mirror at the end of the interferometer arm. The bench consists of a solid ULE plate to which all components are rigidly attached. The components are shown schematically in Figure 5.3. Most components on this structure are passive. Exceptions are a motorised positioner for fibre selection and focusing, photodiodes for signal detection and a phase modulator that allows transfer of information between craft. Light from the laser is delivered to the optical bench by a single-mode fibre. A second fibre coupled to the back-up laser is also provided and may be selected if required.

About 1 mW is split off the main light beam to serve as the local reference for the heterodyne measurement of the phase of the transponded beam returning from the far spacecraft. This splitting is performed by the finite transmission of the polarising beamsplitter in front of the main mirror. Also, in each craft, a few mW is split off and directed towards a triangular cavity. This cavity is used as a frequency reference in the master craft, with those in the other craft being available for backup purposes.

The incoming light from the telescope is reflected off the proof mass and superimposed with the local laser on the phase measuring diode. An optical isolating arrangement consisting of a polarising beamsplitter and a quarter-wave plate is used to allow the required transmission, reception and phase comparison functions to be carried out in a compact way. On the two optical benches in a spacecraft a small fraction ( $100\ \mu\text{W}$ ) of the laser light is reflected off the back of the proof mass and sent to the other optical bench for phase-comparison via the steerable aft-mirror of 1 cm diameter. This mirror is servoed using the signal from an auxiliary quadrant

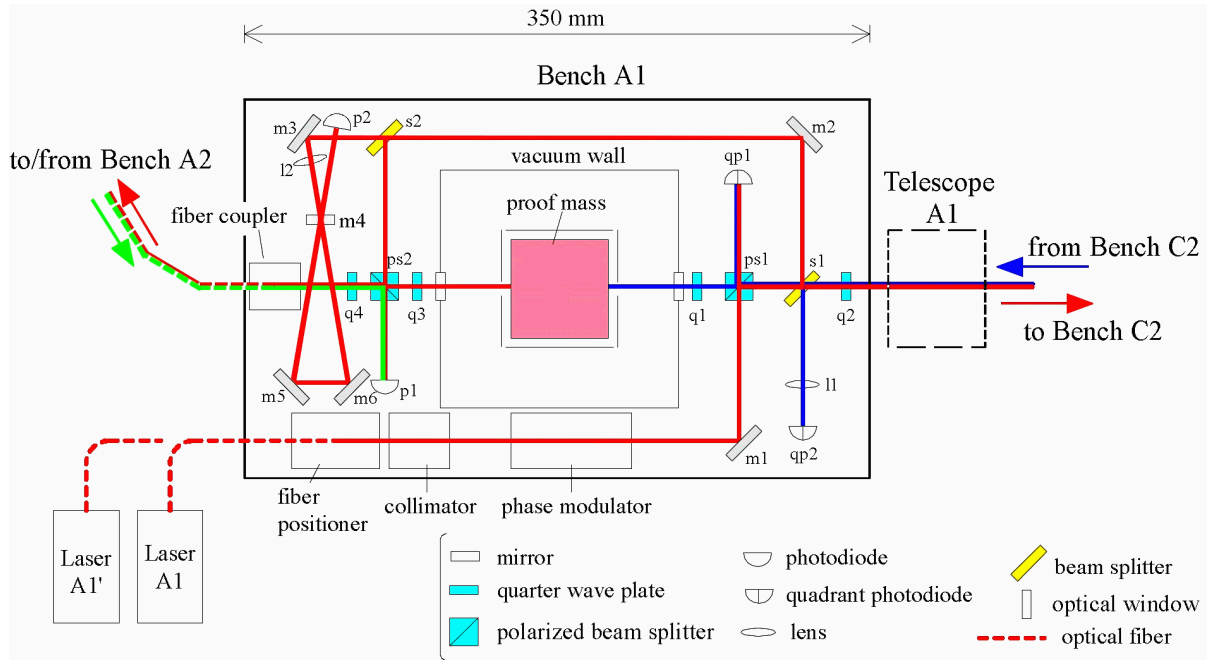


**Figure 5.3** Diagram of the optical bench. The chosen light path renders the measurement insensitive to movement on the spacecraft. The light from the local laser passes through a collimator, a phase modulator and a polarizing beamsplitter to the expanding telescope. The light beam received by the telescope from the distant spacecraft first gets reflected at the proof mass and then interferes with a small fraction of the local laser light at a (quadrant) photodiode (upper right). The diode in the lower left senses the signal for the phase locking between the two lasers at the same spacecraft. The diode in the upper left locks the laser to the reference cavity and the quadrant diode in the lower right is used in pointing the spacecraft.

photodiode which senses both the phase difference between the two beams and the direction of the incoming beam. By bouncing the laser beams off the proof mass in the manner described, the interferometric measurement of proof-mass position is, to first order, unaffected by motion of the surrounding spacecraft. This allows a relaxation of its relative motion specification (though the requirement on proof-mass residual motion with respect to inertial space remains unchanged).

### 5.3.2 Optical bench, revisited

The Pre-Phase A layout of the OB is shown in Figure 5.3 (it refers to the bench A1 according to the nomenclature of Figure 5.1). The OB is composed of a ULE baseplate supporting the inertial sensor and the optical and opto-electronic elements that constitute the LISA laser interferometers.

The laser beam is sent to the bench through a polarisation-preserving fibre that ends in a mechanical positioner for the in-flight fine adjustment of alignment and focus. Then the beam passes through a phase modulator and is split in two components: a small fraction arrives at the quadrant photodiode qp1 (providing the local reference for the phase measurement) while the largest amount is sent towards the telescope for its transmission to the remote spacecraft.

Before leaving the OB another small fraction of the beam is split by s1, which sends it towards

a reference optical cavity (utilised for the laser frequency stabilisation) and to the backside of the proof mass before being sent to the bench A2 via a polarisation-preserving optical fibre. No more than  $100\mu\text{W}$  shall bounce off the back of the proof mass for an acceptable radiation pressure induced acceleration noise). A small fraction of the beam reaches the photodiode p1, which is used for the offset locking of the laser A2 (routed to the bench A1 through the same back fibre) and for removing at first order from the interferometric measurement the effect of the proof mass movement relative to the OB.

The laser beam received from the remote spacecraft C bounces off the front side of the proof mass and is routed by a polarising beamsplitter cube towards qp1 to beat against the local reference. On the reception path, part of the incoming beam is split by s1 towards the quadrant photodiode qp2 utilised for the initial acquisition and tracking of the remote laser.

The main alternative options for the optical bench w.r.t. the Pre-Phase A design considered during the Phase A study are summarised in Table 5.1.

**Table 5.1** *List of the main OB alternative options w.r.t. Pre-Phase A design*

Element	Option	Rationale
Optical cavity	Removal of the optical cavity from the OB and accommodation in a separate enclosure inside the P/L cylinder.	Possibility of improving the dimensional stability thanks to a dedicated thermal insulation.
Phase modulator	Removal of the phase modulator from the OB and accommodation before the optical fiber.	Reduction of the power dissipated on OB and of the radio-frequency interference with the photodiodes. Elimination of beam wandering at the modulator output by the fiber.
Quarter-wave plate q2	a) Placement of the quarter-wave plate q2 before the polarising cube ps1.	Removal of a major straylight source towards the acquisition sensor qp2.
ditto	b) Removal of q2 and OB tilt by $45^\circ$ along the optical axis to rotate the polarisation between the remote OBs.	Removal of an optical element from the OB and of a major straylight source on qp1 and qp2.
Quarter-wave plate q4	Removal of the q4 and twist of the back fibre by $90^\circ$ to rotate the polarisation between the near OBs.	Removal of an optical element from the OB and laser coupled to the fiber with linear polarisation.
Beam expander/compressor	a) Addition of $20\times$ beam expander/compressor at the output/input of the OB	Matching of the incoming beam diameter received by a $30\times$ telescope to the 0.5 mm diameter of qp1.
ditto	b) Addition of $10\times$ beam compressor before the photodiode qp1	Matching of the incoming beam diameter received by a $60\times$ telescope to the 0.5 mm diameter of qp1.
Detectors	a) Addition of a photodiode (p3) for the stabilisation of the laser power.	Obtain the signal for the laser power stabilisation directly on the OB.
ditto	b) Replacement of the quadrant photodiode qp2 with a CCD	Greater sensitivity (critical, because of the tiny power to be detected)
ditto	c) Use p3 as a 4Q-diode for transmitter boresight calibration	Calibration and monitoring sensor for fiber positioner

The proposal of removing the optical cavity from the bench was put aside for the time being, since the required laser frequency stability ( $\delta\nu/\nu \leq 30 \text{ Hz}/\sqrt{\text{Hz}}$ ) can be achieved also with the cavity on the OB if its temperature remains stable within  $10^{-5} \text{ K}/\sqrt{\text{Hz}}$ , a target that seems achievable. This option could be re-considered in the future if the thermal analyses results will indicate that it is critical to maintain such a level of thermal stability for the whole OB, or if more stringent requirements will be placed on the laser frequency stability.

The removal of the phase modulator from the OB has been adopted as baseline solution. Consequently, two alternatives were investigated for the phase modulator type and location:

- Phase modulator integrated in the optical fibre connecting the laser source to the OB
- Bulk phase modulator integrated in the laser head, before the fibre coupling.

With the first solution, the laser head can maintain the very compact and lightweight design defined in the phase A study. The main drawback is that, among all the existing in-fibre phase modulators, very few of them are designed to operate at the 1064 nm wavelength of the LISA laser and all are characterised by small transmission efficiency (less than 40 %, because of the modulator-to-fibre coupling) and cannot accept a large input optical power. Because of the limitations of the present devices, which would impose the development of a new, dedicated in-fibre modulator for LISA, the utilisation of a bulk modulator is considered the baseline solution. Among the available bulk modulators with features close to the LISA needs, the New Focus resonant modulator model 4003 was considered the most suitable, due to its smaller dimensions and power. This device will have to be submitted to space qualification tests to certify its applicability to the LISA mission.

The removal of the quarter waveplate q2 from the OB, with the consequent rotation by  $45^\circ$  of the bench to correctly rotate the linear polarisation between the remote bench pair A1-C2 etc., was rejected after a mechanical analysis of the OB mounted with such a tilt angle that highlighted a higher (and critical) stress in the material w.r.t. the horizontal mounting.

The positioning of the quarter-wave plate q2 before the beam splitter s1 was instead adopted as baseline solution. Consequently a different path of the local laser towards the back of the OB (i.e. towards the reference cavity and the back fibre) was defined, with the addition of another splitter, in order to preserve the linear polarisation of the light following this path and to avoid any possible back-reflection on the acquisition sensor from the optical elements placed on the back of the OB.

The removal of the quarter waveplate q4, with the consequent back fibre twist by  $90^\circ$  to correctly rotate the linear polarisation between the close bench pair A1-A2 etc., was adopted as baseline solution.

The two OB layouts with the  $20\times$  beam expander (coupled with a  $30\times$  telescope) and the  $10\times$  beam compressor before qp1 (coupled with a  $60\times$  telescope) are shown in Figure 5.4. With a  $30\times$  telescope the geometric diameter of the incoming beam on the OB is 1 cm, and the beam outgoing from the bench must have the same gaussian diameter (truncated at  $1/e^2$  intensity) to match the primary mirror diameter. With a beam of such a size on the OB, the utilisation of large optical elements would be required, with serious accommodation problems. Thus this telescope magnification forces the introduction of a beam expander/compressor at the output/input of the OB. With a  $20\times$  magnification a direct matching of the incoming beam to the qp1 size is achieved. The consequences of these optical elements are: large back-reflection towards the OB detectors magnification by a factor 600 of the incoming beam tilt on the OB due to the PAA effect. For these reasons this option was dropped in favour of the  $60\times$  telescope. In this case, in fact the beam diameter on the OB is 5 mm and can still be “handled” with an optical element size that can be accommodated on the bench. Thus no beam expander/compressor is needed

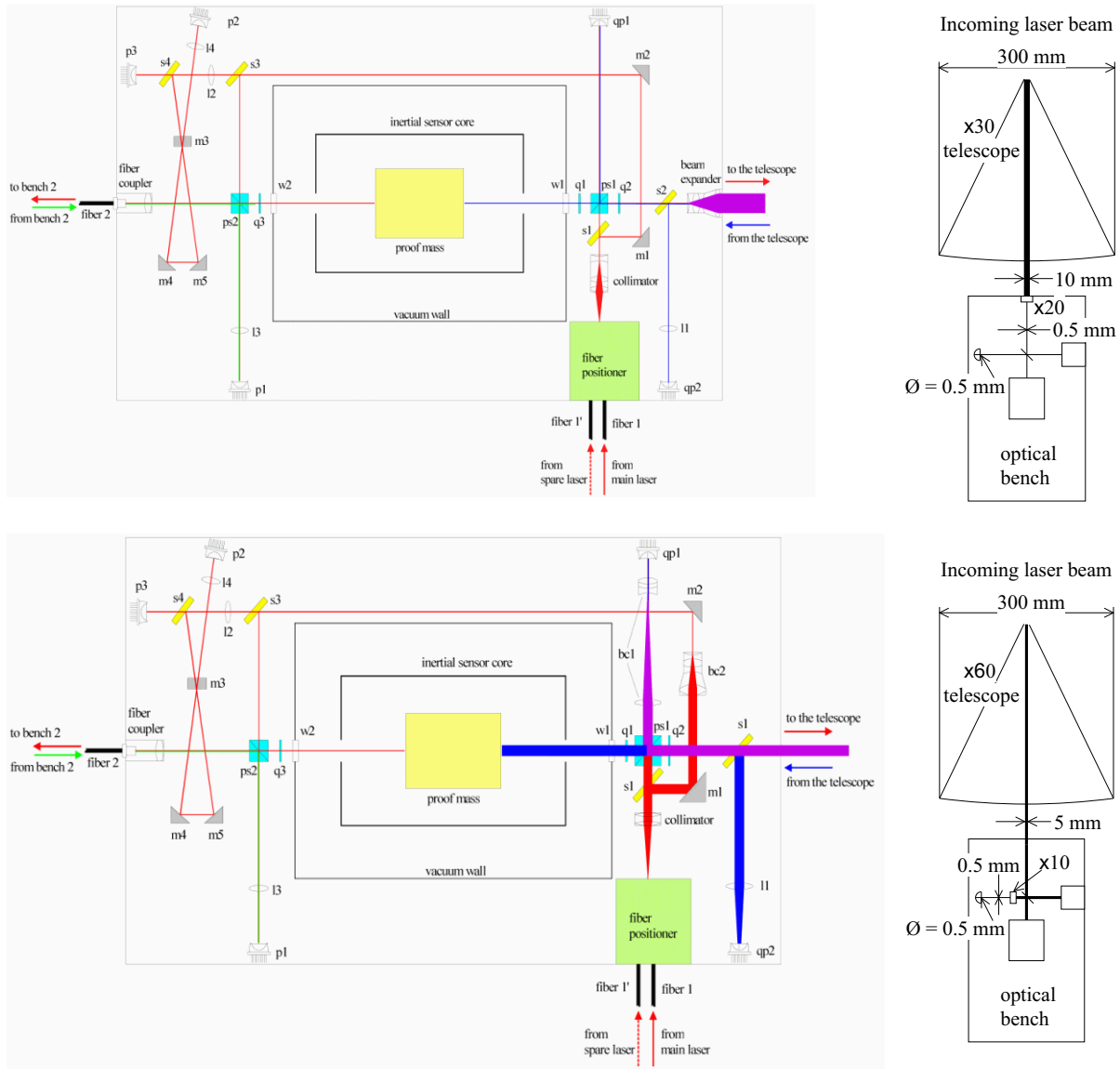


**Figure 5.4** *OB layout for the 30 $\times$  telescope (above) and for the 60 $\times$  telescope (below)*

at the OB output/input, but only a 10 $\times$  beam compressor just before qp1 (a second compressor is added in the path towards the back of the OB to reduce the size of the successive optical elements). Here the PAA is amplified by only 60 times on the OB, thus its compensation is simplified. About the PAA compensation the preferred solution is to receive the incoming beam off-axis and to tilt the proof mass to maintain it parallel to the local beam at qp1. The alternative option of transmitting the outgoing beam off-axis, using the fiber positioner to change its orientation, was discarded because of the large beam shifts and tilts induced in the rest of the OB.

About the detector options, the addition of the photodiode p3, to be used for the laser power stabilisation, was included in the baseline OB design, as well as the replacement of qp2 with a CCD as initial acquisition sensor. In fact, this device enables to achieve a much better SNR figures w.r.t. silicon avalanche photodiodes or InGaAs photodiodes in presence of the tiny amount of power (few pW) to be detected. Among the existing devices, the CCD02-06 deep depletion CCD

manufactured by [EEV](#) is the one that best meets the [LISA](#) needs and has therefore been assumed as the baseline.

### 5.3.3 Telescope assembly

The receiving and transmitting telescope is a Cassegrain system with integral matching lens mounted from the payload support cylinder and protected by a thermal shield. The primary mirror is a double-arch light-weight ultra-low expansion ([ULE](#)) design with a diameter of 30 cm. The mirrors are aspherics and need careful positioning. For more details see [Section 8.7](#) and [Appendix A.6](#).

## 5.4 System requirements

### 5.4.1 Laser power and shot noise

To attain the desired gravitational wave sensitivity the system must keep the noise in measuring the differences in round trip path length between two arms below  $40 \times 10^{-12} \text{ m}/\sqrt{\text{Hz}}$ , over a frequency range from  $10^{-3}$  to  $10^{-1} \text{ Hz}$ . A number of noise sources limit the performance, as will be seen in the noise budget given in [Section 4.2](#). However the fundamental, and most significant, noise source will be due to photoelectron shot noise in the detected photocurrents. Consideration of the noise budget suggests that the limitation due to photoelectron shot noise in each detector should not exceed about  $10 \times 10^{-12} \text{ m}/\sqrt{\text{Hz}}$ . The amount of light used in the measurement depends both on the laser power and the efficiency of the transmission of light from the emitting laser to the detection diode on the far spacecraft. This efficiency is limited by the divergence of the laser beam as it is transmitted over the  $5 \times 10^6 \text{ km}$  arm and losses in the various components in the optical chain.

### 5.4.2 Beam divergence

Even the best collimated laser beam will still have some finite divergence governed by the size of the final optic. With a Gaussian beam optimised for transmission between mirrors of diameter  $D$ , with an arm length  $L$ , and a transmitted power  $P$ , the power received at the far craft is given by

$$P_r = 0.50 \frac{D^4}{\lambda^2 L^2} P. \quad (5.1)$$

This is the case when the Gaussian beam has a waist (of radius  $w$ ) at the transmitting craft that almost fills the final telescope mirror,  $w = 0.446 D$ .

### 5.4.3 Efficiency of the optical chain

There are a large number of components in the optical chain. The main ones contributing to a loss of transmitted power are listed below, beside an estimate of the likely achievable power transmission. All other components in the optical chain are assumed to be perfect.

<i>Component</i>	<i>Efficiency</i>
Fibre	.70
Isolator	.96
Modulator	.97
Splitter plate	.90
Splitter plate	.90
Mirrors + lenses	.88
Interference	.81
Quantum efficiency	.80
Total	.30

The term for interference is to allow for the fact that some signal is lost due to the imperfect matching of the local reference beam and the received light from the far craft: the local reference beam is Gaussian and the received beam is a ‘Top Hat’ mode.

#### 5.4.4 Shot noise limit

Single frequency laser light of significant power from a lightweight reliable system is best provided by a monolithic Nd:YAG laser pumped by laser diodes. With this type of laser up to 2 W of light is currently achievable. In order to obtain high reliability from such a system in a space environment it is reasonable to derate the laser by a factor of two and use only  $P = 1$  W of output power. The laser system is described in detail in Section 5.5. Using this laser and taking into account the overall optical efficiency we find that shot noise limits the minimum detectable change<sup>1</sup> to

$$\widetilde{\delta x} = 11 \times 10^{-12} \left( \frac{\lambda}{1064 \text{ nm}} \right)^{\frac{3}{2}} \left( \frac{0.3 \text{ W}}{\varepsilon P_0} \right)^{\frac{1}{2}} \left( \frac{L}{5 \times 10^9 \text{ m}} \right) \left( \frac{30 \text{ cm}}{D} \right)^2 \text{ m}/\sqrt{\text{Hz}}, \quad (5.2)$$

where  $L$  is the arm length,  $\lambda$  the wavelength and  $P_0$  the power of the laser, the efficiency of the optical chain is  $\varepsilon$ , and  $D$  is the diameter of the transmitting and receiving optics. Thus with an optical chain with a realistic efficiency of  $\varepsilon = 0.3$  and a mirror of diameter of  $D \approx 30$  cm the target shot-noise performance can be achieved.

## 5.5 Laser system

### 5.5.1 Introduction

The laser system to be used in the LISA mission is a diode-laser-pumped monolithic miniature Nd:YAG ring laser which can generate a continuous diffraction-limited infra-red beam at  $1064 \mu\text{m}$  of up to 2 W.

The arguments leading to this choice are given in Appendix A.5.

Diode-pumped solid-state lasers, operating in a single transverse mode, are well known as compact, reliable and highly efficient sources of stable radiation. In the case of the NPRO (Non Planar Ring Oscillator), TEM00 mode operation is achieved by focussing the diode-laser beam

<sup>1</sup>The convention above and throughout this paper is that a ‘tilde’ over a quantity indicates that it is a linear spectral density, *e.g.*  $\widetilde{\delta x}$  is the linear spectral density of  $\delta x$ .



into the crystal (see below). When the beamwidth of the diode laser radiation is smaller than the diameter of the **TEM00** mode in the absorption length of the pump radiation, the laser is forced to operate in a single transverse mode.

Homogeneously broadened solid-state lasers oscillate on several longitudinal modes even at low output power because of the spatial hole-burning effect. To enforce single-frequency operation, resonator internal elements can be applied. However, the additional intracavity elements strongly reduce the efficiency and stability of the laser system. The monolithic **Nd:YAG** ring laser enables single-frequency operation at high output power without intracavity elements. Unidirectional and hence single-frequency oscillation is enforced by an intrinsic optical diode.

The optical beam path in the crystal is determined by three total reflections and one reflection at the negatively curved front surface. The front surface is dielectrically coated, reflecting about 97 % of the 1064 nm laser radiation and highly transmitting the pump radiation at 808 nm (see Figure 5.5). The high frequency stability required for the **LISA** mission can only be achieved

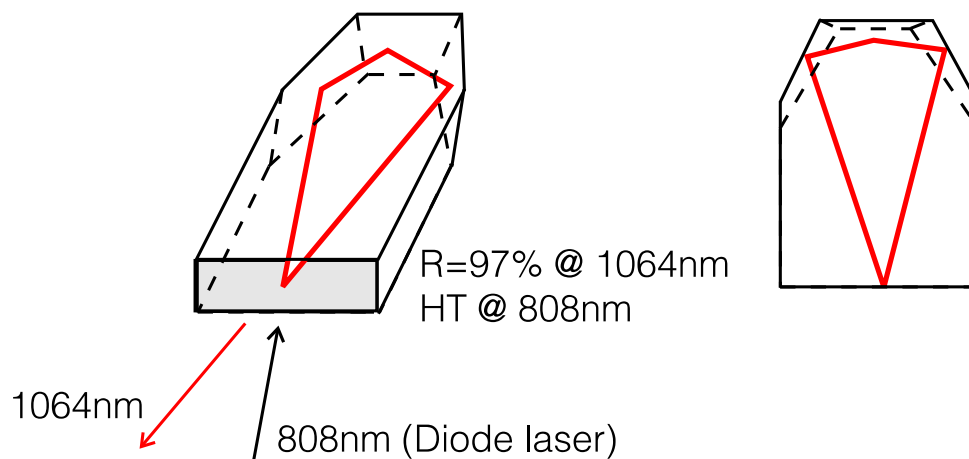


**Figure 5.5** The beam path in the monolithic, nonplanar ring resonator is determined by three total reflections and one reflection at the dielectrically coated front surface.

because of the high intrinsic stability of the **NPRO** (see Section 5.6). This stability results from the monolithic and compact design of the resonator and from the outstanding properties of host material **YAG** (Yttrium Aluminum Garnet  $\text{Y}_3\text{Al}_5\text{O}_{12}$ ). Low **CTE** ( $7 \times 10^{-6} \text{ K}^{-1}$ ) and low temperature dependence of the index of refraction ( $9.05 \times 10^{-6} \text{ K}^{-1}$ ) make the laser rather insensitive to temperature fluctuations.

The hardness of the **YAG** material makes it possible to reduce form errors of the crystal surface below  $\lambda/10$ . Typically 1 % of the  $\text{Y}^{3+}$ -ions are replaced by  $\text{Nd}^{3+}$ -ions. Higher doping rates would be desirable, but would cause mechanical stresses. The active ion  $\text{Nd}^{3+}$  absorbs the radiation of the pumping diode lasers at 808 nm and emits radiation at 1064 nm. Due to that quantum limit the efficiency of the laser is limited to  $\approx 75 \%$ . The 25 % energy loss is dissipated into the crystal.

To date there are few alternatives to **Nd:YAG**. Ytterbium can be used as the active ion, because the efficiency is higher than for  $\text{Nd}^{3+}$  (Neodymium)-ions, but the pump power requirements are also higher because Yb is a three level-atom rather than the four level Nd. Yttrium vanadate ( $\text{YVO}_4$ ) is an alternative candidate for the host material, because it supports the optical diode by introducing an extra polarization selective element, but the thermal properties are much worse than those of the **YAG**. So it is unlikely that the active material of the **NPRO** will be changed from **Nd:YAG** to some alternative material.



### 5.5.2 Laser system components

The complete laser system consists of four major components: the laserhead, the supply unit, the electro-optic modulator and the stabilization photodiode. Each component has its own housing and the block diagram of the system is shown in Figure 5.6 for identification of the different interfaces. Both the laserhead and the supply unit are mounted on a carbon-carbon radiator, whereas the modulator and the photodiode are mounted directly onto or near the optics bench.

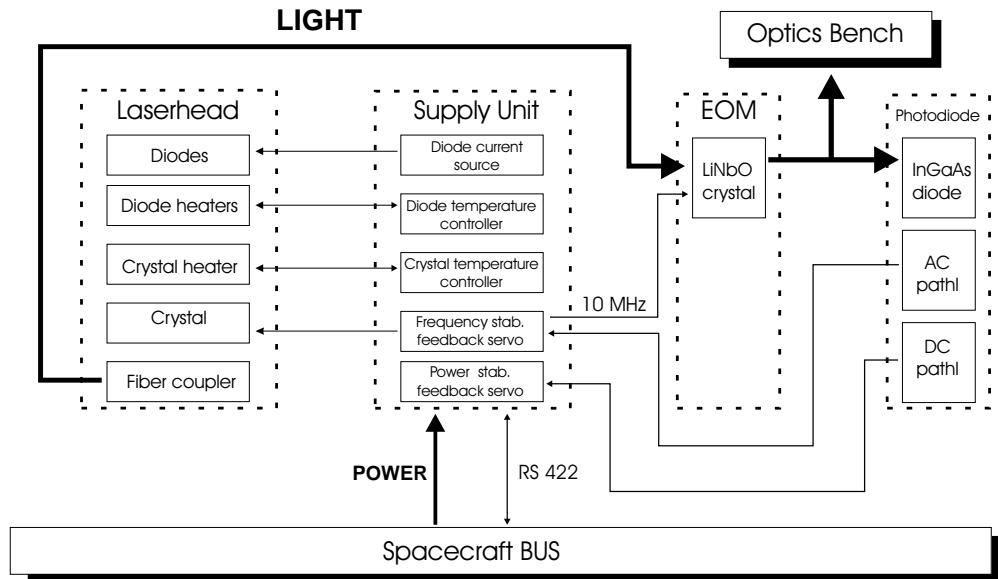


**Figure 5.6** *Laser system block diagram for the identification of the components and interfaces.*

The **laserhead** consists of a Nd:YAG crystal pumped by two long life aluminum-free InGaAsP laser diodes. These single stripe devices have maximum cw output power of 2000 mW. The nominal single-mode, cw output power of the NPRO in this configuration is 1500 mW, but this is downrated for LISA to 1000 mW to improve lifetime and reliability properties. The nominal constant power consumption for the 1000 mW of output power of the complete laser system will be approximately 10 W.

The pump light from each laser diode is transferred into the crystal by imaging the emitting area of  $1\,\mu\text{m} \times 200\,\mu\text{m}$  at unit magnification onto the entrance surface of the crystal, using two identical lenses with plano-convex surfaces to minimize spherical aberration (best form lens shape). A polarizing beamsplitter is inserted between the two lenses to combine the pump light from the two diodes, which are orthogonal in polarization.

All of the above mentioned components are glued to a solid fused silica spacer to ensure mechanical stability. Glued to that spacer are three heat sinks, which serve as the mechanical and thermal interface to the radiator plate. There is a heater integrated in each heat sink to control the operating temperature of the diodes and the crystal.

The **supply unit** mainly contains two current sources for the laser diodes, three temperature controllers, two for the diodes and one for the crystal, the mixer and feedback servo for the frequency stabilisation and the feedback circuit for power stabilisation. The supply unit power interface to the S/C power subsystem shall be the only power interface between the laser system and the S/C.

The **electro-optic modulator** (EOM) is a resonant phase modulator. These devices use lithium niobate crystals as the electro-optic medium, where a few volts drive voltage induce a change in the crystal's refractive index. The only electrical interface to the EOM is the *rf* supply.

The **stabilisation photodiode** is a InGaAs diode operated with a few volts reverse voltage in order to reduce its capacitance. That capacitance is part of a LC-circuit that resonantly enhances the *rf* signal modulated on the the laser beam. The ac-signal from the photodiode is taken as a voltage from the LC-circuit. The dc-signal is obtained by converting the photocurrent into a voltage with a transimpedance operational amplifier.

## 5.6 Laser performance

### 5.6.1 Laser frequency noise

The presence of laser frequency noise can lead to an error in the measurement of each arm length. If the arms are equal these errors cancel out but if they are unequal, the comparison of lengths used to search for gravitational waves may be dominated by frequency noise.

For an arm of length  $L$  the phase difference between the outgoing and returning light of frequency  $\nu$  is given by:

$$\varphi = \frac{4\pi\nu L}{c}. \quad (5.3)$$

Thus, for slow changes in  $L$  and  $\nu$ ,

$$\delta\varphi = \left[ \frac{4\pi}{c} \right] (L\delta\nu + \nu\delta L) = \frac{4\pi\nu L}{c} \left( \frac{\delta\nu}{\nu} + \frac{\delta L}{L} \right), \quad (5.4)$$

where  $\delta\varphi$  is a phase fluctuation resulting from either a change  $\delta L$  in arm length or a change  $\delta\nu$  in frequency of the laser. In fact a fractional change in frequency of  $\delta\nu/\nu$  gives a signal equivalent to a fractional change in length of  $\delta L/L$ . Thus if the difference in two arm lengths is  $\Delta x$  and the relative frequency stability of the laser is  $\widetilde{\delta\nu}/\nu$  the smallest relative displacement which can be measured is given by:

$$\widetilde{\delta x} = \Delta x \frac{\widetilde{\delta\nu}}{\nu}. \quad (5.5)$$

For the  $5 \times 10^6$  km arms of LISA, a maximum value of  $\Delta x$  of the order of  $10^5$  km is likely. For a relative arm length measurement of  $2 \times 10^{-12} \text{ m}/\sqrt{\text{Hz}}$ , which is needed to achieve the desired overall sensitivity, a laser stability of  $6 \times 10^{-6} \text{ Hz}/\sqrt{\text{Hz}}$  is required.

The monolithic structure of the nonplanar Nd:YAG ring laser and the low technical noise of the supply electronics offer a high intrinsic frequency stability of this laser system. In order to reach the desired sensitivity that intrinsic stability has to be even improved and a high precision frequency stabilisation has to be provided. The primary method of stabilisation is to lock the frequency of one laser in the system on to a Fabry-Perot cavity mounted on one of the craft making use of a *rf* reflection locking scheme known as *Pound-Drever-Hall scheme*. This stability is then effectively transferred to other lasers in the system by phase locking techniques.

With the temperature fluctuations inside each craft limited in the region of  $10^{-3}$  Hz to approximately  $10^{-6} \text{ K}/\sqrt{\text{Hz}}$  by three stages of thermal insulation, a cavity formed of material of low expansion coefficient such as ULE allows a stability level of approximately  $30 \text{ Hz}/\sqrt{\text{Hz}}$ . This level of laser frequency noise is clearly much worse than the required  $6 \times 10^{-6} \text{ Hz}/\sqrt{\text{Hz}}$  and a further correction scheme is required. Such a correction is provided by comparing the mean

phase of the light returning in two adjacent arms with the phase of the transmitted light. The phase difference, measured over the time of flight in the two arms, allows an estimate of laser frequency noise to be made. For each arm  $\widetilde{\delta\varphi} = (4\pi/c) L\widetilde{\delta\nu}$  (since  $\nu\widetilde{\delta L} \ll L\widetilde{\delta\nu}$ ) and thus if the spectral density  $\widetilde{\delta\varphi}$  is measured, the spectral density  $\widetilde{\delta\nu}$  can be estimated. A detailed analysis of this scheme is given in Section 7.1.

### 5.6.2 Laser power noise

The tolerable limit to laser power noise is to a large extent set by the radiation pressure effects of the beam to the adjacent craft at a vertex, this beam being reflected off the proof mass in the accelerometer. As will become clear from discussions in Section 6.1, we want few spurious accelerations of the proof mass above a level of  $10^{-16} \text{ m s}^{-2}/\sqrt{\text{Hz}}$ . For a proof mass of 1.3 kg and a reflected light power of  $100 \mu\text{W}$ , the proof mass will undergo a steady acceleration of  $5 \times 10^{-13} \text{ m s}^{-2}$ . To keep the fluctuating acceleration below  $10^{-16} \text{ m s}^{-2}/\sqrt{\text{Hz}}$  the power stability of the reflected light, and hence of the laser, must be better than  $\widetilde{\delta P}/P = 2 \times 10^{-4}/\sqrt{\text{Hz}}$ .

The fundamental limit of the power noise for a free-running laser is set by the quantum properties of light. In principle diode-pumped solid-state lasers offer the potential to reach this quantum noise limit (QNL). However, in real systems the power fluctuations are many orders of magnitude larger. In the LISA frequency band this is mainly due to pump noise transfer.

Substantial power noise reduction has been demonstrated for Nd:YAG ring lasers by application of electronic feedback loops. A fraction of the laser light is detected with a photo diode and the AC components are appropriately amplified to generate an error signal. This signal is fed back to the pump diodes (see Figure 5.7). The noise is less than 10 dB above the quantum noise limit down to a frequency of 10 kHz, corresponding to a relative power noise of less than  $5 \times 10^{-8}/\sqrt{\text{Hz}}$ . To reach the above-mentioned requirements the existing noise reduction scheme has to be extended to the low frequency regime.

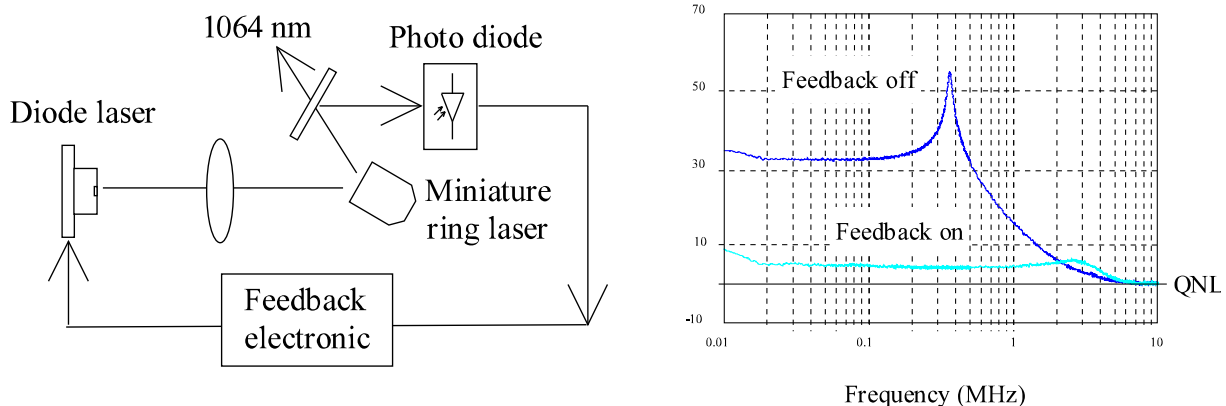


**Figure 5.7** Scheme of power noise reduction setup and intensity noise power spectrum in dB relative to quantum noise limit (1 mW optical power detected).

### 5.6.3 On-board frequency reference

A further technical problem, that of the Doppler shift, occurs if there is a relative velocity between the two spacecraft in an arm, producing a frequency shift in the returned light and

causing a beat signal when the phase comparison is made. For the particular orbits chosen (see Section 5.2), the relative velocities of the spacecraft in arm 3 will be up to about 15 m/s. The corresponding beat frequencies are then less than 15 MHz.

A signal from an ultra-stable oscillator (USO) is required in each arm to allow the Doppler beat frequency to be reduced to a manageable level for later signal processing. The clock signal should be stable enough to contribute a level of phase noise less than that from an arm length change of  $2 \times 10^{-12}$  m/ $\sqrt{\text{Hz}}$ , *i.e.*  $\widetilde{\delta\varphi} < 1.2 \times 10^{-5}$  rad/ $\sqrt{\text{Hz}}$ . The noise  $\delta F$  of the clock frequency  $F$  is related to the phase noise  $\delta\varphi$  at any frequency  $f$  by  $\delta F = f \times \delta\varphi$ , so at  $10^{-3}$  Hz we require a clock with a noise  $\widetilde{\delta F} \leq 1.2 \times 10^{-8}$  Hz/ $\sqrt{\text{Hz}}$ .

If the clock frequency is, say, 15 MHz, the required relative stability of the clock is approximately  $8 \times 10^{-16}/\sqrt{\text{Hz}}$ , an Allan variance<sup>2</sup> of  $3 \times 10^{-17}$  at  $10^{-3}$  Hz. This demand is considerably stronger than can be fulfilled by any flight qualified USO currently available; for example the one used on the Mars Observer had an Allan variance of  $2 \times 10^{-13}$  at  $10^{-3}$  Hz. The stability of the USO can however be improved to the desired level by modulating the clock frequency onto the laser light and stabilising this frequency to the arm length in a scheme analogous to that used to stabilise the laser frequency. To be more precise the USO in the master spacecraft is considered as the master oscillator in the system, and its phase fluctuations are measured by comparing the phase of the outgoing 200 MHz modulation sidebands with the incoming ones in one arm, the incoming ones being offset by a given frequency determined by an NPO on the distant spacecraft. The presence of this offset is essential to allow the phase measuring system to separate the signals related to the beating of the sidebands from the signals related to the beating of the carriers. It should be noted that the phase measuring system requires an accurate measurement of the relevant Doppler signal also to be given to it.

Note that the USO on each craft is effectively phase locked to the master USO by controlling an NPO on the output of each by means of a signal derived from the beating of the modulation sidebands on the incoming and outgoing light. This is elaborated in Section 7.2.2.

## 5.7 Beam pointing

### 5.7.1 Pointing stability

The requirements of the interferometry place constraints on the allowed angular fluctuations of the various interfering beams. The level of pointing control required of each spacecraft is set by the level of phase front distortion in a transmitted beam. If the beam deviates from having perfect spherical wavefronts centred on the transmitting craft, then angular changes of the transmitting craft produce changes in the phase of the received light, and hence apparent gravitational wave signals. From diffraction arguments the largest effect is from a first order curvature error of the wavefront (equivalent to a defocus in one or the other dimension). In this case the apparent phase change,  $\delta\varphi$ , due to movement of the beam in the far field is given by:

$$\delta\varphi = \frac{1}{32} \left( \frac{2\pi}{\lambda} \right)^3 d \cdot D^2 \vartheta_{\text{dc}} \delta\vartheta, \quad (5.6)$$

where  $D$  is the diameter of the mirror,  $d$  is the amplitude of curvature error in the wavefront,  $\vartheta_{\text{dc}}$  is the static offset error in the pointing and  $\delta\vartheta$  is the angular fluctuation. In this case with

<sup>2</sup>For a clock with white frequency noise, the relationship between the Allan variance and the relative frequency stability of the clock at a Fourier frequency  $f$  is given by  $\sigma_{\text{Allan}} = \sqrt{2 \ln 2} \times (\widetilde{\delta F}/F) \times \sqrt{f}$ .

an allowed phase error from this source of  $\widetilde{\delta\varphi} = (2\pi/\lambda) \times 10^{-12} \text{ rad}/\sqrt{\text{Hz}}$  for a single transit,  $d \sim \lambda/10$ , and a mirror diameter  $D = 30 \text{ cm}$ , we need to achieve

$$\vartheta_{\text{dc}} \widetilde{\delta\vartheta} \leq 140 \times 10^{-18} \text{ rad}^2/\sqrt{\text{Hz}}. \quad (5.7)$$

Thus if  $\vartheta_{\text{dc}} \sim 20 \text{ nrad}$ , the required pointing stability of the spacecraft is  $\widetilde{\delta\vartheta} \sim 7 \text{ nrad}/\sqrt{\text{Hz}}$ .

The orientation of the spacecraft with respect to the incoming light may be determined by a wavefront sensing technique. The interference between the local laser and the received light occurs on the main quadrant diode, any angular difference between the two beams will result in a phase difference between the signals in the different quadrants and hence the orientation of the spacecraft can be measured.

### 5.7.2 Pointing acquisition

A star tracker would be used for initial attitude control; this should allow alignment of each of the spacecraft to  $\sim 10^{-4} \text{ rad}$  (20 arcsec). The divergence of the main beam from each craft is considerably smaller than this at  $4 \times 10^{-6} \text{ rad}$  so there is an initial problem in using the main beam for alignment. A solution is to increase the divergence of the main beam by a factor of three during the acquisition phase by a small movement of the output end of the optical fibre. (This system would also provide active focus control.) One spacecraft would use its proof mass as its pointing reference and scan through a  $10 \times 10$  grid of step size  $10^{-5}$  radians. The other spacecraft would note when it received light from the transmitter and pass this information, via the ground, to the transmitter which could then point itself appropriately. The receiving spacecraft would then align its outgoing light to the received light using the wavefront sensing technique described earlier. With light now going in both directions along the arm the original transmitter would now switch to also using wavefront sensing to maintain alignment.

### 5.7.3 Final focusing and pointing calibration

We saw earlier in this section that any defocus of the transmitted light, along with pointing noise, would produce a spurious signal in the interferometer. We can use this effect to optimise the focus for each of the spacecraft in turn. The pointing of one spacecraft is modulated at a known frequency, this will cause a signal at the output of the interferometer at multiples of the modulation frequency. The magnitude and sign of the focus error in the transmitting craft can be deduced from the size and phase of these signals, and hence the focus and ‘dc’ pointing may be optimised.

### 5.7.4 Point-ahead angle

The orbits of the spacecraft, combined with the very long arm length of the interferometer and the finite speed of light, give rise to an angle between the incoming beam and the direction of the beam to be transmitted to the counterpart spacecraft. This point-ahead angle is in the order of  $3.5 \times 10^{-6} \text{ rad}$ .

The orbit dynamic analysis during the Industrial Study [2] has uncovered an unexpectedly strong variation of this point-ahead angle with the orbital period. This variation is caused by the fact that the triangle formed by the spacecraft is both rotating around its normal axis and, simultaneously, its plane is nutating with the orbital period. Thus, each spacecraft as seen from the other spacecraft has an apparent lateral motion, which leads to a varying offset angle

between the emitted and received beams. Although this effect does not constitute a critical issue, it does have some technical implications on the system design and on assembly level.

The dynamic analysis generated the following results :

- In-plane bias  $3.3 \mu\text{rad}$ ; variation  $\pm 55 \text{ nrad}$ ;
- Out-of-plane bias  $85 \text{ nrad}$ ; variation  $\pm 5.7 \mu\text{rad}$ .

These values are defined in free space (telescope entrance) and vary approximately sinusoidally with the orbital period of one year.

The constant in-plane bias can be compensated for by proper parts alignment, e.g. by tilting the polarising beam splitter (PBS), as proposed in previous studies.

The in-plane  $55 \text{ nrad}$  variation is marginally critical only for the transmitter bias relative to the nominal position (specification is  $< 30 \text{ nrad}$ ), because the S/C attitude reference is the received beam wavefront tilt, which is tracked with better than  $8 \text{ nrad}/\sqrt{\text{Hz}}$  on the heterodyne detector.

While the out-of-plane bias of only  $85 \text{ nrad}$  does not present a problem, the out-of-plane variation of  $5.7 \mu\text{rad}$  is the most critical factor. It translates for the relevant beam size on the optical bench (baseline selected  $5 \text{ mm}$  diameter at telescope magnification  $60\times$ ) into  $\pm 342 \mu\text{rad}$  variation perpendicular to the plane for the required offset angle between TX and RX beam at bench level.

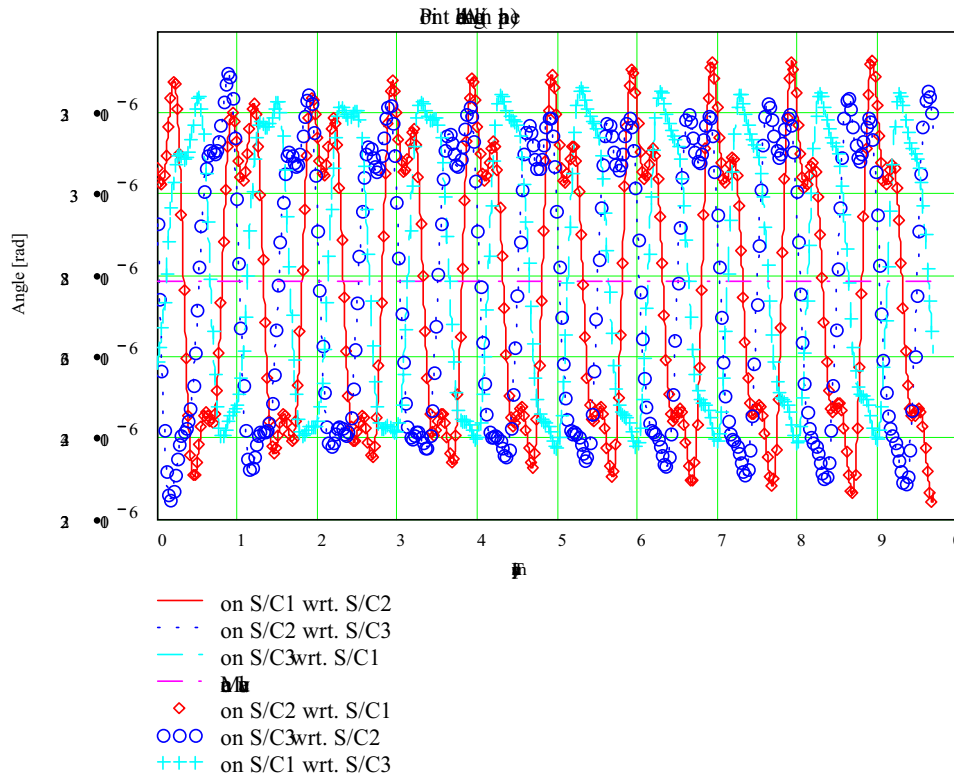


**Figure 5.8** *In-plane point-ahead angle variation over orbital periods*

Due to the limited study resources, several options to cope with this situation could only briefly be addressed:

- 1) Do nothing: the S/C keeps tracking the received beam, but the transmitted beam would be mispointed in the order of the central lobe divergence: not acceptable
- 2) Use the fibre positioner to adjust the offset angle (periodically or continuously) and the transmitter beam axis: This was the first idea, but will misalign the complete optical bench,

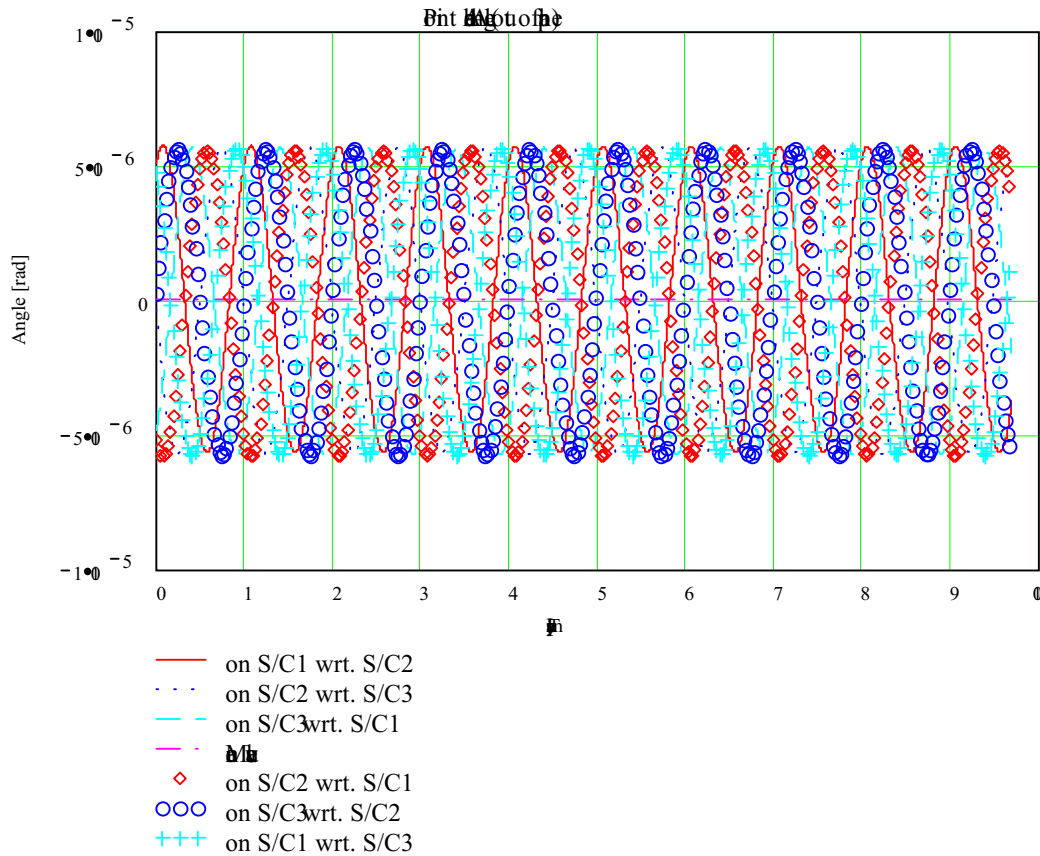


**Figure 5.9** Point-ahead angle variation out-of-plane over orbital periods

especially the local oscillator beam and the beam to the rear interferometer and reference cavity. Of course additional pupil shifting optics or/and additional **DOF** in the fibre positioner assembly could possibly mitigate the impact, but it complicates the situation significantly. In addition, the transmitter beam is tilted towards the optical axis and may lead to a degradation of the far field wavefront (however, should be ok for  $5.7 \mu\text{rad}$ ).

- 3) Use an additional active element in the dedicated transmitter or alternatively receiver beam; e.g. move lens groups or tilt the **PBS** by **PZT**: Implies complication by additional noise sources, control elements and thermal sources, but is otherwise a clean solution.
- 4) Use the proof mass as an already existing active mirror to tilt the received beam (open loop or by using tracking information from the heterodyne detector as error signal for the **IRS**-control: This is the proposed baseline, provided, the associated problems in **IRS** design can be solved. But this function is required anyway to initialise and calibrate the proof mass mirror as an optical element after launch.

The problems that are introduced when considering the latter solution are:

- The tilt angle of  $\pm 171 \mu\text{rad}$  for the proof mass attitude is too large for the present **ONERA** design. A budget has already to be allocated for the initialisation, which must be added to this requirement. **ONERA** quotes that currently about  $50$  to  $70 \mu\text{rad}$  may be acceptable, which is not yet sufficient. Unfortunately, this became apparent only at the end of the study and is only a crude estimate. The physical effects are: the performance of the capacitive sensors, non-linearities and internal **DOF** cross-talk need to be analysed in more detail.



- The rear interferometer will be misaligned during the process. An additional lens introduced to translate the angular tilt into a slight parallel displacement has no direct impact. A transfer function between proof mass attitude noise and rear interferometer phase noise is also introduced, which is assessed to be acceptable (TBC).

The tilt angle at proof mass level can be reduced by selecting a larger beam diameter on the optical bench (or at least at proof mass level by introducing a beam expander in front of the mirror surface). E.g. a factor of 4 brings the tilt angle down to  $43 \mu\text{rad}$ . In addition, also a slight but defined wavefront tilt at the heterodyne detector may be acceptable.

The inertial sensor (IRS) is already a critical assembly in the payload, and the design should not be driven too much by the point-ahead angle requirement. Hence, although it is cautiously adopted as present study baseline, alternatives shall still be considered.

## 5.8 Thermal stability

A high level of thermal stability is required by the interferometer. Thermal variation of the optical cavity to which the lasers are stabilized introduces phase variations in the interferometer signal, which have to be corrected for by using data from the two arms separately. Thermally induced variations in the dimensions of the transmit/receive telescope will lead to changes in the optical path length. Variations in the dimensions of the spacecraft will change the positions of components which cause a change in the mass distribution and hence cause an acceleration of the proof mass.

The thermal stability needed is achieved by using structural materials with low thermal expansion coefficient and by using multiple stages of thermal isolation. The spacecraft and payload structural elements will be made of composite materials with thermal expansion coefficient less than  $1 \times 10^{-6}/\text{K}$ . The optical bench and telescope are supported by the payload cylinder which is weakly thermally coupled to the payload thermal shield which in turn is weakly coupled to the spacecraft body. This provides three stages of thermal isolation for the payload from solar and spacecraft electronics thermal input.

The main source of thermal variation is due to changes in the solar intensity around its mean value of  $1350 \text{ W m}^{-2}$ . Observed insolation variations from 0.1 mHz to 10 mHz can be described [104] by a spectral density with a shallow frequency dependence:

$$1.75 \times \left( \frac{f}{1 \text{ mHz}} \right)^{-1/3} \text{ W m}^{-2}/\sqrt{\text{Hz}}.$$

To quantify the effects of solar and electrical variations, a simple thermal model for the spacecraft was formed with single nodes for the spacecraft body, solar panels, optical bench, telescope, laser radiator and electronics disk. The temperature fluctuations of the optical bench due to solar fluctuations were found to be well under the value of  $10^{-6} \text{ K}/\sqrt{\text{Hz}}$  at 1 mHz used in the analysis of the laser phase noise. To keep the power variations from producing thermal noise in excess of this, the power dissipation of the payload electronics will have to be controlled to  $10 \text{ mW}/\sqrt{\text{Hz}}$  and the power dissipation of the photodiodes on the optical bench will have to be controlled to better than  $50 \mu\text{W}/\sqrt{\text{Hz}}$ . The needed control can be achieved with small heaters and voltage and current sensors. The spacecraft electronics do not need to be controlled to better than the 0.1 % typical of flight-qualified units.

The secondary mirror of the telescope is supported from the primary by a graphite-epoxy spider with length 40 cm and thermal coefficient of expansion  $0.4 \times 10^{-6}/\text{K}$ . The thermally-induced



path-length variations using the thermal model were found to be less than  $2\text{ pm}/\sqrt{\text{Hz}}$  at 1 mHz, and so are not a major source of noise.

The accelerations caused by changes in the mass distribution of the payload were assessed. The primary payload masses are the optical bench, the telescope, the payload electronics, and the laser/radiator combination. The proof-mass acceleration noise caused by solar fluctuations was found to be less than  $1 \times 10^{-16} \text{ m s}^{-2}/\sqrt{\text{Hz}}$  at 1 mHz. The acceleration noise due to thermal variations in the dimensions and component positions of the spacecraft body has not yet been assessed.



# 6 Inertial Sensor and Drag-Free Control

## 6.1 The inertial sensor

### 6.1.1 Overview

The three [LISA](#) spacecraft each contain two inertial sensors, one for each arm forming the link to another [LISA](#) spacecraft. The proof masses of the inertial reference sensors reflect the light coming from the [YAG](#) laser and define the reference mirror of the interferometer arm. The same proof masses are also used as inertial references for the drag-free control of the spacecraft which constitute a shield to external forces. Development of these sensors is done at various institutions. The description here will be based on the choice made for [PPA 2](#).

The proposed sensors (called [CAESAR](#): Capacitive And Electrostatic Sensitive Accelerometer Reference) can be derived from existing space qualified electrostatic accelerometers already developed for the [ESA](#) projects, like the [GRADIO](#) accelerometer or the [ASTRE](#) sensor delivered to [ESTEC](#) for micro-gravity spacelab survey [[105](#), [106](#), [107](#)]. The last one has flown three times on board the [COLUMBIA](#) shuttle in 1996 and 1997. The [STAR](#) accelerometer, based on the same configuration, will also be delivered to [CNES](#) and [DLR](#) in order to be integrated on board the German geodetic satellite [CHAMP](#) launched in 2000. All these sensors are based on a three axis electrostatic suspension of the proof mass with capacitive position and attitude sensing.

Since the laser beam is directly reflected off the proof mass, the noise of the [CAESAR](#) proof-mass position sensing with respect to the sensor cage does not affect directly the interferometer resolution. A resolution of  $10^{-9} \text{ m}/\sqrt{\text{Hz}}$  is nevertheless needed to limit the disturbances induced by relative motions of the satellite with respect to the proof mass, for instance, the disturbances due to the spacecraft self gravity or to the proof-mass charge. Furthermore, this resolution is compatible with the control of the proof-mass orientation to better than  $5 \times 10^{-8} \text{ rad}/\sqrt{\text{Hz}}$ .

What is more demanding for the definition of [CAESAR](#) is the level of the disturbing accelerations induced by the sensor back-action and by the parasitic forces that may be applied directly on the proof mass. This level must be limited to  $3 \times 10^{-15} \text{ m s}^{-2}/\sqrt{\text{Hz}}$  in the frequency domain from  $10^{-4} \text{ Hz}$  to a few  $10^{-3} \text{ Hz}$ .

Contrary to the space accelerometers, no accurate measurement of the acceleration is needed because the scientific data are obtained through the interferometer outputs. Thus, there are no very stringent requirements on the scale-factor accuracy, on stability or on the sensor linearity when the the drag compensation system of the satellite is operating.

The sensor can be considered in two ways. On the one hand, [CAESAR](#) is simply composed of an inertial reference proof mass with surrounding capacitive position sensors that provide the measurement of its attitude and its position with respect to the sensor cage and thus to the satellite. On the other hand, [CAESAR](#) can operate as an accelerometer with its proof mass servo-controlled such as to be motionless with respect to the cage, and the sensor output is then representative of the satellite acceleration. Both ways are proposed to be used during the mission to compensate the spacecraft external forces and torques.

Based on the same concept and technology as the [STAR](#) accelerometer, the [CAESAR](#) sensor design (geometry, performances and accommodation on board the spacecraft) has to be optimised to fit the mission requirements. Fortunately, the sensor will benefit from the thermal stability of

the optical-bench environment of the **LISA** satellite, i.e.  $10^{-6} \text{ K}/\sqrt{\text{Hz}}$ , and of the materials that will be involved in the sensor mechanics exhibiting very low coefficient of thermal expansion (CTE) and ensuring a high geometrical stability.

### 6.1.2 CAESAR sensor head

As shown in Figure 6.1, the **CAESAR** sensor head is mainly constituted by

- a proof mass made of gold-platinum alloy,
- three gold-coated sets of electrode-plates made in **ULE**
- a reference base plate made also in **ULE** that constitutes the mechanical interface with the optical bench,
- a blocking mechanism with gold-coated fingers that should be necessary to maintain the proof mass motionless during the launch vibrations,
- a tight housing made of titanium.

The proof-mass alloy of 90% Au and 10% Pt is presently selected because of its high density of  $20 \text{ g/cm}^3$  and because of its weak magnetic susceptibility, in order to minimise the effects of the magnetic environment fluctuations induced by the interplanetary magnetic field or the magnetic field gradient due to the satellite itself. The drawback of a metallic mass is its thermal expansion coefficient, quite one thousand times greater than the **ULE** cage, but it presents the advantage of a high density and a much better resistance to shocks and vibrations. Fortunately, the mass temperature fluctuations are very limited because it is well thermally decoupled and because the laser beams that are reflected off it exhibit high power stability. Furthermore, the electrode

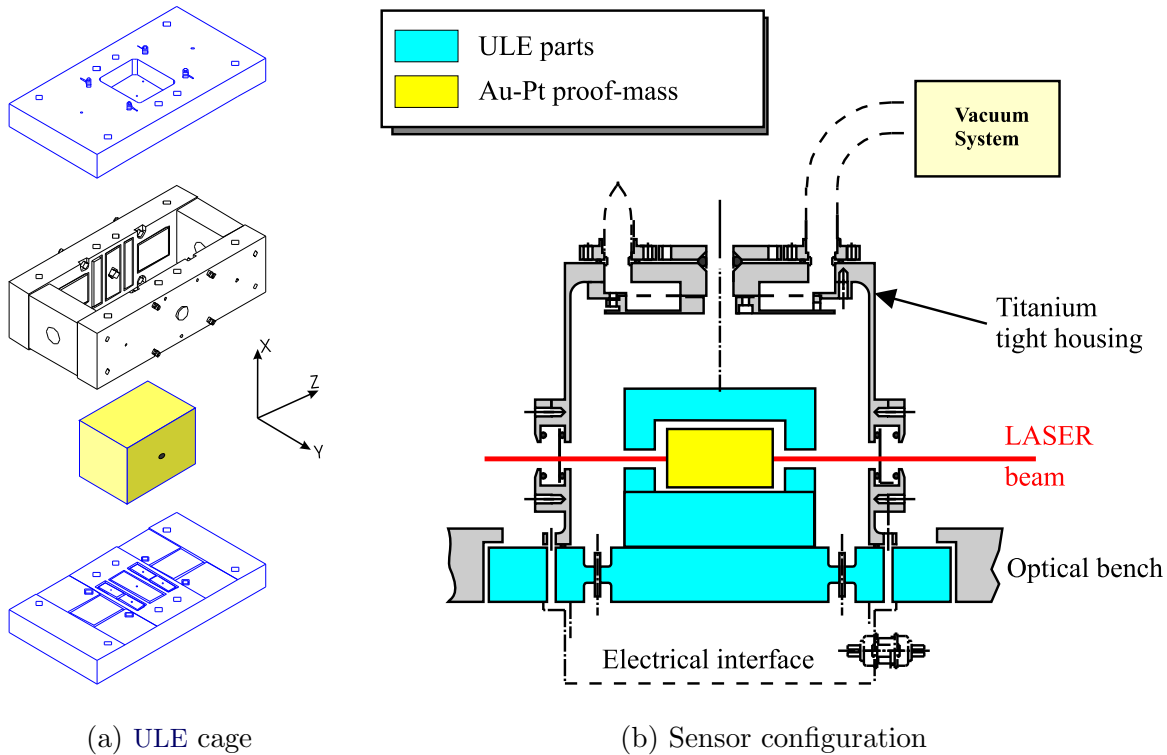


**Figure 6.1** *CAESAR* overview.

configuration is such that the mass expansion does not affect at first order the characteristics of the sensor.

Around the nearly cubic proof mass of about 4 cm side along the X and Y axes and 5 cm along Z (defined by the laser beam direction), the **ULE** sensor cage presents a set of six (or eight) pairs of electrodes used for capacitive sensing of its attitude and its position. The sensor could be realised with the technology developed and exploited for the production of space accelerometers. The **ULE** plates can be obtained by ultrasonic machining and grinding in order to benefit by a high geometrical accuracy and flatness. The gold coating necessary to define the electrode set is obtained by sputtering. In the case of **CAESAR** a specific effort will have to be devoted to the machining and the grinding of the proof mass: the characteristics of the capacitive sensing will depend on its geometry, on the parallelism and on the orthogonality of the faces. Two faces of the mass are also used as mirrors to reflect the laser beam.

The **CTE** of the **ULE** sensor cage is as low as a few  $10^{-8}/\text{K}$  around  $25^\circ\text{C}$ . Associated with the expected very weak thermal variations, it ensures the geometrical stability of the cage. Furthermore, the proof-mass temperature is very steady because, when electrostatically suspended, the thermal exchanges of the proof mass are only radiative: experiments have shown that the proof-mass temperature of the **STAR** accelerometer reacts with a response time of 20 hours, ensuring a very good filtering of the thermal fluctuations of the environment. With a much larger mass, the response time should be even two times larger.

The **CAESAR** cage must be implemented in a tight housing, and the whole sensor electronics could be accommodated on board of the satellite at a distance as large as one meter from the cage without affecting the performances too much. This allows a rather low power consumption inside the sensor head that is fixed on the satellite optical bench to the benefit from its thermal stability.

The titanium tight housing is necessary to maintain all the sensor core in a very clean vacuum after integration of the parts that will be out-gassed. In flight, the tight housing is opened to space vacuum and a very low residual pressure ( $< 10^{-6}\text{ Pa}$ ) is expected inside the **ULE** cage in order to minimise the gas damping effects. A getter material can also be integrated inside the housing as it is done for the already developed space accelerometers.

### 6.1.3 Electronics configuration

The electronics is composed of 6 independent servo loops, each including a capacitive sensor with analog-to-digital sigma-delta converter, an electrostatic actuator and a digital control electronics. Each loop, corresponding to one pair of electrodes, can be used to control one degree of freedom of the proof mass. The proposed configuration for the electrodes is presented in Figure 6.2.

The electrode areas are evaluated to  $8\text{ cm}^2$  for the Z axis and to  $1.5\text{ cm}^2$  for the other two directions. The gaps between the electrodes and the proof mass will result from a compromise between the position-sensor resolution, the electrostatic actuator strength and the level of the disturbing effects resulting from the presence of the instrument cage near the mass. Currently selected are gaps of 1 to 2 mm for the Z-axis electrodes and of 0.3 mm for the X and Y axes.

Then, the setting of the configuration parameters results from the trade-off between the position sensing resolution and the back-actions induced on the proof-mass motion by the detection voltage, i.e. a negative electrostatic stiffness and an electrostatic acceleration when the configuration is not fully symmetric.

As presented in Figure 6.3, the sensitivity of the capacitive position sensor can be adjusted according to the three following parameters: the amplitude of the sine wave detection voltage,  $V_d$ , applied to the proof mass via injection electrodes, the gain of the electronics that collect

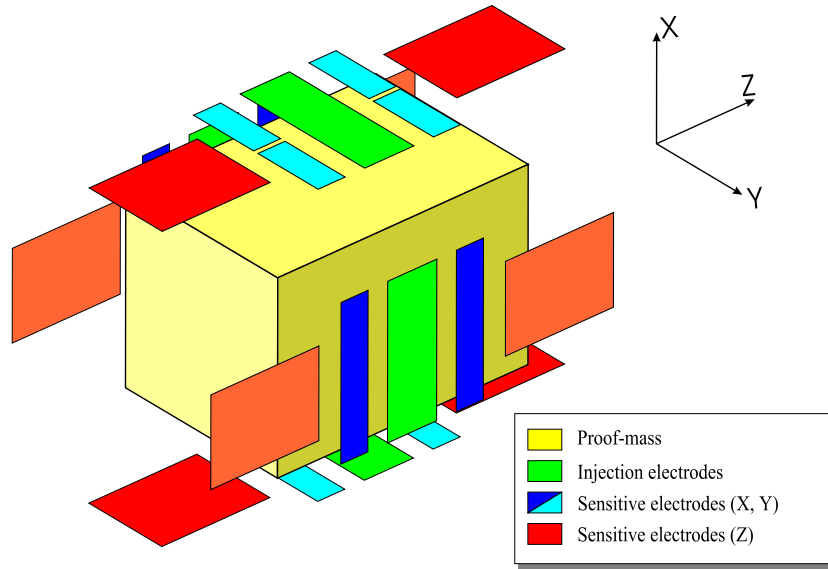


**Figure 6.2** *Electrodes set configuration.*

the detection signal through the two sensing electrodes corresponding to the sensor, and the distance between the electrodes and the proof mass.

As a matter of fact, the capacitive sensor resolution is mainly driven by the thermodynamic noise of the capacitive bridge formed by the proof mass, the opposite sensing electrodes and the differential transformer, and it can be expressed by:

$$C_n(f) = \frac{1}{V_d} \sqrt{\frac{2kTC_e}{\pi f_d Q}} \quad (\text{F}/\sqrt{\text{Hz}}), \quad (6.1)$$

with  $C_e$  the whole capacitance seen at the transformer input and with  $Q$  the quality factor of the LC detection circuit. With a detection voltage level of  $5 \text{ V}_{\text{rms}}$  and a sensitivity of  $50 \text{ V/pF}$  a resolution of  $1.2 \times 10^{-7} \text{ pF}/\sqrt{\text{Hz}}$  has been obtained with space qualified hybrids. Using a reduced

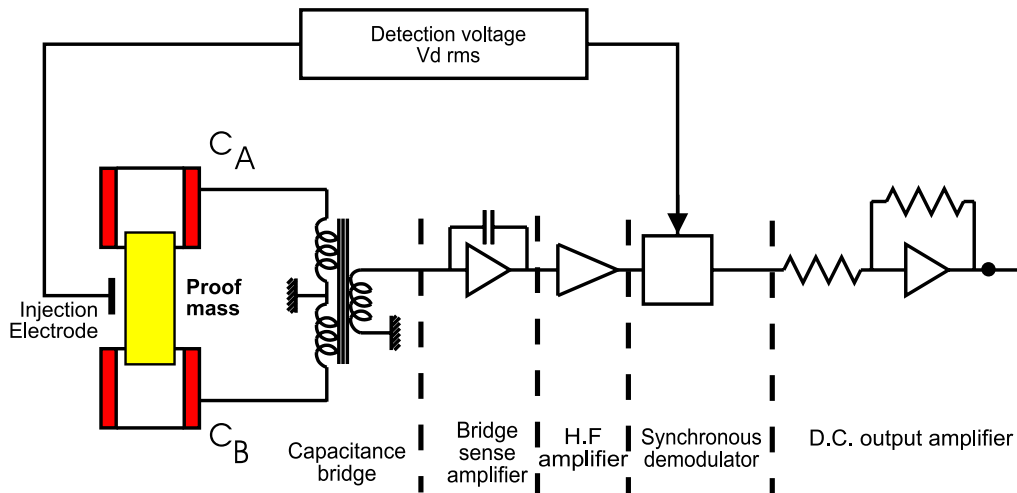


**Figure 6.3** *Scheme of the capacitive sensing.*

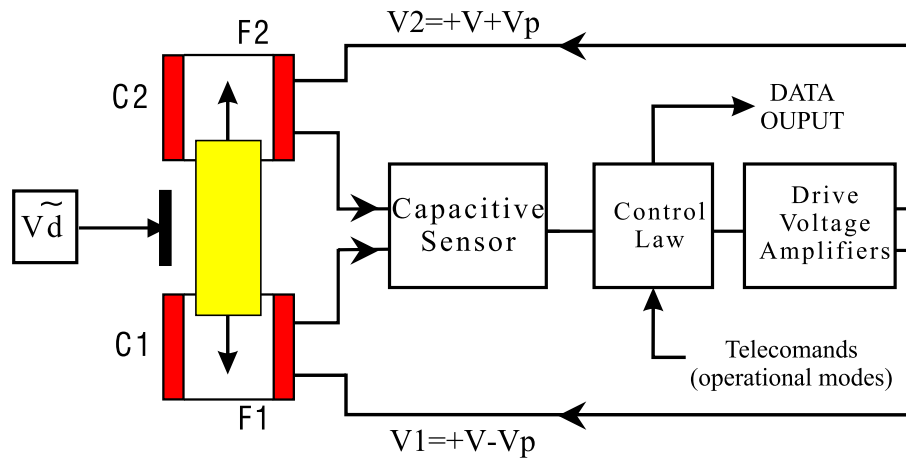


**Figure 6.4** Scheme of one channel loop.

detection voltage of only  $1 V_{\text{rms}}$  and a gap of 1 mm, in order to minimise the effects of the negative electrostatic stiffness, a resolution of  $2 \times 10^{-10} \text{ m}/\sqrt{\text{Hz}}$  should be achieved. Moreover, recent improvements of the resolution of the capacitive sensor could be beneficial to the CAESAR electronics development: the corner frequency of the  $1/f$  sensor noise can be lowered under certain conditions to frequencies below  $10^{-4} \text{ Hz}$ .

The negative electrostatic stiffness induced by the detection voltage is reduced along the Z axis with respect to the two other ones by the electrode configuration and by the distance between the mass and the cage increased to 15 mm. The capacitance variations, measured by the sensor along this axial direction and due to the proof-mass motion, are no longer induced by the variations of the gaps between the proof mass and the sensing electrodes but by the variations of the proof-mass areas in view to these electrodes.

The electrostatic forces are generated by applying the same control voltage  $V$  on the opposite electrodes (see Figure 6.4). This control voltage is generated from the output of the corrector. Opposite DC voltages  $\pm V_p$  are added in order to linearise the electrostatic forces that become proportional to  $V_p$  when the configuration is symmetric. Both electrodes attract the proof mass with forces  $F_1$  and  $F_2$  proportional to the gradients of the capacitances  $\nabla C_i$  and to the square of the potential differences between the proof mass and the electrodes. The resultant force is expressed by

$$F = F_1 + F_2 = \frac{1}{2} (\nabla C_2 V_2^2 + \nabla C_1 V_1^2). \quad (6.2)$$

Because of the geometrical symmetry we have

$$\nabla C_2 = -\nabla C_1 = \nabla C, \quad (6.3)$$

and the resultant force  $F$ , linearised by the use of biasing voltages  $\pm V_p$ , is made proportional to the control voltage  $V$ :

$$F = (2\nabla C V_p) V. \quad (6.4)$$

At low frequencies, inside the control bandwidth, the proof mass is kept motionless in the accelerometer cage, and  $V$  is representative of the acceleration  $\Gamma_{\text{cage}}$  of this cage:

$$(2\nabla C V_p) V \approx m \Gamma_{\text{cage}}, \quad (6.5)$$

with  $m$  being the mass of the levitated proof mass. In the above two expressions, the terms in parentheses represent the instrument scale factor. The value of  $V_p$  is selected according to the



full scale range of acceleration required for the control of the proof mass. It shall be changed according to the different operation modes from tens of volts to hundreds of milli-volts.

A supplementary set of electrodes, called injection electrodes in Figures 6.2, 6.3 and 6.4, is used to control the proof-mass electrical potential, in particular at the pumping frequency of the capacitive sensing. This solution has been preferred to a thin gold wire used in other space accelerometers because of the stiffness and of the damping that the wire may generate. Experimental investigations have demonstrated that the wire is only compatible with a resolution of several  $10^{-14} \text{ m s}^{-2}/\sqrt{\text{Hz}}$  at room temperature [108].

#### 6.1.4 Evaluation of performances

The performances of the inertial reference sensor have been evaluated by considering the geometry and the characteristics of the sensor head, the characteristics of the electronics configuration and the environment on board the LISA satellite. In particular this last point leads to a required pressure inside the housing of less than  $10^{-6} \text{ Pa}$ .

The evolution of the charge  $Q$  of the isolated proof mass is one of the most critical error sources. On the one hand, the proof mass is subjected to the electrostatic forces appearing with the image charges on the electrodes in regard to the proof mass; the resultant of these forces is not null when the configuration is not perfectly symmetric, in particular for any off-centering of the proof mass with respect to the sensor cage. On the other hand, this charge  $Q$  induces a Lorentz force when it moves in the interplanetary magnetic field.

In fact  $Q$  is the sum of the charge acquired when the proof mass separates from the accelerometer cage at suspension switch-on, and of the charge resulting from the cosmic particle bombardment, especially from the proton flux over 100 MeV. When considering a charging rate of  $10^{-17}$  to  $10^{-18} \text{ C/s}$  [109, 110], the  $2 \times 10^{-14} \text{ C}$  limit required is reached in less than one hour. Therefore the charge has to be measured exploiting the electrostatic device itself, and the proof mass has to be discharged, continuously or time by time, for instance by photo-electric emission induced by ultraviolet light [109].

Other electrostatic-force noises must be considered: they are induced either by the fluctuations of the applied voltages, of the contact potential differences and of the patch effects [111], or by the proof-mass motion; they are reduced by the expected geometrical accuracy of the ULE cage and of the proof mass ( $1 \mu\text{m}$ ), by the large gaps and by the servo-loop controls which maintain the proof mass motionless.

The parasitic effects due to the residual pressure are limited by the good vacuum and the high thermal stability. The proof-mass magnetic moment is very weak because of the choice of a material having very low magnetic susceptibility, and the magnetic behaviour of the satellite should be acceptable. Furthermore, a magnetic shield could be implemented if necessary.

This preliminary error budget shows that such a sensor concept appears compatible with the LISA mission requirements. A detailed definition of the sensor, of its operation and of the envisaged environment on board the satellite is necessary to refine and to confirm the evaluation of performances. Experimental investigations will be necessary to assess the behaviour of the sensor and to optimise the configuration. Both activities are being undertaken. The sensor configuration could be tested in the laboratory under normal gravity if a lighter proof mass, made in ULE for instance, is used, and if dedicated electronics units are employed for the one- $g$  proof-mass suspension. Such an ULE proof mass will weight less than 100 g while the suspension of a 320 g accelerometer proof mass has already been performed with quite the same  $16 \text{ cm}^2$  cross-section available for the electrodes used for the one- $g$  suspension. These investigations will be performed in 1999 after the production of such a laboratory model. Even with dedicated

laboratory facilities, the ground tests are limited in resolution by the seismic noise and by the coupling with the one- $g$  suspension, but these tests can be performed over very long periods. They should be complemented by free fall tests in a drop tower that provides the micro-gravity environment, but for only very short test periods of 4.7 s. The [ASTRE](#) accelerometer, being realised in the frame of the [ESA COLUMBUS](#) program and flown on board the shuttle, has been successfully tested in the Bremen drop tower [112]. The instrument currently under development, the configuration of which is very similar and representative to the one proposed for [LISA](#), could be much better evaluated on board a  $\mu$ -satellite with a drag compensation system.

### 6.1.5 Sensor operation modes

The proof mass can be kept motionless in position and attitude by means of six servo-control channels acting separately. It can be shown that the operation of the drag-free control can be represented by two loops. The first loop ensures the electrostatic suspension which can maintain the proof mass at the centre of the cage with electrostatic forces. The second one is the satellite drag-free control loop which compensates the satellite external forces using thrusters.

In the [LISA](#) mission, the absolute acceleration of the proof mass should essentially depend only on the gravitational field. Three sources of disturbances can be considered: the position-sensor noise, the satellite acceleration depending on the drag-free control performances, and the parasitic forces acting directly on the proof mass that cannot be minimised by any servo loop. The first two sources can sufficiently be reduced at low frequencies, when the electrostatic loop stiffness is adequately lower than the satellite control-loop stiffness. On the contrary, the stiffness of the electrostatic loop must be sufficient to easily control the proof-mass motion and attitude, in particular when the drag-free control is not fully operational, at the beginning of the experiment for instance. A trade-off between these requirements could be obtained with a specific configuration of the loop electronics that introduces varying control stiffnesses according to the applied acceleration.

### 6.1.6 Proof-mass charge control

Charge control of the proof-mass is crucial if spurious electromagnetic forces are to be kept at a level such that they do not compromise the science goals. As noted earlier the nominal requirement is to limit the free charge on the proof mass to  $< 2 \times 10^{-14}$  C in the presence of a continuous charging rate of  $10^{-17}$  to  $10^{-18}$  C/s [113]. This charge limit comes from considering the Lorentz force acceleration noise induced in an unshielded charged proof-mass interacting with the interplanetary magnetic field and it is explained in more detail in Section [A.2](#). It is conceivable that a factor of up to 100 might be recovered by shielding provided by the metallic vacuum enclosure around the sensor. Shielding beyond that level will be very difficult, given the need for access holes in various positions, and moreover, noise caused by electrostatic interactions of the free charge with the surrounding electrode structure then becomes significant anyway (see Appendix [A.2](#)).

The baseline charge control technique involves illuminating both the proof mass and its surrounding electrodes with ultra-violet light to release photoelectrons from both surfaces, and then to use bias voltages on the electrodes to control the nett transfer of charge. This technique has been demonstrated already for [GP-B](#) [114], albeit at a somewhat higher level of charge ( $10^{-9}$  C) and much coarser control authority than those required for [LISA](#). Laboratory tests using 2.5 W low-power mercury discharge lamps of two different types (rf discharge for [GP-B](#) and dc electric discharge for [ROSAT](#) [115]) have shown that sufficient photoelectric emission

can be achieved from gold surfaces in both direct and reflected illumination. The low magnetic susceptibility of the Au/Pt proof-mass alloy unfortunately results in a particularly high work function and it may be that a gold coating is necessary on the proof-mass.

The level of bias voltage required to effect sufficient charge control depends on the detailed electrode geometry, the gaps to be used and the mode of introducing the UV. In the current scheme, which offers the simplest mechanical solution, the UV will be introduced onto the central sections of two opposite transverse faces of the proof-mass. The facing electrodes will then be illuminated by reflection. This scheme gives a bipolar discharging capability. However with our current understanding of the charging mechanisms the belief is that the proof-mass will charge positively and hence the bias voltage will need to work against the inherent tendency of this implementation. An alternative scheme which would avoid the need for significant bias voltages could be to illuminate the electrode and proof mass with quasi-independently controllable UV fluxes. This is mechanically more challenging. Laboratory tests are planned to investigate these options further.

There are a number of possible operational modes for the charge control system. One is to allow the UV to illuminate the proof mass continuously and only rely on the bias voltages to control the charge. The bias voltage itself would be derived from measurements of the charge using a dither voltage applied in the transverse direction at a frequency above the science measurement band. Alternatively it might be better to ‘apply’ the UV in a gated fashion only when it was necessary to discharge the proof-mass or in a timed sequence aimed at matching the charging rate. For these modes we need some means of controlling the UV intensity. This can be done using the lamp drive power over a limited range by programming its supply current. A wider dynamic range can either be achieved using a load switching technique or by using an electro-optic switch (Pockels cell). A system to control the UV intensity involving a Pockels cell has been demonstrated in the laboratory [116].

The UV discharge system incorporates 2 low-pressure mercury discharge lamps, associated optical components, power supplies and control electronics contained within a single enclosure measuring 10 cm × 15 cm × 7 cm. The system is internally redundant and only 1 unit is required per spacecraft. The unit is located on the radiator plate. Two electrical connectors provide power and control function interfaces respectively. A digital control interface, including internal h/k conversion, is assumed. Four optical fibre couplings provide interfaces to fibre optic cables delivering independent UV photon fluxes to the proof-masses within the telescope structures.

## 6.2 Drag-free/attitude control system

### 6.2.1 Description

LISA requires that the acceleration noise imposed on each proof mass in the sensitive direction is smaller than

$$\widetilde{\delta a} < 3 \times 10^{-15} \left[ 1 + \left( \frac{f}{5 \times 10^{-3} \text{ Hz}} \right)^2 \right] \text{ m s}^{-2} / \sqrt{\text{Hz}} \quad (6.6)$$

within the measurement bandwidth (MBW) from  $10^{-4}$  to  $10^{-1}$  Hz. In terms of the requirements on spacecraft control, taking into account the optical referencing from both opposing faces of each proof masses, the LISA drag-free & attitude control system (DFACS) must ensure that each spacecraft is controlled in translation and orientation such that the relative displacement between the spacecraft and the proof mass in the sensitive direction of each telescope arm is less

than

$$\widetilde{\delta z} < 2.5 \times 10^{-9} \text{ m}/\sqrt{\text{Hz}} \quad (6.7)$$

within the MBW. In the other axes, the requirement is relaxed to

$$\widetilde{\delta x} = \widetilde{\delta y} < 2.5 \times 10^{-6} \text{ m}/\sqrt{\text{Hz}} \quad (6.8)$$

within the MBW. The relative attitude requirement between each proof mass and the spacecraft is

$$\widetilde{\delta \vartheta} < 1.5 \times 10^{-7} \text{ rad}/\sqrt{\text{Hz}} \quad (6.9)$$

within the MBW. The attitude of the spacecraft relative to each incoming wavefront must be controlled to within the dc value of

$$\varphi_{\text{dc}} < 3 \times 10^{-8} \text{ rad}, \quad (6.10)$$

with a pointing stability requirement of

$$\widetilde{\delta \varphi} < 8 \times 10^{-9} \text{ rad}/\sqrt{\text{Hz}} \quad (6.11)$$

within the MBW.

The DFACS on each spacecraft uses the signals from the two accelerometers and the quadrant photodiodes to generate commands to the spacecraft thrust system via the control laws implemented on the payload processor. The required computational throughput for the DFACS control laws will be less than 2 MIPS, easily accommodated on the RAD 6000-SC. Two autonomous star trackers on each spacecraft are used for coarse attitude information. Owing to the intimate relationship between the DFACS performance and the instrument sensitivity, and since the DFACS relies completely on the key payload sensors (accelerometers and photodiodes), the entire DFACS subsystem — with the exception of the spacecraft thrusters and drive electronics — will be a PI-provided contribution to the LISA payload.

### 6.2.2 DFACS controller modes

The spacecraft coarse attitude controller prevails upon separation from the propulsion module, maintaining a power-positive orientation. During this phase, the spacecraft has access to all of the enabled components on the bus. The coarse attitude control system establishes an inertial orientation using Sun sensors and/or the payload star trackers, plus the spacecraft thrusters. Then, from either realtime ground command or deferred store command, the payload processor is powered on and loaded from the spacecraft processor. The memory load is stored in the solid state recorder (SSR) non-volatile memory. It is fetched from the SSR by the spacecraft processor and routed to the payload processor via the 1553 interface to the payload processor bootstrap loader. Following a successful load, the payload processor is activated and enters a standby mode. Upon command from the spacecraft processor, the payload processor transitions to an intermediate mode whereby the 1553 bus control is transferred from the spacecraft processor to the payload processor. At this transition, the payload processor also takes over the coarse attitude control. Following a sequence of payload setup procedures (e.g. setting up the accelerometers and photodiodes), the payload processor transitions to successive higher modes of drag-free/fine-attitude control. For example, the next mode after coarse attitude control is the acquisition mode whereby the payload processors on each spacecraft command a sequence of manoeuvres for establishing laser links between all spacecraft. The ultimate mode of DFACS operation is the high-performance drag-free and attitude control required during science data gathering.

At all times, the spacecraft processor monitors the coarse attitude sensors and the status of the payload (by means of a watchdog signal from the payload processor) and intervenes by reclaiming bus control and coarse attitude control if a significant problem is detected. If the payload detects a problem (which is not yet severe enough to warrant the spacecraft processor to reclaim control), the payload processor will attempt to deal with it by dropping back to intermediate mode and switching from String A to String B. If not resolvable in this mode, then bus control and coarse attitude control is returned to the spacecraft processor, remaining there until commanded from the ground.

### 6.2.3 Autonomous star trackers

Each [LISA](#) payload will include four star tracker heads, mounted in pairs on the outside of the thermal shield, one pair aligned with each of the two telescopes. Only two are nominally operational – one on each telescope – the others serve as backups. Each has a field of view of  $22^\circ \times 16^\circ$  and can provide attitude knowledge of about 2 arcsec in two axes and 16 arcsec in their boresight roll axis. Star processing at an update rate of 1 Hz will require a total of 16 [MIPS](#) of throughput for both operational trackers. This is provided by a dedicated processor shared by the two optical heads. The processor unit must be mounted remotely, away from the payload thermal shield. (An alternative option is to use the payload processor instead of a dedicated processor, but this is not the current baseline.)

The star trackers will be fully autonomous, and can tolerate direct Sunlight without damage.

Field of view	$22^\circ \times 16^\circ$
Pitch, yaw accuracy	2 arcsec $\approx 10 \mu\text{rad}$
Roll accuracy	16 arcsec $\approx 80 \mu\text{rad}$
Update rate	1 Hz
Tracking rate	$0.2^\circ \text{ s}^{-1} \approx 3.5 \text{ mrad/s}$
Number of stars tracked	$\leq 50$
Tracking sensitivity	$7.5 \text{ m}_v$
Guide stars in database	5650
Auxiliary stars in database	22600
Communications I/F	<a href="#">1553</a> or <a href="#">RS 422</a>
Output format	quaternions, Euler angles
Operating temperature	$-30^\circ$ to $+50^\circ \text{ C}$
Radiation tolerance	1 kJ/kg

**Table 6.1** *Star tracker specifications (per optical head).*

The performance specifications of the star trackers are summarised in Table 6.1. The mass, power, and volume budgets are summarised in Table 6.2. The data in these tables is based on the system under development for the Oersted mission. Since the payload star trackers are on the [1553](#) bus, they may also be accessed by the spacecraft computer for coarse attitude control.

<i>Items</i>	<i>Number of Units</i>	<i>Unit Mass (kg)</i>	<i>Total Mass (kg)</i>	<i>Power per Unit (W)</i>
Optical head + immediate electr.	4	0.25	1	5
Baffle	4	0.5	2	—
Data processing unit incl. shielding	2	1.5	3	3
<b>Totals</b>			<b>6 kg</b>	<b>13 W</b> (2 heads + 1 proc.)
Dims. of each optical head plus baffle: $100 \times 100 \times 300 \text{ mm}^3 = 3 \text{ litres}$ Dims. of proc. unit (housing both processors): $100 \times 100 \times 100 \text{ mm}^3 = 1 \text{ litre}$				

**Table 6.2** *Star tracker mass, power, volume budgets (for one spacecraft).*

### 6.3 Accelerations directly affecting the proof-mass

There are various accelerations that directly affect the proof-mass, even through the shielding that the drag-free environment provides.

Two such acceleration effects stem from the charging of the test mass in interaction with outside magnetic fields, the other from the gravitational influence of smaller masses, minor celestial bodies, that come close to the [LISA](#) instrument.

The effect of these accelerations are discussed in detail in the Appendices [A.2](#) and [A.3](#).





# 7 Signal Extraction and Data Analysis

## 7.1 Signal extraction

### 7.1.1 Phase measurement

Information is extracted from the beat signal as a time series of phase measurements. The phase of the beat signal between the received and transmitted beams is measured with the time base provided by the on-board USO in each of the spacecraft. The two laser beams being beat together have different frequencies because of gradual changes in arm length and because of the roughly 10 kHz offset frequencies used in the locking scheme. The expected Doppler shifts for arms 1 and 2 (see Sections 5.1 and 5.2 and Figure 5.1) are of the order of 1 MHz for annual orbit corrections, and could be kept below 20 kHz if necessary by monthly orbit corrections. For arm 3, the Doppler shifts may be as high as 15 MHz.

The phase of the laser heterodyne signals needs to be measured with an accuracy much better than the total error allocation of  $40 \text{ pm}/\sqrt{\text{Hz}}$  and with a dynamic range of roughly  $10^9$  in order to perform the laser phase noise cancellation scheme. Forty picometers corresponds to  $4 \times 10^{-5}$  of a cycle, and the expected laser phase noise was estimated earlier to be roughly  $30 \text{ Hz}/\sqrt{\text{Hz}}$  at 1 mHz (see Section 5.5). This corresponds to roughly  $3000 \text{ cy}/\sqrt{\text{Hz}}$  for the phase noise at 1 mHz. In order to measure the phase to the necessary accuracy and with the desired dynamic range, the signal from each optical heterodyne detector is beat again against a suitable reference frequency from a comb of frequencies separated by intervals of 50 kHz, which are generated from the USO. The reference frequencies are chosen to place the final beat frequencies in the range of 75 to 125 kHz. A tracking filter is then used to remove phase noise above roughly 100 Hz in order to prevent aliasing of such noise into the phase measurements.

The resulting signals are then sent to the phase meters, where they are strongly amplified, clipped, differentiated, and clipped again to give positive-going zero-crossing pulses with standard shapes. In each measurement interval, the delay between the USO clock pulse defining the interval start and the next zero-crossing pulse is timed, and the total number of zero-crossing pulses is counted. From this information the integer and fractional numbers of zero crossings are determined for each interval. The results are then filtered to remove phase variations at frequencies above about 1 Hz, and the data set is reduced to a time delay and a count every 0.5 s.

## 7.2 Frequency-domain cancellation of laser noise

### 7.2.1 Laser noise

One feasible scheme of cancelling out the noise due to phase jitter of the laser can be applied in the Fourier domain.

The data are affected by the phase noise of the master laser in S/C 1, as well as orbital motions and gravitational waves affecting the long arms. However, the variations in the arm lengths in the frequency band of interest, roughly 0.1 mHz to 1 Hz, are small. Thus the apparent variations in the length of any of the arms can be analyzed to determine the laser phase noise as a function

of time. For simplicity only arms 1 and 2 will be discussed here, but similar results can be obtained for observables that include arm 3 also.

The accuracy of the phase noise measurements will be degraded near harmonics of the frequencies corresponding to the round-trip travel times for the two arms. A weighted mean of the results for the two arms can be used to avoid this problem, but we assume here that arm 1 is used and that the frequency of interest is well separated from any of the harmonics.

Following approximately the notation of Giampieri *et al.* [117], except using units of meters, the phase outputs of the diodes of spacecraft 1 and 2 are

$$\begin{aligned} s_1(t) &= p(t - 2L_1/c) - p(t) + n_1(t) + h(t), \\ s_2(t) &= p(t - 2L_2/c) - p(t) + n_2(t) - h(t), \end{aligned} \quad (7.1)$$

where  $p(t)$  is the laser phase noise,  $L_1$  and  $L_2$  are the arm lengths,  $n_1$  and  $n_2$  are the separate shot noises and any other noises that are not common to the two arms, and  $h$  is the gravitational radiation signal. Transforming to the frequency domain we get

$$\begin{aligned} s_1(f) &= p(f)(e^{4\pi i f L_1/c} - 1) + n_1(f) + h(f), \\ s_2(f) &= p(f)(e^{4\pi i f L_2/c} - 1) + n_2(f) - h(f). \end{aligned} \quad (7.2)$$

An estimate of the clock signal is formed from arm 1 by

$$\hat{p}(f) = \frac{s_1(f)}{e^{4\pi i f (L_1 + \delta L_1)/c} - 1}, \quad (7.3)$$

where our knowledge of the arm length  $L_1$  is in error by an amount  $\delta L_1$ . Including the definition of  $s_1$  we get

$$\hat{p}(f) = p(f) \frac{e^{4\pi i f L_1/c} - 1}{e^{4\pi i f (L_1 + \delta L_1)/c} - 1} + \frac{n_1}{e^{4\pi i f (L_1 + \delta L_1)/c} - 1} + \frac{h}{e^{4\pi i f (L_1 + \delta L_1)/c} - 1}. \quad (7.4)$$

Using the estimate  $\hat{p}$  and the definition of  $s_1$  we define

$$\begin{aligned} \hat{s}_1 &= \hat{p}[e^{4\pi i f (L_1 + \delta L_1)/c} - 1], \\ \hat{s}_2 &= \hat{p}[e^{4\pi i f (L_2 + \delta L_2)/c} - 1]. \end{aligned} \quad (7.5)$$

We then form the difference

$$(s_1 - s_2) - (\hat{s}_1 - \hat{s}_2) = P + N + H, \quad (7.6)$$

with

$$\begin{aligned} P &= p(f) \left[ e^{4\pi i f L_1/c} - e^{4\pi i f L_2/c} - \frac{e^{4\pi i f L_1/c} - 1}{e^{4\pi i f (L_1 + \delta L_1)/c} - 1} \left( e^{4\pi i f (L_1 + \delta L_1)/c} - e^{4\pi i f (L_2 + \delta L_2)/c} \right) \right] \\ N &= n_1(f) - n_2(f) - n_1(f) \frac{e^{4\pi i f (L_1 + \delta L_1)/c} - e^{4\pi i f (L_2 + \delta L_2)/c}}{e^{4\pi i f (L_1 + \delta L_1)/c} - 1} \\ H &= h(f) \left[ 2 - \frac{e^{4\pi i f (L_1 + \delta L_1)/c} - e^{4\pi i f (L_2 + \delta L_2)/c}}{e^{4\pi i f (L_1 + \delta L_1)/c} - 1} \right]. \end{aligned}$$

Expanding by using  $4\pi f\delta L_1/c \ll 4\pi fL_1/c \ll 1$  and  $4\pi f\delta L_2/c \ll 4\pi fL_2/c \ll 1$  these become

$$P \approx p(f) \frac{L_1\delta L_2 - L_2\delta L_1}{L_1} 4\pi if/c \quad (7.7)$$

$$N \approx \frac{n_1(f)L_2 - n_2(f)L_1}{L_1} \quad (7.8)$$

$$H \approx h(f) \frac{L_1 + L_2}{L_1}. \quad (7.9)$$

From the above expressions for  $P(f)$ , it is clear that the laser phase noise can be corrected for to the measurement noise level  $N(f)$  if the arm lengths are known accurately enough, and if the measurement system has sufficient dynamic range.

In general, we assume that the difference in length of the two arms is known to 200 m, and the mean length to 20 km. The error in the arm length difference can then cause an error of  $4 \times 10^{-9}$  of the laser phase noise at  $f = 1$  mHz, and  $4 \times 10^{-10}$  at  $f = 0.1$  mHz. If the fractional difference in arm lengths is 1%, the errors in the laser phase noise corrections due to the uncertainty in the mean arm length are the same magnitude as the values given above.

Our model for the laser phase noise before correction at frequencies of 0.1 mHz to 1 Hz is based on the thermal stability of the reference cavity to which the laser in spacecraft 1 is locked for frequencies below about 3 mHz, plus the noise in locking to the cavity at higher frequencies. Our estimate for the locking noise comes from the results of Salomon *et al.* [118]. As a typical case, we take the fractional frequency noise in the laser to be  $2 \times 10^{-11}/\sqrt{\text{Hz}}$  at 0.1 mHz,  $1 \times 10^{-13}/\sqrt{\text{Hz}}$  at 1 mHz, and  $2 \times 10^{-15}/\sqrt{\text{Hz}}$  at 10 mHz. As an example, the frequency noise at 1 mHz corresponds to a phase noise level of  $5 \times 10^{-3} \text{ m}/\sqrt{\text{Hz}}$ . To correct for this to a measurement noise level of  $4 \text{ pm}/\sqrt{\text{Hz}}$  requires a phase noise reduction of a factor  $8 \times 10^{-10}$ .

The measurement of the difference in arm length for arms 1 and 2 is then corrected for the laser phase noise, using the approximately known lengths of the arms. The requirement on knowing the difference in arm lengths is about 200 m, as assumed earlier. The arm lengths will be determined by combining ground tracking of the spacecraft with the observed arm length changes from the laser phase measurements, or, alternatively, by measuring a group delay with a modulation tone on the laser beam. If the arm lengths are very close to equal, the noise at the harmonics of the round-trip travel frequency will be less well determined, but the accuracy will still be sufficient for correcting the measured arm length difference. A similar process is used to correct the time series of the length of arm 3 minus the average for arms 1 and 2.

The advantage of on-board correction for the laser phase noise is that the data can be compressed by a factor of perhaps 5 before they are transmitted to the ground. This is because the arm length changes will be very smooth and the gravitational wave signals relatively small. The one disadvantage of having to correct for the laser phase noise is that a small fractional error will be made in the amplitude and phase of the gravitational wave signals in some cases. However, this error appears to be correctable for sources where the source direction and polarization can be determined.

## 7.2.2 Clock noise

An ultra-stable oscillator (USO) is required onboard for the phase measurements, for compensation of the orbital Doppler shifts, and for providing offset frequencies for laser phase locking. Because of phase noise limitations for available space-qualified USOs, either the Doppler shifts must be kept very small or the USO phase noise must be measured. Current USOs have a stability

(Allan standard deviation) of  $1 \text{ to } 2 \times 10^{-13}$  for periods of 1 to 1000 s. At 1 mHz, this corresponds to a fractional frequency noise level of about  $7 \times 10^{-12}/\sqrt{\text{Hz}}$ . For a round-trip Doppler shift of 10 kHz and  $5 \times 10^6$  km arm lengths, the resulting noise in measuring variations in the length of one arm is  $9 \text{ pm}/\sqrt{\text{Hz}}$ .

As a practical matter, it would require frequent orbit corrections to keep the Doppler shifts small for even two arms of the interferometer, and the Doppler shift for the third arm would still be large. To avoid the USO stability limitation, the USO phase noise will be measured with a method suggested by Danzmann. In this method, sidebands of perhaps 200 MHz derived from the USOs will be modulated onto the laser beams sent both ways over arms 1 and 2 and one-way over the three short spacecraft separations. The received modulation signals will be used to successively phase-lock all of the USOs except the one in S/C 1 and to determine the phase noise of that USO in the same way as the laser phase noise is measured.

It is assumed that 10 % of the laser power on spacecraft 1 goes into each of two 200 MHz modulation sidetones, and that one of them is filtered out of the transmitted signal. A similar carrier and sidetone with a somewhat different offset frequency are generated on the other spacecraft and offset phase locked to the received signals. When these signals arrive at spacecraft 1, phase measurements are made on both the carrier and the sidetone. For the carrier, the error budget allows about  $\frac{1}{\sqrt{2}} \times 40 \text{ pm}/\sqrt{\text{Hz}}$  for the phase error. For the sidetone, the factor 10 lower intensity will make the shot noise contribution to the error about three times larger. However, some of the systematic error sources will be common to the sidetone and the carrier, and will not affect the measurement of the sidetone frequency. As a rough estimate, we take  $40 \text{ pm}/\sqrt{\text{Hz}}$  for the error in the measurement of the phase of the sidetone after the roundtrip over arm 1.

Because of the transit time over the arm, the error in determining the phase noise of the USO will be increased by a factor  $1/K$ , where  $K$  is the time delay factor from the previous section:

$$K = \left| e^{4\pi i f L/c} - 1 \right|. \quad (7.10)$$

Here  $f$  is the frequency of the phase noise. For  $f \ll 4.77 \text{ mHz}$ , we get  $K \sim f/(4.77 \text{ mHz})$ . To reduce the phase noise in the Doppler correction signal to the level of  $10 \text{ pm}/\sqrt{\text{Hz}}$  used later in our error budget, it can be shown that the following relationship is required:

$$0.25K > \nu_{\text{Doppler}}/(200 \text{ MHz}). \quad (7.11)$$

For a roundtrip Doppler shift of 1 MHz, this holds above about 0.1 mHz, except for very narrow bands around harmonics of the roundtrip travel frequency 30 mHz. For 15 MHz instead of 1 MHz, the relationship holds above 1.4 mHz, except for bands of width 3 mHz about harmonics of 30 mHz. Somewhat better performance can be obtained by using similar information from arm 2. These limitations would not seriously compromise the performance of arm 3 of LISA, and would have essentially no effect for arms 1 and 2.

### 7.2.3 Other approaches

An even more elaborate approach at assessing, and to a large part cancelling, various noises is given in Appendix A.1, ‘Detailed Noise Analysis’.

## 7.3 Time-domain cancellation of laser phase noise

Equal-arm interferometric detectors of gravitational radiation allow phase measurements many orders of magnitude below the intrinsic phase stability of the laser injecting light into their arms.

This is because the noise in the laser light is common to both arms, experiencing exactly the same delay, and cancels when it is differenced at the photo detector. **GW** sensitivity is then set by much lower level secondary noises. **LISA** will necessarily have slightly different arm lengths, so laser noise experiences different delays in the two arms and will not fully cancel at the detector. This section outlines a computationally-simple, time-domain method which exactly cancels the laser noise in the **LISA** one-bounce unequal-arm Michelson interferometer [119].

If the armlengths are unequal by an amount  $\Delta L = L_2 - L_1 \equiv \varepsilon L_1$  (with  $\varepsilon \simeq 3 \times 10^{-2}$  for **LISA**), simple subtraction of, e.g., the two two-way Doppler data streams gives a new data set that is still affected by the laser fluctuations by an amount

$$C(t - 2L_1) - C(t - 2L_2) \simeq 2\dot{C}(t - 2L_1)\varepsilon L_1. \quad (7.12)$$

Here  $C(t)$  is the laser phase/frequency noise process. For example, at a frequency of  $10^{-3}$  Hz and for a laser of frequency stability of about  $10^{-13}/\sqrt{\text{Hz}}$ , the uncanceled laser frequency fluctuations are about  $10^{-16}/\sqrt{\text{Hz}}$ . To reach **LISA**'s design sensitivity it is crucial to cancel laser frequency fluctuations by many more orders of magnitude.

The method relies on a linear combination of phase/frequency differences made separately in each arm. These are obtained by interfering the returning laser light in each arm, which has been coherently transponded by the end spacecraft, with the outgoing light. Let these two time series of phase difference be  $\varphi_i$ ,  $i = 1, 2$ . By forming

$$[\varphi_1(t - 2L_2/c) - \varphi_1(t)] - [\varphi_2(t - 2L_1/c) - \varphi_2(t)], \quad (7.13)$$

where  $L_i$  are the arm lengths, gravitational wave signals remains while the laser noise is cancelled [119]. Analysis of required arm length knowledge and the time scale over which the arm lengths can change is given in [119]. Adopting the criterion that uncanceled laser phase noise should have a spectral level below that of the secondary noises gives a condition on arm-length knowledge. For the expected **LISA** noise spectra, the most stringent constraint occurs near  $f = 10^{-3}$  Hz and implies required accuracy in the armlengths of about 30 meters.

It is also necessary to calculate the time scales during which the arm lengths will change by an amount equal to the accuracies themselves. This identifies the minimum time required before updating the round-trip-light-times during the implementation of the unequal-arm algorithm. This is analyzed for the spacecraft dynamics of the nominal **LISA** mission in [119]. The result depends on which arms are being considered and on time during the mission, and is sufficiently slowly-varying for practical application of the method.

Alternative procedures for canceling laser noise, involving operations on the Fourier transforms of the data from each arm, have been proposed. These frequency domain (**FD**) methods cancel the laser noise in the limit where the duration of the data goes to infinity. A comparison of the time domain method, above, and **FD** methods is given in [119].

## 7.4 Alternative laser-phase and optical-bench noise-canceling methods

The unequal-arm Michelson interferometer data, appropriately processed [119], cancels **LISA**'s leading noise source (laser phase/frequency fluctuations). The interferometric combination is not the only laser-noise-canceling procedure, however. This section describes, and summarizes sensitivity for, **LISA** data combinations which both cancel laser phase noise and non-inertial motions of the optical benches [120]. These alternatives may offer design flexibility (and robustness against some types of instrumental problems) for **LISA**.

### 7.4.1 Notation and geometry

This section closely follows [121] and [120]. LISA is treated in terms of six one-way Doppler links connecting the six optical benches. Figure 7.1 (from [120]) shows the geometry in the plane of the three spacecraft. The spacecraft are labeled 1, 2, and 3, and are equidistant (distance =  $\ell$ ) from point O. Relative to O, the spacecraft are located by the coplanar unit vectors  $\hat{p}_1$ ,  $\hat{p}_2$  and  $\hat{p}_3$ . As indicated in Figure 7.1, the lengths between pairs of spacecraft are  $L_1$ ,  $L_2$  and  $L_3$ , with  $L_i$  being opposite spacecraft  $i$ . Unit vectors along the lines connecting spacecraft pairs are  $\hat{n}_1$ ,  $\hat{n}_2$  and  $\hat{n}_3$ , oriented such that  $\hat{n}_1$  has its foot at spacecraft 3 and its arrow pointing at spacecraft 2,  $\hat{n}_2$  has its foot at spacecraft 1 and its arrow pointing toward spacecraft 3, and  $\hat{n}_3$  has its foot at spacecraft 2 and its arrow pointing toward spacecraft 1. Thus,  $L_1\hat{n}_1 + L_2\hat{n}_2 + L_3\hat{n}_3 = 0$ . This terminology allows cyclic permutation of the indices in subsequent equations, resulting in compact notation and facilitating coding of sensitivity calculations.

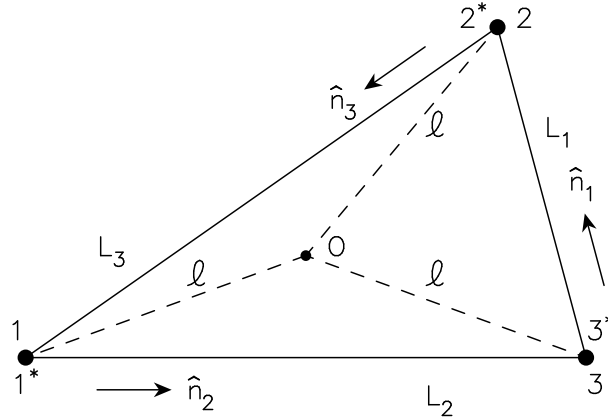


**Figure 7.1** Geometry: Each spacecraft is equidistant from point O, with unit vectors  $\hat{p}_i$  indicating directions to the three spacecraft. Unit vectors  $\hat{n}_i$  point between spacecraft pairs with the indicated orientation.

Laser beams exchanged between spacecraft pairs have fractional frequency shifts,  $y_{ij} = \Delta\nu/\nu_0$ , where  $\Delta\nu$  is the frequency deviation from the center frequency  $\nu_0$ . The subscripts label the transmitting and receiving spacecraft. The convention is that  $y_{31}$  is the beam received at spacecraft 1 and transmitted from spacecraft 2,  $y_{21}$  is the beam received at spacecraft 1 and transmitted from spacecraft 3, etc. Internal metrology signals to correct for optical bench motions are denoted by  $z_{ij}$ , with information content and labeling convention described below. Delay of laser data streams, either by time-of-flight or in post-processing, is indicated by commas in the subscripts:  $y_{31,2} = y_{31}(t - L_2)$ ,  $y_{31,23} = y_{31}(t - L_2 - L_3) = y_{31,32}$ , etc. ( $c = 1$  is used in the formulation with conversion to physical units done for the results.)

Figure 7.2 shows the proof-mass-plus-optical-bench assemblies for LISA spacecraft 1 [122, 120]. The left-hand optical bench is “bench 1”, while the right-hand bench is “bench 1\*”. The photodetectors where data  $y_{21}$ ,  $y_{31}$ ,  $z_{21}$ , and  $z_{31}$  are measured at spacecraft 1 are shown. The lasers are assumed to have the same nominal center frequency and it is assumed that the first order Doppler shift is removed. The fractional frequency fluctuations of the laser on optical bench 1 is denoted  $C_1(t)$ ; on optical bench 1\* it is  $C_1^*(t)$ ; these are independent (the lasers need not be “locked”, but see below). The cyclic terminology for indices applies: at vertex  $i$  ( $i = 1, 2, 3$ ) the random velocities of the two proof masses are respectively denoted  $\vec{v}_i(t)$  and  $\vec{v}_i^*(t)$ , and the random velocities (perhaps several orders of magnitude greater) of their optical benches are correspondingly denoted  $\vec{V}_i(t)$  and  $\vec{V}_i^*(t)$ . Note that this analysis does not assume that pairs

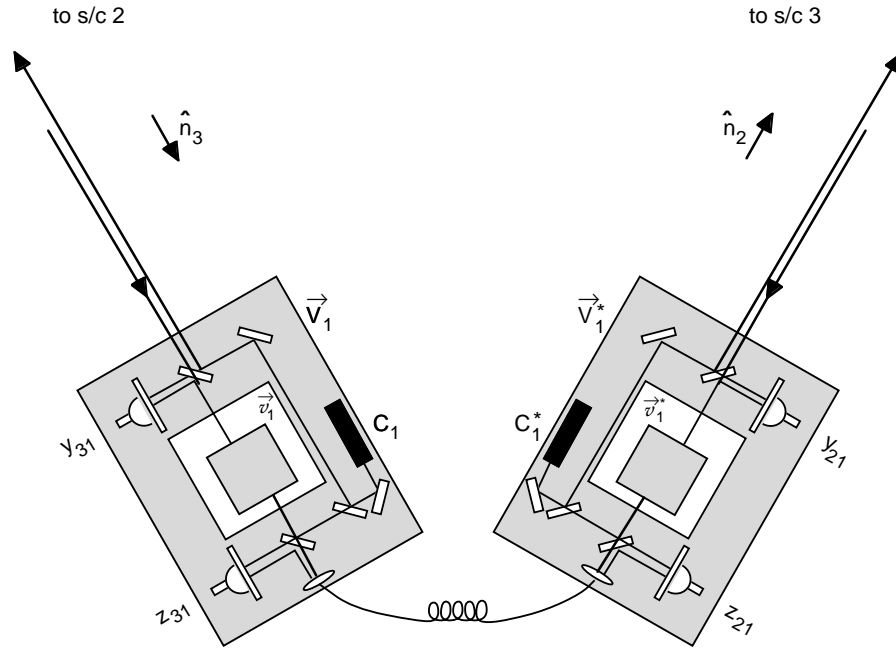


**Figure 7.2** Diagram of *LISA* spacecraft 1, showing the two lasers and the two proof masses enclosed in the two optical bench assemblies. Proof mass and optical bench motions are indicated by lower case ( $v$ ) and upper case ( $V$ ) symbols, respectively. The readouts for the interspacecraft Doppler links ( $y_{ij}$ ) and intraspacecraft metrology links ( $z_{ij}$ ) are shown. Equations for the Doppler and metrology links are given in the text and are the basis for determining laser- and optical-bench-noise-canceling linear combinations and for computation of the transfer functions of the residuals (proof mass and optical path) noises.

of optical benches are rigidly connected, i.e.  $\vec{V}_i \neq \vec{V}_i^*$ , in general. The present *LISA* design shows optical fibers transmitting signals between adjacent benches. Intraspacecraft time-delay effects for the  $z_{ij}$  are ignored and  $\eta_i(t)$  are the frequency shifts upon transmission through the fibers (ultimately due to a component of the relative bench motions,  $\vec{V}_i - \vec{V}_i^*$ ). The frequency shift  $\eta(t)$  within a given spacecraft is the same for both local beams, positive if the benches are approaching and negative if separating.

The light paths for the  $y_{i1}$ 's and  $z_{i1}$ 's can be traced in Figure 7.2. An outgoing light beam transmitted to a distant spacecraft is routed from the laser on the local optical bench using mirrors and beam splitters; this beam does not interact with the local proof mass. Conversely, an incoming light beam from a distant spacecraft is bounced off the local proof mass before being reflected onto the photodetector where it is mixed with light from the laser on that same optical bench. These data are denoted  $y_{31}$  and  $y_{21}$  in Figure 7.2. Beams exchanged between adjacent optical benches however do precisely the opposite. Light to be *transmitted* from the laser on an optical bench is *first* bounced off the proof mass it encloses and then directed to the other optical bench. Upon reception it does not interact with the proof mass there, but is directly mixed with local laser light. They are  $z_{31}$  and  $z_{21}$  in Figure 7.2. This configuration allows the twelve Doppler data streams to be combined so as to eliminate all laser phase noises (the  $C_i$  and  $C_i^*$ ) and optical bench buffeting (the  $\vec{V}_i$  and  $\vec{V}_i^*$ ) noises from GW-sensitive data combinations.



### 7.4.2 Gravitational wave signal transfer function to single laser link

The response of the one-way Doppler time series  $y_{31}$  and  $y_{21}$  excited by a transverse, traceless plane gravitational wave having unit wavevector  $\hat{k}$  is [123, 124]:

$$y_{31}^{\text{gw}}(t) = \left[ 1 + \frac{\ell}{L_3}(\mu_1 - \mu_2) \right] (\Psi_3(t - \mu_2\ell - L_3) - \Psi_3(t - \mu_1\ell)) \quad (7.14)$$

$$y_{21}^{\text{gw}}(t) = \left[ 1 - \frac{\ell}{L_2}(\mu_3 - \mu_1) \right] (\Psi_2(t - \mu_3\ell - L_2) - \Psi_2(t - \mu_1\ell)) \quad (7.15)$$

where  $\mu_i = \hat{k} \cdot \hat{p}_i$ , and  $\Psi_i$  is

$$\Psi_i(t) = \frac{1}{2} \frac{\hat{n}_i \cdot \mathbf{h}(t) \cdot \hat{n}_i}{1 - (\hat{k} \cdot \hat{n}_i)^2} \quad (7.16)$$

and where  $\mathbf{h}(t)$  is the first order spatial metric perturbation at point O. Note that  $L_1\hat{k} \cdot \hat{n}_1 = \ell(\mu_2 - \mu_3)$ , and so forth by cyclic permutation of the indices. The gravitational wave  $\mathbf{h}(t)$  is  $[h_+(t) \mathbf{e}_+ + h_\times(t) \mathbf{e}_\times]$ , where the 3-tensors  $\mathbf{e}_+$  and  $\mathbf{e}_\times$  are transverse to  $\hat{k}$  and traceless. The GW contribution of the other four  $y_{ij}$ 's can be obtained by cyclic permutation of the indices.

### 7.4.3 Noise transfer function to single laser link

The noise contributions to  $y_{ij}$  and  $z_{ij}$  Doppler measurements can be developed from Figures 7.1 and 7.2. Consider  $y_{31}$ . The  $y_{31}$  photodetector on the left bench of spacecraft 1, moving with velocity  $\vec{V}_1$ , reads the Doppler signal  $y_{31}$  by mixing the beam originating from distant optical bench 2\* in direction  $\hat{n}_3$  (laser noise  $C_2^*$  and optical bench motion  $\vec{V}_2^*$ , delayed by propagation along  $L_3$ ), after one bounce off the proof mass ( $\vec{v}_1$ ). This mixing process is done with optical bench 1's local laser light ( $C_1$ ). The  $z_{31}$  measurement results from light originating at the right-bench laser ( $C_1^*$ ,  $\vec{V}_1^*$ ), bounced once off the right proof mass ( $\vec{v}_1^*$ ), and directed through the fiber (incurring Doppler shift  $\eta_1(t)$ ), to the left bench, where it is mixed with laser light ( $C_1$ ). Similarly the right bench records Doppler observations  $y_{21}$  and  $z_{21}$ . The *noise-only* contributions to the four photodetector readouts at vertex 1 are thus:

$$y_{21}^{\text{noise}} = C_{3,2} - \hat{n}_2 \cdot \vec{V}_{3,2} + 2\hat{n}_2 \cdot \vec{v}_1^* - \hat{n}_2 \cdot \vec{V}_1^* - C_1^* + y_{21}^{\text{shot}} \quad (7.17)$$

$$z_{21} = C_1 + 2\hat{n}_3 \cdot (\vec{v}_1 - \vec{V}_1) + \eta_1 - C_1^* \quad (7.18)$$

$$y_{31}^{\text{noise}} = C_{2,3}^* + \hat{n}_3 \cdot \vec{V}_{2,3}^* - 2\hat{n}_3 \cdot \vec{v}_1 + \hat{n}_3 \cdot \vec{V}_1 - C_1 + y_{31}^{\text{shot}} \quad (7.19)$$

$$z_{31} = C_1^* - 2\hat{n}_2 \cdot (\vec{v}_1^* - \vec{V}_1^*) + \eta_1 - C_1 \quad (7.20)$$

The  $z_{ij}$  contain no GW signal, so the “noise” superscript is omitted for them. Eight other relations, for the readouts at vertices 2 and 3, are given by cyclic permutation of the indices in the above equations. The  $z_{ij}$  measurements will be made with high SNR so that shot noise is negligible for them. The transfer of instrumental noise to the Doppler observables ( $y_{ij}$ ) and the intraspacecraft metrology signals ( $z_{ij}$ ) is explicit in the above equations and will be used to compute aggregate noise power spectra.

### 7.4.4 Combinations that eliminate laser noises and optical bench motions

Data combinations which cancel all laser noises and all optical bench motion noises are given in [120]. These combinations retain gravitational waves, proof mass motions  $\vec{v}_i^*$  and  $\vec{v}_i$  (acceleration noise) and readout errors (shot noise). The combinations are not independent, but span a three-dimensional function space [121].

#### 7.4.4.1 Unequal-arm length interferometric combinations

The nominal LISA configuration is an unequal-arm Michelson interferometer (see Figure 7.3).

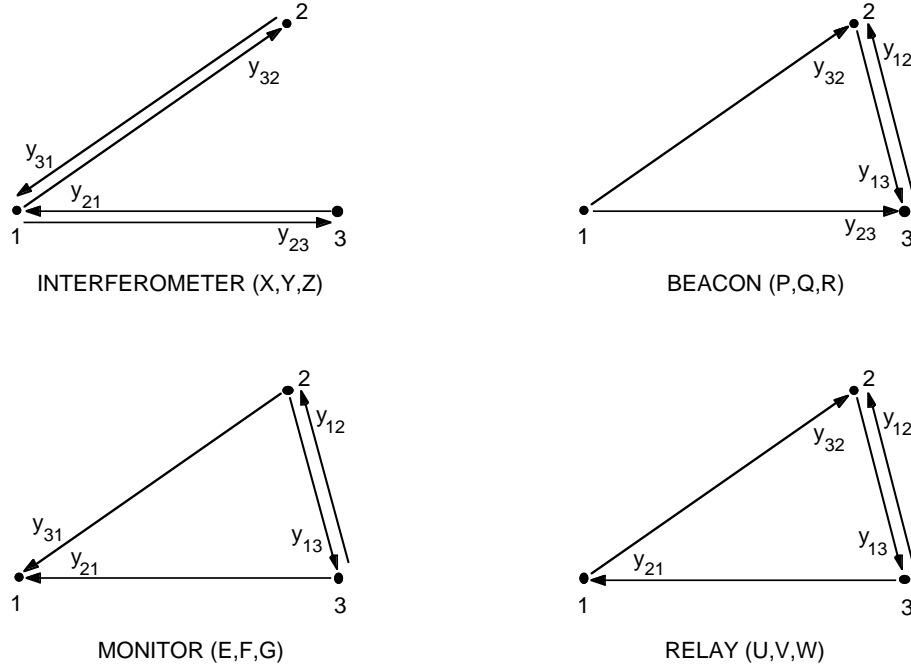


**Figure 7.3** The four-link LISA data combining possibilities.

Appropriate time-domain combinations of the  $y_{ij}$  from the two arms and the intraspacecraft  $z_{ij}$  cancel laser and optical bench noises [119, 120]. There are three possible interferometers (X, Y, Z); the unequal-arm-length interferometric combination X is:

$$\begin{aligned}
 X &= y_{32,322} - y_{23,233} + y_{31,22} - y_{21,33} + y_{23,2} - y_{32,3} + y_{21} - y_{31} \\
 &\quad + \frac{1}{2} (-z_{21,2233} + z_{21,33} + z_{21,22} - z_{21}) \\
 &\quad + \frac{1}{2} (+z_{31,2233} - z_{31,33} - z_{31,22} + z_{31})
 \end{aligned} \tag{7.21}$$

Combinations Y and Z are given by cyclic permutation of the indices. Explicit substitution of the definitions of the  $y_{ij}$  and  $z_{ij}$ , above, shows that all six laser phase noises (the  $C_i$  and  $C_i^*$ ) and all six optical bench motions (the  $V_i$  and  $V_i^*$ ) cancel exactly. The gravitational wave signal maps to X as a superposition of eight realizations:

$$\begin{aligned}
 X^{\text{gw}} &= \left[ 1 - \frac{\ell}{L_3} (\mu_1 - \mu_2) \right] (\Psi_3(t - \mu_1 \ell - 2L_3 - 2L_2) - \Psi_3(t - \mu_2 \ell - L_3 - 2L_2)) \\
 &\quad - \left[ 1 + \frac{\ell}{L_2} (\mu_3 - \mu_1) \right] (\Psi_2(t - \mu_1 \ell - 2L_2 - 2L_3) - \Psi_2(t - \mu_3 \ell - L_2 - 2L_3)) \\
 &\quad + \left[ 1 + \frac{\ell}{L_3} (\mu_1 - \mu_2) \right] (\Psi_3(t - \mu_2 \ell - L_3 - 2L_2) - \Psi_3(t - \mu_1 \ell - 2L_2)) \\
 &\quad - \left[ 1 - \frac{\ell}{L_2} (\mu_3 - \mu_1) \right] (\Psi_2(t - \mu_3 \ell - L_2 - 2L_3) - \Psi_2(t - \mu_1 \ell - 2L_3)) \\
 &\quad + \left[ 1 + \frac{\ell}{L_2} (\mu_3 - \mu_1) \right] (\Psi_2(t - \mu_1 \ell - 2L_2) - \Psi_2(t - \mu_3 \ell - L_2))
 \end{aligned}$$

$$\begin{aligned}
 & - \left[ 1 - \frac{\ell}{L_3}(\mu_1 - \mu_2) \right] (\Psi_3(t - \mu_1\ell - 2L_3) - \Psi_3(t - \mu_2\ell - L_3)) \\
 & + \left[ 1 - \frac{\ell}{L_2}(\mu_3 - \mu_1) \right] (\Psi_2(t - \mu_3\ell - L_2) - \Psi_2(t - \mu_1\ell)) \\
 & - \left[ 1 + \frac{\ell}{L_3}(\mu_1 - \mu_2) \right] (\Psi_3(t - \mu_2\ell - L_3) - \Psi_3(t - \mu_1\ell))
 \end{aligned} \tag{7.22}$$

with  $\Psi_i$ ,  $\ell$ ,  $\mu_i$ ,  $L_i$  given in terms of the wave properties and detector geometry as above. (This equation can be derived by direct substitution of the  $y_{ij}^{\text{gw}}$  into the definition of  $X$ , above.) A  $\delta$ -function GW signal would produce eight pulses in  $X$ , at times depending on the arrival direction of the wave and the detector configuration:  $\mu_1\ell$ ,  $\mu_2\ell + L_3$ ,  $\mu_3\ell + L_2$ ,  $\mu_1\ell + 2L_3$ ,  $\mu_1\ell + 2L_2$ ,  $\mu_3\ell + L_2 + 2L_3$ ,  $\mu_2\ell + 2L_2 + L_3$ , and  $\mu_1\ell + 2L_2 + 2L_3$ .

The noise in  $X$  due to proof-mass motions,  $\vec{v}_i$  and  $\vec{v}_i^*$ , is:

$$\begin{aligned}
 X^{\text{proofmass}} = & \hat{n}_2 \cdot (-\vec{v}_{1,2233}^* + \vec{v}_{1,22}^* - \vec{v}_{1,33}^* + \vec{v}_1^* + 2\vec{v}_{3,233} - 2\vec{v}_{3,2}) \\
 & + \hat{n}_3 \cdot (-\vec{v}_{1,2233} + \vec{v}_{1,33} - \vec{v}_{1,22} + \vec{v}_1 + 2\vec{v}_{2,223}^* - 2\vec{v}_{2,3}^*)
 \end{aligned} \tag{7.23}$$

Shot noise enters only in the  $y_{ij}$ . The power spectra of the acceleration and shot noise components of  $X$ , assuming independent individual proof mass acceleration noises (with equal raw spectra), and independent shot noises (with equal raw spectra) and for the equilateral triangle ( $L_1 = L_2 = L_3 = L$ ) case is [120]:

$$S_X = [8 \sin^2(4\pi fL) + 32 \sin^2(2\pi fL)] S_y^{\text{proof mass}} + 16 \sin^2(2\pi fL) S_y^{\text{optical path}} \tag{7.24}$$

It is assumed that shot noise and optical path noise (i.e. total optical path noise, as specified in [1]) have the same transfer functions.

#### 7.4.4.2 The $\alpha$ , $\beta$ , $\gamma$ combinations

Another three independent linear combinations of the Doppler data which do not contain laser or optical bench noises are:

$$\begin{aligned}
 \alpha = & y_{21} - y_{31} + y_{13,2} - y_{12,3} + y_{32,12} - y_{23,13} \\
 & - \frac{1}{2} (z_{13,2} + z_{13,13} + z_{21} + z_{21,123} + z_{32,3} + z_{32,12}) \\
 & + \frac{1}{2} (z_{23,2} + z_{23,13} + z_{31} + z_{31,123} + z_{12,3} + z_{12,12})
 \end{aligned} \tag{7.25}$$

with  $\beta$ , and  $\gamma$  given, as usual, by cyclical permutation of the indices. The gravitational wave response of  $\alpha$  is:

$$\begin{aligned}
 \alpha^{\text{gw}} = & \left[ 1 - \frac{\ell}{L_2}(\mu_3 - \mu_1) \right] (\Psi_2(t - \mu_3\ell - L_2) - \Psi_2(t - \mu_1\ell)) \\
 & - \left[ 1 + \frac{\ell}{L_3}(\mu_1 - \mu_2) \right] (\Psi_3(t - \mu_2\ell - L_3) - \Psi_3(t - \mu_1\ell)) \\
 & + \left[ 1 - \frac{\ell}{L_1}(\mu_2 - \mu_3) \right] (\Psi_1(t - \mu_2\ell - L_1 - L_2) - \Psi_1(t - \mu_3\ell - L_2)) \\
 & - \left[ 1 + \frac{\ell}{L_1}(\mu_2 - \mu_3) \right] (\Psi_1(t - \mu_3\ell - L_1 - L_3) - \Psi_1(t - \mu_2\ell - L_3)) \\
 & + \left[ 1 - \frac{\ell}{L_3}(\mu_1 - \mu_2) \right] (\Psi_3(t - \mu_1\ell - L_3 - L_1 - L_2) - \Psi_3(t - \mu_2\ell - L_1 - L_2)) \\
 & - \left[ 1 + \frac{\ell}{L_2}(\mu_3 - \mu_1) \right] (\Psi_2(t - \mu_1\ell - L_2 - L_1 - L_3) - \Psi_2(t - \mu_3\ell - L_1 - L_3))
 \end{aligned} \tag{7.26}$$

A  $\delta$ -function GW,  $\mathbf{h}(t) = \mathbf{H} \delta(t)$ , would produce six pulses in  $\alpha$ , located with relative times depending on the arrival direction of the wave and the detector configuration:  $\mu_1\ell$ ,  $\mu_3\ell + L_2$ ,  $\mu_2\ell + L_3$ ,  $\mu_2\ell + L_1 + L_2$ ,  $\mu_3\ell + L_1 + L_3$ , and  $\mu_1\ell + L_1 + L_2 + L_3$ .

The power spectra of the acceleration and shot noise components of  $\alpha$ , assuming equal and independent individual proof mass acceleration noises, equal and independent shot noises, and the equilateral triangle ( $L_1 = L_2 = L_3 = L$ ) case are:

$$S_\alpha = [8 \sin^2(3\pi fL) + 16 \sin^2(\pi fL)] S_y^{\text{proof mass}} + 6 S_y^{\text{optical path}} \quad (7.27)$$

#### 7.4.4.3 The (P,Q,R), (E,F,G), and (U,V,W) combinations

An interesting and potentially useful subset of laser- and optical-bench-noise-free data combinations involve data taken using only four laser links [120]. These combinations are shown schematically in Figure 7.3; they have obvious utility in the event of selected subsystem failures. The following cancel laser and optical bench noises:

$$\begin{aligned} P &= y_{32,2} - y_{23,3} - y_{12,2} + y_{13,3} + y_{12,13} - y_{13,12} + y_{23,311} - y_{32,211} \\ &\quad + \frac{1}{2}(-z_{21,23} + z_{21,1123} + z_{31,23} - z_{31,1123}) \\ &\quad + \frac{1}{2}(-z_{32,2} + z_{32,112} + z_{12,2} - z_{12,112}) \\ &\quad + \frac{1}{2}(-z_{13,3} + z_{13,113} + z_{23,3} - z_{23,113}) \end{aligned} \quad (7.28)$$

with  $Q$  and  $R$  given by index permutation. The gravitational wave contribution to  $P$  is given by:

$$\begin{aligned} P^{\text{gw}} &= \left[1 - \frac{\ell}{L_3}(\mu_1 - \mu_2)\right] (\Psi_3(t - \mu_1\ell - L_3 - L_2) - \Psi_3(t - \mu_2\ell - L_2)) \\ &\quad - \left[1 + \frac{\ell}{L_2}(\mu_3 - \mu_1)\right] (\Psi_2(t - \mu_1\ell - L_2 - L_3) - \Psi_2(t - \mu_3\ell - L_3)) \\ &\quad - \left[1 + \frac{\ell}{L_1}(\mu_2 - \mu_3)\right] (\Psi_1(t - \mu_3\ell - L_1 - L_2) - \Psi_1(t - \mu_2\ell - L_2)) \\ &\quad + \left[1 - \frac{\ell}{L_1}(\mu_2 - \mu_3)\right] (\Psi_1(t - \mu_2\ell - L_1 - L_3) - \Psi_1(t - \mu_3\ell - L_3)) \\ &\quad + \left[1 + \frac{\ell}{L_1}(\mu_2 - \mu_3)\right] (\Psi_1(t - \mu_3\ell - 2L_1 - L_3) - \Psi_1(t - \mu_2\ell - L_1 - L_3)) \\ &\quad - \left[1 - \frac{\ell}{L_1}(\mu_2 - \mu_3)\right] (\Psi_1(t - \mu_2\ell - 2L_1 - L_2) - \Psi_1(t - \mu_3\ell - L_1 - L_2)) \\ &\quad + \left[1 + \frac{\ell}{L_2}(\mu_3 - \mu_1)\right] (\Psi_2(t - \mu_1\ell - 2L_1 - L_2 - L_3) - \Psi_2(t - \mu_3\ell - 2L_1 - L_3)) \\ &\quad - \left[1 - \frac{\ell}{L_3}(\mu_1 - \mu_2)\right] (\Psi_3(t - \mu_1\ell - 2L_1 - L_2 - L_3) - \Psi_3(t - \mu_2\ell - 2L_1 - L_2)) \end{aligned} \quad (7.29)$$

The proof mass noise contribution is:

$$\begin{aligned} P^{\text{proof mass}} &= \hat{n}_1 \cdot (\vec{v}_{2,2} - 2\vec{v}_{2,13} + \vec{v}_{2,112} + \vec{v}_{3,3}^* - 2\vec{v}_{3,12}^* + \vec{v}_{3,113}^*) \\ &\quad + \hat{n}_2 \cdot (-\vec{v}_{1,23}^* + \vec{v}_{1,1123}^* + \vec{v}_{3,3} - \vec{v}_{3,311}) \\ &\quad + \hat{n}_3 \cdot (-\vec{v}_{1,23} + \vec{v}_{1,1123} + \vec{v}_{2,2}^* - \vec{v}_{2,112}^*) \end{aligned} \quad (7.30)$$

The power spectra of the acceleration and shot noise components of  $P$ , assuming equal and independent individual proof mass acceleration noises and equal and independent shot noises, are:

$$\begin{aligned} S_P = & [8 \sin^2(2\pi fL) + 32 \sin^2(\pi fL)] S_y^{\text{proof mass}} \\ & + [8 \sin^2(2\pi fL) + 8 \sin^2(\pi fL)] S_y^{\text{optical path}} \end{aligned} \quad (7.31)$$

The “monitor” combination  $E$  is illustrated in Figure 7.3.  $E$  equals  $\alpha - \zeta_1$  and is, explicitly:

$$\begin{aligned} E = & y_{12,21} - y_{13,31} - y_{12,3} + y_{13,2} + y_{31,11} - y_{21,11} - y_{31} + y_{21} \\ & - \frac{1}{2} (z_{13,2} + z_{21} + z_{32,3} - z_{13,112} + z_{23,112} - z_{32,113}) \\ & + \frac{1}{2} (z_{23,2} + z_{31} + z_{12,3} - z_{12,113} + z_{21,11} - z_{31,11}) \end{aligned} \quad (7.32)$$

As before, the shot noise enters only in the  $y_{ij}$ . The power spectra of the acceleration and shot noise components of  $E$ , assuming independent individual proof mass acceleration noises and independent shot noises, and for the equilateral triangle case are:

$$\begin{aligned} S_E = & [32 \sin^2(\pi fL) + 8 \sin^2(2\pi fL)] S_y^{\text{proof mass}} \\ & + [8 \sin^2(\pi fL) + 8 \sin^2(2\pi fL)] S_y^{\text{optical path}} \end{aligned} \quad (7.33)$$

Combinations  $F$  and  $G$  are obtained from cyclic permutation of the indices in the above equations.

The “relay” combination  $U$  is illustrated in Figure 7.3.  $U$  is  $\gamma_1 - \beta$ :

$$\begin{aligned} U = & y_{21,113} - y_{21,3} - y_{12,123} + y_{13,1} - y_{13,23} + y_{32,11} - y_{32} + y_{12} \\ & - \frac{1}{2} (z_{31,3} + z_{12} + z_{23,23} + z_{32,11} + z_{13,1123} + z_{21,113}) \\ & + \frac{1}{2} (z_{21,3} + z_{32} + z_{13,23} + z_{12,11} + z_{23,1123} + z_{31,113}) \end{aligned} \quad (7.34)$$

The power spectra of acceleration and shot noise components of  $U$  (with independent individual proof mass and shot noises and for the equilateral triangle case) is:

$$\begin{aligned} S_U = & [16 \sin^2(\pi fL) + 8 \sin^2(2\pi fL) + 16 \sin^2(3\pi fL)] S_y^{\text{proof mass}} \\ & + [4 \sin^2(\pi fL) + 8 \sin^2(2\pi fL) + 4 \sin^2(3\pi fL)] S_y^{\text{optical path}} \end{aligned} \quad (7.35)$$

The combinations  $V$  and  $W$  are derived from the above, as usual, via index permutation.

#### 7.4.4.4 Long-wavelength limits

Although [LISA](#) will not operate exclusively in the long-wavelength limit, [LWL](#), analytical results are obviously very useful. In the [LWL](#), the gravitational wave can be expanded in terms of spatial derivatives, e.g.

$$\mathbf{h}(t - \mu_2 \ell - L_3) = \mathbf{h}(t) - (\mu_2 \ell + L_3) \mathbf{h}'(t) + (1/2)(\mu_2 \ell + L_3)^2 \mathbf{h}''(t) + \dots$$

The  $y_{ij}^{\text{gw}}$  are of order  $\mathbf{h}'$ , while  $\alpha$ ,  $\beta$ ,  $\gamma$ ,  $\zeta$ ,  $X$ ,  $Y$ ,  $Z$ ,  $P$ ,  $Q$ , and  $R$  are of order  $\mathbf{h}''$ . The long wavelength expansions for many combinations are given explicitly by [\[121\]](#).

### 7.4.5 Gravitational wave sensitivities

This section describes the sensitivity computations of alternative *LISA* configurations. The conventional *LISA* sensitivity criterion (strength of a sinusoidal GW required to achieve  $\text{SNR} = 5$  in a one-year integration time as a function of Fourier frequency) is assumed. To compute the sensitivity, both the signal and noise responses are required.

The GW signal response of the noise-cancelling combinations is described in [121] and [120]. Those references give curves of the GW signal response for various noise-canceling combinations, averaged over the celestial sphere and over general elliptical polarization state. A nominal *LISA* configuration (equilateral triangle with  $L_1 = L_2 = L_3 = 10\sqrt{3}$  light seconds) is assumed in the plots.

To compute the noise spectra of the data combinations  $X$ ,  $\alpha$ ,  $\zeta$ , etc., the shot noise spectrum (aggregated here as the true shot noise plus all other optical path noise) for an individual laser link is taken to be  $20 \times 10^{-12} \text{ m}/\sqrt{\text{Hz}}$  [1]. In terms of the one-sided spectrum of fractional frequency fluctuations,  $y_{ij}$ , this becomes:  $S_y^{\text{shot}} = 5.3 \times 10^{-38} [f/1 \text{ Hz}]^2 \text{ Hz}^{-1}$ . Acceleration noise for an individual proof mass is currently expected [1, Table 4.2] to be  $3 \times 10^{-15} \text{ m sec}^{-2}/\sqrt{\text{Hz}}$ , which is equivalent to:  $S_y^{\text{proof mass}} = 2.5 \times 10^{-48} [f/1 \text{ Hz}]^{-2} \text{ Hz}^{-1}$ . The frequency-domain transfer functions of these noises to the noise-canceling observables ( $X$ ,  $\alpha$ , etc.) were given above and the aggregate noise spectra are plotted in Figure 7.4 for several combinations.

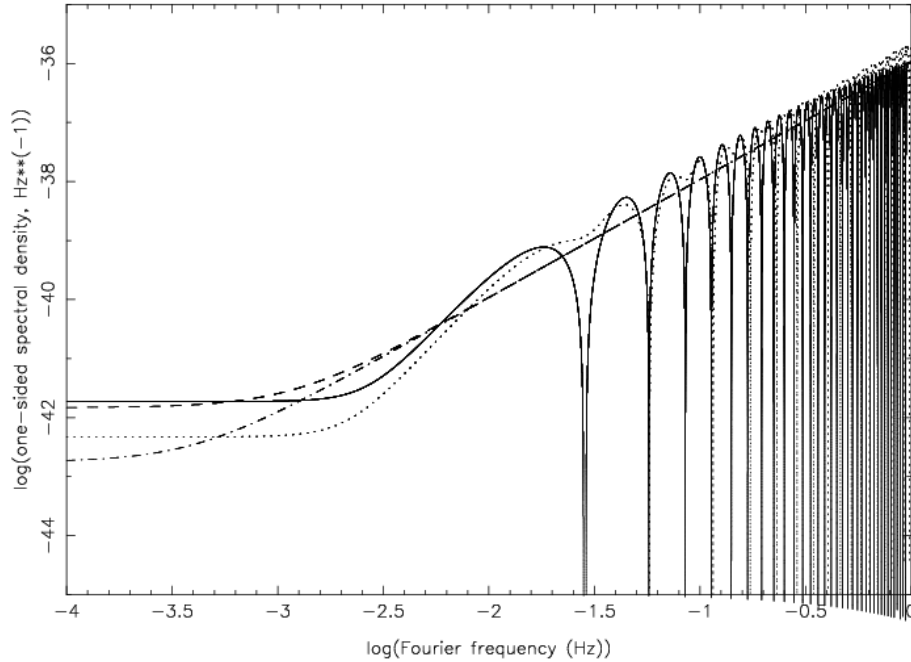


**Figure 7.4** Noise spectra for  $\alpha$  (dashed),  $\zeta$  (dotted-dashed),  $X$  (full), and  $P$  (dotted) using the raw spectra of shot and acceleration noise expected for *LISA* combined with the noise response functions, for  $L_1 = L_2 = L_3 = 10\sqrt{3}$  light seconds.

GW sensitivity is computed as:  $5 \sqrt{S_i(f) B} / G_j^{\text{GW}}$ , where  $G_j^{\text{GW}}$  is the *rms* gravitational wave response for data combination  $j$ , i.e. for  $\alpha$ ,  $\zeta$ ,  $X$ ,  $P$ , etc. The bandwidth,  $B$ , was taken to be  $3.17 \times 10^{-8} \text{ Hz}$  (i.e., one cycle/year). The factor of 5 is for  $\text{SNR} = 5$  in a one-year integration. Figure 7.5 shows the GW sensitivity for  $X$ , assuming  $L_1 = L_2 = L_3 = 10\sqrt{3}$  light seconds. Figures 7.6 to 7.9 show the sensitivity for  $\alpha$ ,  $\zeta$ ,  $E$ ,  $P$ , and  $U$  under the same noise assumptions.

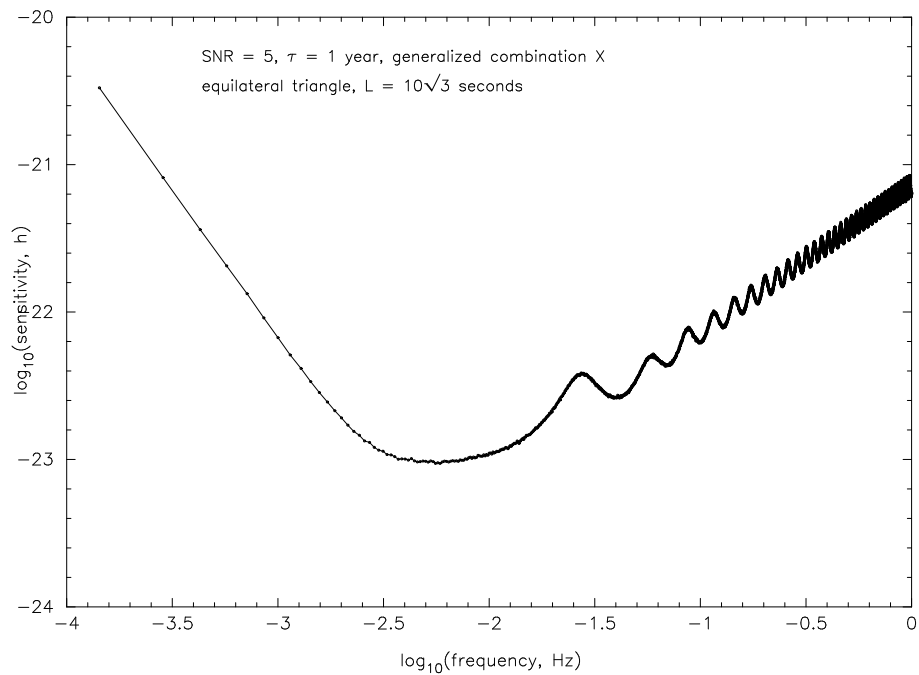


**Figure 7.5** Sensitivity plot for the unequal-arm Michelson combination,  $X$ . Arm lengths:  $L_1 = L_2 = L_3 = 10\sqrt{3}$  light seconds.

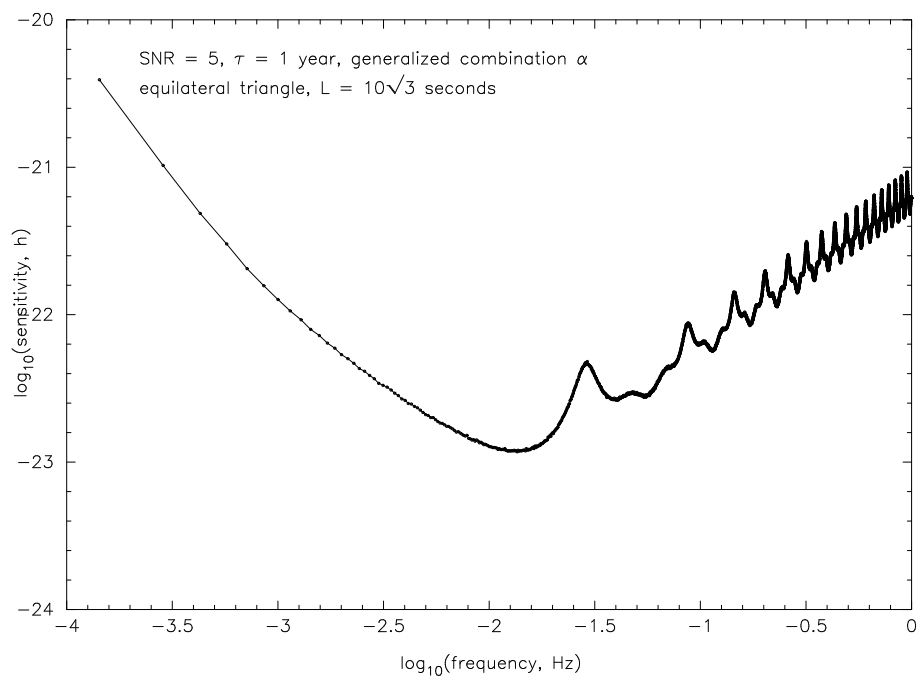


**Figure 7.6** As Figure 7.5, but for  $\alpha$ .



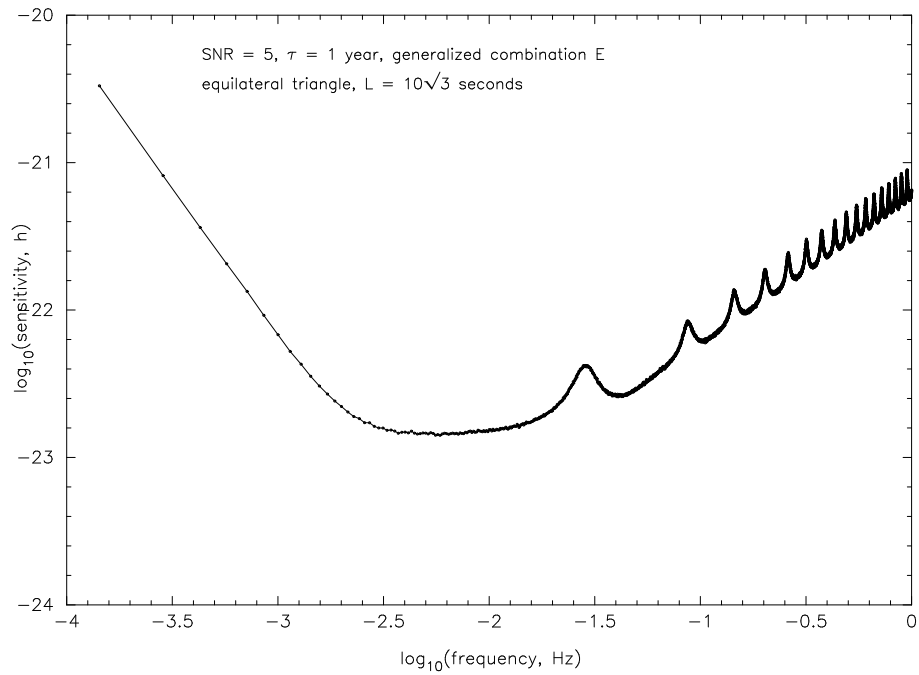


**Figure 7.7** As Figure 7.5, but for *E*.

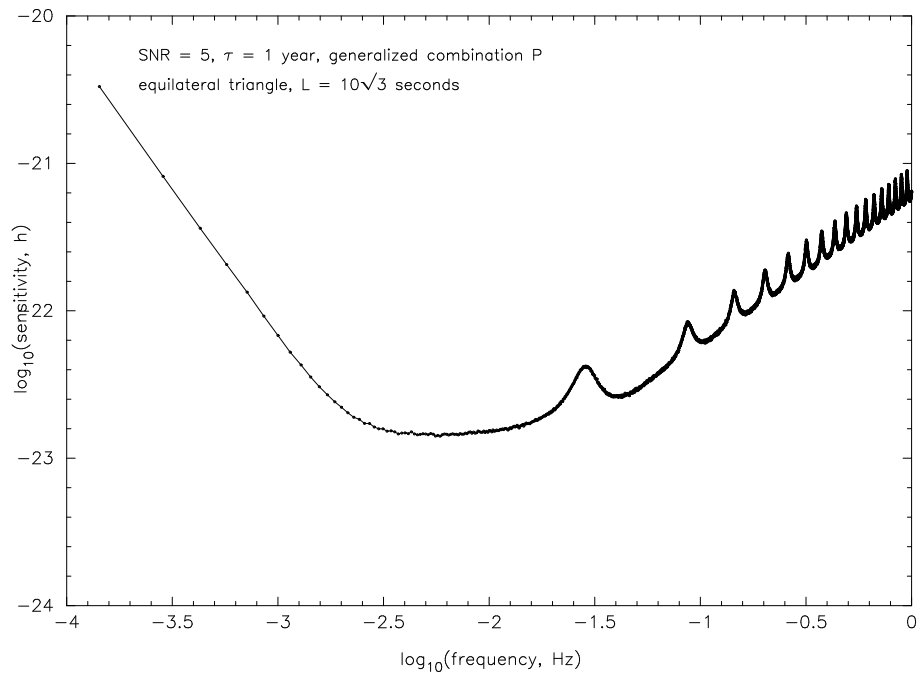


**Figure 7.8** As Figure 7.5, but for *P*.

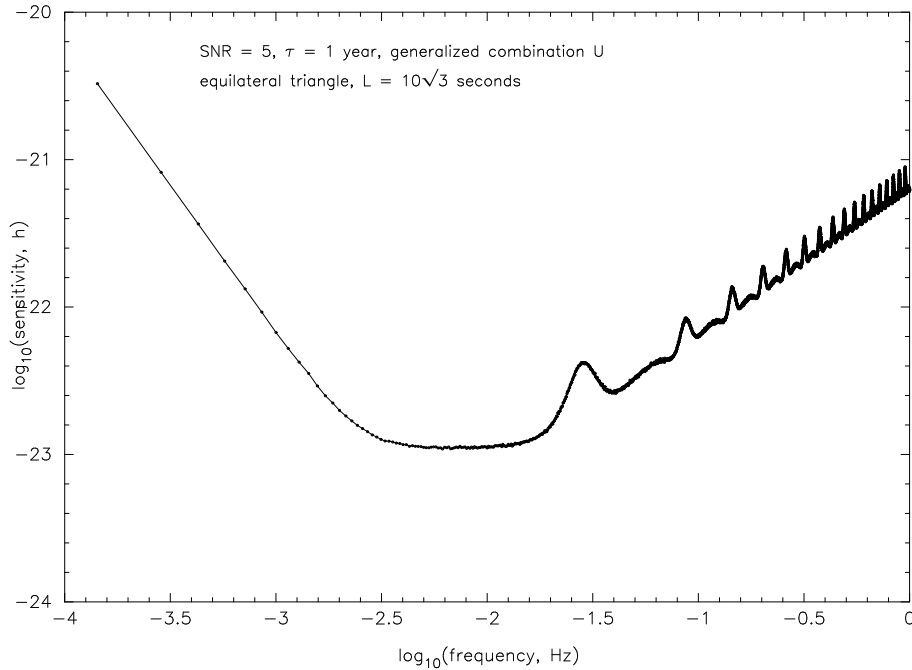


**Figure 7.9** As Figure 7.5, but for  $U$ .

## 7.5 Data analysis

The objective on data analysis for a gravitational wave detector is to reconstruct as far as possible the incoming gravitational wave. From the reconstruction, it is possible to make the kind of inferences about sources that we have described in Chapter 1. The parameters that describe the wave are:

- Its direction on the sky in, say, galactic coordinates  $(\ell, b)$ . These are constants that must be maintained during the observation. Proper motion and parallax are unlikely because the observations of Galactic objects are unlikely to attain better than a few arcminutes directional accuracy. (A stochastic background will not have a precise direction, but that caused by binaries may be anisotropic on the scale of tens of degrees.)
- Its amplitude and polarisation, or alternatively the amplitudes of two independent components  $h_+$  and  $h_\times$ , and their relative phase. For most *LISA* sources, these are constant in time, or at least very slowly varying. Binary orbital precession will cause an intrinsic amplitude modulation of the signal. As *LISA* orbits the Sun, the projection of the wave on the detector will change, which also causes an apparent amplitude modulation, even if the intrinsic amplitude and polarisation of the signal remain constant.
- Signal phase  $\Phi(t)$ . Gravitational wave detectors are coherent detectors, because their operating frequencies are low enough to allow them to track the phase of the signal. The phase, as a function of time, contains interesting information if it is not regular: binaries that chirp, or even coalesce, provide important clues to their masses and distances in the phase function, and the phase function of a black-hole binary allows *LISA* to track the orbit to test general relativity.

The extraction of this information from the *LISA* data will use the same principles that have been developed for ground-based interferometers. But there are a number of important differences

from ground-based instruments:

- *LISA*'s data rate will be  $10^3$  times less than that from a ground-based detector, because *LISA* operates at much lower frequencies. The massive data-handling problems faced by ground-based interferometers [125] will not exist for *LISA*. All its data for one year will fit on a single disc, and the computational demands of the analysis are modest. In this section we will assume that the signal stream from *LISA* will consist of two 2-byte data samples per second. The actual data stream may be sampled more rapidly, but there is no useful gravitational wave signal data above 1 Hz, so the data stream will be anti-alias filtered and resampled at the Nyquist rate of 2 Hz.
- *LISA*'s 3 arms form 2 independent detectors, in the sense that they record two independent components of the incoming gravitational wave. Ground-based detectors will also operate in groups of 2 or more for joint detection, but signal reconstruction and direction finding are very different, because the detectors are well-separated. *LISA* can, in the unfortunate event of the failure of one spacecraft, still reliably detect gravitational waves even operating as a single detector. This is possible because of the next important difference.
- *LISA* observes primarily long-lived sources, while ground-based detectors are expected to observe mainly bursts that are so short that frequency modulation is unimportant. *LISA* is able to find directions and polarisations primarily from the phase- and amplitude-modulation produced by its motion during an observation. Ground-based detectors will, of course, look for radiation from rotating neutron stars, and for this case the detection and signal reconstruction problem are similar to that for *LISA*, but *LISA*'s lower data rate and lower frequency makes the analysis considerably easier.
- If *LISA* sees a gravitational wave background, it cannot identify it by cross-correlation with another independent detector. We will show in Section 7.5.5 below how *LISA* can discriminate one background from another and from instrumental noise.

In what follows we will consider in turn the methods used for data analysis and the expected manner and accuracy of extraction of the different kinds of information present in the signal.

## 7.5.1 Data reduction and filtering

### 7.5.1.1 Noise

The fundamental principle guiding the analysis of *LISA* data is that of *matched filtering*. Assuming that the *LISA* detector noise  $n(t)$  is stationary (an assumption that is only a first approximation, but which will have to be tested), the noise power can be characterised by its spectral density, defined as

$$\mathcal{S}_h(f) = \int_{-\infty}^{\infty} \langle n(t)n(t+\tau) \rangle e^{-2\pi i f \tau} d\tau, \quad (7.36)$$

where the autocorrelation of the noise  $\langle n(t)n(t+\tau) \rangle$  depends only on the offset time  $\tau$  because the noise is stationary. The subscript “ $h$ ” on  $\mathcal{S}_h$  refers to the gravitational wave amplitude, and it means that the detector output is assumed normalised and calibrated so that it reads directly the apparent gravitational wave amplitude.

So far we have not assumed anything about its statistics, the probability density function (PDF) of the noise. It is conventional to assume it is Gaussian, since it is usually composed of several influences, and the central limit theorem suggests that it will tend to a Gaussian distribution. However, it can happen that at some frequencies the noise is dominated by a single influence, and

then it can be markedly non-Gaussian. This has been seen in ground-based interferometers. An important design goal of *LISA* will be to ensure that the noise is mainly Gaussian, and during the analysis the characterisation of the noise statistics will be an important early step.

### 7.5.1.2 Maximum likelihood and the matched filter

The most common way of assessing whether a signal of some expected form is present in a data stream is to use the *maximum likelihood criterion*, which is that one uses as the detection statistic the ratio of the probability that the given data would be observed if the signal were present to the probability that it would be observed if the signal were absent. This ratio has a *PDF* that depends on the *PDF* of the noise.

If the noise is Gaussian, then it can be shown that an equivalent statistic is the output of the *matched filter*. The prescription is as follows. Suppose one is searching for a signal of known form  $s(t)$ , with Fourier transform  $\tilde{s}(f)$ . Then the matched filter for this signal is a function  $q(t)$  whose transform is

$$\tilde{q}(f) = \frac{\tilde{s}(f)}{\mathcal{S}_h(f)}. \quad (7.37)$$

This equation shows that the filter is the signal weighted inversely by the noise *power*. This weighting cuts out frequency ranges that have excessive noise. The filter's output is simply the linear product of the filter with the data stream  $x(t)$

$$c = \int_{-\infty}^{\infty} x(t)q(t)dt = \int_{-\infty}^{\infty} \tilde{x}(f) \tilde{q}^*(f) df. \quad (7.38)$$

For Gaussian noise the statistic  $c$  has a Gaussian *PDF*, so rare signals can be recognised at any desired confidence level by observing the standard deviation of  $c$  when the filter is applied to many data sets, and applying an appropriate decision threshold. Because this is the equivalent of the maximum likelihood criterion, the matched filter is the best linear filter that one can use to recognise signals of an expected form.

### 7.5.1.3 Detection in a continuous stream

In practice we don't know when to expect the signal  $s$ , so its filter must contain a time-of-arrival parameter  $\tau$ : the filter must be made from the transform of  $s(t - \tau)$  for an arbitrary  $\tau$ . Using the shift theorem for Fourier transforms gives us the statistic that we expect to use in most cases,

$$c(\tau) = \int_{-\infty}^{\infty} \tilde{x}(f) \tilde{q}^*(f) e^{2\pi i f \tau} df = \int_{-\infty}^{\infty} \frac{\tilde{x}(f) \tilde{s}^*(f)}{\mathcal{S}_h(f)} e^{2\pi i f \tau} df. \quad (7.39)$$

This last form is simply an inverse Fourier transform. For data sets of the size of *LISA*'s it will be efficient and fast to evaluate it using the *FFT* algorithm.

One recognises a rare signal in the data set by identifying times  $\tau$  at which the statistic  $c(\tau)$  exceeds a predetermined threshold confidence level. Of course, one must be confident that the detector was operating correctly while the data were being gathered, and this usually requires examining "housekeeping" or diagnostic data. If the data pass this test, then one has not only identified a signal  $s(t)$  but also the fiducial time  $\tau$  associated with it. The confidence level is set on the basis of the empirical *PDF* of the statistic  $c(\tau)$  at times when no signal appears to be present.

### 7.5.1.4 Parameters

Of course, predicted signals are actually families whose members are parametrized in some way. Black-hole binaries emit waveforms that depend on the masses and spins of the two holes. Galactic binaries that do not chirp have a unique frequency (in the Solar barycentric frame). All discrete sources have a location on the sky, a polarisation, an amplitude, and a phase at the fiducial time  $\tau$ . One has to construct families of filters to cover all possible parameter values. The usual covariance analysis allows us to estimate the likely errors in the determination of parameters, and this is the basis of the estimates made below of angular accuracy, polarisation, and so on.

Filtering for families of expected signals raises the possibility that the family could be so large that the computational demands would be severe. This is certainly the case for ground-based detectors, where an all-sky all-frequency search for unknown rotating neutron stars in data sets of order one year in length will require a teraflop computer to carry out to the sensitivity limit of the detectors. But in the low-frequency range of *LISA*, the demands are considerably reduced. One year of data might occupy 250 MB of storage. Given what is today an easily achieved computing speed of 1 Gflop and a memory of 512 MB, a computer could perform a Fourier transform (the basis of the matched filter) in a time of order one second. Searching up to  $10^4$  error boxes on the sky for binaries, or  $10^4$  different chirp masses between  $1 M_\odot$  and  $10^8 M_\odot$  for coalescing binary systems, could be done in a day. By the time *LISA* is launched these will be even easier to do.

What is not trivial is searching for neutron stars and black holes falling into massive black holes. Here the parameter space is considerably larger, since even in a few orbits the signal can be dramatically affected by the spins of the objects and the amount of eccentricity of the orbit. Work is underway to estimate the computational demands of this problem, but we are confident that, by the time *LISA* is launched, even this filtering will not be very difficult.

### 7.5.1.5 Other signals

The *LISA* data will also be searched for unexpected signals. By definition, one cannot construct a matched filter for these. Instead, one implements a robust filter that responds to a wide range of signals of a given type. Candidates for these “discovery” filters are wavelets, fractional Fourier transforms, and nonlinear techniques like adaptive filters. These will be developed and proved intensively on the ground-based detectors, and *LISA* will benefit from that insight.

One source that is different from others is a possible random background of gravitational waves. This appears as an extra component of the noise  $\mathcal{S}_h$ . We will consider how to recognise it and determine its origin in Section 7.5.5 below.

## 7.5.2 Angular resolution

### 7.5.2.1 Introduction

The *LISA* mission consists of 3 spacecraft forming a laser interferometric antenna in a plane inclined  $60^\circ$  with respect to the ecliptic, the complete constellation describing an Earth-like orbit at a distance of  $R = 1 \text{ AU}$  from the sun and trailing the earth in its orbit by  $20^\circ$  [126]. One spacecraft is placed at each corner of an equilateral triangle with baselines of  $5 \times 10^9 \text{ m}$ , as was sketched in Figure 3.1.

As the *LISA* configuration orbits around the Sun, it appears to rotate clockwise around its center, as viewed from the Sun, with a period of one year. This is indicated in Figure 7.10. As a

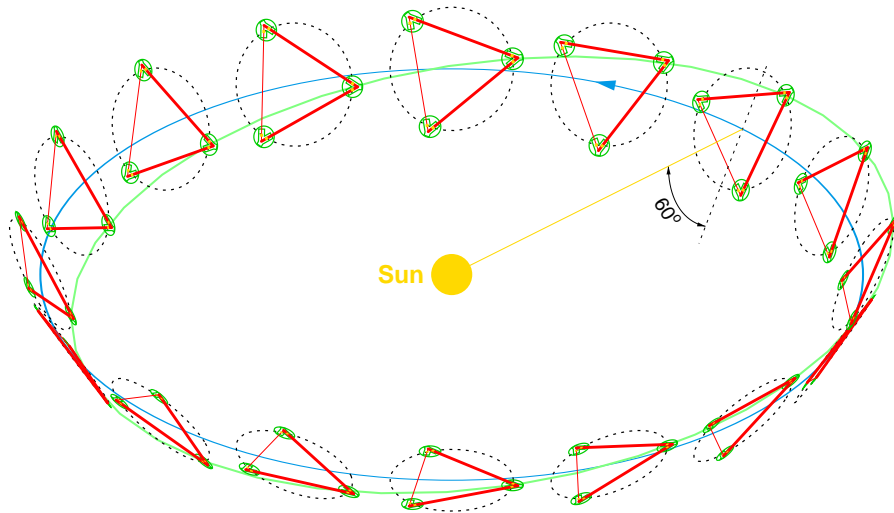


**Figure 7.10** Annual revolution of *LISA* configuration around the Sun, describing a cone with  $60^\circ$  half opening angle. One selected 2-arm interferometer is highlighted by heavier interconnecting laser beams. The “tumbling” motion of a single *LISA* interferometer allows the determination of the position of the source as well as of the polarisation of the wave. The green trajectory of one individual spacecraft is shown, inclined with respect to the blue Earth orbit.

nonmoving detector would reveal no information about the directional parameters of the source of the gravitational wave, all the information about the source parameters is contained in the variation of the detector response that results from *LISA*’s orbital motion.

Firstly, the detector’s sensitivity pattern is not isotropic; rather it projects a quadrupolar beam pattern onto the sky, which rotates with the detector. This rotating beam pattern modulates both the amplitude and phase of the measured waveform.

Secondly, the detector is moving relative to the source due to the periodic motion of its center around the Sun. This Doppler-shifting of the measured gravitational wave frequency of the results in a further phase modulation of the detector output. Both the beam-pattern modulation and Doppler modulation will spread a sharply peaked monochromatic signal into a set of sidebands separated from the carrier at integer multiples of the fundamental frequency  $(1 \text{ year})^{-1}$ . It is easy to see that the effects of the beam-pattern modulation and Doppler modulation are of roughly the same size. Consider a monochromatic signal with frequency  $f_0$ . In Fourier space, the effect of the beam-pattern modulation is to spread the measured power over (roughly) a range  $f_0 \pm 2/T$ , where  $T$  is one year. (The factor of 2 arises because the beam pattern is quadrupolar.) The effect of the periodic Doppler shift coming from the detector’s center-of-mass motion is to spread the power over a range  $f_0(1 \pm v/c)$ , where  $v/c \sim 10^{-4}$ . These two effects are therefore of roughly equal size at  $f_0 \sim 10^{-3} \text{ Hz}$ , which is near the center of the *LISA* band; beam-pattern modulation is more significant at lower frequencies and Doppler modulation is more significant at higher frequencies.

In the following chapters we review the way the source position, polarisation and intrinsic amplitude are encoded in the *LISA* datastream. After reviewing some standard methods of parameter estimation, we then present results on how accurately these physical parameters can be determined for two *LISA* sources of particular interest: stellar-mass binaries and merging MBH binaries. We refer the reader to [127, 128] for more details.

### 7.5.2.2 The beam-pattern modulation

The beam-pattern modulation can be calculated by transforming the metric-tensors

$$\mathbf{h}_\times := h_\times \begin{pmatrix} 0 & 1 & 0 \\ 1 & 0 & 0 \\ 0 & 0 & 0 \end{pmatrix} \quad \text{and} \quad \mathbf{h}_+ := h_+ \begin{pmatrix} 1 & 0 & 0 \\ 0 & -1 & 0 \\ 0 & 0 & 0 \end{pmatrix} \quad (7.40)$$

that are defined in the source frame, i.e. a system with its x-axis in the x-y-plane of the barycentric frame, its z-axis pointing towards the sun and the source at its origin. The transformation is split into one transforming the source system into the barycentric system and another one from the barycentric frame into the detector frame, which is rigidly fixed to the interferometer arms.

Let  $\vartheta$  and  $\varphi$  be the Euler angles that define the source position in the barycentric frame, with its x-y-plane in the ecliptic, as indicated in Figure 7.11.

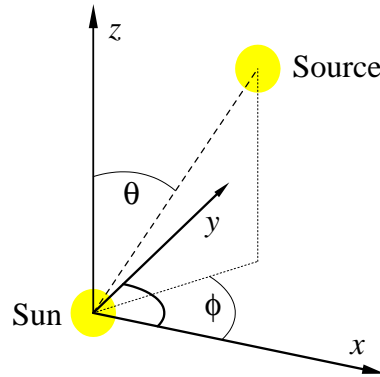


**Figure 7.11** Orientation of the source in the barycentric frame.

The transformation into the source system is composed of two rotations. The first, realized by the rotation matrix  $\mathbf{a}_1$ , turns the y-axis of the barycentric frame on the projection of the line connecting sun and source on the ecliptic, that is counterclockwise through an angle  $\varphi - 90^\circ$  around the z-axis,

$$\mathbf{a}_1 := \begin{pmatrix} \sin \varphi & -\cos \varphi & 0 \\ \cos \varphi & \sin \varphi & 0 \\ 0 & 0 & 1 \end{pmatrix}. \quad (7.41)$$

A second rotation  $\mathbf{b}_1$  turns the system counterclockwise around the new x-axis by  $180^\circ - \vartheta$ . With  $\mathbf{T}_1 := \mathbf{b}_1 \mathbf{a}_1$  the matrix  $\mathbf{h}_+$  of Eq. (7.40) is transformed from the source system into the barycentric frame by

$$\mathbf{h}_+ \rightarrow \mathbf{T}_1^t \mathbf{h}_+ \mathbf{T}_1. \quad (7.42)$$

The following angles are used to calculate the transformation into the detector system :

$$\psi_a := 2 \frac{\pi t}{T} \quad \psi_b := \frac{1}{3} \pi \quad \psi_c := -2 \frac{\pi t}{T} + \alpha \quad (7.43)$$

where  $\frac{1}{3} \pi$  is the angle of LISA with respect to the ecliptic and  $\alpha$  is the phase between LISA's motion around the sun and the motion around its center of mass.

Now a rotation matrix  $\mathbf{a}_2$  turns the frame of reference in the barycentric system counterclockwise around the z-axis by  $\psi_a$ , so the new y-axis points towards [LISA](#). Then  $\mathbf{b}_2$  turns it by  $\psi_b$  out of the ecliptic. Finally  $\mathbf{c}_2$  turns it clockwise around the new z-axis by  $\psi_c$ . A vector is transformed from the barycentric into the detector system by  $\mathbf{T}_2 = \mathbf{c}_2 \mathbf{b}_2 \mathbf{a}_2$ . Therefore e.g. the matrix  $\mathbf{h}_+$  is transformed as :

$$\mathbf{h}_+ \rightarrow \underbrace{\mathbf{T}_2 \mathbf{T}_1^t}_{=:\mathbf{T}} \mathbf{h}_+ \mathbf{T}_1 \mathbf{T}_2^t. \quad (7.44)$$

### 7.5.2.3 The Doppler modulation

The translational motion of the detector relative to the source leads to a phase modulation of the measured gravitational wave signal. This modulation can easily be calculated with the so-called barycentric transform between time of arrival at the Solar System and time at the detector [[129](#)]. In the former system, which can be considered to be a convenient inertial frame, the signal is not modulated and therefore of fixed frequency. Let  $s_d$  and  $s_b$  be the signals at the detector and at the barycenter, respectively; then by definition

$$s_d(t_d) = s_b(t_b[t_d, \vartheta, \varphi]), \quad (7.45)$$

where  $(\vartheta, \varphi)$  is the angular position of the source (see [Figure 7.11](#)). The relation between the two time variables  $t_b, t_d$  is given by

$$t_b[t_d, \vartheta, \varphi] = t_d + \frac{\vec{n}(\vartheta, \varphi) \vec{d}(t_d)}{c}, \quad (7.46)$$

with  $\vec{n}$  being a unit vector pointing towards the source and  $\vec{d}$  a vector connecting [LISA](#) and the sun:

$$\vec{n} = \begin{pmatrix} \cos \varphi \sin \vartheta \\ \sin \varphi \sin \vartheta \\ \cos \vartheta \end{pmatrix} \quad \vec{d} = R \begin{pmatrix} \cos \frac{2\pi t}{T} \\ \sin \frac{2\pi t}{T} \\ 0 \end{pmatrix}. \quad (7.47)$$

Therefore the relation between the two signals  $s_d$  and  $s_b$  as functions of time is

$$s_d(t_d) = s_b \left( t_d + \frac{R \sin \vartheta}{c} \cos \left( \frac{2\pi t}{T} - \varphi \right) \right). \quad (7.48)$$

So if the signal in the inertial frame is pure sinusoidal of frequency  $f_{\text{GW}}$ , in the detector response it appears as

$$\begin{aligned} s_d(t_d) &= \sin(2\pi f_{\text{GW}} t_b) \\ &= \sin \left( 2\pi f_{\text{GW}} t_d + \underbrace{\frac{2\pi f_{\text{GW}} R \sin \vartheta}{c} \cos \left( \frac{2\pi t}{T} - \varphi \right)}_{\Phi(t)} \right), \end{aligned} \quad (7.49)$$

including a phase modulation  $\Phi(t)$  with a modulation index  $m$  of :

$$\begin{aligned} m &= \frac{2\pi f_{\text{GW}} R \sin \vartheta}{c} \\ &\approx \pi \sin \vartheta \left( \frac{f_{\text{GW}}}{1 \text{ MHz}} \right). \end{aligned} \quad (7.50)$$



### 7.5.2.4 The **LISA** response to a gravitational wave

A gravitational wave which is purely sinusoidal in the barycentric frame causes a detector response given by :

$$\mathbf{H} = \mathbf{T} \begin{pmatrix} 0 & 0 & 0 & 0 \\ 0 & h_+ & h_\times & 0 \\ 0 & h_\times & -h_+ & 0 \\ 0 & 0 & 0 & 0 \end{pmatrix} \mathbf{T}^t \exp \{i[2\pi f_{\text{GW}}t + \Phi(t)]\}, \quad (7.51)$$

with the phase modulation  $\Phi(t)$  as given in Eq. (7.49) and the modulated amplitude  $\mathbf{T}(\mathbf{h}_+ + \mathbf{h}_\times)\mathbf{T}^t$  (cf. Eq. 7.44). To see how the gravitational-wave detector works, recall that General Relativity predicts that a ray of light connects a set of points by an interval of zero or

$$ds^2 = 0. \quad (7.52)$$

For simplicity, let us consider first one arm of the the detector, which we take to lie in first quadrant of the x-y plane, at an angle  $\alpha$  to the x-axis. The above equation then becomes

$$\begin{aligned} 0 &= ds^2 \\ &= g_{\mu\nu} dx^\mu dx^\nu \\ &= -c^2 dt^2 + (1 + H_{xx}(t, \vec{x})) dx^2 + (1 + H_{yy}(t, \vec{x})) dy^2 + H_{xy}(t, \vec{x}) dx dy \\ &\quad + H_{yx}(t, \vec{x}) dy dx \\ &= -c^2 dt^2 + [(1 + H_{xx}(s)) \cos^2 \alpha + (1 + H_{yy}(s)) \sin^2 \alpha \\ &\quad + (H_{xy}(s) + H_{yx}(s)) \sin \alpha \cos \alpha] ds^2, \end{aligned} \quad (7.53)$$

where  $ds \equiv \sqrt{dx^2 + dy^2}$ . In the standard deDonder gauge in which we are working, the freely falling masses at the two ends of the arm maintain fixed coordinate locations  $(x, y, z)$ . Thus the light travel time  $\tau$  between the two ends is determined by

$$c \int_0^\tau dt = \int_0^L \sqrt{1 + H_{xx}(s) \cos^2 \alpha + H_{yy}(s) \sin^2 \alpha + \frac{1}{2} (H_{xy}(s) + H_{yx}(s)) \sin 2\alpha} ds. \quad (7.54)$$

Equivalently, we can say the arm length has changed by an amount  $\delta L$  given by (treating the metric perturbation as approximately constant during the trip, and expanding the square root):

$$\delta L = \frac{1}{2} L [H_{xx} \cos^2 \alpha + H_{yy} \sin^2 \alpha + H_{xy} \sin(2\alpha)]. \quad (7.55)$$

**LISA** is designed to measure the *difference* in the arm length changes,  $\delta(L_1 - L_2)$ . Actually, since there are three arms, **LISA** can measure two independent differences. We shall refer to the combination  $L_1 - L_2$  as interferometer I, and to the combination  $(L_1 + L_2 - 2L_3)/\sqrt{3}$  as interferometer II. For simplicity, we let  $L_1$  make a  $15^\circ$  angle to the x-axis, while  $L_2$  makes a  $75^\circ$  angle (i.e.,  $\alpha = \pi/12$  and  $5\pi/12$  for  $L_1$  and  $L_2$ , respectively).

From Eq. (7.55) one easily shows that the strains associated with these particular combinations are

$$\begin{aligned} h_{\text{I}} &= \frac{\sqrt{3}}{4} (H_{xx} - H_{yy}), \\ h_{\text{II}} &= \frac{\sqrt{3}}{4} (H_{xy} + H_{yx}). \end{aligned} \quad (7.56)$$

Thus  $h_I$  and  $h_{II}$  directly measure the  $+$  and  $\times$ -polarisation components of a wave travelling perpendicularly to the plane of the detector. One can therefore think of LISA as operating effectively like a pair of two-arm interferometers that measure orthogonal polarisations.

How is the noise in interferometer I correlated with that in interferometer II? This has not yet been analyzed in detail. However one can show that if the detector noise in the three individual arms is totally symmetric (so that all three arms have the same rms noise amplitude, and the correlation between any pair of arms is also the same), then the noise correlations between interferometers I and II exactly cancel out; they can be regarded as statistically independent detectors [128]. As a first approximation, then, we treat the noises in interferometers I and II as uncorrelated. It seems unlikely that a small correlation between them would significantly affect the results presented below.

A signal that is intrinsically monochromatic will be spread into a set of sidebands by the motion of the detector. The modulation contains all the information about the source position. This is illustrated in Figures 7.12 and 7.13, which show line spectra for one year of integration, for two different source locations. The frequency of the gravitational wave is 3 mHz and the dimensionless amplitude  $h_+$  equals one; the output of interferometer I is shown.

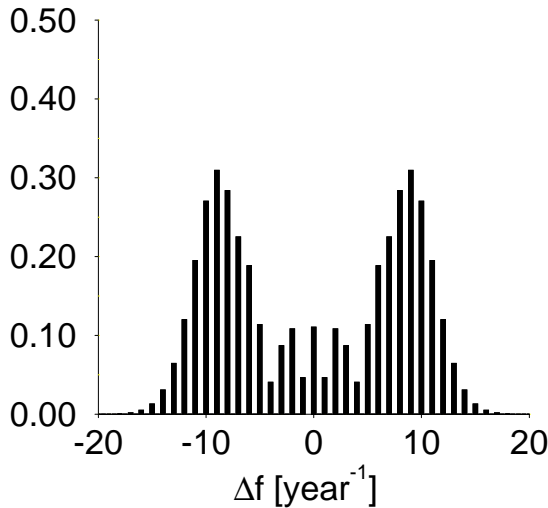


Figure 7.12 Source at  $\vartheta = \frac{\pi}{2}$ ,  $\varphi = 0$ .

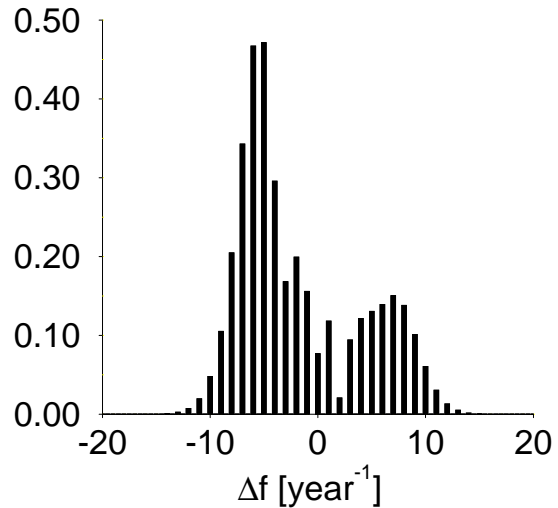


Figure 7.13 Source at  $\vartheta = \frac{\pi}{4}$ ,  $\varphi = 0$ .

### 7.5.2.5 Review of parameter estimation

The problem of measurement is to determine the values of some or all parameters of the signal [130]. It will be shown how accurately that can be done. In this section for simplicity we will consider a single datastream produced by a single interferometer (e.g., interferometer I); the generalization to a pair of outputs I and II is straightforward.

Consider a stream  $s(t)$  that represents the pure detector output  $h(\vec{\mu})$ , parametrized by several unknown parameters  $\mu_i$  collectively denoted as  $\vec{\mu} = (\mu_1 = \vartheta, \mu_2 = \varphi, \dots)$  plus additional noise  $n(t)$ . Now one has to find a probability density function  $\mathcal{P}(\vec{\mu}, s)$  for the parametrization  $\vec{\mu}$  that characterizes the detector output  $h(\vec{\mu})$ . Assuming that  $n(t)$  is a Gaussian process with zero mean, characterized by the one-sided power spectral density  $\mathcal{S}_n(f)$ , it can be shown [131] that

$$\mathcal{P}(\vec{\mu}, s) \sim \exp \langle s, h(\vec{\mu}) \rangle, \quad (7.57)$$

where the symmetric inner product is defined as

$$\langle s, h \rangle = 2 \int_0^\infty \frac{\tilde{s}(f) \tilde{h}^*(f) + \tilde{h}(f) \tilde{s}^*(f)}{\mathcal{S}_h(f)} df. \quad (7.58)$$

From that definition it follows that, for a waveform  $h(\vec{\mu})$ , the signal-to-noise ratio is approximately given by

$$\frac{S}{N} [h(\vec{\mu})] = \frac{\langle h(\vec{\mu}), h(\vec{\mu}) \rangle}{\text{rms}(\langle h(\vec{\mu}), n \rangle)} = \sqrt{\langle h(\vec{\mu}), h(\vec{\mu}) \rangle}. \quad (7.59)$$

The error in measurement is taken to be the width of the probability density function  $\mathcal{P}(\vec{\mu}, s)$  for the measured value  $\hat{\vec{\mu}}$ , i.e. the variance-covariance matrix

$$\Sigma_{ij} = \int (\mu_i - \hat{\mu}_i)(\mu_j - \hat{\mu}_j) \mathcal{P}(\vec{\mu}, s) d^n \mu. \quad (7.60)$$

For high signal-to-noise,  $\Sigma_{ij}$  is well approximated by  $(\Gamma^{-1})_{ij}$ , where  $\Gamma_{ij}$  is the so-called Fisher matrix, given by

$$\Gamma_{ij} = 2 \int_0^\infty \frac{\partial_i \tilde{h}(f) \partial_j \tilde{h}^*(f) + \partial_j \tilde{h}(f) \partial_i \tilde{h}^*(f)}{\mathcal{S}_h(f)} df, \quad (7.61)$$

where  $\partial_i \equiv \partial/\partial\mu_i$ .

### 7.5.3 Polarization resolution and amplitude extraction

One can clearly estimate the amplitude of the waveform directly from the signal-to-noise of the detection; they are directly proportional. Given the output of both interferometers I and II, [LISA](#) should be able to extract both the amplitude and polarisation of the incoming wave, to an accuracy of order the inverse of the signal-to-noise ratio (though again the accuracy that is achievable also depends on correlations with the other parameters that one is trying to extract). Even if only a single interferometer output is available, [LISA](#) can still extract the amplitude and polarisation of the wave due to the rotation of the detector during its orbit. But clearly the yearly rotation of the detector is less helpful for determining the polarisation of shorter-lived sources such as merging [MBH](#) binaries, where most of the signal-to-noise will typically be accumulated in the final week before merger.

The same Fisher matrix calculation that tells us the angular resolution of the detector will simultaneously tell us how accurately the polarisation and amplitude of the source can be determined.

#### 7.5.3.1 Results for monochromatic sources

In terms of sheer numbers, stellar-mass binaries will undoubtedly be the dominant [LISA](#) source. There are so many white dwarf binaries in the galaxy that they effectively form a stochastic background. In this section we consider measurements of a binary that is sufficiently close that it can be detected individually; i.e., its signal stands up above the detector noise and above the background from other binaries.

Binaries with small eccentricity are essentially monochromatic sources. To see this, note first that because the binary orbit is periodic, in Fourier space its gravitational radiation is made up

of discrete lines at  $f = 2/P, 4/P, 6/P$ , etc., where  $P$  is the orbital period. (The sequence is multiples of  $2/P$  instead of  $1/P$  because the dominant radiation is quadrupolar.) For eccentricity  $e < 0.2$ , more than 60% of the power comes out at the “fundamental” frequency  $f = 2/P$ , so in a first approximation we can ignore the higher harmonics. Next note that for an observation time of  $T_0 \sim 1$  yr, the discrete Fourier transform sorts monochromatic signals into frequency bins of width  $\Delta f = 1/T_0 \sim 3 \times 10^{-8}$  Hz. The typical timescale on which these binaries evolve is  $\gtrsim 10^7$  yrs; so in one year’s observation, a binary’s emitted GW frequency changes by  $\lesssim f/10^7 = 10^{-10}(f/10^{-3})$  H, i.e., much less than the width of one bin.

So a stellar-mass binary with roughly circular orbit is a monochromatic source, and conversely any monochromatic source can be thought of as a circular-orbit binary: possible polarisation states of the monochromatic source are in 1-to-1 correspondence with possible directions for the binary’s angular momentum vector. Seven parameters are needed to completely characterize the waveform: its intrinsic frequency  $f_0$ , the source position  $\vartheta$  and  $\varphi$ , the binary’s orientation angles  $\vartheta_L$  and  $\varphi_L$ , its overall amplitude  $\mathcal{A}$  (proportional to  $\mu(\pi M f_0)^{2/3}/D$ ), and its phase  $\varphi_0$  at time  $t = 0$ . As emphasized above, one must extract all these parameters simultaneously; covariances between parameters invariably degrade the accuracy with which any particular parameter can be extracted.

The error box for the position measurement covers solid angle  $\Delta\Omega$ , given by

$$\Delta\Omega = 2\pi \sqrt{(\Delta\mu \Delta\varphi)^2 - \langle \Delta\mu \Delta\varphi \rangle^2}, \quad (7.62)$$

where  $\mu \equiv \cos \vartheta$ . The second term in brackets in Eq. (7.62) accounts for the fact that errors in  $\mu$  and  $\varphi$  will in general be correlated, so that the error box on the sky is elliptical in general. The overall factor of  $2\pi$  in the definition of  $\Delta\Omega$  is chosen so that the probability  $P(\beta)$  that the source lies *outside* an (appropriately shaped) error ellipse enclosing solid angle  $\beta\Delta\Omega$  is just  $P(\beta) = e^{-\beta}$ . Knowing the waveform’s polarisation is equivalent to knowing the angular momentum direction  $\hat{L}$  of the corresponding circular-orbit binary. The accuracy with which this direction can be determined is similarly given by  $\Delta\Omega_L$ , where

$$\Delta\Omega_L = 2\pi \sqrt{(\Delta\mu_L \Delta\varphi_L)^2 - \langle \Delta\mu_L \Delta\varphi_L \rangle^2}. \quad (7.63)$$

Table 7.1 illustrates the accuracy LISA will have in measuring the source direction, polarisation, and amplitude of a monochromatic wave. Results are for one year of observation, normalized to total  $S/N = 10$  for both interferometers I and II. (Thus, the S/N for interferometer I alone would be approximately  $10/\sqrt{2} \approx 7.07$ .)  $\Delta\Omega$  is the size of LISA’s error box (in steradians) in source position,  $\Delta\Omega_L$  the error box for the binary’s orientation, and  $\Delta\mathcal{A}/\mathcal{A}$  is the relative accuracy of the amplitude measurement. Cases A, B, and C refer to three representative choices of the four angles  $(\mu, \varphi, \mu_L, \varphi_L)$ . These angles are: (0.3, 5.0,  $-0.2$ , 4.0) for A; ( $-0.3$ , 1.0,  $-0.2$ , 4.0) for B; and ( $-0.3$ , 1.0, 0.8, 0.0) for C. Each case is illustrated for three gravitational wave frequencies:  $f = 10^{-4}, 10^{-3}, 10^{-2}$  Hz. The subscript ‘I’ on  $\Delta_I$  indicates that the measurement corresponds to detection by interferometer I alone.  $\Delta$  without a subscript indicates the result is for a combined measurement by interferometers I and II.

Table 7.1 shows that for monochromatic sources, having two independent outputs improves the position and polarisation resolution,  $\Delta\Omega$  and  $\Delta\Omega_L$  by a factor of only  $\sim 2$ ; i.e., just the improvement that comes from the increased signal-to-noise. This basically tells us that the rotation of the detector over a one year observation time does indeed allow interferometer I alone to measure both polarisations rather effectively. LISA’s  $\Delta\Omega$  for monochromatic sources at  $f = 10^{-3}$  Hz is typically  $\sim 10^{-3} - 10^{-2}$  sr; LISA’s angular resolution improves at higher

$f$ [Hz]	Case	$\Delta_I \Omega$ [sr]	$\Delta_{II} \Omega_L$ [sr]	$\Delta_I \mathcal{A}/\mathcal{A}$	$\Delta \Omega$ [sr]	$\Delta \Omega_L$ [sr]	$\Delta \mathcal{A}/\mathcal{A}$
$10^{-4}$	A	$2.15 \times 10^{-1}$	$3.81 \times 10^{-1}$	$3.22 \times 10^{-1}$	$8.27 \times 10^{-2}$	$1.99 \times 10^{-1}$	$2.04 \times 10^{-1}$
	B	$2.23 \times 10^{-1}$	$2.81 \times 10^{-1}$	$2.38 \times 10^{-1}$	$7.89 \times 10^{-2}$	$9.78 \times 10^{-2}$	$1.53 \times 10^{-1}$
	C	$1.23 \times 10^{-1}$	$8.48 \times 10^{-2}$	$1.57 \times 10^{-1}$	$7.11 \times 10^{-2}$	$4.00 \times 10^{-2}$	$1.02 \times 10^{-1}$
$10^{-3}$	A	$1.07 \times 10^{-1}$	$3.38 \times 10^{-1}$	$3.21 \times 10^{-1}$	$3.98 \times 10^{-2}$	$1.69 \times 10^{-1}$	$2.04 \times 10^{-1}$
	B	$1.03 \times 10^{-1}$	$1.62 \times 10^{-1}$	$2.21 \times 10^{-1}$	$3.83 \times 10^{-2}$	$7.34 \times 10^{-2}$	$1.53 \times 10^{-1}$
	C	$6.51 \times 10^{-2}$	$6.88 \times 10^{-2}$	$1.56 \times 10^{-1}$	$3.14 \times 10^{-2}$	$3.44 \times 10^{-2}$	$1.03 \times 10^{-1}$
$10^{-2}$	A	$2.57 \times 10^{-3}$	$3.50 \times 10^{-1}$	$3.12 \times 10^{-1}$	$1.08 \times 10^{-3}$	$1.53 \times 10^{-1}$	$2.04 \times 10^{-1}$
	B	$2.90 \times 10^{-3}$	$1.26 \times 10^{-1}$	$2.21 \times 10^{-1}$	$1.15 \times 10^{-3}$	$5.78 \times 10^{-2}$	$1.53 \times 10^{-1}$
	C	$1.95 \times 10^{-3}$	$4.22 \times 10^{-2}$	$1.54 \times 10^{-1}$	$7.66 \times 10^{-4}$	$1.94 \times 10^{-2}$	$1.02 \times 10^{-1}$

**Table 7.1** *LISA*’s measurement accuracy for monochromatic sources, for a few representative choices of angles and gravitational wave frequency. Results are normalized to a combined  $S/N = 10$ . Cases A, B, and C refer to source direction and orientation angles, and are defined in the text. Error boxes  $\Delta \Omega$  (for source position) and  $\Delta \Omega_L$  (for source orientation) are in steradians. Results for interferometer I alone have subscript ‘I’; other results are for the pair of outputs I and II.

frequencies due to the increased impact of the Doppler shift. *LISA*’s polarisation resolution for these sources is typically  $\Delta \Omega_L \sim 0.1$  sr, and  $\Delta \mathcal{A}/\mathcal{A} \sim 0.1 - 0.2$ . Here, too, if only a single interferometric output is available, the degradation in measurement accuracy comes mostly just from the loss in total signal-to-noise.

#### 7.5.4 Results for MBH coalescence

Coalescences of *MBH* binaries, if they occur at sufficient rates to be observable, will be an exceptionally strong *LISA* source, with signal-to-noise ratios of  $10^3 - 10^4$ . Clearly, detecting a population of *MBH* binaries would teach us a great deal about the early evolution of galaxies and the processes by which massive black holes are formed in the centers of those galaxies. There is also a possibility that several detections would allow us to determine the basic cosmological parameters,  $H_0$ ,  $\Omega_0$ , and  $\Lambda_0$ , to high accuracy. The idea is that from the gravity-wave signal one should be able to read off the luminosity distance  $D_L$  to the source to roughly 1% accuracy. (A naive estimate is that one should determine  $D_L$  to an accuracy of order  $(S/N)^{-1} \sim 0.01 - 0.1$  %, but correlations with other parameters increase the error  $\Delta D_L$  to of order 1%; see below.) If one could identify the host galaxy or galaxy cluster, then one could determine the redshift  $z$  of the source optically. Clearly a handful of such measurements would suffice to determine  $H_0$ ,  $\Omega_0$ , and  $\Lambda_0$  to roughly 1% accuracy. So an important question is, will *LISA* have sufficient angular resolution to determine the host galaxy or cluster?

In principle we can answer this question in the same way as for monochromatic sources: just calculate the Fisher matrix and invert it. However for *MBH* mergers the parameter space is much larger and the signals much more complex. The physical parameter space  $\mathcal{N}$  for *MBH* mergers is 17-dimensional:

$$\mathcal{N} = \left( D_L, M_1, M_2, \mu, \varphi, \vec{S}_{1,0}, \vec{S}_{2,0}, \mu_{L,0}, \varphi_{L,0}, e_0, t_0, \psi_0, \varphi_0 \right), \quad (7.64)$$

where  $D_L$  is the luminosity distance;  $M_1$  and  $M_2$  are the masses of the two *BH*’s;  $\vec{S}_1$  and  $\vec{S}_2$  are the spins;  $\mu, \varphi, \mu_L$ , and  $\varphi_L$  give the direction and orientation of the binary;  $e$  is the eccentricity;

$t_0$  is the instant of time at which the orbital period has some fiducial value  $P_0$ ; and  $\psi_0$  and  $\varphi_0$  indicate the direction of the semi-major axis and the value of the orbital phase at  $t = t_0$ . The subscript ‘0’ added to  $\vec{S}_1$ ,  $\vec{S}_2$ ,  $\mu_L$  and  $\varphi_L$  also refer to the values of these physical quantities at  $t = t_0$ ; these quantities will generally vary with time due to the Lense-Thirring effect, which couples the spins of the bodies to their orbital angular momentum.

To date, the Fisher matrix for this problem has only been calculated under the following simplifying assumptions [128]: that  $e = 0$ , that  $\vec{S}_1$  and  $\vec{S}_2$  are both parallel to the orbital angular momentum  $\vec{L}$  (so that there is no precession of the orbital plane), and that both these facts are known *a priori*. By essentially ignoring some parameters, this simplified calculation is likely to overestimate somewhat the accuracy with which LISA can determine the others.

From the simplified calculation the following results emerge. The angular resolution  $\Delta\Omega$  achievable by interferometers I and II combined is typically of order  $10^{-4}$  steradians, or 0.3 square degrees. The angular resolution depends strongly on the masses and the particular angles involved, however.  $\Delta\Omega$  is roughly in the range  $10^{-5} - 10^{-3}$  steradians for masses in the range  $10^5 - 10^7 M_\odot$ ; it is somewhat larger than this for lower-mass black holes, because the total  $S/N$  is generally smaller for lower masses. For MBH mergers, the angular resolution achievable by interferometers I and II combined is roughly an order of magnitude better than that achievable with detector I alone. This is quite different from the case of monochromatic sources, where the improvement was only a factor of  $\sim 2$ . This is because, in the MBH case, the time-scale over which most of the signal-to-noise is accumulated is typically a few weeks. Thus during time that the source is most visible, LISA’s orientation hardly changes, and so having only one interferometric output would effectively restrict LISA to measuring a single polarisation.

LISA’s distance determination accuracy  $\Delta D_L/D_L$  for MBH mergers will be roughly in the range 0.1%–30%, with  $\sim 1\%$  being typical. This is much worse than the naive guess of  $\Delta D_L/D_L \approx (S/N)^{-1}$ , due to correlations between  $D_L$  and the various angles describing the source. Large values of  $\Delta D_L/D_L$  have a strong positive correlation with large uncertainties  $\Delta\Omega_L$  in the binary’s orientation. However LISA should determine the masses of the two BH’s to very good accuracy indeed: typically  $\Delta M_i/M_i \sim 0.1\% - 1\%$ .

From the simplified calculation we have described, it is clear that LISA will not have sufficient angular resolution to determine the location of the merging MBH binary from the gravitational waveform alone. This is because one square degree contains of order  $10^4 L_*$  galaxies. However, LISA could have sufficient angular resolution to facilitate simultaneous detections in the electromagnetic spectrum. This is because for events with  $S/N \sim 10^3 - 10^4$ , LISA should detect the inspiral several weeks before the final merger phase, and LISA’s *one-degree* error box will be available more than a day before the final merger. Thus the source position will be known in time to train a battery of optical, radio, and X-ray telescopes at the roughly the right location on the sky, at precisely the right time. One can hope that some electromagnetic flare accompanies the MBH merger (due to the remnants of an accretion disk that one or both holes might carry with them), which would then identify the source. Clearly this would revive the possibility of using LISA to measure the cosmological parameters.

### 7.5.5 Estimation of background signals

Several types of background signals which either will or may be observable have been discussed previously. These are:

- a confusion-limited background due to unresolved galactic binaries;
- a similar background due to extragalactic binaries;



- possible cosmic backgrounds due to phase transitions in the early universe; and
- a possible primordial cosmic background due to quantum fluctuations before inflation.

An important issue for [LISA](#) is how well we can expect to do in identifying, separating, and quantifying these types of backgrounds.

As described earlier, backgrounds due to galactic neutron star binaries and white dwarf binaries will be observed at frequencies up to about 1 mHz. Hundreds to thousands of binaries of these kinds also will be observed as resolved signals, which are considerably stronger than the background or instrumental noise. Most of these will be at frequencies of roughly 1 mHz and higher. Their distribution in different parts of the galaxy such as the disk and the bulge will be determined from the measured directions and the statistics of the signal strengths. With this information, the galactic backgrounds can be modeled quite well, and fitted to the observations. The galactic backgrounds will be quite anisotropic because of the geometry of the galaxy.

The unresolved background due to extragalactic binaries will be quite different in nature. A few individual binaries from the [LMC](#) and other nearby galaxies probably will be resolvable. However, the universal background will have comparable contributions from equal thickness shells ranging all the way out to cosmological distances, and thus will be nearly isotropic. The small anisotropies in the background due to nearby concentrations of stars such as the [LMC](#), M31, and the Virgo cluster, as discussed by Lipunov *et al.* [132], will be difficult to detect.

The only handle for separating the possible cosmic backgrounds from the dominant isotropic part of the extragalactic binary background is the spectrum. There is enough uncertainty in the ratios of the numbers of binaries of various kinds in other galaxies to the numbers in our galaxy so that the strength of the extragalactic binary background cannot be predicted reliably. However, since the types of binaries contributing most strongly at the frequencies of interest probably will be evolving mostly by emitting gravitational radiation, the spectrum may be known quite well. If the spectrum of a cosmic background were significantly different and the amplitude were large enough, such a background could be separated and quantified.

Perhaps the most significant question is how well all of the backgrounds can be separated from instrumental noise. To discuss this question, it is useful to divide the instrumental noise above roughly  $10^{-4}$  Hz into three different types. One is stationary noise with steady amplitude at all frequencies of interest. The second is noise which varies at one and two cycles/year, in such a way that it mimics the interaction of the galactic background with the rotating antenna pattern. The third is noise with all other types of time variations. The first and second types cannot be separated from isotropic and galactic backgrounds, respectively, except if they are substantially higher than experimental limits which can be put on instrumental noise. The third type of noise would not be confused with real background signals.

For measuring the difference in distances between proof masses, the main noise sources are photon shot noise and phase shifts from fluctuations in laser beam pointing. The shot noise contribution can be calculated from the received light level and at least partly subtracted out. For beam pointing fluctuations, it is difficult to say how much of the noise may be of the first two types, but an estimate of a third or less of the level given in the error budget seems reasonable. Specific experiments during the mission to characterize the noise by changing the gain of the beam-pointing servo loops and temporarily defocusing the beams somewhat should be considered.

For spurious accelerations of the proof masses, there are a number of items of comparable size in the error budget. A few, like random residual gas impacts on the proof masses, may be quite stationary, although they also may have variations at annual and six month periods from spacecraft temperature variations. However, it seems likely that most of the spurious acceleration

sources will not be predominantly stationary. For example, this would apply to sources such as the interaction of the average charge on the proof mass with the fluctuations in the solar wind magnetic field. Consideration will be given to including diagnostic experiments, such as changing the average proof-mass charge or changing how tightly the spacecraft follow the proof masses, in order to characterize the spurious acceleration noise sources as well as possible.

Overall, it seems reasonable to estimate that perhaps a third of the total instrumental noise in the distance measurement and spurious acceleration error budgets would be difficult to separate from real background signals. The extent to which data from the third arm of [LISA](#) would aid in searching for background signals has not yet been investigated.



# 8 Payload Design

## 8.1 Payload structure design concept

The [LISA](#) payload has been analysed in detail in previous investigations [1, 133]. The specification of the (Payload Definition Document [133]) has been adopted as a baseline for the subsequent Industrial Study [2].

As a major result of the Industrial Study, the baseline concept at the recent level of investigations turns out to be a valid approach, with some modifications necessary on assembly level (e.g. the implementation of point-ahead angle compensation).

The design objectives for the payload structure are:

1. To ensure that the structure exhibits no modes of vibration below 60 Hz during launch.
2. To ensure that the structure exhibits no modes of vibration between 0.1 Hz and  $10^{-4}$  Hz during operation.
3. To allow independent pointing adjustment for the two laser systems.
4. To minimise gravitational and optical disturbances due to thermally induced distortions.

In preparation of the Pre-Phase A Study [1] an iterative design study, involving 3D-CAD modelling and Finite Element Analysis, has produced a conceptual design that met the first three requirements. The fourth requirement is met to a greater extent, but further work was required to quantify acceptable levels of distortion and to model the behaviour of the structure in more detail. These further studies were part of the charge of the Industrial Study [2].

The design has a number of features that arise from the requirement specifications:

- All of the optical components are mounted together within rigid subassemblies – the *optical assemblies* – to minimise changes to critical alignment dimensions.
- These two subassemblies are enclosed within the arms of the rigid Y-shaped payload thermal shield. They are attached to the inside by flex-pivot assemblies and pointing actuators to allow the alignment of the optical assemblies to be adjusted. These adjustments are made by moving each entire optical assembly within the payload thermal shield; the shield itself does not move with respect to the spacecraft during alignment.
- The payload thermal shield acts as the main structural member. In addition to the optical assemblies, the radiator plate is supported from the Y-tube's underside. It carries the lasers and their drive electronics, along with the [UV](#) discharge unit. Mounting the radiator plate in this manner minimises the number of interfaces with the spacecraft.
- Finite Element Analysis has shown that additional load paths are required to achieve the first structural design objective. These load paths take the form of launch-locks, which are retracted after launch.

The following sections describe the structural components and launch-lock concept in more detail.

## 8.2 Payload structural components

### 8.2.1 Optical assembly

One set of optical components (telescope, optical bench and support electronics), together with a payload cylinder, make up one optical assembly, as shown in Figure 8.1 (from [1]). Minor modifications, such as suggested in the course of the recent study [2] will be given in later subsections.

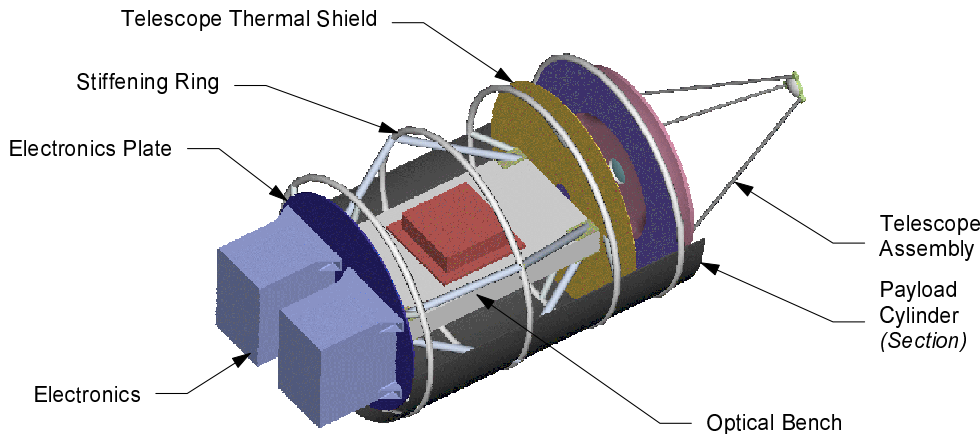


**Figure 8.1** *Optical assembly, section view, from [1].*

**Payload cylinder** The payload cylinder is a graphite-epoxy tube, 360 mm in diameter, 500 mm long and 2 mm thick. It is fabricated in at least two parts, so that sections can be removed in turn to allow access to the internal components after integration.

The cylinder is reinforced at intervals along its length by stiffening rings, suitably positioned to form mounting points for the optical components (see Figure 8.1). These rings are tubes, made from graphite-epoxy, 10 mm in diameter and 2 mm in wall thickness. They are either fabricated individually, then bonded onto the payload cylinder sections, or formed in sections as integral parts of the payload cylinder panels during their manufacture. Each ring is equipped with fittings into which the appropriate component support struts are attached (see descriptions to follow).

**Telescope assembly** The telescope assembly is mounted from the first stiffening ring. It uses graphite-epoxy or stainless steel blade mounts to accommodate the radial thermal expansion of the ULE primary mirror and the payload cylinder. For further details see Appendix A.6.

**Telescope thermal shield** The telescope thermal shield is mounted from the second stiffening ring. It is a disc of graphite-epoxy, 350 mm in diameter and 1 mm thick, with a 40 mm diameter hole through the centre to allow passage of the laser light. The shield is mounted to the stiffening ring with four Pyroceram support tubes, each 5 mm in diameter and 1 mm wall thickness, approximately 80 mm long.

### 8.2.2 Optical bench

The optical bench is suspended from the third stiffening ring by eight Pyroceram support tubes (each 10 mm in diameter, 2 mm wall thickness and approx. 200 mm long) to four points on the ring. The orientation of these tubes and their attachment points are indicated in Figure 8.2.

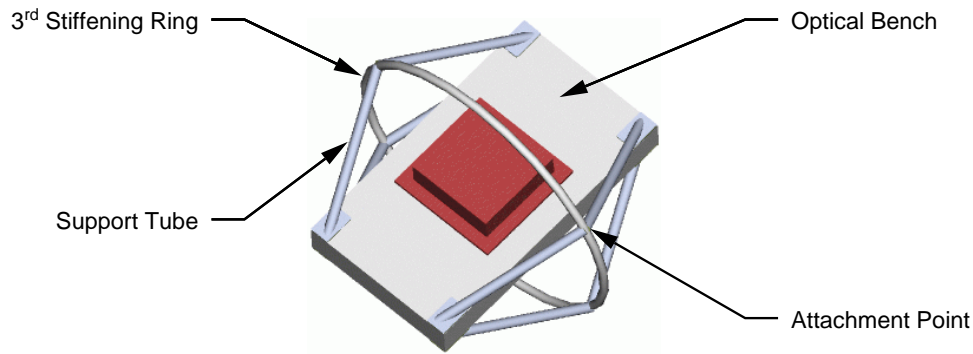


**Figure 8.2** *Optical bench attachment.*

The use of four attachment points, rather than two, significantly increases the rigidity of the assembly, enabling it to meet the stiffness requirements for launch.

**Flex-pivot assembly** In the Pre-Phase A Report [1], the relative orientation of the telescopes, to adjust to the annual change in subtended angle, was done by anchoring the optical assemblies at their very ends with flex-pivots.

The rear of each optical assembly was to be attached to the payload thermal shield by four flex-pivot beams. One end of each beam was attached to the fourth stiffening ring of the optical assembly. The other end was attached to one of two flex-pivots, situated inside the payload thermal shield where the two Y-tube arms intersect, see Figure 8.3 .

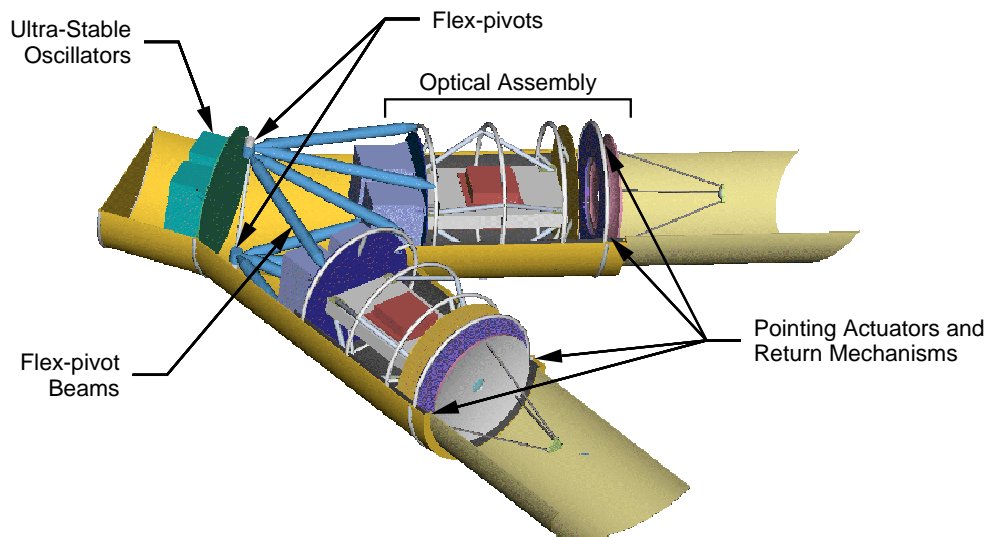


**Figure 8.3** *Flex-pivot assembly, section view.*

This scheme has been superseded by a mechanism described in detail in Appendix A.7 The particular improvement in this revised scheme is the more central location of the rotation axis, which is now very close to the proof-mass position.

### 8.2.3 Payload thermal shield

The payload thermal shield is an assembly of graphite-epoxy cylinders (two Y-tube arms, the Y-tube stub and the two baffles), reinforced by stiffening rings at various locations, as shown in Figure 8.4.

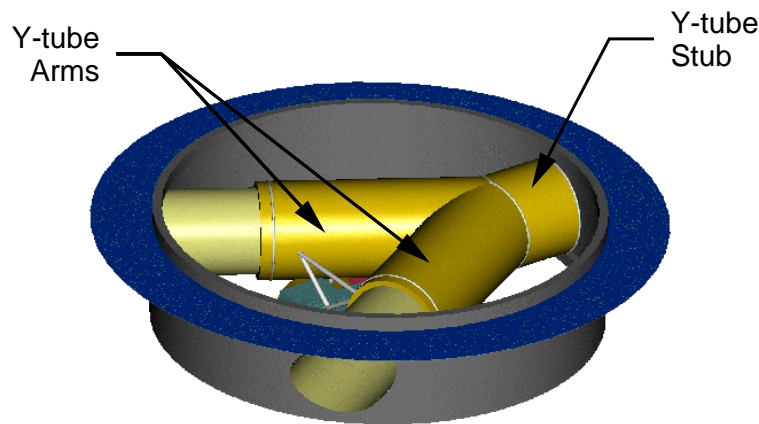


**Figure 8.4** Y-shaped payload thermal shield

The “stub” of the payload thermal shield houses the ultra-stable oscillators, and is connected to the Spacecraft via three stressed fibreglass bands around its circumference. Blade-mounts attach each “arm” of the payload thermal shield to the spacecraft, at the point where the baffles meet the spacecraft ring. These blade-mounts allow longitudinal expansion of the Y-tube arms (due to thermal effects), whilst preventing motion in other directions.

**Launch-locks** Finite Element Analysis has shown that launch-locks will be required if the payload is to achieve the first structural design objective, i.e. to avoid resonances below 60 Hz during launch.

The first set of launch-locks reinforce the attachment of the payload to the spacecraft structure. They connect the baffles to the spacecraft ring during launch.

The second set of launch-locks attach the rear of the optical assemblies directly to the inside of the payload thermal shield. They are positioned at the top and bottom of the fourth stiffening ring.

A very detailed analysis of both the payload and spacecraft structures was one of the charges of the Industrial Study. They are the underlying motivations for various changes and improvements that now represent the [LISA](#) baseline.

## 8.3 Mass estimates

A very detailed analysis of both the payload and spacecraft structures was one of the charges of the Industrial Study. They are the underlying motivations for various changes and improvements that now represent the [LISA](#) baseline.

The earlier mass estimates for the payload structural components are listed in Table 8.1. The results of the recent study deviate from these first assessments, but they are not significantly higher. The specifications for the mass total for a Delta II launch are still easily met.

<i>Item</i>	<i>Number per S/C</i>	<i>Mass (g)</i>	<i>Mass (kg)</i>	<i>Mass (kg)</i>
<b>Optical Assembly Structure</b>	<b>2</b>			<b>&lt; 5.8</b>
Payload cylinder			1.74	
Telescope support			0.64	
<i>Support</i>		550		
<i>Stiffening ring</i>		87		
Telescope thermal shield			0.32	
<i>Shield</i>		145		
<i>Stiffening ring</i>		87		
<i>Support tubes and fittings</i>		92		
Optical bench support			0.47	
<i>Stiffening ring</i>		87		
<i>Support tubes and fittings</i>		385		
Electronics Plate			0.61	
<i>Plate</i>		393		
<i>Stiffening ring</i>		87		
<i>Support tubes and fittings</i>		129		
Pointing assembly			< 2.00	
<i>Flex-pivots</i>		< 1000		
<i>Flex-pivot beams</i>		500		
<i>Pointing actuators</i>		< 500		
<b>Payload Thermal Shield</b>	<b>1</b>			<b>&lt; 11.5</b>
Baffles			1.8	
Y-tube			7.5	
Stiffening rings			0.7	
Launch-locks			< 1.5	
<b>Ultrastable-Oscillator Plate</b>	<b>1</b>			<b>0.5</b>
<i>Plate</i>		394		
<i>Support tubes and fittings</i>		130		
<b>Radiator Plate Structure</b>	<b>1</b>			<b>1.3</b>
Plate and rim			1.0	
Support struts			0.3	
<i>Short supports (all 4)</i>		48		
<i>Fifth support</i>		251		

Table 8.1 Estimated masses of the payload components.

## 8.4 Payload thermal requirements

The major science requirement on the payload thermal control subsystem is one of temperature stability, with the optical bench fluctuations due to solar intensity variations and other sources of disturbances kept below  $10^{-6} \text{ K}/\sqrt{\text{Hz}}$  at  $10^{-3} \text{ Hz}$ . The telescope thermal stability should be below  $10^{-5} \text{ K}/\sqrt{\text{Hz}}$  at  $10^{-3} \text{ Hz}$  to achieve the desired performance.

The optical bench part of the payload shall be maintained at  $20^\circ\text{C} \pm 10^\circ\text{C}$ , but should be known with an accuracy of TBD  $^\circ\text{C}$  at the design stage. Temperature gradients within the optical bench

should be less than  $\text{TBD}^{\circ}\text{C}$ . Electronics boxes need to be maintained within their operational temperature limits of  $\text{TBD}^{\circ}\text{C}$  to  $\text{TBD}^{\circ}\text{C}$ .

The laser diodes are to be kept at their operational temperature, and this will reduce over the mission life from  $295 \pm \text{TBD K}$  at BOL to  $280 \pm \text{TBD K}$  at EOL (beginning, end of lifetime), to accommodate changes in the diode operating wavelength.

In addition to the specific thermal requirements defined above the thermal design must, together with the thermoelastic design, prevent deformations of the structure that compromise the scientific performance of the payload.

## 8.5 Payload thermal design

It is clear that many thermal and system level trade-offs need to be performed before an optimised thermal design may be established. However some thermal analysis has been performed and has enabled the definition of certain design parameters.

The first stage of isolation from the sun should be provided by the spacecraft as either a solar shield with optimised  $\alpha_s/\varepsilon$  or, preferably, multilayer insulation (MLI). This would probably be at the level of the top of the spacecraft structural ring. A second stage of solar isolation is provided by the Y-shaped thermal shield. This will be goldized as extensively as possible on external and internal surfaces, although if the electronics boxes are radiatively cooled then certain parts of this thermal shield will have to be blackened, and also the internal surfaces of the baffles forward of the primary mirrors will probably be blackened for control of scattered light.

The external and internal surfaces of the optical bench support cylinders are goldized to radiatively isolate them from the Y-shaped tube, thus providing a third stage of radiative isolation from the sun. The optical bench and sensor assemblies have been assumed to have their natural surface properties, but further modelling may show that these too need to have controlled low emissivity coatings.

Conductive isolation is used throughout the payload and at the interfaces with the spacecraft as defined in Section 8.2. For this purpose, Pyroceram cylinders are used to support the optical benches, the electronics plates and the telescope thermal shields off the internal support cylinders. Glass fibre reinforced bands are assumed for mounting the internal support cylinders off the Y-shaped tube and carbon fibre brackets for mounting the laser radiator off the Y-shaped tube and the primary mirror off the support cylinder.

Current modelling has indicated that the electronics boxes operate somewhat warm at about  $30^{\circ}\text{C}$  but the current design study considered radiative losses only from the box to the Y-shaped tube and from there to the spacecraft. It is conceivable that an additional radiator could be accommodated in plane with the laser radiator and with heat straps to the payload electronics boxes. The straps would be fairly long and a 30 K temperature drop could result, but the radiator, seeing deep space, could be operated at a cold enough temperature with little difficulty. This approach would also improve the stability of the optical bench since the whole of the Y-shaped tube could be goldized and furthermore the ‘transfer function’ relating payload power to optical bench temperature fluctuations would be somewhat reduced.

The laser radiator requires a radiative coupling in the order of  $0.113 \text{ m}^2$  to space, equivalent to an actual black painted radiator diameter of about 0.4 m. The laser diode temperatures are actively controlled using heaters.

## 8.6 Thermal analysis

Geometrical mathematical models of the [LISA](#) payload were established for the calculation of radiative couplings using ESARADv3.2.6 and thermal mathematical models were established using ESATANv8.2.3. These models assume a solar shield instead of [MLI](#) on the sun facing side ( $\alpha_s/\varepsilon = 0.265$ ) and radiative cooling of the electronics boxes in the Y-shaped tube. They include major service module surfaces (the solar array, top sunshield, ring, and bottom cover) in order to calculate radiation exchanges with these, and to determine the sensitivity of the payload to changes in spacecraft temperature and solar intensity.

The thermal mesh permits the calculation of axial and circumferential gradients within the arms of the Y-shaped tube and internal support cylinders. Significant thermal components of the payload (the proof mass, sensor, titanium housing, optics bench, telescope shield, electronics plate, electronics boxes, primary mirror, secondary mirror, spider) were each represented by one node.

A detailed optical bench model was also established with the bench represented by a total of 28 nodes to allow the prediction of two-dimensional temperature gradients – those through the thickness of the bench are not calculated. A ‘nominal’ steady state calculation case was established using boundary conditions and payload power dissipations as given in [Table 8.2](#).

<i>Item</i>	<i>Value</i>	<i>Unit</i>
Solar constant	1370	W/m <sup>2</sup>
Sunshield $\alpha_s/\varepsilon$ ( <a href="#">BOL</a> value)	0.265	–
Spacecraft ring/base temperature	20	°C
Optics bench dissipations	$2 \times 0.9$	W
<a href="#">USO</a> electronics dissipations	$3.0 \pm 1.3$	W
Analogue electronics (on plates)	$2 \times 4.0$	W
Digital electronics (on plates)	$2 \times 4.5$	W
Radiator plate dissipation (lasers, control, discharge)	41.4	W

**Table 8.2** *Nominal model boundary conditions.*

Resulting temperatures are summarised in [Table 8.3](#).

When the results for the nominal steady state case are applied to the detailed optical bench model the maximum temperature predicted, in the region of the [EOM](#), is 22.9 °C and the minimum temperature predicted is 20.1 °C. For the housing the maximum temperature difference between sides is 1.4 °C. The temperature sensitivity of various components compared with these nominal temperatures is given in [Table 8.4](#) for various changes in the thermal boundary conditions.

The steady state results indicate that the optical bench should come to equilibrium within the required temperature range of  $20 \pm 10$  °C under “nominal” conditions. However this temperature is sensitive to the payload power dissipation and the spacecraft temperature in particular, and to a lesser extent to a number of other parameters. If the spacecraft temperature and payload power dissipation are kept constant then seasonal and sunshield surface degradation effects will result in long term variations limited to 3 or 4 °C (with seasonal changes alone accounting for about 0.5 °C).

Service module temperature changes could dominate the payload long term temperature variations, with a sensitivity of nearly 0.5 K/K. The electronics boxes on the electronics plate are a little on the warm side (in excess of 30 °C). Large temperature differences (nearly 80 °C) exist along the front sections of the Y-shaped tube due to the aperture seeing deep space. The payload



<i>Location</i>	<i>T</i> (°C)	<i>Location</i>	<i>T</i> (°C)
Optics bench	21.0	Support cylinder stiffening ring 4 (front)	2.2
Proof mass	20.4	Support cylinder middle	14.3
Sensor	20.4	USO box plate	24.7
Titanium housing	20.4	USO box	26.6
Primary mirror	−19.7	End plate of Y-shaped tube	19.8
Secondary mirror	−45.3	Y-tube apex (surrounding USO boxes)	19.8
Telescope thermal shield	4.4	Y-tube, from USO plate to electronic plate	23.0
Electronics plate	32.1	Y-tube, from electronics plate to primary mirror	11.8
Analogue electronics box on plate	33.6	Y-tube in front of primary mirror, aft end	−33.2
Digital electronics box on plate	33.8	Y-tube in front of primary mirror, middle	−49.0
Support cylinder stiffening ring 1	18.6	Y-tube in front of primary mirror, front end	−65.4
Support cylinder stiffening ring 2	16.0	Laser electronics radiator	12.2
Support cylinder stiffening ring 3	9.7	Sunshield	

**Table 8.3** *Nominal case temperature distribution.*

support cylinder itself maintains a temperature difference along its length of about 18 °C.

To model the transient performance of the payload, numerical convergence criteria were set to sufficiently small values so as to allow the detection of the very small temperature changes important for LISA. Frequency response simulations were made at  $10^{-4}$ ,  $10^{-3}$  and  $10^{-2}$  Hz and sets of ‘transfer functions’ relating the *rms* temperature of various payload components to *rms* fluctuations in boundary conditions were calculated. Assuming the power spectral density for observed insolation variations  $\widetilde{\delta L}_{\odot}$  is given as

$$\widetilde{\delta L}_{\odot} = 1.3 \times 10^{-4} f^{-1/3} L_{\odot} \text{ W m}^{-2}/\sqrt{\text{Hz}}, \quad (8.1)$$

then for the optical bench we get temperature fluctuations of  $2.0 \times 10^{-4} \text{ K}/\sqrt{\text{Hz}}$  at  $10^{-4}$  Hz,  $4.3 \times 10^{-7} \text{ K}/\sqrt{\text{Hz}}$  at  $10^{-3}$  Hz, and  $< 8.0 \times 10^{-1} \text{ K}/\sqrt{\text{Hz}}$  at  $10^{-2}$  Hz due to these solar fluctuations.

The requirement of  $1.0 \times 10^{-6} \text{ K}/\sqrt{\text{Hz}}$  at  $10^{-3}$  Hz is met, but only by a factor 2. In this case the fluctuations at  $10^{-3}$  Hz in power dissipation for the payload electronics on the electronics plate would have to be less than  $6.8 \times 10^{-4} \text{ W}/\sqrt{\text{Hz}}$  and variations in optical bench power dissipation would have to be less than  $5.2 \times 10^{-6} \text{ W}/\sqrt{\text{Hz}}$ . Spacecraft temperature variations

<i>Item</i>	<i>Proof Mass</i>	<i>Optics Bench</i>	<i>Payload Electron.</i>	<i>Primary Mirror</i>	<i>Support Cylinder</i>
<i>Nominal case temperature (°C)</i>	20.4	21.0	33.6	−19.7	14.3
SVM Base/Ring increased by 10 °C	+4.5	+4.5	+4.8	+4.2	+4.9
Solar Constant increased by 50 W/m <sup>2</sup>	+0.5	+0.5	+0.5	+0.5	+0.6
Shield $\alpha_s$ incr. by 0.052 W/m <sup>2</sup> (to EOL value)	+3.1	+3.1	+3.2	+2.7	+3.4
Electronics power increased by 1 W	+1.4	+1.4	+2.5	+0.9	+1.4
Optical bench power increased by 0.5 W	+9.4	+10.0	+1.3	+2.8	+4.9
CFRP conductivity doubled	−1.3	−1.3	−0.8	+4.2	−2.2

**Table 8.4** *Component temperature changes (°C) compared with nominal case.*



would have to be less than  $1.6 \times 10^{-3} \text{ K}/\sqrt{\text{Hz}}$  and laser electronics dissipation variations less than  $1.7 \times 10^{-1} \text{ W}/\sqrt{\text{Hz}}$ .

## 8.7 Telescope assembly

### 8.7.1 General remarks

The telescope has to fulfil two demands:

- The light power transmitted via the telescopes from the near to the far spacecraft has to be as high as possible in order to reduce the shot noise level in the optical readout system (see Eq. (5.2)).
- The wavefront of the outgoing beam has to be as flat as possible in order to minimize the coupling of beam motions to the interferometer signal (see e.g. Eq. (5.6)).

Increasing the diameter of the primary mirror allows to reduce the divergence of the outgoing beam and thus increases the intensity of the laser light at the far spacecraft. In addition, the power picked up by the far telescope is proportional to the area of the primary mirror there. The received lightpower is therefore proportional to the fourth power of the mirror diameter  $D$  (see Eq. (5.2)).

Once a particular diameter of the primary mirror is given, the intensity at the beam axis in the far field is highest when the Gaussian diameter of the outgoing beam equals the diameter of the primary mirror. The beam is then truncated at the  $1/e^2$  contour line of its intensity. In this case the power picked up at the far spacecraft is given by Eq. (5.1). For reasons of cost and weight a diameter of only 30 cm for the primary mirrors was chosen; it is adequate for the envisaged sensitivity level.

Coupling of changes in beam orientation to the interferometer signal is minimal when the center of curvature of the wavefront at the receiving spacecraft sits inside the emitting spacecraft. For the wavefront of a laser beam in the far field the center of curvature coincides with the focus of the beam. The outgoing wavefront has therefore to be flat. The final quality of the plane wavefront leaving the telescope is specified as  $\lambda/10$ .

### 8.7.2 Telescope concept

The telescope widens the diameter of the beam from a few mm to 30 cm. Since the space available is very limited, spherical optics would cause huge aberrations. Therefore conical sections are used for the mirror surfaces instead of spherical ones. In this case the imaging properties for point sources can in principle be perfect, if the focus of the beam is positioned exactly at the focus of the particular mirror. This is the idea behind the original Cassegrain telescope, where the primary is chosen to be a paraboloid and the secondary a hyperboloid. Unfortunately, the tolerances for misalignments and the usable field of view are very small in this case. There are several improvements over the original Cassegrain, e.g. the Ritchey-Chretien telescope, minimising the first three Seidel aberrations.

The transmitting and receiving telescope in [LISA](#) is therefore an improved Cassegrain system, including an integral matching lens. It is mounted from the payload support cylinder and protected by a thermal shield. The primary mirror is a double-arch light-weight ultra-low expansion [ULE](#) design and has a diameter of 30 cm and also a focal length of 30 cm. The secondary mirror, supported by a three-leg carbon-epoxy spider, is mounted 27.62 cm from the primary and has a diameter of 3.2 cm and a focal length of 2.6 cm. The beam from the

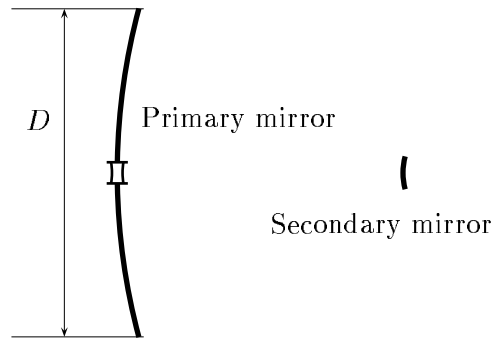


**Figure 8.5** *Geometrical arrangement of the telescope components*

instrument package to the secondary mirror is expanded to a diameter of approximately 3 cm by a suitable lens in the plane of the primary mirror. As just mentioned, the optical elements are aspherics to reduce aberration in the  $f/1$  telescope, and they require careful positioning. Active focus control will be necessary to compensate for any long-term deformations, caused e.g. by temperature drifts. The most critical geometrical parameter seems to be the separation between primary and secondary; a change of about one micron already deforms the outgoing wavefront by the specified tolerance of  $\lambda/10$ .

The temperature fluctuations at the telescope must be less than  $10^{-5} \text{ K}/\sqrt{\text{Hz}}$  at  $10^{-3} \text{ Hz}$  to achieve the desired performance.

### 8.7.3 Telescope development

A very detailed analysis of various telescope options was conducted in the Industrial Study [2]. The salient features of this analysis are presented in Appendix A.6.

## 8.8 Payload processor and data interfaces

### 8.8.1 Payload processor

Each LISA spacecraft includes a PI-provided payload computer comprising a payload processor plus the associated peripherals (I/O etc.), which performs all payload management functions as well as implementation of the drag-free and fine attitude control (DFACS) laws. The current baseline is to use the RAD 6000-SC computer which is a radiation-hardened version of the IBM RS/6000 processor developed for the Mars Surveyor Program (MSP). The nominal performance is 22 MIPS. The payload computer contains 128 Mbytes of DRAM and 3 MBytes of PROM. The relatively low data rates for science and telemetry permits all data to be buffered and stored in DRAM on the payload computer. This eliminates the need for a separate mass memory board, thereby reducing the subsystem mass and power. Likewise, the spacecraft computer which will handle the telemetry (and coarse attitude control/safe modes) does not need to have storage capability for the science data.

Table 8.5 summarises the payload processor specifications. The payload computer will be fully redundant, consisting of two identical units operating in a String A and a String B fashion. String B acts as a warm backup and receives state data from String A at specified intervals. String B will contain a watchdog timer to monitor String A. If this timer runs out, String B will take over as the payload processor. The payload computer component cards will be mounted in a VME chassis.

Processor type	<a href="#">RAD 6000-SC</a> , floating point included
<a href="#">RAM</a>	128 Mbytes radiation tolerant <a href="#">DRAM</a>
Nominal performance	22 <a href="#">MIPS</a> at 10.5 W (21.6 SPECMark)
Mass	< 0.9 kg
Temperature range	−30 ° to +75 °C at the cold plate
Memory protection	on chip <a href="#">EDAC</a> as well as system level <a href="#">EDAC</a>
<a href="#">SEU</a> bit error rate	4/MFC/year <a href="#">GCR</a> (Galactic Cosmic Rays)
Processor total dose	> 20 kJ/kg Total Ionizing Dose ( <a href="#">TID</a> )
<a href="#">DRAM</a> total dose	> 0.3 kJ/kg ( <a href="#">TID</a> )

**Table 8.5** *Payload processor specifications.*

### 8.8.1.1 Payload computer mass, power, volume budgets

The mass, power, and volume budgets of the payload computer subsystem are listed in [Table 8.6](#). The entries for mass include the [VME](#) connectors.

<i>Units</i>	<i>Number of Units</i>	<i>Total Mass (kg)</i>	<i>Power per Unit (W)</i>	<i>Notes</i>
Processor	2	2.3	10.5	
X-strap board	2	1.8	0.75	between A & B strings
<a href="#">1553</a> board	2	1.8	1	<a href="#">1553</a> bus controller
<a href="#">RS 422</a> board	4	1.8	2	Serial I/O for accels., etc
<a href="#">VME</a> chassis	2	1.8	–	composite material
Shielding	–	1	–	
<b>Totals</b>		<b>10.5 kg</b>	<b>14.25 W</b>	
Dimensions of complete payload computer: $233 \times 199 \times 321 \text{ mm}^3 = 14.9 \text{ litres}$				

**Table 8.6** *Payload computer mass, power, volume budgets.*

## 8.8.2 Payload data interfaces

The data interfaces between the payload subsystems and the spacecraft are shown in [Figure 8.6](#). The baseline approach is to use a [MIL-STD-1553](#) data bus to link all of the [DFACS](#) hardware elements to the payload processor, with the exception of the accelerometers (including [UV](#) discharge system) and interferometer electronics which are directly linked to the payload processor via an [RS 422](#) interface. The payload processor is linked to the spacecraft processor via the [1553](#) bus.

If it turns out to be feasible in terms of bus management and reliability, the [1553](#) interfaces may be replaced throughout by [RS 422](#) interfaces, with considerable cost benefit. For the time being, however, the [1553](#) protocol is the baseline choice.

### 8.8.2.1 Bus control

The [MIL-STD-1553](#) protocol requires no more than one bus controller. Initially, the spacecraft processor is the bus controller for coarse attitude control. During a transition phase, after the

payload processor (nominally String A) is brought on line, bus control is transferred from the spacecraft processor to the payload processor. This is accomplished by a “dynamic bus control” command which is available within the framework of the 1553 standard. (Alternatively, the spacecraft processor could retain control of the bus and use remote-terminal-to-remote-terminal transfers.)

### 8.8.2.2 Payload command and data handling software

The payload command and data handling (C&DH) software layer resides on the payload processor and includes the 1553 interface and data structures for normal payload operations, plus the RS 422 interface with the accelerometers and interferometer electronics. The command handler accepts and routes commands either directly from the 1553 interface, or as stored program commands loaded into the payload processor memory. These program commands may be time-tagged with absolute or relative time, or may be conditional commands. The spacecraft computer which controls the telemetry must be configured such as to accept/send data packets from/to the payload processor as commanded by the payload C&DH layer. All payload flight software will be developed using commercial compilers (C, C++, or Ada).

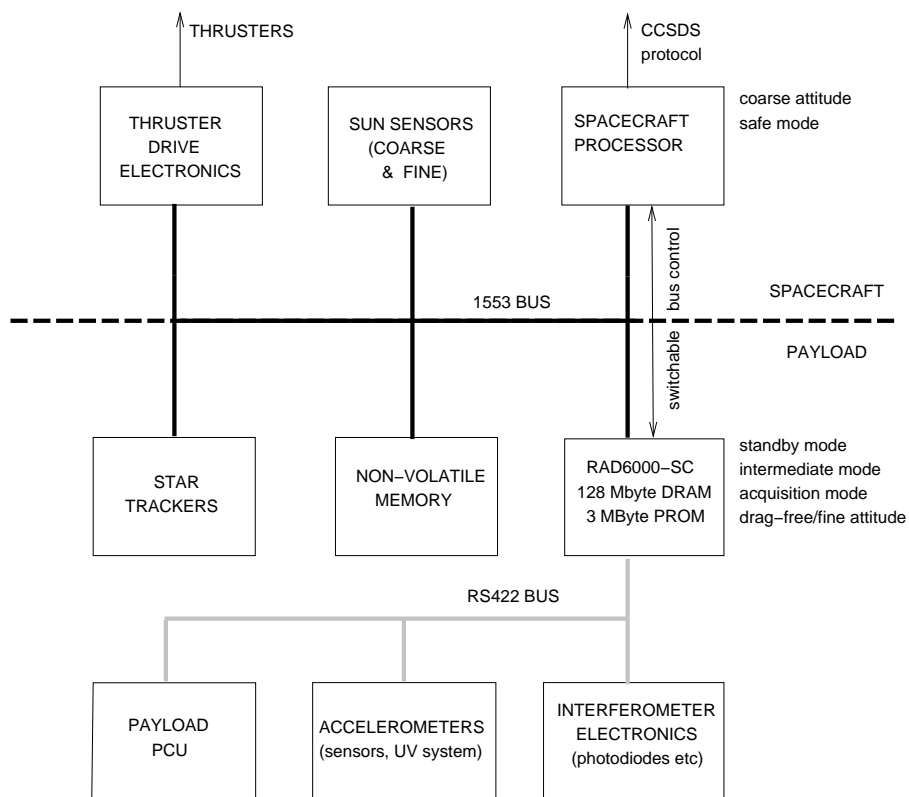


Figure 8.6 *Payload data interfaces.*

## 9 Spacecraft Design

### 9.1 The Pre-Phase A spacecraft design

#### 9.1.1 The spacecraft

The mechanical structure of the [LISA](#) spacecraft is perhaps the part that has most strongly profited from the recent Industrial Study [\[2\]](#).

We will briefly introduce the major issues using the 1998 baseline of [PPA 2](#), and then in [Section 9.3](#) discuss the modifications envisaged since.

The original spacecraft configuration is shown in [Figure 9.1](#). It consists of a cylinder with a height of 480 mm and a diameter of 1800 mm. It supports a Y-shaped tubular structure, the payload thermal shield, which serves to reduce the effects of changes in the solar luminosity on the optical assemblies contained in the two arms of the Y. A top lid across the cylinder (not shown in [Figure 9.1](#)) prevents sunlight from striking the payload thermal shield. The spacecraft equipment is mounted on the inside wall of the structural cylinder. Extending out from the structural cylinder is a sun shield that keeps sunlight off the cylinder wall. The main solar panels are mounted on this sun shield. The spacecraft structural cylinder and the payload

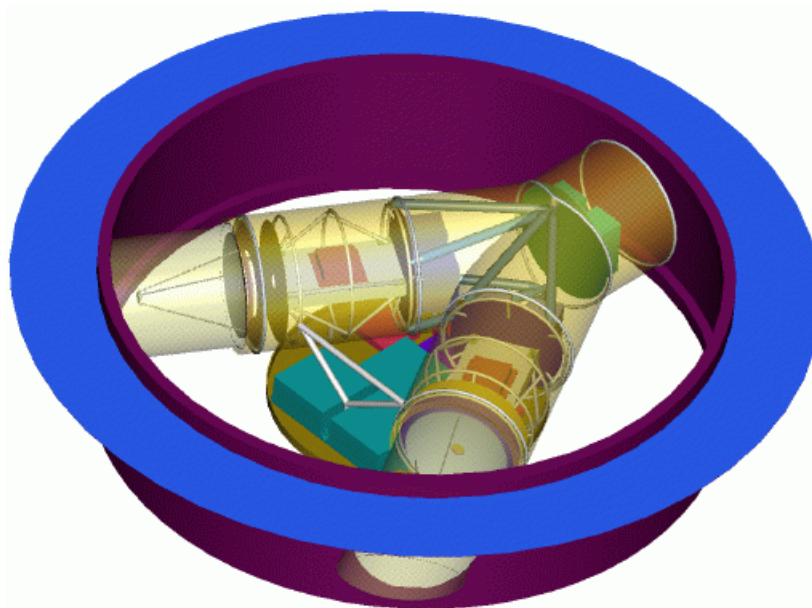


**Figure 9.1** One of the three identical *LISA* spacecraft, as in [\[1\]](#), The main structure is a ring with a diameter of 1.8 m, and a height of 0.48 m, made from graphite-epoxy for low thermal expansion. A lid on top of the spacecraft is removed to allow view at the Y-shaped thermal shield (indicated here as semitransparent) encasing the two payload arms.

thermal shield are made of a graphite-epoxy composite chosen for its low coefficient of thermal expansion. The payload thermal shield is gold-coated and suspended by stressed fiberglass bands from the spacecraft cylinder to thermally isolate it from the spacecraft. The optical

assemblies are in turn thermally isolated from the payload thermal shield. On the outside of the spacecraft cylinder the [FEEP](#) (Field Emission Electric Propulsion) thruster blocks are mounted in six clusters of four thrusters each.

Outside of the payload thermal shield, pointing parallel to the arms, star trackers are mounted on the lower side of the solar panel rim. For redundancy, a total of 4 star trackers are used. In addition Fine Sun Sensors and Sun Acquisition Sensors are mounted on the spacecraft.

Two steerable 30 cm diameter high-gain X-band antennas are mounted via suitable interface structures on the outside of the spacecraft, far enough inside the central cylinder diameter to avoid interference problems during separation. The antennas, used during the operational phase, provide the necessary  $2\pi$  coverage in azimuth. Low- and medium-gain antennas are mounted on short booms at the lower side of the structural cylinder.

In the operational heliocentric orbit the spacecraft nominal orientation is such that the YZ-plane coincides with the plane of the interferometer. Thus the spacecraft X-axes make an angle of  $30^\circ$  with the Sun direction. The angle between the X-axis and the Earth direction varies between about  $78^\circ$  and  $84^\circ$ . The major part of this variation is due to the eccentricity of the Earth orbit. As the interferometer rotates in the apparent orbital plane, making one revolution per year, while the apparent plane moves along the Earth orbit around the Sun, the spacecraft rotate about their X-axes at a rate of about  $1^\circ/\text{day}$ , while the X-axes precess at about the same rate.

### 9.1.2 Propulsion module

At launch, each spacecraft is attached to a propulsion module. The propulsion module provides the capability to maneuver the spacecraft/propulsion module composites into the final orbits, using solar electric propulsion ([SEP](#)).

After reaching the final orbits, about 13 months after launch, the propulsion modules are separated from the spacecraft to avoid having excess mass and solar panels near the proof masses within the spacecraft.

With the single Delta II 7925 H launch and the assumed excess energy of the initial orbit, the spacecraft will slowly drift behind the earth and a continuous low thrust will take the spacecraft to their final operations configuration in 400 days, using 19.1 kg, 13.9 kg, and 17.7 kg of xenon propellant, respectively (20 kg corresponding to a  $\delta V$  of 1305 m/s). The ion engine needs to generate about 20 mN of thrust, using about 500 W of electrical power. Various manufacturers have eligible thrusters. Two ion engines will be carried on each propulsion module, but only one will be used at a time. The second engine is for redundancy and balances the launch load.

For attitude and small orbit trimming manoeuvres, a monopropellant hydrazine system is provided. It is a simple blowdown system with one tank and four 4.45 N and four 0.9 N thrusters, requiring about 5 kg of hydrazine.

The propulsion module structure consists of a 1800 mm diameter central cylinder and two interface rings for the separation system. The total height of the P/M is 400 mm. The cylinder is constructed as a Carbon Fibre Reinforced Plastic ([CFRP](#)) honeycomb structure with a total thickness of 20 mm. The interface rings are made from aluminium.

For initial rate reduction and during orbit manoeuvres, rate sensors are desirable. The P/M therefore also accommodates two Inertial Reference Units (one redundant) and their electronics.

### 9.1.3 Launch configuration

The spacecraft size and shape are approximately optimized to contain the two optical assemblies within the payload thermal shield. This shape combined with the desire to fit the three spacecraft with their propulsion modules into the Delta II fairing places volume constraints on the propulsion modules.

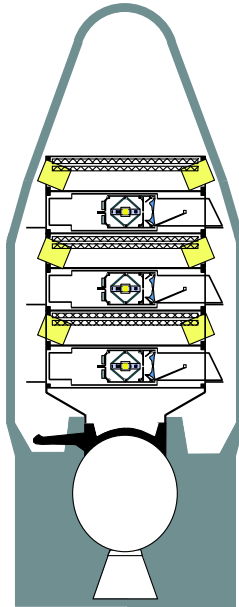


**Figure 9.2** The three *LISA* spacecraft, each with attached propulsion module, within the 9.5 foot fairing for the Delta II 7925 H. The launch stack is attached to the upper stage by a custom launch adapter. Baseline configuration of *PPA 2*.

As is shown in Figure 9.2, the available static envelope within the 9.5 foot fairing allows for the accommodation of the launch stack of three composites with a propulsion module on the top. Preliminary analysis has shown that the first lateral eigenfrequency of the lower stack meets the Delta II requirement ( $> 15$  Hz), and so does the first axial frequency ( $> 35$  Hz).

## 9.2 Spacecraft subsystem design

### 9.2.1 Structure

The spacecraft structure is composed of the following elements:

- An exterior cylinder with top and bottom plate to stiffen the cylinder and provide mounting points for the subsystems. Made from CFRP honeycomb with 0.3 mm CFRP skins and a 10 mm CFRP core.
- Interface rings at each side of the cylinder. These interface rings are made in AFRP (Aramid Fibre Reinforced Plastic) or Carbon/Carbon material.
- Two CFRP support structures for mounting the high-gain antennas and their pointing mechanisms.

The payload module, which on the outside includes a thermal shield made of CFRP with a thickness of 1.5 mm, is attached to the central cylinder, with a system of Kevlar straps.



The two startrackers are supported by suitable interface brackets on the [PLM](#) thermal shield.

### 9.2.2 Thermal control

The thermal control subsystem of the spacecraft is basically a passive system with heaters and their associated controls as the only active elements. All units will have primary and redundant survival heaters controlled by thermostats. These heaters will only be used during the transfer phase or in contingency situations. During the routine operational phase, operation of the heaters will not be required. All units attached to the side panels and the internal surfaces of the side panels will have low emissivity surfaces so that most of the thermal energy is radiated to space, via radiators on the side panels.

### 9.2.3 Coarse attitude control

The main requirements on spacecraft drag-free and attitude control derive from payload constraints. The drag-free control system must force the spacecraft to follow the proof mass to  $1 \text{ nm}/\sqrt{\text{Hz}}$ . The control signals are derived from the payload-provided electrostatic accelerometer as described in [Section 6.1](#). The attitude control system points each spacecraft towards the spacecraft at the other end of its optical path. The pointing tolerance is  $5 \text{ nrad}/\sqrt{\text{Hz}}$  for frequencies above about  $10^{-4} \text{ Hz}$  and  $30 \text{ nrad}$  for lower frequencies and DC. The operational attitude control signals for pointing of the Z-axis (telescope axis) will be provided by the main signal detecting diodes, the difference between the signals from their quadrants giving information on the wavefront tilt.

Initial beam acquisition will rely on the startrackers which are co-aligned with the main telescope. A pointing accuracy of about  $100 \mu\text{rad}$  is sufficient. Once this is established, the laser beam will be defocussed from its diffraction-limited divergence and imaged in the receiving spacecraft on the quadrant diodes. The resulting signal will be used to iteratively repoint the spacecraft until the laser beam divergence can be reduced to the minimum value.

The control torques and forces for the attitude and drag-free control during the operational phase are provided by the Field Emission Electric Propulsion ([FEED](#)) subsystem. The thrusters of this subsystem are composed of an emitter, an accelerator electrode and a neutralizer and use liquid cesium as propellant. Their specific impulse is of the order of  $10\,000 \text{ s}$  and they can provide a controlled thrust in the range of  $1$  to  $100 \mu\text{N}$ , with a noise below  $0.1 \mu\text{N}$ . Six clusters of four thrusters each are mounted on the spacecraft equipment panels. The major force to be compensated is the solar radiation pressure, which, if the spacecraft is completely closed on the top (thermal shield), has a magnitude of about  $50 \mu\text{N}$ .

As the drag-free and attitude control is so intimately related to the experiment and payload, a more detailed description of these subsystems is given in [Sections 3, 6.1 and 9.7](#), also including more details on the [FEED](#) thrusters. Because of this close relation, the drag-free control system is a [PI](#)-provided item and described in [Section 6.2](#).

During the early orbit and transfer phase, the primary attitude sensors to be used are the startrackers ([ST](#)) and Fine Sun Sensors ([FSS](#)) of the top spacecraft of the composite. As the startrackers cannot measure large rates, an Inertial Reference Unit ([IRU](#)) is required as primary sensor during some phase of the early orbit and transfer phase, e.g. during rate reduction after separation from the launcher, during slew manoeuvres and during  $V$  manoeuvres. The [IRU](#)'s will not be required during the operational phase and are mounted on the propulsion module.

During the initial Sun acquisition phase and during emergency safe modes, Sun Acquisition Sensors will be used.



### 9.2.4 On-board data handling

The spacecraft controller consists of two identical units operating in a String A and String B fashion. String B acts as a warm backup and receives state data from String A at specified intervals. String B will contain a watchdog timer to monitor String A. If this timer runs out, String B will take over as the primary spacecraft controller.

The spacecraft controller will perform the command and data handling functions, attitude determination, and control functions as well as processing science data. These functions include science and engineering data collection and data storage. Power to the controller will be supplied by the spacecraft.

A RAD 6000 flight computer as used in the Mars Surveyor Program is suggested for the spacecraft. It contains 128 Mbytes of DRAM and 3 Mbytes of PROM. The relatively low data rates for science and telemetry permits all data to be buffered and stored in DRAM on the flight computer board, thus reducing the subsystem mass and power.

### 9.2.5 Tracking, telemetry and command

The TT&C functions are provided by an X-band telecommunications system, consisting of transponders, a Radio Frequency Distribution Unit (RFDU) and antennas. The transponder subsystem features two basic transponder units, each with its own solid-state power amplifier. Each transponder operates with the receivers in hot redundancy. The transmitters are configured for cold redundancy and can be switched on and off by telecommand. The function of the RFDU is to control the routing of telecommand and telemetry data between the two transponders and the antennas. The signal routing provides efficient redundancy for both telecommand and telemetry functions.

During the operational phase, two steerable high-gain antennas configured on top of the spacecraft are used. These have a diameter of 30 cm and a nominal boresight gain of 25 dBi. The 3 dB two-sided beam width of the antenna is about  $8^\circ$  and an elevation mechanism can be avoided. A mechanism providing  $2\pi$  coverage in azimuth is required, however.

To obtain the required omni-directional coverage for telecommand, two low-gain antennas are mounted on opposite sides of the spacecraft. These, however, cannot provide for the telemetry during the transfer phase, and medium gain antennas, accommodated according to the spacecraft-Earth direction during the transfer, are required.

### 9.2.6 Power subsystem and solar array

Each LISA composite consists of two modules. A propulsion module jettisoned at the end of cruise, and a sciencecraft module. The sciencecraft is a flat cylinder, 1.8 m in diameter by 0.5 m thick. An external sunshade is added to the outer sciencecraft edge on the sun side. This shade combined with the nominal sciencecraft flat surface provides a total sun-facing diameter of 2.2 m with a total surface area of  $3.8 \text{ m}^2$ .

The orbital configuration allows the sciencecraft to be in sunlight at all time, with a maximum off sun angle of  $30^\circ$  (during science operations). Sun facing surfaces are expected to reach  $80^\circ\text{C}$ . GaAs solar cells with 19 percent efficiency are used for power generation for both the sciencecraft and the SEP arrays. The batteries are of the Lithium-ion type, providing 80 Whr/kg specific energy density and 140 Wh/l volumetric density. Integrated Multichip Module to VME board technology is used for power control, management and distribution, and laser pyro drivers. This technology is expected to be demonstrated and qualified before 2001.

## 9.3 The revised spacecraft design

### 9.3.1 The constraints

At an early stage in the [LISA](#) study, a number of constraints were recognised that dictated to a large degree how the satellite element of the [LISA](#) mission would be configured. These still hold. The first constraint involves the method of transfer from a point near the Earth at escape velocity, to the operational orbit and location of each of the three identical spacecraft that form the mission constellation. It was concluded that each of the 3 vehicles shall be delivered by its own propulsion system, rather than having one large propulsion system to deliver each one after the other to the three different operational orbits.

The second factor was the decision to have for each satellite a separate and separable propulsion module. This choice removes all the potential disturbances on the operational satellite that could be caused by the remainder of the transfer fuel and the large solar array required for the ion motors in the transfer phase.

The third factor driving the configuration is the [LISA](#) instrument. This is a large Y-shaped fork whose dimensions are such as to dictate that the satellite configuration is formed around the instrument.

The fourth factor is the launcher selected as baseline for the study. The available volume under the fairing compared to the dimensions of the instrument forced the three satellites and their propulsion modules to be a vertical stack with each instrument fork laid across the stack. The resulting height of this stack limited the overall diameter of both the science and the propulsion modules, because the stack, including a launch adapter, intruded into the conical portion of the 9.5 ft fairing.

These factors and decisions had already been recognised in a previous study [1], and resulted in the configuration shown in [Figure 9.1](#) and [Figure 9.2](#). Here a stack of three satellites (named science modules) and their associated propulsion modules are seen in the original baseline Delta II 7925 H launcher with the 9.5 ft diameter metal fairing. The launcher performance then placed a limit on the maximum mass each satellite could have, and this allowed a total launch mass of 1407 kg.

The direction of illumination from the sun in operational orbit also played a part in the overall configuration.

The two arms of the instrument fork are aligned along the optical axes of the laser telescopes contained in these arms, which are at  $60^\circ$  to each other. The plane containing the optical axes is itself at  $60^\circ$  to the sun-satellite line. This means that the sidewalls of the science module must then be conical with half-angle  $30^\circ$  to avoid sun illumination, making the anti-sun surface smaller in diameter than the sun face with its solar array.

Two basic assumptions regarding the configuration were also made for the earlier study. The first was that the basic structure was a cylinder, carried through each science and propulsion module, with appropriate separation mechanisms. The second was that all the electronic and mechanical units could be accommodated within the volume between the instrument fork and the cylindrical walls, plus the small volume available outside the cylinder, allowing for the restriction caused by the conical outer side walls.

### 9.3.1.1 Review of the science module configuration concept approach

To ascertain whether the configuration concept of the earlier study could be confirmed, or whether any changes or alternative concepts were necessary, it was first necessary to establish the subsystem elements definition, for mass, thermal dissipation, power consumption and size. This also applied to all the units associated with the payload experiment.

The extent to which the payload in particular has demanded more mass than originally foreseen can be seen from Table 9.1 (the original list is in Table 9.2). This is partly due to a reassessment of which units can remain in the Y-fork tubes while maintaining the stable thermal conditions in these tubes.

It then became clear that the originally conceived volume was inadequate, and that the baseline science module constraints must be reassessed.

It was initially thought that all the units must be mounted directly to the radiator on the anti-sun side of the spacecraft, to assist in the thermal stability of the satellite interior. Further, since the side walls of the satellite “cylinder” should also not be illuminated by the sun, this anti-sun area is more limited than the surface under the solar array panels.

**Table 9.2** *Original payload definition at start of study*

Unit/Element	No. of Units
Fork assembly	1
Payload shield	2
Laser Electronics	3
Laser	4
UV Unit	1
Radiator plate	1
Total Mass	84.2 kg

### 9.3.1.2 Amendment to Launcher Baseline

The first relaxation in this situation was to allow the use of the newer 10 ft composite fairing for the Delta II, which replaced a heavier metal one. In consequence the launcher performance was not significantly reduced (1380 kg down from 1407 kg), while gaining significantly in volume. The full 10 ft diameter is advantageous since the cylindrical portion of this fairing is longer than that of the 9.5 ft fairing. That new launch configuration is shown in Figure 10.3.

### 9.3.1.3 Assessment of structural/mechanical concept

The major change was the use of the triangular rather than the circular structural wall concept. This is mainly a consequence of a review of the separation joint concept for the stack of modules. It also has the fortunate advantage of being more efficient for unit accommodation than the circular concept as originally conceived.

**Table 9.1** *Payload and platform unit definitions*

Unit	No.	Total Mass [kg]
Laser head (incl. phase mod)	4	8
Laser head electronics	2	4
USO	2	0.8
Inertial sensor	2	13
IRS Electronics	2	4
UV box	2	1
Interfer. analogue elec.	2	3
Interfer. digital elec.	2	7
Instrument control elec.	1	4.5
Optical bench	2	11.2
Fibre Positioner	2	0.6
Telescope	2	13
Optical assy. structure	2	10
Optical assy. mechanisms	2	4
Optical assy. thermal	2	2
Str/Therm. shield	1	13
Total		99.1

The change to a triangle formed around three strong columns is also a consequence of reviewing the instrument fork structure and its mounting. It is necessary to retain the outer fork of two tubes and the “root” as a stand-alone structure containing the instrument telescope elements and front end electronics.

To avoid any undesired distortion and thermal effects from the main structure feeding into the fork, and thus its internal elements, the attachments for the fork must be so designed to carry the expected loads but be so arranged to minimise carry-over of distortions. This means the walls themselves should not be the main load carriers throughout the entire satellite stack as were the cylindrical walls. The introduction of the columns is then necessary for the transfer of loads between stacked satellites.

The ends of these columns are used as the load transfer points between modules and are fitted with hold-down and release mechanisms. These mechanisms form two groups. The first group connects each science module to its partner propulsion module forming a combination, and the second group connects each module combination to each other, and the lowest to the launcher

adapter.

These mechanisms carry the high launch loads, and after launch each science/propulsion module combination is released to enter its own unique transfer orbit. The separation shock caused by these mechanisms are not significant for this operation. However, for the separation of science and propulsion module at the operational orbit they become important. The science module is only equipped with **FEED** thrusters, and these cannot deal with high tip-off rates at separation. The separation must thus have a very low tip-off rate and a low separation velocity. To achieve this a fourth separation mechanism is incorporated at the centre of the circular anti-sun face of the science module and the adjacent propulsion module face, and does not carry the main launch loads. First the three main mechanisms are released, but the combination remains together using the central attachment. This, with its small separation forces, is then actuated to perform the delicate separation of the propulsion module in the operational orbit.

The consequence of the adoption of the three-column approach is that a dedicated adapter must be developed for the Delta II to interface with the three load-carrying columns of the payload.

To ensure that the structure modal response remains comfortably within the requirements of the launcher, the upper and lower circular plates of the science module are joined around the rim by a conical wall, broken where necessary for telescope apertures and the rear fork radiator. Holes or cut-outs in the solar array caused by interfaces between modules are minimised by using the 3-column approach. This eases the accommodation of solar arrays, especially for the propulsion module, which requires a large area and further avoids the implementation of deployable panels for the propulsion module.

#### 9.3.1.4 Other unit accommodation aspects

Using the revised structural concept, a review of all the units and elements to be accommodated in the science module was undertaken. Allowing for the small but significant growth in the assumed telescope outer tube diameter, driven by mirror mounting constraints, it was possible to mount some of the units on the backside of the sun illuminated wall. The volume and surface areas then proved adequate, as is seen in the internal layout shown in Figure 9.3.

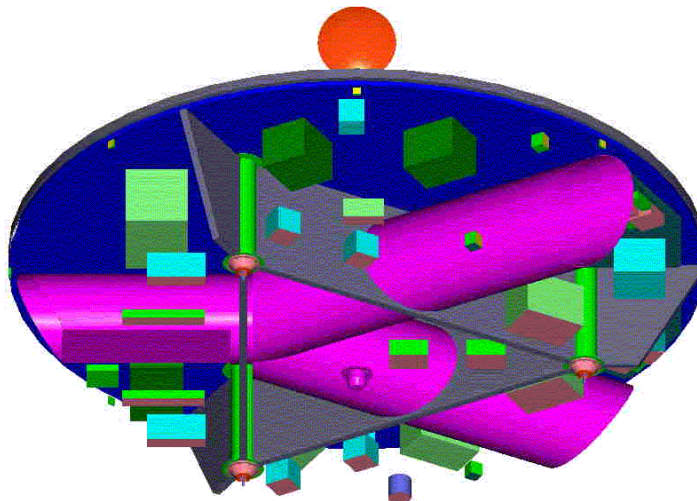


**Figure 9.3** *Internal layout of the science module*

The star trackers are collocated alongside the two telescope apertures and aimed in the same

directions, so that each telescope has one coaligned **ST**. The telescope baffles themselves have ejectable doors, necessary to prevent sun radiation damage during the **LEOP** and transfer phase when the satellite combination may assume any attitude.

The thrusters are required to be arranged as in Figure 9.4.

This means that they may be conveniently be attached to the supporting triangular substructures on the periphery of the larger science module upper structural plate. They are also thus located away from the telescope apertures, avoiding contamination of the optics.

It is essential that the main internal volume of the science module has stable and moderate thermal conditions. To achieve this there is an additional thermal shield plate attached to the sun facing circular surface by thermally isolating mountings with a small gap between the thermal and structural plate. This thermal shield can then carry the relatively small solar array on its front face and thus also protects the structure from thermal heating effects of the solar array itself.

It should be noted that the science module carries no battery, since no failure case is envisaged where solar power is not available. Power for heating during the transfer phase must then come from the propulsion module, with the corresponding electrical connecting interfaces between science and propulsion module.

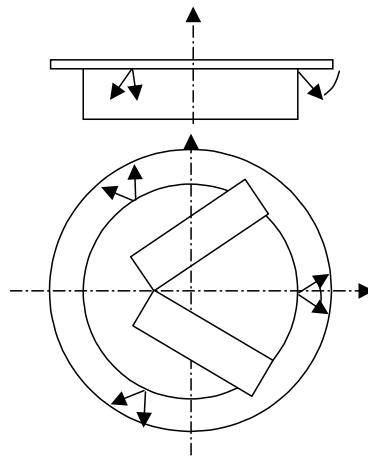


**Figure 9.4** *FEEP Thruster arrangement*

### 9.3.1.5 Communications antenna mounting

External to the science module satellite body are the communication antennas. There are 4 basic configurations for the antenna, which consists of a 30 cm diameter dish and feed pointing at Earth about  $10^\circ$  away from the plane of the front face of the science module towards the sun. A  $360^\circ$  rotational scan of the antenna around an axis perpendicular to the module front face plane is also required during 1 year.

There are the following four options for the antenna mounting:

- 1 A central antenna on the sun face is the obvious candidate if the science module was on its own. However the limited stack height drives the option to need either a large hole in the modules above it, or a stowage mechanism that would still be too thick for the total allowable stack height.
- 2 A single antenna at the anti-sun side has the additional disadvantage of requiring a long post to allow the antenna to look past the satellite rim with the required  $10^\circ$  angle, as well as a

stowage mechanism with the disadvantages of option 1. Also the post and its joints must be very stiff to avoid disturbances to the science measurements.

- 3 Two antennas, each with  $180^\circ$  motion on opposite sides of the science module seem attractive, as this saves on stack height. However, too much of the module body must be cut away to allow a satisfactory field of view at the limits of the  $180^\circ$  arc.
- 4 Utilising the concept of option 3, but with the advantages of option 1 in being mounted on the front face of the satellite. There is enough volume available at the rim of the science module due to the conical shape of the body to allow the antennas from one module to intrude into the vacant space of the module above. Two antennas are needed since both must be moved in unison to minimise the disturbances to the science measurements.

This Option 4 is the option that has been selected for all the above stated reasons.

#### 9.3.1.6 Factors influencing the science module height

In minimising the height of the science module cylinder, some factors need to be taken into account.

To accommodate the nominal 300 mm diameter instrument telescope mirror, mountings and alignment equipment, the outer diameter of the instrument fork structure tube is around 400 mm. Additionally the solar array is mounted directly on the thermal shield with a gap between the shield and the main module. When the science module structure, thermal shield and separation mechanisms are taken into account, then the total height of the science module is 592 mm, for an overall diameter of 2700 mm, matching the 2743 mm available from the 10 ft fairing. This is seen in Figure 9.5 below.

The resulting overall configuration of the Science and Propulsion module combination is shown in Figure 9.6 and Figure 9.7.

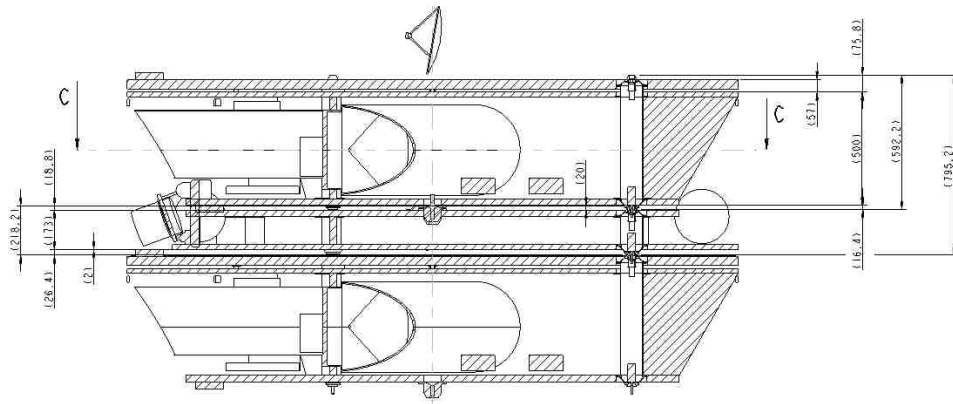


**Figure 9.5** *Cross section of one propulsion module sandwiched between two science modules*



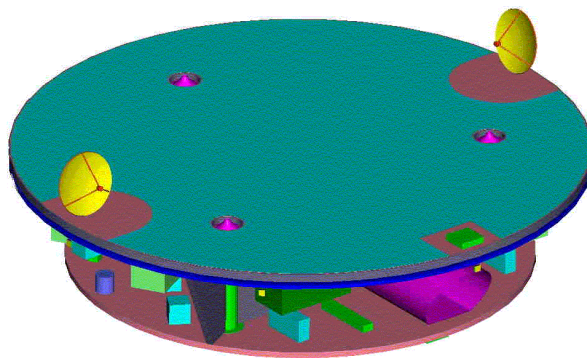


**Figure 9.6** *Overall Configuration of one science module*

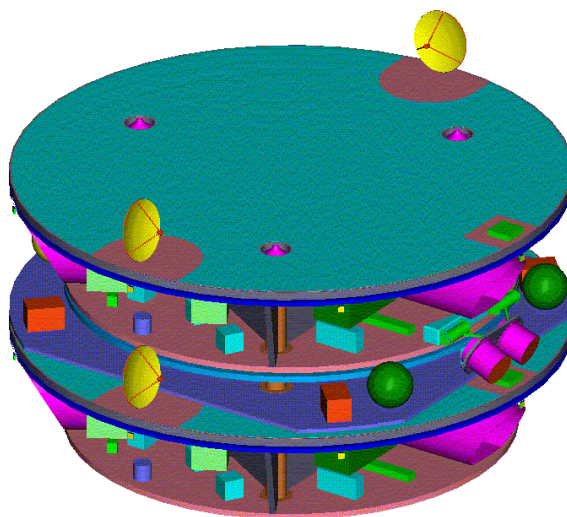


**Figure 9.7** *Overall Configuration of one propulsion modules between two science modules*

## 9.4 Structure and Mechanisms

### 9.4.1 Requirements

#### 9.4.1.1 Compatibility with the Delta II launch

The [LISA](#) spacecraft design shall ensure compatibility with a Delta II launch. Although this launch vehicle will most probably no longer be available at the envisaged launch date, it shall be shown that a spacecraft design with the limited mass and volume capacity of a Delta II class launcher is possible.

- The resulting limitations on spacecraft size and mass have been discussed in Section [9.1.1](#).
- The required minimum fundamental frequencies are 15 Hz for the lateral modes and 35 Hz for axial modes, which are values typically found for several launchers
- The Delta II only allows for a limited distance of the spacecraft [CoG](#) from the separation plane resulting in severe limitations on spacecraft height



- A clamp band fixation shall be avoided for mass saving reasons, thus loads have to be transferred via individual separation devices. Although the 3-stage Delta II only provides clamp band interfaces, the 2-stage 6915 PAF adapter was considered, assuming that it would be possible to adapt it to the 3-stage launcher.

#### 9.4.1.2 Launch in a stack

The launch has to be performed in a stack of three science modules (S/M) and three propulsion modules (P/M). Separation into three pairs of S/M and P/M occurs immediately after separation from the launch vehicle, the separation of S/M and P/M occurs only after achieving a final operational orbit. Thus:

- 6 separation planes with the associated separation mechanism, interface fittings and connectors are needed
- The individual modules, especially the P/Ms have a very small height to diameter ratio. The structure has to accommodate the units under these conditions
- The separation devices have to be compatible with
  - the loads to be transferred
  - the transfer phase duration of one year
  - a final orbit achievement accuracy of 0.3 cm/s
  - electrical connectors between S/M and P/M
- the antenna has to be accommodated in a way that does not interfere with the stacking.

#### 9.4.1.3 Payload performance related

In order to limit the disturbances on the payload specific constraints result:

- The solar array has to be thermally decoupled from the spacecraft. The solar array it self has to provide shielding of temperature fluctuation for which a core layer of 20 mm Polyimide foam is needed. The equipment accommodated on the top of the solar array (e.g. sun sensor, antenna) shall preferably be mounted on the outer face sheet. If this is not possible, the mounting has to provide a very efficient thermal decoupling.
- The fixation of the payload Y-shaped tube has to account for differential thermal deformation. Due to the required stability of the gravitational field, deformations occurring on the spacecraft side may not be transferred into the payload tube. A thermal decoupling is also needed, however less stringent than in the case of the solar array because the radiative coupling is dominating. This is not a design driver because it will be automatically provided as a side effect of the required mechanical decoupling.
- For thermal and configuration reasons, the heat rejection of the units can occur to the conical rim of the spacecraft. In this direction only one wall between any dissipating unit and space is acceptable.

### 9.4.2 Structure Design

#### 9.4.2.1 Science Module

The principle design of the science module structure is shown in Figure 9.8.

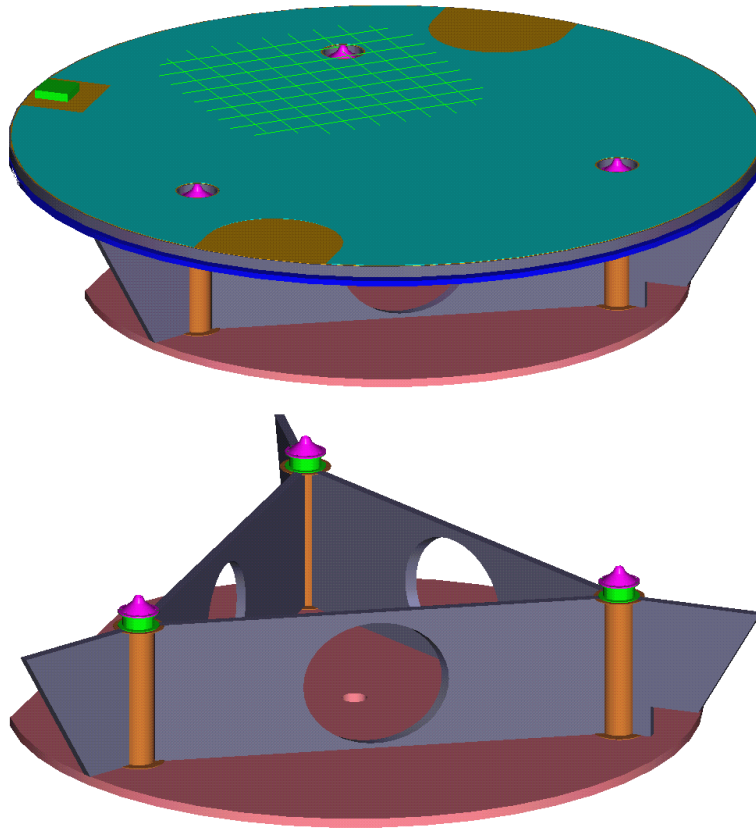


**Figure 9.8** Science module structural design: Upper figure: top and bottom plates, connected; Bottom figure: showing the three connecting Al tubes and the triangular shear wall between them. Holes to accommodate the Y-shapes Payload.

In the Science module the three tubes are connected by a shear wall. These tubes provide for

- Overall lateral bending stiffness of the stack
- Mounting provision for the payload Y-shaped tube
- Transfer of loads from the top and bottom plate into the tubes
- Stiffening of top and bottom plate

All equipment outside the payload Y-shaped tube is accommodated on the top and bottom plate. From the thermal stability point of view it is required to place all dissipating units on the bottom plate. This was not possible because of lack of available space. A less favourable, but still acceptable place are the areas on top and bottom plate close to the rim. This now leads to a mechanically unfavourable mass distribution. Besides the stiffening provided by the shear walls, also the conical rim of the module has to be closed by a conical panel.

Considering the stiffness and thermo-elastic behaviour, an all aluminium structure could be used. However, for mass reasons, CFRP panels with aluminium honeycomb are needed. The solar array panel serves as a thermal shield. Initially a sandwich with pure foam core was selected. However, this did not provide sufficient stiffness. Thus a double sandwich with a foam core for thermal isolation and a aluminium honeycomb core for stiffness is used. The solar array is mounted on 13 thermally insulating attachment provisions.

Main plates: 30 mm sandwich consisting of 0.5 mm CFRP face sheets and an aluminium honeycomb core with a density of  $50 \text{ kg/m}^3$

Stiffening Webs: 20 mm sandwich consisting of 0.5 mm CFRP face sheets and an aluminium honeycomb core with a density of  $50 \text{ kg/m}^3$

Connecting tubes: Aluminium tubes with outer diameter 100 mm and 2.5 mm wall thickness

Solar array: sandwich consisting of: (starting from solar cell side)

- 0.6 mm CFRP facesheet
- 20 mm polyimide foam
- 0.6 mm CFRP facesheet
- 20 mm aluminium honeycomb core
- 0.6 mm CFRP facesheet

#### 9.4.2.2 Propulsion Module

The structural design of the propulsion module is shown in Figure 9.9. The main driver is the very small available height. For thermal reasons, the solar array panel cannot be used for unit accommodation. Therefore, all the propulsion module units have to be accommodated on the module rim.

Instead of the triangular shear walls, a cylinder is used in order to also provide for a stiffening of the panel at the outer rim. This is still not sufficient, additional webs have to be used locally at unit mounting positions. The top plate is needed for the solar cell fixation. Some mass savings could be cut-outs in the bottom plate.

In any case the very stringent limitation in height does not allow to apply lightweight design principles. Essential mass savings can only be achieved by material selection, e.g. by using CFRP facesheets composed of strands with some spacing between each other.

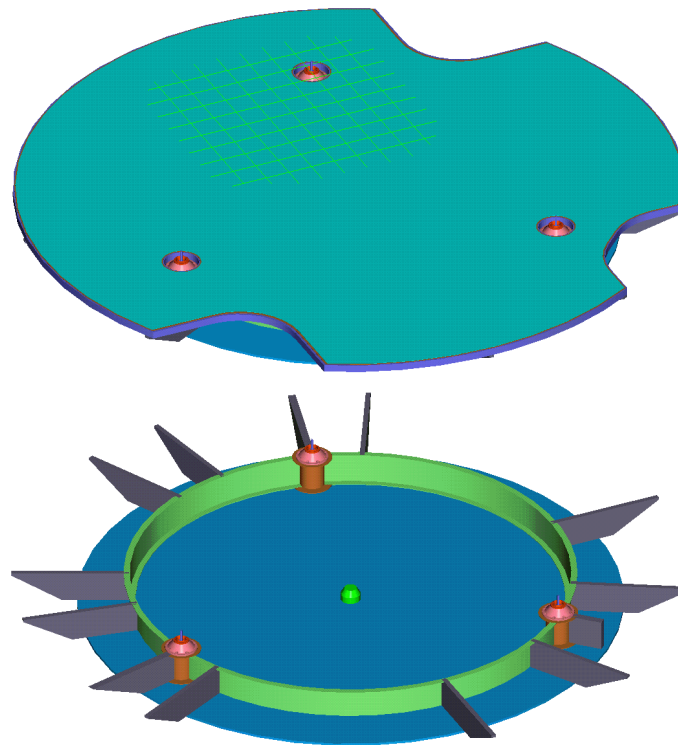


**Figure 9.9** *Propulsion Module structural design*

### 9.4.3 Structure Performance

#### 9.4.3.1 Stiffness

The stiffness of the overall spacecraft is defined by the minimum fundamental frequencies which have been determined in a [FEM](#) analysis. The achieved frequencies are well within the Delta II requirements of  $< 15$  Hz for the lateral and  $< 35$  Hz for the axial modes.

#### 9.4.3.2 Stability

Generally an aluminium structure should be preferred because of the better stability from ambient to vacuum due to moisture release. The advantage of the smaller coefficient of thermal expansion can hardly be used because the electronic units present most of the mass and show the largest temperature fluctuations. Using a different material than aluminium for housing of the electronics seems not to be feasible. Thus the fluctuations of the gravity field would be determined by the thermal deformation of the units themselves. Except for the very high modulus carbon fibres, the thermal conduction of aluminium is higher than that of [CFRP](#).

Use of an all aluminium structure avoids the problems of moisture release. The created thermal deformations have a magnitude that can not be avoided anyhow as long as aluminium housings are used. Aluminium allows for a more uniform temperature distribution which can even reduce the thermal deformation effects.

### 9.4.4 Mechanism Design

#### 9.4.4.1 Spacecraft separation mechanism ([SSM](#))

The [SSM](#) separates the three spacecraft from the launcher. After separation from the launcher the spacecraft are separated from each other. In all cases the same mechanism will be used. The mechanism has to separate at the 3 interface points provided by the launcher. Between each spacecraft, the same arrangement of interface points is given due to the tubes used for load transfer through all spacecraft. A cup-and-cone connection will be used, the fixation is provided by a preloaded bolt which is separated by a Pyronut. Such a mechanism has already been defined in the [DSS](#) phase A study for Mars Express.

#### 9.4.4.2 Module separation mechanism ([MSM](#))

The separation into modules is done at the final orbit position. The orbit position has to be achieved with a very high accuracy, the allowable uncertainty must be less than 3 mm/s. Since the science module attitude control relies on the [FEEPs](#) which only provide very low thrust levels, also the rotation rates after separation have to be limited to less than 1 mrad/s. Electrical connection between the 2 modules is needed during transfer phase. Thus also an electrical connector has to be separated.

Separation will be performed in two steps:

- Immediately after injection into the transfer orbit, a separation of the load carrying parts will be done. This is a mechanism identical to the one used for [SSM](#). This avoids cold welding effects during transfer. During transfer a spindle will maintain both spacecraft connected to each other. The interface forces only result from the ion thrusters which is less than 0.1 N.
- After injection into the final orbit the spindle drives will be operated to separate the two modules. The separation direction has to be fixed by the propulsion module [AOCS](#), the

spindles will than produce an exactly defined separation velocity, high enough to bring them at a safe distance in an acceptable time. The solar radiation pressure will ensure steadily increase of this separation.

## 9.5 Thermal control

### 9.5.1 Requirements

#### 9.5.1.1 Temperature requirements

The standard requirement is as always to maintain the temperatures within their acceptance temperature range. Besides that there are two important requirements on temperature stability and on stability of a temperature gradient within the measurement frequency range:

- Minimise temperature fluctuations on the optical bench with a goal of  $\Delta T \leq 10^{-6} \text{ K}/\sqrt{\text{Hz}}$ . The requirement actually results from optical path length variations within the laser cavity and thus potentially only applies locally. The required value rather represents the value found to be achievable in Pre-Phase A and is considered as a design goal
- Maintain the fluctuation of the temperature difference across the proof mass cavity below  $\Delta(\Delta T) \leq 2 \times 10^{-5} \text{ K}/\sqrt{\text{Hz}}$ .

#### 9.5.1.2 Implicit thermal requirements

Implicit requirements result from requirement on the gravitational field. They concern both, the long term drift and the stability within the measurement frequency range.

- Long term drifts in the temperature field shall be limited such that changes in the self-gravitation field are  $\Delta a \leq 10^{-9} \text{ m s}^{-2}$ .
- the temperature stability of the spacecraft shall provide a stability of the self-gravitational field of  $\widetilde{\Delta a} \leq 10^{-15} \text{ m s}^{-2}/\sqrt{\text{Hz}}$ .

The effect on the gravitational field strongly depends on the distance from the proof mass location. In order to provide a guideline for the thermal design a temperature fluctuation budget can be established. If it is assumed that all items contribute statistically to the overall disturbance and if the mass of all individual items is in the same order of magnitude, a budget only depending on the distance from the proof mass can be established. The acceptable values under these assumptions were analysed for short-term and long-term behaviour, and they can be used for preliminary judgment on the acceptability of unit temperature fluctuations without the need to perform an overall thermo-elastic and gravitational analysis.

### 9.5.2 Thermal design

#### 9.5.2.1 Science module

The thermal design principle is shown in Figure 9.10. As a general design principle no MLI has been used in order to prevent any effects from changing properties due to crinkling by thermal or ageing effects.

The solar array is used as sun shield in order to isolate the science module from the disturbances created by the solar constant fluctuations right at the source. All areas not needed for solar cells will be covered with SSM to minimise the absorbed solar flux and to reduce the solar array

temperature. The reduction in temperature reduces the radiative couplings and thus improves the isolation. No illumination of any other science module surface shall occur. The size of the solar array is limited by the launcher fairing diameter. Thus all other external surfaces have to be within a  $30^\circ$  cone behind the solar array. By this approach only the solar array experiences temperature fluctuations due to the solar constant variation.

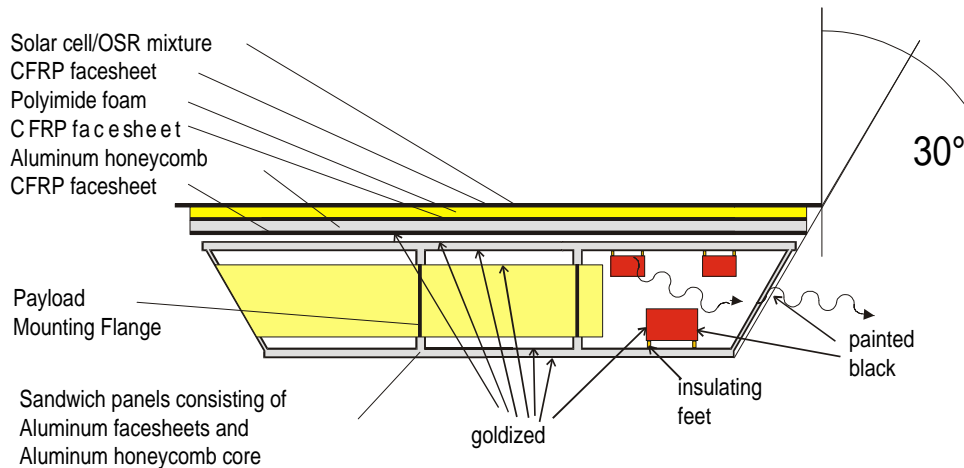


**Figure 9.10** *Thermal design principle*

The transfer of these temperature fluctuations into the science module needs to be minimised by an effective thermal decoupling. The solar array panel is built-up by CFRP face sheets with a polyimide foam core. This reduces the transfer of temperature fluctuations to the solar array rear side by both, insulation and thermal capacitance. On the rear side insulating fixation elements are used for mounting the solar array to the structure. A main contributor is the thermal radiation from the rear side because of the large area and the direct transfer to the payload tube. This is limited by a gold coating on all surfaces in the view of the solar array rear side and the solar array rear itself.

The sensitive payload parts are accommodated within the Y-shaped tube, therefore the tube surface is goldized to provide radiative decoupling also on the inside. The mounting of the tube is via a thin walled flange to accommodate differences in coefficient of thermal expansion, further decoupling is not needed because of dominating radiative coupling

Difficulties arise from the disturbances in dissipating of the electronic units. Ideally they would all be mounted on the rear side of the science module, insulated from the structure as good as possible and directly reject their heat to space. This is not possible for accommodation reasons. Both, bottom and top plate of the structure have to be used for the mounting of the units. In order to limit the transfer of temperature fluctuations from these units to the structure, they are mounted on insulating feet. Heat rejection is done by radiation the science module side wall which acts as a screen radiator. The radiative coupling from these units to the payload tube is reduced by covering the areas with direct view to the payload tube with gold. For smaller boxes eventually doubler plates have to be used or such units have to be mounted on the bottom plate for direct heat rejection. Due to the current status of design this is not yet investigated in detail

The payload tube is very well decoupled from the rest of the science module, this efficiently filters temperature disturbances and allows a very stable optical bench. The telescope will be provided with low emissivity coatings as far as possible to thermally de-couple from the tube. The temperature level inside the optical bench is only determined by the dissipation inside the

tube and the remaining small radiative exchange through the telescope aperture. A calculation of actual temperature level will contain high uncertainties and the system will react very sensitive to parameter changes.

### 9.5.3 Thermal performance

#### 9.5.3.1 Temperature level

The temperatures of electronic unit can be adjusted by the size of the conical radiator. A trimming of this radiator was performed in order to achieve an overall temperature level of about 20°C. The actual temperatures of the units were determined, for different scenarios, and they range from 97°C for the solar array to −15°C for the telescope primary mirror.

All units have to reject their heat by radiation from their housings. Due to the varying ratio of unit size to unit dissipation, the actual temperatures cover a rather wide range which gives in some cases values outside the acceptable temperatures. Therefore, this range needs to be reduced by an individual trimming of the units. For hot units this can be achieved by placing a doubler plate under the unit, cold units can be covered with low emissivity coating. This also needs to be addressed in conjunction with the transfer of temperature disturbances to the payload, this needs a low emissivity on the unit areas facing the Y-shaped tube. This type of design activity needs to know the exact shape and dissipation of each unit. Since major changes are expected towards the real start of LISA phase B activities, the detailed thermal design was not covered in detail. The overall solution is compatible with the system needs, for the trimming of individual units sufficient trimming capability is available and this also allows for sufficient growth potential of the system.

#### 9.5.3.2 Temperature stability

With respect to temperature stability the following cases have to be considered:

##### **Temperature fluctuations due to solar constant fluctuation.**

The fluctuation of the solar constant is given as a spectral density, thus it is only required to determine the frequency dependant transfer function. This was done by performing a transient thermal analysis at three different frequencies. The temperature response is always decreasing with the frequency, thus three cases are sufficient. The solar constant fluctuation is given as

$$1.75 \left( \frac{f}{1 \text{ mHz}} \right)^{1/2} \text{ W m}^{-2}/\sqrt{\text{Hz}} \quad (9.1)$$

in the Pre-Phase A Report. The thermal analysis made use of rounded values.

For frequencies around  $10^{-4}$  Hz, the transfer functions would be  $2.9 \times 10^{-7}$  K/W for the optical bench, and  $2.6 \times 10^{-7}$  K/W for the primary mirror.

The issue for the performance is the temperature difference across the proof mass cavity. This temperature difference is not represented in the model because it depends too much on the actual configuration which is not known in full detail today. However, the fluctuation in temperature difference will be similar to the fluctuation in temperature level on the optical bench. The actual fluctuation of the temperature difference will be at about  $1.1 \times 10^{-6}$  and will thus be a factor of 20 better than the requirement.



### Temperature fluctuation due to a correlated fluctuation of unit dissipations

Such a correlated fluctuation could occur due to fluctuation in the voltage of the power supply or due to operation profile characteristics with effect on the dissipation of many units. Only the lowest frequencies are of concern in this case. The resulting temperature amplitude can be taken to determine the maximum acceptable dissipation fluctuation. Once a transfer function from voltage to dissipation fluctuation is known, a requirement for the voltage stability can be derived. The dissipation stability's can be specified in terms of spectral densities, respectively in terms of upper limits to the response to voltage fluctuations. Therefore it was sufficient to consider only the lowest frequency which is the worst case A . In Table 9.3 the resulting temperature fluctuations and transfer functions are summarised.

As for solar constant fluctuation, the temperature difference across the proof mass cavity is important. The required  $2 \times 10^{-5} \text{ K}/\sqrt{\text{Hz}}$  are exceeded. The correlated fluctuation of dissipations should be less than 0.2 %.

**Table 9.3** *Temperature fluctuations due to 1 % dissipation variation in the electronic units, at  $10^{-4} \text{ Hz}$*

	Temperature Response in K	Transfer Function in K/ppm
Optical Bench	$6.5 \times 10^{-5}$	$6.5 \times 10^{-9}$
Titanium Housing	$2.0 \times 10^{-5}$	$2.0 \times 10^{-9}$
Primary Mirror	$3.0 \times 10^{-5}$	$3.0 \times 10^{-9}$
Secondary Mirror	$5.0 \times 10^{-5}$	$5.0 \times 10^{-9}$
Payload Analogue E-box	$1.0 \times 10^{-3}$	$1.0 \times 10^{-7}$
Payload Digital E-box	$1.0 \times 10^{-3}$	$1.0 \times 10^{-7}$
USO box A	$8.5 \times 10^{-3}$	$8.5 \times 10^{-7}$
USO box B	$8.5 \times 10^{-3}$	$8.5 \times 10^{-7}$

### Temperature fluctuations due to single events

Such single events are e.g. switch on and off of the down-link assembly. Although it is foreseen to keep all components permanently switched on, this case was used to establish an upper limit for any single event dissipation change. For the resulting temperature disturbance a spectral analysis has to be performed in order to achieve the resulting spectral densities in temperature fluctuation. However, the result also depends on the bandwidth which is used to derive spectral density from the amplitude at discrete frequencies. For this case a more specific definition of the requirement is needed.

In the analysis a down-link event leading to an additional dissipation of 36 W over 3 hours was considered. The resulting temperatures of optical bench, titanium housing and the temperature difference between both was calculated.

In order to check against the temperature fluctuation requirements, a Fourier analysis has been performed. From the Fourier coefficients the spectral densities were then derived using 1-octave intervals. The same spectral analysis was also performed for the temperature difference. It can

be seen that in the interesting frequency range the spectral densities of both are almost the same.

The result was that the response (to the 36 W surge) is about a factor of 100 above the requirement. Thus any switch-over in electronic units needs to be limited to less than 0.36 W.

### 9.5.3.3 Verification of thermal performance

Because of the specific thermal design of the science module, the verification of the system will be difficult and has to be investigated in detail at an early stage. For the verification of “standard” thermal requirements the simple environment will allow end-to-end verification by test. However, the extreme thermal decoupling will result in very long stabilisation periods.

For the verification of temperature stability requirements test chamber environment will not be sufficiently stable. Also the long stabilisation period will only allow for few parameters to be tested. Therefore the verification has to be performed in terms of transfer functions.

Verification of the acceleration noise requirements has at least to be supported by analysis. The acceleration noise calculation needs knowledge of displacements of science module. Anyhow, the structure can only reduce acceleration noise by material selection. TCS has to reduce disturbances from solar constant and unit dissipation fluctuations. From achievable TCS filtering, the upper limit of unit dissipation fluctuations can then be established in terms of dissipation fluctuation spectral density and worst case dissipation profile in time domain. These are then the parameters that can be tested, for all the remaining ones one has to rely on analysis.

## 9.5.4 LISA spacecraft system options and trade-off

### 9.5.4.1 Configuration concept options and trade-off

The design of the spacecraft stems from a trade-off of several issues. Some options, though now dismissed, will be briefly listed.

The configuration concept of the LISA spacecraft is dictated by two factors. The first is the large instrument assembly for the two laser telescopes, and the second is the restriction from use of the Delta II launcher.

The possible concepts for carriage of three identical spacecraft have then to be of a short cylindrical form. Within this form two basic arrangements are possible:

- Integrated science module (instrument, bus) and propulsion module.
- Autonomous science module as one element, and a separable propulsion module.

The propulsion elements are to provide the energy for transfer from near-Earth to the operational orbit.

It was decided early in the study to choose the separable version, due to the potential disturbances to the science operation by the propulsion elements that may deteriorate measurement accuracy. Only the separable version has thus been considered in detail and represents the baseline concept.

It had been briefly discussed early in the study to use one or all of the separated propulsion modules during the operational mission phase as data relay stations to earth, a concept, having some advantages for the communication link. However, due to the then increased complexity of the whole mission operation and the availability of alternative solutions for communication this option has not been pursued.

Further trade-offs to be considered for the instrument and bus (science module) configuration are as follows:

- Optimisation of diameter to height
- Location of star trackers
- Structure concept for the carry-through structure of the stack of three spacecraft combinations
- Optimisation of unit accommodation within the allowed volume
- Thermal measures to allow for the inclined flight attitude of the satellite to the sun-satellite line
- Accommodation of the link antenna
- Accommodation of the [FEEP](#) thrusters
- Arrangement of the propulsion motors to allow for centre of gravity movement during transfer orbit

These factors do not allow a clean and simple classical trade-off, since almost all the items are related to each other. In consequence the derivation of the optimised configuration is discussed further in Section [9.3](#) and forms part of the description of the final concept.

### Integrated module concept

Driven by the requirement to minimise the stack height of the three spacecraft configuration, as dictated by the launcher selection, the propulsion module comes out as a very flat cylinder, surrounding the science module (see Section [9.4](#)). This has negative consequences for the structural concept and solar array arrangement, increasing e.g. the mass budget. Hence, re-consideration of the integrated module configuration, taking into account these constraints may be of interest in further studies. Of course, the concerns related to the instrument operation remain valid:

More components need to be included into the detailed thermal and gravity model to model gravity effects at the proof mass locations. Especially critical are uncertainties in remaining propellant distribution from the coarse [AOCS](#) subsystem. A nearly reaction-free venturing prior to science operation appears necessary. Similarly, the mass distribution of the ion engine Xenon propellant would need careful balancing.

The spacecraft mass to be handled by the fine [AOCS](#) system ([FEEPs](#)) is increased.

**EMC aspects:** The sensitivity of the proof masses to magnetic stray fields, leading to torque and accelerations due to interacting magnetic moments from the interplanetary field, the spacecraft internal fields and the induced proof mass field requires a compensation of potential internal sources. In the propulsion module main candidates are the ion engines and propellant valves. Dornier Satellitensysteme has gained experience from careful compensation of magnetic stray fields from valves and other sources (e.g. electrical harness) in the [CLUSTER](#) spacecraft design, aiming at minimisation of disturbance for the magnetometer measurements. This gives confidence, that the problem can be handled in a similar way for [LISA](#); exact requirements are however still lacking, as the magnetic susceptibility of the proof mass alloy is presently not specified (see Section [3.9](#)). The [RITA](#) ion engines developed at Dornier Satellitensysteme do not employ any permanent magnets and hence are essentially stray-field free when shut off.

On the other hand, the availability of the ion engines during the whole mission would maintain coarse  $\Delta V$  capability. This could be of interest for an extended mission duration, in order to keep the triangle configuration within constraints in terms of relative spacecraft velocities and arm lengths.

Mechanisms: An integrated module would of course require no internal separation mechanisms, thus increasing the mission reliability and reducing complexity. Possible detrimental gravity effects from mechanically moving parts as engine pointing mechanisms and loose valve components, caused by unknown mass distributions at the end, need to be investigated in detailed modelling.

#### 9.5.4.2 Structural concept options and trade-off

The overall configuration is driven by the available fairing size. The potential structural concepts are further constraint by thermal needs. Thus only a very limited number of options are available:

- The solar array either needs to be stiff in itself or needs a large number of fixation points. The number of fixation points has to be minimised in order to maintain sufficient thermal decoupling, therefore a sandwich design is needed. For reasons of thermal decoupling a 20 mm Polyimide foam shall be used in the sandwich core. The mechanical properties of that material do not allow to rely on that foam core also for panel stiffness. An additional sandwich layer with an aluminium honeycomb core has to be introduced. As an alternative also a Nomex or Kevlar honeycomb could be used, which could save mass and provide additional thermal insulation. The solar array of the Mars Pathfinder e.g. made use of a Nomex honeycomb. The solar array is a driver for the thermal stability performance and also significantly adds to overall mass. Full use of Nomex properties could be made if the honeycomb cells could be filled with foam. This is considered to be a technology problem to be covered separately. As baseline the aluminium honeycomb was used. In case a foam filled Nomex honeycomb could be made available, the thermal performance could be improved and some mass savings achieved. The stiffness is driven by the panel thickness and the material selection for the face sheets. CFRP face sheets are selected and the panel thickness is adapted for the required stiffness.
- The transfer of loads through the modules requires three tubes which are connected by shear walls. Plane walls are used as well for structural as for unit accommodation reasons. Cylindrical walls neither provide better mechanical behaviour nor allow for more space for unit accommodation.
- For the accommodation of units a top and a bottom plate are needed. They have to provide sufficient stiffness to carry the mass of all units. Since the shear walls cannot support the outer parts of the plates, additional webs are needed. Radial webs cannot be used for accommodation and thermal reasons. Since the circumference would have to be closed anyhow, a conical wall connecting top and bottom plate is used. This gives a closed casing with sufficient stiffness.
- The material selection is not driven by stiffness considerations since all facesheets of the sandwich panel are at the minimum acceptable value from manufacturing and handling point of view. However, CFRP could provide for mass savings because of its lower density.

#### 9.5.4.3 Thermal concept options and trade-off

Since space for unit accommodation is very limited, there is little freedom in the thermal design. Ideally, all dissipating units would have been placed on one plate on the shadow side of the science module thermally insulated from the rest of the module. For unit accommodation reasons however, top and bottom plate had to be used. This only leaves the conical sidewall as radiating surface for heat rejection. For payload units relying on very stable temperatures, also a dedicated insulated radiator on the anti-sun side can be provided.

Normally [MLI](#) would be used as thermal insulation material. The insulation properties of [MLI](#) can only be predicted with a limited accuracy. Furthermore the properties undergo changes due to handling on ground and due to deformation of the foils because of moisture release and other effects in orbit. Therefore gold coatings will be used as insulation.

In case of the solar array, also heat capacity is needed to reduce the transfer of solar constant induced temperature fluctuations from the front to the rear side of the solar array. In this case a polyimide foam is used, which gives a very uniform insulation over the whole solar array area.

The thermal coupling of the rear of the solar array to the rest of the science module is driven by radiation and thus increases with  $T^4$ . Therefore the solar array temperature has to be minimised. This is achieved by covering all solar array areas which is not needed for solar cells with [OSR](#).

All electronic units will show some variation in their dissipation. In order to reduce resulting temperature disturbances of the payload, the heat has to be rejected as directly as possible to space. This is achieved by mounting the units on insulating feet and by providing a gold coating on the faces of the units with view to the payload. A limited number of units could be mounted on the anti-sun side with a dedicated radiator insulated from the rest of the science module. This has to be done for all units showing a fluctuation of dissipation of more than 0.1 W. However, due to limited space, this is only an alternative for a very limited number of units.

#### 9.5.4.4 Electrical architecture concepts and trade-off

##### Centralised Processing System Concept

For Phase A2 an early decision has been made to aim for a centralised processor system ([CPS](#)) for the adoption of the [S/W](#) tasks for [C&DH](#), [AOCS](#), and Instruments because of the necessity for complex integrated control during the science phase, i.e. mainly telescope pointing, fibre positioning, proof mass control with drag-free control. The envisioned processor module is based on an ERC-32 single chip microprocessor which implements SPARC V7 architecture. The performance provides 17 Mips / 3.4 Mflops at 24 MHz which is manifold (factor of  $\approx 15$ ) the performance of the 31750 processor of [ROSETTA](#).

As it would be a major design driver to implement also the electrical physical layer interface into a centralised unit this [CPS](#) must be supported on this physical layer by a dedicated [LISA](#) Instrument Controller (controller in this sense is a very simple micro-controller which cannot run complex control software but adopts the electrical interface to the instrument sensors, actuators and data front-ends.

##### [LISA](#) telemetry Ka-band versus X-band trade-off

Ka-band would seem to offer the advantage of a possible higher data rate compared with X-band.

Ka-band pros:

- increased gain with respect to that provided by an X-Band antenna at same diameter

Ka-band cons:

- $G/T$  for the [DSN](#) Ground Stations is lower for Ka-Band than for X-Band
- free space losses are higher
- limited data transfer times because of atmospheric losses at low elevation angles of [GS](#) antenna
- for tracking of the Earth the antenna drive mechanism would have to provide a second degree of freedom for the antenna elevation pointing ([LISA](#) specific)

- disturbance torques will have a greater effect owing to the necessity to change the boresight pointing of the antenna more frequently

In fact a link budget shows that the X-Band solution offers the more favourable margin.

The X-Band solution appears to be the best, both electrically and mechanically.

### Power Concept

The requirements on thermal stability and magnetic cleanliness (initially, but potentially relaxed at the end of the study) can either be fulfilled by a linear control of the power subsystem (realised on [CLUSTER](#)) or a Maximum Power Point Tracker ([MPPT](#)).

The linear shunt concept has been rejected because of the high power dissipation behind the thermal shield or even inside the [S/C](#) via power dumpers. The [MPPT](#) concept has been selected for the Science Module as well as for the Propulsion Module. Each [PCDU](#) can be mounted with recurring modules in a common procurement.

There is no explicit need for energy storage on the Science Module yet, a potential loss of attitude which would totally de-point the [SA](#) from the sun has not yet been expected to be a credible failure which the [S/C](#) should cope with. Therefore the battery has been allocated to the propulsion Module. This gives several benefits for the Science Module design.

Recent an analysis for reorientation with stored energy for the [FEEPs](#) instead indicate that such a disorientation failure could be corrected with a battery of some 100 Wh of energy.

Thermal stability is maintained at quasi-constant load within the measurement frequency band, e.g. the power consumers like the [RF](#) transmitter will be active during the whole science phase.

## 9.6 Spacecraft electrical subsystems

The [LISA](#) electrical configuration concept is primarily composed of the electrical subsystems on the Science Module and necessary add-ons on the Propulsion Module according to the sketch of Figure 9.11:

- the Avionics subsystem which includes the classical Command and Data Handling ([C&DH](#)) and the [AOCS/RCS](#); today's Avionics applies an integrated processing system with the [C&DH](#) and [AOCS](#) software task running quasi in parallel in the so called Control and Data Management System ([CDMS](#), nomenclature of [ROSETTA](#) and Mars Express)
- the Ion Propulsion subsystem on the Propulsion Module
- the Power subsystem and the Solar Array with some dedicated parts on the Propulsion Module
- the [RF](#) Communication subsystem
- thermal control ([T/C](#)) equipment
- and dedicated external and internal functional/electrical interface.

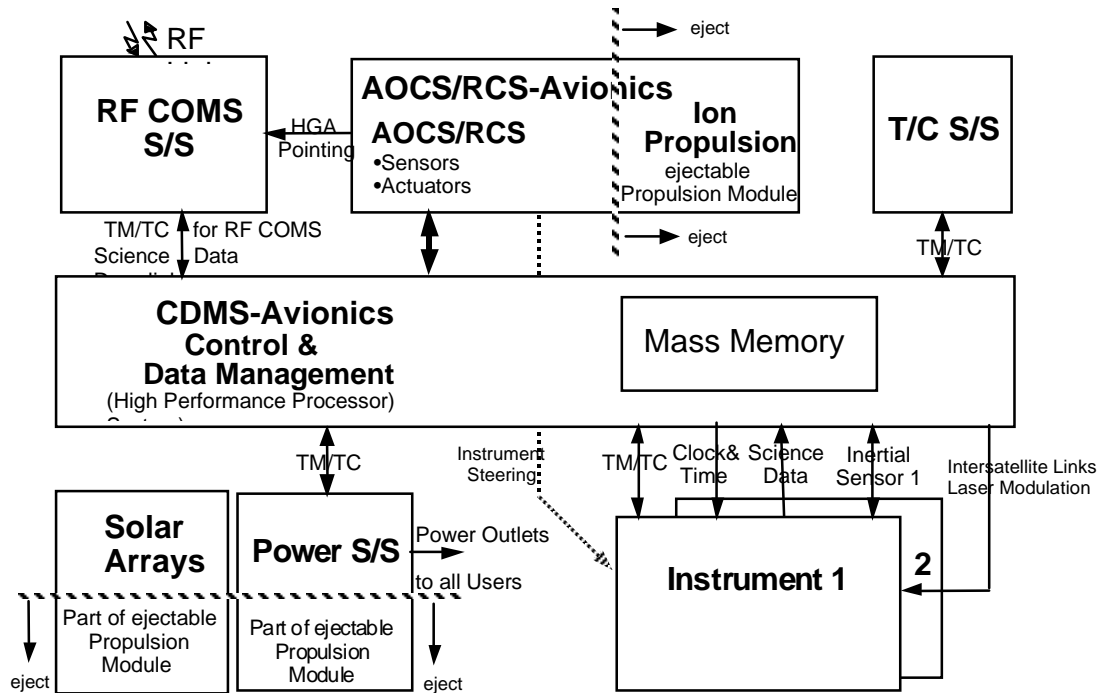


Figure 9.11 Survey of Electrical Subsystems

The aim within this study was to define and design a system fulfilling all mission and payload requirements in a reliable, effective way with the heritage of European state of the art subsystems and units, in order to meet the mass, schedule, and cost constraints.

The Pre-Phase A Avionics system instead had been designed with US heritage based on the recent Mars missions recurring units with the VME backplane Bus (in the Processing Unit) and high performance RAD6000-SC processors.

## 9.6.1 System electrical architecture

### 9.6.1.1 LISA specific functions and requirements

The electrical spacecraft functions for the LISA mission involve classical subsystem services as well as some interdisciplinary features with the integrated satellite.

The LISA specific functions are:

- Attitude and orbit control with chemical propulsion and ion propulsion for LEOP and cruise phase; both propulsion systems will be installed on the propulsion module; if ion thrusters are mounted on optional gimbals the chemical propulsion could be deleted
- FEPPs for coarse acquisition after separation of the propulsion module, and for fine pointing during nominal operations phase;
- In this nominal operations phase the Instrument Inertial Sensor (Proof Mass) and the additional elements for instrument control (telescope pointing, fibre positioning) and spacecraft control are to be combined in close control loops to serve for drag free attitude control and undisturbed science data measurement.
- telemetry (H/K and science data), tracking, and commanding in X-band with DSN 34m antenna



- accommodation of two high or medium gain antennas with 1 DOF to rotate  $\pm 180^\circ$
- providing external and internal umbilical/harness for the stacked composites on the Launcher which shall allow for soft separation of the propulsion modules from the Science Modules
- the power and energy concept only needs stored energy (from battery) during LEOP, the cruise phase, and the turning of the stack before separation of the propulsion stage; thus the battery is only proposed to be accommodated on the Propulsion module (Safe Mode of the Science Module later is sun pointing of the SA, beyond that the Power subsystem will always safely start-up when the solar generator will be illuminated by the sun)
- the functional interface between the Central Processing System and the instruments, as there are sensor raw data acquisition, instrument sensor and actuator control, synch. interface, and inter-satellite communications data.

### Conceptual Design

The electrical service functions have to be allocated to units with a minimum of overhead to serve the stack of Science and Propulsion Modules as well as the separated Science Modules during the Nominal Mission Phase.

The proposed allocation of units to the electrical subsystems and the interconnecting interface is closely oriented at state-of-the-art ESA electrical design concepts of today's scientific satellites, but also respects the specific functions of the previous section. The centralised processor system runs the DMS tasks, AOCS tasks, and Instrument tasks with the estimated processor loads as indicated in the figure, instrument tasks run only on the Application Layer.

The applied background colours correspond with the allocation of responsibilities and competence (H/W tree), design, for cost estimates in the early phases, and later-on for procurement.

The baseline design is the implementation of the functional breakdown into an architecture. It is composed of state of the art subsystem designs for ESA spacecraft and comprises the following functions:

- The avionics system comprises the classical Command and Data Handling System (C&DH) and the AOCS sensors and actuators electrical interface. The avionics system is applying an integrated avionics processor system sharing the processor for the C&DH, the AOCS/RCS, and the Instrument tasks. To ease the graphical lay-out the green AOCS interface module and the (Remote) Terminal Module are drawn separately from the CPS but in the baseline design they are embedded
- The power discipline is realised by two sets of Power Conditioning and Distribution Unit (PCDU) and solar array, one set for each of the two modules. The battery is accommodated only on the propulsion module. The PCDU and the solar arrays are designed for the selected power control concept (PPT).
- The RF communication system is an X-band system with two transponders at 5 W RF power outlet. Six low gain patch antennas provide a quasi-omnidirectional coverage in LEOP, Cruise and Safe Modes. Two HGAs (1 DOF) compensate the torque disturbances when rotated. Only one HGA will be active at a time in nominal science phase. A Radio Frequency Distribution Unit (RFDU) performs the selection of the transmitting antenna.
- Thermal control electrical items are the heater mats, thermistors, thermal control power outlets in the PCDU for survival heater power switching; nominally the temperature control is performed via software controlled circuits.
- The interconnecting medium is the serial MIL-STD-1553 B data bus.

- The satellite operations interfaces will be applied via the Command and Data Handling System (C&DH) of the avionics system and will be based on the ESOC SOIRD (S/C Operations Interface Requirements Document).

### 9.6.2 Electrical power subsystem

#### Major Requirements

- According to the strong requirements on AOCS control stability, very low electromagnetic\* and thermal disturbances shall be generated by the Power subsystem.
- The solar panel shall not generate temperature gradients during the measurement phase, which requires a SA power control scheme, that exploits the SA power homogeneously but not in switched strings or sections.
- The battery shall generate low magnetic moment\*, magnetic materials shall be omitted as far as possible.

The Power subsystem and the solar arrays shall comply with the calculated total power demand of Table 9.4.

#### Power Design

EPS Units:

- Science Module Solar Array
- Propulsion Module Solar Array
- Power Control and Distribution Unit (PCDU) with Maximum Power Point Tracker (MPPT), Main Regulator and Main Error Amplifier (MEA), one of these on each of the modules
- Power Distribution of the Science Module with a Pyro Module
- Battery of Li-Ion type; charge and discharge regulators are located in the PCDU of the Propulsion Module.
- The MPPT builds a closed control loop with power regulators of the buck converter type, which transfer the SA power into a 28 V regulated main bus voltage. During LEOP and the cruise phase the SA and/or battery power of the Propulsion Module is transferred to the main bus of the Science Module. For separation of the composites after cruising this power path shall be disconnected at zero current flow to avoid potential connector welding by arcing.
- Main bus voltage regulation, performed by a 2 out of 3 hot redundant voltage controller, including the main error amplifier (MEA), which delivers the control signal of the primary power control loop, built by SA power regulators – only on the Propulsion Module together with the battery charge and discharge regulators (BCR and BDR).
- The primary power distribution interface to the users must be designed that no single failure at a distributed power line can lead to a permanent shutdown of the main bus. The PCU power bus (on both modules) recovers automatically from any shutdown transition if the cause of it is disappeared.
- The PCDU will be designed such that it safely starts up when it receives power from the SA. Battery charging and survival heating shall not prevent the PCDU from start up capability, even when the battery is fully discharged.

---

\*The initial stringent requirement for low magnetic moment was the design driver but has been ‘provisionally’ relaxed, refer also to Section 9.6.5.

- The [EPS](#) is monitored and controlled by the Data Management System ([DMS](#)) via a serial data bus and discrete command lines from the (Remote) Terminal Module ([RTM](#)).

### Power Design Option

The Electrical Power Subsystem ([EPS](#)) architecture chosen was a compromise with some advantages for the power discipline (mass and cost reduction) but also disadvantage on system level for thermal aspects.

The initial reason for a separate [SA](#) on the propulsion module has been the initially smaller area of the Science Module [SA](#) because of its location in the cone of the fairing. The constraints of the Launcher [CoG](#) reduced the height of the Propulsion Module and caused the upside down orientation of the composite stack on the Launcher, thus the area of the Science Module [SA](#) increased to  $5.7\text{ m}^2$ .

Deleting the [SA](#) on the Propulsion Module would demand for a complete lay-out of the Science Module upper plate with solar cells which does no longer allow to optimise its thermal control with second surface mirrors.

### Solar Array

The solar array of the Science Module under normal operating conditions is orientated to the sun under an aspect angle of  $60^\circ$ . In order to cover the maximum bus power demand of  $315\text{ W}$  any type of solar cells could be applied for this Module. In a common procurement with the solar array of the Propulsion Module the triple junction GaAs cells are baseline.

There remain large areas for the application of Second Surface Mirrors for thermal design on the Science Module [SA](#) and to add [SA](#) strings from redundancy reasons (one failure tolerance at minimum). The minimum cell area must be  $1.9\text{ m}^2$  (without string redundancy).

Each of the [SA](#) string is terminated with a protective diode to avoid propagation of short-circuit failures into the power system.

**Table 9.4** *Detailed Power Budget with Power Demand of the Solar Arrays*

Sub-system	No.	Unit name	Ops power / unit [W]	No. of operating units	Average [W]	Contingency factor	Gross total science module [W]	Gross total propulsion module [W]
AOCS	1	Star camera assembly	7.6	1.0	7.6			
	4	Coarse sun sensor	0.2	0.0	0.0			
	1	Fibre optical gyro unit	12.0	1.0	12.0			
	2	HGA drive	2.5	2.0	5.0			
		AOCS					0.10	27.1
Instrument	2	Laser assembly	5.0	2.0	10.0			
	2	Laser phase modulator	6.0	2.0	12.0			
	2	USO	0.6	1.0	0.6			
	2	UV discharger	3.0	2.0	6.0			
	2	Interferometer:						
	2	optical bench	4.5	2.0	9.0			
	2	electronics box	11.9	2.0	23.8			
	2	DHU	10.0	2.0	20.0			
	2	Inertial reference EL	5.0	2.0	10.0			
	2	LISA instrument controller	8.0	1.0	8.0			
	2	Instruments total					0.25	124.3
Power	1	PCDU basic power	6.0	1.0	6.0			5
		Battery trickle charge						
		Power subtotal					0.10	6.6
CDMS	1	Centralised processor	23.0	1.0	23.0			
	2	Solid state mass memory	2.0	1.0	2.0			
		OBDH subtotal					0.10	27.5
RF COMS	4	LGA X-band						
	1	RFDU	1.0	1.0	1.0			
	2	Transponder X-band	5.0	2.0	10.0			
	2	HGA X-band		1.0	0.0			
	2	Modulator in TRSP	2.0	1.0	2.0			
	2	SSPA (5 W RF power)	30.0	1.0	30.0			
	1	WG, switch,cabling		1.0	0.0			
		RF COMS subtotal					0.10	47.3
FEEPs	2	FEEP electronics	8.0	2.0	16.0			
	3	FEEP clusters	2.8	3.0	8.4			
		RCS subtotal					0.25	30.5
Propulsion	1	Electric propulsion				0.15		676.2
		Propulsion subtotal		588.0				
Thermal		S/S thermal stabilisation						
		Instrument						
Total power required							263	784
PCDU load depend. losses and harness : 8 %							23	68
Module power							286	852
System margin						0.10		
SA power demand							315	938

### 9.6.3 Command and data handling/avionics

State-of-the-art Control and Data Handling systems also serve the interfaces to the [AOCS/RCS](#) sensors and actuators and run the [C&DH](#) and the [AOCS](#) software in their common processor system. For these systems the expression ‘AVIONICS’ is well established.

For [LISA](#) the Avionics System also has been envisaged to run the instrument specific [S/W](#) to ease the integrated scientific control applications. Thus a ‘Centralised Processor System’ is a [LISA](#) specific item.

The functional interface with the instruments which will serve for

- Sensor raw data acquisition
- Sensor and Actuator Control
- Synchronisation
- and Inter-Satellite Communication Data transfer.

will be implemented via the [MIL-STD 1553 B](#) data bus and a specific simple [LISA](#) Instrument Controller.

[LISA](#) Instrument Controller:

Proposed definition of general tasks and implementations:

- Acquisition of instrument raw data and formatting into [CCSDS](#) Source Packets
- Monitoring and reporting of all instrument modules/units ([H/K-TM](#) acquisition, formatting to [CCSDS](#) Source Packets and distribution to system [DMS](#), i.e. the [CPS](#))
- Serving all instrument sensors and actuators on their lower [OSI](#) layers - as Data Link and Physical Layer ([ISO/OSI 7](#) layer structure as reference); the Application Layer (e.g. complex control algorithms for drag-free control) are processes in the [CPS](#)
- Timing Synchronisation, e.g. 1 Hz clock via [MIL-STD-Bus Broadcast](#) correlated to [S/C](#) elapsed time (in [CCSDS](#) Unsegmented Time Code), if necessary a dedicated [TBD](#) MHz clock for sub-seconds counts at high resolution could be amended.
- Inter-Satellite Communication data will simply be identified according to their Application Process [ID](#).

The [LISA](#) Instrument Controller is proposed to be designed of one single cold redundant unit. It shall incorporate for each redundant path:

- one Processor board with a rather simple controller, baseline could be 80 C 32 (radiation tolerant design, Temic), [ROM](#), [EEPROM](#), and [RAM](#) on board
- one interface board with [ADC](#) for analog status and thermistor acquisition, a set of pulse command outlets, detector telemetry [I/F](#): one serial [IEEE 1355](#) link (link performance  $\approx$  100 Mbps) or optionally [RS 422 I/F](#) with [UART](#) (link performance  $\approx$  10 Mbps for 10 m cable length) to the dedicated data electronics, a set of digital status acquisition lines and the System interfaces [MIL-STD 1553 B](#) RT, Clock and Time synch. [I/F](#).
- one [DC/DC](#) converter.

#### 9.6.3.1 Avionics system design

The proposed avionics design for the Centralised Processor System ([CPS](#)) is based on an Integrated Platform Computer ([IPC](#)) named [LEONARDO](#).

**LEONARDO** (LEo On-board Novel ARchitecture for Data handling) is a novel Integrated System especially suited for small and medium size satellite.

The **CPS** gathers, in a unique mechanical box, Command, Data Handling, Attitude and Orbit Determination/Control and Housekeeping capabilities, with great advantages in terms of compactness. A local Solid State Mass Memory module can also be included In the same housing.

The **CPS** is based on an internal modular fault tolerant architecture employing fast internal serial lines (**IEEE-1355 DS-link**/“Spacewire”) for communication among the various modules. A **MIL-STD 1553 B** bus is adopted as a main avionics system bus and also internally to transfer data between the Processor and the peripheral **I/O** modules.

### CPS Description

The **CPS** is the core of the Satellite avionics and includes in the same box the typical Data Handling and Attitude/Orbit Determination and Control functions.

For this purpose it interfaces:

- The **S/C** subsystems via **MIL-STD-1553** bus and discrete **TM/TC** channels
- The **AOCS** sensors and actuators via either **MIL-STD-1553** bus or dedicated specific interfaces
- The Payload via **MIL-STD-1553** bus and discrete **TM/TC** channels
- The **TT&C** and **RX** Payload for Ground Telecommands processing and execution and for sending Telemetry to Ground.

**LEONARDO** hosts a dual redundant electronics.

Normally the main modules are switched on (except the **TC** decoders that are both powered on). In case of failure the redundant module can be switched over independently from the other modules: a full cross-strap is in fact implemented within the unit to allow any module to exchange data with all of the others. Moreover the unit is conceived in such a way to allow switching on both redundancies at the same time (for emergency or diagnostics reasons).

The **CPS** basic modules are:

- **TC** Module implementing a fully compliant **ESA PSS-04-107** Packet Telecommand Decoder: Video **BPSK** or digital input interfaces towards **TT&C** Receivers and **EGSE**, telecommand video **BPSK** stream digital demodulation, single **ASIC** Telecommand Decoder Core functions including internal standard Authentication Unit and Command Pulse Distribution Unit logic. Moreover, High Priority command pulse drivers, **MAP** demultiplexing and distribution interfaces are housed in the same module.
- **TM** Module implementing a fully compliant **ESA PSS-04-106** Telemetry Generator providing on the same module up to 4 Virtual Channels, Virtual Channels multiplexing, Telemetry formatter and Telemetry Interfaces towards **TT&C** Transmitter and **EGSE**. Essential telemetry generation **H/W** is also provided.

The Reconfiguration Module is connected to the nominal and redundant Processor Modules through **DS-Links IEEE-1355** (“Spacewire”)

- **Processor Module**. The Processor Module is based on an **ERC-32** single chip microprocessor (**TEMIC TSC695E**), which implements **SPARC V7** architecture. The Processor Module features 17 Mips / 3.4 Mflops at 24 MHz. Thanks to this performance it is possible to execute on the same Processor Module the classic Data Handling tasks, Attitude/Orbit Control tasks as well as Payload specific tasks with great advantage at system level in terms of mass and power consumption. The Processor Module comes with Start-up/Boot **PROM**, Application **S/W EEPROM** and **S/W Working SRAM**.

The following Interfaces are foreseen: serial MAP I/Fs toward TC module; 6 IEEE-1355 DS-Links towards TM/RM modules.

- Reconfiguration Module. The Reconfiguration module gathers all of the functions pertaining to Failure Detection Isolation and Recovery (FDIR). In details, it provides: the Reconfiguration Function, the Protected Resources, the On Board Time counter, the Reconfiguration Commands logic and drivers. The Reconfiguration Module is connected to the Nominal and redundant Processor Modules through IEEE-1355 DS-Links.
- Attitude Control Electronics (ACE) Module. The ACE module is in charge of interfacing the AOCS actuators and sensors. It provides functions for AOCS command distribution/actuation and data acquisition. The ACE module can support the LISA AOCS Sensors: Sun Sensors, Star Trackers and Fibre Optic Gyros (in case they request particular interfaces different from MIL-STD-1553B). The Propulsion Actuators (FEEP as well as Chemical propulsion systems) are also supported. This module interfaces the Processor Module via MIL-STD-1553B data bus.
- Housekeeping Module. The PF-H/K module interfaces the MIL-STD-1553B data bus and collects standard acquisitions and distributes standard commands from/to external users, implementing the classical OBDH Remote Terminal Unit (RTU). Acquisition interfaces include: Analogue, Digital Bi-level, Relay status, Digital Serial and Thermistor channels; commands interfaces are for Digital Memory Load and for discrete Pulse Command. I/O Interfaces are ESA TTC-B-01 compliant.

LEONARDO heritage and future improvements:

LEONARDO has been developed for the Italian standard satellite platform PRIMA, intended to be mainly exploited for small/medium class satellites (<1000 kg) carrying either Scientific or Earth Observation Payloads.

Every module is implemented on the basis of the LABEN experience in designing On Board Electronic equipment: most of the proposed electronics is inherited from existing hardware already flown or installed on current space programmes.

The Processor Module is an evolution of the one developed for the Italian Star Tracker which will fly on board the SAC-C satellite. TM, TC and Reconfiguration modules largely take into account the experience gained on Cluster/XMM/Integral CDMUs. The Housekeeping I/O Standard (Analogue, bi-level and digital channels, discrete Pulse commands) are based on the above programmes Remote Terminal Units (RTUs), while interfaces towards actuators and sensors are based on ARTEMIS Remote Unit A which has been designed to support command and control of Propulsion System, Reaction and Momentum Wheels, Gyros, Earth and Sun sensors.

Although the present LEONARDO design is based on state-of-art technology with large use of VLSIs (ASIC) and hybrid modules, it can be argued that, considering the schedule of LISA development, new technologies will become available to the space market. This will allow further improvements in terms of compactness, mass, power consumption, capability and processing performances. Some already foreseen expected improvements are for instance:

- 3.3 V digital families, improving power consumption of the logic electronics
- Memory density, allowing to host the requested Mass Memory capacity (256 Mbits) by expanding the one already present on the Reconfiguration Module (currently 64 Mbits)
- Increased adoption of MCM (including 3D) and “system on chip” technology
- Increase of the processing power adopting the forthcoming SPARC V8 which is being developed by ESA

H/W Budgets:



The following budgets have been estimated for the [LISA CPS](#):

- Mass: 15.9 kg
- Dimensions:  $410 \times 243 \times 185$  mm (LxWxH) ( $410 \times 275 \times 190$  including mounting feet and connectors)
- Power consumption: 25 W (average)

### 9.6.3.2 Software design

A reference software layout of the Command and Data handling and [AOCS/RCS](#) systems is proposed to be composed out of three layers:

- 1 basic software,
- 2 standard application software,
- 3 mission specific software.

The standard application software will basically comprise the following functions:

- [TC](#) Handler, [TM](#) Handler, Time Tag Buffer Handler, [H/K](#) Monitor, History Monitor, [TM](#) Transfer Frame Generator, Instrument data formatter ([VCDAU](#)) Handler, [S/W](#) Reporter, [DMS](#) serial links Handler ([IEEE 1355](#)), Data Bus Control Handler ([MIL-STD 1553 B](#)), [CDMS](#)/Avionics Processor Unit Control, [SSMM](#) File Handler, [SSMM](#) Patch/Dump Handler (back-up for failure analyses), [PT](#) to [PT](#) Communication Handler via [MIL-STD-1553 B](#) Data Bus), Time Synchronisation Service

The mission specific software is decomposed into its major constituents servicing the instrument and the individual subsystems (services in this sense are functions not provided by the Standard Application [S/W](#) package). It contains the mission specific criteria and nominal operational cases for which [OBCPs](#) are selected and initiated. In addition, it comprises

- System Nominal Autonomous Control (allowing an unattended operation of [TBD](#) hours)
- High level Anomaly Control, Anomaly Procedures Execution
- Macro Procedures Execution
- Power [S/S](#) Control Service
- Thermal Control Service
- [CandDH](#) Control Service
- Instrument Service
- [RF](#) communication service for [TT&C](#) and Science Data downlink
- Inter-Satellite Laser link communication

Including [AOCS/RCS](#) mode management, attitude and orbit control and orbit maintenance during [LEOP](#) and Cruise, and drag-free control during the science phase..

### 9.6.3.3 Data budget

Data Acquisition (from Master [S/C](#) instruments and also via Laser Inter-Satellite Links), storage, and transmission by [LISA](#) Master [S/C](#):

Science data:  $14 \text{ Variables} \times 24 \text{ bit} \times 2 \text{ Hz} = 672 \text{ bps}$  (desired from instrument experts)

Auxiliary data [TBD](#), assumed: three [S/C](#)  $\times 100 \text{ bps} = 300 \text{ bps}$  (minimum)

[S/C H/K](#) data [TBD](#), assumed: three [S/C](#)  $\times 100 \text{ bps} = 300 \text{ bps}$  (minimum)

Data Formatting into [CCSDS](#) Packets: 5 % overhead

Formatting into Transfer frames for play-back: and [RS](#) encoding: 15 % overhead

**Table 9.5** *LISA on-board Data Rates and Volumes:*

Parameter		Data rates [bps] Status: Start Ph.2updated	
Science data	- raw	1000	672 (3 <a href="#">S/C</a> )
	- compressed	200	
Instrument data (auxiliary data)		100	$3 \times 100$
<a href="#">S/C</a> H/K data		100	$3 \times 100$
Total for master <a href="#">S/C</a>		400	1272
<a href="#">CCSDS</a> packets	into <a href="#">SSMM</a>		1336
Transfer frames factor with <a href="#">RS</a> encoding	during play-back		(1.15)
Data volume	per 48 h	69 Mb	231 Mb
Downlink duration at 7 kbps data rate	per 48 h	2.74 h	9.17 h

As identified in the table above the required data volume of  $\approx 231$  Mb for the ‘Mass Memory’ is far below 1 Gbits. Its implementation can be easily done with the expansion of the processor memory or the Safeguard Memory. From 2002 the available [SSMM](#) boards instead provide a memory capacity of 132 Gbits on just one double-eurobord.

#### 9.6.4 [RF](#) communications

The configuration of the [RF](#) Communications Sub-system is shown in Figure 9.12. It comprises two high gain antennas and six low gain antennas connected to a redundant X-Band Transponder by an [RF](#) Distribution Unit.

The two high gain antennas are steerable dish antennas of 30 cm diameter, each providing  $180^\circ$  coverage in azimuth. They are mounted on the science module to provide a complete  $360^\circ$  of coverage (refer also to the configuration drawings).

During the operational phase the science module makes a stable  $360^\circ$  rotation around its symmetrical body axis once per year. In order to minimise the torque of the antenna to the science module, the antenna drives will be actuated two degrees every second day (two minutes motion time assumed). The antenna actuation will be controlled by the [AOCS](#), the disturbance torque is further minimised by moving the antennas simultaneously in opposite directions. The driving motor could be a piezoelectric drive, if the magnetic moment has to be minimised (refer also to Section 9.6.5).

Each 30 cm diameter dish antenna will have an antenna boresight gain of about 26 dBi and a 3 dB beamwidth of  $\approx 7^\circ$ .

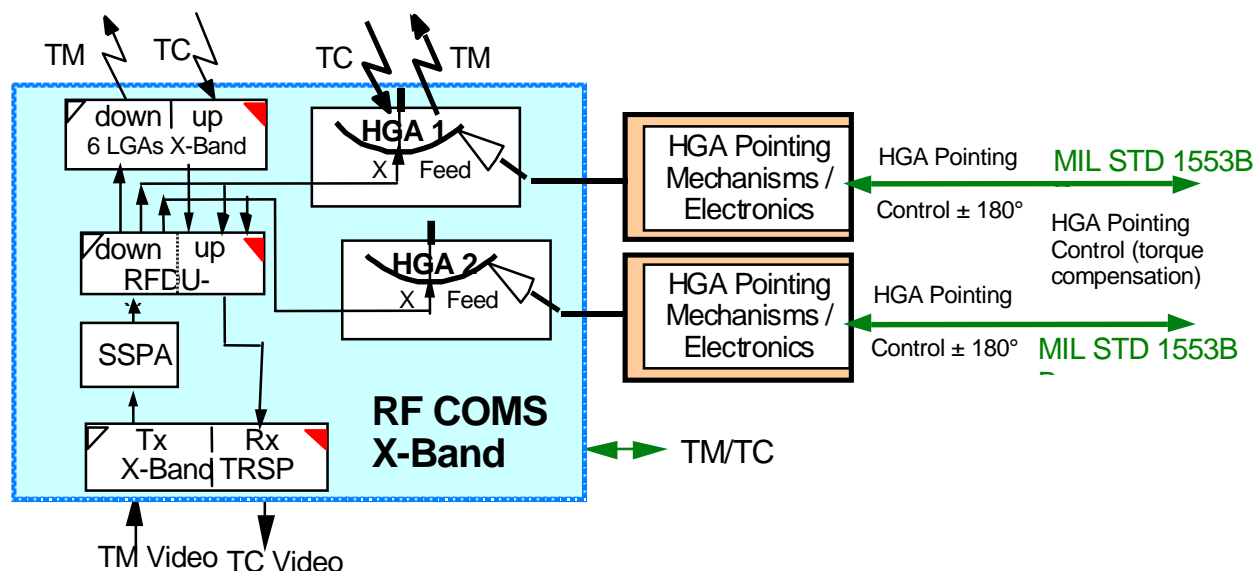


**Figure 9.12** *RF Telecommunications Sub-system Block Diagram*

The antenna movement is done only in azimuth. The boresight in elevation varies by  $\pm 0.5^\circ$  as shown in the orbit analysis. This gives a pointing loss of 0.13 dB. This loss is respected in the link-budget.

An X-Band Standard Deep Space Transponder (recurring from [SMART 1](#), but without Ka-Tx) with a transmission output power of 5 W is baseline (further enhancement by a 20 W [SSPA](#) is an option which would allow to increase the data rate up to 28 kbps and thus reduce the actual downlink transmission time from 9.17 h per two days time intervals below 2.3 h).

Six low gain patch antennas, mounted equidistantly on the spacecraft rim, will provide an quasi-omnidirectional coverage (actually a toroidal pattern around the x axis). If more detailed analyses reveal the necessity for full omnidirectional coverage two additional patches may be adopted into the directions of the main rotational axis.

The [RF](#) Telecommunications has two downlink modes, one with high rate to transmit science and [H/K](#) data in the normal operations mode, another with a 1 bps (at 5 W [RF](#) power (or 5 bps at 20 W [RF](#) power) low rate for the final transfer phase and for spacecraft health and emergencies. At lower distances for the early mission phases this rate should be increased reverse proportionally to the smaller path losses The [DSN](#) 34-m beam waveguide ([BWG](#)) station will receive the X-band downlink in both modes and will also uplink X-band commands at a rate of 2000 bps via the [HGA](#).

The high rate X-band link budget is based on the following parameters:

The 7 kbps downlink uses a modulation index of 1.4 radians peak, directly modulating the carrier. The system will employ rate 1/6, constraint length 15, convolutional code, concatenated with the JPL standard Reed Solomon code. The assumed bit error rate (BER) of  $10^{-6}$  requires an S/N of about 0.81 dB. The antenna will have a 3 dB beamwidth of about  $6.97^\circ$ , and a pointing loss of 0.13 dB (for the boresight elevation variation of  $\pm 0.5$ ). It is assumed the DSN receiver will have a bandwidth of about 5 Hz. With this assumption, the data margin will be  $> 3$  dB and carrier margin will be at least 6 dB. Table 9.6 shows these link budget results. Positive link margins (at least the add-on relative to 3 dB) indicate that the BER will be better than assumed for the link budget calculations.

The low-rate (1 bps) **TM** mode will use six fixed 3 cm low-gain patch antennas (**LGAs**), each

with a 3 dB beam-width of about  $67.2^\circ$ . This link will also use the same coding scheme used by the high-rate downlink. Under these conditions the link will provide a reasonable data margin of 3 dB and a carrier margin of about 6 dB. Table 9.6 also shows the link budget results for this case.

For emergency mode and cruise phase communications, which will use the low-rate mode, the spacecraft will be pointed towards the sun and the one LGA facing the earth will be switched active. It will receive TC and transmit the spacecraft H/K data to the ground. In the case of total failure of the attitude control system the CPS computer will sequentially switch the antennas in a predetermined way and identify the respective antenna active which will cause a receiver locked signal. Emergency commanding will be done using the 34-m BWG antenna to transmit X-band at 20 kW. In both cases the link is a viable link with reasonable margins.

**Table 9.6** *TM Link Budgets Results:*

Antenna	Band	Amplifier W	Gain dBi	Beam deg	EIRP dBWi	Eff. rate kbps	Margin [dB]	
							Carrier	Data
HGA-0.3 m	X	5.0	26	7	63	7	8.12	3.12
	X	20.0	26	7	69	28	14.12	3.10
LGA	X	5.0	0	67.2	37	0.001	3.27	3.21
	X	20.0	0	67.2	43	0.005	8.11	3.69

### 9.6.5 Electromagnetic compatibility

For LISA a spacecraft design resulting in a moderate to low EMI level is proposed. Areas of particular EMC-concern will be

- Grounding and shielding concept of Science Module and Propulsion Module
- EMI Propulsion module to Science Module
- EMI S/C bus to payload
- RF compatibility (RFC)
- Electrostatic charging / ESD.

The grounding concept shall be Distributed Starpoint Grounding (DSPG) for the entire system with the primary starpoint inside the Science Module PCDU. DSPG requires primary isolation within any unit on both Modules as well as signal interface isolation (basically on the receiver end). To achieve a low EMI environment the shielding concept will include requirements for harness-, box, and panel shielding.

For EMI between Propulsion Module and Science Module no major interference is expected due to the fact that the two modules are not going to work simultaneously during the nominal science phase, ie. the EMI driving science instrument will not work during the transfer phase.

EMI to/from the payload is mainly dependent on the satellite design. No particular EMI precautions shall be foreseen according to the actual design. Nevertheless the special voltage stability which is required in the range of  $2.8$  to  $4 \times 10^{-6} \text{ V}/\sqrt{\text{Hz}}$  for some instrument electronic units (Phasemeter electronic, Front-end electronic, ...), which is required by the thermal analysis,

shall not be part of the EMI requirements due to the fact that the voltage stability shall be realised inside each critical unit on secondary voltage level. The required voltage stability shall not be part of the EMI requirements on the power bus. The FEPP thruster system is working at high voltages. The design of the FEPPs and their control electronics shall prevent any radiated emissions EMI.

For Magnetic Cleanliness some analyses were performed. The initial requirement for magnetic moment of  $< 3 \text{ mA m}^2$  is now provisionally relaxed (Memo from S. Vitale, 25.11.1999: "... there is no specific request for the magnetic moment of the spacecraft"; i.e. no particular design needs to be established on LISA according to the referenced document. This information is presently to be consolidated from further experts. If this statement will be revised to a strong requirement on magnetic cleanliness again there will be some possible applications with piezo-electrical drives. Presently there are some activities at the ESTEC mechanisms division for the TRP-Plan (2000-2002) for linear and rotary drives and also for piezo-electrical valves.

RF Compatibility (RFC) will be a minor issue because of the two TT&C high gain antennas (X-band Rx and X-band Tx) on every satellite. The antennas will be mounted on top of the science module with the main beam of each antenna in opposite directions. One antenna only is actively used during each mission phase on every satellite. The coupling between the antennas is therefore reduced by the accommodation and orientation of the antennas. Nevertheless the influence of unwanted coupled signals shall be reduced by the design of the RF communication units and an RFC analysis in future design phases.

The electrostatic charging and ESD respectively depend mainly on the satellite design. The S/C will usually charge up negatively due to the space plasma. Space exposed surfaces must avoid high voltage gradients caused by dielectric materials to prevent ESD (S/C body and SA). The influence of the Ion-Emitter propulsion system on the S/C charging must be investigated. The FEPP thruster system is expected to have no negative influence on S/C charging according to the analysis of ARCS: 'Parameters of the ARCS In FEPP Thruster System', 24./25.10.1999).

## 9.7 Micronewton ion thrusters

The very minute thrusts required in the manoeuvres for pointing (5.7.1) and drag-free operation (3.7) of the LISA spacecraft are best provided by the Field Emission Electric Propulsion (FEPP) thrusters. They operate by accelerating ions in an electric field, and ejecting them to develop the thrust [134]. The ions are generated by exposing a free-surface of liquid metal (cesium or indium) to an electric field.

The shape of this liquid surface is established by the counteracting forces of surface tension and electric field stress along a knife-edge slit with a width of about  $1 \mu\text{m}$ , or at a Tungsten needle with a tip radius of 2 to  $15 \mu\text{m}$ . With an applied voltage between 5 and 10 kV, the ions are ejected at a velocity in the range of 60 to 100 km/s, depending on the propellant and the applied voltage. The mass flow is very low, so the developed thrust is in the desired micro-Newton regime. By smoothly varying the applied voltage, the thrust can be correspondingly controlled, as desired, all the way down to fractions of a micro-Newton. The FEPPs require only about 15 W to develop the necessary thrust. The total propellant (cesium or indium) mass required for the nominal two-year mission is only a few grams per thruster.

There are mainly two designs being pursued by *Centrosazio* (Italy) and at the *Austrian Research Centre Seibersdorf* (ARC). The FEPPs originally developed by *Centrosazio* were designed for thrusts in the milli-Newton regime, as required for communication satellites. For LISA, they had to be scaled-down by a factor of a thousand from the original design. The devel-

opment at [ARC](#), the Indium Liquid-Metal Ion Sources ([In-LMIS](#)) have originally been designed for spacecraft charge control and microanalysis instruments. They have already been flown on various missions and proven their reliability in space during more than 800 hours of operations. The description in the following subsections mainly refer to the *Centrosazio* design. We come back to the [ARC](#) design in subsection [9.7.5](#).

### 9.7.1 History of [FEED](#) development

Research on Field Emission Electric Propulsion ([FEED](#)) using liquid metals has been carried out by [ESA](#) since 1972. The thruster has evolved from a single-pin emitter configuration in 1972, through linear arrays of stacked needles in 1975, to the high-efficiency solid-slit emitter in 1979. During the past phases of the development program, all the components of the system have been designed and tested, and the emitter manufacture problems have been solved. At that time, development had entered the industrialization phase, and research was devoted to the testing of the whole system in view of an application in the milli-Newton range, mainly for North-South station-keeping operations in geostationary telecommunication satellites. The high power-to-thrust ratio of [FEED](#)s, in comparison with other electric propulsion systems now fully developed, made [FEED](#)s lose competitiveness for this specific application. However, a rising interest of the international scientific community in missions requiring micro-Newton thrust levels for ultra-fine pointing operations (such as in [LISA](#)) sparked the present reorientation of [FEED](#) activities to this new thrust range.

### 9.7.2 The Field Emission Electric Propulsion System

In the [FEED](#) system, ions are created directly from the surface of a liquid metal exposed to vacuum, by means of a strong electric field resulting from suitable voltages applied to an emitting unit.

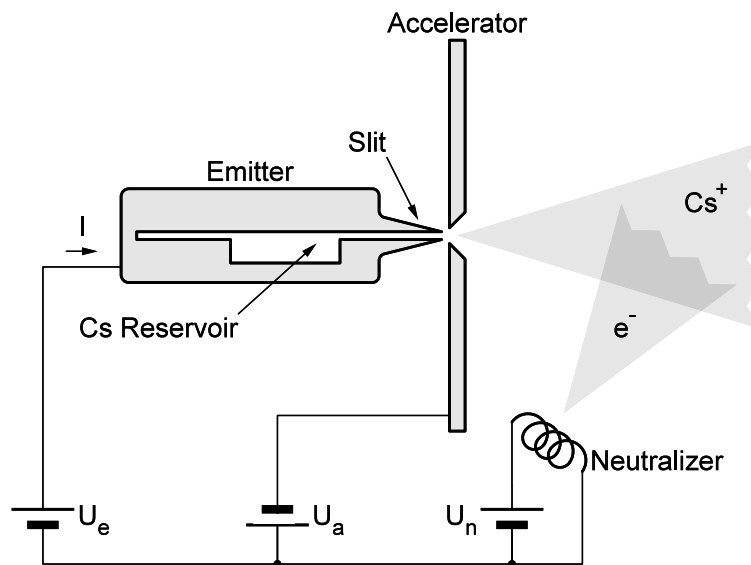


**Figure 9.13** [FEED](#) thruster schematic.

When the surface of a liquid metal is subjected to a strong electric field, it distorts itself into a series of cusps that protrude more and more from the surface plane: the radius of curvature

of the cusp tips becomes smaller and smaller, thus in turn increasing the strength of the local electric field. When the field reaches values of the order of  $10^9$  V/m, the atoms of the metal tip spontaneously ionize, and these ions are accelerated away by the electric field that has created them [135, 136].

Cesium, whose melting point is about  $29^\circ\text{C}$ , has been chosen as propellant because of its low work function, high atomic mass and good properties of wetting on steel surfaces.

The basic FEEP system comprises: a single solid emitter/accelerator system or a cluster of them, a storage and feed system for the Cs propellant, a power conditioning and control unit, and a neutralizer (Figure 9.13).

The main elements of the thruster are the emitter (kept at positive voltage  $V_e$ ) where the ions are created, and the accelerator (kept at negative voltage  $V_a$ ), a counter-electrode to establish the voltage difference  $V_e - V_a$  needed for ionization and acceleration. A threshold voltage of 7 kV is necessary to start the emission.

The emitter consists of a narrow slit between two highly polished metallic plates. On certain regions of one of the inner surfaces several thin dots of Nickel ( $\approx 1\ \mu\text{m}$ ) are deposited by sputtering. When the two halves are tightly clamped together, they are separated by only the thickness of the Ni deposits, thus forming a narrow slit through which the liquid metal is transported to the edges under the action of capillary forces. The present types of emitters have a weight of 15 g. The accelerator is a stainless steel plate placed in front of the emitter; the ion beam is extracted through an elongated slit in front of the emitter blades. The thrust produced by the FEEP system (measured in N) is given by

$$F = 1.66 \times 10^{-3} I_e V_e^{1/2} \frac{\sin \alpha}{\alpha} \frac{\sin \beta}{\beta}, \quad (9.2)$$

where  $I_e$  and  $V_e$  are the emitter current and voltage (measured in A and V, respectively), and  $\alpha$  and  $\beta$  are the divergence angles. By varying just one parameter, the emitter voltage  $V_e$ , the thrust level can be changed.

The neutralizer will supply the electrons needed to neutralize the ion beam created in the emitter/accelerator assembly. Neutralizer concepts requiring only low current and power are currently being evaluated, such as thermionic cathodes and field emission electron sources.

The feeding system consists of a shaped reservoir directly connected to the emitter blades, requiring no external force to drive the propellant to the slit. The small amount of propellant required allows for a self-contained, integral reservoir unit, thus eliminating a complicated feeding system control and reducing the interface with the spacecraft to the electrical connections only. An engineering model of the thruster, including the propellant reservoir, an active thermal control and monitoring system, and a sealed container is already available. This assembly weighs about 300 g and has an overall envelope of 7 cm in height and 6 cm in diameter, and may host about 40 g of propellant. The Power Conditioning and Control Unit (PCU) will provide the adequate voltage and current levels to the different subsystems of the FEEP thruster and will act as interface with the spacecraft power and data buses.

*Centrosazio* (Italy) and *Laben* (Italy) are currently developing the different subsystems for ESA.

### 9.7.3 Advantages and critical points of FEEP systems

The main advantages of the FEEP system for missions like LISA with highly demanding attitude requirements are the following [136, 137]:



- If the forces disturbing the spacecraft are of the order of  $1\ \mu\text{N} - 100\ \mu\text{N}$ , the **FEEP** thruster is the only system capable of providing this kind of thrust level with sufficient accuracy. For the **LISA** mission, the **FEEP** thrust controllability must be able to cover the range  $0.1\ \mu\text{N} - 100\ \mu\text{N}$ , with resolution better than  $0.1\ \mu\text{N}$ . The **FEEP** emitter performance is  $300\ \mu\text{N}$  per centimeter of slit length. The power-to-thrust ratio is  $50\ \text{mW}/\mu\text{N}$ .
- The exhaust velocity of the ions in the **FEEP** thruster,  $\approx 60\ \text{km/s}$ , allows great mass savings compared with other propulsion systems. The total required fuel tankage for the (nominal) duration of 2 years of the **LISA** mission is 9 g per thruster.
- As the **FEEP** system requires only an insignificant amount of propellant, in a compact reservoir, disturbances due to propellant sloshing, or to tidal motion of the gravity center of the propellant under the combined Earth-Moon attraction, affecting the self gravity conditions onboard, are completely negligible.
- The **FEEP** system requires no valve or any other moving parts, and thus any problems of mechanical or gravitational compatibility are avoided.

Possible critical areas to take into consideration when using **FEEP** thrusters for fine attitude control are:

- Reliability: the expected lifetime in space has not been determined; however, at the **ESTEC** Electric Propulsion Test Laboratory, a systematic attempt will be made to determine the lifetime. An endurance test of several months will take place at **ESTEC** in 1998. Preliminary, non-optimal tests demonstrate that laboratory lifetime is in excess of one month in continuous operation, and at least  $10^6$  firings in pulsed mode.
- Repeatability: measurement techniques of **FEEP** micro-Newton levels must be improved in order to fully demonstrate the repeatability of the **FEEP** system working with the high resolution aimed at ( $0.1\ \mu\text{N}$ ). Noise and direct thrust measurements must also be taken into consideration [138, 139].
- Major failure modes in the past have been: (1) clogging of the cesium feed by  $\text{CsOH}$ , produced by the interaction of cesium with ambient laboratory water, and (2) sparking damage to the knife edge of the emitter when the **FEEP** is run at high voltages and high currents. The lower currents required for the low-thrust operation in the **LISA** mission should greatly reduce the danger of sparking damage. Water vapor will not be a problem in orbit or when the thrusters are firing continuously, but the process of bringing the **FEEPs** into space avoiding water vapour during pre-launch, launch and orbit transfer must be carefully designed.

#### 9.7.4 Alternative solutions for **FEEP** systems

As the thrust level for **LISA** is in the range of only micro-Newtons, the old requirement of high atomic mass for the propellant is no longer so important. Therefore, alternative propellants for the **FEEPs** are now becoming attractive, propellants having good wetting characteristics and low ionization energy, without having the problem of reacting with water vapour. The successful operation of an indium field emitter for spacecraft charge control on the Geotail satellite and on the *Mir* station, using the same principle as the **FEEPs**, has focused the attention on this propellant [140, 141]. Further studies on new propellants with the selection of a suitable emitter material and/or surface treatment are being envisaged by **ESA**.

### 9.7.5 Current status

#### 9.7.5.1 Activities at *Centrosazio*

- To avoid contact between the water vapor and the cesium during the pre-launch, launch and orbit transfer, the thruster is placed in a gas-tight cover with an inert gas surrounding it after being operated in the vacuum chamber. This container and the ground equipment required to assemble this system has been manufactured and tested at *Centrosazio*.
- *Centrosazio* has identified the thermoionic neutralizer as the main candidate for the **FEEP** system due to its high reliability with a demonstrated lifetime of more than 10 000 hours. Field emission neutralizers, used in the TV-screen technology, are also being developed by *Centrosazio* because of their low power consumption and low cost.
- Under **ESA** contract, *Centrosazio* has designed, manufactured and tested the integrated emitter/feeding system.
- *Laben* (Italy) is manufacturing the Power Conditioning Unit for the **FEEP** system under **ESA** contract.
- *Centrosazio* and *Laben* are currently preparing a **FEEP** flight experiment on board the space shuttle. This will be the first time that the *Centrosazio* **FEEP** is operated in space.
- A lifetime test of a **FEEP** thruster operating at a certain thrust level ( $1-50\ \mu\text{N}$ ) with neutralizer will take place during 1998 in the **ESTEC FEEP** vacuum facility under the responsibility of *Centrosazio*.
- *Centrosazio* is currently investigating the possibility of using indium as propellant for the *Centrosazio* **FEEP** thruster in collaboration with the *National Physics Laboratory* (United Kingdom).

#### 9.7.5.2 Activities at the *Austrian Research Centre Seibersdorf*

The standard Indium Liquid Metal Ion Source (**In-LMIS**) developed at the *Austrian Research Centre Seibersdorf* is of the central needle type, in which a sharpened tungsten needle of tip radius of a few  $\mu\text{m}$  is mounted in the centre of a heated indium reservoir. For operation, a potential of typically 5–7 kV is applied between the needle and an accelerating electrode. If the needle is well wetted by the liquified indium, the electrostatic stress of the applied field pulls the indium film towards the electrode. This stress is balanced by surface-tension forces which leads to the establishment of a characteristic equilibrium configuration, the so called Taylor cone (see Figure 9.14). Once the electric field at the apex of this cone gets to the order of volts per nanometer, the most protruding surface atoms are field evaporated, ionized and accelerated towards the electrode. Via hydrodynamic flow the atoms leaving the tip area are constantly replenished and a stable emission regime can thus be maintained. Figure 9.15 shows an image of the space qualified indium **LMIS**.

Originally developed for spacecraft potential control instruments these indium **LMIS** so far have been flown on four missions (**GEOTAIL**, **EQUATOR-S** and two times on **MIR**) and are currently scheduled to fly on **CLUSTER-II**, **ROSETTA** and again to the **MIR** station in the next future. A total of 35 ion sources will be used in these three projects. The reliability of the indium **LMIS** design up to now has been proven in more than 800 hours of operation in space. This fact together with the low emission current characteristics of these sources, which could be used to produce a highly controllable micro-thrust ion beam, highlighted the importance of this technology as a complementary low-thrust system to the cesium **FEEP** thrusters. Therefore a

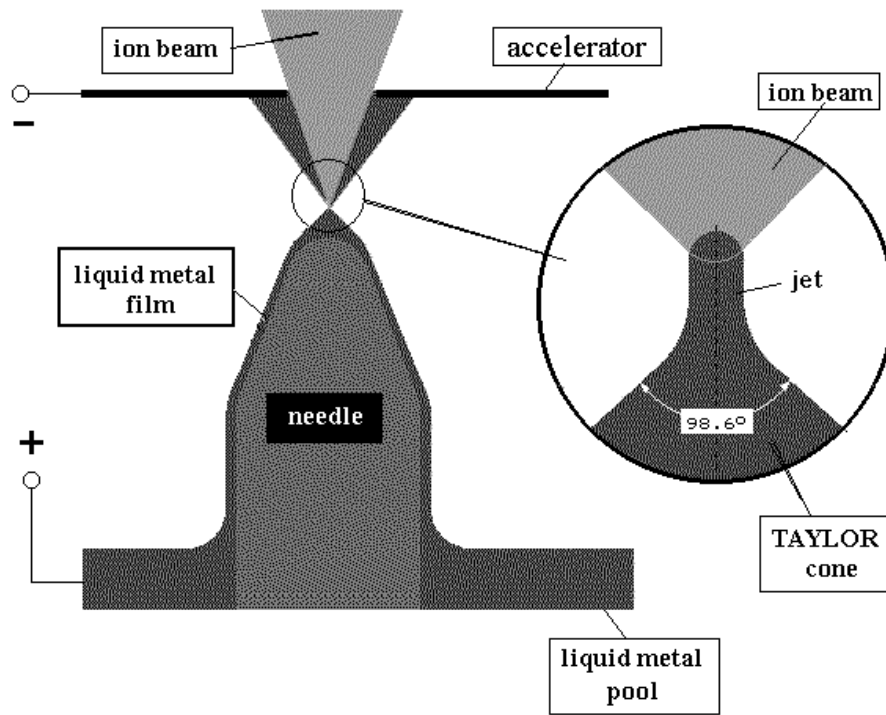


**Figure 9.14** Schematic of the operation of a needle type liquid-metal ion source.

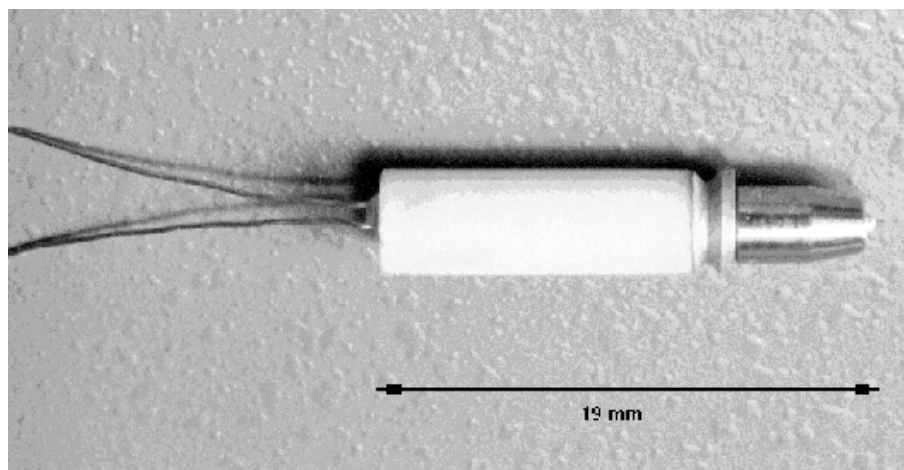


**Figure 9.15** Photograph of an indium *LMIS* developed at Seibersdorf.

small contract for performance characterization, lifetime, reproducibility and controllability of these sources was placed by [ESA](#) with [ARC](#) in 1996. The final results showed that some areas as mass efficiency, specific impulse or thrust controllability were points still to be investigated in order to improve the thruster performance. In particular, the mass efficiency started to diminish when increasing the thrust level above  $8 \mu\text{N}$ . This effect could be due to the uncompleted ionization of the indium species which induces the apparition in the beam of droplets, multi-atomic, single-charged aggregates and multiple-charge ions.

[ARC](#) is currently working in a new [ESA](#) activity dedicated to the understanding of the basic physics regulating the already mentioned phenomena. This first phase will help to optimize this

device which was first designed as a charge compensator. Therefore matters such as distance between electrodes and voltage distribution will be assessed during this activity. Then, the optimized version of this thruster at engineering level will be submitted to characterization tests with thrust levels running from 1 to 25  $\mu\text{N}$ .

### 9.7.5.3 Microthrust measurements

The *National Physics Laboratory* (United Kingdom) is currently developing a microthrust balance for the direct measurement of the **FEEP** thrusters. A prototype of this unit will be ready by the end of 1998. *Centrosazio* is also developing a different concept of a microthrust balance under **ASI** funding.

Direct measurement of **FEEP** thrust will be needed in order to fully characterize the **FEEP** thrusters, including thrust noise evaluation and validation of the theoretical formula at micro-Newton level.

### 9.7.5.4 Future plans

Development and qualification of a Field emission neutralizer as possible alternative to the thermoionic neutralizer. This new concept may improve some system aspects such as power consumption and redundancy.

Miniaturization of the power electronics and redundancy philosophy investigations. Power electronics is the heaviest part of the **FEEP** system and must be reduced.

## 9.8 Mass and power budgets

The spacecraft mass and power budgets are given in Table 9.7 below. Power budgets are given for two cases: power in operational orbit, and power during transfer.

<i>Subsystem</i>	<i>Mass (kg)</i>	<i>Operational Power (W)</i>	<i>Power in Transfer Orbit (W)</i>
Payload	70.0	72.2	
Payload Shield	14.2		
Structure	41.1		
Thermal	1.7		17.0
Attitude Measurement	6.0	2.1	12.7
Propulsion ( <b>FEEP</b> )	22.0		
Telecommunications	9.9	26.4	12.0
Data Handling	14.5	13.1	9.9
Power Subsystem	12.2	14.8	6.8
Cabling	15.1		
Total	202.8	150.6	58.4

**Table 9.7** *Spacecraft mass and power budgets.*

The mass and power budgets of the propulsion module are given in Table 9.8.

The overall launch mass budget is presented in Table 9.9.

<i>Subsystem</i>	<i>Mass (kg)</i>	<i>Power (W)</i>
Structure	52.0	
Thermal	3.0	17.0
Propulsion SEP	44.2	490.0
Propulsion Hydra	7.6	0.8
Power	12.6	26.9
Solar Array	4.2	1.0
Cabling	8.0	
Total	131.6	535.7

**Table 9.8** *Propulsion module budgets.*

<i>Item</i>	<i>Composite 1</i>	<i>Composite 2</i>	<i>Composite 3</i>	TOTAL
S/C	203	203	203	
P/M dry	132	132	132	
Propellant	27	27	27	
Total	362	362	362	1086
Adaptor				21
Contingency (30 %)	100	100	100	300
TOTAL LAUNCH MASS	462	462	462	1407

**Table 9.9** *Total launch mass budget (kg).*



# 10 Mission Analysis

## 10.1 Orbital configuration

The desired configuration for the LISA spacecraft is such that the three spacecraft form an equilateral triangle which changes as little as possible throughout the mission. This desire arises from instrumental noise introduced into the gravitational-wave measurement that must be dealt with if there are changes in the distances between spacecraft. The current nominal orbital configuration places the spacecraft in a triangle with a center 1 AU from the sun and trailing the Earth by  $20^\circ$  in its orbit (see Figure 3.1). From the Earth the triangle appears to rotate about the center with a period of one year (see Figure 7.10). The location of the center of the formation  $20^\circ$  behind the Earth represents a compromise between the desire to have the constellation far from the Earth, to reduce distortions caused by the Earth's gravitational pull, and the desire to be closer to the Earth, to reduce the amount of propellant needed and to ease the requirements on the telecommunications system.

Each spacecraft is in an orbit around the sun with major axis  $D = 2$  AU and eccentricity  $e = d/(D\sqrt{3})$ , where  $d$  is the separation between the vertices (5 million km for the nominal LISA orbits). If the spacecraft were all in the same plane then the separation between spacecraft would vary between  $De$  and  $De/2$  over the course of one year. By giving the spacecraft an inclination  $i = d/D$ , and by appropriate choice of the node, anomaly, and argument of perihelion, the separation between spacecraft is constant to order  $De^2$  [142].

This heliocentric orbital configuration has the property that the directions between spacecraft are always within  $30^\circ$  of being orthogonal to the direction to the sun. This allows the spacecraft to be designed such that sunlight never enters the interferometer optics, and also allows the spacecraft to have the sun always illuminating the same part of the spacecraft.

## 10.2 Launch and orbit transfer

The three spacecraft will be injected into an Earth-escape orbit by a single launch vehicle. The current spacecraft design allows the three spacecraft to fit within the payload fairing and launch capability of a Delta II 7925 H. The Earth-escape orbit has an excess normalized energy of  $C_3 = 1.1 \text{ km}^2/\text{s}^2$  so that the three spacecraft will slowly drift behind the Earth. After launch and injection to the Earth-escape trajectory, the three spacecraft will be separated and individually targeted to their desired operational orbit.

At launch, each spacecraft will be attached to a propulsion module. The propulsion modules will provide the capability to maneuver the spacecraft into the desired operational orbits. After reaching the operational orbits, about 13 months after launch, the propulsion modules will be separated from the spacecraft to avoid having excess mass, propellant, and/or moving parts near the proof masses within the spacecraft. After reaching the final orbits, the spacecraft positions will evolve under gravitational forces only. Micronewton ion thrusters will be used to keep the spacecraft centered about the shielded proof masses within each spacecraft. The thrusters could be used to perform small ( $\Delta V < 1 \text{ cm/s}$ ) maneuvers if required.

Maneuvers with total  $\Delta V \approx 1000 \text{ m/s}$  are needed to reach the desired operational orbits after



launch. If a conventional chemical propulsion system was chosen, each spacecraft would perform two maneuvers of approximately 500 m/s each. The first orbit change maneuver would be a plane-change maneuver to incline the spacecraft orbit by  $i \simeq 1^\circ$  with respect to the ecliptic. The plane-change maneuvers would take place at different times for each spacecraft since the three final orbits are shifted  $120^\circ$  from each other along the ecliptic. For example, one spacecraft might perform a plane-change maneuver shortly after launch, the second spacecraft about 4 months after launch, and the third spacecraft about 8 months after launch. Approximately 13 months after launch, each spacecraft would perform a maneuver to stop the slow drift with respect to the Earth.

The mass of chemical propellant needed to perform the orbit-change maneuvers, combined with the current masses estimated for each spacecraft, would total more than the capability of the Delta II 7925 H launch vehicle. The mass of the propellant can be considerably reduced by use of ion-engines with their much larger specific impulses (velocity with which propellant is ejected) compared with chemical systems. The solar-powered ion engines have an efficiency such that the required propellant mass can be reduced by a factor of approximately 10. This is offset partly by the mass of the additional solar panels needed to provide power for the ion engine.

The required ion-engine thrust is rather small, about 20 mN, if the engine is on during most of the orbit transfer phase. This is much smaller than the thrust of engines designed for interplanetary missions. However, ion-engines developed for station keeping of geosynchronous communications satellites are of an appropriate size. In particular, the *Hughes XIPS* thruster has a thrust of 18 mN [1]. This engine is currently being tested in orbit on a *Hughes* communications satellite.

Well suited are also a radio-frequency thruster *RITA* from *DASA*, Germany, and an electron-bombardment ion thruster *UK-10*, manufactured by *DERA* (or *MMS*) in England. *RITA* has long space experience, and both have had considerable tests. They seem to be equally qualified for the *LISA* mission.

The mass of propellant (xenon) needed for use with these engines to provide the required  $\Delta V$  for the mission is only  $\approx 20$  kg per spacecraft compared with the  $\approx 180$  kg per spacecraft of propellant needed for the traditional chemical system. This reduction in mass is a major factor that enables the current mission design to be launched on a Delta-II class launch vehicle.

The spacecraft transfer trajectories using the ion-engines have not yet been fully optimized. A set of candidate trajectories has been found to establish the engineering feasibility. The candidate trajectories require that the ion-engines be on during approximately 80% of the 13 month transfer phase. The angle between the thrust direction and the direction to the sun for these trajectories ranges from  $10^\circ$  to  $60^\circ$ , making it difficult to provide power with a solar array fixed to the spacecraft body. The current spacecraft design includes steered solar arrays to provide power for the ion-engines during the transfer phase, so that the arrays can be pointed towards the sun regardless of the thrust direction. These arrays would be attached to the propulsion module for each spacecraft and jettisoned, along with the ion engine, after reaching the operational orbits.

### 10.3 Injection into final orbits

The spacecraft will have limited maneuvering capability once separated from the propulsion module, due to the limited impulse of the micronewton thrusters. This requires that the spacecraft be accurately delivered to the final orbits.

If chemical propellant is used in the propulsion modules, a fairly large ( $\Delta V \approx 500$  m/s) insertion maneuver would be needed upon reaching the desired operational orbit. With typical maneuver execution errors of 1%, the error in this maneuver would be about 10 m/s which would

be much too large to be corrected by the micronewton thrusters. Therefore, after the main insertion maneuver, the propulsion module would need to remain attached to the spacecraft while sufficient tracking information is acquired to determine the error in the orbit insertion maneuver.

The propulsion module would then perform a correction maneuver of order 10 m/s. The expected error in a maneuver of this size would be about 10 cm/s which would still be too large for the micronewton thrusters to correct. Another period of spacecraft tracking would be needed to design a final correction maneuver to be executed by the propulsion module. After the execution of the final correction maneuver, the spacecraft would separate from the propulsion module. The separation would be effected by a spring-separation system, with a separation velocity of order 10 cm/s. The error in the separation maneuver is expected to be of order 1 cm/s which can be corrected using the micronewton thrusters.

## 10.4 Orbit configuration stability

Both the nature of the elliptical orbits and planetary perturbations will cause small changes in the lengths of the sides of the triangle formed by the three spacecraft. These orbital changes of distance between spacecraft will impose Doppler shifts on the interferometer signals that will have to be removed using on-board oscillators (clocks). Noise from the oscillators will then corrupt the distance measurements. The amount of noise introduced depends on the size of the Doppler shift and the performance of the oscillator.

The spacecraft are designed to be drag-free so that the only significant forces affecting the proof masses at the center of each spacecraft are gravitational. In the simplest case the only free parameters that can be adjusted to minimize the arm rates-of-change are the initial positions and velocities of the proof masses, which then move under the influence of the gravitational field of the sun and planets. For the heliocentric configuration the typical arm-length changes due to the initial shape of the orbits are of order  $De^2$  with a main period  $T$  of one year. For an arm length  $d = 5 \times 10^6$  km, this implies a maximum arm rate-of-change of order  $v = (2\pi/T)d^2/(3D) \approx 5$  m/s. Perturbations due to the Earth and other planets cause larger changes in the arm lengths after a few years. The degradation is larger when the formation is nearer the Earth.

When the initial positions and velocities for the six spacecraft are chosen to minimize the average rate-of-change of the three arm lengths over a two-year period, the arm rates-of-change are found to vary between  $\pm 6$  m/s [143]. Given the current performance of space-qualified oscillators, removing the Doppler shifts of the nominal orbits introduces more noise in the measurement than can be tolerated. The arm rates of change would have to be less than  $\simeq 10$  mm/s for the noise introduced by a spacecraft clock with Allan deviation  $10^{-13}$  to be at an acceptable level (see Section 7.2.2).

Another option studied was to include occasional maneuvers by the spacecraft to reduce the arm rates-of-change. The idea is that instead of allowing the proof masses to move under only gravitational forces for the entire nominal mission, maneuvers could be done at intervals to keep the arm rates-of-change small. The maneuvers would occur at each spacecraft mainly perpendicular to the direction between the spacecraft. The maneuvers would serve to make small adjustments in the orbit period and eccentricity such that the arm lengths remain more constant. This strategy is limited by the low level of thrust available from the micronewton thrusters planned for the spacecraft. The micronewton thrusters are currently planned to have a maximum thrust of order  $100 \mu\text{N}$ , sufficient to counteract the force on the spacecraft due to the solar luminosity. With these thrusters it would take a long time to execute even small

maneuvers, perhaps one day to change the velocity by 10 cm/s (given the mass of the current spacecraft design). The noise force on the proof masses during the execution of these maneuvers is assumed to be so large as to preclude accurate measurements during that time.

Analysis has been done to show that it is not possible to keep the rates-of-change of all three arms of the heliocentric formation to an acceptable level using the micronewton thrusters [143]. It is feasible to stabilize two of the three arms to an acceptable level with a practical number of small maneuvers. If one particular vertex is considered as the prime vertex, then the same spacecraft oscillator can be used to remove the Doppler shift of the two arms meeting at the prime vertex. Then it is the difference in the rate-of-change of the two arms that introduces noise into the gravitational-wave measurement. An orbit solution has been found with maneuvers taking place once each month, of magnitude 10 cm/s or less, such that the difference in rate-of-change of the two prime arms is kept to an *rms* level of 7 mm/s. The disadvantages of using maneuvers to stabilize one pair of arms is that it does not allow for using the information available from the third arm, and it involves a “dead time” of about one day each month. By not using the third arm the detector is sensitive to only one of the two possible gravitational-wave polarizations at any given time. (The rotation of the formation over the annual period will cause a given pair of arms to be sensitive to different polarizations at different times.)

Another alternative to reduce the noise caused by the Doppler shifts would be to modulate the laser beams with a signal based on the spacecraft oscillators [144]. In this scheme each arm would be essentially used as a delay line to stabilize the oscillators; the returned oscillator signal would be compared with the local oscillator signal and the difference would be used to measure fluctuations in the spacecraft oscillator. This scheme has been adopted as the nominal plan for the *LISA* mission.

With this scheme it is still advantageous to have the arm rates-of-change small since this reduces the dynamic range of the oscillator signal. For example, with arm rates-of-change of 15 m/s and Doppler shifts of 30 MHz, it suffices to use a 200 MHz modulation derived from the spacecraft oscillators on the laser signal [145]. The modulation can be imposed using an electro-optical modulator already planned in the spacecraft payload for other purposes. This is somewhat simpler than the two-laser scheme outlined in Hellings *et al.* [144]. With these clock-noise reduction schemes there are a variety of possible choices of nominal orbits that give acceptable ranges of Doppler shift over the period of the mission.

The nominal operational orbits selected have initial orbits that could, if necessary, be adjusted by small maneuvers each month to keep the rates-of-change of one pair of arms nearly the same throughout the mission. However, no maneuvers are planned if performance is nominal. Figure 10.1 is a plot of the rates-of-change of the three arm lengths for the nominal orbit configuration. (The orbits will change slightly in character depending on the chosen launch date.) The rate-of-change of arm length for two of the arms is almost identical for the first six months of the mission. The difference in rate-of-change of these two arms could be kept small through the use of small maneuvers. The third arm rate-of-change varies between  $\pm 15$  m/s. This could be reduced if all three arms were treated equally, at the cost of not having one pair of arms with similar Doppler rates. However, the Doppler shift caused by an arm rate-of-change of  $\pm 15$  m/s is well within the capability of an electro-optical modulator to perform the clock cancellation scheme.

With the current nominal orbits, the angle between the two distant spacecraft, as seen from any one spacecraft, changes slowly through the year, by  $\pm 1^\circ$  in the worst case. This requires the angle between the two telescopes on each spacecraft to be articulated. Figure 10.2 is a plot of the angle between the two distant spacecraft, as seen from any one of the spacecraft, for these orbits.

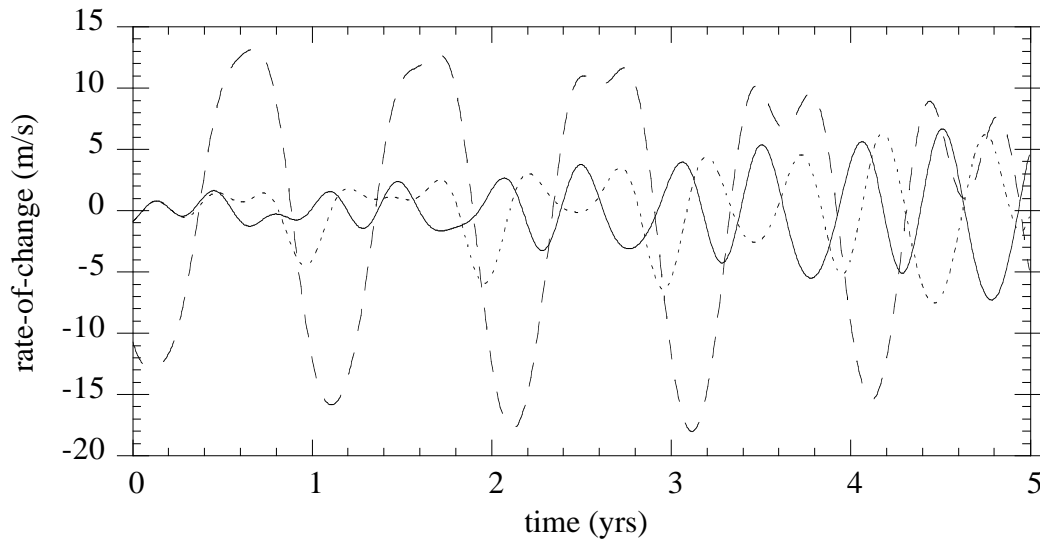


**Figure 10.1** Nominal rates-of-change for the three arms of the *LISA* triangular spacecraft formation, with the spacecraft orbits evolving under only gravitational forces (i.e. with no maneuvers). The rates-of-change of the lengths of arm 1 (solid line) and arm 2 (dotted line) (see Figure 5.1) are almost identical for the first six months of the mission and could be kept nearly identical, if necessary, through the use of occasional small maneuvers.

## 10.5 Orbit determination and tracking requirements

Prior to the separation of the propulsion modules from the spacecraft, the spacecraft positions and velocities need to be accurately determined. The primary requirement is that the spacecraft velocity be known to about 1 cm/s, which is within the capability of the micronewton thrusters. This means that maneuvers, especially the final orbit injection maneuver and propulsion module

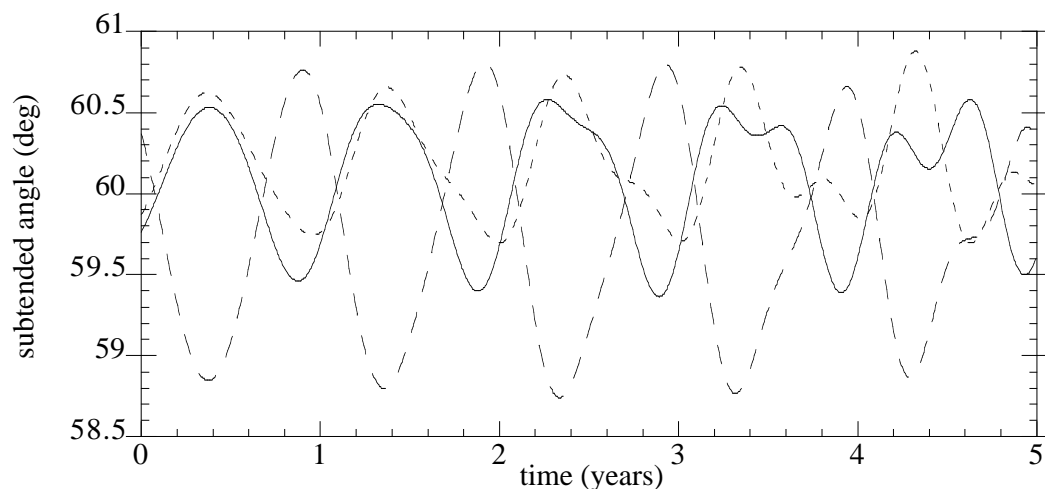


**Figure 10.2** The angle between the two distant spacecraft, as seen from any one of the spacecraft, is shown for the nominal *LISA* orbit configuration. The angle subtended by arm 3 (dashed line), as viewed from spacecraft A, has the most variation with the chosen nominal orbits (see Figure 5.1).

separation, need to be determined to about 1 cm/s. The spacecraft positions should be determined well enough to know the direction to the distant spacecraft within the angle subtended by the laser primary beam width. With laser wavelength  $1\text{ }\mu\text{m}$ , telescope diameter 30 cm, and spacecraft separation  $5 \times 10^6$  km, this implies a position knowledge of approximately 10 km.

During the science-operations phase there are no stringent operational navigation requirements. The spacecraft orbits must be determined with modest accuracy for purposes of ground antenna pointing and frequency prediction. A more stringent requirement arises from the on-board data reduction algorithm for the interferometer data. For this data reduction, the length of each arm needs to be known to better than 200 m at any time (see Section 7.2.1).

Table 10.1 gives a summary of the orbit determination requirements.

**Table 10.1** *Required orbit determination accuracies.*

<i>Phase</i>	<i>Accuracy (<math>\sigma_{\text{rms}}</math>)</i>	<i>Requirements taken into account</i>
Transfer	position: 10 km velocity: 1 cm/s	classical interplanetary navigation, manoeuvre dispersions
Experiment	position: $\leq 10$ km velocity: 2 mm/s arm-length: $\leq 200$ m	laser acquisition, on-board laser phase processing

The navigation performance for the transfer phase is relatively standard for current interplanetary missions that use X-band (8 GHz) radio systems for the acquisition of range and Doppler measurements by tracking stations of NASA's Deep Space Network (DSN). The characteristics of the assumed ground tracking accuracy are:

- Station location uncertainties  $\leq 3$  cm.
- Two-way range data (noise:  $< 2$  m; bias:  $< 10$  m) plus two-way Doppler data (max. error:  $< 0.1$  mm/s for 60 s averaging).
- Ionosphere zenith delay after calibration by means of GPS signals:  $\leq 3$  cm.
- Troposphere zenith delay after modeling:  $\leq 4$  cm.
- Earth orbit orientation error:  $\leq 5$  nrad.

These tracking assumptions are met by the DSN network, and could be met by the ESA Multi Purpose Tracking System after a few enhancements and/or modifications (X-band, GPS-calibration, highly stable frequency standards). With this type of tracking, and assuming that tracking measurements are acquired for each spacecraft throughout 8-hour tracking passes two to three times each week, the navigation requirements for the transfer phase can be met. For the injection into the final orbits, one to two weeks of tracking time may be needed between successive maneuvers until the expected error of the final pre-separation maneuver is less than 1 cm/s.

During science operations, the requirement that the arm lengths be determined to  $\leq 200$  m is not easily met using ground tracking only. However, it will be possible to augment the ground tracking data with data acquired along the interferometer arms. Each interferometer arm will include phase measurements taken every 0.1 s (see Section 7.2.1). Differences in the phase measurements give information on the rate of change of the arm length (i.e. Doppler). The measurements along each arm will be noisy compared with the desired gravitational-wave performance but are sufficient to aid in the determination of the arm lengths. After the arm

lengths are determined, the laser phases can be combined in a manner to cancel most of the phase measurement error and result in the desired instrument performance.

For purposes of determining the arm lengths, a short analysis was performed assuming ground tracking of each spacecraft for 8 hours every other day, and combined with phase measurements from the laser system sampled once every 30 minutes. The phase measurements were assumed to have an accuracy of  $5 \times 10^{-4} \text{ m}/\sqrt{\text{Hz}}$  at the frequency corresponding the round-trip light time. A phase bias needs to be estimated for each arm along with the spacecraft positions and velocities. Uncertainties in the positions of the planets, especially the Earth, have been taken into account, as have uncertainties in station locations and Earth media calibrations. The analysis was performed for a configuration when the LISA constellation was at  $0^\circ$  declination as viewed from the Earth, which is when the poorest orbit determination is expected.

Table 10.2 shows the achievable orbit determination accuracy using combinations of ground tracking and measurements from the laser system. After 16 days of ground and laser tracking, the arm lengths can be determined to about the required 200 m accuracy. The system performance might end up being somewhat better since the assumptions on the laser-system measurements were very conservative.

**Table 10.2** Achievable orbit determination accuracy ( $1\text{-}\sigma$ ).

Case	Accuracy ( $\sigma_{\text{rms}}$ )			
	Position	Arm 1	Arm 2	Arm 3
Radio tracking only over 16 days	5.94 km	3.75 km	1.49 km	5.56 km
Radio and laser tracking over 16 days	1.79 km	0.19 km	0.07 km	0.14 km

If the laser systems include some means of directly measuring the arm lengths, such as incorporation of a ranging signal in addition to the laser carrier phase, then the arm lengths would not need to be inferred from the ground tracking measurements and laser phase measurements. Further studies will need to refine the navigation analysis and determine the optimal means of determining the arm lengths.

## 10.6 Launch phase

### 10.6.1 Launcher and launcher payload

The baseline launcher for the mission originally proposed was the 7925 H with a 9.5 ft diameter metal fairing, but it has been superseded by the same model equipped with the composite 10 ft fairing.

The payload for this launcher is shown in Figure 10.3. It consists of three composite satellite assemblies stacked on top of each other, and is installed in the launcher fairing as illustrated. The total mass of the stack should not exceed 1380 kg, to enable the mission launch profile to be executed.

Further information in relation to the satellite configuration and the launcher accommodation is given in Section 9.3.



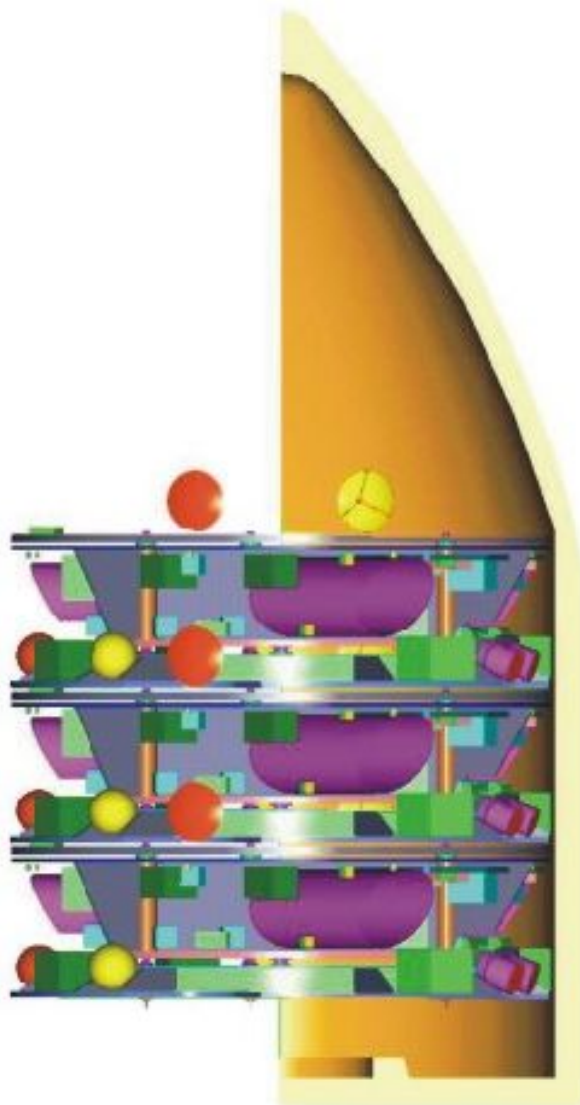


**Figure 10.3** *Three LISA composite spacecraft in the Delta II 10 ft fairing*

### 10.6.2 Analysis of launch phase

The stack of three LISA composite spacecraft is to be launched on a single Delta II 7925 H three-stage vehicle from the Eastern Launch Site. The best mass performances are obtained for a launch flight azimuth of  $95^\circ$ , leading to an orbital inclination of  $28.7^\circ$ , and a perigee altitude of 185 km.

The first part of the ascent phase (main engine of Stage I and the strap-on solid rockets) is followed by a first ignition of Stage II to achieve a circular orbit. Payload fairing separation is performed in this phase. After a coast arc, Stage II is ignited again up to second engine cut-off. The third stage, based on the STAR 48 B solid rocket motor, is spun-up, separated, and fired to inject into the final orbit. The injection orbit is an Earth-escape trajectory with an escape velocity,  $V_\infty$ , of about 1 km/s (the normalised excess energy  $C_3 = V_\infty^2$ ). The third stage can have a yo-yo de-spin system to leave the spacecraft with the required spin velocity which is supposed to be zero.



The three *LISA* composite spacecraft will be separated one by one and will autonomously perform any required attitude manoeuvres to enter into a safe Sun pointing mode. Each spacecraft consists of a Science Module (S/M) and of an attached Propulsion Module (P/M) that provides the capability to individually manoeuvre the composite spacecraft into the required operational orbit. The P/M uses electrical propulsion (one ion engine active, the other one in cold redundancy) with a thrust of about 20 mN.

The mass performance of the launcher depends on the required  $V_\infty$  (near 1 km/s the change is less than 3 kg of payload mass per 100 m/s). The precise conditions of Earth-escape will be selected as function of the launch date and the final S/M and P/M characteristics.

All three composite spacecraft leave the Earth such that after two weeks the distance to the Earth is 1.5 million km, and the relative velocity about 1 km/s when leaving the sphere of influence of the Earth.

Orbit determination during this phase is a standard task of Deep Space Network (DSN).

After injection by the launcher, the conditions of spacecraft illumination by the Sun, and the relative geometry of the spacecraft, Earth and Sun are very similar for launch on any day of the year ensuring the possibility of launch at any day of the year.

## 10.7 Operational orbit injection and composite separation

### 10.7.1 Composite spacecraft

The composite satellite consists of a Science Module (S/M) and a separable Propulsion Module (P/M), as illustrated in Figure 10.4. In this figure the upper two elements are the composite, and are shown attached to the next lower Science Module. The total size of the composite is 2700 mm diameter and 800 mm depth. A more detailed description is provided in Section 9.3.

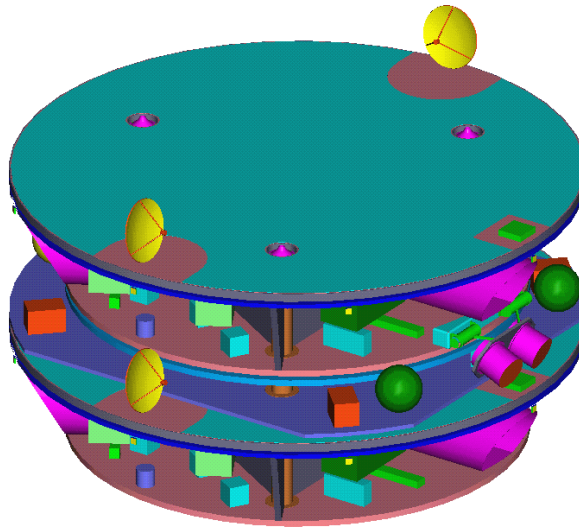


**Figure 10.4** *LISA* composite (attached to the next lower science module)

### 10.7.2 Analysis of injection into operational orbit

The desired operational orbit configuration for the *LISA* spacecraft is such that the three spacecraft are positioned at the vertices of a quasi-equilateral triangle with centre in the ecliptic

plane, about  $20^\circ$  behind the Earth. The side of the triangle,  $d$ , is initially 5 million km. This configuration is achieved by selecting the following orbital elements for the spacecraft orbits:

semi-major axis	$a = 1 \text{ AU} ,$
eccentricity	$e = d/(2a\sqrt{3}) ,$
inclination with respect to the ecliptic	$i = d/(2a) ,$
argument of pericentre	$90^\circ$ or as $270^\circ$ .

The ecliptic longitude of the ascending node,  $O$ , and the mean anomaly,  $M$ , of the three spacecraft differ by  $120^\circ$ :

for S/C 1	$(O, M) ,$
for S/C 2	$(O + 120^\circ, M - 120^\circ) ,$
for S/C 3	$(O - 120^\circ, M + 120^\circ) .$

For a given date,  $O$  and  $M$  are selected such that the centre of the triangle at that epoch is  $20^\circ$  behind the Earth and with the required triangle orientation. When propagating the orbits to a different date the quasi-equilateral triangular configuration is maintained and the orientation of the triangle rotates in a plane that is inclined  $60^\circ$  with respect to the ecliptic.

After spacecraft separation from the launcher the spacecraft will autonomously enter into a safe Sun pointing mode and slowly drift away from Earth. Ground control will initiate the operation of the spacecraft, and control the ion engine to establish the transfer to the operational orbit.

The general characteristics of the transfer trajectories for each spacecraft were analysed as follows: For launch dates in Winter, Spring, Summer, and Fall the period and direction of thrust of the ion-engines has been optimised to generate trajectories to transfer one spacecraft from the Earth to the operational orbit. In this optimisation one has left fixed the parameters  $D0$ ,  $V_\infty$ ,  $\delta_\infty$ ,  $\Theta$ , where  $D0$  is the day of launch,  $V_\infty$  the module of the escape velocity,  $\delta_\infty$  the declination of  $V_\infty$  with respect to the ecliptic, and  $\Theta$  defines the triangle orientation at  $D0$ . The direction of  $V_\infty$  in the ecliptic plane, the sequence and duration of thrust and coast arcs, the arrival date, and the variable thrust direction are left as free parameters to be optimised. The ion engine is either working at full power with 18 mN thrust or switched off. The initial mass of the composite spacecraft is taken as 430 kg.

The results of the optimisation show that:

- The longest transfer time is always less than 15 months, and the difference in time of injection into the operational of the three spacecraft is about 1 month.
- The propellant mass required for the transfer varies between 12.5 kg and 20 kg.
- The angle between the thrust direction and the direction to the Sun, if it is not constrained in the optimisation process, will vary so that the fixed solar array will not always be orthogonal to the Sun but may go up to  $55^\circ$  away. However, the solar aspect angle can be constrained to any desirable value at a modest increase of the propellant mass. This angle can be restricted to less than  $25^\circ$  without propellant mass penalty, and to  $15^\circ$  with a penalty of less than 0.5 kg. The loss of solar power is 10 %, and 3.5 %, respectively.

The design of the [LISA](#) composite spacecraft should support a transfer time of up to 15 months, and have a propellant capability of 20 kg for an initial mass of 430 kg and a 18 mN ion engine. If seasonal launch restrictions are acceptable, this propellant allocation can be reduced to about 16 kg.

For a particular launch day a triangular configuration will be selected from the general characteristics of the transfer trajectories, and the trajectories for the three spacecraft can be re-optimised for a common launch with the same vehicle.

### 10.7.3 Analysis of composite separation

The Propulsion Module (P/M) will deliver the composite spacecraft very accurately to the operational orbit and, before separation from the spacecraft, it will perform an attitude slew manoeuvre to leave it in the proper attitude for operation. A high accuracy of orbit insertion is needed because after the Science Module (S/M) has been separated from the Propulsion Module it has very limited manoeuvre capabilities due to the very low thrust levels of the FEEDs. The required orbital delivery accuracy depends on the tolerable errors in the evolution of the orbital triangular configuration, in particular on the variation of the interferometer arm length change and on the arm length change rate. It has been shown that, using standard X-band radio tracking, delivery errors of 10 km in position and of less than 2 mm/s in velocity are possible and these values are acceptable in view of the evolution of the triangular configuration for periods of several years.

The Propulsion Module will separate from the Science Module by means of a two-stage separation system. This system needs to produce a small relative velocity of separation between the S/M and the P/M ensuring that the two craft will separate safely without risk of collision. The mechanisation error of the separation must, however, not be so big that it takes a long time to correct resulting S/M position and attitude errors with the FEEDs. For a S/M of 250 kg, it takes about 14 hrs to correct 1 cm/s with a thrust of 50  $\mu$ N. The current baseline is to separate the P/M from the spacecraft at a relative velocity of 3 cm/s. This velocity ensures that the distance of the P/M to the plane formed by the three S/Ms is continuously increasing to about 55 km in two months. This period is shorter than the time required for commissioning of the spacecraft and beginning of drag-free control, and this ensures that the Field of view of the telescope will be unobstructed. After the drag-free control is activated the distances between the P/Ms and the triangular plane spanned by the three S/Ms will continuously increase to more than 30 000 km after one year without any risk of collision between craft.

Another matter of importance for the separation is the angular rate imparted to the S/M during separation. Since there is presently no battery foreseen onboard the S/M, this rate must be small enough so that it can be countered by the FEEDs before the solar aspect angle w.r.t. the S/M solar array gets so large that no longer enough power is generated to drive the FEEDs.

## 10.8 Evolution of the operational orbit

The operational orbits of the three S/Ms are selected to maintain these spacecraft at the vertices of a quasi-equilateral triangle with centre in the ecliptic plane, about 20° behind the Earth and with sides of 5 million km length, Figure 10.5.

The orientation of the triangle rotates once a year on a plane that makes an angle of 60° with the ecliptic, and the line of intersection with the ecliptic is orthogonal to the line connecting the Sun with the centre of the triangle. The 20° trailing angle to the Earth results from a trade-off between radio communication links and the orbital perturbation due to Earth and Moon. The distances between spacecraft are dictated by the requirements of the scientific measurements that will be performed by LISA.

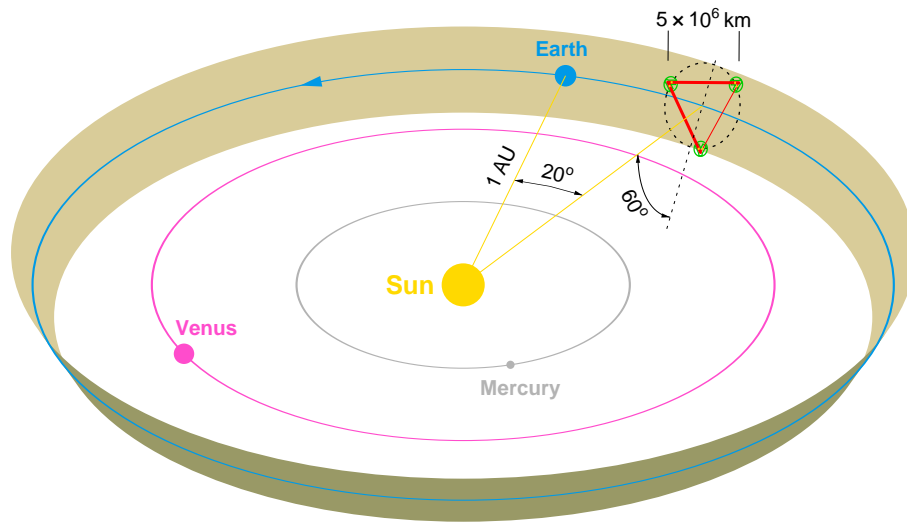


**Figure 10.5** Operational orbit configuration of the three Science Modules

Once in Science Mode operations the S/Ms are controlled in drag-free mode, and, therefore, it is only the gravitational forces of the Sun, planets, and other bodies of the solar system that determine the trajectory of each spacecraft.

Starting with the orbits as described in Section 10.7.2, the initial distance between spacecraft is 5 million km, but this distance varies periodically over one year. Different strategies have been investigated to reduce this variation:

- Passively, by selecting the initial conditions to minimise the variations of one, two, or three arms of the triangle;
- Actively, by performing orbital corrections with the FEEPs. In this case, the analysis shows that it is not possible to stabilise the rate of change of all three arms, but only of one or two arms for a period of a few years. The active control requires as well that manoeuvres may need to be performed for several days every month, with a possible disruption of the scientific measurements.

Therefore, the current baseline is to select the initial orbital conditions so as to minimise the average rate of change of the distance between the three pairs of spacecraft, to let the orbits freely evolve and to avoid orbit control manoeuvres. An alternative would be to select a configuration that keeps the rates-of-change for two arms as small as possible at the cost of increased rates for the third arm (see Section 10.4 and Figures 10.1 and 10.2).

The distances between S/M spacecraft, i.e. the interferometer arm length, will oscillate around the nominal value of 5 million km with an amplitude of less than 30 000 km, and the difference between any two arm lengths can be up to 60 000 km. The velocity along the line of sight of the telescope introduces a measurement noise caused by the Doppler shift that will be corrected by modulating the laser beams. This Doppler compensation is able to cope with the predicted rate of maximum 8 m/s, and with the predicted rate differences between each arm of less than 12 m/s.

The angle between any two S/Ms as seen from the third one changes periodically through the year with variations around  $60^\circ$  with an amplitude of less than  $0.6^\circ$ . This is due to a velocity in the sky plane for each spacecraft as observed by any of the other spacecraft that oscillates between 500 m/s and 1000 m/s. The velocity in the sky plane of spacecraft 2 with respect to spacecraft 1 is the projection on a plane orthogonal to the line from S/C 1 to S/C 2 of the relative velocity of S/C 2 with respect to S/C 1. This velocity necessitates in addition the application of

a point-ahead angle between the transmitted and received laser beams. The point-ahead angle can be split into two components: in-plane and out-of-plane w.r.t. the plane spanned by the three spacecraft. It has been quantified as follows:

In-plane point-ahead angle	Bias: $3.3\ \mu\text{rad}$	Variation: $\pm 55\ \text{nrad}$
Out-of-plane point-ahead angle	Bias: $85\ \text{nrad}$	Variation: $\pm 5.75\ \mu\text{rad}$

The considerable out-of-plane variation is nicely sinusoidal.



# 11 Technology Demonstration in Space

To minimize the cost and risk associated with the full [LISA](#) mission it is essential to have well-understood and proven technology available. A [LISA](#) technology demonstration mission is therefore highly desirable. Such a mission should not just provide a functional test but should instead aim at testing the key technologies required for [LISA](#) to within an order of magnitude of the final performance in the relevant mHz frequency range.

## 11.1 A European LISA Technology Demonstration Satellite – SMART 2

### 11.1.1 Introduction

The proposed European technology demonstration satellite for [LISA](#) aims to test the key technologies of inertial sensing, drag-free control, and low-frequency laser interferometry required for [LISA](#). It could ideally be flown as the up-coming [SMART 2](#) mission.

An even more attractive possibility is to fly a demonstrator jointly with [NASA](#), perhaps in the mission [ST 3](#) or follow-ons.

The single [SMART 2](#) spacecraft will contain two isolated proof masses which will be used as references for the drag-free/attitude control system. The proof masses will also serve as reference mirrors for the laser interferometer package. The interferometer will provide an independent measurement of relative displacement between the masses, allowing a direct assessment of the relative acceleration between the masses. Field emission (ion) thrusters will be the primary actuators for the drag-free/attitude control. An autonomous star-tracker plus Sun sensor will be used for coarse attitude control/safe-mode. A cold-gas system will be used for coarse-attitude control. The target launch year is 2004 (pending the timely development of the key technologies), with a nominal mission duration of six months.

Various candidate orbits and launch options are being considered. It is desirable to have an orbit altitude above 10 000 km in order to avoid the charging of the proof masses due to interaction with trapped protons in the Van Allen Belts. The baseline choice is a Geostationary orbit ([GEO](#)) which avoids the proton belts completely, but which necessitates an apogee kick motor for orbit injection. Another option would be to utilise a shared launch into a suitable orbit without the need for an apogee kick motor. Other suitable sharing options should be investigated. In the worst case, a “de-scoped” option would be a Geostationary transfer orbit ([GTO](#)) which would eliminate the need for a large apogee kick motor, but which would incur much higher charging rates due to traversal of the proton belts. The charge management system would thus have to be enhanced in this option, but the spacecraft and launch costs could be minimised compared with the alternative options.

### 11.1.2 Mission goals

The primary goals of the [SMART 2](#) demonstrator mission are summarised as follows:

1. To demonstrate drag-free/attitude control in a spacecraft with two proof masses in order



to isolate the masses from inertial disturbances. The aim will be to demonstrate the drag-free system with a performance on the order of than  $10^{-14} \text{ m s}^{-2}/\sqrt{\text{Hz}}$  in the bandwidth from  $10^{-3} \text{ Hz}$  to  $10^{-1} \text{ Hz}$ , bearing in mind the [LISA](#) requirement of  $10^{-15} \text{ m s}^{-2}/\sqrt{\text{Hz}}$  for each proof mass (see below).

2. To demonstrate the feasibility of performing laser interferometry in the required low-frequency regime with a performance as close as possible to  $10^{-12} \text{ m}/\sqrt{\text{Hz}}$  in the bandwidth from  $10^{-3} \text{ Hz}$  to  $10^{-1} \text{ Hz}$ , as required by the [LISA](#) mission (see below). Of course, this test only demonstrates the *displacement* sensitivity of the interferometer, not the *strain* sensitivity, which would require large separations ( $5 \times 10^6 \text{ km}$ ) between the proof masses.
3. To assess the longevity and reliability of the capacitive sensors, thrusters, lasers, and optics in the space environment.

In addition to these primary goals, the [SMART 2](#) demonstrator mission will enable systematic tests to be performed on the technology. For example, the characteristics of the thrusters and sensors can be determined over their dynamic range, for use in future design refinements; and the effects of known disturbances (e.g. due to electrical charging of the proof masses) can be assessed. Likewise, various control and calibration strategies can be compared (e.g. using one proof mass as the translational reference, the other as an attitude reference; or defining a virtual drag-free reference from a combination of sensor outputs, etc.)

### 11.1.3 Background requirements

It is useful to consider the requirements of the full-blown [LISA](#) gravitational-wave mission in order to put the [SMART 2](#) demonstrator goals into perspective. The baseline [LISA](#) requirements are summarised as follows:

1. In order to achieve the basic gravitational wave strain sensitivity, each proof mass must be free of spurious accelerations (relative to inertial space) along the interferometer axis to better than

$$3 \times 10^{-15} \left[ 1 + \left( \frac{f}{5 \times 10^{-3} \text{ Hz}} \right)^2 \right] \text{ m s}^{-2}/\sqrt{\text{Hz}}$$

within the measurement bandwidth ([MBW](#)) of  $10^{-4}$  to  $10^{-1} \text{ Hz}$ . The requirements along the other axes are relaxed by approximately two orders of magnitude.

2. In order to suppress the effects of motion-modulation of local (spacecraft-induced) disturbance fields (magnetic, electrostatic, gravitational, etc.) and to suppress the effects of optical-path fluctuations, the relative displacement between each proof mass and the spacecraft, along the interferometer axis, must be less than

$$5 \times 10^{-9} \text{ m}/\sqrt{\text{Hz}}$$

within the [MBW](#). This corresponds to a relative acceleration of

$$\approx 10^{-13} \text{ m s}^{-2}/\sqrt{\text{Hz}} \quad (\text{at } 10^{-3} \text{ Hz}),$$

which is seen to be two orders of magnitude above the requirement on the inertial acceleration of the proof mass (item 1). This means that the spacecraft drag-free control requirement (i.e. relative to the proof mass) is relaxed compared with the requirement on the inertial isolation of the proof mass. This relaxation is made possible by the optical

arrangement whereby the light is effectively referenced to opposing surfaces on each proof mass.

The corresponding relative displacement requirements along the non-sensitive axes arise only from the need to suppress nonlinearities and to avoid sensor saturation (e.g. of the op-amps in the capacitive circuits) which suggests that the displacements must be less than

$$5 \times 10^{-6} \text{ m}/\sqrt{\text{Hz}}$$

within the MBW. However, since each spacecraft contains two proof masses, and since the interferometer axes for each arm are not parallel, the more rigid requirements will prevail in two planar directions, and only the out-of-plane direction will be relaxed.

3. The spacecraft attitude must be precisely controlled for two reasons: (i) to ensure that the receiving spacecraft remains locked-on to the same portion of the incoming, non-perfectly-spherical optical wavefront; and (ii) to ensure that the attitude motion does not yield excessive translational motion at the location of each proof mass (which are spatially separated by tens of centimetres). For nominal parameters, (i) imposes that the pointing must be controlled to within

$$\vartheta_{\text{dc}} \widetilde{\delta\vartheta} \leq 3 \times 10^{-16} \text{ rad}^2/\sqrt{\text{Hz}},$$

where  $\vartheta_{\text{dc}}$  represents the dc pointing error, and  $\widetilde{\delta\vartheta}$  represents the pointing jitter across the MBW. Assuming that  $\vartheta_{\text{dc}}$  can be controlled to  $\approx 3 \times 10^{-8} \text{ rad}$  (depending on photodiode drift, etc.), this imposes a jitter requirement of

$$\widetilde{\delta\vartheta} \leq 10^{-8} \text{ rad}/\sqrt{\text{Hz}}$$

within the MBW. Depending on the actual geometrical layout, condition (i) will be more or less demanding than condition (ii). For example, assuming that the proof masses are spatially separated by 0.2 m, and that the drag-free null passes through the location of one proof mass, then the jitter of  $10^{-8} \text{ rad}/\sqrt{\text{Hz}}$  corresponds to a displacement of  $2 \times 10^{-9} \text{ m}/\sqrt{\text{Hz}}$  at the location of the other proof mass. This is within the allowable limit of item 2, so condition (i) on attitude is more restrictive than condition (ii), etc.

4. In order to achieve the target strain sensitivity across the armlength of  $5 \times 10^6 \text{ km}$ , the interferometer displacement noise must be lower than approximately

$$10^{-11} \text{ m}/\sqrt{\text{Hz}}$$

across the MBW. This includes all optical effects, as well as spurious proof-mass motions. Allowing for reasonable apportioning of errors across the various contributions, the requirement on the optics alone becomes

$$10^{-12} \text{ m}/\sqrt{\text{Hz}}$$

over the MBW.

## 11.2 SMART 2 demonstrator mission profile

### 11.2.1 Orbit – baseline option

For the baseline [GEO](#) option (and for a shared launch into higher orbits), the main disturbance will be radiation pressure with a nominal force magnitude of  $\approx 10 \mu\text{N}$  (solar pressure  $4.644 \times 10^{-6} \text{ N/m}^2$ ; Earth albedo plus [IR](#) pressure  $\approx 0.2$  of solar pressure), modulated at the orbit frequency due to the variation in the direction of the line-of-sight to the Sun. This disturbance will be essentially uniform, with only slight stochastic variations due to solar fluctuations amounting to a few percent of the nominal values. The largest stochastic disturbance is likely to be noise in the thrusters which may be on the order of  $1 \mu\text{N}$  (*rms* across the [MBW](#)).

### 11.2.2 De-scoped option

For the de-scoped option which may be necessary due to cost, the most accessible orbit would be [GTO](#) (Geostationary Transfer Orbit). For example, from a nominal Ariane 5 launch into [GTO](#), the resulting orbit will be low-inclination, highly eccentric, with a perigee altitude of  $\approx 600 \text{ km}$  (velocity  $\approx 9.9 \text{ km/s}$ ), an apogee altitude of  $35786 \text{ km}$  (velocity  $\approx 1.6 \text{ km/s}$ ), and an orbit period of  $\approx 10.6$  hours. In the vicinity of perigee, aerodynamic drag will dominate, with a nominal magnitude of  $\approx 0.1 \text{ mN}$  opposite the direction of travel (atmospheric density  $\approx 5 \times 10^{-13} \text{ kg/m}^3$  at  $600 \text{ km}$ , solar maximum; drag coefficient  $\approx 2.2$ , spacecraft projected surface area  $\approx 1 \text{ m}^2$ ). For most of the orbit, the altitude will exceed  $1000 \text{ km}$ , and the aerodynamic drag will be negligible compared with radiation pressure ( $\approx 10 \mu\text{N}$ ). The comparatively large drag at perigee will saturate the electric thrusters and the inertial sensors, requiring an undesirable switching of electrostatic suspension forces and a corresponding reset and calibration every orbit. It would thus be desirable to boost the orbit perigee to above  $1000 \text{ km}$  in order to overcome this problem. Furthermore, the [GTO](#) trajectory traverses the trapped radiation belts twice per orbit, leading to an integrated electric charge build-up on each proof mass of about  $10^{-10} \text{ C}$  per orbit. However, ground tests have shown that this high charge rate can be managed by enhancing the performance of the discharge system.

### 11.2.3 Coarse attitude control

It is necessary to perform a continuous slewing motion in order to keep the solar array pointed at the Sun to within  $\approx 1^\circ$ . This will require a continuously-varying angular acceleration with a peak value of  $\approx 10^{-7} \text{ rad/s}^2$  which corresponds to a torque of  $\approx 10^{-5} \text{ Nm}$  for nominal spacecraft dimensions. This torque could be supplied by the ion thrusters [[TBD](#)]. However, a cold-gas attitude control system will also be required for safe-modes and for the spin-up/down procedure required for stabilising the satellite during the apogee boost (if a solid apogee boost motor is used to minimise the costs in the baseline option).

The nominal mission lifetime is six months. This is sufficient for testing the performance of the accelerometers, lasers, interferometer, and thrusters, and for partially assessing their longevity and reliability in the space environment. The mission could be extended at the expense of higher operations costs.

## 11.3 SMART 2 demonstrator technologies

### 11.3.1 Capacitive sensor

The capacitive sensors must be designed to meet the appropriate requirements on proof-mass isolation and readout (for control) along all three translational axes. The three attitude degrees-of-freedom of each proof mass must also be measurable and controllable. Existing spaceborne accelerometer technology falls short of the *LISA* requirements by many orders of magnitude. It is necessary to develop the sensor technology dedicated to *LISA*'s requirements. The aim is to test this sensor on *SMART 2*.

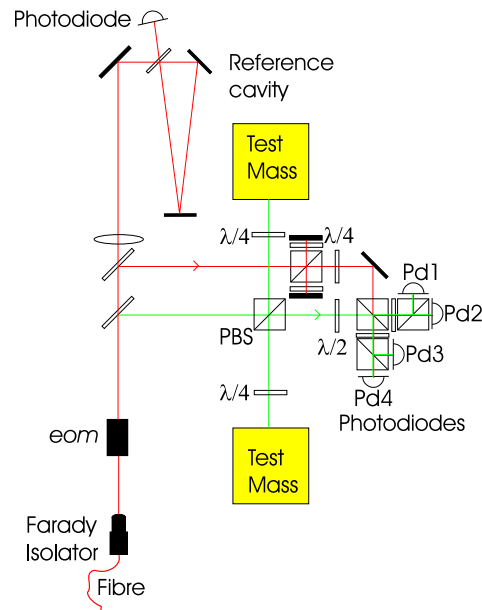


**Figure 11.1** *Interferometry inside the technology demonstrator SMART 2*

### 11.3.2 Laser interferometer

Current ground-based laser interferometry more than meets the requirements of *SMART 2* (and *LISA*), *but only in a much higher frequency regime* (kHz instead of mHz). It is necessary to demonstrate the technology required for low-frequency operation, and to test the functionality in the space environment.

### 11.3.3 Ion thrusters

The main requirements for the *SMART 2* thrust system is to provide sufficient steady-state thrust to offset the external disturbance forces and to provide the six-degree-of-freedom drag-free/attitude control. Existing field-effect ion thrusters operating in the micro-Newton regime are the most suitable technology but have to be further developed for *LISA*. It is known that the thruster noise characteristics play a key role in the noise budget for *LISA* so the thrusters must be developed and flight-tested with these considerations in mind.

### 11.3.4 Drag-free control

Verification of the performance of the drag-free control system is a key element of the [SMART 2](#) mission concept. Since the spacecraft contains two inertial sensors (as with the new [LISA](#) baseline), it cannot be manoeuvred to centre each proof mass within its housing electrodes. Instead, there will be a single location (the “drag-free null”) within the spacecraft where the acceleration is minimised by the drag-free control system. Forces will have to be applied on the proof masses to compensate for any force gradients relative to this drag-free null. [SMART 2](#) will test various control strategies. For example, perhaps the simplest approach is to have the spacecraft translation controlled to centre, in all three components, on one of the two proof masses (i.e. locating the drag-free null at the centre of one proof mass). The attitude of the spacecraft could then be controlled using the information from the other proof mass. The other proof mass will need to have forces applied to it to follow the primary proof mass. These forces would be applied electrostatically by means of its sensing electrodes. The magnitude of the applied force in each component would be comparable to the expected forces on the primary proof mass, i.e. corresponding to an acceleration of order  $10^{-10} \text{ m s}^{-2}$ . A key objective for [SMART 2](#) will be to demonstrate that these forces can be applied in such a way that the noise introduced within the measurement band is acceptable. Also, the orientation of each proof mass needs to be controlled to match the orientation of its housing at the nanoradian level.

## 11.4 SMART 2 satellite design

The [SMART 2](#) system will consist primarily of institute-provided payload elements (e.g. inertial sensors, thrusters, lasers/optical package, flight computer, etc.). The spacecraft, which comprises the structure, power, communication etc. subsystems will be ‘built around the payload’ using commercially-available off-the-shelf components as far as possible. In order to minimise costs, the satellite will be single-string (in terms of failure modes) with limited functional redundancy and graceful degradation of all items.

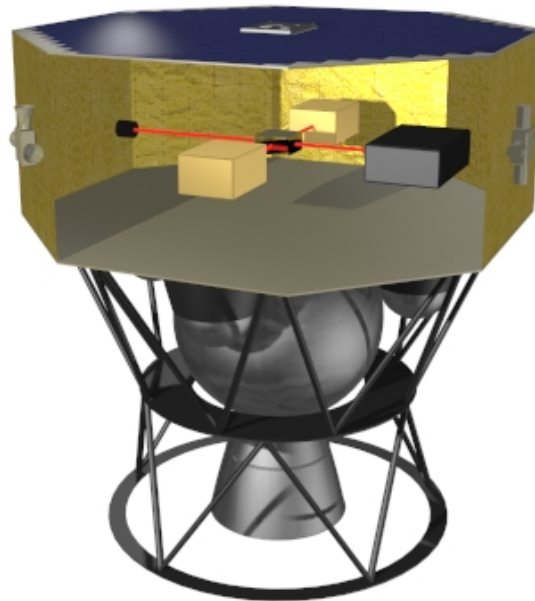


**Figure 11.2** *The demonstrator satellite SMART 2*

### 11.4.1 Power subsystem

For the six-month duration, the [GEO](#) orbit can be chosen to be free of eclipses. Then the nominal continuous power requirement is  $\approx 150$  W, including  $\approx 25$  W for battery charging (for safe-mode).

### 11.4.2 Command and Data Handling

A main central processor unit ([CPU](#), e.g. RAD6000) will be responsible for all command & data handling, and computation of control laws. A smaller backup processor will be used for initial set-up and safe-modes. Command and data [I/F](#) between the processors and all sensors and actuators will be via a 1553 bus with maximum throughput of 100 kbps. [RS 422](#) serial communication may also be an option for some payload items [[TBD](#)]. Control of the 1553 bus can be software-switched between the processors. The main [CPU](#) will incorporate its own warm reset/reboot capability. The backup processor will provide a cold boot capability for the main [CPU](#). Both the main and back-up processors will have anomaly detection and safing functions.

### 11.4.3 Telemetry and mission operations

For the [GEO](#)-type orbit, the nominal operations can be performed via a single ground-station, essentially in real-time. [NORAD](#) and on-board [GPS](#) [[TBD](#) for [GEO](#)] (to  $\approx 100$  m) will provide sufficiently accurate orbit determination so ground-based tracking/ranging will not be required. Telemetry will be packetised according to [CCSDS](#) standards and managed by either the main or backup processor [[TBD](#)]. Standard S-band telemetry rates are: 2 Mbps S-band downlink (11 m ground-station), 1 kbps uplink. If a 1 m portable station is used, the available downlink rate is reduced by an order of magnitude (i.e. to 1.4 kbps) which is, nevertheless, sufficient for [SMART 2](#) (see Table [11.1](#)). For the [GEO](#) orbit, an on-board solid-state storage capability would not be required.

<i>Data Items</i>	<i>Word size (bits)</i>	<i>Words per Data Item</i>	<i>Data size (bits)</i>	<i>Nominal rate (bits/sec)</i>
2 accelerometers				
readout	16	2 x 6 (6 dof per mass )	192	192
servo command	16	2 x 6 (6 dof per mass )	192	192
discharge	16	2 x 2 ( <i>V</i> , <i>I</i> per mass )	64	64
interferometer system				
lasers	16	6 [TBD] (e.g. power, etc)	96	96
readout	16	6 [TBD] (photodiodes)	96	96
Payload thermometers	12	5 [TBD] (different locations)	60	60
Drag-free control vector	16	3 (3 axes)	48	48
Attitude control vector	16	3 (3 axes)	48	48
Star-tracker readout	16	3 (3 axes)	48	48
Thruster commands	16	16 (different thrusters)	256	256
GPS	32	6	192	192
Magnetometers	12	3 (axes)	36	16
Torque rod command	12	1 (axis)	12	12
Sun sensor	12	2 (axes)	24	24
Spacecraft housekeeping	8	4	32	32
<b>Totals:</b>			~1396	~1396

**Table 11.1** *SMART 2 data rates, assuming uniform sample rate of 1 Hz for all data items.*



# 12 Science and Mission Operations

## 12.1 Science operations

### 12.1.1 Relationship to spacecraft operations

Science operations includes all operations related to the operation of the interferometers including the checkout and setting up of the experiment sub-systems. Science operations also includes the following operations that are traditionally regarded to be spacecraft operations, because they affect control loops which directly affect the science data and so need to be under the direct supervision of the experimenters:

- Pointing measurement by startrackers and telescope quadrant detector,
- Attitude control by [FEEP](#) thrusters,
- Acquisition of laser beams,
- Adjustment of spacecraft velocity by means of the [FEEPs](#) to maintain Doppler shifts within the bandwidth of the detector system,
- Control of the scheduling of spacecraft operations in order to maintain thermal stability and avoid sources of systematic noise.

In a traditional space experiment, the need to assure the fundamental safety of the mission would normally result in the above topics being assigned to spacecraft operations. For [LISA](#) the fundamental mission safety will be assured by on-board autonomous systems and ground autonomous systems which will monitor the spacecraft engineering data stream and switch to safe modes if parameters go out of limits. Within planned limits it will be completely safe for the specified spacecraft functions to be under the control of the scientific operations team.

There will be detailed procedures to recover from the various safe modes. The most complex of these will be that following a complete loss attitude and entry into the attitude recovery mode. Spacecraft operations once the satellites are in their final orbits should be limited to this autonomous and manual monitoring and recovery from emergencies or work arounds for observed spacecraft degradation. It is thus envisaged that the spacecraft operations team will be primarily a group of experts who, once the spacecraft and experiment have been successfully commissioned, will only take control on comparatively rare occasions.

### 12.1.2 Scientific commissioning

After the initial switch-on and simple verification of operation of all the scientific sub-systems, the commissioning takes place which includes the following:

- Pointing acquisition using startrackers and laser beams.
- Beam profile characterisation and choice of operating pointing.
- Measurement of orbit parameters using ground stations to track spacecraft, supplemented by observed laser Doppler shifts, and orbit adjustment using [FEEPs](#).

- Establishment of drag-free control loop using the signals from the accelerometer, the star-trackers and the laser interferometer.
- Closing of the phased lock loops on the laser transceivers.

In all these cases there will be tests performed to characterise the operation of subsystems followed by analysis of the data by the experiment team and adjustment of operating parameters. The scientific commissioning will provide the information about the operating conditions which will be used for scientific data acquisition.

### 12.1.3 Scientific data acquisition

During scientific data acquisition the goal will be to operate the observatory with very few interruptions for long periods, typically for half or one year. This will provide near continuous data sets which will be analysed to separate the GW signals resulting from many different astrophysical sources. The steady data acquisition may be interrupted for periods of adjustment such as making changes to the relative space craft velocity. It may also be interrupted by events such as solar flares which may cause disturbances to the drag-free sensor proof mass.

Scientific operations will consist of long periods of routine operations during which searches for transient events will be carried out. This will be followed by computationally intensive data analysis looking for long duration signals. Since the data can be readily stored on board and transmitted to Earth during one 8 hour shift when the constellation is in view of the principal ground station it is anticipated that scientific operations can be organised remotely by networking teams in different laboratories. So the infrastructure for operations will be comparatively modest compared with many space observatories and the operations cost is likely to be modest compared with major ground based optical observatories and ground-based gravitational wave detectors. Thus there should be no financial barriers to exploiting any excess life that the observatory has over and above the design life used for the engineering specifications. It is thus important that if possible the mission consumables are sized to permit extended operations over 10 to 20 years.

## 12.2 Mission operations

In a NASA/ESA collaborative LISA mission, ground systems and mission operations could be provided by NASA. Station support will be through the DSN and so, accordingly, several software subsystems are best taken directly from the DSN Mission Ground Support Operations (MGSO), and adapted for the LISA mission. All navigation functions with the exception of maneuver design will be done by the multimission navigation services.

Some or all of the personnel from design, development, integration, and test will become part of the operations team. Command and telemetry software developed for operations will be used for support in assembly, test, and launch operations.

Upon receipt of the telemetry data, the housekeeping packets will be analysed in order to check the health of spacecraft and instruments. Payload housekeeping and science data will be forwarded to the LISA Science Centre (LSC) located at a PI institute (to be selected through the AO), where the status of the payload will be monitored. Payload Doppler data will be immediately processed, and any desired manoeuvre commands will be sent to the MGSO for uplinking. The LSC will calibrate the interferometer data and distribute them to the PIs.

## 12.3 Operating modes

Six operational modes/mission sequences can be envisaged. During each of these modes the allowable/required payload operations are described in the following Subsections.

### 12.3.1 Ground-test mode

In this mode it will be necessary to exercise as much of the payload functionality and performance as possible. Some subsystems will not be able to be used in full due to  $1g$  operation. Tests may be carried out with payload in any arbitrary orientation. Most tests can be done on single spacecraft.

Functional tests of all electrical/mechanical subsystems, including pointing device, lasers, discharge system, drag-free sensor electronics, drag-free clamping device, [USO](#), interferometer electronics, star trackers, [FEEP](#) electronics, [CPU](#) and [PCU](#).

Performance tests of subset of electrical/mechanical subsystems, including pointing device, lasers, discharge system, [USO](#), interferometer electronics, star trackers, [CPU](#) and [PCU](#).

An end-to-end test with two/three payloads operating together would be desirable.

### 12.3.2 Launch mode

Access is required for late removal of telescope covers.

All payload power should be off.

### 12.3.3 Orbit acquisition

Spacecraft computer performs attitude control and orbit manoeuvres with direct access to star tracker data. During this orbit acquisition phase some subsystem tests are envisaged. Release of drag-sensor vacuum enclosure seal will be done (pyrotechnic device operation). [FEEP](#) seals are released. These activities are initiated by the spacecraft computer.

Functional tests of all electrical/mechanical subsystems, including pointing device, lasers, discharge system, drag-free sensor electronics, drag-free clamping device, [USO](#), interferometer electronics, star trackers, [FEEP](#) electronics, [CPU](#) and [PCU](#). Performance tests of subset of electrical/mechanical subsystems, including pointing device, lasers, discharge system, drag-free sensor electronics, drag-free clamping device, [USO](#), interferometer electronics, star trackers, [CPU](#) and [PCU](#).

Payload orbit/attitude constraints: keep sun outside field-of-view of telescopes.

### 12.3.4 Attitude acquisition

This phase includes calibration activities controlled by spacecraft but where payload computer requires access to star tracker data and [ACS](#) calibration information. There will be a progressive transfer of attitude control from spacecraft computer to payload computer. Full payload functionality is required. Sequential commissioning of drag-free operation under autonomous payload computer control. Data transfer from payload computer to spacecraft computer. Telemetry and ground command is via spacecraft computer with commands passed to payload computer for implementation. Spacecraft computer monitors orbit and attitude, including sun sensor data.

### 12.3.5 Science mode

Attitude control solely by payload computer. Full payload functionality and performance required under autonomous payload computer control. Payload computer is collecting science and housekeeping (h/k) data. Data are transferred from payload computer to spacecraft computer. Telemetry and ground command is via spacecraft computer with commands passed to payload computer for implementation. Spacecraft computer monitors orbit and attitude.

### 12.3.6 Safe mode

This mode may be invoked by the spacecraft in the event of attitude disturbance beyond the range of controllability of the drag-free system putting the mission in jeopardy. In this event the spacecraft computer may invoke safety and power saving routines. Depending on the severity of the situation the power saving priorities are given in the list below:

**Power saving priorities** (first off to last off):

- Discharge system
- Drag-free sensor electronics
- Payload CPU
- Lasers
- Laser electronics
- USO
- Payload PCU

## 12.4 Operational strategy

### 12.4.1 Nominal operations concept

The general concept for operating [LISA](#) is that all activities will be performed according to a master schedule on board each spacecraft, which will be kept updated and harmonised from ground. This on-board master schedule performs the time-tagged commanding of On-Board Control Procedures ([OBCPs](#)) which are to be written in an On-Board Control Procedure Language. The [OBCPs](#) will be defined in a way that they are continued autonomously after simple failures.

All parameters used for autonomous operation including fault management, orbit, drag-free and attitude control etc. will be updateable by telecommand and be available in telemetry.

Time-tagged commands will be applied for scheduled automatic tasking in Routine Phase as well as for event driven procedures. Event driven procedures have to be analysed, a forecast of schedule events from Earth has to be commanded as timeline or in real-time under ground contact.

### 12.4.2 Advanced operations concept

The operations concept briefly outlined in the previous section requires a significant man-power effort for elaborating timelines, since the operation of the three spacecraft is closely interrelated.

The application of an Advanced Timeline Generator on ground (e.g. the [TINA](#) 5.0 system developed by [DSS](#) and already applied in two [ESTEC](#) studies) allows to generate timelines that

contain time windows for the execution of an OBCP with starting and ending times and which contain required key parameter values, required system state and required available resource information. The TINA timeline generator kernel performs the timeline computation based on the commercial ILOG constraint propagation libraries.

The on-board complement for the application of “event driven timeline execution” is already existing as demonstrator application at DSS under the label “System Autonomy Testbed”.

This Autonomy Testbed is based on a modular on-board software architecture which has been developed by DSS in the frame of the project “MARCO” (Modular Architecture for Robotics Control) under DARA contract. It features a modular Ada software concept based on VxWorks real-time operating system.

The controlling component of the architecture is called the Supervisor and is sketched in Figure 12.1. The onboard system supervisor of the Autonomy Testbed is able to execute TINA generated mission timelines which consider both time tags and key parameter values, the system state and resources for execution of OBCPs.

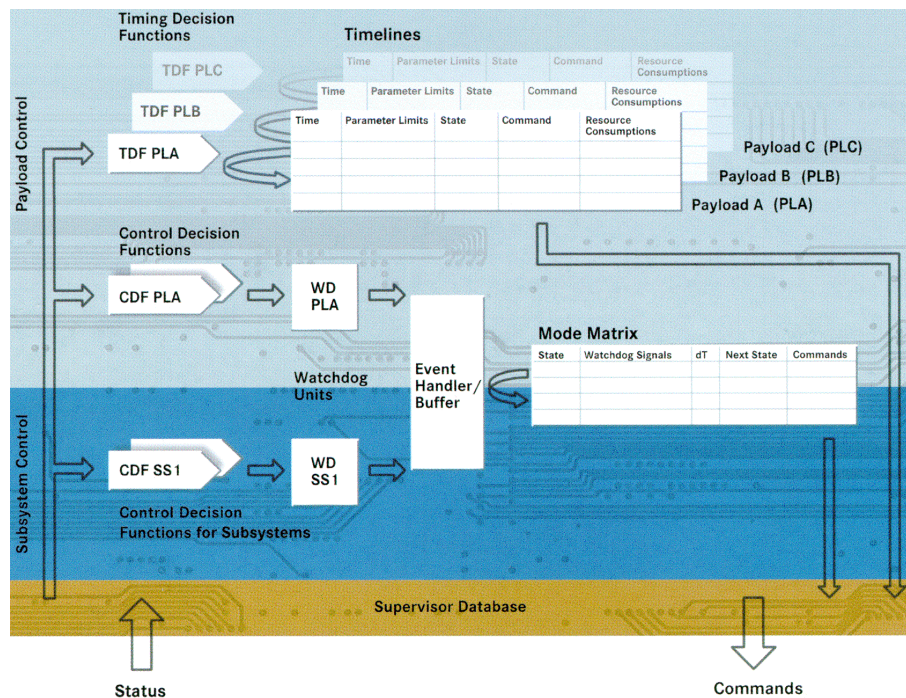


**Figure 12.1** Supervisor functional architecture

This concept has already been proposed to ESA for on-board S/W of PROBA (Project for On-Board Autonomy) and in the “Autonomy Testing” Proposal.

For the LISA mission this advanced operations concept is not mandatory but according to the very complex mission scenario it would give extraordinary advantages for operations in view of flexibility, man power savings, and cost effectiveness. The optimum share between ground and onboard functionality of this supervisor concept for LISA should be elaborated in future phases.

### 12.4.3 Autonomy

For interplanetary missions the need for on-board autonomy is out of question. Signal transmission times between LISA spacecraft and ground in the order of 3 minutes in conjunction with



complex spacecraft interactions, especially for Pointing Acquisition and Tracking, will become extremely difficult otherwise. Moreover, [LISA](#) is required to operate for a period of 72 hours without ground contact. Beyond these 72 hours each spacecraft is required to be able to survive autonomously in a Safe Mode for at least [\[TBD\]](#) days without the need for ground intervention. In order to avoid misinterpretation of the term autonomy a short definition is given hereafter:

“Autonomy or autonomous operations are those on-board actions that are initiated on system level by the spacecraft itself following an on-board event (nominal or failure) in order to fulfil the goal/task of the actual phase or mode. Autonomy can concern nominal operations as well as handling of contingency situations.” All other operations are called predefined or automatic especially if they are handled on subsystem level only.

E.g., the execution of a purely time tagged command timeline is considered an automatic functionality. The execution, however, of a timeline under event driven conditions considering alternatives depending on key parameter values is considered to be an autonomous functionality.

The envisaged autonomy concept can be characterised as follows:

All nominal and contingency operations necessary for the different mission phases are predefined and stored in On-Board Control Procedures ([OBCPs](#)).

The on-board system supervisor executes mission timelines which are conditional to time tags, key parameter values, the system state and the availability of resources. Event driven they initiate execution of the corresponding [OBCPs](#). [OBCPs](#) are defined such that they cover a nominal case and failure cases.

If, in a failure case, the specified corrective action is able to cope successfully with the detected failure, then the mission timeline execution is continued autonomously.

If there is no success of the corrective actions or there is no predefined [OBCP](#), as a last consequence for payload [OBCPs](#) the failing items of the payload, e.g. a particular laser link, will be deactivated and mission timeline execution will continue for all other payload items and subsystems. For non-recoverable spacecraft system failures Safe Mode is entered and autonomously maintained. All parameters used for autonomous operations, including fault management, orbit, drag-free and attitude control, etc., will be updateable by telecommand and related status information available in telemetry.

A demonstrator for such an advanced real-time onboard software controlling a simulated spacecraft by execution of event driven mission timelines has been realised in the System Autonomy Testbed at [DSS](#).

#### 12.4.4 Failure detection, isolation and recovery

The following conceptual definition is based on the [ROSETTA](#) defined levels of on-board autonomous [FDIR](#). Consequently, the levels of autonomous [FDIR](#) for [LISA](#) are structured into four levels:

- 0 is the unit level,
- 1 is the subsystem function level,
- 2 is the high level [DMS](#) surveillance level,
- 3 is the system alarm and reconfiguration module level.

The ground-rule to be observed for [FDIR](#) is that failures should be detected, isolated and corrected on the lowest possible level. Level 0 represents the lowest level. Only the levels 2 and 3 allow for a transition into Safe Mode.

The central item for autonomous [FDIR](#) on level 3 is the Reconfiguration Module. It has the highest level responsibility for the handling of unexpected system alarms.

#### 12.4.5 Ground control

The [LISA](#) operations follow the lines of a survey-type project that will be developed and operated as a Principal Investigator ([PI](#)) mission. Mission operations performed by the Mission Operation and Spacecraft Control Element, [MSCE](#), after separation of the composite spacecraft from the launcher are composed of mission planning, spacecraft monitoring and control, and all orbit and attitude determination and control. The instrument operations will be under the responsibility of the [PIs](#). The co-ordination of the instrument operations and the interface between the [PIs](#) and the [MSCE](#) will be under the responsibility of the Project Scientist supported by members of the [PI](#) teams in the [LISA](#) Science Data Centre [LSDC](#). In support of the instrument operations, the [MSCE](#) will make available to the [LSDC](#) the extracted near real-time payload telemetry packages. It will also process the instrument telecommand and mission planning request from the [LSDC](#), and it will distribute the raw instrument telemetry data augmented by auxiliary data on orbit, attitude, and spacecraft status.

All operations will be executed at the [MSCE](#) according to a Mission Timeline, Flight Control Procedure, and Contingency Recovery Procedures as defined in the Flight Operations Plan. The [FOP](#) will be prepared by the operations staff based on the [LISA](#) Users Manual, and on the [LISA](#) Database. The payload operation support is based on inputs from the experimenters and specified in the Payload Operations Plan.

During routine phase the nominal spacecraft control will be off-line. The period of contact with the spacecraft will be dedicated to collecting science and housekeeping data, for radio tracking measurements, and for up-link of the master schedule for pre-programming the autonomous operation functions of the three [LISA](#) spacecraft. As anomalies will normally be detected with a delay, the mission safety will be ensured by on-board autonomous systems.

## 12.5 Mission phases

The mission is composed of the following operational phases:

- **Launch Phase:** This phase starts with the removal of the umbilical and ends with the separation from the launcher. Throughout the launch the power is provided by batteries.
- **Near Earth Commissioning Phase:** Triggered by the separation from the launcher, the spacecraft activation sequence is started to perform subsystem switch-on, [RCS](#) priming, rate damping and Sun acquisition. The spacecraft is 3-axis stabilised. This phase includes an initial spacecraft check-out and a first payload commissioning.
- **Cruise Phase:** During thrust phases one of the two ion-engines is working at full thrust and operations are reduced to [S/M](#) and [P/M](#) monitoring. Thrust vector orientation is controlled either through the hydrazine thrusters or by swivelling the gimbals of the ion engines. The [P/M](#) is commanded to keep the required thrust conditions. Attitude reference is given by means of the star trackers. Ground contact is restricted to [LGA](#) X-band communication.

During thrustless coast phases [HGA](#) communication may be possible after appropriate attitude adjustments.

- **Commissioning and Verification Phase:** At the end of the Cruise Phase, each composite spacecraft is injected into its required orbit, put into the proper attitude (30° off



Sun pointing), and the S/M separated from the P/M. After P/M separation, the S/M AOCS performs the attitude and position control merely using the FEEDs. Commissioning and verification of all electrical and mechanical systems including the telescope pointing devices, lasers, discharge systems, electronics, clamping devices, and the Ultra Stable Oscillators.

The attitude control for initial laser signal acquisition is preceded by calibration activities between star trackers and acquisition sensors. The laser acquisition will start with the S/Ms controlling their inertial attitudes based on knowledge on-board each S/M of the inertial positions of all 3 S/Ms in order to be able to point their laser beams towards their companion S/Ms. Star trackers supported by Inertial Reference Sensors will be used to ensure stable pointing in the desired direction towards the companion S/Ms. After successful completion of this process all three optical links will have been established and drag-free control enabled. Now the final calibrations are performed. The S/M's FDIR functionality monitors the spacecraft subsystems and the payload and may take over control to enter a pre-established Safe Mode if it detects any failure that puts the mission in jeopardy.

During this phase it will be possible to transmit not only the already compressed but in addition also the raw science data to ground. This gives the ground the means to check the validity of the on-board science-data compression.

- **Routine Phase:** Normal mode in this phase is Science Mode with all three optical links established and drag-free control active. Data will be stored on-board and transmitted to ground during the contact periods with the spacecraft of about 9 hrs every second day. For ground contact there will be a configurable master S/M collecting science and housekeeping data from its companions via the optical links, transmitting these data together with its own to the ground, receiving telecommands from ground and forwarding them via the optical links to its companion S/Ms. The ground will monitor and perform emergency recovery in case of failure or in the short interruptions that may be required to correct external events causing disturbances to the S/M or its sensors (solar flares, interplanetary dust, micro-meteoroids, etc). Operation in the normal Science Mode is supposed to last for long periods of time with very few short interruptions.

A standard DSN X-band network will support the mission from launch until start of the interplanetary Cruise Phase. Afterwards, one single ground station is sufficient to support the mission. Radio tracking from two ground stations will be needed during campaigns to calibrate the orbit determination process.

All over the mission, each S/M will be under the control of its Centralised Processor System. The principal tasks of this system are

- spacecraft control,
- payload control,
- spacecraft and payload data management.

In case of failure, the Centralised Processor System will have the capability of predicting with the required accuracy the position of its own S/M as well as those of the other two spacecraft, the attitude to point to them, and the direction of the Earth, and shall autonomously try to re-establish the triangular spacecraft configuration and establish the optical links.

The Payload Controller will be in charge of accepting and responding to commands and reference values received from the Centralised Processor System. It will condition and forward these commands to the payload, acquire and condition payload signals and transmit them back to the Centralised Processor System.

## 12.6 Operating modes and mode transitions

The basic system modes that are needed to fulfil the operational requirements of the [LISA](#) mission phases are defined below.

The **Prelaunch Mode** will be used during final preparation and checkout activities on the launch pad. It is automatically entered when the spacecraft is switched on. In this way it will be used during all ground testing, but in addition also for loading data for the separation sequence.

The spacecraft is in the **Launch Mode** from removal of umbilical until it has autonomously performed all operations after separation to achieve a safe Sun pointing 3-axis stabilised attitude including [RCS](#) priming and Sun acquisition (Sun incident on the Propulsion Module solar array). Communication via [LGAs](#) is established. These operations are controlled by a dedicated [OBCP](#) which is continued also in failure cases.

The **Activation Mode** follows the Launch Mode when control is taken over from ground. It is used for spacecraft check-out and first payload commissioning. The [AOCS](#) is in Star Sensor Mode. Minor trajectory correction manoeuvres using hydrazine propulsion are performed to compensate for launcher orbit insertion errors. Apart from these manoeuvres the spacecraft is leaving the Earth on a purely ballistic trajectory. The communication goes via [LGAs](#).

The **Cruise Mode** follows on Activation Mode and is used during the interplanetary cruise phase. In this mode a sequence of thrust phases (using ion propulsion) separated by purely passive coast phases is used to transfer each spacecraft to its station. Only restricted communication will be possible, since most of the time the [LGAs](#) will have to be used. Due to their single-axis articulation the [HGAs](#) will normally never be Earth-pointing during cruise, especially, since the [HGAs](#) are mounted on the [S/M](#) which is oriented towards deep space during cruise. During coast phases, however, when the ion propulsion is off, it might well be possible to change the orientation of the spacecraft towards the Earth in a way that the [HGAs](#) can be made use of for extensive spacecraft monitoring and health checking. At the end of the Cruise Phase a precise orbit determination and orbit correction is mandatory to obtain good initial conditions for the mission orbit.

After end of cruise, **P/M Separation Mode** will be entered. In this mode the composite spacecraft will perform a 180° attitude slew in order to have the [S/M](#) and no longer the [P/M](#) solar array Sun pointed. The Propulsion Module will be separated in two stages from the Science Module: first structurally by means of separation nuts and then regarding the electrical connectors smoothly by spindle devices. After end of **P/M Separation Mode** the [P/M](#) is drifting passively away from the [S/M](#). The [EPS](#) of the [S/M](#) is now fully dependent on the power from the [S/M](#) solar array, since the batteries remain on the [P/M](#). Attitude and position control authority is limited now to [FEEPs](#). The [FEEPs](#) have to be used to compensate the separation rates and to reacquire the Sun pointing attitude.

Separation Mode is followed by **On Station Mode**. In this mode the [S/M](#) acquires its nominal attitude 30° off the Sun and then permanently aligns its two telescope lines of sight towards its companion spacecraft. For communication with the ground the [HGAs](#) are used, since they can be permanently be Earth pointed now. Continuous on-board propagation of positions of [S/M](#) 1 to 3 and of Earth provides the knowledge necessary for pointing of telescope lines of sight and of [HGAs](#). Further activities in this mode are related to payload activation: mechanical release of Optical Assemblies, test of Telescope Pointing Mechanisms, release and calibration of proof-masses, alignment calibration between Star Trackers and Acquisition Sensors, test of the laser assembly, of the front end electronics, etc.

**PAT Mode** is the mode in which the optical links between a S/M spacecraft and its two distant companions are established one by one. PAT Mode is necessary in both spacecraft trying to establish an optical link. In PAT Mode drag-free control will be enabled and the proof-masses used as additional inertial sensors to allow for a highly stable pointing towards the opposite spacecraft. The complex pointing acquisition scenario to be observed by both S/Ms in this mode needs only to be initiated from the ground and can then be followed autonomously by the two spacecraft, one being declared Master, the other Slave. For the establishment of a link between a Master S/C and a Slave S/C the steps to be taken in PAT Mode on the Master can briefly be summarised as follows:

- M-1 The Master switches its laser on and slowly performs with the laser beam one full scan over the uncertainty cone surrounding the expected position of the Slave which is propagated over time accordingly. Then the laser is switched off.
- M-2 Under nominal conditions the laser beam transmitted back from the Slave can be detected on the acquisition sensor of the Master immediately after switching off its own laser. The attitude of the Master, of its respective telescope and/or of its proof-mass are adjusted in order to orient the Master with an error smaller than the emitted beam width towards the Slave and to centre the incoming beam on the coherent detector of the Master. If the optical link between the Master and the third S/C has already been established then this attitude adjustment needs to be performed in a way that this link is safely maintained. Finally the laser on the Master is switched on again. After a predefined time the Slave should have accomplished its step S-2 so that the link is operational.

The following steps need to be taken on the Slave S/C:

- S-1 The Slave points towards the expected position of the Master with its local laser off and waits for a beam from the Master (scanning with its laser the uncertainty cone) to be detected on its own acquisition sensor. This allows to determine the direction of the received beam and thus of the Master itself. The attitude of the Slave S/C and of its telescope are adjusted towards the Master with an error smaller than the emitted beam width and then the laser is switched on. Thus it is ensured that the Master will in step M-2 of its PAT sequence detect the beam. If the optical link between the Slave and the third S/C has already been established then this attitude adjustment needs to be performed in a way that this link is safely maintained.
- S-2 After a predefined time the laser is shortly switched off and on again to check that the laser on the Master is on again. If this is the case, then the Slave can reacquire the incoming beam on the acquisition detector and subsequently centre it on the coherent detector by attitude adjustments of the overall Slave S/C, of the respective telescope and/or of its proof-mass. The local laser is now switched on and a frequency scan of the reference oscillator is performed. After detection of the beat signal on its coherent detector the Slave laser frequency is successfully adjusted to the Master frequency and the link is operational and can be used for data transfer between spacecraft.

**Science Mode** is the normal mode during Routine Phase. Normally, via both telescopes of a S/M optical links will be established when being in this mode. In a degraded Science Mode only one link could be operational. In Science Mode drag-free control will be enabled to compensate external disturbances such as solar pressure. Proof-mass discharging will be performed at regular intervals. The measurements obtained from the coherent detectors will be pre-processed and compressed on-board and downlinked every second day via the HGAs. Science data quality should not be impaired by data transmission. Adjustment of the HGAs every second day,

however, is likely to introduce mechanical disturbances that will corrupt science data for some tens of seconds.

**Safe Mode** is primarily designed to ensure a safe power situation (solar arrays Sun pointing) and accessibility from ground. For the different mission phases different safe modes will become necessary:

- Safe Near Earth Mode,
- Safe Cruise Mode,
- Safe On Station Mode.

After an on-board anomaly, the spacecraft will always first attempt to recover from the failure and continue with the mission timeline. Only if this proves to be not feasible Safe Mode will be entered.

**Survival Mode** will be entered in case Safe Mode is unable to achieve a safe attitude due to a major on-board anomaly. In Survival Mode the spacecraft is capable of surviving on its own for a virtually unlimited time.

The transitions between these modes are visualised in Figure 12.2.

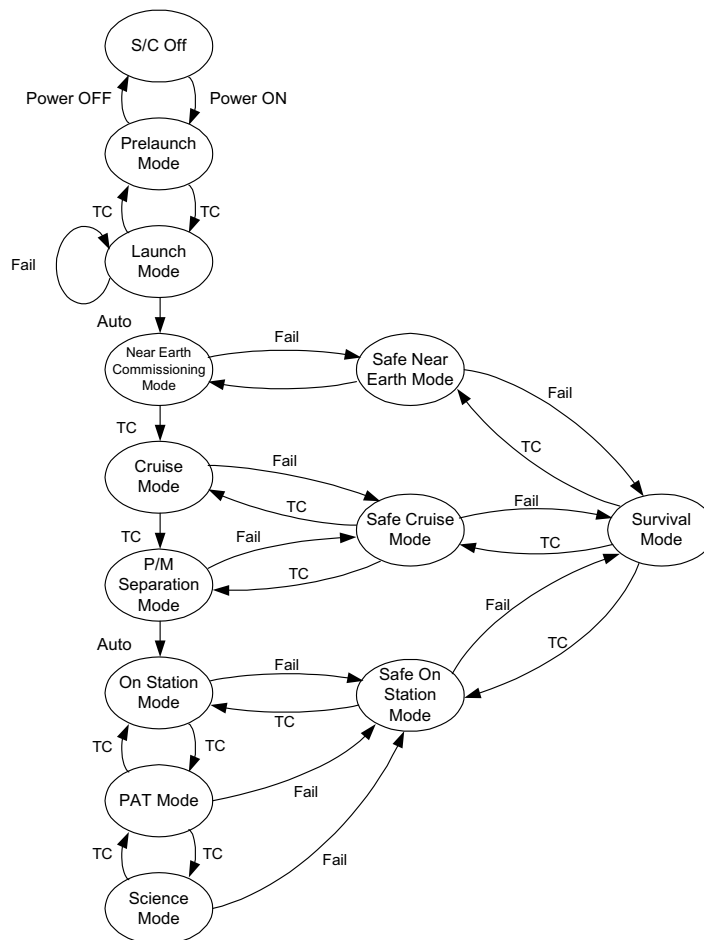


Figure 12.2 System mode transition diagram

## 12.7 Ground segment

Within the [ESA/NASA](#) collaboration in the [LISA](#) mission, [NASA](#) will prepare a Ground Segment comprising all facilities (hardware, software, documentation, and trained staff) that are required to conduct the [LISA](#) operation under all expected conditions. The operations include planning and controlling the mission and the spacecraft operation. All ground facilities to be established for [LISA](#) support will be based on existing ground segment infrastructure tailored to support the specific requirements of [LISA](#). In particular the following sub-systems will be available:

- The Mission Operations and Spacecraft Control Element, [MSCE](#), is to perform all mission operations, spacecraft planning, monitoring and control. It will operate the whole Ground Segment and monitor the facilities, resource and operations of the mission.

The [MSCE](#) will generate the mission operations plan and the derived spacecraft and ground segment operation plan. The spacecraft operations plan shall result in an optimised distribution of functions between the space and the Ground Segment. The [MSCE](#) will interact with the [LSDC](#) for the generation of this plan, and it will report on the actual execution of the operations.

Automatic analysis of essential spacecraft data will be performed to assess the status of the spacecraft and, if needed, to trigger automatically the reaction to planned contingencies.

The [MSCE](#) will be able to start automatically sequences of pre-stored commands for routine operations or for planned contingencies.

For contingency operations, the [MSCE](#) shall be able to handle other [NASA](#) or [ESA](#) ground stations that provide temporarily support.

The [MSCE](#) will include facilities for:

- Telemetry analysis
  - Telecommand generation
  - Flight Dynamics Facility to support the analysis, and execution of: orbit determination and orbit control; attitude determination and attitude control
  - The Spacecraft Software Simulator to be used for Flight Control system and operations procedures validation, and for staff training.
- The Command and Data Acquisition Element, [CDAE](#), to perform all telemetry and command processing. It will be in charge of the Telemetry, Telecommand and Control, [TT&C](#), links with the spacecraft and of the acquisition of the Scientific Payload Data. The [CDAE](#) will receive telecommands from the [MSCE](#) and will uplink them to the spacecraft as scheduled.

All scientific and ancillary data will be processed as required, and temporarily stored for a period of at least one week.

Data will be transmitted from the [CDAE](#) to any other element of the Ground Segment as required for mission operations.

- The Ground Stations and Communications Network will be shared with other users during the mission lifetime. Station support for nominal operations will be through stations of the [DSN](#) network, and the required sub-systems of the [DSN](#) Mission Ground Support Operations will be adapted to the specific requirements of the [LISA](#) mission. Daily use while supporting critical phases ([LEOP](#), insertion into operational orbit, Laser beam acquisition, etc.), and in two days interval while on routine phases.
- The Processing and Archiving Element will provide the required processing of the data received to the level required for efficient archiving and delivery to the [LSDC](#). The [PAE](#)

will perform data quality control, archive the mission data, generate and maintain the data products catalogues, and provide access services to the user community.

- The external connections to the [MSCE](#), [LSDC](#), and the [PIs](#) will use commercial and/or public networks.

Before launch all dedicated [LISA](#) hardware and software will be developed or procured, installed, and verified. All documentation required for operations will be prepared and the operations staff will be trained. The general purpose facilities will be configured and scheduled for [LISA](#) followed by a sequence of Validation Tests and Rehearsals to verify the different elements, and the Ground Segment as a whole system.

For the full duration of the mission and up to ten years after launch the Ground Segment will provide to the [LSDC](#) and to the individual users the primary and the archived data. In routine operations data will be transmitted to the [LSDC](#) within one day from acquisition, and data from exceptional observations or events not later than 3 hours after acquisition at the ground station. The Ground Segment will be prepared in accordance with a Mission Implementation Requirements Document issued in advance.

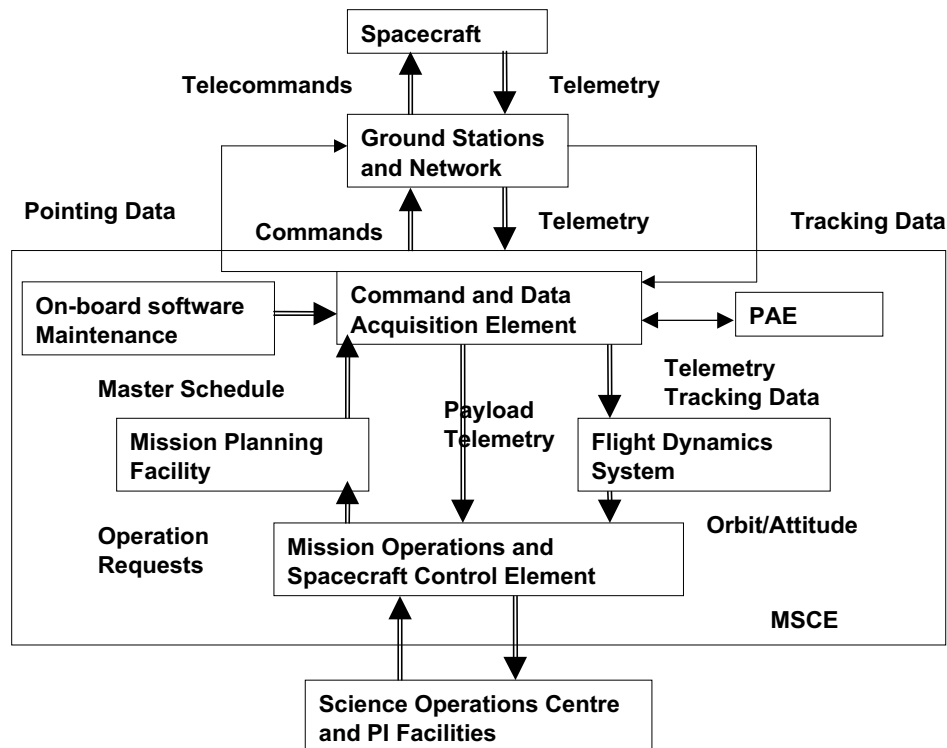


Figure 12.3 *LISA mission operations system*





# 13 International Collaboration, Management, Schedules, Archiving

## 13.1 International collaboration

LISA is envisaged as a NASA/ESA collaborative project in an equal partnering arrangement. This allows both space agencies to participate in this project at moderate cost and also reflects the contributions to the payload and mission design made by the scientific community in the USA and in Europe and by the two space agencies.

Much of the early development work of the LISA payload and project was carried out in the US (then known as the LAGOS project, for details see Section 2.6), while more recently most of the work was done in Europe: study of a 4-spacecraft LISA mission at assessment level in 1993/94 including an in-depth trade-off between the geocentric and the heliocentric option, selection of a 6-spacecraft LISA mission as a cornerstone project in 1995, detailed payload definition and design in 1997/98 and industrial study at Phase A level in 1999.

In early 1997, NASA supported a short LISA study by JPL's Team-X, based on three spacecraft and ion drive propulsion which led to a significant mass and cost reduction (from 6.8 t launch mass and about 800 MECU for the 6-spacecraft configuration excluding the payload to 1.4 t launch mass and \$465 M for the 3-spacecraft configuration including the ion drives, launch vehicle, operations and payload). Towards the end of 1997, NASA decided to form a LISA Pre-Project Office at JPL and in March 1998 to set up a LISA Mission Definition Team.

Currently, both ESA and NASA studies of the LISA mission proceed in parallel, with partial team membership overlap to ensure maximum commonality between the two studies.

From the very beginning, the LISA team consisted of US and European scientists working very closely together and it is difficult for the international LISA team to imagine that LISA could be carried out in any other way than in collaboration between ESA and NASA.

The original proposal of the LISA Project by an international team of scientists to ESA in May 1993 suggested a NASA/ESA collaborative project. Furthermore, in February 1997, ESA's Fundamental Physics Advisory Group (FPAG) strongly recommended to carry out LISA in collaboration with NASA and suggested that *"this collaboration should be put in place as soon as possible"*. Also in February 1997, ESA's LISA Study Team clearly stated that *"the LISA mission should be carried out in collaboration with NASA."* It is assumed that ESA and NASA will explore the possibilities of a collaboration after completion of ESA's industrial study, at a time when the feasibility and the cost of the LISA mission are better known.

Considering that a Delta II class launch vehicle is sufficient to launch the three LISA spacecraft and that a launch vehicle of that class does not exist in Europe (only the much bigger Ariane 5) it would be natural to assume that NASA would provide the launch vehicle in such a collaboration. It would also make sense for NASA to provide the mission and science operations using their Deep Space Network (DSN). ESA would then provide the three spacecraft, presumably including the ion drives. To ensure compatibility with the DSN the telecommunications system will use X-band transmission with the telecommunications system hardware on board the spacecraft provided by NASA. In such an "equal sharing scenario", NASA would provide 50 % of the payload while European institutes funded nationally would provide the other 50 %.

Possible other candidates for cooperation in the [LISA](#) mission could be Japan and Australia, where there are active communities interested in ground-based detection of gravitational waves. Discussions with individual scientists in these countries have taken place which may lead to a collaboration at a later time, presumably at a lower level of investment than the two main partners [NASA](#) and [ESA](#).

After approval of the [LISA](#) project by [NASA](#) and [ESA](#), a Memorandum of Understanding ([MoU](#)) and a Program Plan ([PP](#)) would be prepared jointly by [NASA](#) and [ESA](#). The [MoU](#) would define the agreement made between [NASA](#) and [ESA](#) for the implementation of the [LISA](#) project. It would contain, inter alia, agreements, responsibilities and deliverable items. The [PP](#) is the highest level Project document which defines the objectives, requirements, organization, and management structure of the project.

## 13.2 Science and project management

The proposed procurement scheme for [LISA](#) is based on the concept that the payload will be provided by Principal Investigators ([PIs](#)) with funding from [ESA](#)'s Member States as far as European contributions are concerned, and from [NASA](#) for possible [US](#) contributions. Payload selection would be based on proposals that would be submitted to [NASA](#) and [ESA](#) in response to a single joint [NASA/ESA](#) Announcement of Opportunity ([AO](#)). Payload elements would be selected competitively by a joint [NASA/ESA](#) selection committee after a parallel scientific and technical evaluation of the proposals.

After selection of the payload a [LISA](#) Science Working Team would be formed, comprising the [US](#) and European [PIs](#), the [NASA](#) and [ESA](#) Project Managers and Project Scientists and the Experiment Manager. Nationally funded payload subsystems such as lasers, optical bench, telescope, accelerometer, and structure, will be constructed at [PI](#) institutes. One institute would perform the overall management, integration, and testing of the payload under the responsibility of the Experiment Manager who would be the single-point interface to the [ESA](#) Project Manager.

The [ESA](#) Project Manager would set the requirements for and procure the three spacecraft from industry. He would also be responsible for the integration of the payload into the spacecraft and the overall test programme until delivery of the integrated and tested spacecraft to the launch site.

The [NASA](#) project Manager would interface with the launch vehicle authorities and provide launch operations support. During the flight phase he would also be responsible for the mission operations. Science operations would be carried out at a science institute to be selected competitively a few years before the launch.

## 13.3 Schedule

The schedule for the [NASA/ESA](#) collaborative [LISA](#) Project assumes approval of the project by [NASA](#) and [ESA](#) in 2004 and a 6-year development programme leading to a launch in 2010.

The project development phase is preceded by a 4-year technology development programme in both space agencies starting in the year 2000. In parallel with this technology development programme a joint [NASA/ESA](#) system level study is assumed which would last about a year starting in 2001.

A major element in the schedule is a dedicated small ( $\sim 100$  kg), low-cost (5–20 [MEuro](#)) [LISA](#) Technology demonstration satellite. This could be a European mission ([SMART 2](#)), or a joint

mission with [NASA](#) (possibly on [ST 3](#)), which could be launched as early as 2004 and should not fly later than 5 years before the [LISA](#) launch. [SMART 2](#) could be an [ESA](#) responsibility, a [NASA](#) responsibility could be a ground-based full-scale [LISA](#) simulation facility located at [JPL](#).

## 13.4 Archiving

According to the [ESA](#) policy on data rights, for the first six months after the end of the mission, the team of [LISA](#) investigators will have exclusive rights over their data. Thereafter, all science data (raw, calibrated, housekeeping) will have to be submitted to two [LISA](#) Science Data Archiving Centres ([LSDAC](#)) where the data will be stored on [CD-ROM](#) and can be accessed by the wide scientific community. One candidate for the [LSDAC](#) would be [ESA](#)'s Space Science Department at [ESTEC](#), the other archiving centre would presumably be the National Space Science Data Center ([NSSDC](#)) at [GSFC](#), Greenbelt, [MD](#), [USA](#). The complete [LISA](#) data set comprises:

- interferometer data,
- inertial sensor data,
- drag-free control and [FEEP](#) thruster data,
- [UV](#) control lamp discharging data.

The teams providing the various data sets have the following tasks:

- performing a thorough end-to-end error analysis,
- calibration of the science data,
- development of appropriate software for data analysis,
- production of an explanatory supplement,
- timely (i.e. 6 months after mission end) delivery of the items above to the [LSDACs](#).

The [LSDACs](#) have the following tasks:

- ensuring timely delivery of the items above,
- verification of the contents of the [CD-ROMs](#),
- production of an appropriate number of copies of [CD-ROMs](#) and supplements,
- responding to requests from the user community and sending out [CD-ROMs](#) and supplements as requested.



# Appendix

## A.1 Detailed Noise Analysis

### A.1.1 Overview

The purpose of the [LISA](#) system is the measurement of gravitational waves characterised by the dimensionless amplitude  $h$  which can be viewed as cause of proportional change of the distance between two proof masses induced by the gravitational wave.

Following the Pre-Phase A Report [1] the average sensitivity of a measurement system based on a Michelson-Interferometer can be expressed as

$$\Delta h(f) = \frac{\delta L(f)}{L} \operatorname{sinc}\left(\frac{\pi L f}{c}\right) \sin(\alpha_{\text{arm}}) \frac{\text{SNR}_{\text{desired}}}{T_{\text{observation}}} \beta_{\text{averaging}} , \quad (\text{A.1})$$

where

$\Delta h(f)$	Spectral sensitivity in terms of $h$ [ $1/\sqrt{\text{Hz}}$ ]
$L$	Armlength of Interferometer [m]
$f$	Frequency [Hz]
$\delta L$	Spectral amplitude of error in measurement armlength difference [ $\text{m}/\sqrt{\text{Hz}}$ ]
$\alpha_{\text{arm}}$	Angle between interferometer arms
$\text{SNR}_{\text{desired}}$	Desired <a href="#">SNR</a> (in terms of amplitude) after specified observation time, e.g. 5
$T_{\text{observation}}$	Observation time [s]
$\beta_{\text{averaging}}$	averaging factor resulting from averaging over various polarisations and directions of incidence (assumed to be about $\sqrt{5}$ )
$c$	Velocity of light [m/s]
$\operatorname{sinc}(x)$	$\sin(x)/x$

The angle between the interferometer arms is  $60^\circ$  resulting from the configuration of the three spacecraft in form of an equilateral triangle. The arm length is determined by the separation of the spacecraft ( $5 \times 10^9$  m). The characteristic performance parameter of the [LISA](#) measurement is the uncertainty in the determination of the armlength difference ( $\delta L$ ). This parameter is only of concern within the [LISA](#) measurement bandwidth ( $10^{-4}$  Hz to  $10^{-1}$  Hz). Hence absolute knowledge of the arm length difference is not required.

In the triangular configuration two independent difference measurements can be carried out yielding information on direction and polarisation of the incident gravitational wave.

As  $\delta L$  is defined with respect to the undisturbed proof mass positions it includes not only distance measurement errors but also arm length variations resulting from (unknown) acceleration acting on the proof-masses. This results in a performance model as shown in [Figure A.1](#).

In the Pre-Phase A study an apportionment of the two main error contributors has been performed. [LISA](#) has to show a performance equal or better than the measurement sensitivity that would result from an optical pathlength measurement error of  $40 \text{ pm}/\sqrt{\text{Hz}}$  and an acceleration noise of  $3 \times 10^{-15} \text{ m s}^{-2}/\sqrt{\text{Hz}}$ , both contributions being assumed as white processes in the measurement spectral range. Following these apportionment, effective errors in the optical pathlength difference and resulting averaged sensitivity over one year of observation are shown in [Figure A.2](#) and [Figure A.3](#).

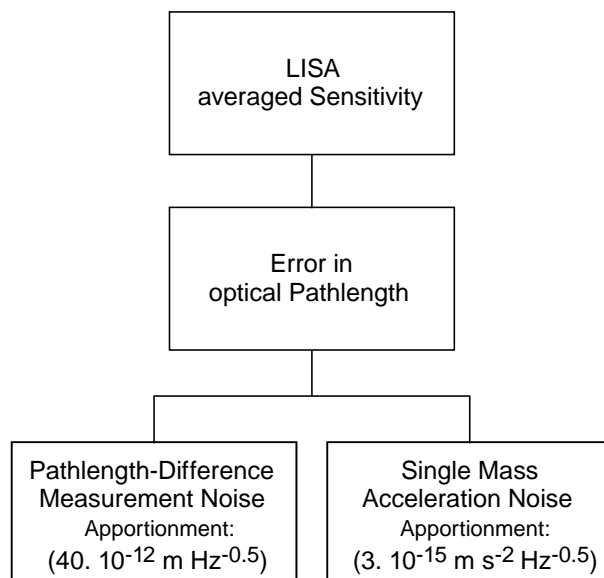


**Figure A.1** *Performance model structure*

In a practical implementation both error contributions are not likely white processes over the whole measurement frequency band. It can be expected that acceleration resulting from the drag-free control loop residual error will rise at the upper edge of the frequency band while measurement noise resulting from uncompensated laser phase noise will rise at the lower band edge. Since however the system sensitivity is dominated by length measurement noise at the high frequencies and by acceleration noise at the low frequencies these effects will not necessarily compromise the overall sensitivity.

The length measurement noise has several causes:

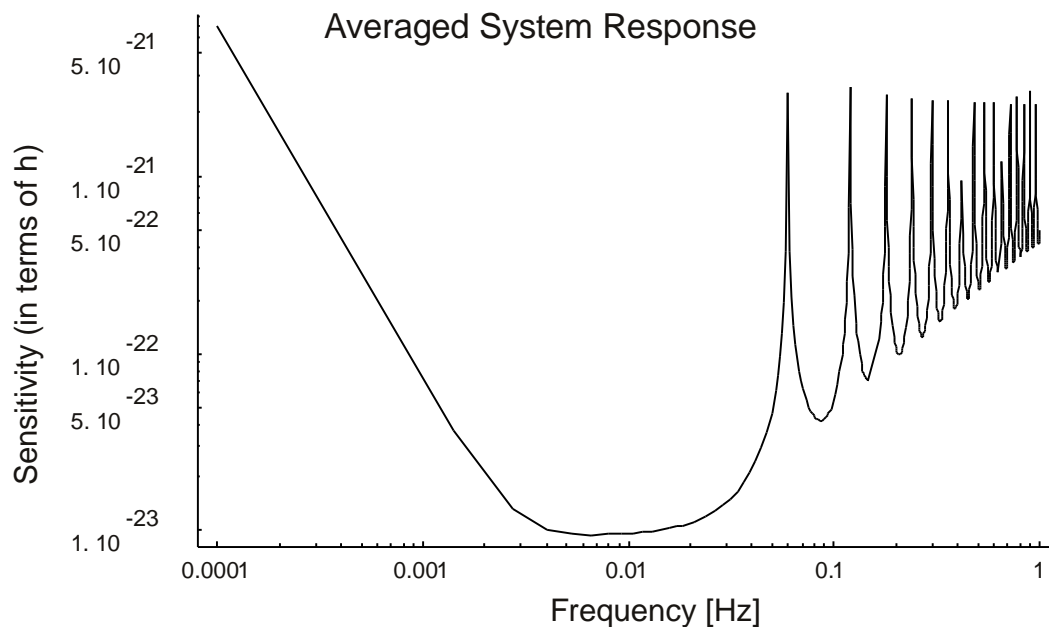


**Figure A.2** *Specified error bound for optical path-length (as phase error)*

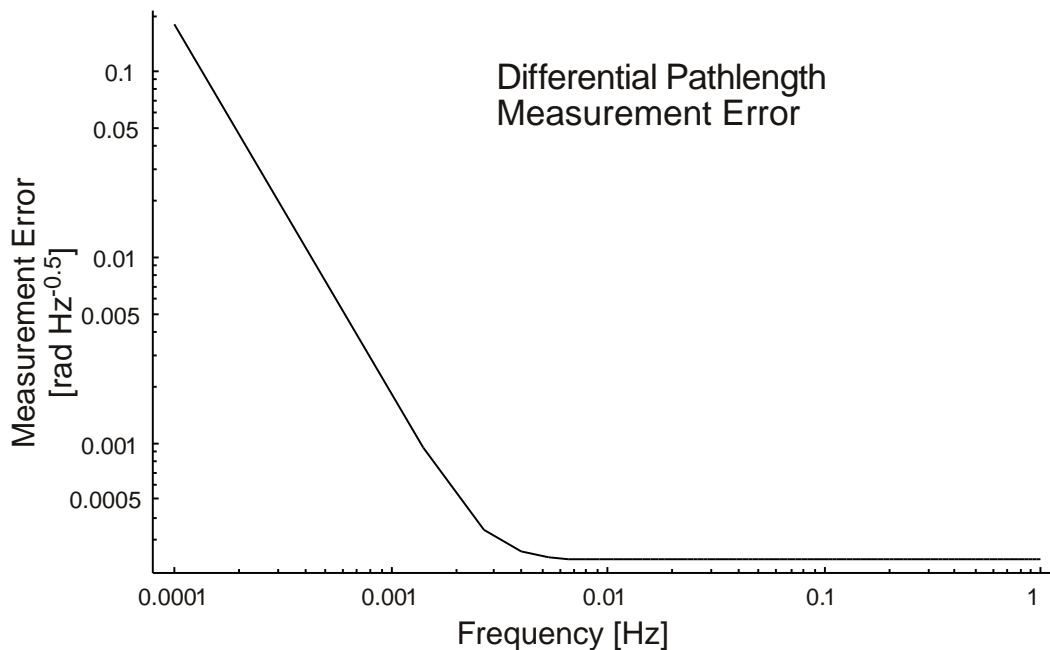


**Figure A.3** Required system sensitivity for one year of observation

- Shot noise due to the limited number of received photons
- Laser phase noise
- Measurement clock phase noise
- Variation of measured phase due to motion of optical components inside the instrument
- Variation of phase due to wavefront curvature and pointing interaction

The unavoidable contribution is the shot noise on the received signal. It is ideally the dominating noise source for the length measurement, determined by telescope diameter and transmitter power. Optical losses, wavefront mismatch at the detector and detector quantum efficiency contribute to the shot noise level. However state of the art optical design is so close to the theoretical limit that practical improvement of shot noise is only expectable via higher transmitter power or larger telescopes. For the required measurement accuracy, a transmitter power of 1 W and a telescope diameter of 0.3 m is sufficient, with some margin to accommodate the above mentioned losses.

Although not limited by first principles it is technologically demanding to reduce the other measurement error contributions to a magnitude comparable with the shot noise as determined above.

The approach to deal with laser phase noise and measurement clock noise is the use of noise cancellation techniques. This eliminates the first order effect of these noise sources to the system measurement sensitivity. However the actual magnitude of the phase noises determines the accuracy required for the cancellation process and hence poses requirements to equipment and accuracy of ancillary data, e.g. phase meter dynamic range and aliasing behaviour.

An ancillary interferometer measurement is assumed to determine the relative motion of proof-mass versus spacecraft to eliminate the dominating internal pathlength variation.

Residual pathlength variations have to be addressed by technological means, i.e. a mechanically and thermally stable design of the optical bench, control of straylight intensity and mechanical



stability of straylight paths. Tight control of transmitter pointing in combination with good optical quality of the telescope (to reduce errors in phasefront curvature) is required to achieve a small pointing-induced measurement error.

The acceleration noise is also resulting from several causes:

- External forces directly acting upon the proof masses coupled by interplanetary magnetic fields (e.g. Lorentz force)
- Forces induced by time varying local fields (gravity, magnetic (gradient))
- Forces directly resulting from the electrostatic actuators of the drag-free control loop
- Forces resulting from gradients of magnetic and gravity fields bound to the spacecraft and relative motion between spacecraft and proof mass

The key element governing the acceleration noise budget is the drag-free control loop. It shields the proof masses from most external forces acting upon the spacecraft, specifically from time-varying radiation pressure originating from the sun. The control loop uses the [FEED](#) thrusters to control spacecraft position and attitude such that the proof masses remain centred in their cages and the telescopes remain pointed to the two other spacecraft of the formation. Since the 6 degrees of freedom of spacecraft position and orientation are not sufficient to achieve the control objective for two proof-masses and two telescopes, additional actuators are employed. Specifically the pointing angle between the telescopes can be controlled and electro-static actuators are employed to impose forces and torque to the proof masses. The design of the control loop is constrained by stability considerations arising from static forces and “spring constants” acting on the proof masses (resulting from field-strength and field-strength gradient of magnetic and gravitational fields). Aim of the control loop optimisation is the minimisation of forces in the measurement bandwidth arising from electrostatic actuator action or resulting from relative motion of the proof-masses with respect to the field gradients coupled to the spacecraft.

The two aspects of [LISA](#) performance (pathlength measurement error and acceleration noise) are discussed and budgeted in the following two sections. Compensation of phase and clock noise as well as accounting for relative motion of spacecraft versus proof masses is essential to measurement performance. The section on the pathlength measurement error includes therefore also the description of the measurement setup and processing strategy addressing these aspects.

### A.1.2 Pathlength Difference Measurement

The basic measurement configuration of the [LISA](#) system is specified in [1] and [133]. One Michelson interferometer is implemented using the payload of three spacecraft. The interferometer setup using spacecraft 2 as centre node and spacecraft 1 and 3 as ends of the two arms is shown in Figure [A.4](#).

Since the formation is an equilateral triangle and all spacecraft are identical, three equivalent setups can be formed by cyclic permutation. However only two simultaneously derived results provide independent information on the gravitational wave.

[TX/RX](#) units assembled on individual optical benches are used at the ends of the interferometer arms. Each spacecraft houses two of such units. Each unit contains:

- an individual transmitter laser
- a phase modulator to create sidebands on the transmitted laser beam used to convey information on the local clock (and for data exchange between the spacecraft)
- an individual proof-mass (with electrostatic sensors and actuators, used by the drag-free control),

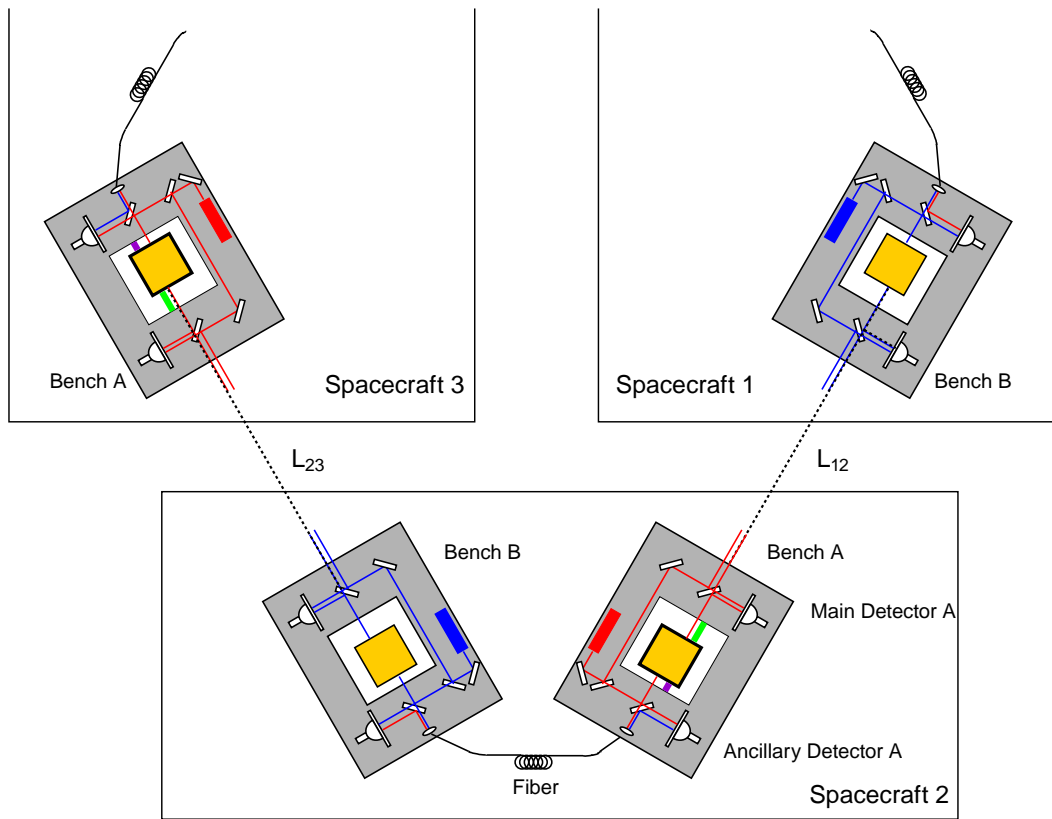


**Figure A.4** *LISA measurement setup*

- a main detector where the interference signal of the received light and a fraction of the light from the local transmission laser is converted to an electrical signal containing the beat note of the carriers and the modulation sidebands (actually the main detector signal is the sum of four quadrant signals of a segmented detector)
- a secondary detector where a heterodyne signal between the two transmitter lasers on board the same spacecraft is generated
- ancillary functions supporting pointing and beam alignment; including quadrant channels of the main detector for measurement of wavefront tilt
- a reference cavity which may be used for stabilising the transmitter laser

The optical signal path is selected such that changes in the distance between the proof masses of an interferometer arm is represented as phase change on the main detectors. Due to the long roundtrip time of about 33 s, relative motion of the optical bench versus the floating proof mass is visible in the main detector signals. Therefore the light path associated with the secondary detector contains a reflection on the backward surface of the proof mass such that an interferometer is formed measuring the motion of the optical bench relative to the proof mass. This information can be used for correcting the spacecraft relative motion effect on the main interferometer. On all detectors light from different laser sources is superimposed. Hence all interferometer signals are heterodyne signals with beat frequencies not necessarily close to zero, even when no significant Doppler shift is involved in the respective light path. The strategy to obtain reasonable frequencies of the detector signals is to use one laser in the configuration as reference and lock the other lasers directly or indirectly to this master laser. The master laser itself is stabilised by a control loop using the above mentioned cavity. The ancillary detectors

serve aside from their function in the backside interferometers as means to establish a phase relation between the two lasers in the same spacecraft. By using offset locking between the different lasers the frequency of the beat signals can be conveniently controlled. However at some detectors a beat frequency as high as the maximum one way Doppler shift between any two spacecraft is unavoidable (about 1 MHz per 1 m/s relative velocity). Handling high frequencies at the input of the phase measurement devices requires appropriately accurate reference clocks.

The desired data product from the described configuration is the armlength difference  $L_{23} - L_{12}$  which should be representative in the measurement bandwidth  $10^{-4}$  Hz to  $10^{-1}$  Hz. It is needed from two of the three possible interferometer configurations in the triangular formation. The main problem in determining these quantities from the measured detector signals is the large phase noise on the laser signals and on the local clock signals which dominate the wanted measurement signal by orders of magnitude.

The Pre-Phase A design has adopted cancellation techniques for both noise types.

The phase noise cancellation technique follows G. Giampieri [117]. It operates in the frequency domain (Fourier transform of the time series from the detector). Essentially instead of  $L_{23}(f) - L_{12}(f)$  the system is solved for  $L_{23}(f) - \gamma(f)L_{12}(f)$ , where  $\gamma(f)$  is a known complex-valued function depending on system geometry with an absolute value close to unity. This particular linear combination can be shown to be independent of the laser noise with perfectly known system geometry. When the absolute values of the interferometer arm length difference is only approximately known the residual amplitude error is proportional to the laser phase noise amplitude and (at least at sufficiently low frequencies) proportional to the error in knowledge of the absolute armlength difference. At low frequencies the residual error follows a  $1/f$  characteristic.

The clock noise compensation is a derivative of the method described by Hellings and Giampieri [144]. (It differs in the method of generation of the clock synchronisation signal.) Basically a high-frequency signal (200 MHz) synchronised to the local reference clock is modulated on each transmitted laser beam and demodulated at each main detector. The demodulated signals allow referencing of the local clocks (one per spacecraft) to exactly monitored delay lines established by the precisely measured path delay on the interferometer arms. The achievable clock noise (at modulation frequency level) after correction is proportional to the shot noise on the ancillary carrier. As the fraction of this noise relevant to the LISA measurement is determined by the ratio of the beat signal frequencies to the ancillary modulation frequency, a sufficiently low corrected clock noise can be achieved for nominal detector signals with frequencies small compared to the modulation frequencies. Generally the residual effect of the clock noise should be negligible when the frequency ratio can be made large compared to the power ratio of laser carrier and used modulation side-band.

#### A.1.2.1 Formal description of the measurement setup.

The setup given in Figure A.4 can be reduced to a formal diagram identifying the relevant optical paths and phase relationships as shown in Figure A.5 for spacecraft 2.

The optical components needed for changing polarisation as needed for the TX/RX beam splitting are not shown. Their effect is included in the relevant optical pathlengths; pathlength variations are assumed negligible in the measurement bandwidth.

Figure A.5 identifies the 6 possible phase measurements per spacecraft:

- $s_{2a}$  beat note of optical carriers in spacecraft 2 for link S/C 1 to S/C 2
- $s_{2b}$  beat note of optical carrier in spacecraft 2 with upper modulation sideband of received signal for link S/C 1 to S/C 2
- $s_{2c}$  beat note of backside interferometer with measurement path via proof mass A2
- $s_{2d}$  beat note of backside interferometer with measurement path via proof mass B2
- $s_{2e}$  beat note of optical carrier in spacecraft 2 with upper modulation sideband of received signal for link S/C 3 to S/C 2
- $s_{2f}$  beat note of optical carriers in spacecraft 2 for link S/C 3 to S/C 2

The unknown quantities are:

Laser and clock phase functions (referenced to the nominal master signals optical respectively USO)

- $p_{B2}$  phase function of laser associated with proof-mass B2 (reference point is polarising beam splitter in front of proof-mass B2)
- $p_{12}$  clock phase function (S/C 2) as modulated onto optical carrier, i.e. as represented by difference of carrier and sub-carrier phase (reference point is polarising beam splitter in front of proof-mass B2, however differences other than a constant phase are not assumed when the modulation is observed at the polarising beam splitter in front of proof-mass A2)
- $p_{A2}$  phase function of laser associated with proof-mass A2 (reference point is polarising beam splitter in front of proof-mass A2)

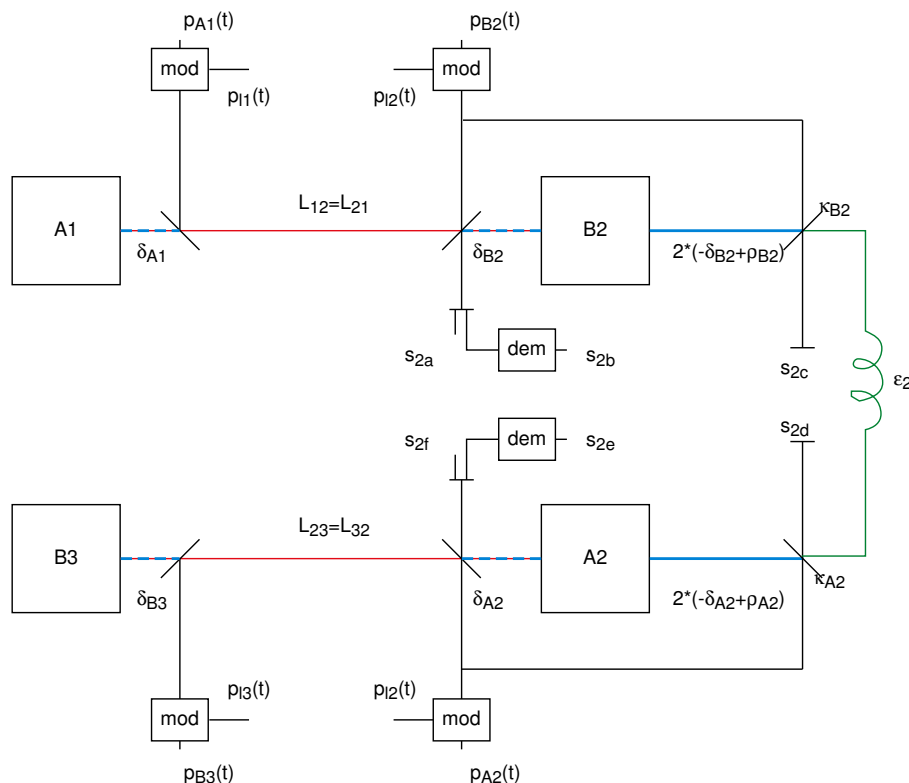


**Figure A.5** LISA measurement setup parameter diagram

Optical path-lengths:

- $L_{12}$  distance between the proof-masses A1 and B2 which is the interferometer arm length S/C 1 to S/C 2,
- $\delta_{B2}$  distance between polarising beam splitter in front of proof-mass B2 and proof-mass B2 (part of optical path from S/C 1 to S/C 2)
- $\delta_{A1}$  distance between polarising beam splitter in front of proof-mass A1 and proof-mass A1 (part of optical path from S/C 2 to S/C 1)
- $\varrho_{B2}$  difference in distance from the front surface of the proof mass B2 to the main beam splitter and the distance from the backside of the proof-mass to the ancillary beam splitter; this quantity is assumed to be constant as it depends only on mechanical dimensions of proof-mass and optical bench
- $\kappa_{B2}$  phase difference between pB2 and the optical phase of the B2 transmitter laser observed at the ancillary beam splitter; this quantity is assumed to be constant as it depends only on mechanical dimensions of the optical bench
- $\varepsilon_2$  optical pathlength of the fibre path between the two ancillary beam splitters; both directions are assumed to exhibit identical optical pathlength (neglected dispersion and polarisation dependence effects)
- $L_{23}$  distance between the proof-masses B3 and A2 which is the interferometer arm length S/C 3 to S/C 2,
- $\delta_{A2}$  distance between polarising beam splitter in front of proof-mass A2 and proof-mass A2 (part of optical path from S/C 3 to S/C 2)
- $\delta_{B3}$  distance between polarising beam splitter in front of proof-mass B3 and proof-mass B3 (part of optical path from S/C 2 to S/C 3)
- $\varrho_{A2}$  difference in distance from the front surface of the proof mass A2 to the main beam splitter and the distance from the backside of the proof-mass to the ancillary beam splitter; this quantity is assumed to be constant as it depends only on mechanical dimensions of proof-mass and optical bench
- $\kappa_{A2}$  phase difference between pA2 and the optical phase of the A2 transmitter laser observed at the ancillary beam splitter; this quantity is assumed to be constant as it depends only on mechanical dimensions of the optical bench

For the purpose of the LISA measurement changes in the quantities describing optical path-lengths are relevant in the picometer scale while the effect of the same quantities in terms of delay as relevant for the measurement of the phase noises is only noticeable in the meter scale. Therefore the equations describing the measurement setup will be formulated in terms of difference quantities  $\Delta L_{12}$ ,  $\Delta L_{23}$ ,  $\Delta \delta_{B2}$ ,  $\Delta \delta_{A1}$ ,  $\Delta \delta_{A2}$ ,  $\Delta \delta_{B3}$ ,  $\Delta \varepsilon_2$ , referring to some arbitrary starting value and of estimates of the absolute quantities as needed for the phase noise cancellation. I.e.  $\Delta L_{12}$  shall be the unknown variation of the interferometer arm length S/C 1 to S/C 2 (relevant in picometer scale) while  $L_{12}$  is the estimate of the absolute value (relevant in meter scale).

The resulting LISA equations for S/C 2 measurements in the time domain are given in Eq. (A.2) below. The equivalent equations for the measurements on the spacecraft 1 and 3 can be derived by cyclic permutation of the indices and assuming the identities  $L_{23} = L_{32}$  and  $L_{12} = L_{21}$ .

In Eq. (A.2)  $n_{2a}$  to  $n_{2f}$  is the shot noise associated with the respective measurements. These noise can assumed to be white in the frequency range of interest. The factors  $a_{2a}$  to  $a_{2f}$  are the fraction of the USO phase noise at modulation frequency to be applicable for the respective phase measurement. This factor is given by the frequency ratio of the beat note at the detector compared to the modulation frequency of the ancillary modulation. The sign depends on which of the two mixed laser frequencies is larger. These factors are treated like the estimate of the absolute arm lengths.

$$\begin{aligned}
2a: \quad s_{2a}(t) &= n_{2a}(t) + \alpha_{2a} \cdot p_{l2}(t) + \frac{2\pi}{\lambda} \cdot \left( \Delta L_{12}(t) + \Delta \delta_{B2}(t) - \Delta \delta_{A1} \left( t - \frac{L_{12}(t)}{c} \right) \right) - p_{A1} \left( t - \frac{L_{12}(t)}{c} \right) + p_{B2}(t) \\
2b: \quad s_{2b}(t) &= n_{2b}(t) + \frac{2\pi}{\lambda} \cdot \left( \Delta L_{12}(t) + \Delta \delta_{B2}(t) - \Delta \delta_{A1} \left( t - \frac{L_{12}(t)}{c} \right) \right) - p_{A1} \left( t - \frac{L_{12}(t)}{c} \right) + p_{B2}(t) + (1 + \alpha_{2a}) \cdot p_{l2}(t) - p_{l1} \left( t - \frac{L_{12}(t)}{c} \right) \\
2c: \quad s_{2c}(t) &= n_{2c}(t) + \alpha_{2c} \cdot p_{l2}(t) + \frac{2\pi}{\lambda} \cdot (\Delta \varepsilon_2(t) - 2\Delta \delta_{B2}(t) + 2\rho_{B2}(t)) - \left( p_{A2} \left( t - \frac{\varepsilon_2(t)}{c} \right) + \kappa_{A2} \right) + (p_{B2}(t) + \kappa_{B2}) \\
2d: \quad s_{2d}(t) &= n_{2d}(t) + \alpha_{2d} \cdot p_{l2}(t) + \frac{2\pi}{\lambda} \cdot (\Delta \varepsilon_2(t) - 2\Delta \delta_{A2}(t) + 2\rho_{A2}(t)) - \left( p_{B2} \left( t - \frac{\varepsilon_2(t)}{c} \right) + \kappa_{B2} \right) + (p_{A2}(t) + \kappa_{A2}) \\
2e: \quad s_{2e}(t) &= n_{2e}(t) + \frac{2\pi}{\lambda} \cdot \left( \Delta L_{23}(t) + \Delta \delta_{A2}(t) - \Delta \delta_{B3} \left( t - \frac{L_{32}(t)}{c} \right) \right) - p_{B3} \left( t - \frac{L_{32}(t)}{c} \right) + p_{A2}(t) + (1 + \alpha_{2f}) \cdot p_{l2}(t) - p_{l3} \left( t - \frac{L_{23}(t)}{c} \right) \\
2f: \quad s_{2f}(t) &= n_{2f}(t) + \alpha_{2f} \cdot p_{l2}(t) + \frac{2\pi}{\lambda} \cdot \left( \Delta L_{23}(t) + \Delta \delta_{A2}(t) - \Delta \delta_{B3} \left( t - \frac{L_{23}(t)}{c} \right) \right) - p_{B3} \left( t - \frac{L_{23}(t)}{c} \right) + p_{A2}(t)
\end{aligned} \tag{A.2}$$

The Fourier transform of equations Eq. (A.2) is given in Eq. (A.3) under the simplifying assumption that the time dependence of  $L_{12}(t)$ ,  $L_{23}(t)$ ,  $L_{13}(t)$  can be neglected. This simplification is equivalent to assuming that the variations of arm lengths and Doppler frequency although significant for the phase of the beat signal are sufficiently small to be ignored in the domain of the phase variations considered as a modulation on the light signal (laser phase noise, phase modulation due to relative proof mass motion). These slow phase variations can be considered as processed representing a wavelength very large compared to the arm length variations in question. Similarly the  $\alpha_i$  are considered constant which assumes negligible Doppler variations. The resulting set of equations is for each given frequency linear with respect to the unknowns. Equations for S/C 2 measurements in frequency domain (transforms of constant values omitted) are shown in Eq. (A.3).

$$\begin{aligned}
2a: \quad s_{2a}(f) &= n_{2a}(f) + \alpha_{2a} \cdot p_{l2}(f) + \frac{2\pi}{\lambda} \cdot \left( \Delta L_{12}(f) + \Delta \delta_{B2}(f) - \Delta \delta_{A1}(f) \cdot e^{-j2\pi f \frac{L_{12}}{c}} \right) - p_{A1}(f) \cdot e^{-j2\pi f \frac{L_{12}}{c}} + p_{B2}(f) \\
2b: \quad s_{2b}(f) &= n_{2b}(f) + \frac{2\pi}{\lambda} \cdot \left( \Delta L_{12}(f) + \Delta \delta_{B2}(f) - \Delta \delta_{A1}(f) \cdot e^{-j2\pi f \frac{L_{12}}{c}} \right) - p_{A1}(f) \cdot e^{-j2\pi f \frac{L_{12}}{c}} + p_{B2}(f) + (1 + \alpha_{2a}) \cdot p_{l2}(f) - p_{l1}(f) \cdot e^{-j2\pi f \frac{L_{12}}{c}} \\
2c: \quad s_{2c}(f) &= n_{2c}(f) + \alpha_{2c} \cdot p_{l2}(f) + \frac{2\pi}{\lambda} \cdot (\Delta \varepsilon_2(f) - 2\Delta \delta_{B2}(f)) - p_{A2}(f) \cdot e^{-j2\pi f \frac{\varepsilon_2}{c}} + p_{B2}(f) \\
2d: \quad s_{2d}(f) &= n_{2d}(f) + \alpha_{2d} \cdot p_{l2}(f) + \frac{2\pi}{\lambda} \cdot (\Delta \varepsilon_2(f) - 2\Delta \delta_{A2}(f)) - p_{B2}(f) \cdot e^{-j2\pi f \frac{\varepsilon_2}{c}} + p_{A2}(f) \\
2e: \quad s_{2e}(f) &= n_{2e}(f) + \frac{2\pi}{\lambda} \cdot \left( \Delta L_{23}(f) + \Delta \delta_{A2}(f) - \Delta \delta_{B3}(f) \cdot e^{-j2\pi f \frac{L_{23}}{c}} \right) - p_{B3}(f) \cdot e^{-j2\pi f \frac{L_{23}}{c}} + p_{A2}(f) + (1 + \alpha_{2f}) \cdot p_{l2}(f) - p_{l3}(f) \cdot e^{-j2\pi f \frac{L_{23}}{c}} \\
2f: \quad s_{2f}(f) &= n_{2f}(f) + \alpha_{2f} \cdot p_{l2}(f) + \frac{2\pi}{\lambda} \cdot \left( \Delta L_{23}(f) + \Delta \delta_{A2}(f) - \Delta \delta_{B3}(f) \cdot e^{-j2\pi f \frac{L_{23}}{c}} \right) - p_{B3}(f) \cdot e^{-j2\pi f \frac{L_{23}}{c}} + p_{A2}(f)
\end{aligned} \tag{A.3}$$

The measurement equations in Fourier representation from all three spacecraft of the LISA configuration can be combined in several ways to form linear equation systems that can be solved for armlength differences representing the desired measurement result. Solution is performed separately and independently for each frequency bin in the interesting frequency range.

### A.1.2.2 Equation systems describing the measurement setups

With the three spacecraft two measurement setups can be formed:

- a closed ring configuration in which all links are supposed to be operational

- a fall-back configuration in which one arm can not be used due to failure of a laser link.

In the closed ring configuration the desired measurement result is a set of two armlength differences, i.e.  $(\Delta L_{12} - \Delta L_{23})$  and  $(\Delta L_{23} - \Delta L_{13})$ , while in the fall-back configuration only one armlength difference is determined (three possible variations depending on the arm with the unused or defective link).

The phase noise compensation technique as described in [117] and the clock noise compensation as described in [144] operate in Fourier space. The equations for the (transformed) phase measurements Eq. (A.3) form a linear equation system with complex frequency dependent coefficients which has to be solved for the desired armlength differences.

### A.1.2.3 Fall-back configuration equation system

In the fall-back system only measurements not depending on the light of one of the two lasers operating on the arm with the failed link can be used. In case of a defective arm from S/C 1 to S/C 3 the usable detector equations are: 1e, 1f, 2a, 2b, 2c, 2d, 2e, 2f, 3a, 3b.

The set of unknowns consists of  $\Delta\Delta L_{123}$ ,  $\Delta L_{12}$ ,  $\Delta L_{23}$ ,  $p_{i1}$ ,  $p_{i2}$ ,  $p_{i3}$ ,  $\Delta\delta_{A1}$ ,  $\Delta\delta_{A2}$ ,  $\Delta\delta_{B2}$ ,  $\Delta\delta_{B3}$ ,  $\Delta\varepsilon_2$ ,  $p_{A1}$ ,  $p_{A2}$ ,  $p_{B2}$ ,  $p_{B3}$ . It is clear that on the two side spacecraft the backside interferometer is not operational, hence no information on the relative movement of the proof-masses can be retrieved (i.e. on  $\Delta\delta_{A1}$ ,  $\Delta\delta_{B3}$ ). However, as will be demonstrated formally below by examination of the Null space of the equation system, this does not affect the ability to solve for the arm length difference. Relative motion of spacecraft versus proof mass affects the armlength measurement due to the round trip delay time: The position of the polarising beam splitter (relative to the proof mass) is the reference point for the phase measurement, it may change during the roundtrip time causing a measurement error. On the side spacecraft however, phase measurement serves only for relating the instantaneous phase of the outgoing beam to that of the incoming beam. Here any change of the beam splitter position is compensated because length changes on the reception path correspond to the same length changes on the transmission path but with opposite sign. This is different for the centre spacecraft as the distance of beam splitter versus proof mass on the transmit path corresponds to the same distance on the receive path at a different instance in time.

From the 10 equations describing possible phase measurements in the fall-back configuration (i.e. disregarding all measurements involving the unused link) only 9 are linearly independent. The USO noise is over-determined by 1e, 2b, 2e, 3b. Dropping any one of these four measurements results in a non-contradicting set.

A further equation has to be added to define the desired result  $\Delta\Delta L_{123}$  which is the armlength difference. This results in 10 linearly independent equations for 15 unknown quantities. This can be written in the form (one equation system per each frequency bin)

$$\mathbf{M} \cdot \vec{\xi} = \vec{s} \quad (\text{A.4})$$

where  $\mathbf{M}$  is the matrix ( $15 \times 10$  for fall-back solution) of complex coefficients applicable at the actual frequency bin,  $\xi$  is the vector of unknowns (length = 15 for fall-back solution),  $s$  is the vector of Fourier transformed phase measurements at the actual frequency.

A unique solution for all unknowns does not exist. An infinite set of solution vectors is compatible with the same measurement input. The structure of the space of solutions is described by the Null space of matrix  $\mathbf{M}$ .



The general form of the solution is:

$$\vec{\xi} = \vec{\xi}_0 + \sum_{j=1}^n \beta_j \cdot \vec{\xi}_j, \quad (\text{A.5})$$

where  $\xi_0$  is an arbitrary solution of the inhomogeneous system Eq. (A.4) (in the practical measurement problem this can easily be determined by standard numerical algorithms to solve linear equations, such as Gauss elimination, the undetermined variables are simply set to zero),  $\xi_j$  are vectors of the Null space of matrix  $M$ ,  $\beta_j$  are arbitrary complex numbers and  $n$  is the number of vectors in the Null space (5 for fall-back solution).

In a useful measurement setup the solution for  $\Delta\Delta L_{123}$  must not depend on the arbitrarily selectable  $\beta_j$  which is equivalent to requiring that in all  $\xi_j$  the element corresponding to  $\Delta\Delta L_{123}$  is zero. In this case the desired measurement result is uniquely defined by the measured phase values. However, some or all of the other unknowns can not be determined unambiguously. For the most obvious definition of  $\Delta\Delta L_{123}$ , i.e.  $\Delta\Delta L_{123} = \Delta L_{12} - \Delta L_{23}$  the resulting equation system lacks the above mentioned property, i.e. a solution is not unambiguously determined by the vector of measurements.

Essentially the laser phase noise cancellation scheme introduced in [117] solves this problem by determining  $\Delta\Delta L_{123} = \Delta L_{12} - \gamma * \Delta L_{23}$ , where  $\gamma$  is a factor depending on frequency and known system geometry determined such that a unique solution for  $\Delta\Delta L_{123}$ . For low frequencies and LISA system geometry  $\gamma$  is a complex number close to  $(1+0i)$ . The definition which yields the uniqueness requirement with the equation system used here is:

$$\Delta\Delta L_{123} = \Delta L_{12} - \frac{\exp\left(\frac{2\pi i f (L_{23} - L_{12})}{c}\right) \cdot \left(\exp\left(\frac{2\pi i f L_{12}}{c}\right) - 1\right)}{\exp\left(\frac{2\pi i f L_{23}}{c}\right) - 1} \cdot \Delta L_{23}. \quad (\text{A.6})$$

The resulting equation system has been analysed using a formula manipulation program. The Null space has been determined as is shown in Table A.1.

This demonstrates that  $\Delta\Delta L_{123}$  is indeed uniquely determined while ambiguous solutions exist for  $\Delta L_{12}$  and  $\Delta L_{23}$ . When examining the vectors of the Null space it becomes apparent that the main source of ambiguity is that laser phase-noise ( $p_{xx}$ ), proof-mass relative motion ( $\Delta\delta_{xx}$ ) and effective length of the coupling fibre ( $\Delta\epsilon_2$ ) have indistinguishable effects. This is a specific feature of the layout of the backside interferometer following [146]. It is characterised by routing the light from the laser associated with a proof-mass via the backside of that proof-mass and then interfere with the light of the other laser on the same spacecraft which has not been reflected at any proof mass. Using the proof-masses over cross would for example not lead to an equation system with unique solution for  $\Delta\Delta L_{123}$ .

The above results have been obtained assuming that the absolute optical length  $\epsilon_2$  of the fibre is insignificant to the phase noise of the lasers as observed by the detectors at either end, i.e.  $\exp(-2\pi i f \epsilon_2 / c)$  is assumed to be exactly 1. This is only then an acceptable assumption when the difference between the correct number and unity is small compared with the ratio of shot noise induced phase measurement error and laser phase noise. With an arbitrary length fibre a unique solution for  $\Delta\Delta L_{123}$  or a similar linear combination has not been identified.

#### A.1.2.4 Nominal configuration equation system

Similar to the fall-back solution equation system an equation system for the complete configuration can be established. The equations for the 18 detector signals contain 4 linearly dependent

**Table A.1** Null space of the equation system for the fallback configuration

$\xi_1$	$\xi_2$	$\xi_3$	$\xi_4$	$\xi_5$	Unknown
1	0	0	0	0	$p_{B3}$
0	1	0	0	0	$p_{B2}$
0	0	1	0	0	$p_{A2}$
0	0	0	1	0	$p_{A1}$
0	0	0	0	1	$\Delta\delta_{B3} * 2\pi/\lambda$
1	0	0	-1	1	$\Delta\delta_{A1} * 2\pi/\lambda$
2	-1	-1	0	2	$\Delta\varepsilon_2 * \pi/\lambda$
1	-1	0	0	1	$\Delta\delta_{B2} * 2\pi/\lambda$
1	0	-1	0	1	$\Delta\delta_{A2} * 2\pi/\lambda$
0	0	0	0	0	$p_{i3}$
0	0	0	0	0	$p_{i2}$
0	0	0	0	0	$p_{i1}$
$\exp\left(-\frac{2\pi i f L_{23}}{c}\right)$	0	0	0	$\exp\left(-\frac{2\pi i f L_{23}}{c}\right)$	$\Delta L_{23} * 2\pi/\lambda$
$\exp\left(-\frac{2\pi i f L_{12}}{c}\right)$	0	0	0	$\exp\left(-\frac{2\pi i f L_{12}}{c}\right)$	$\Delta L_{12} * 2\pi/\lambda$
0	0	0	0	0	$\Delta\Delta L_{123} * 2\pi/\lambda$

left sides. This is due to the over-determination of **USO** noise by equation 1b, 1e, 2b, 2e, 3b, 3e only three of which are needed for an unambiguous determination of the **USO** noises. Dropping for example the “b” equations leads to a valid set. In a practical implementation the remaining three measurement values can be utilised to improve the **USO** phase estimate in the presence of measurement noise. Aside from selecting only 3 of the 6 **USO** equations it is also necessary to drop one of the 6 backside interferometer equations 1c, 1d, 2c, 2d, 3c, 3d. The unused measurement has to be on the spacecraft not used as vertex of one of the two armlength differences, i.e. with  $\Delta\Delta L_{123}$  and  $\Delta\Delta L_{231}$  as differences to be determined 1c or 1d must be selected. The remaining backside interferometer measurement on that spacecraft does not lead to a contradiction in the equation system, but it is also not required to determine the armlength differences and therefore it can also be omitted. (Using all 6 equations is equivalent to trying to synchronise all lasers to each other in a ring structure. Dropping one equation cuts the ring to a chain synchronised to the master. The information coming from the backside interferometer is not required on the wing spacecraft for the same reason as in the fall-back configuration, allowing to drop the mentioned fifth equation as well. The fibre connection associated with the two unused detectors is then also not needed allowing to remove the change of fibre optical pathlength  $\Delta\varepsilon_1$  from the list of unknowns.)

Together with the defining equations for  $\Delta\Delta L_{123}$  and  $\Delta\Delta L_{231}$  these considerations lead to a system of 15 equations with 22 unknowns ( $\Delta\Delta L_{123}$ ,  $\Delta\Delta L_{231}$ ,  $\Delta L_{12}$ ,  $\Delta L_{23}$ ,  $\Delta L_{13}$ ,  $p_{i1}$ ,  $p_{i2}$ ,  $p_{i3}$ ,  $\Delta\delta_{A1}$ ,  $\Delta\delta_{B1}$ ,  $\Delta\delta_{A2}$ ,  $\Delta\delta_{B2}$ ,  $\Delta\varepsilon_2$ ,  $\Delta\delta_{A3}$ ,  $\Delta\delta_{B3}$ ,  $\Delta\varepsilon_3$ ,  $p_{A1}$ ,  $p_{B1}$ ,  $p_{A2}$ ,  $p_{B2}$ ,  $p_{A3}$ ,  $p_{B3}$ ). The defining

equations for  $\Delta\Delta L_{123}$  and  $\Delta\Delta L_{231}$  are given by Eq. (A.6) and

$$\Delta\Delta L_{231} = \Delta L_{23} - \frac{\exp\left(\frac{2\pi i f(L_{13}-L_{23})}{c}\right) \cdot \left(\exp\left(\frac{2\pi i f L_{23}}{c}\right) - 1\right)}{\exp\left(\frac{2\pi i f L_{13}}{c}\right) - 1} \cdot \Delta L_{13} . \quad (\text{A.7})$$

Again the Null space has been determined, this time however using numerical methods instead of symbolical calculations because of the complexity of the involved expressions. For representative geometry at frequency 1 mHz the vectors of the Null space are given in Table A.2.

The vectors are normalised to their largest element. Hence the absolute values below  $10^{-14}$  effectively represent zero. The null space has essentially a structure similar to that of the fall-back configuration:

- unambiguous solutions for  $\Delta\Delta L_{123}$ ,  $\Delta\Delta L_{231}$  exist

**Table A.2** *Null space of nominal configuration equation system*  
(absolute values of numerical solution at 1 mHz)

$ \xi_1 $	$ \xi_2 $	$ \xi_3 $	$ \xi_4 $	$ \xi_5 $	$ \xi_6 $	$ \xi_7 $	Unknown
1	0	0	0	0	0	0	$p_{B3}$
0	1	0	0	0	0	0	$p_{A3}$
0	0	1	0	0	0	0	$p_{B2}$
0	0	0	1	0	0	0	$p_{A2}$
0	0	0	0	1	0	0	$p_{B1}$
0	0	0	0	0	1	0	$p_{A1}$
0	0	0	0	0	0	1	$\Delta\epsilon_3$
0.5	0.5	$3.93 \times 10^{-17}$	0	0	$2.64 \times 10^{-19}$	0.5	$\Delta\delta_{B3}$
0.5	0.5	$1.39 \times 10^{-17}$	0	0	$2.64 \times 10^{-19}$	0.5	$\Delta\delta_{A3}$
1	1	1	1	0	$3.93 \times 10^{-18}$	1	$\Delta\epsilon_2$
0.5	0.5	1	0	0	$1.88 \times 10^{-18}$	0.5	$\Delta\delta_{B2}$
0.5	0.5	$1.12 \times 10^{-16}$	1	0	$1.88 \times 10^{-18}$	0.5	$\Delta\delta_{A2}$
0.5	0.5	$2.78 \times 10^{-17}$	0	1	$3.72 \times 10^{-19}$	0.5	$\Delta\delta_{B1}$
$1.11 \times 10^{-16}$	1	0	0	0	1	0	$\Delta\delta_{A1}$
$2.22 \times 10^{-16}$	$2.18 \times 10^{-16}$	0	0	0	$1.45 \times 10^{-17}$	$2.22 \times 10^{-16}$	$p_{i3}$
$2.22 \times 10^{-16}$	$9.27 \times 10^{-16}$	$8.88 \times 10^{-16}$	0	0	$1.45 \times 10^{-17}$	$2.22 \times 10^{-16}$	$p_{i2}$
$4.44 \times 10^{-16}$	$1.00 \times 10^{-15}$	$8.88 \times 10^{-16}$	0	0	$1.45 \times 10^{-17}$	$4.44 \times 10^{-16}$	$p_{i1}$
0.056	0.056	$5.72 \times 10^{-17}$	0	0	$7.41 \times 10^{-19}$	0.056	$\Delta L_{13}$
0.054	0.054	$1.24 \times 10^{-16}$	0	0	$7.74 \times 10^{-19}$	0.054	$\Delta L_{23}$
0.053	0.053	$1.73 \times 10^{-18}$	0	0	$2.82 \times 10^{-20}$	0.053	$\Delta L_{12}$
$4.20 \times 10^{-17}$	$3.85 \times 10^{-17}$	$1.79 \times 10^{-17}$	0	0	$2.02 \times 10^{-19}$	$4.51 \times 10^{-17}$	$\Delta\Delta L_{231}$
$6.19 \times 10^{-19}$	$5.04 \times 10^{-17}$	0	0	0	$7.61 \times 10^{-19}$	0	$\Delta\Delta L_{123}$

- ambiguities exist between laser phase noises and various variables describing relative position between S/C and proof masses or fibre delays
- USO phases are unambiguously defined

Again the restriction applies that the effective path-delay in the optical fibres must be negligible in the sense described above for the fall-back configuration.

If the only relevant cause of armlength changes in the interesting frequency range where gravitational waves a relation between the three armlengths variations could be established. Introduction of such a condition e.g.  $\Delta L_{12} + \Delta L_{23} + \Delta L_{13} = 0$  for a setup in form of an equilateral triangle reduces the Null space from seven to 6 vectors and allows unambiguous solution for  $\Delta L_{12}$ ,  $\Delta L_{23}$ ,  $\Delta L_{13}$ . It is not longer necessary to solve for the linear combinations  $\Delta\Delta L_{123}$  and  $\Delta\Delta L_{231}$  to get an unambiguous solution, i.e. to cancel the phase noise. However length variations due to spacecraft relative motion do not obey the relations between the arm-lengths as derived from gravitational wave properties. Introduction of properties of gravitational waves into the equation system is therefore only permissible for frequency intervals in which the motion introduced spectral components of the armlength variation are negligible. However assimilation of the data to gravitational wave amplitudes is probably better left to a post-processing step where more observations can be combined and interfering effects can be calibrated out than is possible on the basis of a single observation.

#### A.1.2.5 Numerical condition of the equation system

The numerical condition of the equation systems has been analysed using singular decomposition. The ratio of the largest to the smallest singular value, sometimes referred to as condition number is about 10 for both configurations. This indicates that no major problems with the accuracy of numerical solutions are to be expected.

#### A.1.2.6 Sensitivity to phase measurement noise

The determination of one solution of the equation system as it may be obtained by a variety of numerical methods may also be expressed as matrix operation

$$\vec{\xi}_0 = \mathbf{R} \cdot \vec{s}. \quad (\text{A.8})$$

As described above,  $\xi_0$  is only one arbitrarily selected solution of the equation system, but the vector component representing the result variable(s) are unambiguous.

If the desired result variable is the  $i$ th component of  $\xi_0$ , the standard deviation  $\sigma_i$  resulting from the standard deviations of the phase measurements  $s_j$  can be calculated as

$$\sigma_i = \sqrt{\sum_j (\mathbf{R}_{ij} \cdot \text{stdev}(s_j))^2}. \quad (\text{A.9})$$

Phase measurements in the LISA measurement setup are performed on heterodyne signals resulting from beating two laser beams on a photodiode. Shot noise limited heterodyne detection is approximated when receiving the weak signals on the inter-satellite links. In this detection mode the local oscillator (LO) intensity is increased until the shot-noise of the LO signal renders technical noise from the electrical pre-amplifiers insignificant. As the amplitude of the beat signal in terms of detector current increases proportional to the electric field amplitude of both received signal and LO, and the shot noise in the detector signal (in terms of current *rms* fluctuation) increases also proportional to the electric field amplitude, an operating point can be

reached where noise sources other than the quantisation of the received signal (i.e. the weaker of the two heterodyned light signals) can be neglected. The electrical signal exhibits in this case a carrier-to-noise density  $C/N_o$  ideally identical to the photon rate (in terms of photons per second) of the received signal incident at the detector. Practically, however, this figure is reduced by imperfect matching of LO and received signal wavefronts (accounted for in terms of modulation efficiency  $\eta_h$ ; typical value in the order of 0.9) and by a detector quantum efficiency  $\eta_q$  smaller than 1 (typical value in the range 0.7 to 0.8). An ideal phase measurement on a sinusoidal signal with a given carrier to noise density results in a (phase) measurement noise of  $N_o/C = N\varphi$  [in terms of  $\text{rad}^2/\text{Hz}$ ]. Hence the phase noise (squared) is inversely proportional to the power of the received light signal.

In the *LISA* setup three different types of beat signals are measured:

- Main link detector signals ( $s_{1a}, s_{1f}, s_{2a}, s_{2f}, s_{3a}, s_{3f}$ ) resulting from beating the carrier of the received signal with a fraction of the transmitter signal used as LO. The phase noise  $N_{\text{main}}$  determined by the power of the received carrier signal on the inter-satellite should ideally constitute the largest part of the random measurement error.
- Ancillary carrier detector signals ( $s_{1e}, s_{2e}, s_{3e}$ ) resulting from beating a USO synchronized subcarrier of the received signal with a fraction of the transmitter signal used as LO. The power of the subcarrier is a comparatively small fraction of the main carrier power. Nominally a fraction of 10 % is foreseen. Consequently a factor of  $\sqrt{10}$  increased *rms* phase noise must be expected.
- Backside interferometer signals ( $s_{2c}, s_{2d}, s_{3c}, s_{3d}$ ) resulting from beating fractions of the two transmitter signals on a spacecraft on the detectors of the backside interferometer setup. The backside interferometers have not the typical setup of a shot-noise limited heterodyne detector with a dominating LO signal and a received signal of considerably lower power. Instead two beams of about the same power (order of 100 mW) are used. This will not necessarily lead to a shot-noise limited operation but this is by far not necessary in view of the high photon count available. However considering the high phase noise of the laser signals, the dynamic range of the phase detectors will not allow to utilize a very largely improved analog input signal to its full extent without adaptation in the phase meter electronics. In the following discussion on noise sensitivity therefore a moderate improvement of only 20 dB lower phase noise for this signals as compared to the main link signals has been assumed.

Table A.3 shows the sensitivity of the estimate of the armlengths differences to measurement phase noise. The column “Signal” identifies the measured signal following the convention of Figure A.5. The column “Incident Noise Power” specifies the applicable measurement noise in terms of multiples of the main link phase noise [ $\text{rad}^2/\text{Hz}$ ]. The other columns show the factors  $R_{ij}$  as for Eq. (A.9) for both result variables  $\Delta\Delta L_{12}$  and  $\Delta\Delta L_{23}$  at different frequencies (0.1 mHz, 1 mHz, 5 mHz and 10 mHz).

Relatively large differences between armlengths (order 10 %) have been assumed for the calculation to demonstrate the range of variability of sensitivity factors due to geometry. In a perfectly symmetrical configuration the factors associated with measurements on the two contributing arms are identical.

The following can be observed:

- The factors associated with the main link detector signals (orange shading) are for frequencies below 5 mHz approximately independent of frequency and are close to the expectable value of 0.5. Deviations result from armlength differences in combination with the phase noise compensation scheme.
- The factors associated with the backside interferometer signals are approximately linearly

**Table A.3** Sensitivity of measured arm length differences from measurement phase noise (arm length differences expressed in units of  $\lambda/2\pi$ )

	0.1 mHz		1 mHz		5 mHz		10 mHz		
Signal	$2\pi/\lambda$	$2\pi/\lambda$	$2\pi/\lambda$	$2\pi/\lambda$	$2\pi/\lambda$	$2\pi/\lambda$	$2\pi/\lambda$	$2\pi/\lambda$	Incident
	$\times$	$\times$	$\times$	$\times$	$\times$	$\times$	$\times$	$\times$	Noise
	$\Delta\Delta L_{123}$	$\Delta\Delta L_{231}$	$\Delta\Delta L_{123}$	$\Delta\Delta L_{231}$	$\Delta\Delta L_{123}$	$\Delta\Delta L_{231}$	$\Delta\Delta L_{123}$	$\Delta\Delta L_{231}$	Power
$s_{1a}$	0.	0.491	0.	0.491	0.	0.510	0.	0.578	$N_{\text{main}}$
$s_{1e}$	0.014	0.027	0.014	0.028	0.023	0.038	0.336	0.341	$10*N_{\text{main}}$
$s_{1f}$	0.486	0.027	0.486	0.028	0.495	0.038	0.912	0.341	$N_{\text{main}}$
$s_{2a}$	0.500	0.	0.501	0.	0.518	0.	0.581	0.	$N_{\text{main}}$
$s_{2c}$	0.005	0.	0.053	0.	0.264	0.	0.509	0.	$0.01*N_{\text{main}}$
$s_{2d}$	0.005	0.	0.053	0.	0.264	0.	0.509	0.	$0.01*N_{\text{main}}$
$s_{2e}$	0.011	0.015	0.012	0.016	0.025	0.025	0.326	0.355	$10*N_{\text{main}}$
$s_{2f}$	0.502	0.485	0.503	0.485	0.524	0.494	0.577	0.931	$N_{\text{main}}$
$s_{3a}$	0.490	0.500	0.491	0.501	0.509	0.519	0.575	0.585	$N_{\text{main}}$
$s_{3c}$	0.	0.005	0.	0.054	0.	0.269	0.	0.518	$0.01*N_{\text{main}}$
$s_{3d}$	0.	0.005	0.	0.054	0.	0.269	0.	0.518	$0.01*N_{\text{main}}$
$s_{3e}$	0.026	0.015	0.026	0.015	0.036	0.028	0.322	0.345	$10*N_{\text{main}}$
$s_{3f}$	0.026	0.506	0.027	0.506	0.036	0.529	0.322	0.595	$N_{\text{main}}$
Total (rms)	0.99	1.00	1.00	1.00	1.04	1.04	2.27	2.37	$N_{\text{main}}$

increasing with frequency. However the magnitude of the factors seen in combination with the applicable measurement noise shows that the contribution to the total measurement error is always negligible in the measurement frequency range.

- The factors associated with ancillary carrier detector signals are only weekly frequency dependent (factor 2 over the interval 0.1 mHz to 5 mHz). They are well below the factors associated with the main link detector signals ( $< 1/20$ ) which is needed to allow for the higher phase noise associated with the ancillary phase measurement. These factors depend linearly on the ratio of main detector signal beat frequency versus ancillary modulation frequency. The values in the table have been calculated assuming ratios in the order of  $1/40$  which is compatible with a modulation frequency of 200 MHz and beat signals in the 5 MHz range. Due to the use of the transmitter lasers as local oscillators on the receive channels the control of beat frequencies is restricted by the Doppler shift. In particular it is impossible to generate beat notes on both detectors of an interferometer arm with frequencies below the 1 way Doppler shift. At  $1\mu\text{m}$  wavelength an assumption of 5 MHz main carrier beat frequency corresponds therefore to relative velocities of the two related spacecraft below or equal 5 m/s. The sensitivity factors shown in Table A.3 lead to negligible contribution to the total measurement error in the frequency range below 5 mHz when considering the assumed phase measurement noise on the ancillary signals. However considering the dependence on spacecraft relative motion, maintaining some margin is reasonable.
- Generally the calculated sensitivities are such that below 5 mHz the expected simplified behaviour of the LISA setup is closely met: In a simple interferometer system with active transponders at the edge spacecraft without any ancillary measurements for phase

noise compensation etc., the expectable *rms* error in armlength difference should be  $0.5(\lambda/2\pi) \times \sqrt{4N_{\text{main}}}$  (where the factor 0.5 results from armlength difference being half as large as the optical pathlengths difference and the factor  $\sqrt{4}$  results from the four measurements entering with equal weight). The calculated values are within 4 % of this simple model in the frequency range below 5 mHz.

- A frequencies of 10 mHz and above the sensitivity factors are dominated by the extrema/poles resulting from the phase noise compensation scheme. With all interferometer arms at equal length of  $5 \times 10^6$  km a pole would be expected at about 30 mHz. The calculated values show that the increase in sensitivity to phase measurement noise is already significant at 10 mHz (factor 2.3); i.e. one of the consequences of implementing the phase noise cancellation scheme is an increase of noise in the measured quantity (arm length difference) in the vicinity of frequencies determined by  $1/(\text{round-trip-delay})$  and multiples thereof. For the use of the frequency band 10 mHz to 100 mHz a degeneration of the measurement due to the combined effects of
  - System response Eq. (A.1) (the frequencies of the error maxima are multiples of the 1-way propagation delay)
  - Measurement error due to laser phase noise Eq. (A.12) (the frequencies of the error maxima are multiples of the roundtrip delay)
  - Measurement error due to shot noise (described above) (the frequencies of the error maxima are multiples of the roundtrip delay)

has to be accounted for.

#### A.1.2.7 Sensitivity of solutions to uncertainty of knowledge of absolute armlength

If the coefficients of the Matrix  $\mathbf{M}$  in Eq. (A.8) are only approximately known, such that instead of the correct matrix  $\mathbf{M}$  an approximation  $\mathbf{M} + \Delta\mathbf{M}$  is used, an error  $\Delta\xi$  follows for the result vector  $\xi$ . The matrix  $\Delta\mathbf{M}$  is the matrix of the errors in components of  $\mathbf{M}$ .

$$\begin{aligned}
 (\mathbf{M} + \Delta\mathbf{M}) \cdot (\vec{\xi} + \Delta\vec{\xi}) &= \vec{s} \\
 \mathbf{M} \cdot \vec{\xi} + \mathbf{M} \cdot \Delta\vec{\xi} + \Delta\mathbf{M} \cdot \vec{\xi} + \Delta\mathbf{M} \cdot \Delta\vec{\xi} &= \vec{s} \\
 \mathbf{M} \cdot \Delta\vec{\xi} &\approx -\Delta\mathbf{M} \cdot \vec{\xi} \\
 \Delta\xi_0 &\approx -\mathbf{R} \cdot \Delta\mathbf{M} \cdot \vec{\xi}
 \end{aligned} \tag{A.10}$$

For the unambiguous components of  $\xi$  the appropriate component of  $\xi_0$  can be interpreted as the error in the calculated measurement result originating from assuming a matrix which is wrong by  $\Delta\mathbf{M}$ .

The matrix  $M_{ij}$  depends on only approximately known properties  $\xi$  of the system such as the absolute armlengths  $L_{12}$ ,  $L_{23}$ ,  $L_{13}$ , and the input frequency to modulation frequency ratios  $\alpha_{1a} \cdots \alpha_{3f}$ . Using the result from Eq. (A.10) the standard deviation of the armlength difference can be calculated from the magnitude of the unknowns and the standard deviation of the parameters used for the establishment of the Matrix coefficients. Note that the actual values of the unknowns are treated here as uncorrelated random variables.



$$\begin{aligned}
-\mathbf{R} \left( \frac{\partial \mathbf{M}}{\partial x_j} \cdot \text{stdev}(x_j) \right) &= \mathbf{N}_j \\
\Delta \Delta L_{123} &= \xi_1 \\
\text{stdev}(\Delta \Delta L_{123}) &\approx \sum_j \sum_i |\mathbf{N}_{1,i}|^2 \cdot |\xi_i|^2
\end{aligned} \tag{A.11}$$

This approach has been used to assess the sensitivity of the measurement results to uncertainties in the above mentioned parameters. To test the credibility of the approach the numerical results have been compared with the analytical results obtained by Giampieri [117] for a simplified configuration. The analytical expression for the sensitivity follows from Equation [14a] of the reference:

$$\text{stdev} \left( \frac{2\pi}{\lambda} \Delta L_{123} \right) = 0.5 \frac{4\pi f \cdot p_{\text{laser}} \cdot \text{stdev}(L)}{c} \sqrt{\left| e^{\frac{4\pi i f \cdot L_{23}}{c}} \right|^2 + \left| e^{\frac{4\pi i f \cdot L_{12}}{c}} \cdot \frac{e^{\frac{4\pi i f \cdot L_{23}}{c}} - 1}{e^{\frac{4\pi i f \cdot L_{12}}{c}} - 1} \right|^2} \tag{A.12}$$

The factor 0.5 results from the fact that the Giampieri equation is expressed in terms of path-length while here the difference of arm lengths is used as result parameter.

With the nominal system geometry at 1 MHz the following results were obtained:

$$\begin{aligned}
\text{stdev}(\Delta L_{123} 2\pi/\lambda) &= 2.079 \times 10^{-11} [\text{m}^{-1}] p_{\text{laser}} \text{stdev}(L) \quad \text{following Eq. (A.11)} \\
\text{stdev}(\Delta L_{123} 2\pi/\lambda) &= 2.993 \times 10^{-11} [\text{m}^{-1}] p_{\text{laser}} \text{stdev}(L) \quad \text{following Eq. (A.12)}
\end{aligned}$$

where  $\text{stdev}(L)$  stands for the uncertainty in armlength in a standard deviation sense and  $p_{\text{laser}}$  for the phase noise magnitude in  $\text{rad}/\sqrt{\text{Hz}}$ . The approximate factor of  $\sqrt{2}$  between the analytical prediction and the numerical result is probably due to using only a single arm for phase noise estimation in the original Giampieri paper, therefore a slight improvement when using both arms is not unreasonable. Typical laser phase noise at 1 MHz is about  $10^{-6} \text{ rad}/\sqrt{\text{Hz}}$  and the desired noise floor for  $\text{stdev}(\Delta L_{123} 2\pi/\lambda)$  is about  $8 \times 10^{-5} \text{ rad/Hz}$ . To achieve this, a highly accurate determination of armlength (or differential armlength) is required (in the low meter range).

#### A.1.2.8 Impact of laser phase noise

To achieve reasonable suppression of laser phase noise, joint optimisation of the system elements is needed:

- the laser transmitter (phase noise properties)
- the main detector phase meter
- the arm length estimation procedure.

Laser frequency noise is typically close to  $1/f$  characteristics in the measurement frequency range. At frequencies above 1 Hz the noise characteristics depends on the employed control concept. With additional effort, e.g. involving the use of an electro-optical modulator, the  $1/f$  characteristics can be maintained until the resulting phase noise falls below the main link shot noise threshold. With more conventional concepts a flat plateau in terms of frequency noise exists above 1 Hz until at several kHz the system behaves like a free running laser, again exhibiting an approximate  $1/f$  characteristics. In Figure A.6 resulting phase noise intensity is shown for a transmitter laser system conforming to the assumptions given in LISA Pre-Phase A report [1] and (based on LZH experience) for predicted laser performance with and without

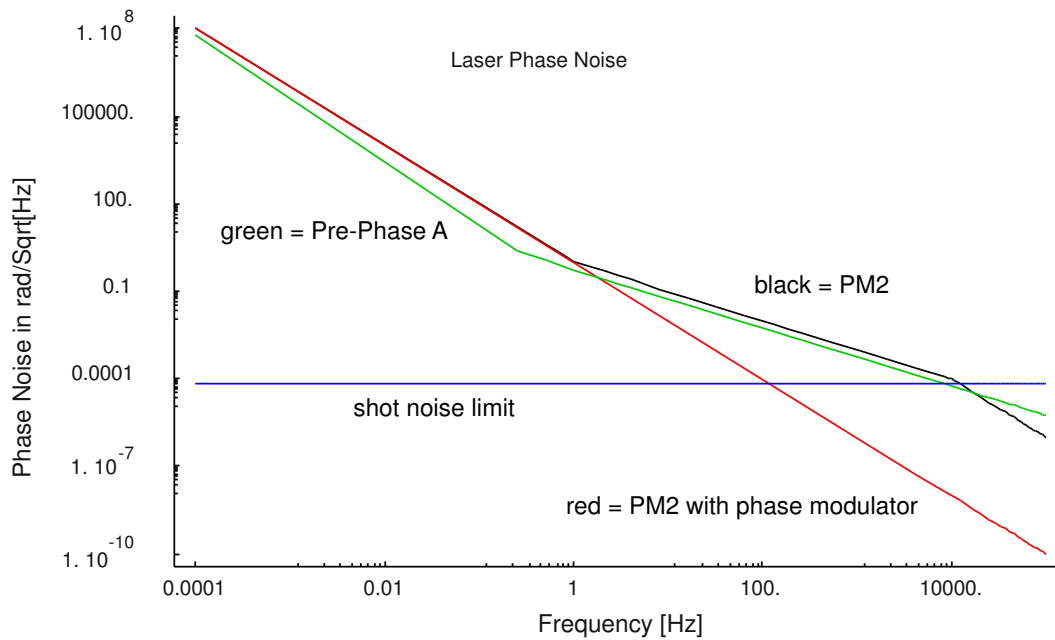


**Figure A.6** Typical laser phase noise

enhanced regulation at frequencies above 1 Hz. At the frequencies in the measurement bandwidth the **LZH** figures are somewhat above the Pre-Phase A assumptions ( $10^{-6}$  rad/ $\sqrt{\text{Hz}}$  versus  $3 \times 10^{-4}$  rad/Hz, both at 1 mHz).

As described in Section A.1.1, the total measurement error of the **LISA** system is composed of a contribution resulting from unknown parasitic accelerations acting on the proof-masses and the measurement error of the interferometer system. The measurement error itself results from phase measurement noise as discussed in the earlier section “Sensitivity to phase measurement noise”, the residual error of the phase noise cancellation as discussed in the previous section and additional contributions resulting from pointing errors and thermoelastic deformation of the optical setup. If the latter contributions are negligible the total error of the pathlength difference measurement has a typical behaviour as shown in Figure A.7 (red curve). The error is given in terms of effective phase measurement error. At low frequencies (below 2 mHz) the total error is dominated by acceleration effects (blue curve). Likewise at high frequencies the phase measurement noise (mostly resulting from shot noise) dominates (horizontal plateau of the red curve). Depending on the accuracy of the absolute pathlengths estimation the laser phase noise residual error may affect the total measurement error in the transition region between acceleration error dominated frequency region and shot noise error dominated frequency region. In Figure A.7 the green curve for the residual error from laser phase noise has been calculated for 20 m *rms* estimation error of armlength and **LZH** laser phase noise characteristic.

This error contribution scales proportionally with the *rms* estimation error of the armlengths. With 20 m estimation accuracy there is just a small impact in the transition frequency region. The laser phase noise residual error is entirely negligible for better armlength estimation accuracies and for inferior estimation accuracies it becomes significant in the 1 mHz to 10 mHz frequency interval. However the armlengths can be determined from the nominal measurements itself. One method would be to minimise the effective noise power in the corrected difference estimates by variation of the assumed armlengths. The most appropriate frequency range for this operation would be above the transition region as there are more frequency bins available and the noise floor from the shot noise can be assumed to be more stable than that from the

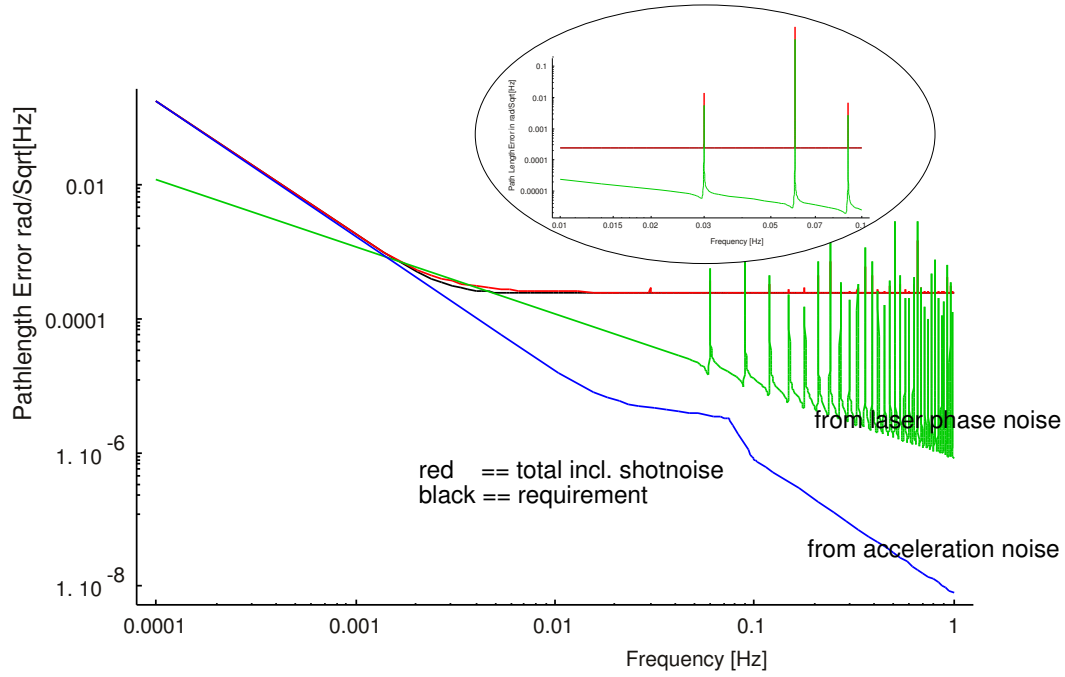


**Figure A.7** Effect of laser phase noise to system measurement error (large scale plot does not show all poles due to plot resolution limits, see inserted image for details)

acceleration as it is created by a comparatively simple process. Within the frequency interval where the pathlength estimation is performed a suppression of the residual phase noise level well below the shot noise level is reasonable, because many frequency bins can be averaged (in terms of noise power) for this operation thus allowing improved accuracy for the determination of noise power levels. In principle the accuracy of the mentioned armlength estimation procedure can be improved just by artificially adding a phase modulation on the laser signal at some frequency above the scientifically relevant frequency range. The armlength estimation procedure would then use this “artificially introduced laser phase noise”.

The laser phase error is not perfectly compensated and therefore leads to a residual error that may affect a particular frequency interval in the final measurement result. As shown above this leads however not to a direct requirement on laser phase noise because the quality of compensation depends in first order on the accuracy of the arm length estimation which has no obvious limit in the range of the required accuracies. With the proposed technique the arm length estimation accuracy is even linked to the laser phase noise compensation technique such that it provides sufficient accuracy for any laser phase noise. The requirements to the transmitter laser phase noise characteristics are therefore not determined by first order effects (as they are compensated by the phase noise cancellation) nor by first order effects of the cancellation procedure itself (because its first order efficiency can be arbitrarily improved by the mentioned improvement of arm length estimation accuracy).

The next order effects that can limit the correction capability for large laser phase noises are

- Limited accuracy of the assumptions underlying the measurement equation system Eq. (A.3)
- Limitation of phase meter measurement accuracy when subjected to phase noise many orders of magnitude above the white shot noise

The most important simplification in the equation system in the Fourier domain is the summation of a negligible effect of arm length variations with respect to the calculation of the Fourier transform of a phase spectrum after a round trip. When considering required armlength accuracies in the order of 20 m *rms* relative velocities between spacecraft of 5 m/s and a time interval for a discrete Fourier transform of  $> 10\,000$  s (to resolve to 0.1 mHz) this is likely not sufficiently accurate. In the Fourier representation a time variation of the arm lengths adds considerable complexity. In particular the transform of Eq. (A.2) will in general no longer result in a linear equation system when  $L_{12}$ ,  $L_{23}$ ,  $L_{13}$ , are considered to be time depending.

The following refinements could be considered:

- implementing the special case of constant spacecraft relative motion (e.g.  $L_{12} = at + b$ ) (this still leads to a linear equation system in the Fourier domain, however different frequency bins are now coupled)
- solve for the armlength difference in time domain (the solution Eq. (A.8) has a time domain representation which can be obtained by inverse Fourier transform; the  $\Delta\Delta L_{123}(t)$  can be represented as a sum of measured phase values  $s_i(t)$  each convolved with a function obtained by inverse Fourier transform of the frequency depending matrix coefficients  $R_{ij}(f)$  (assuming that  $\Delta\Delta L_{123}(f)$  is the  $i$ -th component of the solution vector  $\xi_0(f)$ ; under the simplifying assumptions of constant armlengths this represents a linear time invariant system linking the measured time series of phase values with the desired output variable; this could be generalised by considering time depending armlengths, which would lead to a linear time variant system)

Within this study no further investigations about refinement of the [LISA](#) equations in the above mentioned sense have been performed. However it is likely that any desirable degree of accuracy in the description of the delay effects is obtainable but the required effort for solving the equations will increase when higher precision is needed. With the relatively low data rate of the [LISA](#) experiment this may not constitute a problem if the data evaluation including low level processing is performed on earth but it would be difficult to perform the part of the processing that compensates for phase noise on board (which might be useful to save data volume on the space to earth link). Nevertheless it is not assumed that the complications to data evaluation that are caused by high laser phase noise establish a firm requirement for the tolerable laser phase noise.

The relation of the transmitter laser properties to the phase detector properties results from the necessity to represent the phase of the received signal in the measurement bandwidth with an accuracy not inferior to the shot noise limit. Neither intermodulation or clipping effects due to the large signal dynamic nor aliasing effects resulting from representation in a discrete time series must introduce errors larger than the shot noise. The normalisation to the shot noise results from the fact that the [LISA](#) link is dimensioned such that the length measurement error due to shot noise consumes most of the allowance in the measurement error budget.

When considering the transmitter laser performance using only thermal control (black curve in Figure A.6), the phase noise resulting from laser frequency noise in the measurement bandwidth (0.1 mHz to 1 Hz) is 198 dB above the shot noise, which would require about 33 bit representation for a discretisation noise comparable with the shot noise. However this large dynamic is largely due to slow drifting of frequency, i.e. the dynamic range increases with about 30 dB for extending the measurement frequency range for a decade towards lower frequencies. The 33 bit dynamic in the measurement bandwidth is however not necessarily the driver for data rate on the links or length of registers in the phase measurement devices. Simple encoding techniques such as [BAQ](#) can be used to reduce data rate on links and software unwrapping of a phase meter which uses a modulo  $n$  representation of its measured value can be used to reduce the required register

size in the phase meter. A representation comparable to 24 bits per sampled value on links and phase registers is likely sufficient as it represents approximately the dynamic range in a 0.01 Hz to 1 Hz intervals of the order 100 s for unwrapping of modulo counters and block coding.

Therefore the dynamic range in the phase measurements resulting from laser phase noise as it is represented in data rate and detector numerical resolution is also not a design driver.

More difficult is the avoidance of errors introduced by filtering and aliasing. The laser phase noise spectrum exceeds the phase noise induced by shot noise on the main links over a frequency range much exceeding the measurement frequency band. Referring to Figure A.6 the phase noise of the envisaged laser (LZH) reaches the shot noise limit on the main link at about 12 kHz (break even point). When an optical phase modulator is included in the control loop the laser can achieve a break even point of about 200 Hz. For the thermally controlled laser the power of the laser phase noise in the frequency interval from the upper edge of the measurement bandwidth (1 Hz) to the break even point is about 83 dB above the main link shot noise level in the measurement interval. It is not significantly lower (78 dB) for the alternative laser with additional phase modulator as the higher frequencies do not significantly contribute to the total noise power.

The importance to the phase detector design arises from the fact that a digital representation of the measured phase at a low sampling rate is needed to maintain low data rates. Representation with 2 Hz sampling frequency requires filtering of the out-of-band phase noise at the detector input such that aliasing products within the measurement bandwidth are negligible compared to the in-band shot noise level. A suppression of about 90 dB for frequencies above 1 Hz (with relaxing requirements at higher frequencies) is required. On the other hand a precise control of the pass-band attenuation is needed: the relative amplitude error due to uncertainty in pass band attenuation must be comparable to the ratio of in-band laser phase noise to shot noise induced phase noise. These demanding requirements are probably only feasible if numerical filtering is applied. The primary digitalisation process is therefore to be performed at a considerably higher sampling rate. Depending on the type of phase detector the digitalisation is either performed explicitly by an ADC sampling the down-converted detector signal (the phase detection is then numerically performed by various techniques) or the digitalisation is implicit in the phase measurement principle such as for counter based detectors evaluating the zero crossings of the detector signal in comparison to a reference signal. In any case the effective sampling frequency should be selected (slightly) above the break even frequency to avoid aliasing in the first processing step without relying on (high performance) analog pre-filtering for the purpose of laser phase noise rejection (some pre-filtering will nevertheless be required to avoid aliasing from the shotnoise itself).

Phase estimates are then generated at a comparatively high sampling rate (12 kHz or 200 Hz for the modulator controlled laser) and must be digitally filtered with a decimation filter meeting the filtering requirements driven by the laser phase noise.

Laser development and detector development have to be seen as a joint effort where properties of both equipment can be traded:

- efforts on the laser to suppress out-of-band noise (above 1 Hz), e.g. by employing an optical modulator trades against internal sampling frequency in the detector equipment related to internal timing requirements and numerical work load in the decimation filtering
- efforts in the laser to suppress in-band phase noise are related to the stability requirement of the in-band filter characteristics (in addition to the already mentioned impacts to dynamic range of the data representation and the accuracy required for the interferometer arm length estimate).

### A.1.2.9 Laser synchronisation

The properties of the [LISA](#) measurement equation system in nominal or fall-back configuration do not depend on any assumption about the locking of the laser frequencies or [USOs](#) to each other. The only requirement is to maintain the beat frequencies of the signals heterodyned at the various detectors within an acceptable frequency range. The allowable frequency range is determined by the capability of the [USO](#) phase noise compensation scheme which is reflected in the sensitivity of the measurement result to the noise on the  $s_{1e}$ ,  $s_{2e}$ ,  $s_{3e}$  signals (see discussion of Table [A.3](#)). With the baseline design the beat signal frequencies should be below 10 MHz (except for the modulation signal). This condition is not achievable with lasers individually locked to their reference cavities. Hence some form of (offset) locking of all employed lasers to a single reference is required while no explicit locking of [USOs](#) is needed.

If the lasers are named according to their optical bench (see Figure [A.4](#)) a typical chain of synchronisation is:

$$A2 \rightarrow B3 \rightarrow A3, \quad A2 \rightarrow B2 \rightarrow A1 \rightarrow B1,$$

where A2 is the master laser synchronised to its cavity and “ $x \rightarrow y$ ” means laser y is offset locked to laser x. Whenever the lasers locked to each other are not on the same spacecraft an inter-satellite link is used. Therefore the frequency of both lasers differ not only due to the deliberately introduced offset but also due to the Doppler shift. In general the frequency offsets are selected such that beat frequencies close to zero are avoided and that the maximum beat frequency does not exceed the maximum allowable one-way Doppler shift.

Introduction of frequency locking does not change the structure of the [LISA](#) equation system nor the magnitude of the phase noises of the laser. The laser phase noises become however correlated. The characteristic of the phase signal derived from the detector signals differs from the free running case. While in the free running case all signals show the large phase noise which results from the independent phase noise of the two heterodyning laser sources this is different for synchronised lasers as the phase noises are now correlated. The shot noise is the same in both cases, it depends only on the light intensity on the respective detectors (see Table [A.3](#)). In a measurement setup with synchronised lasers three different types of phase characteristics can be observed:

- for the detectors used for the frequency control of a laser the phase is entirely predictable, it depends only on the used offset frequency; if the synchronisation is not perfect the measurable phase deviates from the prediction value in the sense of a control loop error
- for detector signals of the backside interferometers that are not used for synchronisation and for modulation signals on detectors that are used for laser synchronisation the phase varies with low dynamic relative to the predictable mean resulting from the offset locking of the two involved lasers. These small phase variations carry information on relative proof-mass movement or [USO](#) phase noise
- for the remaining signals a phase noise resulting from main laser phase-noise superimposed to itself after a round-trip delay is present; the phase noise spectrum is comparable to that of the main laser itself except for an attenuation at frequencies below  $1/\text{Roundtrip\_delay}$ .

For the above proposed hierarchy of laser synchronisation the different characteristics are distributed among the 18 phase signals as shown in Table [A.4](#). The signal names refer to Figure [A.5](#) and a full [LISA](#) configuration (two differences measured) is assumed. There are 5 signals with high phase dynamic, 8 signals with low phase dynamic and 5 signals that are either entirely predictable or exhibit a low phase dynamic (depending on properties of the phase locked loops). As phase locking does not change the shot noise level and the master laser phase noise charac-



**Table A.4** *Properties of the detector signal in a LISA setup with laser phase locking*

Spacecraft	Detector signals to which a laser is locked (ideally entirely predictable)	Detector signals with low phase dynamic	Detector signals with high phase dynamic
1	$s_{1f}, s_{1d}$	$s_{1c}, s_{1e}$	$s_{1a}, s_{1b}$
2	$s_{2d}$	$s_{2c}$	$s_{2a}, s_{2b}, s_{2e}, s_{2f}$
3	$s_{3a}, s_{3c}$	$s_{3b}, s_{3d}$	$s_{3e}, s_{3f}$

teristics the measurement accuracy is not affected. The essential properties of phase detectors in a synchronised system also do not differ significantly from the un-synchronised case as the characteristics of the signal with high phase dynamic differs from the case with unsynchronized lasers only with respect to the low frequency dynamic range which is of little impact to the detector design and the data rate.

The impact of using a synchronised measurement setup is therefore, apart from the purpose to maintain a desirable frequency separation of the individual lasers, mainly a reduction in raw data rate, however, by less than a factor of 2. Instead of avoiding the 5 measurements on the signals used for locking entirely by appropriate design of the control loops it is probably more efficient to perform this measurements and relax on the control loop requirements.

To relax the requirements to the accuracy of the phase noise cancellation as reflected in the need to determine absolute armlength and the required precision in the representation of the measurement equation system and to the in-band transfer characteristic of the phase meters, a reduction of low frequency phase noise is highly desirable. In the synchronised setup this affects only the master laser which in the baseline design is stabilised by coupling to its reference cavity. It has not been investigated in this study whether a potential exists to reduce the in-band phase noise by synchronising the master laser to the delay line provided by the round trip on one interferometer arm. A combined use of detector signals from the reference cavity and from the main link phase detector signal associated with the reference laser ( $s_{2f}$  if the master laser is A2) could be used to reduce in-band phase noise.

#### A.1.2.10 Summary on Pathlength Difference Measurement

The pathlength difference measurement including all necessary corrections can be performed with the baseline measurement setup.

The achievable accuracy is (almost) entirely determined by the main link phase noise (in the way it would be expected in a simple setup that would not need any of the corrections foreseen for the LISA setup): laser phase noise, clock phase noise and proof-mass relative motion.

With the conditions described in the sections above (sufficiently low Doppler shift, phase detector quality matched to laser phase noise, accuracy of representation of the measurement equation system) the residual impact of the error sources for which compensation is implemented can be neglected, except for a small impact of laser phase noise close to the frequency where acceleration noise dominates the system sensitivity. This residual error is mostly depending on the principle of arm length estimation and not so much on the magnitude of the phase noise itself.

The most critical problem is the matching of the capabilities of the phase detector to the laser phase noise properties. Due to the large magnitude of the laser phase noise, compared with the main link shot noise, small parasitic errors in the phase detection process (aliasing, non-linearity) may severely affect the measurement accuracy.



### A.1.3 Residual Proof Mass Acceleration

The budgeting of parasitic acceleration effects acting on the proof masses follows the Pre-Phase A Study [1]. In Table A.5 the respective budget is repeated. The effects have been grouped according to error mechanism into following groups:

- Acceleration resulting from external magnetic fields. Magnetic effects of fluctuating interplanetary magnetic fields (coupling with static local fields) and Lorentz forces acting on the charged proof-mass have been considered.

**Table A.5** Acceleration budget following Pre-Phase A Study [1]

Error Source	Acceleration @ $10^{-4}$ Hz [ $10^{-15} \text{ m s}^{-2}/\sqrt{\text{Hz}}$ ]	Number of effects per proof-mass	Sum of group ( <i>rms</i> ) [ $10^{-15} \text{ m s}^{-2}/\sqrt{\text{Hz}}$ ]	Description of Group
Magnetic force on proof mass from fluctuating interplanetary field	0.50	1	1.12	External effects directly acting on proof mass
Lorentz force on charged proof mass from fluctuating interplanetary field	1.00	1		
Noise due to dielectric losses	1.00	1	2.00	CAESAR internally generated Acceleration
Electrical force on charged proof mass	1.00	1		
Temperature difference variations across cavity	1.00	1		
Residual gas im- pacts on proof mass	1.00	1		
Thermal distortion of spacecraft	1.00	1	1.22	Gravitational effect due to thermally induced mass displacement
Thermal distortion of payload	0.50	1		
Telescope thermal expansion	0.50	1		
Gravity noise due to spacecraft displacement	0.50	1	0.50	Contributor to residual acceleration resulting from control loop action
Other substantial effects	0.50	4	1.56	Other effects
Other smaller effects	0.30	16		
Total effect of acceleration			3.07	

- Acceleration resulting from [CAESAR](#) internal effects
- Acceleration resulting from displacement of masses on board the spacecraft due to thermo-elastic distortion and due to antenna motion
- Acceleration resulting from relative motion of spacecraft versus proof mass as result of residual [DFC](#) control loop error in reaction to external forces acting on the spacecraft
- Other effects not specified in detail

Work within this study has concentrated on

- Analysis of local gravitational field
  - [DC](#) acceleration at center of test mass
  - Gradient at center of test mass
  - Dynamic-parasitic acceleration over measurement band (driven by thermoelastic distortion)

From these analyses only the last item “Dynamic-parasitic acceleration” enters directly in the performance budget while the other two aspects constitute boundary conditions for the analysis of the drag-free control loop.

- Analysis of the drag-free control loop (covering item “Gravity noise due to spacecraft displacement” and some of the unspecified effects). The analysis covers properties of [CAESAR](#) including inter-axis cross coupling, modelling of external disturbing forces and impact of [FEEP](#) noise. The mayor input into the analysis except for [CAESAR](#) properties and [FEEP](#) characteristics is the assumption on the magnitude of the “negative spring stiffness” resulting from gravitational field gradients and magnetic field gradients on which control loop properties critically depend. The latter issue enters in terms of requirements into “Analysis of static gravitational field gradients” and “Derivation of requirements to internal magnetic field generation”. As the gravitational analysis has been performed in parallel with the analysis of the drag-free control an assumption on negative spring stiffness has been used in the latter analysis. The gravitational calculations now available justify the assumptions although some mass balancing is needed to meet the [DC](#) acceleration assumptions. The gradient assumptions are already close to the required values without compensation measures.
- Derivation of requirements to internal magnetic field generation for compatibility with “Magnetic force on proof mass from fluctuating interplanetary field” assumption and negative spring stiffness requirement.

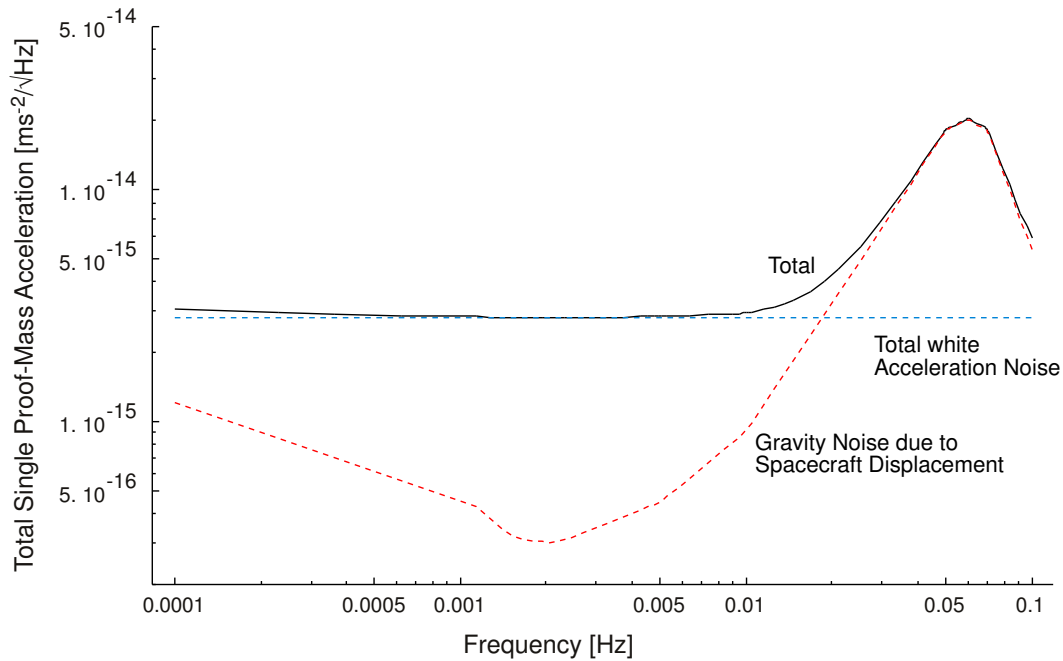
The updated acceleration noise budget per proof-mass assumes a constant acceleration spectrum except for the residual acceleration resulting from the [DFC](#). The constant part is budgeted in [Table A.6](#), the total acceleration spectrum acting on a single proof-mass is shown in [Figure A.8](#). Note that the increase of parasitic acceleration towards higher frequencies is uncritical because the effects will be masked by the white noise component of the interferometric measurement.

#### A.1.4 Optical Path-Noise Budget

The measurement errors not resulting from accelerations acting on the proof-masses are summarized in the optical path-noise budget. The main component is the error of the interferometric measurement itself as described in [Section A.1.2](#). It is composed from shot-noise error and residual effects from compensated laser phase noise. However the optical-path noise budget also contains thermo-elastic pathlength variations in optical bench and telescope, straylight effects and interaction of pointing jitter on the transmitted beam with wavefront curvature. The optical

**Table A.6** Acceleration budget resulting from this study (white noise part)

Error Source	Acceleration @ $10^{-4}$ Hz [ $10^{-15}$ m s $^{-2}$ /√Hz]	Comment
External effects directly acting on proof mass	1.12	Taken from Pre-Phase A Report
CAESAR internally generated Acceleration	2.00	Taken from Pre-Phase A Report
Gravitational effect due to thermally induced mass displacement	0.13	See FTR [2]
Gravity noise due to spacecraft displacement	no flat spectrum	Analysis result shows essentially non-white behaviour; the effect is therefore handled separately, refer to Figure A.8
Other Effects	1.56	Taken from Pre-Phase A Report; this is slightly pessimistic as some of the effects enter into “Gravity noise due to spacecraft displacement”
Total effect of acceleration (white noise)	2.8	

**Figure A.8** Single-proof-mass acceleration spectrum

path-noise budget as assessed in the LISA Pre-Phase A study is given in Table A.7 for reference. It is expressed in terms of length variation of the total optical path (4 space links).

**Table A.7** Pre-Phase A optical-path noise budget [1]

Error Source	Magnitude 1-way [pm/ $\sqrt{\text{Hz}}$ ]	Number in Path
Main detector Shot Noise	11	4
Master Clock Noise	10	1
Residual laser phase noise after correction	10	1
Laser phase measurement and offset lock	5	4
Laser beam pointing instability	10	4
Scattered-light effects	5	4
Other substantial effects	3	32
Total	40	

The shot noise dependent measurement error is budgeted in Table A.8:

- A detailed optical power budget is used as input.
- Energy loss on the main carrier resulting from modulation is taken into account.
- Numerically calculated modulation efficiency of the heterodyning at the main detector is used.
- Electrical and phase measurement noise is accounted for.

The resulting effective phase noise ( $8.5 \times 10^{-5} \text{ rad}/\sqrt{\text{Hz}}$ ) and the corresponding optical path-length error is slightly larger than predicted in the previous project phase. In the last row of Table A.8 another degradation of about 4% has been introduced to account for the effect of noise on the ancillary detectors as described in Section A.1.2.

The effect of transmitter pointing jitter on optical pathlength is budgeted in Table A.9. As the pointing performance of the DFC and the optical quality of the telescope are both predicted to be better than the respective values used in the Pre-Phase A study the resulting effect is now smaller than previously assumed.

The path-noise budget is summarized in Table A.10. The evolution from Pre-Phase A can be observed by comparison with Table A.7:

- The shot noise dependent contribution has increased. This is partly due to some loss factors not previously accounted for. However electrical noise and phase measurement noise are now included in this budget point.
- A residual effect of USO noise could not be demonstrated
- The residual impact of laser phase noise is separately accounted for because of its frequency dependence (see also discussion in Section A.1.2)
- With the proposed data evaluation technique the error in the locking process of the lasers does not create a measurement error (it just serves to reduce phase noise on some measured signals)
- Scattered light effects have been analysed in this study. However the dominant straylight paths mainly involving the sub and main reflector enter directly in the pathlength budget, hence the pathlength effect of the stray light is negligible (small compared to the direct effect).

**Table A.8** Shot-noise budget on main link (phase standard deviation)

Parameter	Value	Remark
Received signal power on main detector ( $P_{\text{in}}$ )	65 pW	
Fraction thereof attributable to main carrier ( $\eta_{\text{mc}}$ )	0.8	10 % for subcarrier
Modulation Efficiency ( $\eta_{\text{mod}}$ )	0.9	numerical simulation
Detector Quantum Efficiency ( $\eta_{\text{qe}}$ )	0.56	resulting from 0.65 A/W sensitivity
Resulting electrical carrier to noise density	81.4 dBHz	$\text{PND} = \frac{\eta_{\text{mc}} \cdot \eta_{\text{mod}} \cdot \eta_{\text{qe}} \cdot P_{\text{in}}}{h\nu}$
Resulting phase standard deviation not accounting for electronics/phase meter errors	$8.5 \times 10^{-5} \text{ rad}/\sqrt{\text{Hz}}$	$\text{stdev}_{\varphi} = \frac{1}{\sqrt{\text{PND}}}$
Analog electronics error contribution	$3 \times 10^{-6} \text{ rad}/\sqrt{\text{Hz}}$	
Phase meter error contribution	$6 \times 10^{-6} \text{ rad}/\sqrt{\text{Hz}}$	
Resulting phase standard deviation	$8.5 \times 10^{-5} \text{ rad}/\sqrt{\text{Hz}}$	(phase meter and electrical noise is almost negligible)
Equivalent error in optical pathlength measurement	28.5 pm/ $\sqrt{\text{Hz}}$	
Accounting for noise on ancillary detectors	29.6 pm/ $\sqrt{\text{Hz}}$	estimated using the results from Table A.3

**Table A.9** Effect of beam pointing instability

Parameter	Value	Remark
Wavelength	1.06 $\mu\text{m}$	
Transmitted beam pointing offset error	30 nrad	requirement to pointing acquisition procedure
Transmitted beam pointing jitter	6 nrad	see analysis 4.6.3
Telescope diameter	0.3 m	design parameter
Telescope wavefront error (as fraction of wavelength)	1/30	telescope manufacturing quality
Resulting phase error due to pointing jitter	3.73 mrad/ $\sqrt{\text{Hz}}$	using relation 3.6 of [1]
Equivalent 1 way pathlength error	3.95 pm/ $\sqrt{\text{Hz}}$	

Since it was not clear which other stray paths have been accounted for in Pre-Phase A the old values have been taken over as margin. The same has been applied to the unspecified

effects.

- Two types of thermo-elastic pathlengths changes have been accounted for
  - variation of the optical pathlength on the optical bench (mainly resulting from thermal effects on components)
  - variation of the optical pathlength in the telescope

Two types of telescope design have been analysed. Very good stability could be reached with a design using CFRP struts. This has been selected as baseline and the respective performance has been used in the budget. However an all-SiC design can reach pathlength effects in the order of  $17 \text{ pm}/\sqrt{\text{Hz}}$  which also comes close to useful performance.

**Table A.10** *Optical-path noise budget*

Error Source	Magnitude 1-way [pm/ $\sqrt{\text{Hz}}$ ]	Number in Path	Remark
Pathlength error due to phase measurement noise	29.6	1	See Table A.8 The value Includes <ul style="list-style-type: none"> <li>• shot noise on all detectors (incl. ancillary)</li> <li>• electrical and phase meter noise</li> </ul>
Master Clock Noise	negligible	-	
Residual laser phase noise after correction	see Figure A.9	1	separately accounted because of frequency dependence
Laser phase measurement and offset lock	-	-	phase measurement noise included in point 1; offset lock error is transparent for selected processing principle
Laser beam pointing instability	4.0	4	See Table A.9
Scattered-light effects	5	4	from Pre-Phase A Report
Other substantial effects	3	32	from Pre-Phase A Report
Optical Pathlength Variation on bench	5.8	4	see Table A.7 <i>rms</i> sum of $3.9 \text{ pm}/\sqrt{\text{Hz}}$ and $4.3 \text{ pm}/\sqrt{\text{Hz}}$
Optical Pathlength Variation within telescope (1-way)	0.6	4	Composite telescope with CFRP struts SiC telescope design would contribute $17 \text{ pm}/\sqrt{\text{Hz}}$
Total	38.3		Use of SiC telescope would result in $51.2 \text{ pm}/\sqrt{\text{Hz}}$ optical path error

A graph of the optical path-noise budget including the frequency dependent residual error from laser-phase noise is shown in Figure A.9. An accuracy of 20 m (*rms*) for absolute arm-length determination and the LZH laser phase noise characteristic has been assumed in accordance with the argumentation presented in Section A.1.2.

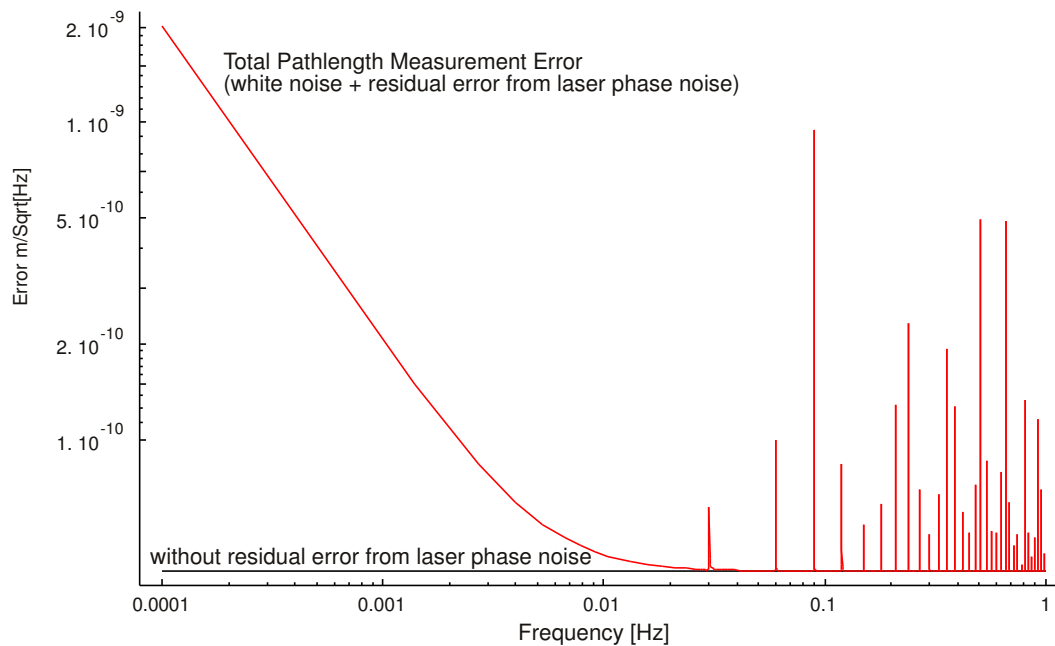


**Figure A.9** Total path-length measurement error

### A.1.5 Conclusion

The combined effect of proof-mass acceleration and measurement errors budgeted in the preceding sections is shown in Figure A.10. All effects are presented in terms of optical pathlength error.

It can be seen that the assumed white components of the acceleration budget and the path-noise budget dominate over most of the measurement frequency range. The white acceleration errors dominate below about 3 mHz, the white pathlength errors above 5 mHz. In the transition region residual effects from laser phase noise play a role. How large this effect is and whether it is possible to suppress it entirely depends on the strategy of arm length determination as described in Section A.1.2. It is not directly linked to the magnitude of the laser phase noise except when an independent technique not depending on the laser phase noise is used for the arm length determination.

The residual acceleration resulting from the DFC action does at no frequency significantly influence the total error budgets. At the high frequencies where the DFC residual acceleration exceeds the white acceleration noise the total error is dominated by the white pathlength noise by more than an order of magnitude.

From the total measurement error the system sensitivity for gravitational waves can be predicted. The resulting sensitivity for 1 year averaging and gravitational  $\text{SNR} = 5$  is shown in Figure A.11. As reference the sensitivity that would result from the Pre-Phase A report budget values for acceleration noise ( $3 \times 10^{-15} \text{ m s}^{-2}/\sqrt{\text{Hz}}$ ) and pathlength noise (40 pm/Hz) is drawn as requirement curve. The deviation is mainly resulting from the residual effect of laser phase noise.



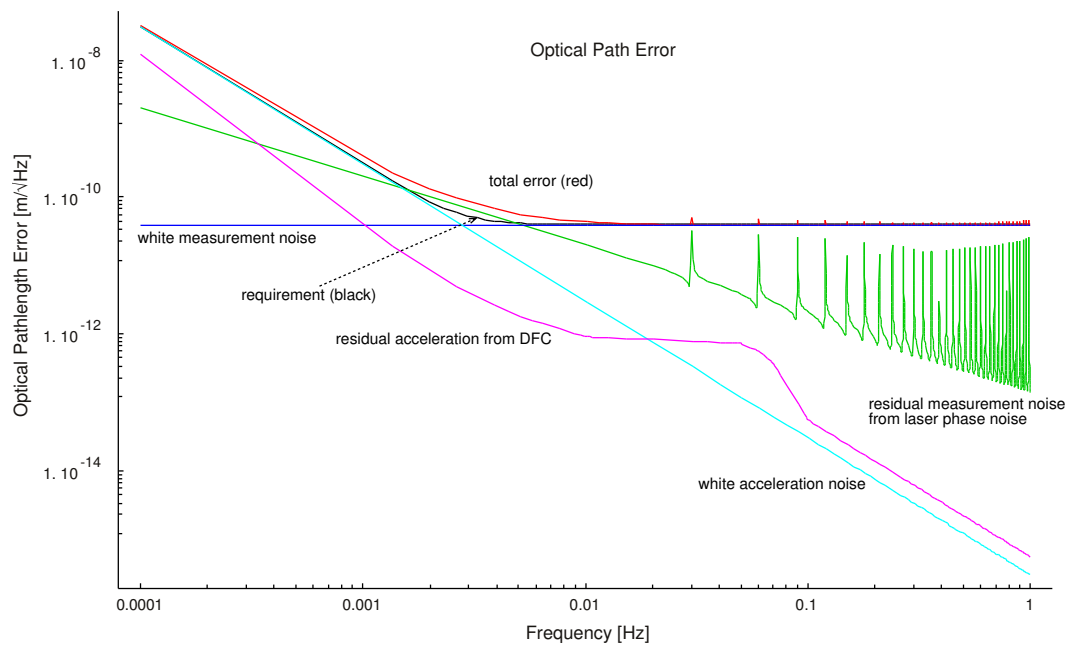


**Figure A.10** Synthesis of all error components (in terms of pathlength error)

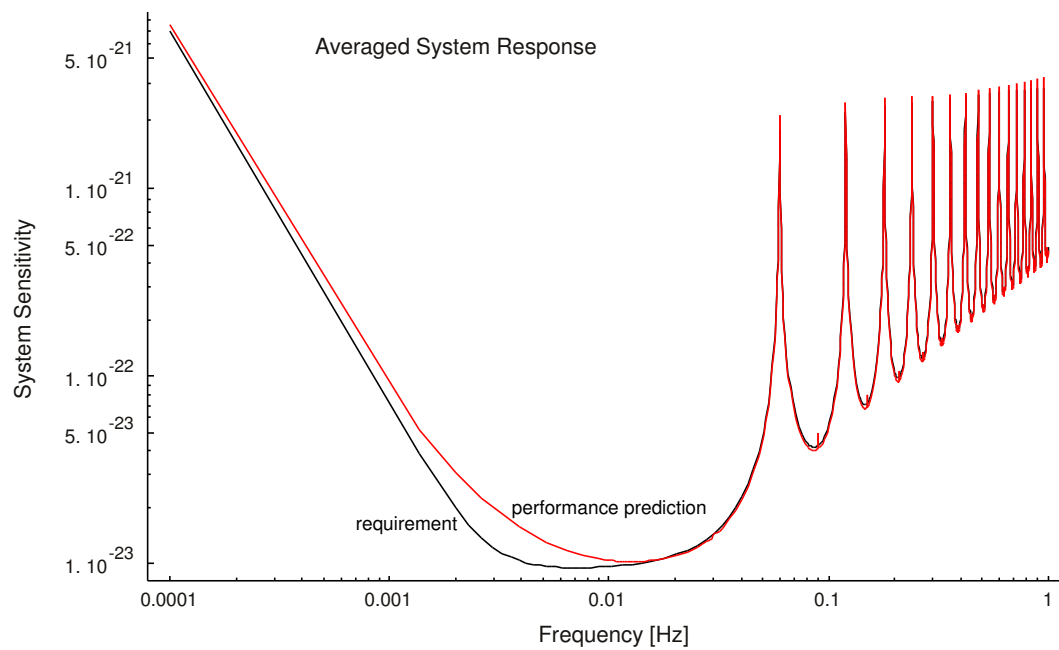


**Figure A.11** Total system sensitivity (1 year averaged gravitational wave amplitude)

## A.2 Proof-mass charging by energetic particles

As described in Section 6.2, the drag-free controller provides isolation from *external* dynamic disturbances, analogous to the seismic isolation on the ground-based gravitational-wave detectors. However, the system cannot cancel any forces that *act directly on the proof masses (mirrors)*. Of particular importance are those due to electrostatic charging, which are now discussed in detail.

### A.2.1 Disturbances arising from electrical charging

Proof mass charging due to cosmic rays will produce spurious forces resulting from Lorentz forces due to the motion of the charged proof mass through the interplanetary magnetic field, and from Coulomb interaction between the charged proof mass and surrounding conducting surfaces. These forces must be adequately attenuated.

Figure A.12 shows the spectra for the most abundant primary cosmic ray constituents (protons and helium nuclei) inside the heliosphere. As far as LISA is concerned, these primary fluxes can be considered to be isotropic.

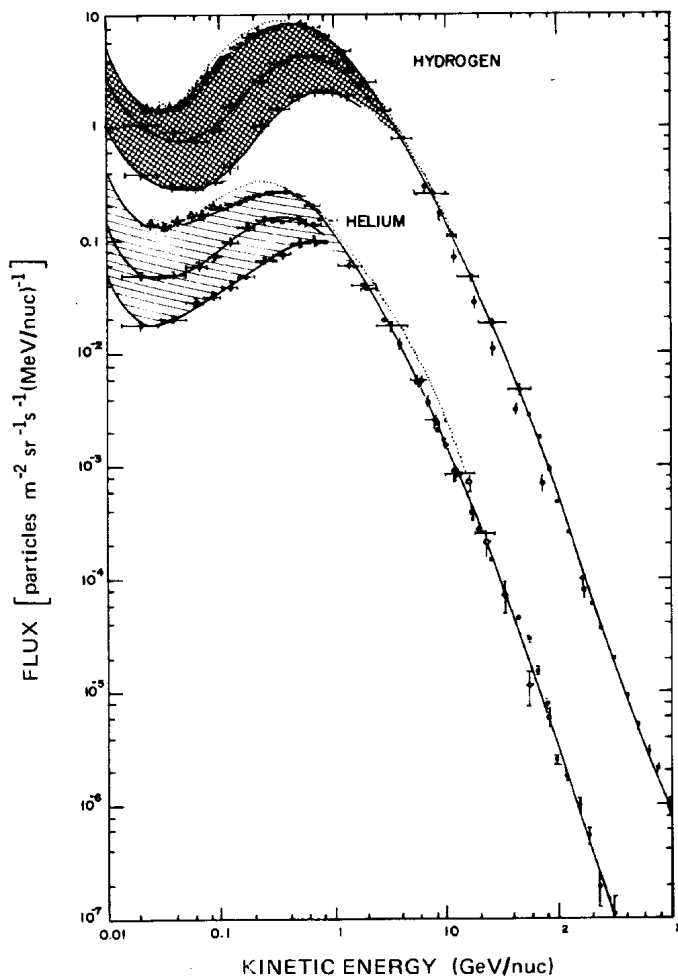


**Figure A.12** Cosmic ray differential energy spectrum (reproduced from [147]). The hydrogen spectrum has been multiplied by a factor of 5 to avoid clutter. For each species, the upper envelope indicates the solar minimum spectrum, the lower envelope indicates the solar maximum spectrum. The shaded area indicates the range of the solar modulation over a solar cycle.

### A.2.2 Modelling the charge deposition

Charge deposition depends significantly on secondary particle generation and detailed geometry, both of which are complicated to model analytically. Consequently, the [GEANT](#) radiation transport code [148] has been used. The code employs Monte Carlo particle ray-tracing techniques to follow all particles (incident and generated) through three-dimensional representations of the [LISA](#) spacecraft geometry, taking into account all significant interactions. Table A.11 shows the interactions that are currently modelled by [GEANT](#). A more detailed discussion of the use of [GEANT](#) for this type of application can be found in [149].

**Table A.11** *Interactions modelled by [GEANT](#) (adapted from [148]).*

<b>Processes involving the photon</b>	$(e^+, e^-)$ pair conversion Compton collision Photoelectric effect Photo fission of heavy elements Rayleigh effect
<b>Processes involving <math>e^+/e^-</math></b>	Multiple scattering Ionisation and $\delta$ -rays production Bremsstrahlung Annihilation of positron Generation of Čerenkov light Synchrotron radiation
<b>Processes involving <math>\mu^+/\mu^-</math></b>	Decay in flight Multiple scattering Ionisation and $\delta$ -rays production Ionisation by heavy ions Bremsstrahlung Direct $(e^+, e^-)$ pair production Nuclear interaction Generation of Čerenkov light
<b>Processes involving hadrons</b>	Decay in flight Multiple scattering Ionisation and $\delta$ -rays production Hadronic interactions Generation of Čerenkov light

The geometric model constructed for [LISA](#) is summarised as follows: the 4 cm gold cubical test body is surrounded on all faces by 25  $\mu\text{m}$  gold electrodes mounted on a cubically-symmetric 15 mm shell of quartz, enclosed in a 5 mm thick titanium vacuum housing, surrounded by 1 cm of carbon-epoxy representing the spacecraft structure. On two opposing faces of the cube, quartz windows (7 mm diameter) have been inserted in the titanium, quartz, and electrode layers, representing the access windows for [LISA](#)'s laser beams. Although this is a somewhat simplified representation, it does contain the key elements for accurate modelling, namely, a three-dimensional description of the intervening layers of material between the proof mass and the exposed spacecraft outer surface.

Figure A.13 shows the computed net charging of the *LISA* proof mass as a function of incident particle energy. To produce this curve, *GEANT* was used to analyse the effect of isotropic particles striking the outer spacecraft walls, for a range of energies from 100 MeV to 10 GeV. For each data point on the curve,  $10^6$  particles of a fixed energy were aimed randomly at the model (yielding adequate convergence of the Monte Carlo statistics). The curve contains no information on the actual spectrum of cosmic ray particles (this comes later).

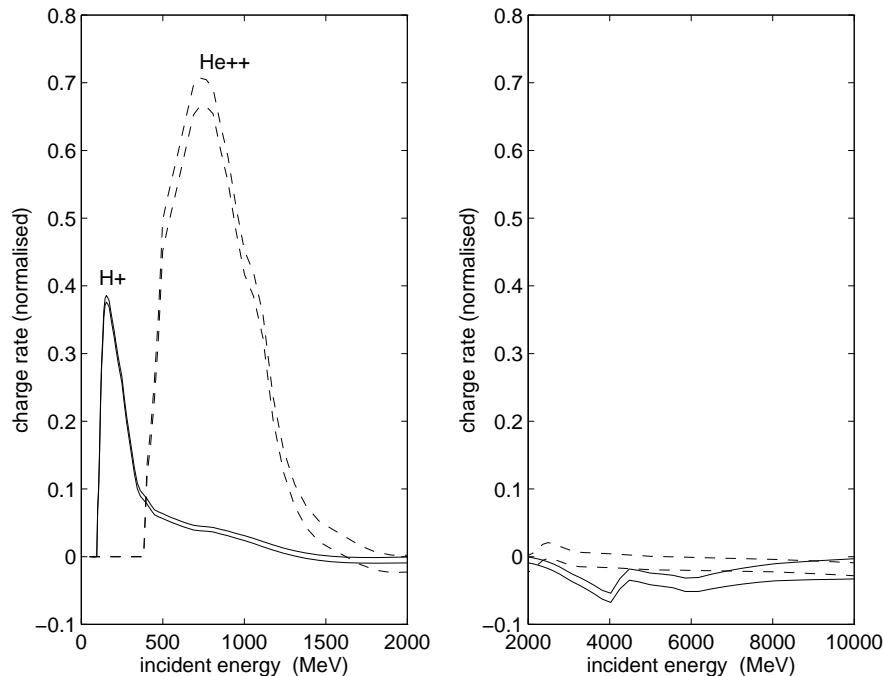


**Figure A.13** *LISA* proof-mass charging versus incident particle energy. (The normalisation is described in the text.) For each species, there are two closely-spaced curves which differ only by the inclusion of low-energy electrons (see text).

In the figure, the charging has been normalised to the ‘bare entry flux’ which is a purely artificial number defined as *the effective isotropic flux of particles at a given energy which would enter the cube if it were freely exposed*. For example, consider the proton curve in Figure A.13 which has a peak of 0.4 at an energy of 200 MeV. The ‘bare entry flux’ at this peak is defined as the number of 200 MeV particles which would enter an isolated cubical proof mass exposed to an isotropic flux of 200 MeV protons (it does not address the number of particles which then leave the body). The curve can thus be interpreted as saying that the number of 200 MeV protons stopped in the cube happens to be 0.4 of the ‘bare entry flux’. These stopped protons are a combination of original (incident) protons which reach the proof mass having penetrated the intervening structure, as well as secondary protons generated somewhere along the way, which then end up reaching the proof mass. Therefore, the normalised plot contains information on the combined shielding power of the structure and the proof mass.

It turns out that the peak of the proton curve corresponds to the energy at which incident protons actually come to rest in the proof mass, having passed through the spacecraft structure. At higher energies, the charging is reduced but remains positive, and is due mostly to secondary protons stopping in the proof mass (most of the primary protons pass right through). At even higher energies ( $> 2000$  MeV), the charging actually becomes negative, and is dominated by secondary electrons which stop in the proof mass (most protons, primary and secondary, pass

right through). The curve for helium follows a similar trend, but is shifted to higher energies (by virtue of their larger size, helium nuclei require more energy to penetrate a material).

**GEANT** is only valid for energies in excess of 10 keV. To check whether low energy ( $\leq 10$  keV) electrons unmodelled by **GEANT** could significantly affect the charge deposition, the ITS Monte Carlo code [150] was used to analyse the transport of low energy electrons in the near vicinity ( $1\text{ }\mu\text{m}$ ) of surfaces. This explains the two closely-spaced curves for each species in Figure A.13. The slight difference between the curves represents the inclusion of the effects of low-energy electrons. It is seen that the differences only become significant at high incident particle energies ( $\sim 1000$  MeV) when the electrons are generated in large quantities.

The ‘raw responses’ in Figure A.13 can now be ‘folded in’ with the cosmic ray spectra (Figure A.12) to yield the desired result, namely, the charge rates due to cosmic rays. The results of this convolution are shown in Figure A.14. It can be seen that the charging is significant

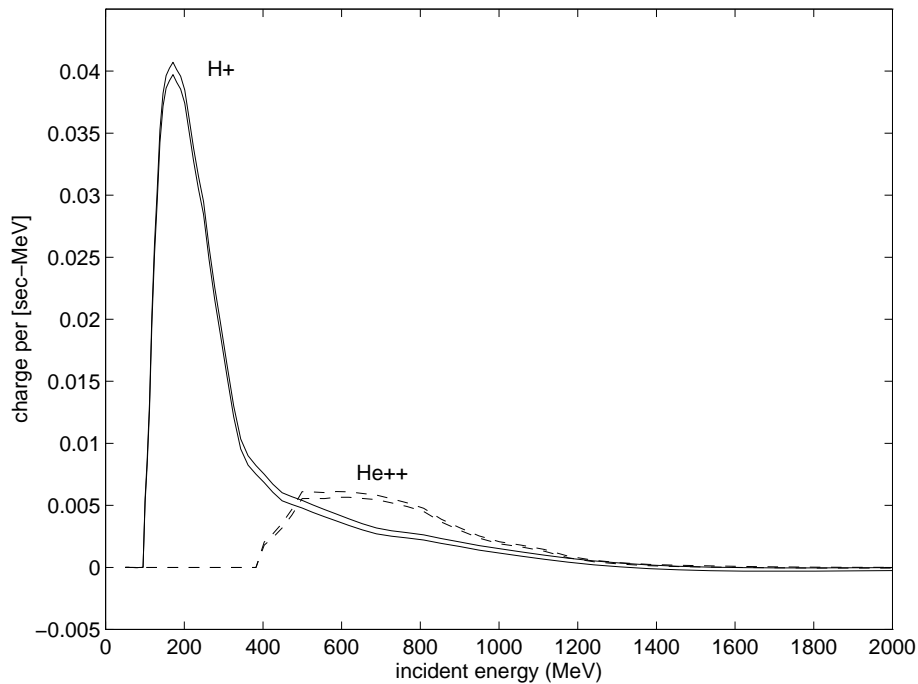


**Figure A.14** *Computed cosmic ray charging spectrum for the **LISA** proof mass. The results shown are for solar minimum, (and should be reduced by a factor of 4 for solar maximum).*

for incident particle energies up to 1000 MeV. To shield against these would require in excess of 25 cm tungsten, totally impractical for a space mission.

Integrating over energy yields a total charge rate of 11 protons/s ( $2 \times 10^{-18}$  C/s) at solar minimum, with a discrepancy of  $\pm 10\%$  corresponding to the effects of low-energy electrons. Additional errors come from uncertainties in the cosmic ray spectra (error bars in Figure A.12) which amount to  $\pm 30\%$  in computed charge rate. Therefore, the actual charge rate can be expected somewhere between 6 and 16 protons/s for solar minimum (and between 1 and 4 protons/s for solar maximum). It is interesting to note that although helium accounts for only 10 % of the cosmic ray incident flux, it is found to produce 30 % of the charging, owing to the comparatively high numbers of secondaries generated. Another interesting quantity is the ratio of stopped charge to the total rate of charges entering the proof mass if it were exposed directly to the cosmic ray flux. This ratio turns out to be 1:20 which shows that, (very) roughly speaking, 95 %

percent of the cosmic rays pass straight through without any effect.

The cosmic rays are the dominant species only when the Sun is inactive. When it is active, an average solar flare will send out protons with sufficient energy to produce a charging of about  $4 \times 10^7$  protons integrated over the event (calculated using [GEANT](#) with solar proton flux models from [\[151\]](#)). An anomalously large flare leads to  $4 \times 10^{10}$  protons. As discussed in [\[149\]](#), the frequency of flare events is skewed and asymmetric with respect to the solar cycle. In the seven-year neighbourhood of solar maximum, about eight average flares per year can be expected. In the three-year neighbourhood of solar minimum, the frequency drops to about one per year. An anomalously large event can occur at any time in the cycle. However, a more recent reference [\[152\]](#) including information on solar flare cosmic rays from 1972–1987 with energies high enough to affect [LISA](#) indicates a considerably lower frequency of such events than the earlier data did. Although the charge rates are significant, the time history of the charging is correlated with the history of the flare event which lasts typically for a few hours, so the science data can simply be ignored during flares (as long as a subsequent discharging procedure is employed).

No account has been made for the errors in the [GEANT](#) modelling. These are difficult to assess. For conservativeness, a factor of two should be assumed.

### A.2.3 Lorentz forces

For a given charge  $Q$  on the proof mass as it moves at velocity  $\mathbf{v}$  through the interplanetary magnetic field  $\mathbf{B}$ , the acceleration disturbance is given by

$$\mathbf{a}_n = \frac{Q}{m} \mathbf{v} \times \mathbf{B}. \quad (\text{A.13})$$

In order to investigate the spectral distribution of the disturbance, Eq. [A.13](#) can be expressed as follows,

$$\mathbf{a}_n = \frac{1}{m} \bar{Q} t \mathbf{v} \times \bar{\mathbf{B}} + \frac{1}{m} \delta Q \mathbf{v} \times \bar{\mathbf{B}} + \frac{1}{m} \bar{Q} t \mathbf{v} \times \delta \mathbf{B}, \quad (\text{A.14})$$

where  $\bar{Q} t$  is the mean charge (at a given time),  $\bar{\mathbf{B}}$  is the mean magnetic field,  $\delta Q$  are the fluctuations of charge about the mean value, and  $\delta \mathbf{B}$  are the fluctuations in the magnetic field (higher order terms in  $\delta Q$  and  $\delta \mathbf{B}$  have been neglected). The first term in Eq. [A.14](#) induces a drift of the proof mass, resulting in an armlength change. The rate of change of armlength is negligibly small, and, moreover, its noise components are insignificant in the measurement band.

Consider now the fluctuating terms in Eq. [A.14](#). In order to characterise the charge fluctuations ( $\delta Q$ ), it can be assumed that the charging occurs in equal increments (one proton at a time) which are distributed randomly in time (a Poisson process). The (single sided) spectral density in the current flowing onto the proof mass ( $S_I$ ) is then given by [\[153\]](#):

$$S_I(f) = 2e\bar{Q} \quad (\text{A}^2/\text{Hz}). \quad (\text{A.15})$$

(Compare this with the well-known representation for electrical ‘shot noise’.) To convert from current to charge, the expressions for current must be integrated over time. This yields

$$Q(t) = \bar{Q} t + \delta Q(t), \quad (\text{A.16})$$

where the first term ( $\overline{\dot{Q}}t$ ) represents the average linear growth, and the second term ( $\delta Q$ ) represents the fluctuations with a spectral density ( $\mathcal{S}_Q$ ) given by

$$\mathcal{S}_Q = \frac{2e\overline{\dot{Q}}}{(2\pi f)^2} \quad (\text{C}^2/\text{Hz}). \quad (\text{A.17})$$

(The appearance of  $f$  in the denominator corresponds to the process of integration.) Substituting this into the second term in Eq. A.14 yields the spectrum of acceleration disturbance corresponding to  $\delta Q$ , namely

$$\sqrt{\mathcal{S}_a} \approx \frac{1}{m} \frac{\sqrt{2e\overline{\dot{Q}}}}{2\pi f} (\mathbf{v} \times \overline{\mathbf{B}}) \quad (\text{m s}^{-2}/\sqrt{\text{Hz}}). \quad (\text{A.18})$$

Putting in numbers, and imposing a limit of  $10^{-16} \text{ m s}^{-2}/\sqrt{\text{Hz}}$  for the acceleration, yields an upper limit of  $2 \times 10^{-12} \text{ C/s}$  for the mean charge rate. This is almost six orders of magnitude above the expected charge rate, and so this effect can be neglected.

For the final term in Eq. A.14, recent measurements of the interplanetary magnetic field variations (from the Ulysses spacecraft at 1 AU) have been used to derive  $\delta \mathbf{B}$  and place limits on the allowable charge at which 10 % of the acceleration noise budget is reached. These are shown, versus frequency, in Figure A.15. Also shown is the time taken to reach these limits, assuming the charging rates computed by GEANT (with a factor of two margin). It is clear that for low

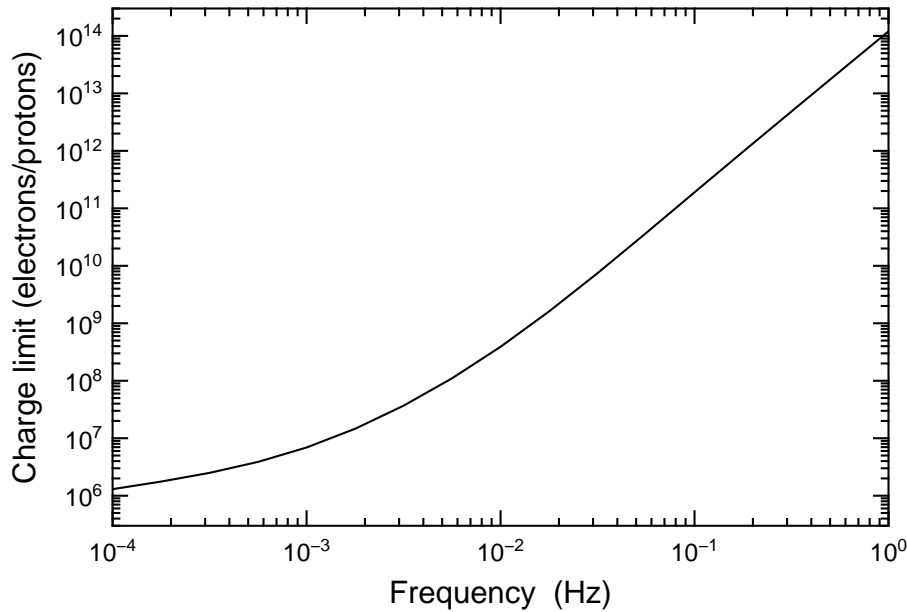


**Figure A.15** Limit on allowable charge due to the Lorentz force disturbance as a function of frequency.

frequencies ( $10^{-4} \text{ Hz}$ ) the charge build-up exceeds the allowable levels after an hour or so (the situation is less severe at higher frequencies), which means that the charge must be removed rather frequently. In principle this limit could be relaxed somewhat by employing closed electromagnetic shielding around the accelerometer. The precise extent to which this can be done is unclear but it is certainly reasonable to expect to be able to obtain an order of magnitude reduction in charge sensitivity. In fact it turns out that additional constraints on the charge level become the limiting factors beyond this level of shielding anyway. These are explored in the following sections.



### A.2.4 Coulomb forces

Electrically the conducting proof mass surrounded by electrodes can be thought of as a bank of capacitors with the proof mass forming a common central electrode. The proof-mass potential,  $V_T$ , due to any applied potentials,  $V_i$ , will be

$$V_T = \frac{1}{C} \sum_{i=1}^n V_i C_i, \quad (\text{A.19})$$

where the summation is over all electrodes and the total capacitance is  $C = \sum_{i=1}^n C_i$ . If a free charge,  $Q$ , resides on the proof mass then the arrangement will have a total energy,  $E$ , which is a combination of stored energy in the electric fields, energy associated with the ‘batteries’ providing the applied potentials, and the interaction energy between the free charge and the applied potentials. This is given by

$$E = \frac{1}{2} \sum_i C_i (V_i - V_T)^2 + \frac{1}{2} \frac{Q^2}{C} + QV_T + \sum_i Q_{Bi} V_i. \quad (\text{A.20})$$

Forces will act on the proof mass primarily through the capacitance gradients. In any direction,  $k$ ,

$$F_k = -\frac{\partial E}{\partial k} = \frac{1}{2} \sum_i \frac{\partial C_i}{\partial k} V_i^2 + \frac{Q^2}{2C^2} \frac{\partial C}{\partial k} - \frac{Q}{C} \sum_{i=1}^n V_i \frac{\partial C_i}{\partial k}, \quad (\text{A.21})$$

where we have assumed for simplicity that the electrostatic control system would normally ensure that  $\sum_i C_i V_i = 0$ , i.e. that

$$V_T = 0 \text{ and } \frac{\partial V_T}{\partial k} = \frac{1}{C} \sum_{i=1}^n V_i \frac{\partial C_i}{\partial k}. \quad (\text{A.22})$$

The first term represents the electrostatic suspension and control forces, the second term is from spurious forces due to the interaction of any free charge with the surrounding electrode structures, and the third contains the interplay between the free charges and the applied potentials on the surrounding electrodes.

All terms involve the gradient of the capacitance which must be evaluated for the specific geometry of the proof mass and its surrounding electrode structure. For a simple displacement type sensor geometry, as used on the transverse degrees of freedom of the proof mass, the total capacitance gradient,  $\frac{\partial C}{\partial k}$ , comes from differencing the gradients from the opposing surfaces with the result that  $\frac{\partial C}{\partial k} = 4\epsilon \frac{A}{g^3} \delta k$ , where  $A$  is the electrode area,  $g$  is the gap between the electrode and the proof mass,  $\epsilon$  is the permittivity of free space and  $2\delta k$  is the difference in the gaps at the two opposing sides; i.e. the asymmetry in the arrangement. For an overlap type sensor geometry, as proposed for the sensing in the sensitive direction, the total capacitance gradient is again determined by asymmetries between the two ends. However in this case it is differences in the transverse dimensions of the electrodes and the transverse gaps which are important. For the [LISA](#) configuration each micron asymmetry in each of the critical dimensions gives rise to a capacitance gradient of typically  $6 - 9 \times 10^{-13} \text{ F/m}$ .

The total proof-mass capacitance with respect to its surroundings is  $\approx 70 \text{ pF}$ . The electrostatic force acting on the proof mass due to free charge on it is then (using the second term in equation [A.21](#))  $\approx 2.3 \times 10^{-30} n_e^2 (\text{N } \mu\text{m}^{-1})$ , where  $ne$  is the number of free charges on the proof mass. The corresponding acceleration is  $\approx 1.8 \times 10^{-30} n_e^2 (\text{m s}^{-2} \mu\text{m}^{-1})$ .

The charge build-up will be the result of the random arrival of cosmic rays, with each ‘hit’ depositing a variable amount of charge according to the stochastic nature of the interaction process. Following an argument similar to that already used for Lorentz force noise it turns out that the acceleration *noise* arising from this process can be approximated by

$$\tilde{a}_n = 10^{-29.9} n_e \sqrt{\dot{n}_e} f^{-1} \text{ (m s}^{-2}/\sqrt{\text{Hz}} \text{)}. \quad (\text{A.23})$$

In order to keep this acceleration noise below its budget allocation the amount of accumulated charge must be controlled such that

$$n_e \leq 2 \times 10^{13} f \left[ 1 + \left( \frac{f}{3 \times 10^{-3} \text{ Hz}} \right)^2 \right] \text{ electrons/protons}. \quad (\text{A.24})$$

This limit is much less severe than that from the Lorentz force noise. It has been based on a  $1 \mu\text{m}$  ‘asymmetry’ assumption. Whether this is a reasonable figure to use remains to be confirmed.

Another source of acceleration noise which will occur if the proof mass becomes charged is through displacement noise modifying the electrostatic force. There are two components (arising from the second term in equation A.21) due to changes in the total capacitance and in the asymmetry factor, which in turn affects the capacitance gradients. Adding these two in quadrature gives an acceleration noise (for the displacement type sensor geometry)

$$\tilde{a}_n = \frac{Q^2}{mC^2} \frac{\partial C}{\partial k} \sqrt{\frac{1}{4\delta k^2} + \frac{1}{C^2} \left( \frac{\partial C}{\partial k} \right)^2} \tilde{k}_n \text{ (m s}^{-2}/\sqrt{\text{Hz}} \text{)}, \quad (\text{A.25})$$

where  $\tilde{k}_n$  is the spatial displacement noise spectral density and all other symbols retain their earlier meanings. Putting in the numerical values for the LISA sensor design and using  $\tilde{k}_n = 10^{-9} \text{ m}/\sqrt{\text{Hz}}$  gives  $\tilde{a}_n = 1.8 \times 10^{-33} n_e^2 \text{ m s}^{-2}/\sqrt{\text{Hz}}$ .

The final noise source which will be discussed in this section arises from the interaction between any free charges on the proof mass and the applied control voltages,  $V_i$ , and any associated voltage noise,  $V_{ni}$ . Using the third term in equation A.21 this noise component is given by

$$a_n^2 = \frac{Q^2}{m^2 C^2} \left( \sum_{i=1}^n V_{ni} \frac{\partial C_i}{\partial k} \right)^2 + \frac{Q^2}{m^2 C^4} \left( \sum_{i=1}^n V_i \left( \frac{\partial C_i}{\partial k} \right)^2 \right)^2 k_n^2 \text{ (m}^2 \text{ s}^{-4}/\text{Hz} \text{)}. \quad (\text{A.26})$$

The electrostatic forces which come about through the proof mass becoming charged bring with them associated effective spring constants. There are three effects, two of which involve the applied potentials and one which does not, which have been considered. The two involving the applied potentials are given by terms of the form  $|K| \approx \frac{QV_{\text{cm}}}{C} \frac{4\epsilon A}{g^3}$  and  $|K| \approx \frac{2QV_{\text{cm}}}{C} \frac{\partial^2 C_i}{\partial k^2}$ , where  $V_{\text{cm}}$  and  $V_{\text{dm}}$  are the voltages applied in common mode and differential mode to electrodes on opposite sides of the proof mass. The second of these two spring constant terms is the most significant for the current sensor design. The spring constant term arising out of pure electrostatic interaction with the surrounding conducting surfaces is of the form (for displacement type sensor geometries)  $|K| \approx \frac{Q^2}{2C} \frac{4\epsilon A}{g^3}$ . This term is not significant. A charge limit is then derived by requiring that these spring constant terms do not upset the nominal spring constant from the electrostatic control system by more than 10%.

### A.2.5 Summary of charge limits

The above charge limits for the LISA proof mass are summarised in Table A.12.. The most stringent limit comes from Lorentz force noise (note a factor of 10 is included to allow for some electromagnetic shielding from the partial titanium enclosure around the sensor). The next most critical effect is modification of the spring constant.

**Table A.12** Summary of proof-mass charge limits and charge build up times

<i>Effect</i>	<i>Charge Limit</i> [electrons/protons]	<i>Charging Time</i> [days]
Lorentz force acceleration noise	$2 \times 10^6$	0.7
Electrostatic acceleration noise		
Stochastic charge arrival	$4 \times 10^{10}$	$1.4 \times 10^4$
Displacement noise	$5 \times 10^8$	187
Control voltage noise	$2 \times 10^{11}$	$7 \times 10^4$
Spring Constant	$10^7$	3.7

### A.2.6 Charge measurement using force modulation

The force modulation technique depends on applying oscillating potentials (dither voltages) to the electrode structure around the proof masses which then exert forces on the charged proof mass via the third term in equation A.21. This induces an oscillatory motion in the proof mass which can be detected capacitively. The amplitude and phase of the response give the size of the charge and its sign. It turns out there is sufficient sensitivity in the displacement sensor for the dither to be applied in the transverse direction. If two opposing electrodes are used then the dither force is

$$F_d = -\frac{Q}{C} \left( V_1 \frac{\partial C_1}{\partial k} + V_2 \frac{\partial C_2}{\partial k} \right), \quad (\text{A.27})$$

where  $C$  is again the *total* capacitance and  $\frac{\partial C_i}{\partial k}$  is the capacitance gradient associated with an individual surface. Assuming the proof mass is reasonably well centred within the two opposing electrodes, such that  $\frac{\partial C_1}{\partial k} = -\frac{\partial C_2}{\partial k} = \frac{\partial C_o}{\partial k}$  and we apply equal and opposite voltages to the two sides (i.e.  $V_1 = -V_2 = V_d$ ) then the dither force is

$$F_d = -\frac{2QV_d}{C} \frac{\partial C_o}{\partial k}. \quad (\text{A.28})$$

The charge measurement sensitivity is here defined as the charge,  $Q_s$ , at which the induced acceleration just equals the system acceleration noise,  $\Delta a_n$ :

$$Q_s = \frac{m\Delta a_n C}{2V_d} \left( \frac{\partial C_o}{\partial k} \right)^{-1}. \quad (\text{A.29})$$

The acceleration noise,  $\Delta a_n$ , will depend on the spectral noise density,  $\tilde{a}_n$ , and the measurement bandwidth of the dither sensing. The dither frequency must be high enough that the measurement time does not impinge much on the science observations. With a mean charging rate of  $5 \times 10^{-18}$  C/s the charge limit of  $2 \times 10^6$  electrons is reached in some  $6.4 \times 10^4$  seconds and so any charge measurement, whether it be continuous or intermittent, must have a response time small compared to this. The integration time,  $\tau$  ( $\sim$  inverse bandwidth), needed to achieve the required charge sensitivity is

$$\tau = \frac{m^2 a_n^2 C^2}{4V_d^2 Q_s^2} \left( \frac{\partial C_o}{\partial k} \right)^{-2}. \quad (\text{A.30})$$

The integration times given by this equation using a 1 volt dither voltage are completely negligible compared to the charge build-up time and dither frequencies can be selected just above the science signal measurement range.

The proposed technique for control of the charge on the proof mass is described in section 6.1.6.

### A.2.7 Momentum transfer

Performing an analysis using poissonian statistics for arrival times to calculate the fluctuating force due to *momentum* imparted from cosmic ray interactions yields the following expression for the spectral density of momentum transfer in a given direction

$$\mathcal{S}_M \approx 2 p^2 \lambda \quad (\text{N}^2 \text{s}^2 / \text{Hz}), \quad (\text{A.31})$$

where  $p$  is the momentum (in the given direction) per particle stopped in the proof mass, and  $\lambda$  is the number of particles stopped per second. Summing the effects of all particles (protons and helium), taking into account their directions, yields an acceleration of  $\sim 2 \times 10^{-18} \text{ m s}^{-2} / \sqrt{\text{Hz}}$ , which is two orders of magnitude below the desired sensitivity.

### A.3 Disturbances due to minor bodies and dust

In order to provide a rough estimate of how often spurious signals might be generated by gravity forces due to minor bodies or dust grains passing by one of the [LISA](#) spacecraft, it is assumed that the disturbances take place with the point of closest approach along one of the interferometer arms. Only the acceleration of one proof mass is considered. Then the Fourier component of the proof mass acceleration at angular frequency  $\omega$  is given by

$$a(\omega) = \frac{GM}{\omega R^2} \int_{-\infty}^{\infty} \frac{z^3 \cos y}{(z^2 + y^2)^{3/2}} dy, \quad (\text{A.32})$$

where  $R$  is the distance of closest approach,  $V$  is the minor body relative velocity,  $M$  is the disturbing mass, and  $z$  is defined as  $z = \omega R/V$ . Since

$$\int_{-\infty}^{\infty} \frac{z^2 \cos y}{z^2 + y^2} dy = \pi z e^{-z} \quad (\text{A.33})$$

and

$$\int_{-\infty}^{\infty} \frac{z^4 \cos y}{(z^2 + y^2)^2} dy = \frac{\pi}{2} z(1 + z) e^{-z}, \quad (\text{A.34})$$

it is expected that the effective value of  $a(\omega)$  will be approximately proportional to the *rms* of the above two expressions:

$$a(\omega) \approx \pi z \frac{GM}{\omega R^2} \sqrt{\frac{5}{8} + \frac{z}{4} + \frac{z^2}{8}} e^{-z} = \frac{\pi GM}{RV} \sqrt{\frac{5}{8} + \frac{z}{4} + \frac{z^2}{8}} e^{-z}. \quad (\text{A.35})$$

We take the signal of interest to be the second derivative of the difference in length of two of the interferometer arms. For frequencies higher than the corner frequency  $f_c$  for the [LISA](#) antenna of about 3 mHz, the expected acceleration noise level  $\tilde{a}_n$  for [LISA](#) is given roughly by

$$\tilde{a}_n = \tilde{a}_c \left( \frac{\omega}{\omega_c} \right)^2, \quad (\text{A.36})$$

where  $\tilde{a}_c = 6 \times 10^{-15} \text{ m s}^{-2}/\sqrt{\text{Hz}}$  and  $\omega_c = 2\pi f_c$ . Below  $f_c$ ,  $a_n$  is equal to  $a_c$  down to at least  $1 \times 10^{-4} \text{ Hz}$ , and then increases again at some lower frequency. Thus, for fixed  $R$ , since  $a(\omega)$  is a monotone decreasing function of  $\omega$ , the ratio of  $a(\omega)$  to  $\tilde{a}_n$  will be a maximum somewhere below  $f_c$ . For simplicity, it is assumed below that  $\tilde{a}_n = \tilde{a}_c$  down to zero frequency, although this won't be the case in reality.

The square of the signal-to-noise ratio  $S/N$  for detecting the disturbance is given by

$$(S/N)^2 = 2 \int \frac{a(\omega)^2}{a_n^2} df. \quad (\text{A.37})$$

In terms of the dimensionless variable  $z = \omega R/V$  this becomes

$$(S/N)^2 = \frac{V}{\pi R} \int \frac{a(z)^2}{a_n^2} dz. \quad (\text{A.38})$$

The integral divides naturally into two parts:

$$(S/N)^2 = \frac{\pi(GM)^2}{R^3 V a_c^2} (I_1 + I_2), \quad (\text{A.39})$$

where

$$\begin{aligned} I_1 &= \int_0^{z_c} \left( \frac{5}{8} + \frac{z}{4} + \frac{z^2}{8} \right) e^{-2z} dz = \frac{13}{32} - \left( \frac{13}{32} + \frac{3}{16} z_c + \frac{1}{16} z_c^2 \right) e^{-2z_c}, \quad \text{and} \\ I_2 &= \int_{z_c}^{\infty} \frac{z_c^4}{z^4} \left( \frac{5}{8} + \frac{z}{4} + \frac{z^2}{8} \right) e^{-2z} dz = \left( \frac{5}{24} z_c - \frac{1}{12} z_c^2 + \frac{5}{24} z_c^3 \right) e^{-2z_c} - \frac{7}{12} z_c^4 E_1(2z_c), \end{aligned} \quad (\text{A.40})$$

with  $z_c = \omega_c R/V$ . Here  $E_1$  is the usual exponential integral.

It is useful to approximate  $\frac{32}{13} (I_1 + I_2)$  by  $H(z_c)$ , where  $H(z_c)$  is defined as  $H(z_c) = 2z_c$  for  $z_c < 1/2$ , and  $H(z_c) = 1$  for  $z_c > 1/2$ .  $H(z_c)$  is a maximum of 41 % too high at  $z_c = 0.5$ , but is a very good approximation for both low and high values of  $z_c$ . Thus  $(S/N)^2$  can be approximated by the following expressions:

$$\begin{aligned} (S/N)^2 &= \frac{13}{16} \pi \omega_c \left( \frac{GM}{RV a_c} \right)^2 \quad \text{for } R < V/(2\omega_c), \\ (S/N)^2 &= \frac{13}{32} \pi \frac{(GM)^2}{VR^3(a_c)^2} \quad \text{for } R > V/(2\omega_c). \end{aligned} \quad (\text{A.41})$$

Even if the event time were known, the signal would not be detectable unless  $S/N > 3$ . The differential rate  $r(M)$  of small-body events with  $S/N > 3$  is

$$r(M) = \pi R_{(S/N=3)}^2 F(M), \quad (\text{A.42})$$

where  $F(M)$  is the differential flux of minor bodies and dust grains. From Eqs. (A.41), with  $V = 2 \times 10^4$  m/s, we get

$$\begin{aligned} \pi R_{(S/N=3)}^2 &= 5.2 \times 10^{-3} M^2 \quad \text{for } R < 5.3 \times 10^5 \text{ m}, \\ \pi R_{(S/N=3)}^2 &= 2.9 \times 10^2 M^{4/3} \quad \text{for } R > 5.3 \times 10^5 \text{ m}. \end{aligned} \quad (\text{A.43})$$

The flux of minor bodies and dust grains with masses less than about 0.1 kg is given by Grun *et al.* [154]. The results from their Table 1 can be fit for the higher part of the mass range by

$$I(M) = 2.1 \times 10^{-19} M^{-1.34} \text{ m}^{-2} \text{ s}^{-1}, \quad (\text{A.44})$$

where  $I(M)$  is the integral flux of all bodies with masses greater than  $M$ . This expression gives a good approximation to their results down to about  $10^{-9}$  kg, but is several orders of magnitude too high at lower masses.

For higher masses, estimates of the integral flux versus mass from Shoemaker [155] can be used. They are based on counts of impact craters versus size on the Moon, and careful analysis of the relation between crater size and the energy of the impacting body. The results appear to be consistent within the uncertainties with those from other sources of information.

Figure 1 of reference [155] gives an estimated curve represented by large black dots for the cumulative frequency per year of impacts on the Earth versus the equivalent energy of the

impacts in megatons of TNT. Since 1 megaton of TNT is equivalent to  $4.2 \times 10^{15}$  J, for a typical impact velocity of  $2 \times 10^4$  m/s, 1 megaton corresponds to an impact by a mass of  $2.1 \times 10^7$  kg. Thus the results of Figure 1 of reference [155] can be converted to the integral flux of bodies with masses between roughly  $2 \times 10^4$  and  $2 \times 10^{12}$  kg in the neighborhood of the Earth's orbit. Shoemaker's results can be approximated by the following two power law expressions for the integral flux:

$$I(M) = 4.2 \times 10^{-18} M^{-0.88} \text{ m}^{-2} \text{ s}^{-1} \quad \text{for } 2 \times 10^4 \text{ kg} < M < 2 \times 10^{10} \text{ kg}, \quad (\text{A.45})$$

$$I(M) = 1.7 \times 10^{-21} M^{-0.55} \text{ m}^{-2} \text{ s}^{-1} \quad \text{for } 2 \times 10^{10} \text{ kg} < M < 2 \times 10^{12} \text{ kg}. \quad (\text{A.46})$$

Eq. (A.45) intersects Eq. (A.44) at  $1.5 \times 10^{-3}$  kg, and it will be used, for simplicity, over the extended range from  $1.5 \times 10^{-3}$  to  $2 \times 10^{10}$  kg, even though it may well be too high below  $2 \times 10^4$  kg. It will turn out that this doesn't affect the final results appreciably.

From the above approximate integral flux curves, the differential flux versus mass  $F(M)$  can be obtained by differentiating  $I(M)$ . Thus the differential rate  $r(M)$  of small-body disturbances can be obtained from Eq. (A.42), using the expressions for  $\pi R_{(S/N=3)}^2$  from Eq. (A.43). Integrating  $r(M)$  over different mass ranges will then give the corresponding estimates of the contributions to the event rate  $Q$ .

For masses less than  $1.5 \times 10^{-3}$  kg,  $R_{(S/N=3)}$  is much less than  $3.5 \times 10^5$  m, and

$$Q(M < 1.5 \times 10^{-3}) \approx 3 \times 10^{-23} \text{ s}^{-1}. \quad (\text{A.47})$$

For larger masses up to  $1.3 \times 10^7$  kg,  $S/N = 3$  requires  $R < 5.3 \times 10^5$  km, and we get

$$Q(1.5 \times 10^{-3} < M < 1.3 \times 10^7) \approx 1.6 \times 10^{-12} \text{ s}^{-1}. \quad (\text{A.48})$$

The next contribution, still using the integral flux from Eq. (A.45), but with a distance of  $R_{(S/N=3)} > 5.3 \times 10^5$  m, yields

$$Q(1.3 \times 10^7 < M < 2 \times 10^{10}) \approx 1.1 \times 10^{-10} \text{ s}^{-1}. \quad (\text{A.49})$$

And, using Eq. (A.46) for the highest mass range, we have

$$Q(2 \times 10^{10} < M < 2 \times 10^{12}) \approx 1.5 \times 10^{-9} \text{ s}^{-1}. \quad (\text{A.50})$$

From the above estimates in Eqs. (A.47-A.50), it is clear that most of the probability for an event observable by LISA comes from objects with large masses. Thus, improved estimates can be made for the important range of masses using the fact that  $z_c$  will be large. For  $M > 4.1 \times 10^8$  kg,  $R_{(S/N=3)}$  will be  $> 5.3 \times 10^6$  m, and  $z_c > 5$ .

Two of the approximations made were that the point of closest approach for the disturbing body was along an interferometer arm, and that only one proof mass would be disturbed. It is estimated that removing these approximations would reduce the calculated disturbance probability by about a factor two. However, there are three spacecraft that can be disturbed, so a better estimate for the total LISA disturbance rate by masses of up to  $2 \times 10^{12}$  kg is about  $2.4 \times 10^{-9}$  per second, or roughly 8% per year.

In considering the above estimate, it should be remembered that the instrumental acceleration noise was assumed to be constant below 3 mHz. With this assumption and for  $M = 2 \times 10^{12}$  kg, the distance of closest approach is  $R_{(S/N=3)} = 1.5 \times 10^9$  m. The time for the disturbing body to travel this distance is about  $7.5 \times 10^4$  s. Thus, if the acceleration noise level starts to rise at a



shorter period than this, the probability of reaching  $S/N = 3$  will be reduced. Also, as noted earlier, a  $S/N$  of 3 is adequate to observe the disturbance only if the time of the event is known. The diameter for an asteroid with a mass of  $2 \times 10^{12}$  kg is roughly 1 km. At present less than 10 % of the Earth-crossing asteroids of this size or larger are believed to be known [156, 157], but future observing programs may detect most of them in the next 25 years. If LISA detected a disturbance with a period of a few hours to a few days, a rapid optical search for a nearby disturbing body should be feasible. Disturbances by comets also are possible, although their flux is believed to be somewhat lower in the mass range of interest and they generally have higher relative velocities.

## A.4 Alternative Proof-Mass Concepts

### A.4.1 Single (spherical) proof mass

In a first approach, the payload concept alternatives identified have been focused on the desire to reduce complexity by replacing the two proof mass concept in each spacecraft by a single proof mass, serving as an inertial reference for both line of sight directions. A further reduction potential for the degrees of freedom to be controlled has been tentatively identified by replacing a (single) cubic proof mass by a sphere.

The number of degrees of freedom in the inertial reference system that need to be controlled would be reduced from 12 (two proof masses) to 6 (one cubic proof mass) or even to 3 (one spherical proof mass), leading to a simplified control architecture. On the other hand, the two adjacent laser interferometer arms would be tightly coupled and in case of failure of the single proof mass, the mission would terminate. This is not the case for two independent optical assemblies in each spacecraft, because one Michelson interferometer could be still kept operational on two arms. A further complication is the requirement to continuously adjust the angle between the lines of sight by about  $\pm 1^\circ$  over a period of one year. As a consequence either additional degrees of freedom have to be introduced in the interferometric optical path or the reference reflector, i.e. the proof-mass mirror, has to be shaped accordingly, e.g. as a spherical surface. A conceptual sketch is shown in Figure A.16 for the case of a spherical proof mass and a tetrahedral geometry optical read out system for proof mass to cage position. In order to meet optical alignment requirements, the proof mass as part of the interferometer optics has tight position tolerances in all three DOF, which may be in the same order as already required from self-gravity effects minimisation (few nm) and which are well in the reach of optical read out systems. However, the necessary control stiffness needs to be assessed in a detailed analysis as well as the consequences for operation in the LISA desired low stiffness inertial mode (within the measurement band). The sensor is invariant to the attitude DOF for a perfect sphere only. Spheres can at present be manufactured to about 30 nm surface rms and bulk density variations of  $10^{-6}$  (Silicon; Physikalisch-Technische Bundesanstalt Braunschweig). Rotating the sphere at

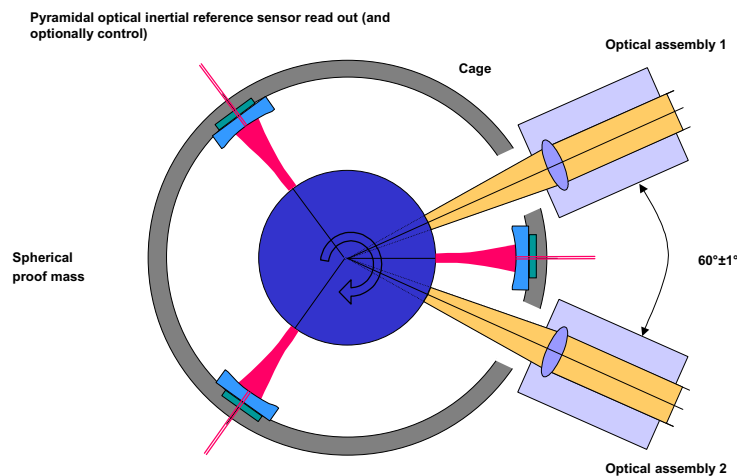


**Figure A.16** *Spherical proof mass inertial reference sensor concept, featuring an all optical read out, based on cavity gauge laser interferometers in a pyramidal geometry. Surface deformations can be averaged out by rotating the sphere at a sufficiently high rate.*

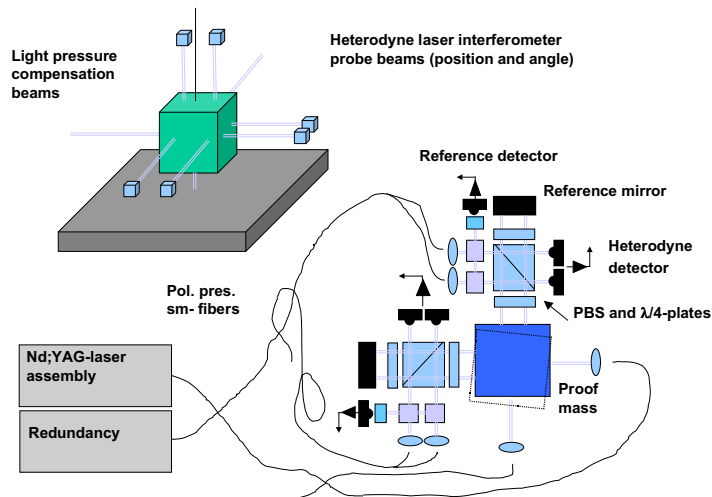


**Figure A.17** *Inertial reference sensor all optical read out concept utilising pm-resolution polarisation / heterodyne laser metrology.*

a rate larger than the measurement bandwidth would average out surface deformations. The rotation could e.g. be excited prior to the measurement phase by a rotating electro-magnetic field.

#### A.4.2 IRS optical read out

Simplification potential has been identified in replacing the electrostatic capacitive internal sensors in the inertial reference by optical interferometric sensors, i.e. an overall optical readout assembly.

Laser interferometer measurement systems are already commercially available with nm resolution and -on laboratory or prototype level- with few pm resolution for relative distance change measurement. Two principles are prime candidates for this application : Heterodyne polarisation interferometers and resonant cavity gauge interferometers, both verified technologies. Principle layouts are shown in Figure A.16 and Figure A.18. (Small) attitude changes can be monitored in addition to position by using e.g. two adjacent probe beams or alternatively by quad-cell heterodyne detectors in the same way as already baselined for the LISA interferometer coherent tracking sensor. In the case of resonant cavities, the excitation of higher order cavity modes could also provide attitude information. The advantage of pm-optical read-out sensors over the baselined capacitive sensors would be a higher resolution, the possibility of a large gap between probe mass and cage (cm) and a large linear measurement range not affected by electrostatic stray fields between electrode arrangements. The laser source can be conveniently generated by splitting off a tiny fraction of the highly frequency stable LISA transmitter laser beam already on board. On the other hand, any probe beam light pressure accelerates the proof mass at a level, exceeding for the required power levels ( $\mu\text{W}$ ) already the requirements. Hence a light pressure compensator beam is required and only differential effects (differential intensity fluctuations, straylight induced light pressure and thermal effects) need to be controlled.



#### A.4.4 Laser metrology harness

Once an optical read sensor for the inertial reference sensor has been developed which has pm-resolution capability, this subsystem could be extended to an optical assembly internal laser metrology harness (operating at a different wavelength, e.g.  $1.5\ \mu\text{m}$ ), monitoring all critical internal optical paths with pm accuracy and, hence, allowing a discrimination between laser phase changes generated by detrimental effects inside the spacecraft and those stemming from outside. However, despite of introducing a rather complex all optical active monitoring subsystem, it is not clear at the moment, whether this would detect all relevant internal optical path noise sources in a proper way. An advantage of such an approach would be, that the LISA laser interferometer could be optically separated from the inertial reference sensor, by having the reference mirrors on the optical bench rather than on the proof masses, Figure A.19. Any relative movements of proof mass and reference mirrors would be monitored and these signals could be integrated into the data reduction. Only one proof mass would be necessary. Also the annual angular variation of the line of sight directions could be implemented in a simple way.

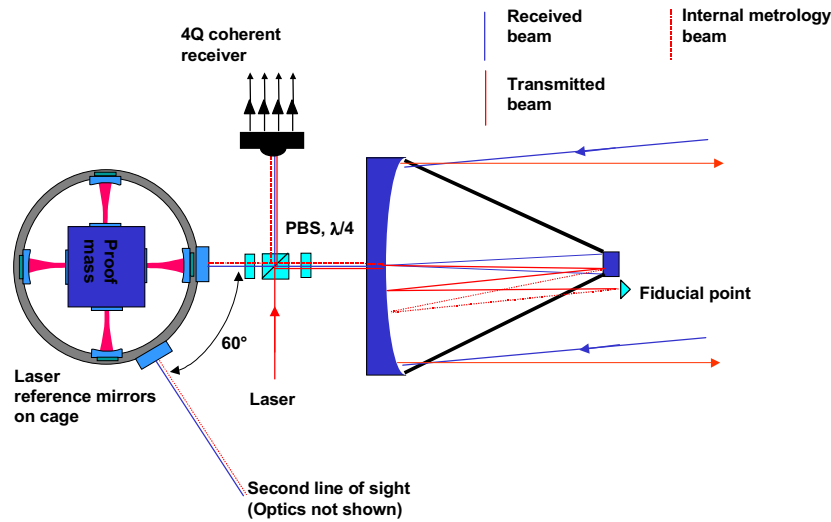


**Figure A.19** Internal laser metrology harness to monitor all relevant distance changes at pm resolution. One single proof mass (all optical read out to provide the necessary pm accuracy) is the inertial reference. The LISA laser interferometer reference mirrors are rigidly mounted on the optical bench. They can be shaped to allow the annular angular variation of line of sight without introducing additional degrees of freedom in the interferometer path.

#### A.4.5 Single proof mass as accelerometer

In combination with a sensitive optical monitoring system for all internal critical spatial degrees of freedom as sketched above, it could be interesting, to operate the inertial reference as an accelerometer. That means strong coupling to the spacecraft and precise monitoring of proof mass position by dedicated picometer-resolution laser metrology. Again, the LISA laser interferometer reference mirror could be located on the optical bench and the spacecraft motion, while freely floating, is affecting the heterodyne beat. Its influence, however, could be separated by employing the accelerometer read out for data reduction.

## A.5 Laser Assembly Concepts

### A.5.1 Laser requirements

The following requirements (given in Tables 3.1 to 3.3) apply for the laser assembly:

- Output power and output power noise:  
The nominal output power available on the optical bench shall be at least 1 W. The required laser power stability of the actively stabilised system between  $10^{-4}$  Hz and  $10^1$  Hz is:

$$\frac{\widetilde{\delta P}}{p} \leq 4 \times 10^{-4} / \sqrt{\text{Hz}}$$

- Beam quality and Polarisation:  
The laser beam quality shall be single transverse TEM00 mode. Polarisation shall be linear.
- Laser frequency noise:  
The laser frequency noise between  $10^{-3}$  Hz and 1 Hz shall be less than

$$\widetilde{\delta P} \leq 30 \text{ Hz} / \sqrt{\text{Hz}}$$

- Mass and power budget:  
Due to the limited capacity of the LISA spacecraft, the laser systems dimensions, mass and power requirement shall not exceed the following limitations:

Dimensions  $10 \text{ cm} \times 10 \text{ cm} \times 10 \text{ cm}$

Mass 1.5 kg

Power input total 15 W

The LISA mission requires a 1 W laser system with single-frequency operation and very high frequency and amplitude stability. In what follows the possible options for a single frequency laser will be discussed and the most suitable options for the LISA mission proposed.

The above mass and power constraints can only be met by a solid state laser system.

### A.5.2 Single-frequency solid state laser alternatives

In general four mechanisms are possible to achieve the single-frequency emission of solid state lasers:

- 1 In the case of a homogeneously broadened laser material, the unidirectional operation of ring laser.
- 2 Utilisation of filter elements (e.g. etalons) in the resonator or frequency selective end mirrors.
- 3 Micro chip laser arrangement, i.e. utilisation of a small laser crystal length with a free spectral range larger than the gain width of the laser material.
- 4 Injection locking with a single frequency seed laser (not appropriate here).

In what follows, the most suitable design concepts using the techniques 1–3 are reviewed in more detail.

#### A.5.2.1 Monolithic, nonplanar ringlaser (NPRO)

In the case of the NPRO (Non Planar Ring Oscillator) TEM00 mode, hence single transverse mode, operation is achieved by focussing the diode laser-beam into the crystal. When the

beamwidth of the diode laser radiation in the crystal is smaller than the diameter of the **TEM<sub>00</sub>** mode over the absorption length of the pump radiation, the laser is forced to operate in a single transverse mode.

Nevertheless, homogeneously broadened solid-state lasers oscillate on several longitudinal modes even at low output power because of the spatial hole burning effect. To enforce single-frequency operation, intra-resonator elements can be applied. However, these additional intracavity elements strongly reduce the efficiency and stability of the laser system. The monolithic **Nd:YAG** ring laser enables single-frequency operation at high output power without intracavity elements. Unidirectional and hence single-frequency oscillation is enforced by an intrinsic optical diode. This diode is formed by the laser material with a non-zero Verdet constant in a magnetic field in combination with a polarising output coupler.

The optical beam path in the crystal is determined by three total reflections and one reflection at the negatively curved front surface. This front surface is dielectrically coated, reflecting about 97 % of the 1064 nm laser radiation and highly transmitting the pump radiation at 808 nm (Figure A.20). A very high intrinsic frequency stability results from the monolithic and compact design of the resonator and from the excellent thermal properties of the host material.

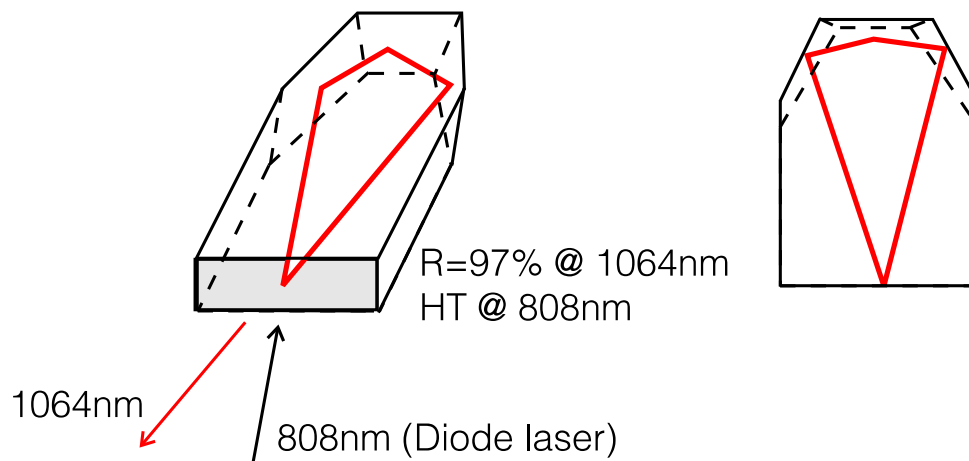


**Figure A.20** Arrangement of the monolithic non-planar **Nd:YAG** ring laser

#### A.5.2.2 Microchip laser

Microchip lasers are miniature solid-state lasers commonly emitting radiation in the near infrared frequency range (**NIR**) and pumped by a diode laser. A small crystal-chip (feasible length is about 1 mm) constitutes both the active medium and the resonator of the microchip laser i.e. the resonator mirrors are directly coated onto the surfaces of the chip. The setup is quite simple: The significant elements required are a lens focusing the pump beam on the crystal front face and a heat sink cooling the chip. Figure A.21 shows the arrangement of a microchip laser longitudinally pumped with a diode-laser pump module.

Single-frequency operation of microchip lasers is based on the realisation of a small resonator length, which results in a mode spacing larger than the gain bandwidth of the laser medium. One example is a monolithic **Nd:YAG** chip pumped by a diode laser. Measured short-term linewidths of the free-running laser are below 1 kHz. However, the **Nd:YAG** chip shows an induced birefringence, which is not easy to control. Further disadvantages of microchip lasers are the high sensitivity on back-reflections, beam walking problems and low efficiency.



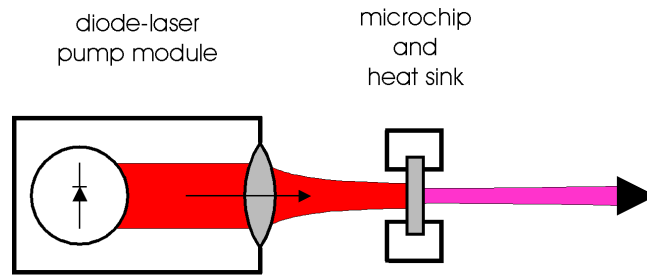


**Figure A.21** *Experimental setup of a diode-pumped microchip laser*

High output powers can be obtained but a quite high pumping power is required, because the optical to optical efficiency is below 10 %. Extra thermal contacts are necessary to ensure proper cooling of the crystal's surfaces, e.g. clamping the chip between sapphire plates.

Furthermore, whatever the operating output power is, the small laser crystal exhibits a high sensitivity to environmental temperature changes. This leads to frequency fluctuations which can only be suppressed by a very accurate temperature stabilisation of the laser crystal and its environment.

### A.5.2.3 External-cavity diode lasers

Diode lasers are compact, reliable, efficient and cost effective light sources in combination with a simple handling. In addition, the wide variety of visible and near-infrared frequencies (600–1600 nm), tuneability and output power practicable up to several ten watts make diode lasers suitable for many applications.

The use of diode lasers for the LISA laser system demands frequency narrowing due to the big linewidth of the common laser diodes (10–100 MHz). This can be realised with frequency selective component inside the laser resonator. DFB and DBR lasers (as described below) and external-cavity lasers are well established using internal frequency selection.

An External-cavity diode laser usually uses an external diffraction grating for frequency selection. The resonator is composed of a laser-diode with one AR coated surface and the external grating (Littrow configuration) or an additional mirror reflecting the light of the first order of diffraction (Littman configuration). In both configurations order 0 of diffraction is used as light output. Figure A.22 demonstrates a setup with Littman configuration.

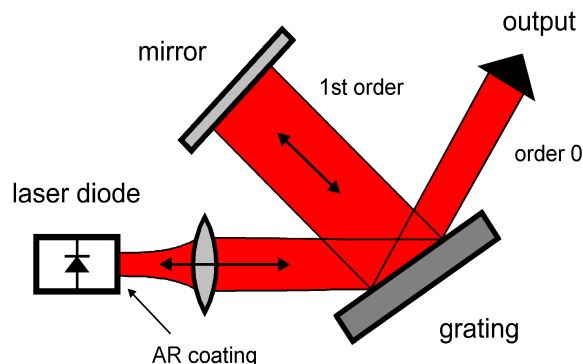


**Figure A.22** *External-cavity diode laser in Littman configuration*

Diode lasers with external cavity provide stable single mode operation with achieved linewidths

of less than 100 kHz in the visible or infrared range. Tuneability of 20 nm and more is possible with precise rotating of the grating (and additional movement of the mirror in Littman configuration). The main disadvantage seems to be the great sensitivity to mechanical instabilities which prevents long term reliable operation that is necessary for space applications. A horizontal misalignment in the dispersion plane of the grating corresponds to a wavelength detuning. But a vertical one in the sagittal plane is critical because only a few  $\mu$ m shift is enough for total misalignment of the external cavity. For that reason maintenance of alignment requires the possibility of adjusting the components during the use of the laser. Self aligning techniques could solve this problem so a reliable operation using these techniques may make this type of lasers available for satellite flights.

Also the output power of state-of-the art external cavity diode lasers are too low (20 mW) for an application as the LISA laser system.

#### A.5.2.4 DFB/DBR laser diodes

Another possibility for frequency narrowing is to connect the active semiconductor medium directly to Bragg gratings used as frequency selective components: DFB and DBR diode lasers (DFB: distributed feedback, DBR: distributed Bragg reflection) are laser diodes which compose small quasi-monolithic external cavities together with integrated Bragg gratings. They combine the small dimension, reliability and stable operation of a laser diode with a comparable narrow linewidth.

A DBR laser resonator contains the active region and one or more Bragg gratings used as reflectors instead of the high-reflection coatings of a common laser diode. The DFB laser integrates a Bragg grating directly into the active layer, so the regions of gain and reflection are not separated. That means an optical wave travelling in one direction is continuously scattered into the optical wave in the reverse direction. This concept represents a combination of continuous feedback and gain.

However, frequency tuning is very difficult since several modulation currents are to be controlled. Typical frequency modulation coefficients of 5 MHz/ $\mu$ A imply that an electronic power supply with very low current noise is necessary. Therefore, a stability and tuneability corresponding to the LISA requirements seems difficult to achieve. Additionally, neighbouring mode suppression is problematically, so these devices tend to multi-frequency operation, which would be catastrophic for the signal detection process. Furthermore, DFB/DBR laser diodes have the disadvantage of a very high sensitivity to back-reflections.

The output power of a typical DFB/DBR laser is very low, so as LISA laser system they will require an additional power amplifier. For this purpose monolithic master oscillator power amplifiers (M-MOPA) are well established. These are monolithic assemblies of a DFB/DBR laser as master oscillator and a connected gain region as power amplifier. Figure A.23 shows a M-MOPA with single mode waveguide, edge emission and an integrated DBR semiconductor laser as master oscillator.

A variety of DFB/DBR diode lasers with appropriate performance characteristics is available at the telecommunication wavelengths 1310 nm and 1550 nm because of the huge demand. However, 1064 nm is a critical wavelength for diode laser and only so-called strained InGaAs material can be used. Output power in the order of 100 mW is available from commercial strained InGaAs DFB or DBR laser diodes, but these devices are usually quoted preliminary products and SDL, the largest diode manufacturer, even ceased the production because of too small customer interest. Also a laser linewidth of less than 5 MHz is a major problem because of the huge free spectral range of laser diodes as such.

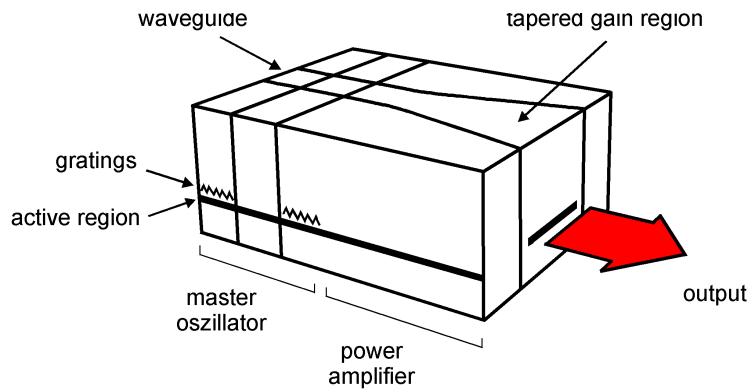


**Figure A.23** *M-MOPA with DFB semiconductor master oscillator*

#### A.5.2.5 Fibre laser

Development of diode-pumped fibre lasers is a fast growing field of research. Fibre lasers are very suitable and easy scaleable in laser power. However, the emission bandwidth is very high (several nm) and the fibre resonator is sensitive on temperature, stress etc. By the implementation of fibre Bragg gratings single-frequency operation was already demonstrated. However, the linewidths are around several MHz and not suitable for the LISA laser system. Also radiation hardening of doped fibres has only been investigated very barely and seems to be a major problem.

#### A.5.2.6 Master oscillator power fibre amplifier (MOPFA)

The non-resonant amplification of a low noise, low power master oscillator (e.g. NPRO or external cavity diode laser) is another approach to fulfil the LISA laser requirements. For this type of laser the radiation from the stable master oscillator is mode matched into the approximately  $10\text{ }\mu\text{m}$  wide inner core of a double clad fibre (see Figure A.24). This inner core consists of (e.g. Nd) doped glass.

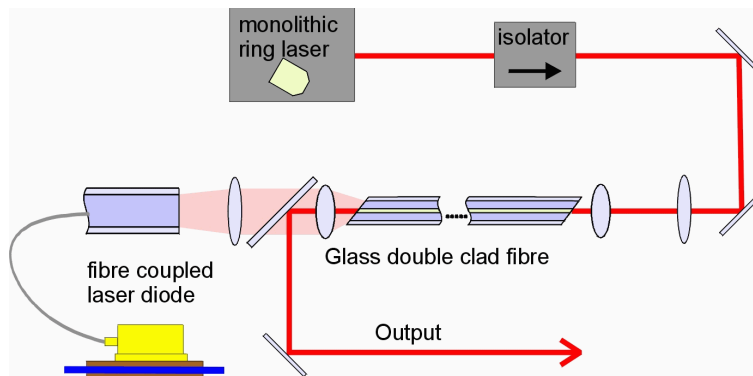


**Figure A.24** *Arrangement of master oscillator power fibre amplifier (MOPFA)*

The inner undoped cladding of the fibre, which serves as the pump core, has a diameter of several hundred  $\mu\text{m}$ . A silicone outer cladding protects the glass fibre and leads to a NA of approximately 0.4 for the pump light. The fibre amplifier is pumped with one laser diode bar, which is available with output up to 30 W at 809 nm. The light is matched into the outer core of the fibre.

The phase noise characteristics of the master laser are usually maintained through the amplification process, whereas the low frequency power fluctuations are significantly increased due to the noisy high power diodes. More than 5 W amplified emission at 1064 nm have been demonstrated using a 500 mW **NPRO** as the master oscillator and 25 W of 809 nm radiation. This corresponds to 20 % optical-to-optical efficiency. For the **LISA** mission the master laser power would be reduced to approximately 50 mW, suitable for high frequency phase modulation, which could be amplified to more than 4 W. The main drawback of the **MOPFA** system are its low efficiency and the large number of optical components that are fragile and costly to qualify. Also the high radiation sensitivity of the doped fibre is an unsolved problem.

### A.5.2.7 Concept selection

Table A.13 summarises the system properties of the different laser alternatives.

**Table A.13** *Laser Concept Trades*

	<b>NPRO</b>	Micro Chip Laser	External Cavity Laser	<b>DFB/DBR M-MOPA</b>	Fibre Laser	<b>MOPFA</b>
Power	+	0	-	+	++	++
Beam Quality	+	+	+	+	+	+
Power Stability	+	-	-	-	-	0
Frequency Stability	+	-	-	-	-	+
Efficiency	+	0	+	++	+	0
Physical Dimensions	+	++	+	++	++	0
Technology Status	+	0	-	0	-	+

++ meets the requirements with large margin, standard space component

+ meets the requirements, commercial product with potential for qualification

0 meets the requirements only with additional development, requires development

- does not meet requirement, requires basic technology development

Based on the advantages and drawbacks as shown in Table A.13 the **NPRO** laser concept is clearly identifiable as superior to the other alternatives and it is therefore selected as the baseline. However, the **MOPFA** concept shall be regarded as the second option, as no major obstacles are identified and the possibility of scaling the output to higher power is very attractive.

### A.5.3 Laser components identification and trades

Based on the laser concept selection as shown in the preceding section, trades for specific laser components have been performed. The following parts and components have been identified that are required for the utilisation of a laser diode pumped non-planar ringlaser (**NPRO**) for the **LISA** laser system:

- Laser crystal
- Laser diode pump source

- Pump light optics
- Electro-optic modulator (EOM)
- Faraday isolator
- Fibre coupler

#### A.5.3.1 Laser crystal

The only laser crystal material that has been taken into account is **Nd:YAG**, which stands for neodymium doped yttrium aluminium garnet. The reason for this are the unique laser specific properties of **Nd:YAG**, such as excellent thermo-optical properties and good quantum efficiency, combined with extensive space heritage.

Two different mechanical designs of the non-planar ring oscillator (**NPRO**) have been experimentally investigated regarding their suitability for the **LISA** laser system, the so-called “standard” design and the “**ETR**” design. The main difference is the overall dimension of the crystal and therefore the overall optical path length inside the laser resonator. The crystal dimensions are  $3 \times 8 \times 12 \text{ mm}^3$  for the standard geometry and  $2 \times 4 \times 7 \text{ mm}^3$  for the **ETR** geometry. The main advantage of the **ETR** is an increased mode-hop free tuning range of approximately 30 GHz. Also the optical to optical efficiency is slightly higher. The main drawback of the **ETR** geometry is the decreased size of the required pump radiation focus.

Due to the small laser focus that puts demanding constraints on the pump source beam quality, the baseline for the **LISA** laser system is the standard crystal geometry. However, an intermediate crystal design should be investigated.

#### A.5.3.2 Laser diode pump source

The two main options for the laser diode pump source are direct imaging of the radiation from the semiconductor chip into the laser crystal or application of fibre coupled laser diodes and imaging the radiation from the fibre end. The advantages of fibre coupled diodes are a separate thermal management of the laser system and the pump unit, the availability of higher pump power levels and the possibility of switching between more than two redundant devices. The advantages of direct pumping are infinitely small pump power losses and therefore high optical to optical efficiency and a rigid connection of the laser crystal and the pump that is insensitive to misalignment and introduces no additional optical components such as fibres and fibre couplers and no additional pump units.

As direct pumping can be done with two polarisation coupled laser diodes, sufficient pump power and redundancy are guaranteed. Therefore direct pumping is selected as the baseline for the **LISA** laser system.

A number of specific laser diodes have been experimentally investigated regarding their suitability for the **LISA** laser system. Firstly direct diode parameters have been measured and then the devices have been used to pump a **NPRO** laser crystal to determine laser threshold and optical-to-optical efficiency.

The laser Coherent laser diode is selected as the baseline for the **LISA** laser system, because the physical laser related properties are clearly superior to the other devices. Also, Coherent is the only manufacturer that uses aluminium free semiconductors for the diodes, which improve lifetime properties.

**Table A.14** *Experimental results on laser diode properties*

Laser Diode	Coherent S-81-3000C-200-H	Opto-Power D003-808-HB100	Siemens SFH 487401
Power [W]	3	3	1
Emitter Size [ $\mu\text{m}$ ]	200	100	100
(Half) divergence angle [ $^\circ$ ]	8	13	16
Treshold [mA]	611	4000	400
Electrical-optical Efficiency [W/A]	1.0	0.5	0.6
<b>FWHM</b> Linewidth [nm]	1	1	1.5
<b>NPRO</b> threshold [mW]	130	196	235
Optical-optical Efficiency [%]	66	50	42
Qualificatio aspects investigated	No	No	YES

#### A.5.3.3 Pump light optics

The collimation and of the pump radiation is done with a aspherical, plano-convex fused silica lenses per diode. The two collimated beams are combined on a polarising beam splitter and focused into the laser crystal with a single aspherical, plano-convex fused silica lens.

No alternatives to this pumping scheme have been identified. The redundancy concept appears sufficient with respect to the expected lifetime and reliability figures of then available pump laser diodes. It could be further improved, if necessary, by using fibre coupled pump units and fiber switches for example.

#### A.5.3.4 Electro-optic modulator (**EOM**)

In the Pre-Phase A design, the phase modulator was placed on the optical bench. Another option is to have the phase modulator placed inside the laser head. Figure A.25 shows the two options. Table A.15 summarises the advantages and the drawbacks for the two options.

Based on these advantages and drawbacks the second option, phase modulator inside the laser head, has been identified as superior and selected as the baseline for **LISA** laser system.

#### A.5.3.5 Faraday isolator

A Faraday isolator is required to suppress back reflection into the laser crystal. Any light that is redirected to the crystal must be attenuated by at least 26 dB or it will lead to self injection locking phenomena and disturb the single frequency operation. Two options for the Faraday isolator have been identified:

- A fibre-optic isolator
- Free space beam isolator.

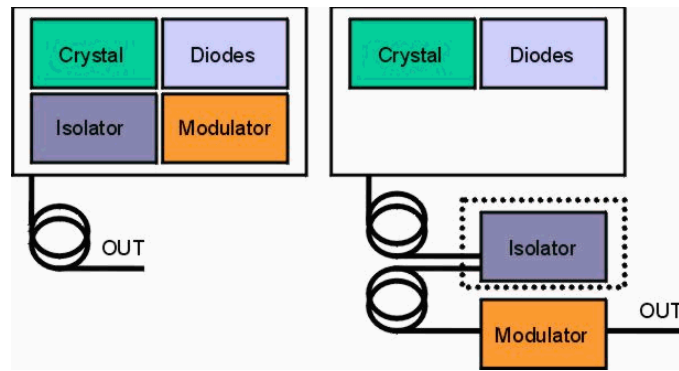


**Figure A.25** Options for the laser head (left : baseline; right : Pre-Phase A, dotted box : option)

**Table A.15** Advantages and drawbacks for the phase modulator placement options

Option	Advantages	Drawbacks
PM on optical bench	Reduced mass and size Mechanical stability Simple design	Modulator development High coupling losses
PM inside laser head	Standard modulator use Low coupling losses	Complex design Increased mass and size

As the baseline for the EOM foresees the location of the phase modulator inside the laser head, the baseline for the Faraday isolator must be a free space beam isolator inside the laser head.

#### A.5.3.6 Fibre coupler

Two options have been evaluated for the fibre coupler : A standard fibre coupler with a movable lens in combination with a rigidly fixed fibre end and secondly a movable fibre end with a lens permanently glued to the fibre. The advantage of the former is a high maximum coupling efficiency ( $\approx 100\%$ ). The latter has the advantage of low sensitivity to misalignment, a coupling efficiency of more than  $80\%$  is possible.

A fibre coupler with a movable fibre end with a lens permanently glued to the fibre is selected as the baseline.

#### A.5.4 Photodiodes

Table A.16 lists the photodiodes that have been identified for use in the laser subsystem. Those devices are not space qualified; nonetheless, the manufacturer has qualified similar devices for particular programs.



**Table A.16** *Photodiodes for use in the laser subsystem*

Diode	Type	Model	Purpose
p1	InGaAs PIN	EG&G C30619G	Laser phase locking
p2	InGaAs PIN	EG&G C30619G	Laser frequency stabilisation
p3	InGaAs PIN	EG&G C30665G	Laser power stabilisation

**Table A.17** *EG&G photodiodes characteristics*

Part #	$\phi_{\text{active}}$ (mm)	Responsivity (A/W)		$I_d$ (nA)	NEP (pW/ $\sqrt{\text{Hz}}$ ) (c)	$C_d$ (pF) (d)	$BW$ (MHz) (e)	$P_{\text{max}}$ (dBm)	Bias (V) (b)
		(a)	(b)						
C30619G	0.5	0.2	0.86	5	8	350	> +13	5	< 0.1
C30665G	3.0	0.2	0.86	25	1000	3.0	+11	0	0.2

(a): at 850 nm; (b): at 1300 nm; (c): at 100 kHz; (d): into 50  $\Omega$ ; (e): for 0.15 dB linearity

## A.6 Telescope

### A.6.1 Telescope design drivers

#### A.6.1.1 Performances and interface requirements

The design drivers considered for the telescope definition are the following:

- afocal design,
- imaging quality (performance to be met at end of life in-orbit over the full field of view)
  - emitted beam: wavefront error better than 35 nm rms ( $\lambda/30$  rms at  $1.06\ \mu\text{m}$ )
  - received beam: wavefront error better than 90 nm rms ( $\lambda/12$  rms at  $1.06\ \mu\text{m}$ )
- straylight minimisation on both acquisition and coherent sensors,
- mechanical interface ( $\varnothing$  360 mm cylinder), overall mechanical envelope minimisation.
- afocal magnification  $g_\alpha = 60$  ( $g_\alpha = 30$  acceptable if the performance requirements can not be met with a  $g_\alpha = 60$  design),

The FOV considered for telescope optical design is  $\pm 10\ \mu\text{rad}$ , according to the analysis in Section 7.1.1.

#### A.6.1.2 Telescope thermal environment

The main characteristics of the telescope thermal environment are:

- an operational temperature estimated to  $-15^\circ\text{C}$ ,
- an considerable longitudinal gradient between the primary mirror, located close to the optical bench thermal shield, and the secondary mirror close to the space aperture,
- an expected change over life time of  $5^\circ\text{C}$  (from Pre-Phase A study).

The telescope will therefore work far from its alignment temperature and in presence of considerable gradients. This is of major importance for the determination of the structure and mirrors materials.

The telescope short term thermal stability will depend on its decoupling from the environment. A high decoupling shall be preferred to improve the telescope intrinsic stability performances.

### A.6.2 Review of possible optical and mechanical telescope designs

#### A.6.2.1 Possible optical designs

This section presents the possible optical designs a priori compatible with the LISA telescope requirements. The next section (A.6.2.2) will then review the materials and technologies available to manufacture the mirrors and structures corresponding to the possible optical designs, and assess their performances.

A two-mirrors design enables to meet the required imaging performance over the narrow FOV. Optical designs with convex or concave secondary mirrors can be considered:

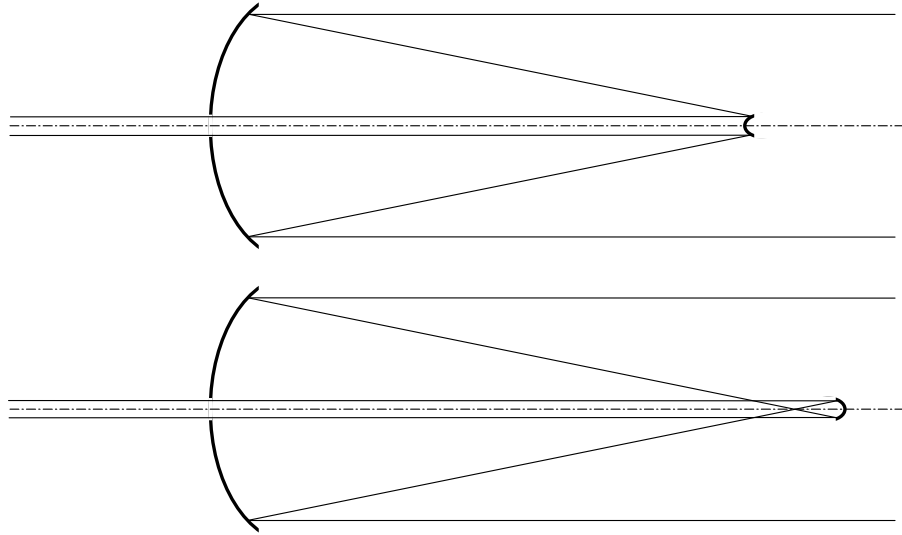


**Figure A.26** Telescope design with convex (upper figure) or concave (lower figure) secondary mirror

Remark: because of the afocal design, the primary and the secondary mirrors have the same numerical aperture.

Two optical combinations can be considered to meet the required performance:

- Cassegrain type design:
  - both [M1](#) and [M2](#) are parabolic,
  - design corrected of all primary order aberrations but field curvature.
- Dall-Kirkham type design:
  - quasi parabolic [M1](#) ( $K \approx -0.97$ ),
  - spherical [M2](#),
  - design corrected on-axis from spherical aberration, coma in [FOV](#).

The Cassegrain telescope features the best imaging quality for a two mirrors afocal design. The small [LISA](#) telescope [FOV](#) however enables to consider a design not corrected from field aberrations. The main advantage of the Dall-Kirkham design is its spherical [M2](#), which enables an easy and cost effective high quality manufacturing.

The performances achievable with both designs will be compared in the next sections, taking into account the mirrors' achievable [WFE](#) and roughness as well as the imaging quality sensitivity to aberrations induced by initial alignment and long term effects.

#### A.6.2.2 Primary mirror technologies and related performance

The primary mirror will be aspherical (parabolic or elliptical).

##### Zerodur mirrors

A mirror [WFE](#) of 25 nm *rms* can be considered the best achievable quality for a 300 mm diameter parabola of 1.2 to 1.5 numerical aperture made of Zerodur or [ULE](#). Such a performance requires a final polishing step using ion beam figuring. A roughness of 10 Å can be obtained.

The [SILEX](#) terminals primary mirrors are representative of the ultimate polishing performance obtained on Zerodur. The mirrors are 250 mm diameter, 1.5 numerical aperture parabola, which

have been polished using ion beam figuring to a 28 nm *rms* WFE and feature a 10 Å roughness (performances at mirrors delivery).

### SiC-100 mirrors

The polishing of SiC-100 is comparable to glass polishing. A thin layer of SiC CVD (50 to 100  $\mu\text{m}$ ) is applied on the SiC-100 substrate after grinding, in order to overcome the residual intrinsic porosity of the bulk material and obtain low scattering performances. The achieved polishing equals that achieved on glass and exceeds it when ion beam figuring is used for the final polishing. A WFE of 8 nm *rms* is achievable with a 10 Å roughness for a 300 mm diameter parabola of 1.2 to 1.5 numerical aperture.

The DetelSiC primary mirror (diameter 200 mm, numerical aperture 1.46, asphere  $K = -0.96$ ) is representative of the polishing quality achievable with ion beam figuring for the LISA telescope primary mirror. A WFE of 5.4 nm *rms* has been obtained, corresponding to  $\lambda/196$  at 1.06  $\mu\text{m}$ .

Remark: this higher efficiency of the SiC ion beam polishing is due to the material's high thermal conductivity which avoids local surface distortions.

#### A.6.2.3 Secondary mirror achievable performance

The polishing quality achievable for the secondary mirror depends on the selected optical design as well as on the mirror material.

- The secondary mirror can be either convex or concave. For a small parabola, discussions with mirrors manufacturers show that there is no major feasibility difference between a convex and a concave shape. The concave shape requires an additional optics to be tested (Hindel sphere), which manufacturing is not challenging nor cost driving for a small mirror. A concave secondary mirror is therefore preferred, as it enables to minimise the telescope overall mechanical envelope.
- In the case of a Dall-Kirkham design, the secondary mirror is spherical. There is then no diameter limitation, and a 8 nm WFE *rms* polishing quality is achievable on Zerodur or SiC with a surface roughness of 5 to 10 Å.
- In the case of a Cassegrain design, discussions with optics manufacturers have enabled to estimate the feasibility limits of a 1.2 to 1.5 numerical aperture high quality parabolic mirror:
  - a 10 mm diameter mirror (required in the  $g_\alpha = 30$  option) can be manufactured with a 15 nm *rms* WFE and 10 Å roughness (challenging but achievable target for a Zerodur or SiC mirror),
  - a 5 mm diameter mirror (required in the  $g_\alpha = 60$  option) can be manufactured with a 25 nm *rms* WFE and 15 Å roughness.

Remark: ion beam figuring can not be used for the secondary mirror polishing as the mirror is too small with respect to the ion beam diameter (about 10 mm).

#### A.6.2.4 Structure design and performances

##### Main structure requirements

The telescope structure shall:

- ensure constraints-free interfaces to the mirrors so that their initial WFE and alignment is not jeopardised by mechanical stresses,

- minimise external straylight (due to sun illumination) and internal straylight (retro-reflection of the emitted beam toward detectors),
- provide a high long term relative stability between both mirrors, as well as between the telescope and the payload structure, taking into account the [LISA](#) mission environments (thermal interfaces, launch loads etc.),
- feature low mass / high stiffness performances,
- minimise costs.

### Selection of the structure material

A high long term stability is required to maintain the imaging quality performance over the life time, which limits the choice of the structure material to the followings:

- [CFRP](#), associated with Zerodur or [ULE](#) mirrors,
- Carbon-carbon, associated with Zerodur or [ULE](#) mirrors,
- [SiC](#), associated with [SiC](#) mirrors,
- Beryllium, associated with beryllium mirrors,
- Zerodur, associated with Zerodur mirrors.

[SiC](#) has been preferred after comparison of the figures of merits of these materials, taking into account their mechanical and thermal properties, as well as the cost aspects.

The major advantages of the [SiC](#) are :

- The cost, the [SiC](#) solution being the cheapest of the five listed above.
- The high specific stiffness (Young modulus over mass density or  $E/\rho = 420 \text{ GPa}/3250 \text{ kg m}^{-3}$ ) which allows a high level of alleviation, thus considerable mass savings. With respect to classical materials such as Zerodur, the mass saving is about 2 for the primary mirror. Only Beryllium alloys meet the [SiC](#) performance in this respect, but it shows out several drawbacks in terms of health hazard during manufacture and overall manufacturing costs.
- The high thermal distortion figure of merit, i.e. thermal conductivity over thermal coefficient of expansion or  $\lambda/\alpha = (160 \text{ W/mK})/(2 \times 10^{-6}/\text{K})$ . This ratio quantifies the impact of a thermal gradient on the deformation of the optical surface in steady state conditions. There again, the high thermal conductivity of the [SiC](#) coupled to a very low thermal expansion coefficient makes the [SiC](#) the best optical material, far above Beryllium alloys.
- The impacts of thermal transient can be quantified through an additional figure of merit which takes into account the specific heat of the material and the mass of the mirror, through the material mass density and its thermal conductivity. This figure is expressed as the ratio of the mass density times the specific heat times the thermal conductivity over the [CTE](#) ( $\rho C_p \lambda / \alpha$ ). The higher the figure, the better can the material either spread the heat in its bulk or store it with a minimum temperature change, thus minimum distortion. For this figure again, the [SiC](#) features the best behaviour.

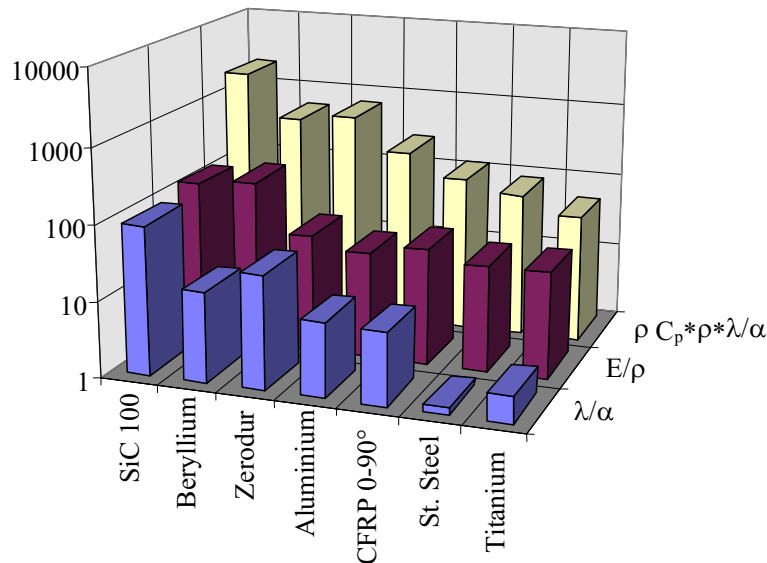
The [SiC](#) exhibits the best overall behaviour, as indicated by its first ranking for all figures of merit (for specific stiffness it is second to Beryllium alloy, but the [SiC](#) low [CTE](#) of  $2 \times 10^{-6}/\text{K}$  and high conductivity allows outstanding stability performances). Other fields of interest brought by [SiC](#) are the following:

- Total insensitivity to hygroelastic phenomena (moisture desorption) w.r.t. [CFRP](#) materials,
- ability to be polished to the highest [WFE](#) performance using ion beam figuring,

- good compressive holding and high friction coefficient ([SiC/SiC](#)) used for direct linkage compatible with stability criteria under launch environment (enabling mirrors central mount, thus minimising parts number),
- possible suppression of surface coating such as black painting due to high thermo-optical coefficient ( $\varepsilon = 0.8$ ).

**Table A.18** *Relative materials mechanical properties*

Material	Density (kg/m <sup>3</sup> )	Young's Modulus (Gpa)	Stiffness-to- Weight Ratio (10 <sup>6</sup> Nm/kg)	Thermal Conductivity (W m <sup>-1</sup> K <sup>-1</sup> )	CTE (10 <sup>-6</sup> /K)
<a href="#">SiC</a>	3200	420	131	170	2
Aluminium (2024)	2800	70	25	225	24
Beryllium	1850	304	164	220	11
Titanium (TA-6V)	4430	110	25	7.2	8.6
<a href="#">CFRP</a> (GY70 Isotropic)	1800	100	56	35	0.02
Zerodur	2530	91	36	1.6	0.05

**Figure A.27** *Relative figures of merit of the most space usual materials*

### Identification of an alternative structure material

The all-Zerodur design has been successfully used for the [SILEX](#) program. It is however discarded for the [LISA](#) telescope as more recent materials enable to reach equivalent or better performances at lower costs.

The carbon-carbon solution is also discarded for its much higher cost.

A telescope with a CFRP structure and Zerodur mirrors would feature high mechanical performances and excellent thermal stability, which makes this solution a technically valid alternative to the SiC design. But though cheaper than the above listed solutions, it remains more expansive than the all SiC design. The CFRP + Zerodur design is therefore considered as a back-up for the telescope design.

### Selection of the mechanical design

**Primary mirror design** Designs based on a structural primary mirror are rejected, as they are not compatible with high WFE performances. The telescope design will instead include a baseplate supporting the primary mirror as well as the secondary mirror spider structure. The primary mirror is linked to the baseplate by a central attachment, which is a compromise between several opto-mechanical aspects:

- mechanical stress under quasi-static load,
- mechanical stress under interface default and bolts preload,
- impact of mounting default on the WFE optical quality,
- impact of thermo-elastic effects due to local thermal gradient on the WFE optical quality.

This design enables to limit the impact of mounting distortion on mirror WFE to 5 nm *rms* (verified on the representative Ø 200 mm DetelSiC demonstrator).

In a conservative approach, the lightweighting ratio proposed for the primary mirror is of 0.4, which leads to a quite massive mirror and takes a maximum benefit of the SiC conduction to minimise potential thermal gradients impact on WFE. According to the result of detailed thermal analyses, a 60 % lightweighted primary mirror could be considered, enabled by the SiC stiffness.

**Secondary mirror support** The low mass of the secondary mirror ( $\approx 20$  g) enables to consider two solutions for the M2 supporting structure:

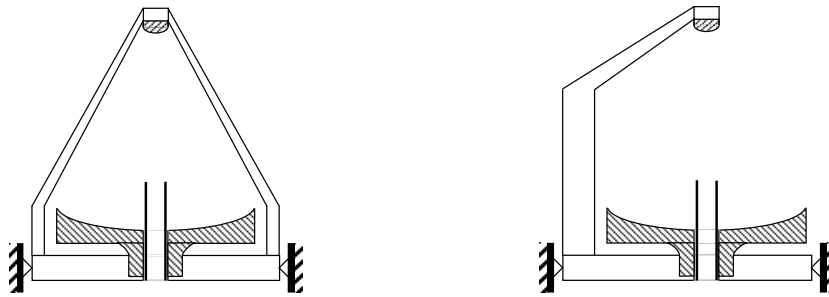


**Figure A.28** left: Concept 1, three-legged spider, as in PPA 2 [1]; right: Concept 2, one mast, as in FTR [2]

Both concepts are compatible with a SiC structure. The mast design however features the following advantages with respect to the spider one:

- reduction of the number of structure elements inducing costs saving,
- straylight minimisation.

The mast design is therefore preferred.

Remark: a classical three spiders design is also compatible with the SiC design and remains a possible back-up if strong short term thermal fluctuations shift the optical axis and induce



pointing bias and jitter. The high SiC thermal conductivity should however minimise this type of effect.

**Telescope baffling** In addition to the interface tube preventing any direct solar illumination on the telescope, an internal baffle is foreseen to minimise the straylight that could reach the optical bench after diffusion on the interface tube. The length of this internal baffle is set a priori to 70 mm from M1 apex, this value being to be optimised according to detailed optical assembly straylight studies. The internal baffle will be made of black painted aluminium, and be attached to the interface plate.

### Alignment principle and performances

The proposed alignment principle aims at reducing the number of components. For that purpose, all alignments are performed at the secondary mirror assembly level:

- the primary mirror will be mounted on the telescope baseplate. There are no alignment capabilities at this level, but tight M1 interfaces manufacturing tolerances will be required (typically 0.05 mm),
- the secondary mirror will be aligned with respect to the M1 using appropriate focus shims and step by step eccentrics. The angle of the focus shim will enable to adjust the mirror tilt.

During the alignment, the telescope will be in auto-collimation in front of an interferometer (for example Zeiss D100 featuring a  $\lambda/100$  resolution), and the imaging quality will be monitored for each iteration. The alignment criteria will be the minimisation of focus and coma aberrations.

The following alignment accuracy can be achieved:

- adjustment of the inter-mirrors distance  $\pm 3 \mu\text{m}$
- M2 / M1 centring resolution  $\pm 10 \mu\text{m}$
- M2 / M1 tilting resolution  $\pm 300 \mu\text{rad}$

It is to be noted that M2 / M1 tilt and decentring both induce coma aberration. The residual M2 tilt will therefore be compensated by a M2 decentring (within centring resolution).

### Long term stability

The long term stability of the telescope imaging quality covers all WFE evolutions from end of on-ground alignment to in-flight end of life.

The effects to be considered for the long term stability performance are the following:

- microsettling due to launch loads,
- thermal effects (impact of homogeneous temperature variations and gradients),
- gravity release (alignment under 1 g, operation at 0 g),
- radiations.

**Microsettling** Though no detectable microsettling has been observed on the available SiC structures, an allocation corresponding to a  $0.5 \mu\text{m}$  IMD variation and a  $2 \mu\text{m}$  M2/M1 lateral shift is considered for the telescope performance analyses. These figures, conservative in the case of a all-SiC telescope, are deduced from the maximum displacements observed at the optical equipments interfaces for both SILEX and GOMOS instruments.

**Thermal stability** The all-SiC telescope has a homothetic dilatation under homogeneous temperature changes which has no impact on the imaging quality. The influence of gradients is minimised thanks to the material high thermal conductivity. Both homothetic behaviour and gradients resistance have been experimentally verified on the DetelSiC telescope:

- no WFE impact over a  $-100^{\circ}\text{C}/+ 60^{\circ}\text{C}$  uniform temperature range,
- $\Delta T$  of  $5^{\circ}\text{C}$  between M1 and M2 in a  $100^{\circ}\text{C}$  gradient environment.

A conservative allocation of  $1\ \mu\text{m}$  IMD variation,  $5\ \mu\text{m}$  M2/M1 lateral displacement is however considered for the stability estimation, to be replaced by the results of a detailed thermo-elastical analysis when thermal data are available.

**Gravity release** A FEM mechanical analysis of DetelSiC telescope enables to estimate the gravity release worst case influence on the LISA telescope alignment and imaging quality:

- |                                |                    |
|--------------------------------|--------------------|
| - IMD variation                | $1\ \mu\text{m}$   |
| - M2 / M1 lateral displacement | $6\ \mu\text{m}$   |
| - M1 WFE distortion            | $5\ \text{nm rms}$ |

The gravity release impact on IMD will be compensated by refocalisation on the emitted path, which is not the case for the lateral displacements. A vertical telescope orientation during the alignment however enables to minimise the lateral displacements induced by gravity release.

**Radiations** It has been verified experimentally that a SiC telescope imaging quality shows no sensitivity to radiations. A SiC-100 mirror has been irradiated (200 Mrad of gamma rays) without showing a measurable WFE distortion.

The long term telescope structural stability taken into account for the performances assessment is then the following (quadratic summation of contributors):

- |                                |                    |
|--------------------------------|--------------------|
| - IMD variation                | $1.6\ \mu\text{m}$ |
| - M2 / M1 lateral displacement | $8\ \mu\text{m}$   |
| - M1 WFE distortion            | $5\ \text{nm rms}$ |

The refocalisation capability implemented on the emitted beam optical path enables to correct the IMD errors due to the initial alignment and to the long term stability. An allocation of  $1\ \mu\text{m}$  for a residual IMD error is however considered for the performances evaluations, which covers the accuracy of the focus correction as well as the acceptable focus evolution between two focus corrections.

### A.6.3 Selection of the telescope optical design

This section proposes a performance analysis of both Cassegrain and Dall-Kirkham designs according to the mirrors f-numbers, assuming the following hypotheses (from above sections).

All optical performances have been computed using the CodeV software.

The imaging quality requirement being more stringent on the emission path, the reception path is not taken into account for the design versus performance trade-off. The performance on the reception path will only be computed for the selected design. It is therefore assumed for all following performances computations that the focalisation is optimised with a residual  $1\ \mu\text{m}$  error.

The optical aberrations and sensitivities to M1/M2 decentring depend only on the mirrors numerical apertures so the only distinction between the  $g_{\alpha} = 30$  and  $g_{\alpha} = 60$  designs is the mirrors manufacturing limits. This is why the same performance is achieved whatever the  $g_{\alpha}$  in the case of the Dall-Kirkham design.

The choice of the telescope mirrors aperture is made taking into account the imaging performance as well as the telescope overall mechanical envelope.

The Dall-Kirkham design is preferred for its simpler and cheaper secondary mirror. It enables to reach a 60 magnification ratio with the required performances for a telescope numerical aperture set to  $N=1.4$ , which leads to a design in line with the telescope envelope current hypotheses (550 mm).

#### A.6.4 Design and performance summary

##### A.6.4.1 Optical design and performance

The baseline telescope optical design is a Dall-Kirkham lay-out, with  $g_\alpha = 60$  and  $N=1.4$  mirrors apertures.

##### A.6.4.2 Mechanical design and mass budget

The drawing Figure A.29 corresponds to the baseline SiC design described above.

The telescope interfaces with the payload structural tube using tangential titanium blades featuring an isostatic interface. These blades also provide a high conductive decoupling with respect to the tube (the mechanical and thermal design of these fixations has been validated on the Meteosat SEVIRI telescope). If the tube diameter is to be maintained at 360 mm, a slight decentring (27 mm) between the tube axis and the optical beam is necessary. This decentring is suppressed if the tube diameter can be increased to 400 mm. The following drawings take into account the 360 mm diameter hypothesis.

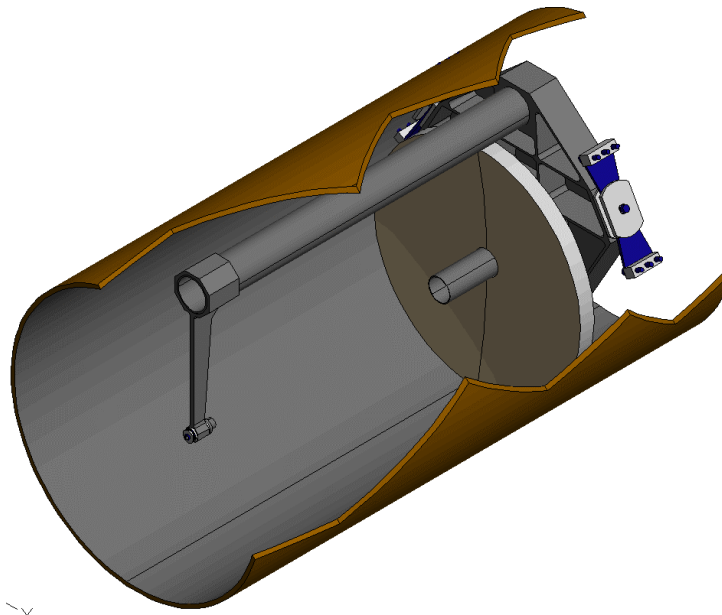


**Figure A.29** *LISA telescope, version with one-mast mounting*

On the basis of the above mechanical design, a telescope mass budget has been estimated:

	Baseline : 40 % lightweighted M1	60 % lightweighted M1 hypothesis
Primary mirror	3.2 kg	2.1 kg
M1 fixation ring	0.2 kg	0.2 kg
Secondary mirror	0.02 kg	0.02 kg
Mast and M2 support	0.7 kg	0.7 kg
Baseplate	1.6 kg	1.6 kg
Isostatic mountings	0.6 kg	0.6 kg
Baffle, bolts etc.	0.3 kg	0.3 kg
Total	6.6 kg	5.5 kg

## A.7 Line-of-Sight Orientation Mechanism

The angle under which one spacecraft sees the other two varies through the year by about  $\pm 0.6^\circ$ . The line-of-sight pointing must therefore allow an orienting mechanism, which had in the PPA 2 been realised by a flexure mechanism at the end of the optical assemblies, see Section 8.2.1.

Here is a description of the newly adopted line-of-sight orientation mechanism as proposed in the Industrial Study [2].

In line with the nomenclature used in that Study (and in contrast to the preceding appendix, A.6), the term *telescope* will mean *the whole optical assembly*, i.e. optical bench, inertial sensor, structural elements, payload cylinder, thermal shield, flexure mechanism, and the ‘telescope’ in the narrower sense.

### A.7.1 Configuration

The fine pointing of the two telescopes can be realised :

- either by combining a single-axis mechanism, controlling the angle between the telescopes, with the FEEP thrusters controlling the attitude of the entire spacecraft,
- or by dedicated two-axis mechanisms for each telescope

Indeed, a mechanism is at least required to control the angle between the telescopes; this angle is a DOF not controllable by the S/C attitude. Indeed the geometrical configuration of the three LISA satellites is not a constantly perfect equilateral triangle. The spacecraft constellation slowly evolves in time, demanding a fine control of the relative angle between counterpart spacecraft lines of sight.

For LISA, the proposed telescope pointing architecture is the following :

- Use of the attitude control to realise a complete pointing of one telescope – let’s call it telescope A – and of the off-plane angle of the second telescope (telescope B).
- Use of a mechanism to control the in-plane angle of telescope B.
- Implement a spare mechanism on telescope A, so that the roles of telescope A and B can be switched in case of failure.

The resulting architecture is illustrated in Figure A.30.

This choice is based on the ability to perform the fine pointing with the thrusters, without inducing any new or more stringent requirement on the FEEP propulsion. Then, three of the four DOF will be maintained through the 3-axis attitude control.

The objective of this section is to present the mechanism controlling the fourth DOF, independent from the S/C attitude. The following aspects are addressed :

- short synthesis of the requirements applicable to the mechanism
- review of the candidate architectures and design drivers
- identification of a mechanism reference concept : architecture, components
- identification of the component achievable performance
- dynamic simulation, implementing the mechanism components characteristics
- assessment of the overall pointing performances and verification of the adequacy of the mechanism and its control scheme with respect to the performance requirements.

All these points will indicate to which extent the telescope orientation system is feasible and what are potential key issues.

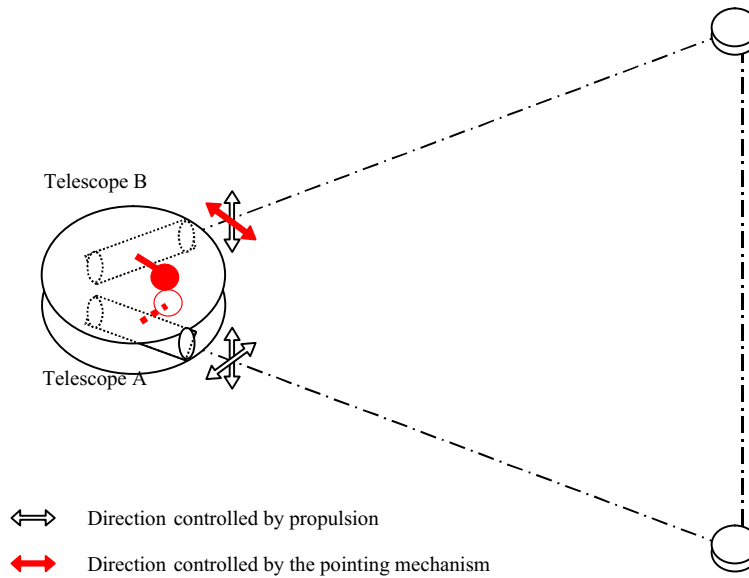


**Figure A.30** Control of the telescope pointing *DOF*

### A.7.2 Pointing mechanism requirements

The main mechanism requirements are indicated hereafter :

- Angular range :
  - overall angular range:  $1^\circ$ . This is driven by the seasonal variations of the three-spacecraft constellation.
  - scanning range:  $\pm 6 \mu\text{rad}$  for the counterpart spacecraft LOS acquisition
- Angular rate :
  - acquisition :  $\pm 20 \text{ nrad/s}$ . This is driven by the requirement to scan the  $12 \mu\text{rad}$  acquisition angle in less than 10 min
  - operational : up to  $\pm 3.5 \text{ nrad/s}$ . This corresponds to the maximum seasonal deformation rate of the constellation (sine motion; magnitude  $1^\circ$ ; period : one year).
- Absolute accuracy : better than  $1 \mu\text{rad}$ . This contributes to the scan angle extension. The current allocation to the mechanism is 10 % of the overall scan angle.
- Angular resolution and noise :  $0.5 \text{ nrad}$
- Stability/noise : based on the instrument performance template
  - allocation :  $0.7 \text{ nm}/\sqrt{\text{Hz}}$  above 40 mHz
  - *rms*: TBD ( $20 \text{ nrad}$ )
- stiffness in operational configuration : around 0.5 Hz. This requirement is selected in order to set the first mechanism resonance higher than the MBW. Conversely, it is selected low enough for allowing active damping by the control loop if required. A priori, such a value is consistent with the heterodyne detector bandwidth. This assumption would need further evaluation and analysis at sensor level.
- Life time : 2 years. Provision for 10 years is considered.

## Telescope mass properties

The mechanism steers the whole optical assembly, here termed ‘telescope’. The following mass properties are assumed:

- mobile mass: 33 kg
- telescope inertia around the centre of mass:  $1.5 \text{ kg m}^2$
- telescope inertia around furthest pivot (PPA 2):  $15 \text{ kg m}^2$ .

## Mechanical environments

The mechanism shall survive the launch loads and shall be fully operational in orbit, with the performances specified before. The assumptions considered with regard to the launch environment are:

- launch: 20 *g* quasi-static
- qualification level: 25 *g*
- sizing level: 30 *g*

In the frame of the study, the critical components of the mechanism are sized considering 30 *g* quasi-static load, assuming that the random levels will not be more critical.

Combined with the telescope mass (33 kg), the mechanical loads are:  $30 \text{ g} \times 33 \text{ kg} = 10\,000 \text{ N}$ .

## A.7.3 Mechanism design drivers

### A.7.3.1 Mechanism complexity.

In general, the launch loads cannot be withstood by the critical elements (guiding), requiring the accommodation of a launch locking device (LLD). The main purpose of the LLD is to avoid the launch loads to pass through the critical elements. Conversely, such accommodation leads to more complex mechanism design, both in terms of analysis (hyperstatic configuration) and hardware: the LLD is in fact a second mechanism. The cost impact is important.

Despite the large mass of the telescope (33 kg), a design without LLD is identified, as shown in the following feasibility assessment.

### A.7.3.2 Location of the rotation axis

The location of the rotation axis with respect to the centre of mass has two main impacts:

- static unbalance: generates disturbing torques during launch
- self gravity, considering the proof masses sensitivity during in-orbit operations.

### A.7.3.3 Actuation resolution

The actuation resolution and noise (0.5 nrad typ.) is very demanding, compared to the angular motion range required ( $1^\circ$ ). This corresponds to a motion dynamics of:

$$1^\circ / 0.5 \text{ nrad} = 35\,000\,000.$$

This is far from the ‘usual’ pointing mechanisms, even for the most constraining applications. This can be compared to high performance steering mechanisms (mirror steering), requiring resolution of few  $\mu\text{rad}$  over  $30^\circ$  typ (motion dynamics = 100 000). The LISA telescope pointing requires motion dynamics three orders of magnitude larger than ‘state-of-the-art mechanisms’; LISA is a very challenging application.



### A.7.4 Location of the centre of rotation.

Three configurations were considered and compared :

- remote centre of rotation
- balanced configuration : rotation axis near the telescope center of mass
- minimum self-gravity oriented : rotation axis near the proof-mass location.

The static unbalance is the separation distance between the rotation axis and the telescope centre of mass. Considering the launch environment, static unbalance generates torques to be compensated to avoid the rotation of the telescope. The selection of small static unbalance is favourable with regard to the design of the device aiming at blocking the telescope rotation during launch.

#### A.7.4.1 Architecture 1 : remote centre of rotation

This (original) configuration [1], illustrated in Figure A.31, does not feature decisive advantages. The drawbacks are:

- the large static unbalance generates high torques during launch. Assuming a static unbalance of 0.5 m, this corresponds to a torque of:  $10 \text{ kN} \times 0.5 \text{ m} = 5\,000 \text{ Nm}$
- generates large self-gravity variations
- corresponds to higher telescope inertia

The large unbalance will require the accommodation of a LLD to withstand high torques during launch.

#### A.7.4.2 Architecture 2 : balanced configuration

This configuration is illustrated in Figure A.32. The rotation axis is selected to include the telescope centre of mass. The purpose is to minimise the static unbalance, ideally down to 0. Residual unbalance in the range of few mm ( $d = 3 \text{ mm}$  for instance) is easily achievable, leading to torques during launch of:

$$C = F \cdot d = 10 \text{ kN} \times 0.003 \text{ m} = 30 \text{ Nm}$$

Assuming the accommodation of a blocking element at 0.5 m, this leads to a blocking force of 70 N, which can be provided by a lot of available, simple, small-volume devices. All the launch load passes through the rotation axis (10 kN). The design of the spacecraft structure shall provide 'hard' points at that location.

The possible drawback is related to the self-gravity if the proof mass is not located at the vicinity of the telescope centre of mass. By design, the separation between the proof mass and the telescope center of mass shall be limited to a few cm.

#### A.7.4.3 Architecture 3 : centre of rotation near proof mass

This configuration is illustrated Figure A.33. The rotation axis crosses the proof mass, minimising the self-gravity variations. This configuration corresponds to a static unbalance of TBD (10 cm max.), generating torque during launch of 1000 Nm (TBC). Loads of 2000 N shall be withstood by the rotational blocking device. Such a value is less favourable compared with the architecture 2, but does not lead to unfeasibility nor severe extra complexity.

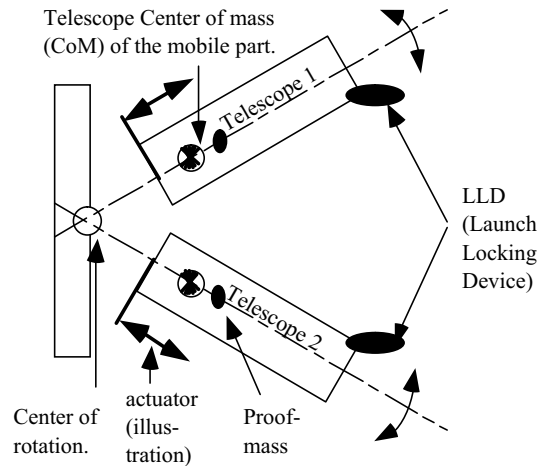


**Figure A.31** *'remote centre of rotation'*

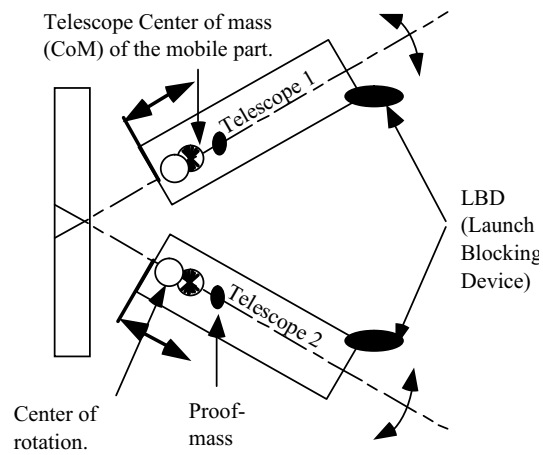


**Figure A.32** *'balanced configuration'*.

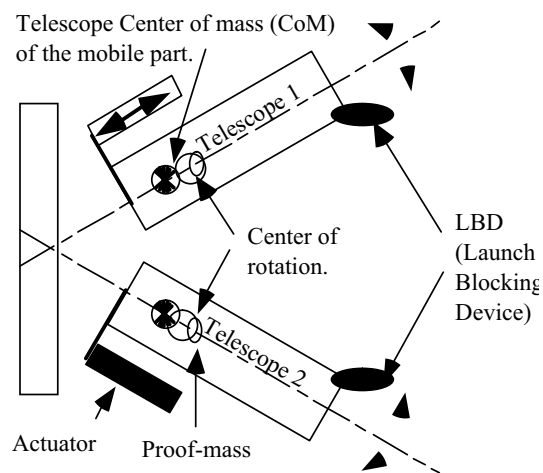


**Figure A.33** *self-gravity oriented : minimum variations.*

#### A.7.4.4 Conclusion

Considering the telescope internal architecture (proof mass location with respect to the telescope centre of mass), the architectures 2 and 3 seem equivalent. Architecture 2 is recommended and considered as the baseline in the following.

#### A.7.5 Candidate technologies

##### A.7.5.1 Actuators

The review of candidate actuators performed for the ‘Fibre Positioner Unit’ (see Section 3.9) is fully applicable and relevant for the telescope pointing application.

##### A.7.5.2 Bearings (guidance)

Considering the bearing (guidance) aspects, the selection of flexural pivots is mandatory due to the very small motion resolution required; for nanometer applications, guiding elements with friction shall be disregarded.

In order to assess the feasibility of the telescope pointing mechanism, standard components are first considered. In case key issues are identified, improvement areas of such components will be listed.

The usual procurement source for flex pivots is the Lucas company (US). R&T efforts were completed in Europe in the past years, allowing to have now alternative European procurement sources.

Considering the Lucas products, high load capability pivots are available, for instance Lucas 5032-400. The characteristics are :

- load capability : 7000 N per pivot
- torsional stiffness :  $\approx 50$  Nm/rad

The telescope guiding can be ensured by implementing a pair of such pivots. Such a pair is able to withstand the launch loads without additional support (LLD for instance). The torsional stiffness of the pair of the guiding element is 100 Nm/rad. Combined with the worst case telescope inertia ( $15 \text{ kg m}^2$ ), this leads to a mechanical eigenfrequency of 0.4 Hz. This resonance frequency is above the scientific measurement band and will not be detrimental to the measurement performance.

##### A.7.5.3 Sensing

A priori, no local sensing device is necessary at mechanism level. The LISA instrument delivers directly the LOS measurement which can be used by the controller to drive the mechanism. Sufficient sensor measurement bandwidth is expectable and can be used for actively damping the telescope eigenfrequency.

#### A.7.6 Mechanism concept

##### A.7.6.1 Performance apportionment

The mechanism design is driven by the very large motion dynamics requirement (40 000 000):

- resolution : 0.5 nrad

- range: 20 mrad ( $1^\circ$ )

A single stage mechanism cannot fulfil such a requirement. A two-stage design is mandatory, with some operational overlapping of the two stages. The apportionment is the following:

Stage	Motion range	Resolution	Dynamics
‘Fine’ stage	$0.5 \text{ nrad} \rightarrow 5 \mu\text{rad}$	0.5 nrad	10 000
‘Coarse’ stage	$0.5 \mu\text{rad} \rightarrow 20 \text{ mrad}$	$0.5 \mu\text{rad}$	40 000
Overlapping zone	$0.5 \mu\text{rad} \rightarrow 5 \mu\text{rad}$	1 ‘coarse’ stage step = 10 % of the ‘fine’ stage range	

The resolution and overlapping allocation aims at ensuring that the ‘coarse’ stage resolution corresponds to 5 to 10 % of the fine stage range capability.

#### A.7.6.2 Mechanism concept

The utilisation of direct drive (not amplified) piezo is compatible of the ‘fine’ stage specification, both in terms of resolution and range.

The telescope overall geometry indicates that a translation mechanism can drive the telescope rotation via a lever arm  $R$ . This is possible in accordance with the overall angular range ( $1^\circ$ ).

The lever arm selection is limited by the following aspects:

- bulkiness: the lever arm shall remain smaller than 300 to 400 mm
- telescope diameter: does not allow accommodation of the mechanism at less than 150 mm of the telescope axis.

Therefore, the selected lever arm is  $R = 200 \text{ mm}$  (TBC).

After selection of the lever arm, the performance apportionment between the two stages (rotation) can be translated into translation requirements, relevant for translation actuators.

For  $R = 0.2 \text{ m}$ , we get:

Stage	Motion range	Resolution	Dynamics
‘Fine’ stage	$0.1 \text{ nm} \rightarrow 1 \mu\text{m}$	0.1 nm	10 000
‘Coarse’ stage	$0.1 \mu\text{m} \rightarrow 4 \text{ mm}$	$0.1 \mu\text{m}$	40 000
Overlapping zone	$0.1 \mu\text{m} \rightarrow 1 \mu\text{m}$	1 ‘coarse’ stage step = 10 % of the ‘fine’ stage range	

Various mechanism architectures were reviewed and compared.

The two main candidate families are:

- ‘fine’ and ‘coarse’ stages in series,
- ‘fine’ and ‘coarse’ stages in parallel.

Concerning the ‘coarse’ stage, the main candidate solutions are:

- spindle-nut,
- voice-coil.

The voice-coil solution would require a linear sensor, as the voice coil generates a force and not directly a position. In that respect, the spindle-nut candidate is the most promising one and its feasibility is further analysed. The coarse ‘stage’ motion resolution is very small:  $0.1 \mu\text{m}$ , not directly achievable with a spindle-nut assembly; a linear motion reducer shall be added.

Classical reducers with gears and friction (at least in the guiding elements) shall be disregarded. The ‘elastic’ reducer principle is very attractive for the application.

Finally, the reference mechanism principle is illustrated in Figure A.34. It includes the two actuators :

- direct drive piezo for the ‘fine’ stage
- spindle-nut drive for the ‘coarse’ stage, driven by a stepper motor

combined with mechanical compliance/stiffness :

- flex pivots, supporting the telescope and featuring torsional stiffness :  $k_{\text{flex}} = 100 \text{ Nm/rad}$  typically.
- Piezo transmission :  $k_{\text{fine}}$ .
- Spindle-nut head transmission :  $k_{\text{head}}$ .

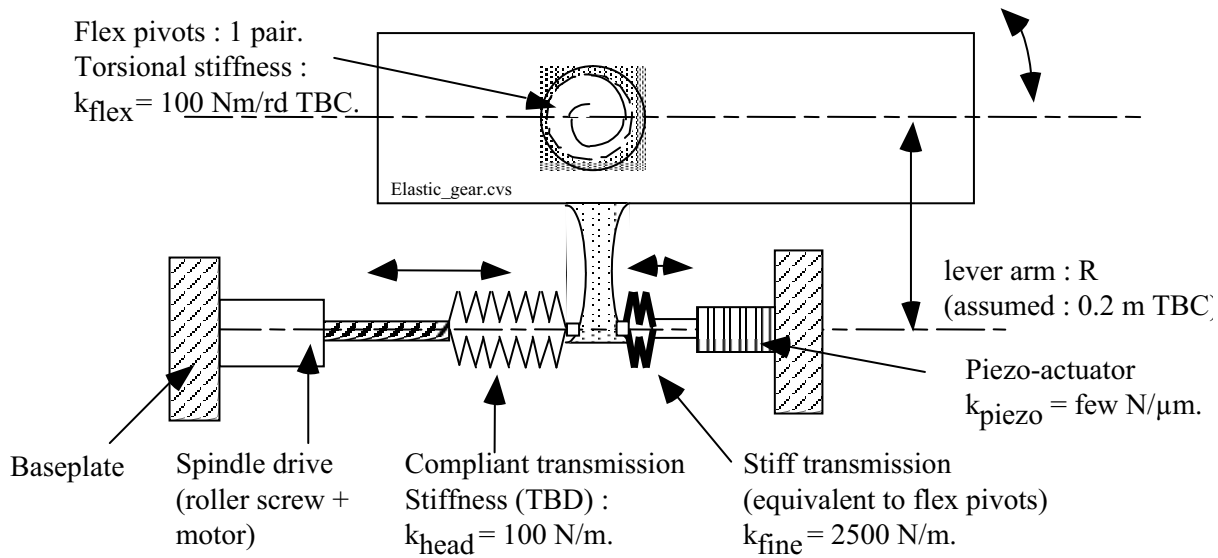


**Figure A.34** Telescope pointing : reference mechanism principle.

The flex pivot torsional stiffness can be translated into equivalent translation stiffness at actuators level:

- $k_{\text{flex}} = 100 \text{ N m/rad}$
- $R = 0.2 \text{ m}$
- Equivalent to :  $k'_{\text{flex}} = k_{\text{flex}}/R^2 = 2500 \text{ N/m}$

In order not to require large increase of the piezo motion range, the following is selected :

- piezo transmission : stiff, equivalent to the flex pivots stiffness  $k_{\text{fine}} = 2500 \text{ N/m}$
- Spindle-nut head transmission : compliant in order to ensure both :
  - a large reduction ratio of the screw-jack motion.
  - a negligible reduction of the piezo motion efficiency

Selected value: 100 N/m

Based on these values, the requirements at stage level can be translated into actuator requirements, considering:

- for the piezo: motion ratio  $\approx k_{\text{fine}}/(k_{\text{fine}} + k'_{\text{flex}}) \approx 0.5$   $\varrho_{\text{fine}} \approx 1/0.5 = 2$
- for the spindle-nut: motion ratio  $\approx k_{\text{head}}/(k_{\text{fine}} + k'_{\text{flex}}) \approx 0.02$   $\varrho_{\text{head}} \approx 1/0.02 = 50$

By applying  $\varrho_{\text{fine}}$  and  $\varrho_{\text{head}}$  to the fine stage and the coarse stage specification respectively, one can derive the actuators specifications:

Stage	Motion range	Resolution	Dynamics
‘Fine’ stage: piezo	0.2 nm $\rightarrow$ 2 $\mu$ m	0.2 nm	10 000
‘Coarse’ stage: spindle nut	5 $\mu$ m $\rightarrow$ 200 mm	5 $\mu$ m	40 000

A piezo of a few mm length provides the 2  $\mu$ m range capability. Longer piezo stacks can be accommodated, in combination with the reduction of the  $k_{\text{fine}}$  stiffness. For instance,  $k_{\text{fine}} = 1000$  N/m can be associated to a piezo motion range of 5  $\mu$ m; including casing, the piezo actuator overall length is then 30 mm.

The motion resolution (and noise) depends mainly on the piezo drive electronics. With low-voltage ceramics (100 V max.), the dynamics requires a resolution/noise of 10 mV. The command covering the 10 000 dynamics corresponds to a 16 bit coding.

Concerning the ‘coarse’ actuator, the motion range of 200 mm drives the choice of the spindle length, leading to 250 mm typ. This aspect is not a severe design driver and is well in accordance with the state of the art.

The 5  $\mu$ m resolution is achievable with a roller screw device; one can consider the following combination:

- spindle pitch: 1 mm
- stepper motor: 200 steps/rev

leading to a motion resolution in full step command: 5  $\mu$ m.

Other combinations can be envisaged, typically:

- spindle pitch: 1.2 mm
- stepper motor: 360 steps/rev

leading to a motion resolution in full step command: 3.33  $\mu$ m.

This indicates that the proposed design includes margins and can be further optimised, based always on the utilisation of well demonstrated components for space applications. For instance, a resolution of 3.33  $\mu$ m instead of 5  $\mu$ m can reduce the spindle motion range down to 133 mm ( $= 200 \text{ mm} \times 3.33 \mu\text{m} / 5 \mu\text{m}$ ).

In order to validate the adequacy of the proposed mechanism concept, a dynamic simulator was developed, including the mechanism components (stiffness, actuators), the telescope inertia and the control loop (LOS control). The results are presented hereafter.

### A.7.7 Dynamic simulations

The simulator has been developed in the MATLAB/SIMULINK environment to assess the overall dynamic performance, including that of the mechanism. This simulator, modelling the behaviour of the mechanism, has also been integrated in the overall DFACS simulator.

The plots that will be presented hereafter correspond to the following assumptions:

- Telescope arm inertia:  $J_{zz} = 15 \text{ kg m}^2$ .
- Stepper motor in full step mode. One full step corresponds to  $3 \mu\text{m}$  of elongation.
- System damping: structural type,  $\xi = 2 \%$ .
- Heterodyne sensor noise:  $3 \text{ nrad}/\sqrt{\text{Hz}}$ .
- Piezo resolution:  $0.2 \text{ nm}$ .
- S/C attitude jitter:  $6 \text{ nrad}/\sqrt{\text{Hz}}$ .

The strategy used to reduce the effect of the motor steps is a feed-forward command to the piezo, synchronous with the motor stepping. With this strategy, the system does no longer see steps, but just impulses, resulting from the error between the motor step and the piezo compensation.

The time history of the pointing error obtained in this simulation and its PSD indicate that, in terms of PSD level, the requirement is met with margins. However two points of concern remain:

- 1 Harmonic peaks due to the periodic steps of the motor are marginally larger than the allowed values. In the time domain, it means that the measurement might be too corrupted for scientific use in the couple of seconds after each step of the motor.
- 2 An oscillating mode at  $0.5 \text{ Hz}$ , with very small damping, induces large pointing errors, up to  $50 \text{ nrad}$ . This might not be acceptable.

To improve these two points, which are marginally critical, MMS recommend the following solutions:

- Utilisation of the stepper motor in ministepping mode. A division by a factor 8 or 16 of the steps is easily achievable, without severe constraints nor really increased complexity.
- Better damping of the oscillations. This can be done by several means: either passively or actively. Passive damping remains an open issue, because it is difficult to guarantee that a technology compatible with the jitter magnitude exists. Active damping with the piezo seems to be the most promising solution. It depends on the heterodyne sensor output frequency: to be faster than  $10 \text{ Hz}$ . If confirmed, the  $0.5 \text{ Hz}$  oscillation can be damped with the attitude controller.

### A.7.8 Conclusion

During the Phase A, MMS has demonstrated the feasibility of a telescope pointing mechanism meeting both constraints of high range and high accuracy. A two-stage mechanism is proposed, relying on very mature technologies, such as stepper motor, roller screw and piezo actuators. The design of the spindle-nut drive is flexible, allowing to separate the resolution (defined by the spindle pitch and the motor step) and the motion range capabilities (defined by the spindle length).

The number of cycles can be estimated from the analysis. The motor stepping rate corresponds to one full step every 100s, worst case S/C constellation seasonal deformation rate. This corresponds to  $0.6 \text{ Msteps}$  for 2 years (3000 rev), with an extension to  $3 \text{ Msteps}$  (15 000 rev) for 10 years. The life time is not a critical issue, as the roller-screw components provide Mrevs capability.

This reliable mechanical design can be further improved in different directions.

The performances obtained with full step command of the spindle drive are acceptable but feature no sufficient pointing margins. Simple improvement of the motor drive – ministepping



instead of full step command – will significantly reduce the magnitude of the disturbance induced by the ‘coarse’ stage and the mechanism eigenfrequency excitation (ratio of 10).

The control strategy including active damping is another promising solution, boosting the mechanism performances at low cost.

The classical stepper motors include permanent magnets and generate magnetic fields (stator windings). This can lead to an open issue with regard to the [PM](#) magnetic requirements. Alternative technologies exist, based on rotary piezo actuators. Such technology is under development under [ESA](#) funding, preparing the validation of this type of motors for future missions. Only a limited torque capability is required for the motor, as a large reduction ratio/torque magnification is provided by the screw-jack device. The volume and the reliability of the motor is improved accordingly.

The analyses performed indicate that the telescope pointing mechanism requirements can be fulfilled with mature technologies. The concept relies in particular on the ‘elastic’ gear principle, which is theoretically simple. Further design activities up to breadboarding are deemed necessary to consolidate the feasibility statement and refine the component specification, selection and definition.



# References

- [1] LISA Study Team, *LISA Pre-Phase A Report*, 2<sup>nd</sup> edition, Report MPQ 233, Max-Planck-Institut für Quantenoptik (Jul 1998). Cited on page 5, 45, 48, 49, 53, 60, 106, 109, 127, 128, 129, 139, 186, 225, 228, 242, 249, 252, 253, 290, 298
- [2] DSS, MMS and Alenia Aerospazio, *LISA Final Technical Report*, Technical report, ESTEC (Apr 2000). Cited on page 5, 45, 53, 59, 60, 79, 127, 128, 136, 139, 251, 290, 295
- [3] C.W. Misner, K.S. Thorne, and J.A. Wheeler, *Gravitation* (Freeman & Co., San Francisco, 1973). Cited on page 7
- [4] P.R. Saulson, *Fundamentals of Interferometric Gravitational Wave Detectors* (World Scientific, Singapore, 1994). Cited on page 7
- [5] B.F. Schutz, *A First Course in General Relativity* (Cambridge University Press, Cambridge, 1985). Cited on page 7
- [6] K.S. Thorne: *Gravitational Radiation*, in *300 Years of Gravitation*, edited by S.W. Hawking and W. Israel (Cambridge University Press, Cambridge, 1987) 330–458. Cited on page 7, 19
- [7] B.F. Schutz and C.M. Will: *Gravitation and General Relativity*, Encyclopedia of Applied Physics **7** (1993) 303–340. Cited on page 7, 16
- [8] J.H. Taylor and J.M. Weisberg: *Further experimental tests of relativistic gravity using the binary pulsar PSR 1913+16*, Astrophys. J. **345** (1989) 434. Cited on page 8, 22
- [9] B.F. Schutz: *Gravitational Waves on the Back of an Envelope*, Am. J. Phys. **52** (1984) 412–419. Cited on page 14
- [10] P.C. Peters and J. Mathews, Phys. Rev. **131** (1963) 435. Cited on page 15
- [11] C.M. Will, *Theory and Experiment in Gravitational Physics* (Cambridge University Press, Cambridge, 1981). Cited on page 16
- [12] G. Giampieri, Mon. Not. R. Astron. Soc. **289** (1997) 185–195. Cited on page 19
- [13] V.N. Mironowskii, Soviet Astron. **9** (1966) 752. Cited on page 21, 25
- [14] I. Iben (1984), workshop on Gravitational Waves and Axions. Cited on page 21
- [15] D. Hils, P.L. Bender, J.E. Faller, and R.F. Webbink, in *11th Int. Conf. on General Relativity and Gravitation: Abstracts of Cont. Papers, Vol. 2* (Univ. of Stockholm, 1986) 509. Cited on page 21
- [16] D. Hils, P.L. Bender, and R.F. Webbink, Astrophys. J. **360** (1990) 75. Cited on page 21, 24, 25
- [17] V.M. Lipunov and K.A. Postnov, Soviet Astron. **31** (1987) 228–230. Cited on page 21

- [18] V.M. Lipunov, K.A. Postnov, and M.E. Prokhorov, *Astron. & Astrophys.* **176** (1987) L1–L4. Cited on page 21
- [19] C.R. Evans, I. Iben, and L. Smarr: *Degenerate Dwarf Binaries as Promising Detectable Sources of Gravitational Radiation*, *Astrophys. J.* **323** (1987) 129–139. Cited on page 21
- [20] R.A. Hulse and J.H. Taylor: *Discovery of a pulsar in a binary system*, *Astrophys. J.* **195** (1975) L51. Cited on page 22
- [21] R.A. Hulse and J.H. Taylor, *Astrophys. J.* **345** (1989) 434. Cited on page 22
- [22] D. Lorimer and E.P.J. van den Heuvel: *On the galactic and cosmic merger rate of double neutron stars*, *Mon. Not. R. Astron. Soc.* **283** (1996) L37–L39. Cited on page 22
- [23] A.V. Tutukov and L.R. Yungelson, *Mon. Not. R. Astron. Soc.* **260** (1993) 675. Cited on page 22, 23
- [24] H. Yamaoka, T. Shigeyama, and K. Nomoto, *Astron. & Astrophys.* **267** (1993) 433. Cited on page 22
- [25] V.M. Lipunov: *Relativistic Binary Merging Rates*, in *Proceedings of the Joint Discussion “High Energy Transients”, XXIIIrd General Assembly of the IAU, Kyoto (1997)* . Cited on page 22
- [26] D.R. Lorimer, A.G. Lyne, L. Festin, and L. Nicastro, *Nature* **376** (1995) 393. Cited on page 22
- [27] F. Verbunt: *Waiting for LISA: binaries with orbital periods less than  $10^4$  s*, *Class. Quantum Grav.* **14** (1997) 1417–1424. Cited on page 22, 24
- [28] C.A. Meegan *et al.*, *Astrophys. J. Suppl.* **106** (1996) 65. Cited on page 22
- [29] J. van Paradijs, P.J. Groot, T. Galama, *et al.*, *Nature* **386** (1997) 686. Cited on page 22
- [30] R. Narayan, T. Piran, and A. Shemi: *Neutron star and black hole binaries in the Galaxy*, *Astrophys. J.* **379** (1991) L17. Cited on page 23
- [31] L. Yungelson and S.F. Portegies Zwart: *Evolution of Close Binaries: Formation and Merger of Neutron Star Binaries*, in *Proceedings of the “Second Workshop on Gravitational Wave Data Analysis”* (1998) . Cited on page 23
- [32] S.F. Portegies Zwart and S.L.W. McMillan, *Astrophys. J. Lett.* **528** (2000) L17–L20. Cited on page 23
- [33] T.R. Marsh, *Mon. Not. R. Astron. Soc.* **275** (1995) L1. Cited on page 24
- [34] T.R. Marsh, V.S. Dhillon, and S.R. Duck, *Mon. Not. R. Astron. Soc.* **275** (1995) 828. Cited on page 24
- [35] G. Nelemans, F. Verbunt, L.R. Yungelson, and S.F. Portegies Zwart, *Astron. Astrophys.* (astro-ph/0006216), in press (2000). Cited on page 24
- [36] R.F. Webbink and Z. Han, in *Laser Interferometer Space Antenna*, edited by W.M. Folkner (AIP Conference Proceedings 456, 1998) 61–67. Cited on page 24

- [37] G. Nelemans, S.F. Portegies Zwart, and F. Verbunt, in *Gravitational Waves and Experimental Relativity* (World Publishers, Hanoi, 1999) 119–124. Cited on page 24
- [38] D.I. Kosenko and K.A. Postnov, *Astron. & Astrophys.* **336** (1998) 786. Cited on page 24
- [39] R. Schneider, V. Ferrari, S. Matarrese, and S.F. Portegies Zwart, *Mon. Not. R. Astron. Soc.* (2000), (astro-ph/0002055), in press. Cited on page 24
- [40] B. Warner, *Astrophys. and Space Sci.* **225** (1995) 249–270. Cited on page 24, 25
- [41] I. Iben and A.V. Tutukov, *Astrophys. J.* **370** (1991) 615. Cited on page 24
- [42] D. Hils, in *Laser Interferometer Space Antenna*, edited by W.M. Folkner (AIP Conference Proceedings 456, 1998) 68–78. Cited on page 25, 30
- [43] A. Tutukov and L. Yungelson, *Mon. Not. R. Astron. Soc.* **280** (1996) 1035. Cited on page 25
- [44] D. Hils and P.L. Bender, *Astrophys. J.* **537** (2000) 334–341. Cited on page 25
- [45] K.S. Thorne, in *Proceedings of Snowmass 1994 Summer Study on Particle and Nuclear Astrophysics and Cosmology*, edited by E.W. Kolb and R.D. Peccei (World Scientific, Singapore, 1995) 160–184. Cited on page 26
- [46] C. Cutler, T.A. Apostolatos, L. Bildsten, L.S. Finn, E.E. Flanagan, D. Kennefick, D.M. Markovic, A. Ori, E. Poisson, G.J. Sussman, and K.S. Thorne: *The Last Three Minutes: Issues in Gravitational Wave Measurements of Coalescing Binaries*, *Phys. Rev. Lett.* **70** (1993) 2984. Cited on page 26
- [47] M.G. Haehnelt, *Mon. Not. R. Astron. Soc.* **269** (1994) 199–208. Cited on page 26, 27
- [48] A. Vecchio, *Class. Quantum Grav.* **14** (1997) 1431. Cited on page 26
- [49] H.C. Ford *et al.*, *Astrophys. J.* **435** (1994) L27. Cited on page 26
- [50] R.J. Harms *et al.*, *Astrophys. J.* **435** (1994) L35. Cited on page 26
- [51] Y. Tanaka *et al.*, *Nature* **375** (1995) 659. Cited on page 26
- [52] M. Miyoshi *et al.*, *Nature* **373** (1995) 127. Cited on page 26
- [53] A. Eckart and R. Genzel: *Observations of stellar proper motions near the Galactic Centre*, *Nature* **383** (1996) 415–417. Cited on page 26
- [54] A.M. Ghez, B.L. Klein, M. Morris, and E.E. Becklin, *Astrophys. J.* **509** (1998) 678–686. Cited on page 26
- [55] R. Genzel, C. Pichon, A. Eckart, O.E. Gerhard, and T. Ott, *Mon. Not. R. Astron. Soc.* (2000), (astro-ph/0001428), in press. Cited on page 26
- [56] T.R. Lauer *et al.*, *Astron. J.* **104** (1992) 552. Cited on page 26
- [57] J. Kormendy and D. Richstone, *Ann. Rev. Astron. & Astrophys.* **33** (1995) 581. Cited on page 26
- [58] K. Gebhardt *et al.*, *Astrophys. J.* (2000), (astro-ph/0006289), in press. Cited on page 26

- [59] M.J. Rees: *Astrophysical evidence for black holes*, in *Black Holes and Neutron Stars*, edited by R.M. Wald (University of Chicago Press, Chicago, 1997) . Cited on page 26, 27
- [60] M.J. Rees, Class. Quantum Grav. **14** (1997) 1411–1416. Cited on page 26, 27
- [61] P. Crane *et al.*, Astron. J. **106** (1993) 1371. Cited on page 26
- [62] T.R. Lauer *et al.*, Astron. J. **110** (1995) 2622–2654. Cited on page 26
- [63] G.D. Quinlan and S.L. Shapiro, Astrophys. J. **356** (1990) 483. Cited on page 27
- [64] M.H. Lee, Astrophys. J. **418** (1993) 147–162. Cited on page 27
- [65] M.G. Haehnelt and M.J. Rees, Mon. Not. R. Astron. Soc. **263** (1993) 168. Cited on page 27
- [66] D.J. Eisenstein and A. Loeb, Astrophys. J. **443** (1995) 11. Cited on page 27
- [67] M. Umemura, A. Loeb, and E.L. Turner, Astrophys. J. **419** (1993) 459. Cited on page 27
- [68] T. Baumgarte and S.L. Shapiro, Astrophys. J. **526** (1999) 941–952. Cited on page 27
- [69] C. Cutler: *Angular Resolution of the LISA, Gravitational Wave Detector*, Phys. Rev. D **57** (1998) 7089–7102. Cited on page 29
- [70] M. Shibata, Phys. Rev. D **50** (1994) 6297. Cited on page 30
- [71] D. Hils and P.L. Bender, Astrophys. J. **445** (1995) L7. Cited on page 30
- [72] S. Sigurdsson and M.J. Rees, Mon. Not. R. Astron. Soc. **284** (1996) 318. Cited on page 30
- [73] S. Sigurdsson, Class. Quantum Grav. **14** (1997) 1425. Cited on page 30
- [74] D. Hils and P.L. Bender (2000), unpublished results. Cited on page 30
- [75] B. Allen, in *Les Houches School on Astrophysical Sources of Gravitational Waves*, edited by J.-A. Marck and J.-P. Lasota (Cambridge University Press, 1996) . Cited on page 32
- [76] C.J. Hogan, in *Laser Interferometer Space Antenna*, edited by W.M. Folkner (AIP Conference Proceedings 456, 1998) 79–86. Cited on page 32
- [77] B. Caldwell and B. Allen, Phys. Rev. D **45** (1992) 3447. Cited on page 33
- [78] A. Kosowsky, M.S. Turner, and R. Watkins: *Gravitational radiation from colliding vacuum bubbles*, Phys. Rev. D **45** (1992) 4514. Cited on page 33
- [79] J. Weber, Phys. Rev. **117** (1960) 306. Cited on page 36
- [80] M. Bassan, Class. Quant. Grav. Supplement A **39** (1994) 11. Cited on page 37
- [81] F.A.E. Pirani, Acta Physica Polonica **15** (1956) 389. Cited on page 37
- [82] M.E. Gertsenshtein and V.I. Pustovoit, JETP **16** (1963) 433. Cited on page 37
- [83] R. Weiss, Quarterly Progress Report of RLE, MIT **105** (1971) 54. Cited on page 37
- [84] G.E. Moss, L.R. Miller, and R.L. Forward, Appl. Opt. **10** (1971) 2495. Cited on page 37

- [85] A. Abramovici *et al.*, Science **256** (1992) 325. Cited on page [38](#)
- [86] G. Bradaschia *et al.*, Nucl. Instrum. and Methods A **289** (1990) 518. Cited on page [39](#)
- [87] K. Danzmann *et al.*: *GEO 600 – A 300 m, laser-interferometric gravitational wave antenna*, in *Proc. of the 1<sup>st</sup> Edoardo Amaldi Conference* (1994) . Cited on page [39](#)
- [88] K. Tsubono and TAMA collaboration: *TAMA Project*, in *Proc. of the TAMA Intern. Workshop on Gravitational Wave Detection*, edited by K. Tsubono, M.-K. Fujimoto, and K. Kuroda (Universal Academy Press, Tokyo, 1997) 183–191. Cited on page [39](#)
- [89] V.M. Kaspi, J.H. Taylor, and M.F. Ryba, Astrophys. J. **428** (1994) 713. Cited on page [40](#)
- [90] Report US Govt. Printing Office No. 1978-261-371:11, Report prepared by NASA Marshall Space Flight Center (1978). Cited on page [41](#)
- [91] R. Weiss, P.L. Bender, C.W. Misner, and R.V. Pound, *Report of the Sub-Panel on Relativity and Gravitation, Management and Operations Working Group for Shuttle Astronomy*, Technical report, NASA, Washington, DC (1976). Cited on page [42](#)
- [92] R. Weiss: *Gravitational Radiation – The Status of the Experiments and Prospects for the Future*, in *Sources of Gravitational Radiation*, edited by L. Smarr (Cambridge University Press, 1979) . Cited on page [42](#)
- [93] R. Decher, J.L. Randall, P.L. Bender, and J.E. Faller: *Design aspects of a laser gravitational wave detector in space*, in *Active Optical Devices and Applications*, vol. 228 (SPIE, 1980) 149–153. Cited on page [42](#)
- [94] J.E. Faller and P.L. Bender (Jun 1981), abstract for the Second International Conference on Precision Measurements and Fundamental Constants. Cited on page [42](#)
- [95] J.E. Faller and P.L. Bender: *A possible laser gravitational-wave experiment in space*, in *Precision Measurements and Fundamental Constants II*, NBS Special Publication 617 (U.S. Govt. Printing Office, Washington, D.C., 1984) 689–690. Cited on page [42](#)
- [96] J.E. Faller, P.L. Bender, J.L. Hall, D. Hils, and M.A. Vincent: *Space antenna for gravitational wave astronomy*, in *Proceedings of the Colloquium on Kilometric Optical Arrays in Space*, SP-226 (ESA, 1985) . Cited on page [42](#)
- [97] D. Shoemaker, R. Schilling, L. Schnupp, W. Winkler, K. Maischberger, and A. Rüdiger: *Noise behavior of the Garching 30 meter prototype gravitational wave detector*, Phys. Rev. D **38** (1988) 423–432. Cited on page [51](#)
- [98] D.I. Robertson, E. Morrison, J. Hough, S. Killbourn, B.J. Meers, G.P. Newton, N.A. Robertson, K.A. Strain, and H. Ward: *The Glasgow 10 m prototype laser interferometric gravitational wave detector*, Rev. Sci. Inst. **66** (1995) 4447–4451. Cited on page [51](#)
- [99] R.E. Vogt *et al.*: *The U.S. LIGO Project*, in *Proc. of the Sixth Marcel Grossmann Meeting on General Relativity*, edited by H. Sato and T. Nakamura (World Scientific, Singapore, 1992) 244–266. Cited on page [51](#)
- [100] S. Peskett, *LISA Payload Pre-Phase A Thermal Study (WP03)*, Technical report, RAL (1999). Cited on page [53](#), [56](#)



- [101] L. Morgenroth, *LISA Phase A Thermal Study Draft Final Report*, Technical report, Dornier Satelliten Systeme (1999). Cited on page 54, 55, 56
- [102] R. Schilling: *Angular and frequency response of LISA*, Class. Quantum Grav. **14** (1997) 1513–1519. Cited on page 57
- [103] P.R. Saulson: *Thermal noise in mechanical experiments*, Phys. Rev. D **42** (1990) 2437–2445. Cited on page 62
- [104] M. Woodard, *Short-Period Oscillations in the Total Solar Irradiance*, Ph.D. thesis, University of California, San Diego (1984). Cited on page 82
- [105] M. Nati, A. Bernard, B. Foulon, and P. Touboul: *ASTRE – a highly performant accelerometer for the low frequency range of the microgravity environment*, in *24th International Conference on Environmental Systems* (1994) . Cited on page 85
- [106] A. Bernard and P. Touboul: *The GRADIO accelerometer: design and development status*, in *Proc. of the ESA-NASA Workshop on the Solid Earth Mission ARISTOTELES* (1991) . Cited on page 85
- [107] P. Touboul *et al.*, *Continuation of the GRADIO accelerometer predevelopment*, Final report 51/6114PY ESTEC (1992) and 62/6114PY ESTEC (1993), ONERA. Cited on page 85
- [108] E. Willemenot, *Pendule de torsion à suspension électrostatique, très hautes résolutions des accéléromètres spatiaux pour la physique fondamentale*, Ph.D. thesis, University Paris-Sud (1997). Cited on page 90
- [109] T.J. Sumner and P. Touboul: *Charge management system for STEP*, in *Proceedings of the STEP Symposium, Pisa (ESA, 1995)* . Cited on page 90
- [110] P. Touboul, M. Gay, B. Foulon, Y. Bienenfeld, and T.J. Sumner: *The charge measurement and control technique for STEP experimentation*, in *The 2nd William Fairbank conference on Relativistic Gravitational Experiments in Space and Related Theoretical Topics, Hong Kong 1993* . Cited on page 90
- [111] Y. Bienenfeld, *Etude des différences de potentiel de contact au coeur des accéléromètres ultrasensibles à suspension électrostatique*, Ph.D. thesis, University Paris 6 (Dec 1994). Cited on page 90
- [112] P. Touboul, B. Foulon, and E. Willemenot: *Electrostatic space accelerometers for present and future missions*, Acta Astronautica (1998). Cited on page 91
- [113] Y. Jafry and T.J. Sumner: *Electrostatic charging of the LISA proof masses*, Class. Quantum Grav. **14** (1997) 1567–1574. Cited on page 91
- [114] S. Buchman, T. Quinn, M. Keiser, D. Gill, and T.J. Sumner: *Charge measurement and control for the Gravity Probe B gyroscopes*, Rev. Sci. Instrum. **66** (1995) 120–129. Cited on page 91
- [115] G.P. Adams, G.K. Rochester, T.J. Sumner, and O.R. Williams: *The ultra-violet calibration system for the UK XUV, telescope to be flown on the ROSAT satellite*, J. Phys. E **20** (1987) 1261–1264. Cited on page 91



- [116] T.J. Sumner and G.K. Rochester, *Technical report on charging rates and discharge studies for LISA*, Report DFSC-FR-DA-001, Daimler-Benz Aerospace (1998). Cited on page 92
- [117] G. Giampieri, R.W. Hellings, M. Tinto, and J.E. Faller: *Algorithms for Unequal-Arm Michelson Interferometers*, Opt. Commun. **123** (1996) 669–678. Cited on page 98, 230, 234, 235, 242
- [118] Ch. Salomon, D. Hils, and J.H. Hall: *Laser stabilization at the millihertz level*, J. Opt. Soc. Am. B **5** (1988) 1576–1587. Cited on page 99
- [119] M. Tinto and J.W. Armstrong, Phys. Rev. D **59** (1999). Cited on page 101, 105
- [120] F.B. Estabrook, M. Tinto, and J.W. Armstrong, Phys. Rev. D **62** (2000), (in press). Cited on page 101, 102, 104, 105, 106, 107, 109
- [121] J.W. Armstrong, F.B. Estabrook, and M. Tinto, Astrophys. J. **527** (1999) 814. Cited on page 102, 104, 108, 109
- [122] M. Peterseim, D.I. Robertson, K. Danzmann, H. Welling, and P. Bender, Adv. Space Res. **25** (2000) 1143. Cited on page 102
- [123] F.B. Estabrook and H.D. Wahlquist, Gen. Relativ. Gravit. **6** (1975) 439. Cited on page 104
- [124] H.D. Wahlquist, Gen. Relativ. Gravit. **19** (1987) 1101. Cited on page 104
- [125] B.F. Schutz, (ed.) *Gravitational Wave Data Analysis* (Kluwer, Dordrecht, 1989). Cited on page 113
- [126] K. Danzmann *et al.*, *LISA – Proposal for a Laser-Interferometric Gravitational Wave Detector in Space*, Report MPQ 177, Max-Planck-Institut für Quantenoptik (1993). Cited on page 115
- [127] M. Peterseim, O. Jennrich, and K. Danzmann, Class. Quantum Grav. **13** (1996) 279. Cited on page 116
- [128] C. Cutler, Phys. Rev. D **57** (1998). Cited on page 116, 120, 124
- [129] B.F. Schutz, in *The detection of gravitational waves*, edited by D. Blair (Cambridge University Press, Cambridge, 1991) 406–452. Cited on page 118
- [130] C. Cutler and E. Flanagan, Phys. Rev. D **49** (1994) 2658. Cited on page 120
- [131] L.S. Finn, Phys. Rev. D **46** (1992) 5236. Cited on page 120
- [132] V.M. Lipunov, S.N. Nazin, I.E. Panchenko, K.A. Postnov, and M.E. Prokhorov, Astron. & Astrophys. **298** (1995) 677–687. Cited on page 125
- [133] LISA Study Team, *Payload Definition Document*, Report (Oct 1998). Cited on page 127, 228
- [134] C. Bartoli, H. von Rohden, S. Thompson, and J. Blommers: *A Liquid Caesium Field Ion Source for Plasma Propulsion*, J. Phys. D: Appl. Phys. **17** (1984) 2473–2483. Cited on page 176

- [135] B.T.C. Zandbergen, *FEEP: the [ESTEC](#) Liquid Caesium Field Ion Source*. An Investigative Report, Ph.D. thesis, Technical University Delft (Jun 1984). Cited on page [178](#)
- [136] C. Bartoli, J. González, G. Saccoccia, M. Andrenucci, S. Marcuccio, and A. Genovese: *Space-Borne Astronomical Gravity wave Interferometer Mission ([SAGITTARIUS](#)): the [FEEP](#) option*, IEPC (1993) 16. Cited on page [178](#)
- [137] J. González, G. Saccoccia, and H. von Rohden: *Field Emission Electric Propulsion: Experimental Investigations on Microthrust [FEEP](#) Thrusters*, IEPC (1993) 57. Cited on page [178](#)
- [138] M. Andrenucci, S. Marcuccio, L. Spagli, A. Genovese, and F. Repola: *Experimental Study of [FEEP](#) Emitter Starting Characteristics*, IEPC (1991) 104. Cited on page [179](#)
- [139] A. Ciucci, G. Genuini, and M. Andrenucci: *Experimental Investigation of Field Emission Electrostatic Thrusters*, IEPC (1991) 103. Cited on page [179](#)
- [140] R. Schmidt, H. Arends, *et al.*: *A novel medium-energy ion emitter for active spacecraft potential control*, Rev. Sci. Instrum. **64** (1993). Cited on page [179](#)
- [141] M. Fehringer, F. Rüdenauer, and W. Steiger: *Space-Proven Indium Liquid Metal Field Ion Emitters for Ion Microthruster Applications*, in 33rd AIAA Joint Propulsion Conference (1997) 3057. Cited on page [179](#)
- [142] M.A. Vincent and P.L. Bender: *Orbital mechanics of a space-borne gravitational wave experiment*, in Proc. Astrodynamics Specialist Conference ([Kalispell USA](#)) (Univelt, San Diego, 1987) 1346. Cited on page [185](#)
- [143] F. Hechler and W.M. Folkner: *Mission Analysis for Laser Interferometer Space Antenna ([LISA](#))*, in Advances in Space Research ([COSPAR](#), 1996) . Cited on page [187](#), [188](#)
- [144] R. Hellings, G. Giampieri, L. Maleki, M. Tinto, K. Danzmann, J. Hough, and D. Robertson: *Heterodyne laser tracking at high Doppler rates*, Opt. Commun. **124** (1996) 313–320. Cited on page [188](#), [230](#), [234](#)
- [145] R.T. Stebbins, P.L. Bender, and W.M. Folkner: *[LISA](#) data acquisition*, Class. Quantum Grav. **13** (1996) A285–A289. Cited on page [188](#)
- [146] M. Peterseim, *LISA Interferometer Sensitivity to Spacecraft Motion*, Work package TN-WP8, Max-Planck-Institut für Quantenoptik (1999). Cited on page [235](#)
- [147] A.S. Jursa (ed.), *Handbook of geophysics and the space environment*, United States Air Force Geophysics Laboratory (1985), document number ADA 167000. Cited on page [257](#)
- [148] R. Brun, F. Bruyant, M. Maire, A.C. McPherson, and P. Zanarini, *[GEANT3](#) User's Guide*, [CERN](#) (1984), dD/EE/84–1. Cited on page [258](#)
- [149] Y. Jafrý and C. Tranquille: *An Assessment of the Charged Particle Environment during the [STEP](#) Mission, and Consequences for the Payload*, in Proceedings of the [STEP](#) Symposium, Pisa 1993 ([ESA](#), 1995) . Cited on page [258](#), [261](#)

- [150] J.A. Halbleib, R.P. Kensek, T.A. Mehlhorn, G.D. Valdez, S.M. Seltzer, and M.J. Berger, *ITS Version 3.0: The Integrated TIGER Series of Coupled Electron/Photon Monte Carlo Transport Codes* (1992), SAND91-1634 UC-405, Sandia National Laboratories, New Mexico. Cited on page 260
- [151] J.H. King: *Solar Proton Fluences for 1977–1983 Space Missions*, J. Spacecraft **11** (1974) 401. Cited on page 261
- [152] J.N. Goswami, R.E. McGuire, R.C. Reedy, D. Lal, and R. Jha: *Solar Flare Protons and Alpha Particles During the Last Three Solar Cycles*, J. Geophys. Res. **93** (1988) A7195–A7205. Cited on page 261
- [153] F. De Coulon, *Signal Theory and Processing* (Artech House, Dedham, MA, 1986). Cited on page 261
- [154] E. Grun, H.A. Zook, H. Fechtig, and R.H. Giese: *Collisional Balance of the Meteoritic Complex*, Icarus **62** (1985) 244–272. Cited on page 268
- [155] E.M. Shoemaker: *Asteroid and Comet Bombardment of the Earth*, Ann. Rev. Earth Planet. Sci. **11** (1983) 461–494. Cited on page 268, 269
- [156] E.M. Shoemaker, R.F. Wolfe, and C.S. Shoemaker: *Asteroid and Comet Flux in the Neighborhood of Earth*, in *Global Catastrophes in Earth History*, edited by V.L. Sharpton and P.D. Ward (Geol. Soc. of America, 1990) 155–170. Cited on page 270
- [157] D. Morrison and C.R. Chapman: *Impact Hazard and the International Spaceguard Survey*, in *Observations and Physical Properties of Small Solar System Bodies*, edited by A. Brahic, J.-C. Gerard, and J. Surdej (Univ. de Liege, 1992) 223–228. Cited on page 270

# Acronyms

– and other abbreviations and mission names

1553	(standardised interface bus)
AC	Alternating Current
ACE	Attitude Control Electronics
ACS	Attitude Control System
Ada	(a programming language)
ADC	Analog-to-Digital Converter
AFRP	Aramid Fibre Reinforced Plastic
AIV	Assembly, Integration and Verification
AO	Announcement of Opportunity
AOCS	Attitude and Orbit Control System
AR	Anti-Reflective (coating)
ARC	Austrian Research Centre, Seibersdorf
ARCS	Austrian Research Centre, Seibersdorf
ARISTOTELES	Applications and Research Involving Space Techniques Observing The Earth field from Low-Earth orbiting Satellite
ARTEMIS	– Remote sensing LIDAR system –
ASCA	– satellite name –
ASI	Agenzia Spaziale Italiano
ASIC	Application Specific Integrated Circuit
ASTRE	Accelerometre Spatial TRIaxial Electrostatique
AU	Astronomical Unit: distance Sun–Earth
AURIGA	Antenna Ultracriogenica Risonante per l’Indagine Gravitazionale Astronomica: cryogenic resonant-mass antenna, Legnaro, Italy
BAQ	Block-Average Quantization
BCR	Battery Charge Regulator
BDR	Battery Discharge Regulator
BER	Bit-Error Rate
BH	Black Hole
BOL	Begin Of Lifetime
BPSK	Binary Phase Shift Keying
BWG	Beam Wave Guide
C	(a programming language)
C++	(an object-oriented programming language)
C&DH	Command and Data Handling
CAD	Computer Aided Design
CAESAR	Capacitive And Electrostatic Sensitive Accelerometer Reference
CASSINI	– NASA space mission (1997) to orbit Saturn –
CCD	Charge-Coupled Device
CCSDS	Consultative Committee for Space Data Systems, telemetry standard
CD-ROM	Compact Disk – Read Only Memory
CDAE	Command and Data Acquisition Element
CDMS	Command and Data Management Subsystem
CDMU	Central Data Management Unit

---

CERN	Conseil Européen de la Recherche Nucléaire
CFRP	Carbon Fibre Reinforced Plastic
CHAMP	– German geodetic satellite –
CLUSTER	– ESA/NASA space mission (1996), 4 S/C to be launched on Ariane 5 –
CLUSTER-II	– ESA/NASA space mission (2000), 4 S/C to be launched on Ariane 5 –
CNES	Centre National d’Etude Spatiales (France)
CO	Carbon-Oxygen
COBE	COsmic Background Explorer
CoG	Centre of Gravity
COLUMBIA	– NASA space shuttle –
COLUMBUS	– ESA space mission, to fly on NASA shuttle, 1996 –
COSPAR	Committee On SPACe Research
CPS	Centralised Processor System
CPU	Central Processing Unit
CTE	Coefficient of Thermal Expansion
CVD	Chemical Vapor Deposition
CWDB	Close White Dwarf Binaries
DARA	Deutsche Agentur für RaumfahrtAngelegenheiten
DASA	Daimler AeroSpace Aktiengesellschaft
DBR	Distributed Bragg Reflection
DC	Direct Current
DERA	(British company)
DFACS	Drag-Free and Attitude Control System
DFB	Distributed FeedBack
DFC	Drag-Free Control
DLR	Deutsches Zentrum für Luft- und Raumfahrt
DMS	Data Management System
DOF	Degree(s) Of Freedom
DRAM	Dynamic Random Access Memory
DS	Deep Space
DSN	Deep Space Network (NASA)
DSPG	Distributed StarPoint Grounding
DSS	Dornier Satellitensysteme
EDAC	Error Detection And Correction
EEPROM	Electrically Erasable Programmable Read-Only Memory
EEV	(company)
EG&G	Edgerton, Germeshausen & Greer
EGSE	Electrical Ground Support Equipment
EIRP	Effective Isotropic Radiated Power
EMC	Electro-Magnetic Compatibility
EMI	Electro-Magnetic Interference
EOL	End Of Lifetime
EOM	Electro-Optic Modulator
EPS	Electrical Power Subsystem
EQUATOR-S	– satellite name –
ESA	European Space Agency
ESD	Electro-Static Discharge
ESOC	European Space Operations Centre
ESTEC	European Space Research and Technology Centre



---

JILA	Joint Institute for Laboratory Astrophysics (Boulder, USA)
JPL	Jet Propulsion Laboratory (Pasadena, USA)
LAGOS	Laser Antenna for Gravitation-radiation Observation in Space
LEONARDO	LEo On-board Novel ARchitecture (for data handling)
LEOP	Low Earth Orbit Phase
LGA	Low Gain Antenna
LHC	Large Hadron Collider (CERN)
LIGO	Laser Interferometer Gravitational wave Observatory (USA)
LISA	Laser Interferometer Space Antenna
LLD	Launch Locking Device
LMC	Large Magellanic Cloud
LMIS	Liquid Metal Ion Source
LO	Local Oscillator
LOS	Line Of Sight
LSC	LISA Science Centre
LSDAC	Lisa Science Data Archiving Centre
LSDC	LISA Science Data Centre
LWL	Long-Wavelength Limit
LZH	Laser Zentrum Hannover
M-MOPA	Monolithic Master Oscillator Power Amplifier
M1	Primary Mirror
M2	Secondary Mirror
MAP	Multiplexed Access Point
MARCO	Modular Architecture for Robotics Control
MATLAB	– Commercial software package –
MBH	Massive Black Hole
MBW	Measurement Bandwidth
MCG	– Catalogue of Galaxies –
MCM	Mult-Chip Module
MD	Maryland (State in USA)
MEA	Main Error Amplifier
MECU	Million ECU (European Currency Unit)
MEuro	Million Euro
MGSO	Mission Ground Support Operations
MIL-STD	MIL-STandarD
MIL-STD-1553	MIL-STandarD interface 1553
MIPS	Million Instructions Per Second
MIR	– Russian space station –
MIT	Massachusetts Institute of Technology (USA)
MLI	Multi-Layer Insulation
MMS	Matra Marconi Space
MOPFA	Master Oscillator Power Fibre Amplifier
MoU	Memorandum of Understanding
MPPT	Maximum Power Point Tracker
MPQ	Max-Planck-Institut für Quantenoptik (Germany)
MSCE	Mission operations and Spacecraft Control Element
MSM	Module Separation Mechanism
MSP	Mars Surveyor Program
NA	Numerical Aperture

NAO	National Astronomical Observatory, Tokyo, Japan
NASA	National Aeronautics and Space Administration (USA)
NAUTILUS	– Cryogenic resonant-mass antenna, Frascati (Italy) –
Nd:YAG	Neodymium-doped Yttrium-Aluminium Garnet
NEP	Noise Equivalent Power
NIR	Near Infra Red
NORAD	NORth American Defense command
NPO	Numerically Programmed Oscillator
NPRO	Non-Planar Ring Oscillator
NS	Neutron Star
NSF	National Science Foundation (USA)
NSSDC	National Space Science Data Center
OB	Optical Bench
OBCP	On-Board Control Procedures
OBDAH	On-Board Data Handling
OMEGA	Orbiting Medium Explorer for Gravitational Astrophysics
ONERA	Office National d’Etudes et de Recherches Aérospatiales (France)
OSI	Open System Interconnect
OSR	Optical Surface Reflector
P/M	Propulsion Module
PAA	Point Ahead Angle
PAE	Processing and Archiving Element
PAF	Payload Attach Fitting
PAT	Pointing Acquisition and Tracking
PBS	Polarising Beam Splitter
PCDU	Power Conditioning and Distribution Unit
PCU	Power Conditioning and Control Unit
PDD	Payload Definition Document
PDF	Probability Density Function
PF	Platform
PI	Principal Investigator
PIN	P-doped – Intrinsic – N-doped semiconductor junction
PLM	PayLoad Module
PM	Proof Mass
PND	Power-to-Noise Density
PP	Program Plan
PPA 2	LISA Pre-Phase A report
PPT	Power Point Tracker
PRIMA	– satellite name –
PROBA	Project for On-Board Autonomy
PROM	Programmable Read-Only Memory
PSD	Power Spectral Density
PT	Packet Terminal
PZT	(piezo-electric transducer, originally from lead[Pb]-Zirkonate-Titanate)
QNL	Quantum Noise Limit
RAD 6000-SC	Radiation-hardened version of IBM RS/6000
RAL	Rutherford Appleton Laboratory
RAM	Random Access Memory
RCS	Reaction Control Subsystem



---

RF	Radio Frequency
RFC	Radio Frequency Compatibility
RFDU	Radio Frequency Distribution Unit
RITA	Radio frequency Ion Thruster
RM	Reconfiguration Module
rms	root mean square
ROM	Read-Only Memory
ROSAT	ROentgen SATellite
ROSETTA	– planned ESA cornerstone mission –
RS	Reed-Solomon
RS 422	(standardised interface bus)
RTM	Remote Terminal Module
RTU	Remote Terminal Unit
RX	Receive(r)
S/C	SpaceCraft
S/M	Science Module
S/N	Signal-to-Noise (ratio)
S/S	SubSystem
S/W	Software
SA	Solar Array
SAC-C	– satellite name –
SAGITTARIUS	Spaceborne Astronomical Gravitational-wave Interferometer To Test Aspects of Relativity and Investigate Unknown Sources
SDL	Spectra Diodes Lab
SEP	Solar Electric Propulsion
SEU	Single Event Upset
SEVIRI	Spinning Enhanced Visible And IR Imager
SiC	Silicon Carbide
SILEX	Semiconductor Laser Intersatellite Link Experiment
SIMULINK	– software –
SMART	Small Missions for Advanced Research and Technology
SNR	Signal-to-Noise Ratio
SOHO	Solar Oscillation and Heliospheric Observatory (1995)
SOIRD	Spacecraft Operations Interface Requirements Document
SRAM	Static Random-Access Memory
SSM	Spacecraft Separation Mechanism
SSMM	Solid State Mass Memory
SSPA	Solid State Power Amplifier
SSR	Solid State Recorder
ST	StarTracker
ST 3	3 <sup>rd</sup> NASA Space Technology mission
STAR	Space Three-axis Accelerometer for Research
STEP	Satellite Test of the Equivalence Principle
SVM	SerVice Module
T/C	Thermal Control
TAMA	– Japanese 300 m GW detector built near Tama, Tokyo –
TAMA 300	– Japanese 300 m GW detector built near Tama, Tokyo –
TBC	To Be Confirmed
TBD	To Be Determined

TC	TeleCommand
TCS	Thermal Control Subsystem
TEM00	Fundamental transverse light mode
TID	Total Ionising Dose
TINA	(commercial software program)
TM	TeleMetry
TNT	TriNitroToluene (an explosive)
TRIAD	– Space mission using drag free control –
TRP	Technology Research Programme
TT&C	Tracking, Telemetry and Command
TX	Transmitter
TX/RX	Transmitter/Receiver
UART	Universal Asynchronous Receiver Transmitter
UK	United Kingdom
ULE	Ultra-Low Expansion glass (trade name)
ULF	Ultra Low Frequency
ULYSSES	– spacecraft tracking mission (1990), orbiting Sun –
US	United States (of America)
USA	United States of America
USO	Ultra-Stable Oscillator
UV	Ultra Violet
VCDAU	Virtual Channel Data Access Unit
VIRGO	– French-Italian laser-interferometric GW detector –
VLSI	Very Large Scale Integration
VME	(interface bus type)
WFE	Wave-Front Error
XIPS	Xenon Ion Propulsion System
XMM	X-ray Multi-Mirror satellite
XUV	eXtreme Ultra Violet
YAG	Yttrium-Aluminium Garnet



